OAK RIDGE NATIONAL LABORATORY LIBRARY
3 4456 0021549 8

AL RESEARCH LIBRARY
UMENT COLLECTION

2

ORNL-4168
UC-41 – Health and Safety

HEALTH PHYSICS DIVISION
ANNUAL PROGRESS REPORT
FOR PERIOD ENDING JULY 31, 1967

OAK RIDGE NATIONAL LABORATORY
CENTRAL RESEARCH LIBRARY
DOCUMENT COLLECTION
LIBRARY LOAN COPY
DO NOT TRANSFER TO ANOTHER PERSON
If you wish someone else to see this document, send in name with document and the library will arrange a loan.
UCN-7969
(3 3-67)

OAK RIDGE NATIONAL LABORATORY
operated by
UNION CARBIDE CORPORATION
for the
U.S. ATOMIC ENERGY COMMISSION

Printed in the United States of America. Available from Clearinghouse for Federal Scientific and Technical Information, National Bureau of Standards, U.S. Department of Commerce, Springfield, Virginia 22151
Price: Printed Copy $3.00; Microfiche $0.65

LEGAL NOTICE

This report was prepared as an account of Government sponsored work. Neither the United States, nor the Commission, nor any person acting on behalf of the Commission:

A. Makes any warranty or representation, expressed or implied, with respect to the accuracy, completeness, or usefulness of the information contained in this report, or that the use of any information, apparatus, method, or process disclosed in this report may not infringe privately owned rights; or

B. Assumes any liabilities with respect to the use of, or for damages resulting from the use of any information, apparatus, method, or process disclosed in this report.

As used in the above, "person acting on behalf of the Commission" includes any employee or contractor of the Commission, or employee of such contractor, to the extent that such employee or contractor of the Commission, or employee of such contractor prepares, disseminates, or provides access to, any information pursuant to his employment or contract with the Commission, or his employment with such contractor.

INTRA-LABORATORY CORRESPONDENCE

OAK RIDGE NATIONAL LABORATORY

ORNL-4168
Errata

Central
Research Library
Document Collection

MAR 28 1968
pdb

HEALTH PHYSICS DIVISION ANNUAL PROGRESS REPORT
FOR PERIOD ENDING JULY 31, 1967

Please insert the attached corrected table, page 225, in your copy of the subject report. The table is printed on gummed stock and may be glued directly on the page.

INTRA-LABORATORY CORRESPONDENCE

OAK RIDGE NATIONAL LABORATORY

RB

To: Recipients of ORNL-4168

Subject: Health Physics Division Annual Progress Report for Period Ending July 31, 1967

The attached page contains corrected versions of Tables 25.5 and 25.6 on page 272 of the subject report. The page is printed on gummed stock so that it may be pasted directly over the copy.

ORNL-4168

Contract No. W-7405-eng-26

HEALTH PHYSICS DIVISION ANNUAL PROGRESS REPORT

For Period Ending July 31, 1967

K. Z. Morgan, Director
W. S. Snyder, Assistant Director
E. G. Struxness, Assistant Director

OCTOBER 1967

OAK RIDGE NATIONAL LABORATORY
Oak Ridge, Tennessee
operated by
UNION CARBIDE CORPORATION
for the
U. S. ATOMIC ENERGY COMMISSION

OAK RIDGE NATIONAL LABORATORY LIBRARY
3 4456 0021549 8

Reports previously issued in this series are as follows:

ORNL-166	Period Ending August 31, 1948
ORNL-227	Period Ending November 30, 1948
ORNL-346	Period Ending February 28, 1949
ORNL-375	Period Ending July 15, 1949
ORNL-495	Period Ending October 15, 1949
ORNL-596	Period Ending January 15, 1950
ORNL-695	Period Ending April 15, 1950
ORNL-786	Period Ending July 15, 1950
ORNL-877	Period Ending October 15, 1950
ORNL-968	Period Ending January 20, 1951
ORNL-1004	Period Ending April 20, 1951
ORNL-1086	Period Ending July 20, 1951
ORNL-1174	Period Ending October 20, 1951
ORNL-1277	Period Ending January 20, 1952
ORNL 1353	Period Ending July 20, 1952
ORNL-1420	Period Ending October 20, 1952
ORNL-1488	Period Ending January 20, 1953
ORNL-1596	Period Ending July 31, 1953
ORNL-1684	Period Ending January 31, 1954
ORNL-1763	Period Ending July 31, 1954
ORNL-1860	Period Ending January 31, 1955
ORNL-1942	Period Ending July 31, 1955
ORNL-2049	Period Ending January 31, 1956
ORNL-2151	Period Ending July 31, 1956
ORNL-2384	Period Ending July 31, 1957
ORNL-2590	Period Ending July 31, 1958
ORNL-2806	Period Ending July 31, 1959
ORNL-2994	Period Ending July 31, 1960
ORNL-3198	Period Ending July 31, 1961
ORNL-3347	Period Ending July 31, 1962
ORNL-3492	Period Ending June 30, 1963
ORNL-3697	Period Ending July 31, 1964
ORNL-3849	Period Ending June 30, 1965
ORNL-4007	Period Ending July 31, 1966

Contents

SUMMARY ix

PART I. RADIOACTIVE WASTE DISPOSAL

1. FATE OF RADIONUCLIDES IN TERRESTRIAL ENVIRONMENT 3
   - Differential Movement of ^{137}Cs and ^{134}Cs on Runoff Plots 3
   - Effect of Soil Moisture Content on Uptake of ^{137}Cs by Plants 7
   - Radionuclide Adsorption Studies 8
2. DISPOSAL BY HYDRAULIC FRACTURING 12
   - Injections of ORNL's Evaporator Concentrate 12
   - Rock Mechanics 13
3. DISPOSAL IN NATURAL SALT FORMATIONS 18
   - Project Salt Vault 18
   - Laboratory Tests on Deformation of Rocks 26
   - Salt Space Requirements for Projected Nuclear Power Economy to Year 2065 29
4. APPLICATION OF MINERAL EXCHANGE TO REACTOR TECHNOLOGY 32
   - Behavior of Sulfur Hexafluoride and Methyl Iodide in an Idaho Soil 32
   - Movement of Curium in Soil Columns 35
   - Processing Organic Reactor Coolants 35
5. ENGINEERING, ECONOMIC, AND SAFETY EVALUATIONS 39
   - Krypton-85 and Tritium in an Expanding World Nuclear Power Economy 39
   - Underground Disposal of ^{85}Kr 43
   - Experimental Studies on the Sorption and Diffusion of Krypton and Xenon in Soil and Underground Materials 45
   - Long-Range Waste Management Study 45
   - Safety Evaluation of Tank Storage 46
6. EARTHQUAKES AND REACTOR DESIGN 49
   - General 49
   - Faults 49
   - Ground Motion 51
   - Tsunamis (Seismic Sea Waves) 52
   - Instrumentation 52

7. DOSE-ESTIMATION STUDIES RELATED TO PROPOSED CONSTRUCTION OF AN ATLANTIC-PACIFIC INTEROCEANIC CANAL WITH NUCLEAR EXPLOSIVES 53
Models for Dose Estimation 53
8. RELATED COOPERATIVE PROJECTS 60
Cooperation of Other Agencies in ORNL Studies 60
Visiting Investigators from Abroad 60
Nuclear Safety Review 60
Committee Work 60
Participation in Educational Programs 60

PART II. RADIATION ECOLOGY

9. RESPONSES OF ANIMAL POPULATIONS TO IONIZING RADIATION 63
Radiation Effects in Blood of Indigenous Small Mammals 63
Radionuclide Excretion in Indigenous Small Mammals 64
Survival of Irradiated Insects in Field Environments 65
Life History Radiation Sensitivity of Bagworms (Lepidoptera: Psychidae) 67
Population Genetics and Radiation Effects Studies 69
Movement of ^{106}Ru, ^{60}Co, and ^{137}Cs in Arthropod Food Chains on White Oak Lake Bed 70
10. RESPONSES OF PLANTS TO IONIZING RADIATION 72
Radiosensitivity of Forest Tree Species to Acute Fast-Neutron Radiation 72
Genetic Modification of Radiosensitivity 74
Dosimetry in Forests Around the HPRR 75
Effects of Internal Emitters on Native Plant Species 75
Radionuclide Uptake as a Measure of Radiation Stress in Single-Component Microcosms 77
11. RADIONUCLIDE CYCLING IN TERRESTRIAL ECOSYSTEMS 79
Summary of Radiocesium Movement in a Forest Landscape 79
Accumulation of ^{137}Cs in Soils of the Tagged *Liriodendron* Forest 80
Microbial Immobilization of Radionuclides in the Field 81
^{137}Cs Transfer in Terrestrial Microcosms 82
Trophic Level Concentration of ^{137}Cs, Sodium, and Potassium in Forest Arthropods 83
Body Size and Bioenergetic Relations in Forest Arthropods 85
Elimination Rates of Radiocesium by Spiders as a Function of Temperature and Body Size 86
Radioactive Tungsten Retention by Insects 88
Cycling of ^{45}Ca by Dogwood Trees 89
Biomass Regression Relations for the El Verde Rain Forest in Puerto Rico 91
Foliar Application of ^{137}Cs on Understory Species of Mesic Forest 91

12. RADIONUCLIDE CYCLING IN AQUATIC ECOSYSTEMS 93
Uptake and Metabolism of Strontium in Bluegill Flesh and Blood 93
Cesium and Potassium in Aquatic Food Chains 97
Radiation Effects on Carp Reproduction 98
Periphyton Growth and Radionuclide Accumulation 99
Community Structure and Function of Benthic Macroinvertebrates in a Constant Temperature Spring 99

13. WATERSHED AQUATIC HABITAT INTERACTIONS 102
Land-Water Interactions 102
Walker Branch Watershed Facility 103
Concentration and Transport of Suspended and Dissolved Material by River Water 108

14. THEORETICAL AND SYSTEMS ECOLOGY 111
The System Identification Problem 111
Radiant Energy Budget of Deciduous Forest 111
Initial Model for Energy Flow in *Liriodendron* Forest 113
Vertical Periphyton Growth 115
Rates of Geochemical Denudation of the Continents 115

15. FOREST MANAGEMENT 117
Forest Management 117
Use of Linear Programming in Forest Regulation 117

PART III. RADIATION PHYSICS

16. THEORETICAL RADIATION PHYSICS 121
Double Plasmon Excitation by Charged Particles 121
Calculation of the Minimum Dipole Moment Required to Bind an Electron to a Finite Electric Dipole 121
Electron Scattering from Atoms of $1s^2 2s^2 2p^q$ Configuration 123
Nonadiabatic Target Distortion in Low-Energy Atomic Scattering 124
Potential Energy Shift at the Atomic Nucleus 127
Electron Mean Free Paths in a Free Electron Gas 129
Effects of Phantom Geometry on Dose Distribution 129
Reformulation of the Dielectric Constant and of Ohm's Law in an Absorbing Medium 130
Characteristic Energy Gain by Fast Electrons in Solids 131
Plasmon Exchange Scattering by Fast Electrons 131
Surface Secondary Electron Emission from Solids 132
Group Theory of Normal Modes and Molecular Orbitals 132
Potential Energy Curves for Diatomic Molecules 133
Oscillator Strengths in Magnesium Porphin 133
High-Energy Dosimetry 134

17. INTERACTION OF RADIATION WITH LIQUIDS AND SOLIDS 135
Photon Excitation of Surface Plasmons: Analysis of Aluminum Data 135
Optical Properties of Certain Insulating Materials 137
A New Method of Kramers-Kronig Analysis 140
Optical Properties of Evaporated Films of Amorphous Selenium 141
Refractive Index of Potassium 142
Measurement of Optical Properties at Long Wavelengths 144
An Angle Doubler for Reflectance Measurements in Evacuated Systems 144
Photoemission Measurements for Silver, Palladium, and Nickel in the Vacuum Ultraviolet 146

18. ATOMIC AND MOLECULAR RADIATION PHYSICS 149
Molecular Scattering of Thermal Electrons 149
Electron Capture by Hydrogen Halides and Their Deuterated Analogs 151
Electron Capture by O_2 (O_2-C_2H_4 and O_2-C_2H_4-H_2O Mixtures) 153
Electron Capture by Aromatic Molecules 154
Electron Capture of Toxic Chlorinated Compounds 154
Temporary Negative Ion Lifetimes 155
Temporary Negative Ion Resonances in Organic Molecules 155
Thermal (Field Free) Electron Capture Rate and Thermal Electron Diffusion Coefficient Determinations from Time-of-Flight (TOF) Studies Using Electron Multiplier Techniques 156
Excitation of Atoms and Molecules by Electron Impact 159
Emission from Organic Liquids Excited by Electron Impact 161
Development of a Nanosecond Pulsed Source for Scintillation Decay Time Measurements 164
Negative-Ion–Molecule Reactions 166
Collisional Detachment Experiments 166
Sensitized Ionization of Molecules 167
Yields of Resolved Transitions in Gases 167
Unimolecular Decompositions 168

19. GRADUATE EDUCATION AND VOCATIONAL TRAINING 169
Graduate Education and Vocational Training 169

20. PHYSICS OF TISSUE DAMAGE 172
Low-Energy Electron Transmission in Solids 172
Excitation of Amino Acids by Electron Bombardment 173
Radiation Interactions with Liquids 174
Organic Scintillators with 2-Ethylnaphthalene as a Solvent 175
Excitation of Volume Plasmons with Low-Energy Electrons 178
Excitation and Ionization Yields in Al 179

PART IV. RADIATION DOSIMETRY

21. ICHIBAN STUDIES 185

Ichiban Liaison 185

Radiation Attenuation by Concrete 186

Operation HENRE – General Operations 187

Preliminary Results of Angular Dose and Neutron Energy Spectrum Measurements Made During Operation HENRE 190

22. SPECTROMETRY AND DOSIMETRY RESEARCH 193

A Possible Nuclear-Accident Dosimeter Based on ^{103}Rh 193

Experimentally Determined Recoil-Particle Energy Spectra Produced in Tissue-Equivalent Material by 3- and 15-Mev Neutrons 194

An Intermediate-Energy Neutron Spectrometer Using Magnetic Analysis of Recoil Protons 197

^{6}LiI Spectrometry 197

23. DOSIMETRY APPLICATIONS 201

Silver-Activated Phosphate Glass Dosimetry 201

Solid-State Track Detectors 203

Dosimetry Intercomparisons with CERN (European Organization for Nuclear Research, Geneva, Switzerland) 206

Third Annual Intercomparison Study 208

"Total" and "Exchangeable" Sodium Studies in Swine and Sheep Using Activation Analysis and Isotopic Dilution 208

High-Sensitivity G-M-Type Gamma-Ray Dosimeter for Operation HENRE 214

Yield, Energy, and Angular Distributions of Neutrons Produced in Graphite, Copper, and Tantalum Targets Irradiated with 63-Mev Protons 216

The Effect of Slant Incidence of a Broad Parallel Beam of Neutrons on the Distribution of Dose in a Cylindrical Tissue Phantom 219

The Calculation of Kerma as a Function of Neutron Energy 223

Results of the Calculations of the Dose Imparted to Small Seeds by the HPRR 225

Results of the Computations of Dose as a Function of Penetration Depth in Mouse-, Rat-, and Guinea-Pig-Sized Cylindrical Tissue Phantoms 226

24. HPRR AND DLEA OPERATIONS 227

Health Physics Research Reactor 227

Radiation Dosimetry Studies at the HPRR 227

Radiation Survey of the HPRR 227

DOSAR Low-Energy Accelerator Modifications and Applications 229

PART V. INTERNAL DOSIMETRY

25. INTERNAL DOSE ESTIMATION 233

Calculating the Effective Energy per Radioactive Decay for Use in Internal Dose Calculations 233

Distribution of Dose in the Body from a Source of Gamma Rays Distributed Uniformly in an Organ 245

The Variation of Dose in Man from Exposure to a Point Source of Gamma Rays 257

An Age-Dependent Model for the Bodily Retention of Cesium 261

A Dosimetric Study for the Administration of Neohydrin Labeled with ^{203}Hg and ^{197}Hg 267

Use of Excretion Data to Predict the Systemic Body Burden of Plutonium 273

26. STABLE ELEMENT METABOLISM 283

Long-Term Study of Intake and Excretion of Stable Elements 283

Tissue Analysis Laboratory 287

PART VI. HEALTH PHYSICS TECHNOLOGY

27. AEROSOL PHYSICS 291

Adhesion of Particles to Particles and to Plane Surfaces 291

Coulometric Electrolytic Tank for Study of Electrical Forces on Particles 293

Exploding-Wire Aerosol Generator 296

Interaction of Airborne Vapors with Particulates 299

Initial Retention of Particles on Skin 301

Expected Dose from "Hot" Particles Deposited on the Skin 302

28. APPLIED INTERNAL DOSIMETRY 304

ORNL in Vivo Gamma-Ray Spectrometry Facility 304

In Vivo Detection and Measurement of ^{90}Sr-^{90}Y Internal Contamination 306

Elimination of Injected ^{203}Hg 306

Absorption of 17 kev X Rays from Transuranic Elements 308

New Procedure for Radiostrontium Analysis of Environmental Samples 308

THESES, PAPERS, PUBLICATIONS, AND LECTURES

THESES 315

PAPERS 316

PUBLICATIONS 323

LECTURES 335

Summary

PART I. RADIOACTIVE WASTE DISPOSAL

1. Fate of Radionuclides in Terrestrial Environment

Field plots were installed and tagged with ^{137}Cs and ^{134}Cs in a design which allowed locating the source of runoff and erosion losses. These plots also served as replicates of earlier ^{137}Cs plots. Results obtained thus far confirm seasonal variation and the basic soil-cesium-loss relationship derived earlier.

Greenhouse studies of radiocesium uptake by plants using a split-root technique have been initiated. The technique allows control of soil moisture at predetermined tensions and permits an evaluation of the role of soil moisture in radiocesium uptake. Laboratory studies of cobalt sorption reactions point to the conclusion that small amounts of sesquioxides of iron and aluminum influence the reaction of the element in tracer concentrations.

2. Disposal by Hydraulic Fracturing

Two injections of medium-level waste concentrate were made during the past year. In the first, on December 12 and 13, 1966, a total of 96,000 gal of slurry, containing 20,000 curies of cesium, was pumped into a slot at a depth of 872 ft, which already contained 215,000 gal of grout from previous experimental injections. In the second, on April 20 and 24, 1967, 230,400 gal of slurry, containing principally 60,000 curies of cesium, was injected into a new slot at 862 ft. The injection plant operated without incident, and the slurry composition that was used appeared to be satisfactory. Measurements in the gamma-ray and rock-cover monitoring wells show that better instrumentation is now required, but every indication is that the operation is well within the limits of safety.

The oil-field technique of hydraulic fracturing has been proposed as a method for measuring the state of stress in the earth's crust. Hydraulic fracturing would have several distinct advantages over existing methods, because the stress itself can be measured rather than the strain of elastic rocks, which is then reduced to stress by use of Hooke's law. The research and development proposed will extend the present limited applicability of earth-stress measurement by hydraulic fracturing and enable the method to become a standard tool for fundamental studies of earthquakes and other geophysical processes, and for gathering design information for underground structures.

3. Disposal in Natural Salt Formations

The second and third sets of Engineering Test Reactor fuel assemblies have been installed in the arrays in the mine at Lyons, Kansas. The first set was returned to Idaho in October 1966. Both the second and third sets contained about 1.5 million curies at the time they were installed. Radiation doses to personnel were low, and no serious problems were encountered.

Doses to the salt exceeded the minimum goal of 5×10^8 rads, and the last two sets of fuel were returned to Idaho in June 1967. Peak array temperatures reached about 200°C after a power boost in January 1967.

The first two objectives of Project Salt Vault – the demonstration of the feasibility and safety and the demonstration of handling equipment and techniques – have been achieved.

Salt flows (thermal expansion and plastic flow) resulted in increased separation (sag) rates of the

2-ft-thick salt layer in the roof. The installation of roof bolts in the entire experimental area eliminated any possible hazard from this source due to startup of the heated pillar test. The heated pillar test was started November 14, 1966, with a power input of 33 kw and is proceeding in expected fashion; that is, greatly increased transverse expansion rates of the pillar produce pillar spalling and large vertical thermal expansion of the floor in the adjoining rooms.

Small quantities of water trapped in negative crystal cavities in the salt have been found to migrate toward a heat source. The water inflow rate in the main and electrical arrays appears to be between 0.3 and 3 ml day^{-1} $hole^{-1}$. In the old mine floor array the water inflow rate is about 40 to 90 ml day^{-1} $hole^{-1}$ due to the presence of water in the embedded shale.

The array in the old mine floor is behaving similarly to the other arrays, except for slightly higher temperature rises, more water inflow, and no roof separation (due to a thicker roof beam).

A detailed stratigraphic study has been completed of the salt section extending from 30 ft below the floor of the old mine workings to 10 ft above the ceiling in the demonstration site, a total thickness of 75 ft. Halite is by far the predominant mineral.

Additional laboratory tests on pillar models have indicated the importance of simulation of roof and floor in quasi-plastic rocks like salt.

Calculations of the gross salt mine space for the projected United States nuclear power economy to the year 2065 indicate that by 2065 an area about 7 miles square (49 square miles, a very small portion of the available area) will have been committed for waste disposal. Only about a third of that will have actually been used at that time, assuming 30 years' interim storage before disposal.

4. Application of Mineral Exchange to Reactor Technology

The behavior of sulfur hexafluoride (SF_6) and methyl iodide (CH_3I) in an Idaho soil was studied. The SF_6 showed little, if any, interaction with the soil material. Methyl iodide was retained to the extent that its movement was about 0.6 that of air.

Curium solutions of various pH levels were passed through columns of hydrobiotite. Instead of normal chromatographic breakthroughs, a constant leakage of curium occurred. The distribution of the curium along the column indicates that a radiocolloid is formed and that the hydrobiotite column acts as a filter.

Several adsorbents have been compared with attapulgite (presently in use) as cleanup agents for organic reactor coolants. Bentonite, activated bauxite, and spent cracking catalyst appear to be superior to attapulgite. Evaluation is based on color, melting point, and molecular weight of the effluent coolant.

5. Engineering, Economic, and Safety Evaluations

Investigation has continued on the degree of safety associated with present methods of radioactive waste management. Studies of ^{85}Kr and ^{3}H have been concerned with acceptable rates of release from a hypothetical fuel-reprocessing plant located in Oak Ridge. A general procedure was developed for estimating permissible atmospheric releases on the basis of average annual meteorological conditions that influence a continuously operating plant. The procedure considers cloud depletion of ^{85}Kr and ^{3}H by washout, fallout, and adsorption on particulate matter in the atmosphere, and buildup of contaminants on the ground surface.

Continuous disposal of ^{85}Kr to suitable geologic formations may be one possible means of reducing or avoiding atmospheric release. Although the apparent advantages of underground disposal are its relative simplicity and its effectiveness, one severe requirement imposed on any disposal formation is that it must be essentially free of vertical channels. The mechanisms considered by which ^{85}Kr may be retained underground include containment and adsorption. In the absence of vertical convective transport, movement is influenced only by molecular diffusion. These mechanisms have been evaluated theoretically for quantities of ^{85}Kr and volumes of off-gas assumed to be produced at a 10 metric ton/day reprocessing plant. Measurements were made of krypton and xenon adsorption by various soil materials.

As a part of the long-range waste management study, projections were made of the nuclear power requirements by regions and of the reactor mix that may accommodate these requirements.

Evaluation of tank safety has been extended to thermal considerations in the event of a leak of

high-level wastes. Preliminary calculations were made for leaks of various sizes using a spherical shell geometry. Transient temperatures are being estimated for various source geometries and heat sinks by use of the computer program TOSS (Transient or Steady State).

6. Earthquakes and Reactor Design

Specific information on earthquake characteristics as they influence site selection, site evaluation, design of nuclear installations, and design of seismic shutdown systems is provided in a state-of-the-art paper on earthquakes and reactor design.

7. Dose-Estimation Studies Related to Proposed Construction of an Atlantic-Pacific Interoceanic Canal with Nuclear Explosives

The phase I dose-estimation studies related to the radiological-safety feasibility of excavating an Atlantic-Pacific interoceanic canal are summarized. Information developed includes methods for estimating external and internal dose equivalents, quantifying the transfer of radionuclides through critical exposure pathways, and identifying the radionuclides likely to be critical, and criteria for evaluating the radiological safety of the operation.

8. Related Cooperative Projects

Representatives of other agencies continued to participate in the Radioactive Waste Disposal Section's studies. Three alien guests were in residence during the year. Members of the section participated in the ASCE Committee on Sanitary Engineering Aspects of Nuclear Energy and in the American Standards Association.

One member served as assistant news editor for the United States for *Health Physics* and as an assistant editor of *Nuclear Safety*. Two members of the section taught courses at the University of Tennessee. Two members of the section participated part time at the Nuclear Safety Information Center.

PART II. RADIATION ECOLOGY

9. Responses of Animal Populations to Ionizing Radiation

Time-related responses in peripheral blood of four species of indigenous mammals were followed after whole-body irradiation. Total leukocyte number in all irradiated groups dropped sharply by one day postirradiation. Decreases in number of lymphocytes primarily accounted for the decrease in total number of leukocytes. By day 20, recovery in leukocyte number was evident for all species (49 to 82% of original values). Erythrocyte count and associated values (hemoglobin concentrations and hematocrits) decreased by day 20 in the rice rat, but these values were not significantly lower in the other species. These studies suggest that the greater radiosensitivity of the rice rat may be attributable to the radiosensitivity of the hematopoietic system of this species.

Loss rates of ^{59}Fe at 25°C were determined in seven species of native rodents in an effort to establish a suitable index to radiation damage in erythropoietic tissues and hemoglobin synthesis in free-ranging animals. Animals were injected peritoneally, and whole body counted until 114 days postinjection. Excretion rates were low for all animals tested. Irradiation (whole body) resulted in decreases in λ_b ranging from 1.9 to 4.4% by day 5 except in *M. musculus*, in which no change occurred. It appears that radiation effects on iron metabolism cannot be detected with this technique, on a short-term basis at least, in animals irradiated at relatively low levels.

The postirradiation survival of brown crickets in a grassland habitat was compared with that in laboratory experiments. Irradiated crickets were released into a field pen and then recaptured nightly in traps. In the laboratory similarly irradiated crickets were maintained at optimum rearing temperatures. Recaptures of crickets suggested a 50% survival time of about 11 days in the meadow environment compared with 21 days in the laboratory. The decreased survival time in the pens indicates that additional mortality factors were operating there; a possibility is predation by wolf spiders, which were observed feeding on these crickets. Further studies were completed on life history stage responses of evergreen bagworms to gamma radiation. For a single end point, LD_{50-20}

day mortality, sensitivities between egg and larval stages varied by a factor of nearly 35.

Fecundity of the mosquito fish, *Gambusia affinis affinis*, which live in White Oak Lake was evaluated. These fish receive approximately 130 rads/year from internal emitters and may receive as much as 10 rads/day from bottom sediments in certain parts of the lake. Fecundity, or brood size, was found to be greater in *Gambusia* from White Oak Lake than in a control population. The average number of viable embryos per fish from White Oak Lake was 44.4 ± 1.83; the average number from the control area was 32.1 ± 1.49. Besides the brood size, percent of dead embryos and abnormalities were greater in the White Oak Lake population. Increased brood size of the chronically irradiated fish may reflect a population adjustment to the increased mortality (exploitation) produced by ionizing radiation.

A comparison was made of the movement of ^{106}Ru, ^{60}Co, and ^{137}Cs in arthropod food chains on White Oak Lake bed. Distribution of ^{137}Cs among biota in the bed was similar to that previously reported. Compared with ^{137}Cs, more efficient food chain movement was suggested by the data for ^{106}Ru and ^{60}Co. Uptake from soil was greater for these latter radioisotopes than for radiocesium. Transfers from vegetation to herbivores and from herbivores to predators also appeared more efficient for ^{106}Ru and ^{60}Co than for ^{137}Cs. In particular, ^{106}Ru concentrations in predators were almost three times higher than those in herbivores. Consequently, the relative abundances of the three radioisotopes became rearranged by food chain processes. Ruthenium-106 had twice the concentration of ^{137}Cs in soils; in predators ^{106}Ru was 20 times more abundant than ^{137}Cs.

10. Responses of Plants to Ionizing Radiation

Responses to fast-neutron radiation in terms of growth, morphological, or mortality criteria have been measured for locally important tree species. These species represent ten families of wide taxonomic distribution. The extreme radiosensitivity of the conifers (*Pinus*) was apparent, with lethal doses being about 12 times less than the average lethal dose for the deciduous species. The most sensitive deciduous trees tested were dogwood (*Cornus florida*), sassafras (*Sassafras albidum*), and sweetgum (*Liquidambar styraciflua*). Doses required to produce lethality and severe growth effects in these species averaged 33 and 35% lower, respectively, than those required to produce these end points in the other deciduous trees. The most resistant species tested were mimosa (*Albizzia julibrissin*) and red oak (*Quercus rubra*). Doses producing lethality and severe growth effects in these species averaged 40 to 57% higher, respectively, than those for other deciduous species.

Nuclear criteria for genotypes of *Populus deltoides* (eastern cottonwood) were investigated to establish whether chromosome-volume differences existed in our populations, which consist of 30 clones representing ecotypes from six states. All clones had the diploid (38) number of chromosomes. The range of the interphase chromosome volumes with their associated standard errors was 2.38 ± 0.07 to 4.24 ± 0.16 μ^3. These two extreme values suggest that a difference in radiosensitivity may exist between these clones due to this 1.8 factor of increase in chromosome size. However, the other clones tested had chromosome volumes differing from one another only by a factor of 1.4 or less. Past work has shown that size differences of this magnitude are not likely to correlate well with exposure predictions for growth or mortality end points.

11. Radionuclide Cycling in Terrestrial Ecosystems

Five years of research, including laboratory experiments on insect feeding, have clarified many problems related to the animal food chains in the ^{137}Cs-tagged forest. Over 2 $\mu c/m^2$ of foliage consumption was necessary to maintain radioactivity levels in canopy insect populations, even though the total activity represented in them was very small (about 0.004 $\mu c/m^2$ at any one time). The contributions of insects, and probably of other animals, to the export of radioactivity from the forest appeared small (less than 0.1 $\mu c/m^2$) by comparison with the measured export in blowing leaves which fell outside the plot boundaries in autumn (5.3 $\mu c/m^2$ in 1963; less in later years). Litter falling inside the plot contributed about 5 $\mu c/m^2$ to animal food chains (especially ground insects and millipedes), which eventually return radiocesium to the litter layer or underlying soil.

Equations that were used previously in mathematical models for accumulations of nutrients in soils, plants, and animals were extended to overall analysis and prediction of radiocesium in and around the tagged forest. The continued decreases in radioactivity of tree foliage imply readjustment toward lower levels of activity throughout the animal food webs. In spite of the tendency of soil minerals to fix cesium ions, recycling into plant roots may lead to an almost steady state, at levels less than 1% of the first year levels of activity, between the fifth and tenth year of the experiment. One model prediction indicates that continued input of activity to the soil may be balanced by radioactive decay in approximately seven years.

Studies on the distribution of three alkali metals (cesium, potassium, and sodium) in arthropod food chains showed that trophic processes do not result in increased concentration of ^{137}Cs and K between arthropod links in the food chains. Since fallout ^{137}Cs often has been reported to be accumulated in vertebrate food chains, it is apparent that the faunistic composition of environmental pathways must be considered before the fate of ^{137}Cs in trophic levels of ecosystems can be assessed.

Laboratory studies of ^{187}W retention were performed with two species of insects to determine what magnitude of food chain transfer might be expected in tungsten-tagged environments. The biological half-lives for tungsten, based on the mean retention estimates at each counting time, were 48 hr for *Acheta* and 58 hr for *Oncopeltus*. Percentage error was found to be about 20%. Radiotungsten absorption and retention parameters appear similar to those for radiocesium in these two insects. From these measurements it is inferred that radiotungsten movements through the arthropod portions of food chains may approximate movement of radiocesium.

12. Radionuclide Cycling in Aquatic Ecosystems

Several types of experiments were done to clarify the respective roles of fish flesh and blood in Sr uptake and turnover in bluegills (*Lepomis macrochirus* Rafinesque). Specific activities or radiostrontium-to-total-Sr ratios were used to determine whether the Sr in flesh and blood was in equilibrium with that in water. The blood incorporated radiostrontium rapidly, reaching about two-thirds of the maximum activity level in 24 hr. The concentration factor rose from 0.124 at 1 day to 0.194 at 35 days. The specific activity in the blood did not change appreciably in the test period, rising from 0.47 at 1 day to 0.74 at 35 days. The greatest rate of ^{89}Sr uptake by the flesh occurred in the first 4 days. The second component of the uptake curve was faster for flesh than for blood, and the maximum concentration factor reached after 35 days was 0.121. Extrapolation of the second component indicates that approximately 72 days are necessary for bluegill flesh to reach a concentration factor of 1, which may be expected from stable Sr analyses.

Uptake responses to different environmental Sr concentrations (0.3 to 30,000 ppb stable Sr) were carried out in bluegills. The concentration factor for radiostrontium was virtually constant within this range. This indicates that the readily exchanged Sr fraction was accumulating Sr in direct proportion to that in the environment. Results of the stable Sr analyses indicated that concentration factors of stable Sr were inversely proportional to the Sr concentration in test waters, except at the two highest environmental concentrations, 3000 and 30,000 ppb. The levels of stable Sr in the flesh of the experimental fish did not change significantly. These results showed that the quickly exchanged fraction of Sr in bluegill flesh was a small proportion of the total Sr in flesh.

Experiments on cesium and potassium turnover in white crappie were performed to test a hypothesis that Cs/K ratios will increase at succeeding trophic levels in the food chain. The results do not support this hypothesis. Field studies on trophic-level increases, using White Oak Lake fish, showed no consistent pattern of Cs content with respect to trophic level. Comparison of Cs and ^{137}Cs analyses from fish from the Clinch River (ORNL), Finnish lakes, and Red Lake, Minnesota, showed that trophic-level increases occurred only part of the time. These differences may be the results of different food chains in different habitats, which in turn affect Cs concentration at succeeding trophic levels. Data available at present do not warrant the general application of trophic-level increases to Cs in food chains.

13. Watershed Aquatic Habitat Interactions

A watershed research program was initiated this year which will unify portions of the terrestrial and aquatic ecology research. The Walker Branch

watershed, having a total area of 241 acres and consisting of two smaller watersheds of 95 and 146 acres, was selected for study. Two permanent spring-fed streams drain the area. Research objectives of the project are to (1) relate water quality and productivity of the stream to the productivity and chemical budget of the adjacent terrestrial ecosystem, (2) equate the net loss of chemical elements to the rate of mineral cycling, (3) establish the relationship between the hydrologic cycle and mineral cycle, and (4) provide benchmark information of natural terrestrial-aquatic ecosystems for comparison with those modified by man's cultural practices.

A base map was prepared from an existing detailed topographic map and from aerial photos taken in October 1966 and February 1967. A four-chain grid system was established with permanent corner markers to facilitate positive field location. The overstory vegetation and soil types have been mapped. Five rain gages were installed, and areas around them were fenced and seeded. Access roads were constructed, and preliminary excavations for the two weirs were completed. Weir design, as well as the design for continuous proportional water samplers which are to be installed at the weir site, was completed. A power line to the weir site was designed and is being installed.

14. Theoretical and Systems Ecology

Data on radiant energy input and productivity were utilized to construct a preliminary model of energy flow in *Liriodendron* (tulip poplar) forest. Values for stem production were 9000 kcal m^{-2} $year^{-1}$, canopy 1950 kcal m^{-2} $year^{-1}$, and 1600 kcal m^{-2} $year^{-1}$ for roots. These values correspond to 0.12, 1.6, and 0.12% of the annual (all wavelength) solar energy input to leaves, stems, and roots respectively. A general instructive model describing vertical periphyton growth was developed on the basis of periphyton studies carried on in White Oak Lake.

15. Forest Management

The Forest Management Program, initiated in 1965, has the responsibility for managing 20,900 forested acres adjacent to the ecology study areas on the AEC Oak Ridge Reservation. A self-financing commercial forest program is conducted in harmony with the research objectives of ORNL. Applied forestry research is conducted as needed to solve specific land management problems.

PART III. RADIATION PHYSICS

16. Theoretical Radiation Physics

The problem of double plasmon excitation by a fast electron is considered a framework which allows for damping of the intermediate states by plasmon interactions together with other possible competing processes. The value of the minimum dipole moment required to bind an electron to a finite permanent electric dipole has been established rigorously to be $D_{min} = 1.625 \times 10^{-18}$ esu-cm. Approximating the polarization potential for electron scattering from atoms of $1s^2 2s^2 2p^q$ configuration, using a polarization potential previously calculated for oxygen and the experimental dipole polarizabilities, calculations of the total elastic scattering cross sections for these atoms have been made; agreement with experiment is rather good. A perturbation method has been used to obtain equations for the dynamic distortion of the target system when low-energy electrons or positrons scatter from atomic or molecular systems. The potential energy of the electronic cloud at the nucleus of an atomic system is of interest in beta decay theory; calculations of this energy for a number of different neutral atoms have been made using the Hartree-Fock equations for the atomic system. Work is continuing on the effect of the exclusion principle in intermediate states of scattering of a hot electron on a free-electron gas. Comparisons of the dose distribution in cylindrical and slab phantoms due to protons of energies in the range 250 to 400 Mev have been carried out. A new formulation of the dielectric constant of an absorbing medium has been made. It is predicted that photon absorption by a fast electron may occur with appreciable probability through the intermediary of a virtual plasmon; estimates show that it may be feasible to observe this process experimentally. Plasmon exchange scattering by two colinear fast electrons of slightly different energies appears more difficult to observe experimentally.

Consideration has been given to the process of surface secondary electron emission from metal through the Auger decay of surface plasmons created by fast charged particles. A procedure has been formulated for choosing the normal modes of motion of nuclei in a molecule so that, when subjected to a symmetry operation of the point group of the molecule, they form bases for irreducible representations of the point group. Work on the Klein method for obtaining the potential vs internuclear distance for diatomic molecules is continuing. Molecular structure calculations of magnesium porphin have been carried out; resulting energy levels and oscillator strengths correspond to two prominent strong absorptions near the experimental values. Studies of the passage of high-energy nucleons through multiregion phantoms, corresponding to soft tissue and bone parts, have been made for protons and neutrons with energies up to 400 Mev.

17. Interaction of Radiation with Liquids and Solids

Optical constants in the vacuum ultraviolet have been determined for single crystals of MgF_2 and MgO and thin films of white Sn, amorphous Se, and K. Reflectance techniques were used, except for K, where the critical-angle method yielded the refractive index directly. For critical-angle measurements an angle doubler, an apparatus for moving the detector at twice the angular velocity of the sample, has been designed. In addition, an ellipsometer and ultrahigh-vacuum chamber were constructed, and optical constants of palladium at long wavelengths were determined from analysis of the ellipticity of light reflected from a flat palladium surface. Photoelectric measurements have been made on silver, palladium, and nickel, with photoelectron energy distribution curves being obtained for various incident-photon energies.

To obtain optical constants from reflectance data, a new method of employing the Kramers-Kronig relations has been devised.

Both optical constants over an extended energy range and photoelectron energy distribution curves yield information about the energy-absorption processes taking place when photons interact with the material. Such information can be related to band structure and to absorption cross sections. For each material studied, structure in the optical constants, in the derived energy-loss functions, and in the photoelectron energy distribution curves has been interpreted in terms of excitons, interband transitions, and collective, or plasma, oscillations. In some cases comparison has been made with characteristic electron energy loss measurements published in the literature. An attempt was made to identify photon excitation of surface plasmons in aluminum using data obtained previously. Positive identification was not possible due to the existence of an interband transition near the surface-plasmon energy.

18. Atomic and Molecular Radiation Physics

The minimum molecular electric dipole moment which is necessary to bind an electron has been calculated and found equal to 1.639 Debye units. An analysis of electron swarm data for electrons traveling through polar gases provided the first experimental evidence for this value.

Investigations of low-energy electron attachment to aromatic molecules have been extended from the halogenated benzene derivatives to benzene itself, naphthalene, and napthalene derivatives. Electron capture in the diatomic molecules HX and DX (X = halogen) revealed new electron attachment processes and provided most interesting results for direct dissociative electron attachment to molecules. Capture cross sections (corrected for the finite width of the electron pulse) as a function of electron energy have been obtained for these molecules. Electron capture in chlorinated linear hydrocarbons provided interesting results which will form the basis of an attempt to relate electron capture with the toxic action of these molecules. Further, a new technique has been developed which allows determination of thermal electron attachment to molecules and thermal electron diffusion under field-free conditions.

Nondissociative electron attachment to O_2 in O_2-C_2H_4 and O_2-C_2H_4-H_2O mixtures has been studied, and the efficiencies of O_2, C_2H_4, and H_2O as stabilizing agents for O_2^{-*} have been investigated. Electrons were found to attach to polyatomic molecules with high probability and for times of the order of 10^{-5} sec. The product of the capture cross section and the corresponding negative ion lifetime has been found to be a strong function of the molecular electron affinity. From a theoretical expression relating the capture cross section, the negative ion lifetime, and the electron

affinity, a calculation has been made of the electron affinity of sulfur hexafluoride, nitrobenzene, diacetyl, and glyoxal. In this respect new experiments have been initiated to study collisional detachment of electrons from negative ions in an effort to measure molecular electron affinity directly.

Short-lived negative ion resonances have been discovered in benzene, seven benzene derivatives, and naphthalene. For benzene derivatives for which dissociative attachment is possible, autoionization and dissociation were found to be in competition. The temporary negative ion resonances observed in benzene and naphthalene gave a lower limit to the electron affinities for these molecules equal to -1.4 and 0.8 ev respectively.

Excitation of hydrogen halide molecules, benzene, seven benzene derivatives, and naphthalene has been studied at the threshold of excitation processes using SF_6 as a scavenger of low-energy electrons. Important results have been obtained, especially with respect to temporary negative ion resonances and triplet state excitation of molecules. The emission from organic liquids excited by electron impact has been found to be completely due to excimers. The characteristic monomer emission observed under ultraviolet and x-ray excitation was completely absent under intense electron bombardment. Ion recombination is believed to be the origin of the excimer emission, while strong ionization quenching of excited monomer molecules is believed to be responsible for the absence of monomer emission. A nanosecond pulsed electron source for scintillation decay time measurements has been developed and will aid our luminescence studies of polyatomic molecules.

Finally, studies have been made of sensitized ionization of molecules, molecular decomposition, and the yields of resolved transitions in gases.

19. Graduate Education and Vocational Training

In the Graduate Education and Vocational Training Program, eight AEC Health Physics Fellows from Vanderbilt University, four from the University of Tennessee, and one from the University of Rochester came to ORNL for summer training in applied health physics and research. Final writing and editing were completed on the book "Principles of Radiation Protection: A Textbook in Health Physics." Page proof was received and publication is expected in time for use during the academic year 1967–68. Nineteen colleges and universities were visited, and health physics research and career opportunities were discussed. Twenty-two graduate students conducted thesis research in the Health Physics Division for the M.S. or Ph.D. during the year. A total of 56 university personnel ranging from undergraduates to professors spent last summer in the Health Physics Division. Several of our staff assisted the UT Physics Department in writing three research proposals to government agencies. A new undergraduate curriculum in health physics was set up at UT with our help. The Division cooperated with Oak Ridge Associated Universities in screening of applicants for USAEC Fellowships; participation in the conference on "Principles of Radiation Protection," which attracted approximately 100 faculty members; and presentation of courses of up to ten weeks duration in health physics for 32 state personnel. Lectures were given at four Medical Radioisotopes Courses, attended by 60 physicians. The Division assisted in the presentation of an eight-week course in health physics for college and university staff members who have responsibility for campus radiation safety. At ORNL, Division personnel participated in the presentation of a two-week course in Radiation Safety for Laboratory staff.

20. Physics of Tissue Damage

In the Physics of Tissue Damage Program, studies of electron transport through tin metallic layers were extended with a new ultrahigh vacuum system and a new electron gun capable of supplying electrons of as little as 1 ev at an arbitrary angle to the layer. An enhancement of surface-plasmon excitation was noted as the electron beam impinged at glancing (as opposed to normal) angles, whereas the absorption due to L-shell ionization decreased. The former behavior was in qualitative accord with theoretical expectations, whereas the latter was not and is not understood. In measurements on amino acid films, electrical characteristics were noted as follows: band gap, 2.7 ev; resistivity, 10^{16} ohm-cm; field strength at

breakdown, 10^5 v/cm. An electron irradiation system was constructed which prevented light from the electron gun from shining on the amino acid target. Optical measurements of the ratio of phosphorescence to fluorescence for tryptophan and tyrosine films showed that the ratio is independent of electron energy from 30 ev to 100 kev, implying that optical excitation is determined entirely by low-energy secondary electrons. The reflectivity of liquid water was measured at angles of 20, 45, and 70° to the normal and in the wavelength region between 1000 and 3000 A. Peaks in reflectivity at 2100, 1700, and 1000 A are attributed tentatively to triplet excitations, singlet excitations, and ionization in the liquid respectively. A peak at 1250 A is unidentified.

Eleven scintillator solutes were studied in the solvent 2-ethylnaphthalene, with emphasis on emission intensities, quenching effects, and pulse heights. This solvent, which emits from excimer formation, was found to be highly efficient and to resist quenching to a much greater extent than other scintillating materials. A preliminary study of light emission from silver irradiated by 200-ev electrons showed a peak at 3900 A, in contrast to the peak at 3300 A found from high-energy (>10-kev) irradiation. Further study is required in order to decide whether this peak arises from surface-plasmon decay or bremsstrahlung. Electron slowing-down spectra from beta-ray sources in aluminum were used to calculate the number of *K* ionizations (~3), *L* ionizations (~300), and plasmon excitations (~18,000) which arise as an Mev beta ray slows down in aluminum. Virtually all beta-ray energy ultimately goes to plasmon formation.

PART IV. RADIATION DOSIMETRY

21. Ichiban Studies

The major emphasis of the program during fiscal year 1967 was on shielding studies associated with the survivors who were exposed in reinforced concrete or other massive structures, liaison, depth-dose calculations, and dosimetry related to Operation HENRE. The calculation of the shielding provided by large structures requires a knowledge of (1) the geometry of exposure (from ABCC records), (2) the energy and angular distribution of the neutrons and gamma rays (from previous dosimetry studies), and (3) the attenuation and buildup factors for the building materials for the exposure geometry. The latter subject was studied extensively both in the laboratory and during Operation HENRE. Two liaison trips to Japan made it possible for ORNL and ABCC to work efficiently on a joint basis. Calculations of depth-dose distributions for various neutron energies and irradiation geometries were continued (see "Dosimetry Applications," Sect. 23).

22. Spectrometry and Dosimetry Research

Spectrometry research for both directly ionizing particles and indirectly ionizing particles and quanta continued to be an important part of the dosimetry program. Silicon diodes were the primary tools for directly ionizing radiations. Neutron spectrometry research was directed to magnetic analyzing devices for elastically scattered protons and to ^{6}LiI scintillation systems. A new detector system for nuclear accidents is based on the use of rhodium. Much of the overall effort was directed to spectrometry for Operation HENRE (see "Dosimetry Applications," Sect. 23). For these studies, the ^{6}LiI spectrometer was most useful because of its great sensitivity compared with other systems.

23. Dosimetry Applications

Development of integrating or "passive" systems of dosimetry for personnel and nuclear accidents was continued, primarily with solid-state devices; these include metaphosphate glass for gamma radiation and fission-foil–solid-state (glass, plastic, etc.) detectors for neutrons.

Intensive intercomparisons of dosimetry systems were completed; both domestic and foreign groups used the HPRR in joint evaluations of a wide variety of systems. These studies are important both as a basis for evaluating the dosimetry systems and as a forum for information exchange. Depth-dose studies were continued for a tissue medium for an assortment of sizes and geometries, and calculations of radiation dose to many varieties of seeds irradiated at the HPRR were made. Measurements of neutron fluence and dose distributions near thick targets of copper and carbon bombarded by 60- and 80-Mev alpha particles were made at the Oak Ridge Isochronous Cyclotron. A more

sensitive Geiger-Mueller tube was adapted to the "Phil" system by designing appropriate shields for eliminating thermal-neutron response and for flattening the response vs photon energy to match the tissue dose curve. A series of measurements were made to determine the exchangeable and total sodium in the human body by isotopic dilution and neutron activation techniques; the study was conducted because a British group reported experimental values which were sufficiently lower than any previous values to require changes in previous ORNL data.

24. HPRR and DLEA Operations

The Health Physics Research Reactor continued to serve as the radiation source for a large fraction of the world's dosimetry research. An increasing percentage of the reactor operations is in the pulsed mode. The DOSAR Low-Energy Accelerator has proved to be a versatile and highly reliable source of low-energy charged particles and 3- and 14-Mev neutrons.

PART V. INTERNAL DOSIMETRY

25. Internal Dose Estimation

Calculation of the average beta-particle energy in beta decay has been computerized, and graphs of the ratio of average energy to end-point energy are presented for allowed, first-forbidden unique, and second-forbidden unique transitions. Computer codes have been developed which calculate the percentages per decay and respective energies of x rays, gamma rays, internal conversion electrons, and Auger electrons for electron capture decay and gamma-ray internal conversion. Illustrative computer outputs are presented.

When a gamma emitter is present in an organ of the body, one needs to know what fraction of the energy released is absorbed in various tissues of the body in order to estimate dose to those tissues. Many oversimplified methods have been used in the past to estimate these "absorbed fractions" as they are often termed, for example, a single interaction calculation, a "straight-ahead" model of scattering, or the use of an "effective radius." This paper defines a mathematical model of the human body and 23 organs, each having approximately the correct size and shape, and a computer code estimates dose to each of these organs from a source uniformly distributed in any one of them. The principal limitation is that the phantom is homogeneous, and efforts are under way to remedy this. However, for energies above 0.2 Mev, the mass absorption coefficients of bone and soft tissue are not very different, and so only sources at or above 0.2 Mev have been used thus far. In general, the "absorbed fractions" obtained by these more exact, multicollision-type estimates are lower than values obtained by the use of an "effective radius" as defined by the ICRP and NCRP, the new values being generally about half those estimated by that procedure.

A Monte-Carlo-type code has been developed at ORNL which permits one to estimate dose in tissue phantoms for a wide variety of exposure situations. This is a report on dose in an anthropomorphic tissue phantom which has approximately the dimensions and masses of "Standard Man." The incident photons emanate from an external point source which is positioned at various distances up to 2 m from the phantom and at several heights. The phantom is divided into 160 subregions. The volume elements nearest the surface of the trunk section have a thickness of 1 cm, and the dose in these volume elements may be expected to approximate the reading of a dosimeter exposed on that portion of the surface of the body. Thus the variation of dosimeter readings when the dosimeter is worn in different positions on the body surfaces can be estimated and compared with the distribution of dose within the body. Each point source is monoenergetic, and the energy of the photons is varied from 0.07 to 1 Mev. The dose at a specified site within the phantom may differ as much as an order of magnitude from the dose indicated by a dosimeter worn at certain locations on the surface of the phantom, the difference depending on the energy of the source and its position in relation to the phantom and the position of the dosimeter.

After an intake of cesium, this element is eliminated over a period of time. It has been found by Richmond *et al.* that a one- or two-exponential retention function is usually sufficient to fit the observed data. This retention model is valid for adults and children, but the elimination rates are different in each case. In this report a mathematical compartment model is proposed which allows compartment size or growth to be included naturally. This model is applied to the retention of ^{137}Cs by humans from birth through adulthood.

The biological half-times predicted with this model compare favorably with experimental values, although there is still much variation of the observed half-times within an age group. The implications of this model in regard to dose from single and continuous intakes are examined.

Detailed estimates are provided of dose within the body from administration of Neohydrin labeled with ^{197}Hg or ^{203}Hg. Such estimates are of interest in deciding the relative merits of the two compounds for extensive clinical use. Dose estimates to (1) cortex of kidney, (2) medulla of kidney, (3) bladder, and (4) ovaries are provided per millicurie-hour of residence of the source in blood (early phase), in cortex, in medulla, and in the bladder (excretory phase). The dose from photons is estimated using the Monte Carlo technique. These estimates are used with available data on residence times to obtain a dose estimate for a typical case. However, they can be easily adjusted in other proportions appropriate for the elimination rates of a particular patient.

The accuracy of computer codes based on excretion data following a single intake to blood for estimating a systemic body burden of plutonium is considered (1) by fitting power functions to data of individuals resulting from a single intake to blood and comparing these functions to determine individual differences, (2) by analyzing day-to-day fluctuations to determine confidence bands about the power functions which include a preassigned percentage of the data, (3) by using computer methods to predict intake or body burdens for known cases where the predictions can be checked, and (4) by using only portions of the excretion data to reveal inaccuracies due to inavailability of all the excretion data. The use of these data on fluctuations of day-to-day excretion and on individual differences to estimate body burdens by computer methods is being explored.

26. Stable Element Metabolism

Long-Term Study of Intake and Excretion of Stable Elements

Statistical studies of the daily elemental dietary intake and urinary and fecal excretion of two men on *ad libitum* diets over a period of four months indicate the influence of the time of intake, of intake of other elements, and of other factors on the excretion of an element. Equations relating these factors have been developed.

Tissue Analysis Laboratory

In the tissue analysis program, attention has been directed to the detection of trace elements in bone. The overall sensitivity has been improved by developing a chemical preconcentration procedure.

PART VI. HEALTH PHYSICS TECHNOLOGY

27. Aerosol Physics

Studies of the adhesion of solid particles to other particles and to solid surfaces have been extended to provide a better understanding of the basic physical mechanisms. Results of earlier ad hoc studies have confirmed the importance of capillary and electrostatic forces; thus, the major emphasis of the present work has been directed toward capillary and electrical phenomena. A theoretical treatment of the capillary force between two spheres of equal radii has shown that there is a maximum size capillary that can exist between two contacting spheres of radius R and that the maximum adhesion force is $5.329R\gamma_s$, where γ_s is the average surface free energy of the solid. A new analog method was developed for determining the charge area density on a conductive particle in contact with a charged conductive surface. The apparatus is described as a coulometric electrolytic tank and employs electrodeposition of metals onto models of the particle shapes under study. The surface mass density of deposited metal is determined by removing known segments of the deposit and weighing them on an ordinary laboratory balance; the distribution of mass per unit area on the model is analogous to the distribution of charge per unit area in the electrostatic case. The interfering effect of ionic diffusion is reduced by proper selection of the plating bath parameters and by control of the maximum current density. The validity of the method is demonstrated by comparing the analog solution for a hemisphere on a plane with the classical solution for a charged plane having a hemispherical boss. Obviously, departure from the known solution for a hemisphere, resulting from diffusion effects, could be treated as a calibration, providing correction factors useful for other geometries; however, the degree of error is seen to be small, and one may determine the surface charge density of rather complex

particle shapes to within less than about 10% error by this method.

The exploding-wire aerosol generator, described in previous reports, has been redesigned, resulting in a more compact, versatile, and portable device. A commercially available 2800-j capacitor and trigger unit form the central core of the exploding-wire device. Various control circuits are included in the new design to improve the safety features developed in operations of the earlier model.

Aerosols generated by the exploding-wire device are being used in a study of the interaction of airborne vapors with particulates. The rate of disappearance of free iodine vapor from a cylindrical tank is about nine times that of sulfur dioxide vapor from the same aerosol chamber in the absence of significant concentrations of condensation nuclei. When nuclei of platinum for iodine and either platinum or ferrosoferric oxide (Fe_3O_4) for sulfur dioxide are added to the chamber, the rate of equilibration of the vapor with the airborne nuclei is about ten times faster in the case of sulfur dioxide. As an adjunct to this study a screening test is being carried out by passing the vapor through a deposit of exploding-wire particulates collected on a membrane filter. Initial studies have been done using 2 different concentrations of sulfur dioxide and 17 different particulate compositions. The preliminary work shows a variety of interactions, some being proportional to concentration and others more related to time of contact.

Investigations of the retention times of particles adhering to the skin have been extended to include estimates of initial retention after impaction at approximately the terminal velocity of the particle in air. All particles less than about 180 μ in diameter were retained, whereas none larger than about 700 μ were retained when the removal force was equal to the force of gravity.

Particle retention time data were combined with measurements of the dose rate in tissue produced by a neutron-irradiated reactor fuel particle to provide an estimate of dose to the skin as a result of "hot" particles being deposited on the skin. The particles were irradiated for 20 min, simulating a short operating time, and, because of the rapid decay of the contained fission products, the expected dose from a given particle depends on the time, after shutdown of the reactor, at which first contact is made with the skin and upon the time of retention. The results are given in terms of the expected dose averaged over an area of 1 cm^2 at a depth of 7.6 mg/cm^2, and the upper and lower limits on the dose are indicated for one standard deviation of the estimate.

28. Applied Internal Dosimetry

During the period June 1, 1966, through May 31, 1967, a total of 896 whole-body counts were made involving 744 persons. Only 10.2% of the persons counted showed detectable amounts of radionuclides other than normal levels of ^{40}K and ^{137}Cs (6 to 9 nc of ^{137}Cs in 1966). Two employees, whose exposure by inhalation of $^{90}SrTiO_3$ particles in January 1964 has been described in earlier reports, have been recounted at approximately monthly intervals for 1260 days; the half-time for lung clearance at the end of the report period appears to be in excess of 1800 days.

The elimination of ^{203}Hg from the body was observed by whole-body counting using a 6-ft arc geometry during the period from 30 to 190 days after injection for medical purposes. In this period the body burden changed by more than two orders of magnitude, and the indicated effective half-life was 25.1 days; based on this, the biological half-life is calculated to be 54 days. Effective half-lives were observed to be 24 days for retention in the liver and 53 days in the kidney region.

The attenuation of x rays from a $^{238}PuO_2$ microsphere was observed as a function of depth in various absorbers simulating tissue as well as in polyvinyl chloride. Because of the presence of chlorine atoms, attenuation is significantly greater in polyvinyl chloride, for which the half-value layer is 120 mg/cm^2 as compared with 680 mg/cm^2 for the other materials. Calibration of a wound probe using the microsphere source indicates that the least detectable amount of ^{239}Pu in a wound varies from 0.01 nc at a depth of 1 mm to 2.4 nc at 33 mm, based on three standard deviations of the background.

A new procedure has been developed to analyze environmental samples for radioactive strontium. The radioisotopes of strontium, barium, and radium are removed from the dissolved sample by retention on a cation exchange resin, and separation of these elements is effected by elution at controlled pH. The recovery of ^{85}Sr tracer in grass, milk, leaves, feces, and bone samples was observed to be greater than 99%.

Part I. Radioactive Waste Disposal

F. L. Parker

1. Fate of Radionuclides in Terrestrial Environment

Tsuneo Tamura
E. R. Eastwood
Joseph Shalhevet[1]
A. S. Rogowski
F. S. Brinkley
O. H. Myers

The soils program includes three major areas of study: (1) from field and laboratory experiments, movement of radionuclides by erosion and runoff is being followed; (2) in the greenhouse, uptake of radionuclides is being investigated, with particular emphasis on moisture content as it affects radiocesium uptake; and (3) in the laboratory, studies are under way to elucidate the mechanism of radionuclide adsorption by natural materials, current emphasis being placed on selective adsorption of tracer levels of cobalt.

DIFFERENTIAL MOVEMENT OF ^{137}Cs AND ^{134}Cs ON RUNOFF PLOTS

A. S. Rogowski E. R. Eastwood

Purpose of the Study

In the study with ^{137}Cs alone, the dependence of cesium loss on soil loss was demonstrated. The time dependence of the cesium-loss function and the seasonal fluctuation of specific loss as a function of time and climatic variables were demonstrated also.[2] The purpose of the differential movement study was to establish the relative contributions of radiocesium in terms of travel distance from the exit drain and its spatial distribution within a plot, thereby providing an additional dimension in the understanding of radionuclide movement by runoff and erosion.

In addition, the new plots were to serve as replicates for the original study, in which ^{137}Cs alone was used. Selection of the dosing date in the spring (March 18, 1966) rather than fall, as was done previously, was to clarify seasonal variations observed before. Application of varying concentrations of radiocesium and stimulation of runoff and erosion on the bare plots were to determine the effects of rate of dosing and the behavior of radiocesium under higher rates of runoff and erosion.

Experimental Procedure

In the spring of 1966 a differential radionuclide movement study was initiated using ^{137}Cs and ^{134}Cs in the study area situated on Captina soil. Three plots were constructed, similar to the plots on which the movement of ^{137}Cs alone was being studied. These 8×8 ft plots (Fig. 1.1) were surrounded by a metal strip sunk into the ground to prevent losses to the outside. They contained runoff sinks in the lowest corners, which were connected to collection pans in which runoff and eroded material could accumulate. The runoff was measured and sampled, and the unused portion was ultimately disposed of into a waste ditch. On the first plot the vegetation was removed entirely; on the second plot the meadow was clipped and allowed to remain on the surface. Both plots received a surface application of herbicide prior to dosing to prevent the reemergence of vegetation.

[1] Visiting Scientist from Rehovoth, Israel.

[2] A. S. Rogowski and Tsuneo Tamura, "Movement of ^{137}Cs by Runoff Erosion and Infiltration: Part 1, Results of Two-Year Study on Small Plots of Captina Soil," to be published.

ORNL-DWG 67-8672

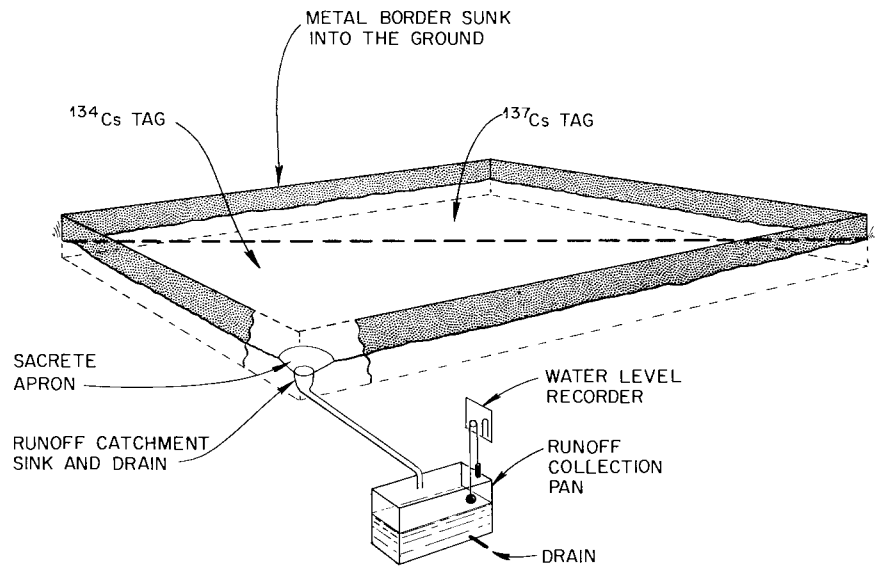

Fig. 1.1. Schematic Diagram of Differential Movement Study Plot. (not to scale)

Table 1.1. Slope, Plot Area, Amounts of ^{137}Cs and ^{134}Cs Applied, Their Respective Areas, and Vegetation Cover on Experimental Runoff Plots

Plot	Slope (%)	Plot Area (m^2)	^{137}Cs ($\mu c/m^2$)	^{137}Cs (m^2)	^{134}Cs ($\mu c/m^2$)	^{134}Cs (m^2)	Vegetation[a] (g/m^2)
1. Bare soil	5	5.6	841	3.0	3869	2.6	
2. Mulch	3	5.7	418	3.0	2397	2.7	582 ± 120[b]
3. Meadow	7	5.1	440	2.7	1462	2.4	802 ± 184

[a]Vegetation given on dry matter basis.

[b]Vegetation on plot 2 was in form of dead grass mulch.

Herbicide treatment turned plot 2 into a mulch plot, simulating initial conditions on the original meadow plot in the previous study. The herbicide chosen for this study, unlike the 2-4-D used previously, was Monobor Chlorate, whose composition was 68% $Na_2B_2O_4 \cdot 4H_2O$ and 30% $NaClO_3$. In addition to killing the vegetation, it was hoped that runoff and erosion rates would be accelerated by inhibiting infiltration through rapid surface sealing with sodium-dispersed clay.

On the third plot the heavy uniform fescue meadow was fertilized at the rate of 300 kg/hectare of nitrogen (applied as ammonium nitrate). Cesium-137 and -134 were applied (Fig. 1.2) to the plots in the form of spray in dilute HCl solution (pH 4). Each plot was divided diagonally (Fig. 1.1) into two halves; ^{134}Cs was applied to the lower half and ^{137}Cs to the upper half. In Table 1.1, prevailing land slope, total plot area, ^{137}Cs and ^{134}Cs concentrations, and their respective areas, as well as the initial vegetation cover, are given.

First Year's Results

In Table 1.2, runoff, soil loss, and ^{134}Cs and ^{137}Cs losses on the bare soil (plot 1), mulch (plot 2), and meadow (plot 3) are given. The

Fig. 1.2. Application of ^{134}Cs and ^{137}Cs on the Differential Movement Study Plots.

Table 1.2. Runoff, Soil Loss, ^{134}Cs Loss, and ^{137}Cs Loss on Three Plots of Differential Movement Study After One Year[a]

Plot	Runoff (liters/m^2)	Soil Loss (g/cm^2)	^{134}Cs Loss (%)	^{137}Cs Loss (%)
1. Bare soil	996	15,255	64.2	76.9
2. Mulch	630	895	40.6	53.2
3. Meadow	336	19	4.1	0.4

[a]Total rain was 121.11 cm (1211 liters/m^2); total energy intensity erosion index was 16.3×10^3 dynes/sec; cesium loss is given as a percent of the total applied originally.

total rain of 48 in. for the year was lower than normal (55 in.) for the area, but the total energy intensity erosion index was a high 16.3×10^3 dynes/sec (expected, 9.9×10^3 dynes/sec). High soil loss on plot 1 (equivalent to 68 tons/acre) and high runoff (82%) are reflected by the high radiocesium loss. Mulch cover on plot 2 afforded some protection with respect to soil loss (4 tons/acre) and runoff (52%), but the radiocesium loss remained high. In the continuing study with ^{137}Cs alone,[2] the radiocesium losses on the clipped meadow plot were also high in proportion to the soil loss. These results suggest that radiocesium on a mulched or clipped meadow is very susceptible to loss by runoff and erosion, perhaps because it can easily be leached from dead vegetation.

Low runoff (28%), low soil loss (0.09 ton/acre), and low radiocesium loss on meadow plot 3 reflect the vigorously growing heavy meadow cover, in contrast to the meadow in the study with ^{137}Cs

alone,[2] where the vegetation was initially dead. Despite a heavy cover, a relatively high loss of ^{134}Cs was observed on the lower half of the plot.

Relative losses of ^{137}Cs from the upper half exceeded those of ^{134}Cs losses from the lower halves of bare soil plot 1 and mulch plot 2. Considering the heavy soil losses from these plots, it is likely that the lower half of the plot acted as an area of deposition for the material eroded from the upper half dosed with ^{137}Cs. Thus the material being eroded in greater proportion appears to have originated in an "upland" area of the plot.

In contrast, on meadow plot 3 little erosion and thus little deposition resulted primarily in the loss of radionuclide from the area adjacent to the exit drain.

In Fig. 1.3, cumulative ^{134}Cs and ^{137}Cs losses are plotted as a function of cumulative soil loss. The dashed line and its equation, $y = 2.2(x/b)^{0.35}$, represent the equilibrium phase curve obtained for the bare soil plot with ^{137}Cs alone.[2] The solid curves were hand-fitted for purposes of illustration, and the resulting equations are included for comparison. The curve for bare soil plot 1 shows good agreement with the previously obtained curve, whereas the curve for mulch plot 2 and the ^{134}Cs curve for meadow plot 3 differ from the original bare soil curve, mainly in the initial amount lost per unit weight as given by the coefficient, although the exponents are also somewhat lower. The ^{137}Cs curve for meadow plot 3 exhibits an exponent (0.92) comparable with that obtained during the initial meadow plot[2] with ^{137}Cs alone (1.0) (curve not shown on Fig. 1.3).

Seasonal variation is particularly apparent if the data points for the ^{137}Cs loss are examined to the left of April 25 and to the right of October 15 (Fig. 1.3) and compared with the data points between these dates. The higher slope of the data points is indicative of the larger exponent. It appears that the increase in radiocesium loss rate, as given by the exponent, takes place mainly in the winter and early spring months in Tennessee; this is due to the climatic variables prevailing in this area.[2] The general orientation of the data points between the dates appears to be flatter. Similar flattening was observed previously and is indicative of decreased loss rates during summer and early fall months.

No apparent differences in the cesium-soil loss relationship could be observed due either to the differences in the rate of dosing or to the increase in the erosion rate, as can be seen from the curves for bare soil plot 1 and mulch plot 2.

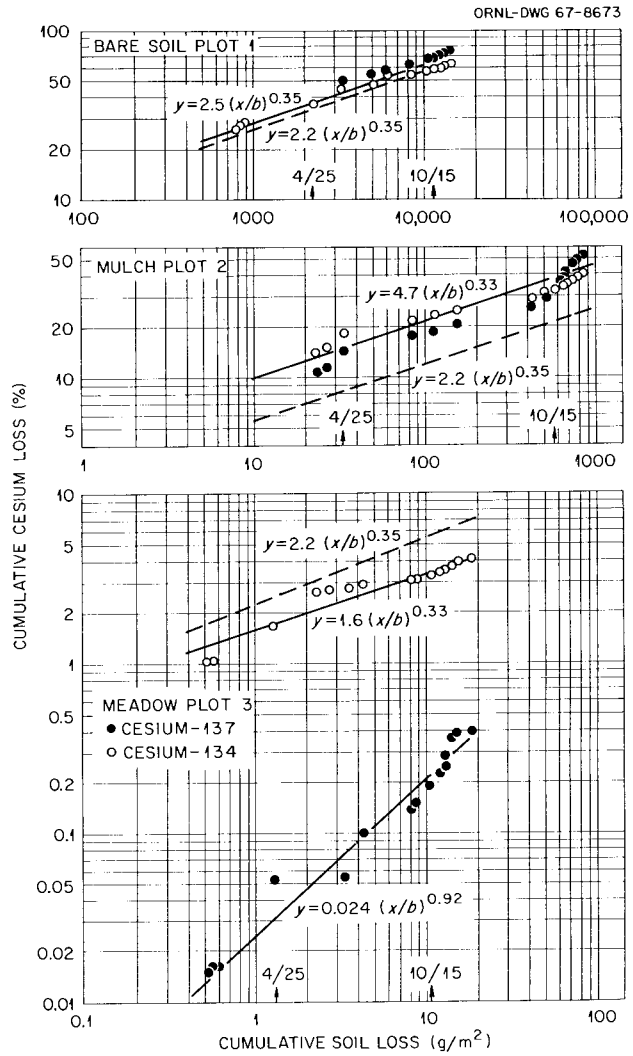

Fig. 1.3. Cumulative Cesium Loss as a Function of Cumulative Soil Loss on Bare Soil Plot 1, Mulch Plot 2, and Meadow Plot 3.

Preliminary Conclusions

On the basis of results of the first year, it is concluded that on the exposed areas, such as the bare soil and mulch plots, radiocesium losses are about uniform, with a higher proportion of radiocesium being lost from the "upland" areas. Under the conditions of heavy cover, such as the meadow plot, radiocesium losses occur primarily from the

area adjacent to the exit drain or, as the case may be, on a watershed with a heavy cover, from the low-lying areas close to the stream bed. It is expected that the relative contribution of radiocesium from the upper portion of the plot will increase with time.

Also the results obtained thus far offer satisfactory replication of the results obtained previously with ^{137}Cs alone.[2] Neither the dosing rate nor the increase in erosion rate appears to influence significantly the basic soil-radiocesium loss relationship.

EFFECT OF SOIL MOISTURE CONTENT ON UPTAKE OF ^{137}Cs BY PLANTS

Joseph Shalhevet Tsuneo Tamura
F. L. Brinkley

Study of the influence of various soil-moisture-content factors on the uptake of radiocesium by plants has some significance in relation to the long-term effects of radioactive fallout or accidental release of radioactivity from nuclear plants.

The present study was undertaken to investigate the role of soil-water content in the recovery of radiocesium by plants. Two different experimental methods were employed to control moisture content. In the first, water content was held relatively constant at various predetermined levels; in the second, water content was allowed to fluctuate – irrigation water was applied as the plants dried the soil to various predetermined levels.

The study consisted of three experiments. In the first, a split-root technique was employed. The growth container, 10 cm in diameter and 20 cm deep, is divided into two chambers by a wax membrane. The membrane is impermeable to water but easily penetrable by roots (Fig. 1.4). The top chamber, 15 cm deep, contains a sand-vermiculite mixture and serves as a water and nutrients supply chamber. The lower chamber, 5 cm deep, contains 18 g of ^{137}Cs-tagged vermiculite mixed with 650 g of fine sand. There are two levels of cesium, 16.4 and 21.8 $\mu c/g$, and three levels of moisutre tension, 30, 45, and 65 millibars, for a total of six treatments in three replications. Porous ceramic disks, placed at the bottom of the lower chambers, were maintained under the desired tensions by hanging water columns of the appropriate lengths. The moisture-characteristic curve of the sand-vermiculite mixture (Fig. 1.5) was determined using the lower chambers. The vertical lines extending from the experimental points in Fig. 1.5 give the range of moisture content from the top to the bottom of the chamber. Tensiometers were placed in the top chambers to indicate irrigation needs.

Fig. 1.4. Experimental Setup.

Results of the second and third harvests are reported in Table 1.3. The first harvest was done shortly after the roots penetrated the lower chamber and discarded, since root development was not the same in all the chambers. The total ^{137}Cs content of the tops is expressed as a ratio of the root weight in the lower chamber. As the soil-moisture tension increased (soil-moisture content decreased), cesium

Table 1.3. Uptake of ^{137}Cs by Sudan Grass as a Function of Suction Applied

	Suction Applied (cm H_2O)					
	30		45		65	
	Expt. 1	Expt. 2	Expt. 1	Expt. 2	Expt. 1	Expt. 2
^{137}Cs content in lower chamber soil, microcuries per gram of soil	0.447	0.594	0.447	0.594	0.447	0.594
^{137}Cs recovered in the plant tops, microcuries per gram of root	0.467	0.580	0.322	0.403	0.208	0.323
Ratio of row 2 to row 1	1.04	0.98	0.72	0.68	0.47	0.54

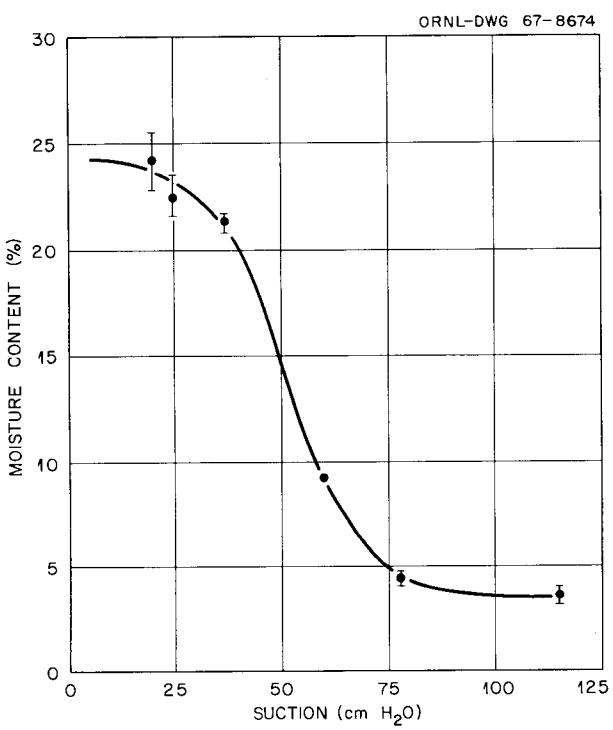

Fig. 1.5. Moisture Characteristics Curve for a Mixture of Vermiculite and Sand (27% Vermiculite) Desorption Cycle.

uptake decreased. The relationship is nearly linear. Uptake was also directly proportional to the ^{137}Cs concentration in the soil (Table 1.3, bottom row). There is very little difference in cesium content in the tops of the plants of each pair with the same moisture tension if uptake is expressed as a ratio of the ^{137}Cs concentration in the soil.

In the second experiment the split-root technique was also used. Placed in the lower chamber were 6.5 g of vermiculite tagged with 20.6 μc of ^{137}Cs per gram mixed with 650 g of fine sand. The sand-vermiculite mixtures were saturated with approximately 150 ml of either 0.01 *N* KNO_3 or 0.01 *N* $Ca(NO_3)_2$ solution. Five days after roots started to develop into the lower chambers, the plants were harvested and suction treatment was initiated. At this writing the plants are growing vigorously, and the first sampling is in progress.

In the third experiment, two naturally occurring soils were used instead of the sand-vermiculite mixture. One soil is predominantly illitic (Sequoia clay loam) and the other predominantly kaolinitic (Fullerton clay loam). Two kilograms of each soil were uniformly tagged with 68.7 μc of ^{137}Cs and placed in 32 plastic containers. The experiment included four irrigation treatments in four replications. The four treatments are: daily watering and watering when the soil moisture suction reaches 0.7, 4.0, or 15 bars. At each watering the soil moisture content was brought back to the 0.1-bar level. Sudan grass plants were used in all three experiments.

RADIONUCLIDE ADSORPTION STUDIES

Tsuneo Tamura O. M. Myers

Studies to characterize the selective adsorption of tracer levels of cobalt in the presence of competing cations (0.1 *N* NaCl) have been in progress

this past year. Initially, these studies confirmed the findings of several earlier workers who found that trioctahedral 2:1 layer lattice minerals sorbed more cobalt than the dioctahedral varieties with the exception of muscovite (di-) and biotite (tri-). Further, it was found that, if the two minerals were acid washed, the muscovite lost its capacity to selectively sorb cobalt, whereas the biotite did not; but, if the muscovite was saturated with aluminum ions, it regained its selective capacity.[3] Other minerals have now been studied, and the results are discussed in this section.

Cobalt Sorption by Hydrobiotite

Hydrobiotite was saturated with Fe^{3+}, Mg^{2+}, Al^{3+}, and Na^{+} ions by adding the appropriate chloride salt, centrifuging, and decanting the supernatant. This was repeated twice. After the third treatment the excess was washed off. In the case of iron saturation, adsorption was followed by $^{59}FeCl_3$ tagging and without repetitive treatment. The sample was therefore only partially (55%) saturated with iron. All other samples were 100% saturated, the method of saturation used being a standard procedure.

The data plotted in Fig. 1.6 represent a solution/solid contact time of one week. The curves depict two types of response. The natural, sodium-, and magnesium-saturated clays sorbed relatively small amounts of cobalt; iron and aluminum clays show low sorption at a pH of around 5, but sorption increases rapidly with increasing pH. The slightly lower adsorption by the iron clay is probably due to the lack of total saturation with iron.

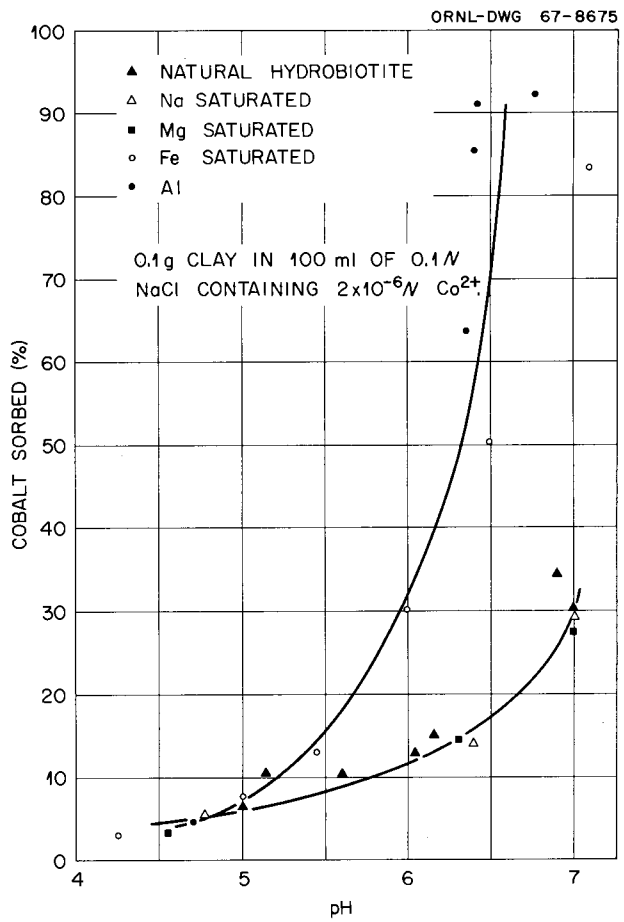

Fig. 1.6. Cobalt Sorption by Hydrobiotite. System contains 0.1 g of clay in 100 ml of 0.1 *N* NaCl containing 2×10^{-6} *N* $CoCl_2$.

Cobalt Sorption by Montmorillonite

Aluminum-saturated montmorillonite sorbed cobalt selectively; however, the natural mineral and sodium-saturated clay sorbed cobalt relatively more efficiently than the hydrobiotite (Fig. 1.7). These responses led to a suspicion that the clay might be "contaminated" with iron or aluminum. To check this possibility, the clay was treated to remove free iron oxide, using the citrate-dithionite technique. The resultant clay showed behavior very similar to hydrobiotite in the sodium- and magnesium-saturated form, as well as in its natural form.

Cobalt Sorption by Illite and Kaolinite

The data in Fig. 1.8 show responses by illite and kaolinite with iron saturation and with the iron removed by the citrate-dithionite treatment, which results in sodium saturation. The kaolinite sample was 100% saturated with iron; however, the illite sample sorbed over 400% of iron as measured by the exchange capacity. This was caused by the presence of calcium carbonate in the sample, which raised the pH and caused hydrolysis of the iron.

[3] Tsuneo Tamura *et al.*, "Fate of Radionuclides in Terrestrial Environment," *Waste Treatment and Disposal Semiannual Progress Report for July–December 1966* (ed. by F. L. Parker and R. E. Blanco), ORNL-TM-1846 (in press).

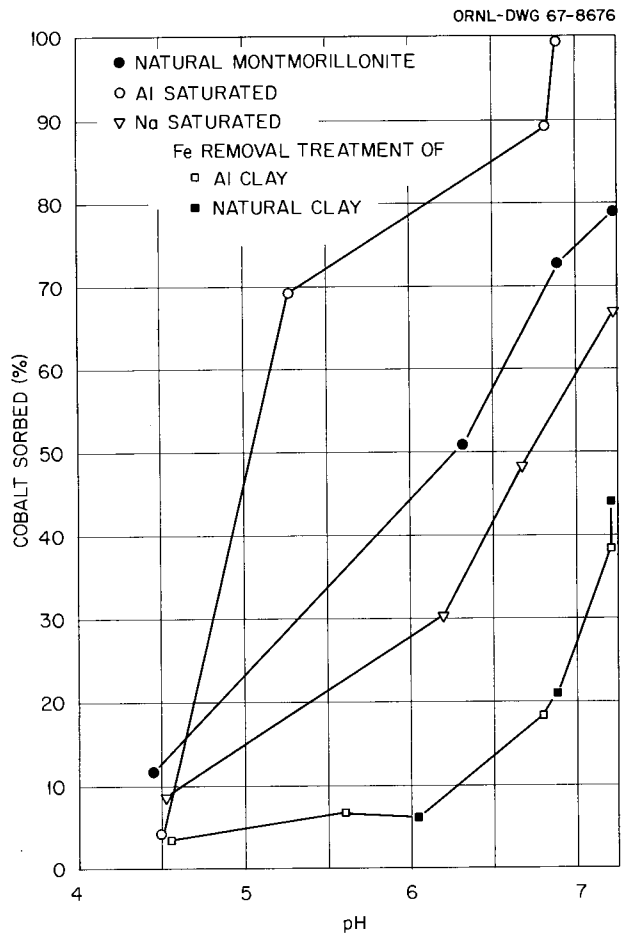

Fig. 1.7. Cobalt Sorption by Montmorillonite (Wyoming Bentonite). System contains 0.1 g clay in 100 ml of 0.1 N NaCl containing 2×10^{-6} N $CoCl_2$.

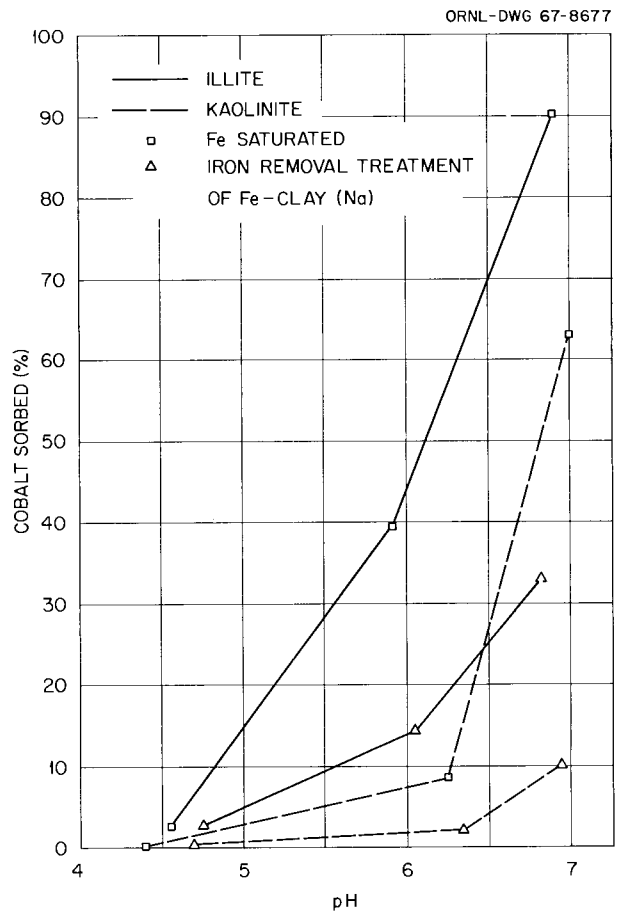

Fig. 1.8. Cobalt Sorption by Fithian Illite and Georgia Kaolinite. System contains 0.1 g clay in 100 ml of 0.1 N NaCl containing 2×10^{-6} N $CoCl_2$.

In both cases the iron-treated clays were superior to iron-depleted clays. The extremely low adsorption by kaolinite may be due to its low exchange capacity (lowest of the four clays), low surface area, and high degree of crystallinity.

Discussion of Results

These results show that aluminum and iron saturation of clays increases their selectivity for tracer levels of cobalt. It is important to note that a decrease in pH of soil systems is accompanied by aluminum saturation of the soil colloids. Furthermore, in the weathering process, iron and aluminum are constantly being released; and iron oxide coatings of minerals are common. Hence, these results with iron and aluminum clays help to understand the natural soil system.

It must be remembered that when tracer levels of ions are involved and when the sorbent materials are "treated" with chemicals, the observed results may not necessarily be due to known effects of the treatment. Small changes of the surface or dissolution of some minor components can accompany the treatment. Indeed, a treatment which is known to work on one mineral may not apply to another. In this regard, results of the iron-removal treatment of the clays can be cited.

The four clays – kaolinite, illite, montmorillonite, and hydrobiotite – were placed in a solution containing $FeCl_3$ tagged with ^{59}Fe. The degrees of ion exchange saturation of the four clays were 100,

460, 82, and 55% for kaolinite, illite, montmorillonite, and hydrobiotite respectively. As noted earlier, the excess sorption by illite was likely due to hydrolysis, since calcium carbonate was present in the sample.

The four clays were then subjected to the iron-removal treatment. Results showed that, based on the initial amount sorbed, removals were 99.1, 98.5, 98.3, and 24.7% for the kaolinite, illite, montmorillonite, and hydrobiotite respectively. Evidently the hydrobiotite did not "release" its iron under this treatment. It was not surprising to find that the hydrobiotite which had been treated by the iron-removal technique did not show a decrease in sorption of cobalt, but it was surprising to find that sorption on the treated sample was even higher than on the 55% iron-saturated clay. A tentative explanation for this might be that the treatment did not remove an appreciable amount of iron sorbed in the interlayer of the mineral but did remove some of the iron from the trioctahedral layer of the mineral, rendering the mineral even more reactive than its original state and the iron-saturated (55%) state.

The exchange capacity of hydrobiotite which had been fully saturated with aluminum was evaluated by the standard technique. The natural material had a capacity of 70 meq/100 g; but after aluminum saturation the material had a capacity of 31 meq/100 g. This shows that about 39 meq (56%) of the aluminum was fixed in the interlayer positions. Such complications make interpretations of results difficult without a thorough study of the system.

2. Disposal By Hydraulic Fracturing

Wallace de Laguna
W. C. McClain
Tsuneo Tamura
F. S. Brinkley

INJECTIONS OF ORNL'S EVAPORATOR CONCENTRATE

Wallace de Laguna Tsuneo Tamura

Progress in fiscal year 1967 was marked by two successful injections of medium-level waste. This is the Laboratory's medium-level waste, concentrated by the new waste evaporator. The injections were not primarily experimental, but were made for the purpose of disposing of this waste. Prime responsibility for the injections rested with the Operations Division, but the work was carried out jointly with the Health Physics Division, the Plant and Equipment Division, and the Halliburton Company. This cooperative arrangement is working well and will probably continue.

The first injection was made on December 12 and 13, the two-day interval being needed to pump more liquid waste over to the disposal plant, as the tank capacity at the plant site was limited. A total of 62,000 gal of liquid waste was mixed with 217 tons of dry solids, largely portland cement, fly ash, and clay, to give a total of 96,000 gal of slurry. The total injection time required on the two days was about $6\frac{3}{4}$ hr, so that the average injection rate was 240 gpm. The waste contained about 20,000 curies of ^{137}Cs, 21 curies of ^{106}Ru, 8 curies of ^{60}Co, and 3 curies of ^{90}Sr. In addition to the liquid waste, about 3800 gal of water was injected for startup and cleanup. The total volume of bleedback from the well was about 2000 gal, but this water contained only 3 curies of activity, largely ^{137}Cs, so the prescribed mix appears to have performed satisfactorily.

The pressure required to start the injection was 1600 psi, and the wellhead pressure remained within about 100 psi of this value during the first day of operation. The pressure required to start the injection the next day was about 1700 psi, and during this operation, also, the pressure remained within about 100 psi of the starting pressure. These relatively low and constant injection pressures were a somewhat unusual feature of the operation.

The slot used for these injections was at a depth of 872 ft, the same slot which had been used for the sixth and seventh experimental injections. During these earlier injections, some 215,000 gal of grout had been injected, so that the total volume pumped into this fracture after the December injection was over 300,000 gal.

The second pair of injections was made on April 20 and 24, 1967. Again, the interval was used to refill the waste storage tanks at the plant site, where the waste storage capacity had been increased to about 80,000 gal. The total volume of waste injected on these two days was 163,000 gal, which, mixed with some 500 tons of dry solids, gave a slurry volume of 230,400 gal. This was injected into a new slot at a depth of 862 ft. The breakdown pressure for this new fracture was 2500 psi. The injection on April 20 started with a pressure of about 2400 psi, which fell to about 2000 psi as the injection continued. On April 24 the injection pressures were virtually identical.

The injection plant proper is now essentially complete, although modifications and some additions will undoubtedly be required later. As yet, only a few wells have been constructed for logging or for tests of the rock cover, so that only fragmentary information is available as to where the grout sheets are going or what may be happening to the rock cover.

Uplift Measurements

A review of the results of the leveling used to measure the surface uplift resulted in a recalculation of the data using a somewhat more sophisticated system for adjusting the traverses. There appear to be two sources of error in this work, one resulting from the limitations in accuracy possible even with the best methods and equipment, and the other from occasional slips, as from the settling of one of the legs of the tripod or from the rod not being vertical. By rerunning a few of the readings following an analysis of the field data, the errors in closure have been cut by about half. These errors are now about 0.002 ft in traverses which, out and back, are nearly a mile long.

The new data suggest that the volume of the surface uplift is somewhat less than first calculated, but it still appears to be greater than the volume of grout injected. Attempts were made to measure the uplift directly in one of the observation wells with a wire anchored at the bottom and held under constant tension at the top, but the wire proved unsatisfactory. It is planned eventually to try again using a rod rather than a wire, but the well will have to be specially constructed for this purpose. The aim is to determine if there is any settling of the cover rock following an injection, which may help to decide if the rock is acting elastically or in part plastically.

Gamma-Ray Logging

The seven wells available have been carefully logged prior to and shortly after each injection using a gamma-sensitive probe containing a scintillation detector. The unit was built to measure the natural radioactivity of rock and had an upper useful limit of 0.2 mr/hr. This was extended to about 3.0 mr/hr by increasing the bias on the preamplifier in the probe. However, tests with a radium source showed that the crystal-photomultiplier module "saturated" at 14 mr/hr, following which the probe appeared to be oversensitive. A new probe with a smaller crystal has been ordered so that the waste-grout sheets may be mapped more accurately. The fields in the gamma-ray logging wells opposite the waste-grout sheets appear to be as high as 100 mr/hr.

ROCK MECHANICS

W. C. McClain

The analysis of stresses induced in the rocks around the injected grout sheets[1,2] has led naturally to the suggestion that hydraulic fracturing can be used for the expressed purpose of measuring the state of stress in the earth's crust. Some knowledge of the state of stress in the earth's crust is essential in the design of underground excavations in the mining-, civil-, and military-engineering fields and would also be helpful in the petroleum industry. However, the largest application of any method capable of measuring earth stresses would probably be in geophysical research. Knowledge of the crustal stress fields and their fluctuations in time and space would contribute significantly to the understanding of deformational processes, especially the origins, mechanisms, and prediction of earthquakes.

The geologic history, which can be read from rocks, indicates that the earth's crust has been subjected to a complex stress history. The rocks are compacted during the deposition and lithification stage, horizontally compressed, folded and thrust faulted up into mountains, stripped of overburden pressures by erosional processes, pulled apart by regional stresses causing normal faults, and crushed against one another in transcurrent faulting. And, yet, the only estimates of the present state of stress in the crustal rocks which can be made are that one of the principal stresses is vertical and due only to the weight of the overlying material [Eq. (1)], and that the horizontal principal stresses are those resulting from either the elastic [Eq. (2)] or the plastic [Eq. (3)] response of the rocks to that vertical stress. These estimates, in mathematical form, are:

$$S_z = -\mu H \ , \tag{1}$$

$$S_x = S_y = \frac{\nu}{1-\nu} S_z \ , \tag{2}$$

$$S_x = S_y = S_z \ , \tag{3}$$

[1]W. C. McClain *et al.*, *Health Phys. Div. Ann. Progr. Rept. July 31, 1966*, ORNL-4007, pp. 10–12.

[2]W. C. McClain *et al.*, *Waste Treatment and Disposal Semiannual Progress Report, July–December 1966* (F. L. Parker and R. E. Blanco, editors), ORNL-TM-1846 (in press).

where

S_z, S_x, S_y = vertical and horizontal principal stress (tension is positive),

ν = in situ Poisson's ratio of the rocks,

μ = density factor (usually taken at 1 psi per foot of depth),

H = depth below ground surface.

Equation (2) requires that the rocks have behaved isotropically and elastically from the moment of their deposition. Equation (3) assumes the rock will flow plastically under any principal stress, resulting eventually in a hydrostatic stress condition. Neither of these assumptions is supported by observational or experimental evidence. For this reason, and their total disregard of the possibility of tectonic stresses, estimates of the state of stress based on Eqs. (2) and (3) must be considered wholly unsatisfactory.

A number of workers[3-8] have attempted to measure the state of stress either by the overcoring method or the flat-jack method from some underground access. In the overcoring method, an instrument sensing diametral deformations is installed in a drilled hole and then is stress relieved by overcoring; that is, cutting the portion of rock containing the instrument away from the formation. The measured strain taking place in the rock between the full-stress and zero-stress conditions yields the two components of the original stress field perpendicular to the axis of the borehole when reduced using the theory of elasticity. In the flat-jack method, the strain on the surface of the rock is measured while a slot is being cut. A pillow-like hydraulic flat-jack is then grouted into the slot and pressurized until the rock strain is exactly counteracted. The fluid pressure in the jack is then equal to the original stress component perpendicular to the plane of the slot. In both methods, the depth into the rock at which the measurement can be made is limited. The measured stresses therefore include the stress concentrations around the access openings. Both methods require a linearly elastic behavior for the sampled portion of rock, which has to be representative of the rock mass. The overcoring method also requires accurate determination of the elastic properties. These restraints severely limit the applicability of these techniques. Even in hard, dense, homogeneous rock, results have shown a wide variability.[4,8] Therefore, there is no way, at the present time, to measure reliably or even estimate the state of stress in the earth's crust.

The possibility of using the standard oil-field technique of hydraulic fracturing for measuring earth stresses has only recently been recognized.[9] In hydraulic fracturing,[10] an oil well is subjected to a high fluid pressure which produces a fracture deep into the reservoir rock, which is then propped open with sand. The fracture provides flow channels and a greatly increased drainage area, thus increasing the effective permeability of the formation and improving the productive performance of the well. Recent theoretical work[11,12] has shown that pump-pressure records obtained during hydraulic fracturing operations can sometimes be used to determine the regional stresses at the fracture point. The system appears to have several attractive advantages for stress measurement:

1. Stresses can be determined at any distance from the access point, limited only by the hole-drilling capability.
2. Earth stresses are measured directly as a fluid pressure, thus eliminating the necessity of sophisticated strain-measuring instruments.

---

[3]Nils Hast, *The Measurement of Rock Pressure in Rivers*, Sveriges Geologiska Undersokning, Stockholm, 1958.

[4]Leonard E. Obert, "In Situ Determination of Stress in Rocks," *Mining Engineering* 14(8), 51–58 (August 1962).

[5]L. A. Panek, "Measurement of Rock Pressure with a Hydraulic Cell," *Mining Engineering* **222**, 282–85 (March 1961).

[6]J. C. Jaeger and N. G. W. Cook, "Theory and Application of Curved Jacks for Measurement of Stresses," pp. 12-1 to 12-21 in *Proceedings of International Conference on State of Stress in the Earth's Crust, Santa Monica, 1963.*

[7]R. H. Merrill, "In Situ Determination of Stress by Relief Techniques," pp. 8-1 to 8-36 in *Proceedings of International Conference on State of Stress in the Earth's Crust, Santa Monica, 1963.*

[8]R. E. Leeman, "The Measurement of Stress in Rock," Parts I, II, and III, *J. S. African Inst. Mining Met.* **65**(2), 45–114; **65**(4), 245–84 (1964).

[9]C. Fairhurst, "Measurement of In Situ Rock Stresses, with Particular Reference to Hydraulic Fracturing," *Rock Mech. Eng. Geol.* **2**(3-4), 139–47 (1964).

[10]Halliburton Co., Frac-Plan, Duncan, Okla., 1960.

[11]A. E. D. Scheidegger, "Stresses in the Earth's Crust as Determined from Hydraulic Fracturing Data," *Geol. Bauw.* **27**(2), 45–53 (1962).

[12]R. O. Kehle, "Determination of Tectonic Stresses Through Analysis of Hydraulic Well Fracturing," *J. Geophys. Res.* **69**(2), 259–73 (Jan. 15, 1964).

3. Since a linear elastic behavior of the rocks is not required, stresses can be determined in a vastly increased variety of rock types and locations.
4. Only the regional stresses are measured without interference from stress concentrations, small local stress anomalies, and internal stresses[13] which give rise to inaccuracies in overcoring methods.

Theory of Stress Measurement by Hydraulic Fracturing

Hydraulic fractures were first discovered by the nuisance they created during other oil-field operations[14] involving high fluid pressures in a well (e.g., squeeze cementing, water flooding, and drilling with high-density mud). Purposely forming these fractures was rapidly developed into a standard well-treatment technique which has been performed over 400,000 times since 1949. For many years, a heated controversy raged over the role of penetrating and nonpenetrating fracturing fluids in the development of vertical or horizontal fractures. This discussion was settled by a pioneering paper by Hubbert and Willis,[15] which proved both theoretically and experimentally that the orientation of hydraulically induced fractures was controlled primarily by the original stress field at the fracture. They showed that the fracture will always be oriented perpendicular to the direction of the least compressive principal stress; that is, where the least amount of work is required to force open the fracture.

The relationship between the regional stresses and the fracturing pump-pressure data implied by Hubbert and Willis was further developed by Scheidegger[11] and Kehle,[12] using the idealized pressure record shown in Fig. 2.1. All fluid pressures are those measured at the fracturing depth and therefore do not include the hydraulic head nor the viscous losses in the well. The signif-

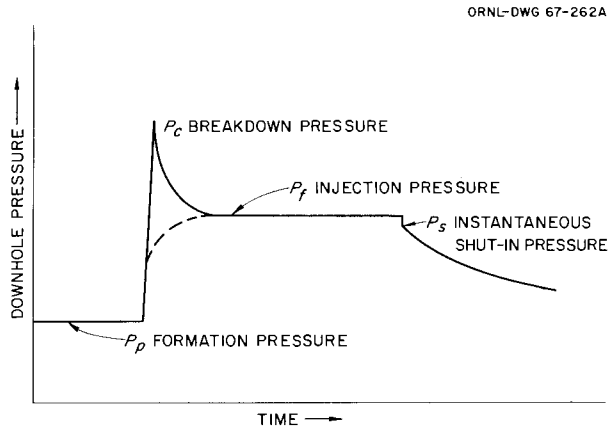

Fig. 2.1. Schematic Pressure Curve for Hydraulic Fracturing Operation.

icant pressures which occur during the fracturing operation are defined as (Fig. 2.1): P_p, the pore or formation pressure, that is, the fluid pressure existing in the pore spaces of the rock; P_c, the breakdown pressure, a pressure maximum which is usually, but not always, attained shortly after the start of the operation and representing the initial rupture of the rocks; P_f, flow or injection pressure, the fluid pressure required to extend the fracture; and P_s, instantaneous shut-in pressure, the fluid pressure immediately after pumping has ceased and the well sealed. Kehle's interpretation of these pressures is based on his analysis of the stresses induced in the rock around a pressurized portion of the borehole delineated by packers (Fig. 2.2). The induced stresses at the wall of the hole, shown on Fig. 2.2 in terms of the fluid pressure in the pressurized interval, define two regions of interest:

1. The central area between the packers, comprising some 80% of the packed-off zone, where the induced tangential stress (σ_θ) is equal to the fluid pressure (P) and the induced vertical stress (σ_z) is nearly zero.
2. A narrow zone at both ends of the packed-off interval and immediately adjacent to the packer, where the induced tangential stress (σ_θ) is essentially zero and the induced vertical stress (σ_z) approaches the fluid pressure (P).

The total stresses at the wall of the hole can be obtained by adding these stresses induced by the fluid pressure to the regional stresses. At this

[13] C. L. Emery, "Strain Energy in Rocks," pp. 4-1 to 4-39 in *International Conference on State of Stress in the Earth's Crust, Santa Monica, 1963.*

[14] W. E. Hassebrock and A. B. Waters, "Advancement Through 15 Years of Fracturing," *J. Petrol. Technol.* **16**, 760–64 (1964).

[15] M. K. Hubbert and D. G. Willis, "Mechanics of Hydraulic Fracturing," *Trans. AIME* **210**, 153–68 (1957).

ORNL-DWG 67-261A

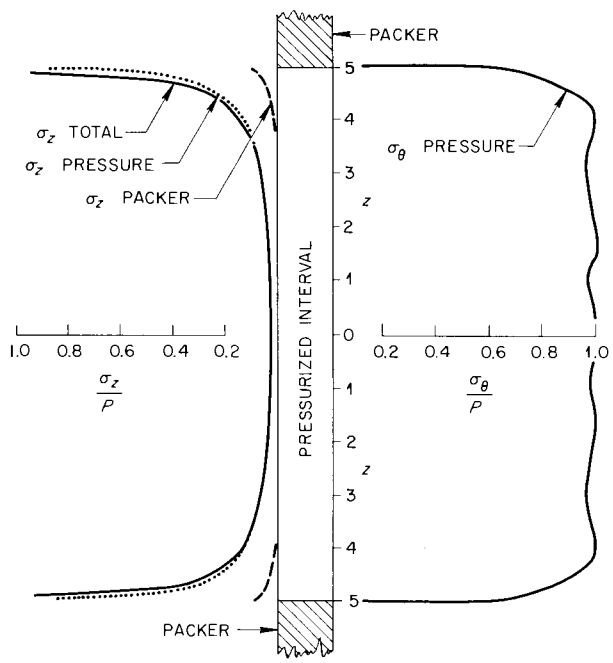

Fig. 2.2. Plot of the Vertical and Tangential Stress Induced by the Well-Fracturing Operation (After Kehle).

point, it is necessary to make the assumptions implied in Eq. (1); that is, one of the principal earth stresses (S_z) is oriented in the vertical direction and is equal to the weight of the overburden. The two horizontal principal regional stresses (S_x, S_y) can be any value, with S_x considered the larger (least compressive). These horizontal stresses will be concentrated around the borehole in such a way that the tangential stress at the wall of the hole is given by:[16]

$$S_\theta = S_x + S_y + 2(S_x - S_y)\cos 2\theta \ , \tag{4}$$

where

S_θ = tangential stress at any point around the hole,

θ = angle between principal stress axis and the point in question on the wall of the hole.

[16]T. Timoshenko and J. N. Goodier, *Theory of Elasticity*, McGraw-Hill Book Company, New York, 506 pp., 1951.

The maximum tangential stress occurs at two points around the hole ($2\theta = 0, \pi$) and is given by

$$S_\theta \max = 3S_x - S_y \ . \tag{5}$$

Therefore, the total radial, vertical, and tangential stresses at the wall of the hole (S_r, S_z, S_θ) for the two areas of interest are: at the center of the pressurized interval

$$S_r = -P \ , \tag{6a}$$

$$S_z = \mu H \ , \tag{6b}$$

$$S_\theta = 3S_x - S_y + P \ ; \tag{6c}$$

and at the ends of the pressurized interval

$$S_r = -P \ , \tag{7a}$$

$$S_z = -\mu H + 0.94P \ , \tag{7b}$$

$$S_\theta = 3S_x - S_y \ . \tag{7c}$$

During the fracturing operation, the fluid pressure (P) is increased until one of the total stresses [Eqs. (6), (7)] reaches the value of the tensile strength of the rock, which then ruptures. This occurs at the breakdown pressure P_c. At the moment of rupture, two possibilities exist: either the fracture is vertical and from Eq. (6c)

$$3S_x - S_y = -P_c + J_x \ , \tag{8}$$

where

J_x = tensile strength of the rock perpendicular to the x direction,

or the fracture is horizontal and from Eq. (7b)

$$S_z = -\mu H + 0.94P_c - J_z \ , \tag{9}$$

where

J_z = tensile strength of the rock perpendicular to the z direction (i.e., horizontally).

After the fracture has been extended beyond the stress concentrations around the hole, the pressure required to extend the fracture (P_f) is only

slightly greater than the stress acting perpendicular to the fracture plane, which is the least compressive of the three principal stresses. The fluid pressure required to just maintain the fracture without any extension should be, therefore, equal to that principal stress. This fluid pressure is the instantaneous shut-in pressure, P_s. For a vertical fracture, where, by definition, $S_x > S_y$,

$$S_x = -P_s \ , \tag{10}$$

and the three principal stress components of the original stress field are completely defined by Eqs. (1), (8), and (10). For a horizontal fracture,

$$S_z = -P_s = -\mu H + 0.94P_c - J_z \tag{11}$$

and the state of stress remains undefined.

A third possibility is that a horizontal fracture could have been initiated which then reverts to its normal vertical orientation and "backs up" into the well. This behavior is a consequence of the concentration of regional stresses around the hole. In this case, two of the principal earth stresses are defined by

$$S_z = -\mu H \ ,$$

$$S_x = -P_s$$

as before, but only the range of the third principal stress can be established:

$$-P_s > S_y > -3P_s + \mu H \ . \tag{12}$$

This theoretical analysis can be modified to include approximately the effects of interstitial pore pressure in the fractured rock by incorporating the concept of "effective stress." If a porous material, permeated with fluid under pressure, is subjected to an external compressive stress, the structure of the material experiences an effective stress equal to the difference between the external stress and the pore pressure. Using this concept, the stresses in Eq. (6) become

$$S_r = -(P - P_p) \ ,$$

$$S_z = -(\mu H - P_p) \ ,$$

$$S_e = 3(S_x + P_p) - (S_y + P_p) + (P - P_p) \ .$$

In summary, it was seen that the state of stress in the earth's crust can be completely determined by the hydraulic fracturing technique if certain conditions are satisfied and if a vertical fracture is developed. If a horizontal fracture is initiated, a complete solution cannot be obtained, although some information concerning the state of stress is recovered. The principal condition which must be satisfied is that one of the principal earth stresses is oriented vertically and is equal to the overburden pressure.

A program to investigate the possibility of developing the earth-stress measuring capabilities of the hydraulic fracturing method is currently under consideration.

3. Disposal in Natural Salt Formations

PROJECT SALT VAULT

R. L. Bradshaw
F. M. Empson
T. W. Hodge, Jr.
B. L. Houser
Hisashi Kubota[1]
T. F. Lomenick
W. C. McClain
Roger Rzekiecki[2]
R. C. Sexton[3]
H. J. Wyrick

Project Salt Vault is a demonstration disposal of high-level radioactive waste solids, with irradiated Engineering Test Reactor fuel assemblies in lieu of actual solidified wastes. This demonstration is being carried out in the Carey salt mine at Lyons, Kansas. Major objectives are the confirmation of feasibility and safety of disposal in salt mines, including demonstration of required waste-handling equipment and techniques, and the collection of rock mechanics data sufficient to establish the basis for the design of a disposal facility.

Fuel Assembly Changeouts and Operational Experience

The first set of irradiated fuel assemblies stored in the relatively pure salt floor in room 1 were transferred in June 1966 without incident to the new experimental facility in room 5 to determine the effects of shale and its included moisture. The second set of 14 irradiated Engineering Test Reactor (ETR) fuel assemblies from the National Reactor Testing Station was shipped from Idaho to Lyons, Kansas, and on June 13 to 15 was lowered 1000 ft into the mine and placed in the experimental facility in room 1. This second shipment contained about 1.5 million curies and was lowered without difficulty. Radiation fields higher than in the previous run were found in the test holes. No personnel exposures greater than 70 millirems were incurred during the transfer operations. Negligible contamination of the shipping cask was found after the discharge of the fuel assemblies.

In October 1966, the first set of fuel assemblies was removed from room 5 and returned to Idaho. The second set of ETR fuel assemblies (which had been installed in the array of holes in the relatively pure salt of room 1 in June) was moved to the array in room 5, in the original mine floor, during the first week of November. On November 7 to 10, 1966, the third set of ETR fuel assemblies (containing a total of about 1.5 million curies) was lowered into the mine and placed in the holes vacated in room 1. The chief difficulty encountered was malfunction in the hydraulic system of the underground transporter caused by pieces of rubber from the inside of the hydraulic hoses.

Each canister contained approximately 200,000 curies of activity when it was received at the mine. All handling operations at the mine were performed by remote control without the aid of hot cells. The highest dose to any of the personnel during the handling operations so far completed was 200 millirads, to the head and hands only. Throughout the operation, there have been no accidental exposures nor any releases of activity to the off-gas system. It is felt that the first two objectives of the experiment – the demonstration of the feasibility and safety and the demonstration of handling equipment – have been successfully achieved.

In addition, as will be explained in the next section, the radiation dose to the salt has exceeded the minimum goal; therefore it was decided to terminate the radioactive phase of the test in June 1967. The fuel cans from room 5 in the original mine floor were returned to Idaho the week of June 12, and those from the main array were returned the week

[1]Analytical Chemistry Division.
[2]Alien guest from France.
[3]Plant and Equipment Division.

of June 26. Other phases of the test will proceed as planned into fiscal year 1968.

Radiation Dose to Salt

The measured peak radiation dose to the salt in the main array, at the junction between the two ETR fuel assemblies, was about 3.7×10^8 rads as of November 1, 1966 (see Fig. 3.1, bottom curve, solid dots). By May 1967 the total was about 5.3×10^8 rads (Fig. 3.1). Generally, the accuracy of the dose measurements themselves is believed to be within about 20%. However, the point at which the measurements of the incident dose to the salt are made (the junction between the assemblies) is such as to produce dose values which are lower than the average incident salt dose (over the 6-ft length of the tandem fuel assemblies) by about

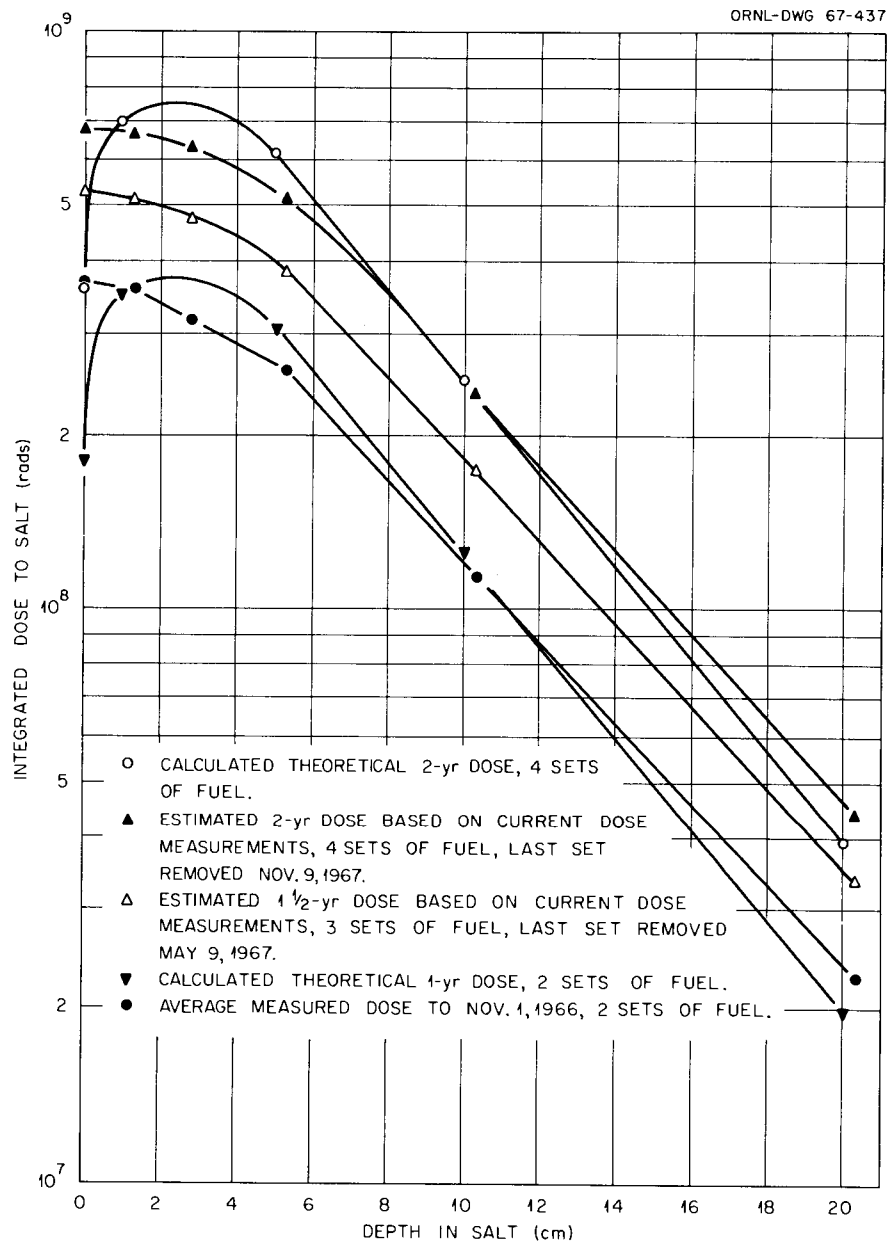

Fig. 3.1. Comparison of Measured and Calculated Doses to Salt in Project Salt Vault.

35%, and lower than the peak dose (near the centers of the individual fuel assemblies) by nearly a factor of 2. The reason for this may be seen in Fig. 3.2, which shows the actual dose distribution measured along the outside of an array hole liner along a line which is about $4\frac{1}{4}$ in. from the center of the liner. The measurements appear reasonable, since the power in the lower fuel assembly was reported by ETR operations to be about 15% higher than in the upper assembly. (Other cans show similar profiles.) For comparison purposes the incident dose measured in the normal manner is shown. This point is 6 in. from the center of the liner, and the relationship between this reading and the one closer to the hole liner is approximately what would be expected when the distance from a cylindrical source is considered.

It should be noted that the measured doses for salt depths up to about 5 cm would also be expected to be lower than the maximum, due to the fact that all of the dosimeters, except the incident, are located at varying distances above or below the junction of the two fuel assemblies. The 10- and 20-cm dosimeters are located near the points of maximum dose, and thus should be approximately correct.

It should also be noted that, *in the following discussions, corrections based on the above considerations have not been taken into account. Thus, in particular, the incident salt doses may be assumed to be quite conservative.*

From Fig. 3.1 it may be seen that if the fourth set of fuel assemblies is assumed to be identical to the third, the peak dose accumulated to next

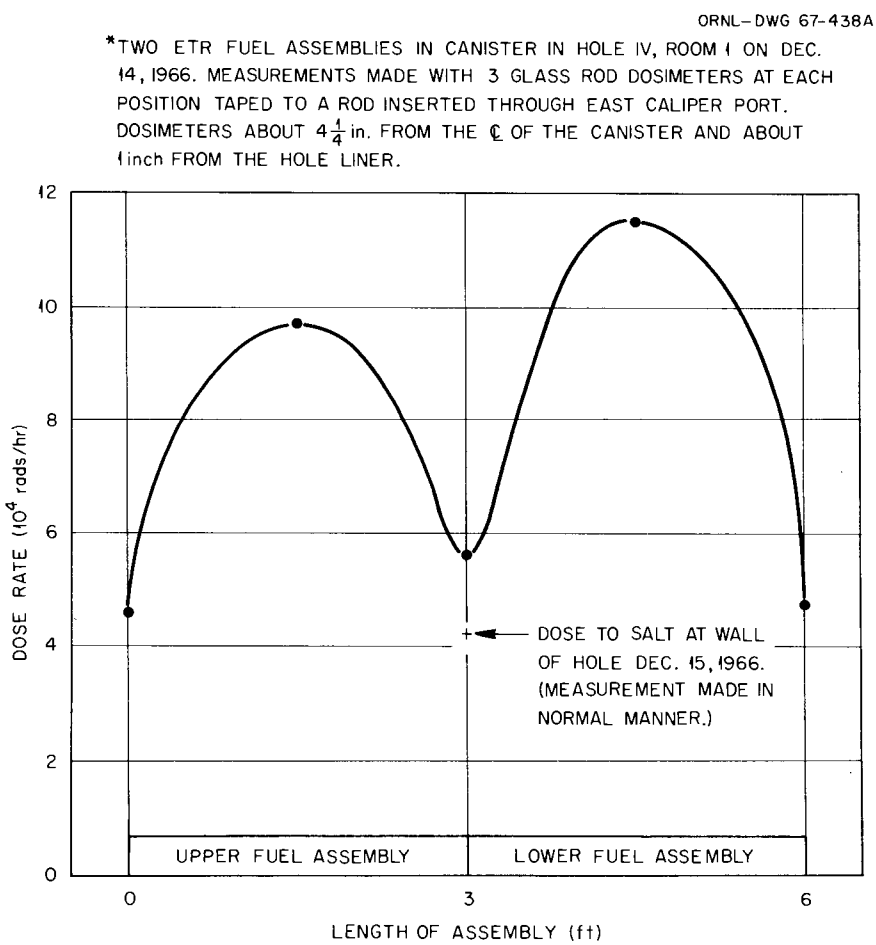

Fig. 3.2. Dose Distribution Along ETR Fuel Assembly Canister.

November would be about 6.8×10^8 rads. This compares favorably with the calculated theoretical curve (Fig. 3.1), which was based on the nominal ETR fuel history used in the design of the experiment. The chief difference is the fact that the peak dose rate appears to be at the salt surface rather than at a depth of about 2 cm. This appears to be of no consequence.

The original goal, to achieve a peak dose of at least 5×10^8 rads, has been met. The 5×10^8 minimum was based on the fact that at 10^8 rads there was no indication of any change in the physical properties of salt, while at 5×10^8 there was an indication of a small change in such properties as the compressive strength. On the other hand, a hypothetical Acid Purex solid waste of the future would deliver a calculated peak dose of about 4×10^9 rads in two years, and more than 10^{10} rads ultimately. It would be impractical to attempt to reach these levels until actual waste solids become available. In any case, only the first few inches of salt adjacent to the containers would be exposed to such levels.

In view of the fact that both field and laboratory studies now confirm that the radiation effects on salt do not appear to have any detrimental effects for waste disposal, there did not appear to be any need for bringing in the fourth set of fuel assemblies. The approximately 30% increase in total dose which would accrue with the fourth set of fuel assemblies would be unlikely to produce any new results. For example, even if the salt around the waste containers were to lose all its structural strength, the extent of the damaged zone (even for the future wastes) would be enough that it should have no significant effect on mine stability.

Effects of Heat and Radiation in Array Rooms

The only distinguishable effect of radiation so far determined has been the intermittent production of extremely small quantities (less than 1 ppm in the off-gas) of an oxidizing gas. The generation of this gas, which is not radiolytic chlorine nor hydrogen peroxide, appears to be a function of dose rate and dependent upon a threshold salt temperature of approximately 175°C. A sample collected in a cold trap and analyzed on a gas chromatograph indicates that the material is a molecule with a weight greater than 200. The material does not appear to attack stainless steel, and the quantities appear to be too low to constitute a health hazard in a waste-disposal operation. Additional samples are being analyzed in an attempt to identify the material.

Peak temperatures in the centers of the arrays were running about 150°C (except in the array in the old mine floor, where they were around 160°C). More heat was being lost to the room air than would be conducted through the salt if the room were backfilled with salt or if there were a solid mass of salt. Consequently, each array was insulated over an area of about 16 ft square (on standard day 1116) to see if this would increase the peak temperature significantly. The net result was higher temperatures in the salt above the centers of the arrays but no appreciable increase in the peak temperature at the periphery of the array holes.

The objectives of the experiment called for achieving a peak temperature of about 200°C. The chief reason why this level had not been reached is that the salt appears to have somewhat better heat dissipation properties than those assumed in the theoretical calculations (200°C values of Birch and Clark). (These somewhat pessimistic values were used for the calculations to make sure the temperatures did not tend to go too high.) In order to reach the desired 200°C, the total power input (fission product plus electrical) was increased about 40% (to 2.1 kw per hole) on January 23, 1967 (standard day 1240 on Fig. 3.3). Peak temperatures in the centers of the arrays at the beginning of June were about 200°C in the main radioactive array (room 1), 195°C in the control array (room 4), and 215°C in the radioactive array in room 5. The upper curve of Fig. 3.3 shows the temperature of salt at a point $1\frac{1}{2}$ ft from the center of the main array.

Some of the deformations of the salt around the main radioactive array are illustrated in Fig. 3.3. These data are also typical of the electrical (control) array. Initially, a constant heat generation of 1.5 kw was maintained on each of the array holes by compensating for the decrease in fuel assembly decay heat by gradually increasing the supplemental electrical heat delivered to each hole. The dashed curve on Fig. 3.3 shows the temperature increase of the salt in the central region of the array. The disrupting influence of the two exchanges of canisters and the effect of the increase in heating rate to 2.1 kw/hole can also be seen. Curve 1 on Fig. 3.3 shows the uplift of the floor

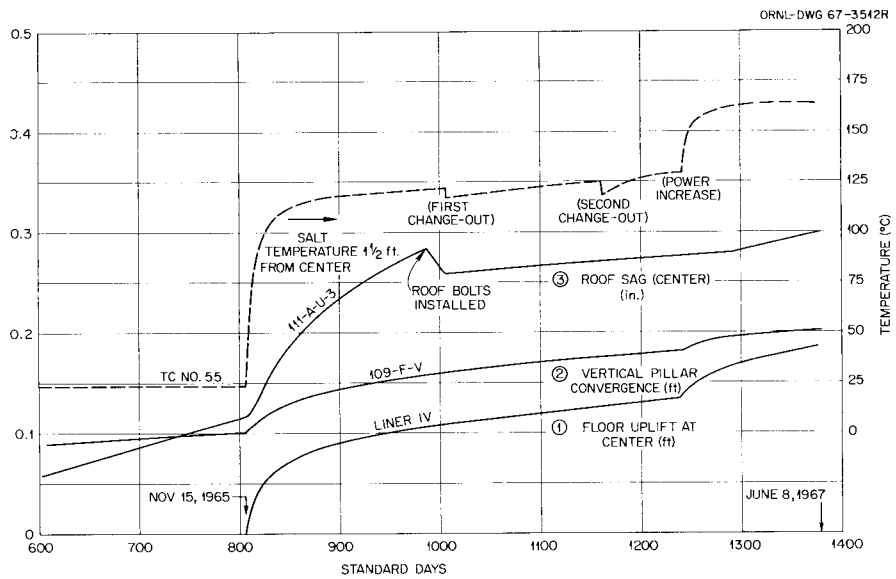

Fig. 3.3. Thermal Effects on Salt Around Experimental Rooms.

(in feet) at the center point of the array due to thermal expansion of the salt. This vertical movement of the floor was distributed across the room in the shape of a normal error curve, the limbs of which extend well beyond the edges of the salt pillars supporting the room. This thermal expansion of the floor under the edges of the pillar caused an immediate acceleration of the deformation of the pillar, the vertical component of which is shown by curve 2 on Fig. 3.3. Although an accelerated deformation of the pillars with heat was anticipated, several weeks were required before there was any significant temperature increase in the pillar.

The immediate roof of the entire experimental area consists of a 2-ft-thick bed of salt which had separated from the overlying material along a thin shale parting. Instruments in the area indicated that this roof bed was sagging into the experimental rooms at the rate of about 0.1 in./year during the period immediately prior to startup on November 15, 1965 (curve 3, roof sag in center of room in *inches*). Roof sags of this type are well known in salt mines, and this sag rate was not considered to be excessive. As can be seen on curve 3, Fig. 3.3, the accelerated deformation of the pillar was transferred to the sagging roof bed in the form of an axial load, which caused a fivefold increase in the rate of sag immediately after startup.

Because of the nature of the experiment and the planned extensive heating of the pillar in the center of the experimental area, roof bolts were installed throughout the area to support the 2-ft roof bed, even though this accelerated sag by itself did not create a hazardous condition. The effect of these roof bolts is shown on the continuation of curve 3, where it can be seen that the roof was lifted slightly at about standard day 1080, and the rate of sag was reduced to about one-fourth of its original (preheating) rate. It may also be noticed from curve 3 that the rate of separation increased slightly after the power increase at 1240 days, but it is still lower than it was before the start of the test in November 1965. Although the curves for the control array (room 4) corresponding to these are essentially the same, the increase in curve 3 after the power boost was not observed. This is *not* interpreted to have anything to do with the absence of radiation, but rather due to slight variations in the salt from room to room.

The results for the second radioactive array (room 5) are similar, except there has been no separation of salt in the roof; and none was expected, since there are no significant shale layers in the first 8 ft of roof. Temperature rises and floor uplift in room 5 are a few percent higher due to the poorer heat transfer properties caused by the presence of layers of shale and anhydrite in the floor.

The experience with the roof bed illustrates several important points pertaining both to the Project Salt Vault demonstration and to the operation of any

high-level disposal facility in salt deposits. First, the structural properties of salt are not completely understood, especially the mechanical behavior at elevated temperatures and under thermal gradients. With the present state of knowledge, it is impossible to predict in detail all the responses of the salt to any given set of thermal conditions. Second, rock mechanics instrumentation should be an integral part of any deep underground disposal experimentation or facility. In the initial phases of such an operation or whenever there is any significant departure from established routine, this instrumentation should be fairly extensive so that (1) incipient structural problems can be detected at any early stage, (2) sufficient information will be available to enable the best solution to those problems to be found, and (3) the solutions can be checked. After routine operations have been established, a limited number of rock mechanics instruments should be maintained for proper control of the operation. Third, underground mine disposal, in salt or any other formation, is still a mining operation. The solutions to any problems should be sought first within the body of existing mining technology.

Water Release and Possible Effects

The small quantities of water trapped in negative crystal cavities in the salt have been found to migrate toward a heat source. This is apparently due to a small salt solubility increase with increasing temperature and to diffusion of salt from a high solution concentration on the hot side of the brine cavity to the lower concentration on the cold side. Based on some approximate calculations and simple laboratory tests, it would be anticipated that the migration rate through the temperature gradients which exist around the holes in the arrays might be somewhere in the range of a fraction of an inch per year to as much as 3 or 4 in./year. Previous measurements have indicated that the water content of the salt is around $\frac{1}{4}$% by volume, so this should produce an inflow of water which might go as high as 2 ml day^{-1} hole^{-1}. Measurements indicate that water is being released into the radioactive and control array holes at the rate of about 0.3 ml day^{-1} hole^{-1} to perhaps as much as 3 ml day^{-1} hole^{-1}. This small quantity of water poses no problems for the demonstration, since it is removed by the off-gas system.

In an actual disposal facility the waste-container holes will be backfilled with crushed salt. In that case the water coming into the hole would move as vapor upward through the void spaces in the crushed salt, where it would condense as it reached cooler regions. The possibility exists that the upper regions of the waste containers (filling neck, void-space zone, etc.) will remain below the boiling point for some extended period of time, and the water could corrode through the container. Even if this happened, there probably would not be any problem so long as the container does not contain appreciable quantities of gases at a positive pressure and the waste product is relatively nonleachable. (So long as most conversion-to-solids processes are functioning properly, there should be no gas buildup. However, in a routine production operation, it may be anticipated that there will be occasional exceptions. These containers might release such gases as oxides of nitrogen, hydrogen, volatile fission product fluorides, ruthenium, or perhaps other unknown compounds. Most of these materials would be expected to remain in the 7 to 8 ft of crushed salt above the waste containers.) As the 100°C temperature front moves up, the water would be expected to move with it, thus eventually finding its way up into the room. In the relatively pure salt (such as is normally mined), free of significant quantities of interbedded shale (which contains several percent water), the water content is generally of the order of less than $\frac{1}{2}$% of volume. Quantities such as this should pose no problem in a disposal operation, since the inflow rate is very low.

The two modified pillar heaters (heaters in sealed cans in holes backfilled with salt as in an actual disposal operation) have been helpful in evaluating the effects of the water in the relatively pure salt. One of these (made of plain carbon steel pipe) has been operating since June 1966 and is still holding pressure. The other (made of 304L stainless steel), started in November 1966, developed a low leak about the middle of February 1967. This leak is believed to be due to pitting corrosion on the stainless steel tubing which comes up out of the hole to the pressure gage. Additional simulated waste container tests are to be started in June. Also, it is planned to calculate the theoretical migration rates of the brine cavities in order to establish the quantities of water which might accumulate in a given hole over any specified time. Some additional laboratory tests may be required in this connection.

In the array in the original mine floor, due to the presence of shale, the water inflow rate is about 40 to 90 ml day^{-1} hole^{-1}, a much more significant volume than in the other arrays. Since in some situations it may not be possible to find suitable salt which does not contain some shale in the region where the holes would be drilled for the waste containers (or one might want to use an old mine area, which would almost invariably contain such shale layers), tests are to be started in June with four simulated waste containers made of mild steel and 304L stainless steel in holes in the original Lyons mine floor. These holes will be backfilled with crushed salt to see what happens to both the integrity of the containers and the fairly large quantities of water.

Heated Pillar Test

A part of the Project Salt Vault experimental program was designed especially to obtain additional information on the thermomechanical properties of salt under transient temperature conditions. This is the heated pillar test, in which a 20-ft-thick pillar between the two central rooms of the experimental area is being extensively heated by a total of 33 kw of electrical power applied in the floor along the sides of the pillar. This configuration represents approximately three times the heat input to the pillar which would be expected if the floor of the rooms were filled with real solidified wastes. In addition, the heat input is concentrated at the pillar; this tends to further exaggerate the time response. The vertical deformation of this pillar, as measured at seven gage points, is shown in Fig. 3.4. The initial portions of the curves represent the normal squeezing and plastic deformation of the pillar resulting from the overburden pressure. The middle part of the curves illustrates the effect of only one of the heaters (adjacent to gage 125), which was started with a 3-kw input as a preliminary to the main experiment. Notice that the effect

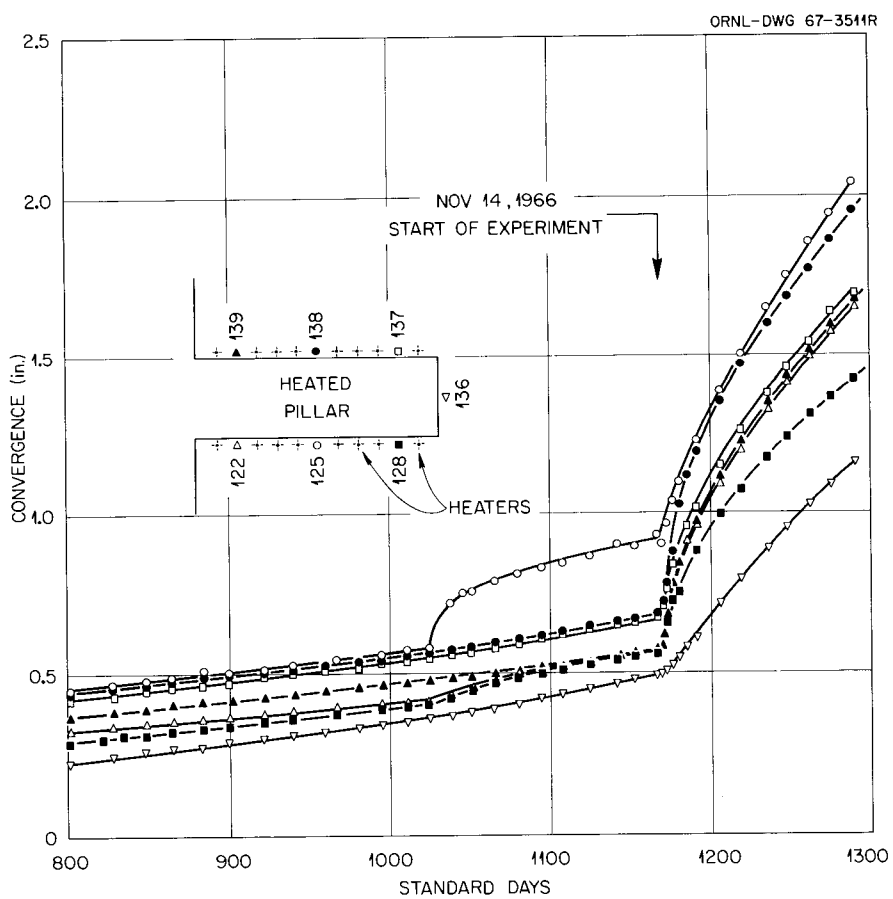

Fig. 3.4. Vertical Deformation (Convergence) of the Heated Pillar.

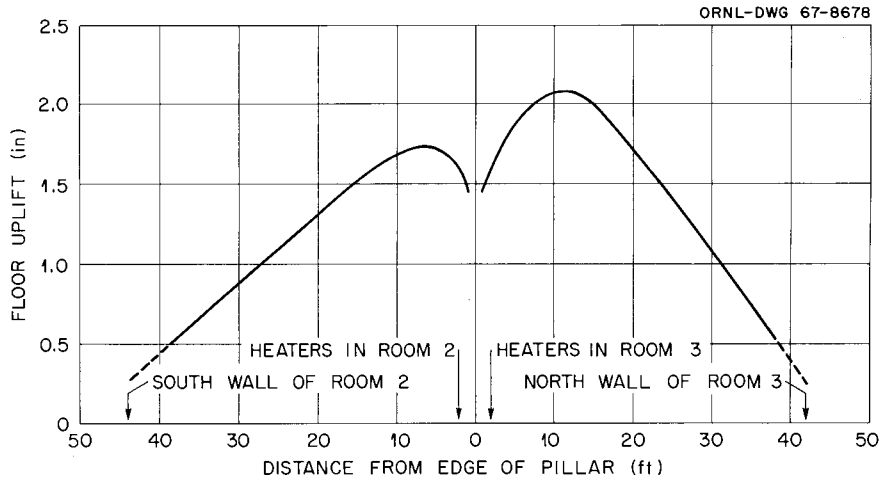

Fig. 3.5. Floor Uplift Along South-North Center Lines of Rooms 2 and 3 as of June 1, 1967 (1369 Standard Days).

of this single heat source can also be seen at gages 122 and 128, 20 ft away.

On November 14, 1966 (standard day 1170), all 22 of the heaters were turned on with a power input of 1.5 kw each. The resulting increase in the rate of convergence of the pillar was about an order of magnitude, from 0.2 to 2.0 in./year. This rate of convergence is approximately the same as would result from a doubling of the overburden pressure or depth. The strong temperature dependence of the pillar deformation is further illustrated by the distribution of the convergence around the pillar. The largest convergence and the greatest rate (gages 125 and 138) occur at the center region of the pillar, which is the hottest. The least amount of convergence (gages 128, 136, and 137) takes place around the end of the pillar, where the heat losses to the air result in the lowest temperatures.

In Fig. 3.5 are shown the floor uplift profiles (in inches) along the south-north center lines of rooms 2 and 3 (which border the heated pillar) as of June 1, 1967. At that time the temperature under the center of the pillar (9 ft down in the salt, at the center plane of the heaters) was 68°C, and at the ends of the pillar at 9 ft depth it was about 50°C. Halfway up the pillar, in the center, the temperature was 43°C. Temperatures in excess of 100°C (at the 9-ft depth) extended to distances of more than 2½ ft from the centers of the heaters. At the 9-ft depth in the center of the rooms, the temperature was 43°C; this same temperature was recorded at a depth of 17 ft.

It will be noted that the uplift in rooms 2 and 3 is not quite symmetrical, with somewhat more uplift being recorded in room 3 than in room 2. This was found to be caused by a separation (floor heave) taking place at some plane of weakness more than 5 ft down into the salt in room 3. Again, this is considered to be a normal variation caused by slight differences in the salt from room to room.

Detailed Stratigraphy of the Salt Section in the Vicinity of the Demonstration Site

A detailed stratigraphic study has been completed of the salt section extending from 30 ft below the floor of the old mine workings to 10 ft above the ceiling in the demonstration site, a total thickness of 75 ft. The section was prepared through examination of numerous exposures in the rooms and haulageways of the old mine workings and the demonstration area, as well as from the core of several holes that were drilled in the roofs and floors of these areas. X-ray diffraction was the principal means used to identify mineral species. Halite is by far the predominant evaporate in the sequence, while anhydrite and polyhalite are prominent in a few localities. Traces of gypsum, dolomite, and calcite have also been identified. Illite and montmorillonite are the principal clay constituents, while quartz is also abundant in the interbedded shales. In general, the salt consists of layers of halite up to several inches in thickness that contain clay as thin laminae or blebs that tend to be concentrated parallel to bedding, thus giving the salt a banded appearance. In that part of the section below the floor of the old mine workings,

halite beds up to several feet in thickness are separated by shale layers that may be as much as 6 in. thick. A few thin anhydrite layers are usually present along with the shale. The 9-ft-thick portion of salt of the old mine workings contains the purest salt in the section examined, although a few blebs or very thin laminae of clay occur with the halite. In the demonstration area the salt section contains several prominent shale layers, the lowermost of which is several feet thick in some places. Polyhalite blebs are distinguishable in this part of the section, and in some places they are concentrated so heavily along bedding that the salt takes on a dark red banded appearance. Anhydrite blebs are commonly associated with the polyhalite. The salt in the roof of the experimental or demonstration area is, in general, quite similar to the salt immediately below it.

LABORATORY TESTS ON DEFORMATION OF ROCKS

T. F. Lomenick H. J. Wyrick

Simulation of Mine Pillars in Scale Models

The deformational characteristics of rocks are an extremely important consideration in the simulation of mine conditions in scale-model tests. For instance, for laboratory tests of rock samples to determine the stability of mine pillars, it is absolutely necessary, in the case of rocks that deform plastically like rock salt, to simulate in the models as near as possible not only the mine pillar but also the roof and floor conditions. However, for brittle rocks like dolomite, the roof and floor apparently do not affect greatly the deformation of the pillar.

This has been illustrated in recent uniaxial tests of model mine pillars of rock salt and dolomite. In both cases, the models were fabricated from 6-in.-diam cores. After cutting the cores to a length of 5 in., a portion of the center of the specimens was ground out to form the pillar (1 in. high by 4 in. in diameter) and the surrounding roof and floor. Steel rings were then "epoxied" to the top and bottom portions of the samples to restrain laterally the deformation of the rock in the roof and floor (as would be the case in actual mine workings). The radial stress on the rings was measured by attaching wire strain gages to the steel rings (see Fig. 3.6). For rock salt samples tested at room temperatures, it was found that the radial stress exerted on the rings increased with increasing axial loads up to approximately 80% (12,000 psi) of the axial load at 15,000 psi. However, for the dolomite samples, it was observed that the radial stress did not exceed about 7% of the axial stress of the pillar load even at loads as high as 23,000 psi. These data indicate that, for materials that deform plastically like rock salt, actual mine conditions are simulated best when the roof and floor portions of the models are constrained laterally. This allows confining stress in the roof and floor to be transmitted into the pillar (at least for samples having a width-to-height ratio of 4), thereby making the pillar stronger. For dolomite the relatively small values of radial stress measured on the confining rings of the models indicate that the roof and floor have less influence on the strength of the pillars, and thus the simulation of the roof and floor in models used to define mine pillar deformation in rocks of this type is not as critical as for rocks that deform plastically under the same conditions.

Size of Model Specimens

The scaling of mine works to a convenient size for laboratory testing is a matter of great concern in model studies of rock deformation, since all geologic features may not be adequately represented in scaled-down laboratory specimens. Perhaps the most important scaling considerations in regard to the modeling of salt mine structures are the size of the test specimens with respect to the grain size of the rock salt and the amount of salt above and below the mine pillars. Leonard E. Obert of the Bureau of Mines has stated that reproducible results are obtained when the pillars of the test specimens have diameters of at least about 10 grains or crystal diameters.[4] Serata has reported that specimens containing about 500 grains should be adequate for test purposes.[5] Both these conditions are met in our "standard test specimen" (a 6 in.-diam core cut to a 5-in. length that includes a 1-in.-high, 4-in.-diam pillar).

---

[4]L. E. Obert, Applied Physics Laboratory, U.S. Bureau of Mines, College Park, Md., personal communication, February 1963.

[5]Shosei Serata, Serata Geomechanics, Berkeley, Calif., personal communications, October 1963.

Fig. 3.6. Model Pillar Specimen in Test Machine. Note wire strain gages on steel rings at top and bottom of the sample.

To evaluate the effects of various salt thicknesses in the roofs and floors of test models, several samples were tested having the same pillar dimensions (4 in. in diameter by 1 in. high) but with different thicknesses of salt ($\frac{7}{8}$, 2, 3, and 4 in.) above and below the pillar. In Fig. 3.7, which shows pillar deformation with time, it is observed that there is little difference in the deformation curves for the samples with 2 in. or more of salt above and below the pillar; however, for the specimen having only a $\frac{7}{8}$-in. layer of salt in the roof and floor, the amount and rate of deformation are markedly greater. It is concluded from these data, along with the measured values of radial stress in the roof and floor of model salt pillars as discussed above, that the thickness of the salt above and below the pillar should be two or more times the height of the pillar to approximate the true strength of actual mine pillars. The effectiveness of shale partings that may lie at the top and bottom of salt pillars in reducing pillar strength has been discussed previously.[6]

In addition to the tests discussed above, one specimen having dimensions twice those of the "standard model specimen," that is, a 2-in.-high, 8-in.-diam pillar with roof and floor thicknesses of 4 in., was tested at a load of 4000 psi at 22.5°C.

[6] F. L. Parker and R. E. Blanco, *Waste Treatment and Disposal Semiannual Progress Report July–December 1965*, ORNL-TM-1465.

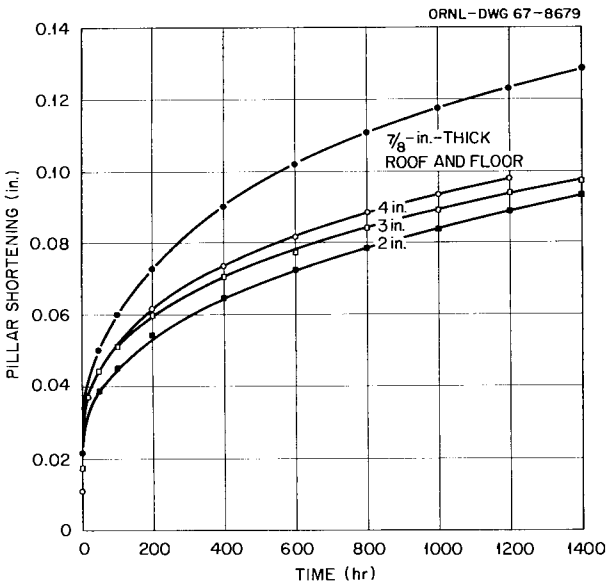

Fig. 3.7. Deformation of Model Pillar Specimens at 22.5°C and 6000 psi with Varying Thicknesses of Salt in the Roof and Floor.

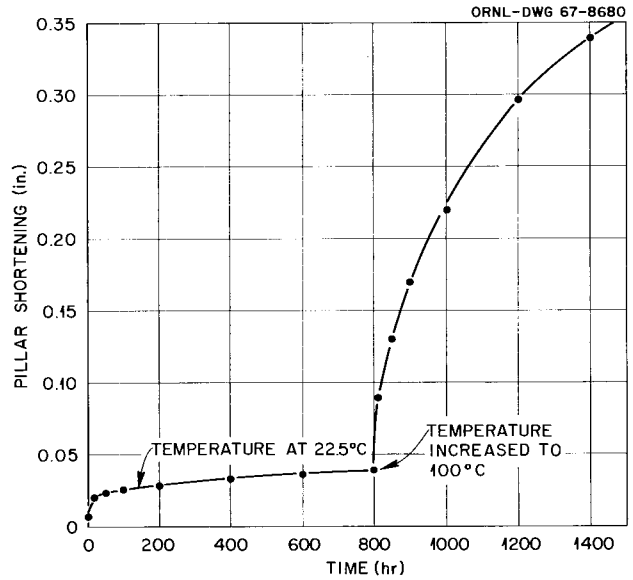

Fig. 3.8. Deformation of Model Salt Pillar at 4000 psi and at 22.5 and 100°C.

The deformation curve for this sample was essentially the same as that for the smaller "standard model" for the same type of rock salt. It is thus concluded that a 5-in.-long, 6-in.-diam core of rock salt ground out in the center to form a 4-in.-diam, 1-in.-high pillar, with 2 in. of salt in the roof and floor above and below the pillar, simulates mine conditions best where the pillar, roof, and floor are essentially all rock salt.

Heat Effects

The effects of heat on the deformation of rock salt have been reported earlier.[7,8] In these tests, carried out to establish empirical relations between temperature, pressure, and time, the samples were first heated and then loaded. However, under actual disposal conditions, the mine pillar would be loaded first and then the salt would be heated as the rooms are filled with waste. To define pillar deformation under the latter conditions, a model specimen was loaded to 4000 psi at room temperature (22.5°C) for about 800 hr, and then the temperature was increased to 100°C. In the case of both the initial loading and the elevation of the temperature, it is observed in Fig. 3.8 that the deformation curve rises sharply initially and then proceeds to rise but at a decreasing rate; however, in the latter case, the total deformation is significantly greater. It is also of interest that on the application of heat (the temperature of the salt was raised from 22.5°C to 100°C over a period of about 4 hr), there was a corresponding increase in the load on the sample. This increase of load, which was due undoubtedly to the thermal expansion of the salt, attained a peak value of 4640 psi (a 16% increase) after the salt had reached a temperature of about 80°C, or approximately 2 hr after the initial temperature rise. It is also significant that at the time the salt temperature had reached its maximum value of 100°C, the load had decreased to the static value of 4000 psi. This test shows that some increase in the load on salt pillars will occur with a significant rise in temperature; however, because of the accelerated flow of salt at elevated temperatures, the load is rather quickly relieved. Since the temperature rise in the salt in an actual mine disposal facility will rise very slowly (probably over periods of many months to years), it is difficult to state precisely, based

[7] R. E. Blanco and F. L. Parker, *Waste Treatment and Disposal Semiannual Progress Report July–December 1964*, ORNL-TM-1081.

[8] T. F. Lomenick *et al.*, *Health Phys. Div. Ann. Progr. Rept. July 31, 1965*, ORNL-3849, pp. 16–18.

on laboratory tests of pillar models that are uniformly heated within a few hours, the nature of the increase in pillar loading and the relieving of this excess load through salt flow. Perhaps a better understanding of this phenomenon will evolve from the heated pillar test now in progress at the Lyons mine.

SALT SPACE REQUIREMENTS FOR PROJECTED NUCLEAR POWER ECONOMY TO YEAR 2065

R. L. Bradshaw

An estimate has been made of the gross area required in salt formations to dispose of high-level wastes from the projected United States nuclear power economy to the year 2065. The estimates of installed nuclear electrical generating capacity up to the year 2000 were taken to be the same as those developed by R. E. Blanco *et al.* in July 1966.[9] From the year 2000 to 2060 the figures were derived from the projections shown in Fig. 3, p. 44, of the 1962 AEC Report to the President on Civilian Nuclear Power.[10] A comparison of the installed electrical capacity derived from this figure for the year 2000 with that of Blomeke and Boegly[9] indicated that the AEC figures were about 14% lower. Thus a multiplying factor of 1.14 was applied to the numbers derived from the AEC Fig. 3 up to the year 2060. The results are shown as the lower curve in Fig. 3.9. All curves were extrapolated to year 2065.

The upper curve of Fig. 3.9 shows the installed nuclear thermal capacity. Again, the Blomeke-Boegly thermal efficiency assumptions were used to obtain this curve; that is, a thermal efficiency linearly increasing from 30% in 1965 to 44% in 2000. Beyond 2000 the efficiency was assumed to remain constant at 44%.

The middle curve of Fig. 3.9 shows the equivalent continuously operating thermal nuclear generation. This, too, is based on Blomeke-Boegly assumptions—reactor load factor constant at 80% until 1980, then linearly decreasing to 70% by 2000, and constant at 70% thereafter.

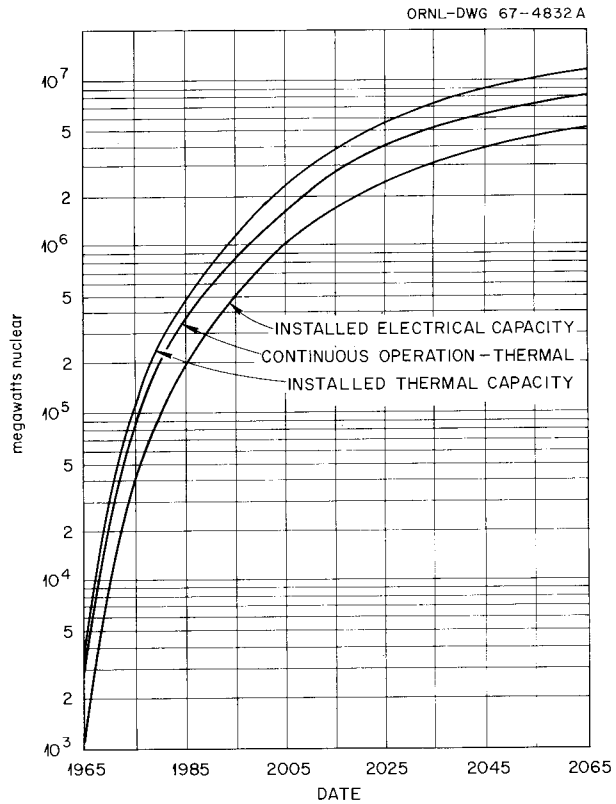

Fig. 3.9. Nuclear Power Projections to Year 2065.

Calculations of mine space requirements were made previously for the joint Health Physics–Chemical Technology waste management economics study.[11] In that study it was found that the overall economics are best when the waste is interim stored for about 30 years before disposal. By that time essentially only ^{137}Cs-Ba and ^{90}Sr-Y are left as significant heat producers. (The same is true for wastes at least ten years old.) Therefore, only the total megawatt-days of operation and not the residence time of the fuel in the reactor (one year in the prior economic study, and perhaps two or more years in future reactors) is important in determining the waste heat-generation rate. Thus the future requirements for salt mine space can be derived directly from the previous study.

The previous economic study assumptions represented the continuous operation of 56,000 Mw (thermal) [15,000 Mw (electrical) continuous operation

[9] R. E. Blanco *et al.*, *Survey of a Site for a Nuclear Fuel Reprocessing Plant and Waste Disposal Area at Oak Ridge*, ORNL-TM-1748 (Jan. 13, 1967).

[10] *Civilian Nuclear Power, a Report to the President – 1962*, USAEC.

[11] R. L. Bradshaw *et al.*, "Disposal of High Activity Power Reactor Wastes in Salt Mines: A Concept and Field Scale Demonstration," *Nucl. Struct. Eng.* 2, 438–46 (1965).

at 27% efficiency]. In that study the peak allowable temperature at the walls of the holes containing the waste cans was assumed to be 200°C. (Based on considerations of the effects of elevated temperature on mine stability and other variables, this figure appears to be realistic, although perhaps slightly conservative.) For the temperature calculations, the cesium and strontium were lumped together and assumed to have a 30-year half-life. In the previous study, for purposes of conservative cost calculations, the infinite array of heat sources was assumed. In that study it was shown that for 30-year half-life wastes (and perhaps for younger wastes also) the temperature rise calculations are conservative by a factor of about 1.7. In this study the more accurate calculations have been assumed (i.e., the space requirements are a factor of 1.7 less than assumed in the economic study).

Other assumptions were that the mine is located at a depth of 1000 ft, typical of many of the deposits in the United States, and that conventional mining practice, modified by the special requirements for handling radioactive materials, is used. (Deeper mines would require more gross space and shallower ones less.)

The gross mine space requirements (storage rooms, access tunnels, and all unexcavated salt left for overburden support, barriers, etc.) for disposing of the 30-year-old waste from the continuous operation of the 56,000 Mw (thermal) nuclear power was 5.25 acres/year (using the 1.7 factor). Thus the yearly space committed in any given year can be determined by ratioing the continuous operation megawatts obtained from the middle curve of Fig. 3.9 to 56,000 Mw (thermal) and multiplying by 5.25 acres. This has been done and is shown in Fig. 3.10. Also shown in Fig. 3.10 is the cumulative gross salt formation space committed up to any given year. This curve was obtained by a graphical integration of the previous curve.

The third curve of Fig. 3.10 shows the gross salt area which might actually be used by any given date. It is merely the second curve shifted 33 years to the right – 30 years for the interim storage period and 3 years for the period from the time the fuel was put into the reactor until the time it was processed.

It is of interest to note that by the year 2065, only about 30,000 acres (an area less than 7 miles square) will have been committed and only about one-third of this will have actually been used.

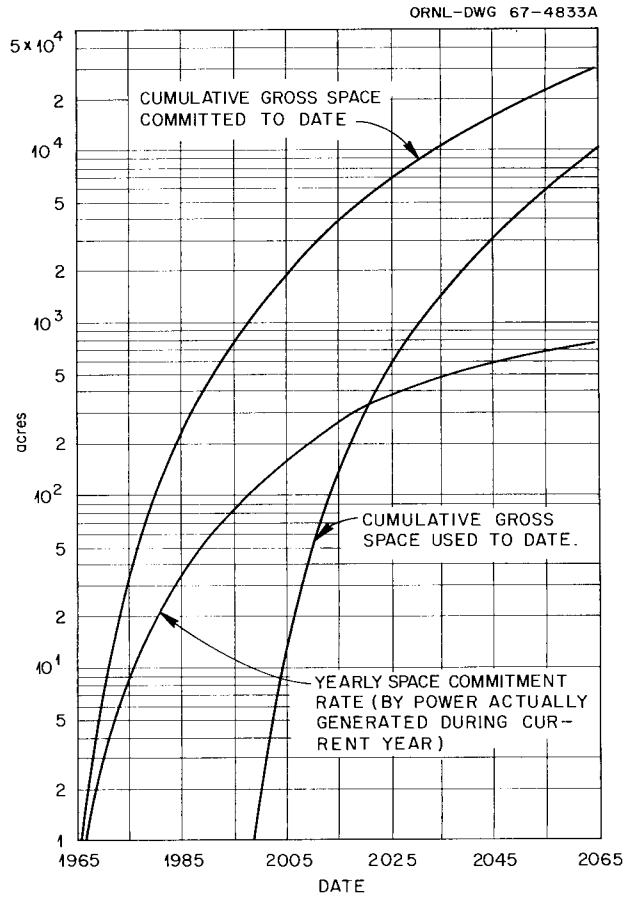

Fig. 3.10. Salt Formation Space Requirements for High-Level Waste Disposal to Year 2065.

Considering the fact that about ¼ to ½ million square miles of the United States is underlain by salt, even though only a small percentage of the area might be suitable for waste disposal, there would not appear to be any scarcity in the foreseeable future. Also, in some of the formations, where the salt deposits are several hundred feet thick, more than one level might be used.

As a point of interest, if the waste were to be interim stored only 10 years instead of 30, the gross space commitments would be increased by about a factor of 1.6. In that case the "space used to date" curve would be shifted back to the left 20 years and multiplied by 1.6. As an example, the space used to year 2045 would then be about 16,000 acres.

Since the 1.7 factor is probably still valid for wastes less than 10 years of age, it is also of interest to consider storing wastes as early as 4

years out of the reactor. If the interim storage period were to be 4 years instead of 30, the gross space commitments would be increased by a factor of about 1.75. This is only about 10% higher than for 10 years' interim storage. For 4 years' interim storage the "space used to date" curve would be shifted back to the left 26 years and multiplied by 1.75. The space used to year 2039 would be about 17,500 acres.

It appears economical to place the wastes in the mine as early as 4 years out of the reactor,[12] but, in the interest of conserving salt space, the longer interim storage period may be desirable.

---

[12] J. O. Blomeke *et al.*, "Estimated Cost of High-Level Waste Management," *Proceedings of International Symposium on the Solidification and Long-Term Storage of Highly Radioactive Wastes, Richland, Washington, February 14–18, 1966*, Conf-660208, pp. 830–43 (Nov. 1966).

4. Application of Mineral Exchange to Reactor Technology

D. G. Jacobs
H. W. Kohn[1]
Y. P. Chou[2]
O. M. Sealand

BEHAVIOR OF SULFUR HEXAFLUORIDE AND METHYL IODIDE IN AN IDAHO SOIL

Sulfur hexafluoride (SF_6) and methyl iodide (CH_3I) have been considered as possible gaseous tracers for evaluating the suitability of a site near the proposed Loss of Fluid Test (LOFT) for containing radioactive gases.

Sulfur hexafluoride, although not a radioactive waste, seems to be a very good tracer for this project. It is inert, nontoxic, and sparingly soluble in water. In addition to its chemical stability, it is very sensitive to electron capture detection for gas chromatographic analysis.[3,4] It has been reported that SF_6 can be detected at levels as low as 10^{-9} ppm.[5]

Methyl iodide has been suggested as a possible tracer since it has been found to penetrate iodine adsorption columns and would likely present a major hazard in the case of a reactor incident.

In order to determine the magnitude of the interaction of CH_3I and SF_6 with soil materials, laboratory studies were conducted using columns of Idaho Falls subsoil that were provided by Bruce Schmalz, USAEC, Idaho Falls.

Adsorption of SF_6 at Room Temperature (26°C)

Idaho soil (20-mesh or less) from a depth of 14 to 15 ft, with a moisture content of 3.8%, was packed in a glass column and flushed with 99% pure SF_6 at the rate of about 20 ml/min for 1 hr. A portion of the treated soil was leached with 0.2 *M* KOH. Both the treated soil and the leached solution were submitted to the Analytical Chemistry Division for analysis, but no satisfactory results were obtained. Infrared measurement showed contradictory results.

Three hundred forty-five grams of the same soil was packed in a glass column. Sulfur hexafluoride was passed through the soil column at a rate of about 18 ml/min for 4 hr and subsequently was purged by helium at the same rate for 2 hr. The soil was then transferred to a 500-ml Erlenmeyer flask connected to a gas-sampling rubber balloon. The soil was heated to about 90°C for 1 hr, and the remaining gas in the flask was blown into the balloon with air. The gas sample was then analyzed by a gas chromatograph with an electron-capture detector.

The sample collected by heating the soil after treatment with SF_6 and helium showed adsorption of 99 ppm. Because of the nonlinearity of the instrument at higher concentrations, the chromatographic peaks obtained from pure SF_6 are probably lower than they should be, and thus the resulting adsorption value of 99 ppm is probably too high.

Three hundred forty grams of soil was packed in the same glass column as in the above experiment. The soil was first flushed with helium for 2 hr to displace all the air in the column, and then SF_6 was admitted at the rate of 12 ml/min. Samples

---

[1]Chemistry Division.

[2]Research participant, Lenoir Rhyne College, Hickory, N.C.

[3]N. L. Gregory, *Nature* **196**, 162 (1962).

[4]C. A. Clemons and A. P. Altshuller, *Anal. Chem.* **38**, 133 (1966).

[5]C. A. Clemons *et al.*, "Sampling and Analysis of SF_6 to 10^{-9} ppm Levels by Concentration on Carbon," to be presented at the 152d ACS National Meeting, New York, Sept. 14, 1966.

were collected in rubber balloons at 8-min intervals for 2 hr. The soil column was eluted with helium at the rate of 7.7 ml/min, and again the sample was collected in a rubber balloon at intervals of 5 min for 105 min. After the soil had been flushed with helium, it was transferred to an Erlenmeyer flask and heated as described above, except that the remaining gas in the flask was blown into the balloon by helium instead of by air. All the samples collected were analyzed chromatographically.

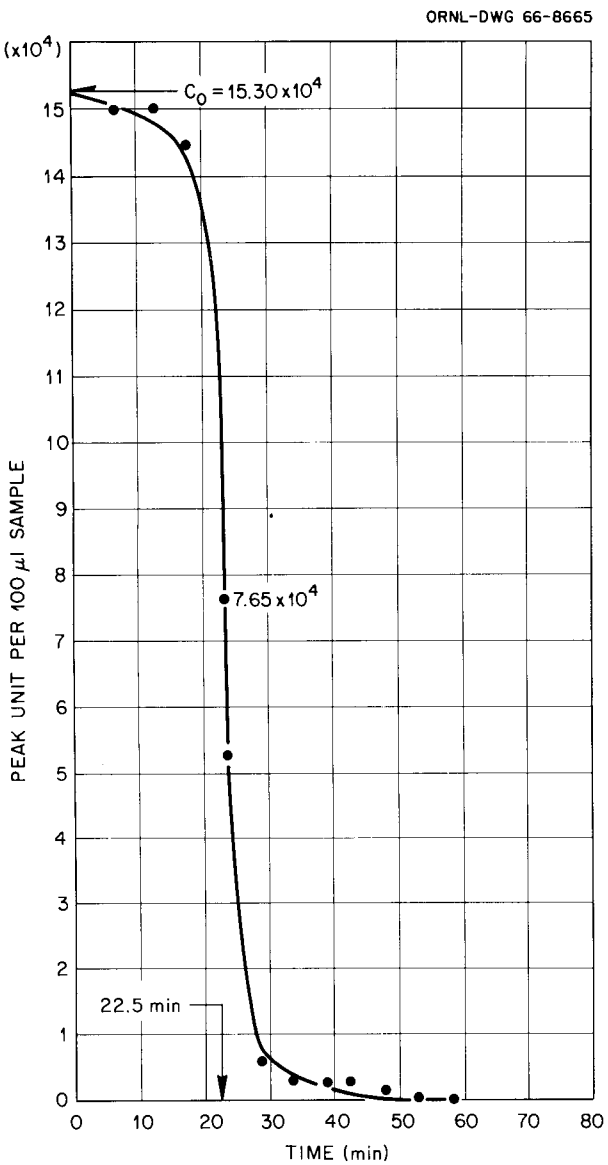

Fig. 4.1. Elution of Sulfur Hexafluoride from a Column of Idaho Falls Soil Using a Helium Purge.

In this experiment the adsorption value of the sample collected from heated soil was 8 ppm. On the other hand, the curve in Fig. 4.1 shows that the half-breakthrough point for the elution of SF_6 by helium was at 22.5 min. Correcting for half the sample size gives a retained volume of 148 ml, compared with an integrated value of 154 ml. The pore volume of the column was 147 ml; thus 4 ± 3 ml of SF_6 was adsorbed on the 340 g of soil. This amounts to 70 ± 52 ppm by weight and includes, of course, the loosely bonded as well as the tightly bonded SF_6. Based on the fact that the solubility of SF_6 in water is 3.3×10^{-4} g/cm^3 and that the soil moisture is 3.8%, all of the first 13 ppm adsorbed would be dissolved in water.

Adsorption of CH_3I at Room Temperature (26°C)

A glass column was packed with 86.1 g of Idaho Falls soil. A known quantity of CH_3I, tagged with ^{131}I and contained in a 125-ml Erlenmeyer flask, was attached to the glass column connected to a glass tube which extends above the scintillator of the counter and finally connects to a U-tube containing 1 *M* $AgNO_3$ solution.

Counts were taken at intervals of 5 or 10 min (except during the night) until a constant count was attained. Then the column was purged with air at the rate of 2.2 ml/min, and a count was taken every 5 min until background was reached. The precipitate formed by the reaction of CH_3I and $AgNO_3$ was dissolved in KCN solution, and the volume of this solution was measured and counted. After the purging of loosely bound CH_3I, the soil column was dissected into five sections, crushed, and exposed to air for 10 min; then the adsorbed $CH_3{}^{131}I$ was counted.

The results of the air elution experiment are shown in Fig. 4.2. From this curve the half-breakthrough point gives 70.4 ml for the total volume of CH_3I retained by 86.1 g of soil. Since the pore volume is 41.2 ml, the CH_3I adsorbed on the soil is 29.2 ml, or 1940 ppm by weight. The integrated value for the sorption of CH_3I is 74.8 ml, which is somewhat larger than the 50% breakthrough value.

The adsorption value obtained directly by counting the soil column, as shown in Table 4.1, was 577 ppm (0.0497 g CH_3I on 86.1 g soil), which may be considered as water-dissolved and nonexchangeable CH_3I. Since the soil moisture is 3.8% and

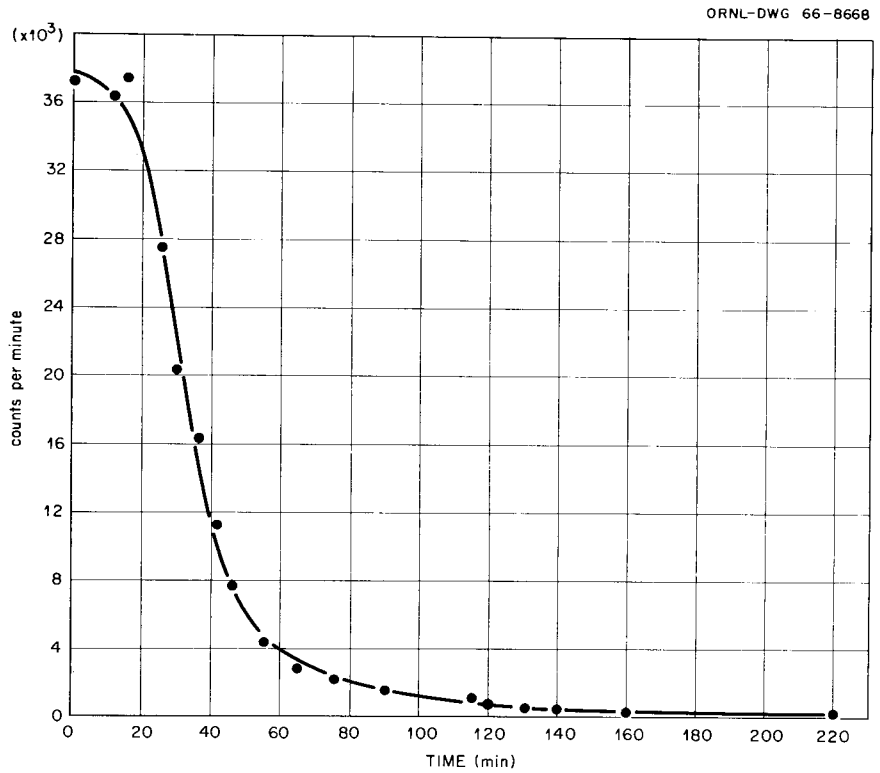

Fig. 4.2. Elution of CH_3I from a Column of Idaho Falls Soil Using an Air Purge.

the solubility of CH_3I in water is 1.4%, then 295 ppm of the retained CH_3I should be dissolved in water, assuming that Henry's law holds in this solid system. (Vapor pressure of CH_3I at 26°C is 410 mm.) There is, however, a discrepancy of 0.1256 g between the amount of CH_3I diffused and collected. This discrepancy may be the result of adsorption on glass and possibly some loss of CH_3I during a short period of failure in making connections.

The diffusion coefficient $\bar{D}$ was estimated to be 3.3×10^{-3} cm²/sec. For comparison, a value of the molecular diffusion constant D for CH_3I diffusing in air was calculated with the Chapman-Enskog formula:[6]

$$(D_m)_{AB} = 1.8583 \times 10^{-3} \frac{T^3[(1/M_A) + (1/M_B)]}{P\sigma^2_{AB}\,\Omega_{AB}}$$

$$= 0.07 \text{ cm}^2/\text{sec} ,$$

where

T = absolute temperature, 299.2°K,

P = total pressure, 0.975 atm,

σ_{AB} = collision diameter, 4.218 A (for CH_3I, estimated for atomic radii),

Ω_{AB} = Lennard-Jones molecular parameter 1.6 (for CH_3I, assuming $T_c \cong 3/2\ T_b$),

M_A = molecular weight of CH_3I (142 g/mole),

M_B = average molecular weight of air (28.8 g/mole).

This value corresponds closely to the diffusion constant of ^{131}I in air, 0.0784 cm²/sec.[7]

The value for the diffusion coefficient of CH_3I in air must be corrected for the porosity of the soil column and by a tortuosity, or path length, factor; this gives a value of 0.024 cm²/sec for the diffusion of CH_3I in the soil column. In

[6]R. B. Bird *et al.*, *Notes on Transport Phenomena*, p. 306, John Wiley, New York, 1958.

[7]E. R. Bennett and W. J. Kaufman, "Molecular and Convection Dispersion," notes of meeting on Ground Disposal of Radioactive Waste, University of California, Berkeley, January 28–29, 1965.

Table 4.1. Mass Balance of CH_3I

	Grams
Weight of CH_3I	19.7166
Weight of CH_3I after diffusion	18.8346
Total weight of CH_3I diffused	0.8820
Weight of CH_3I collected in $AgNO_3$ solution	0.7067
Weight of CH_3I remaining on soil	0.0497
Discrepancy	0.1256

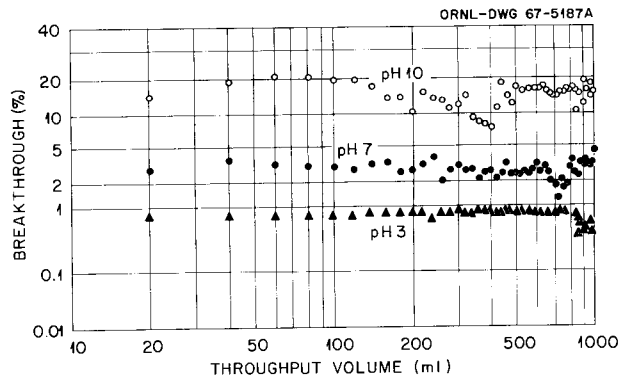

Fig. 4.3. Leakage of ^{242}Cm Through a 1-g Column of Hydrobiotite Using a Carrier Solution of 0.1 *M* $NaNO_3$.

addition, the total distance between the source of the CH_3I and the detector must be modified for the adsorptive properties of the soil for CH_3I. This would account for the additional difference of an order of magnitude between the extracted and the calculated values.

MOVEMENT OF CURIUM IN SOIL COLUMNS

Sodium nitrate solutions (0.1 *M*) tagged with ^{242}Cm were passed through 1-g columns of hydrobiotite preequilibrated with untagged solutions of the same chemical composition. Approximately 1 liter of solution was passed through each column. The concentration history of the effluent is shown in Fig. 4.3. The concentration did not follow a normal chromatographic breakthrough; instead, the leakage was fairly constant during the entire time. The average leakage through the columns was: at pH 3, 0.80 ± 0.09%; at pH 7, 2.75 ± 0.41%; and at pH 10, 15.0 ± 2.5%. Also, as the pH was increased, ^{242}Cm precipitated from the stock solution, reducing the activity of the influent solution.

After the runs the columns were disassembled to ascertain the distribution of activity along the column. Most of the activity was found in a glass wool plug above the column and in the first segment of the column. This indicates the importance of precipitation on the behavior of curium. The leakage of the curium through the column suggests that the mobile species is probably a radiocolloid that is small enough to avoid filtration by the hydrobiotite.

PROCESSING ORGANIC REACTOR COOLANTS

H. W. Kohn D. G. Jacobs

Attapulgus clay columns are presently used at the Whiteshell reactor to purify organic reactor coolants. On the basis of molecular size and pore structure considerations, it would appear that other adsorbents – bentonite, activated bauxite, or possibly spent cracking catalyst – would be superior to attapulgite. Several of these proposed adsorbents were evaluated in this program.

Slow percolation tests were done in all-glass systems at 350°C at flow rates of 0.45 to 1 cm/min. On the basis of the amount of material which could be collected before the dark material[8] broke through, the yellowness of the collected fractions, and the melting point of the coolant (see Fig. 4.4), the indications are that if slow percolation were the purification method used, bentonite, activated bauxite, and cracking catalyst would be superior to attapulgite. Actually, the tests are not conclusive, since percolation at this temperature involves a number of uncontrolled processes – flash evaporation, washing the column by reflux, filtration, possibly cracking or other chemical reactions, as well as adsorption. However, these factors may also play a part in the actual (fast column flow) purification procedure presently in use.

Part of the purification by slow percolation is due simply to filtration. The demarcation lines

[8]The material tested was coolant irradiated for about one month at the Whiteshell reactor.

can be seen in Fig. 4.5 (arrows). Since the columns are darkened throughout after use, this demarcation cannot be due to preferential adsorption. Indeed, the filtering action was demonstrated by a run using glass wool as the adsorbent.

Several adsorbents other than those listed in the tables were tested but proved to be of limited interest (clinoptilolite, coconut charcoal, Norit, montmorillonite, vermiculite).

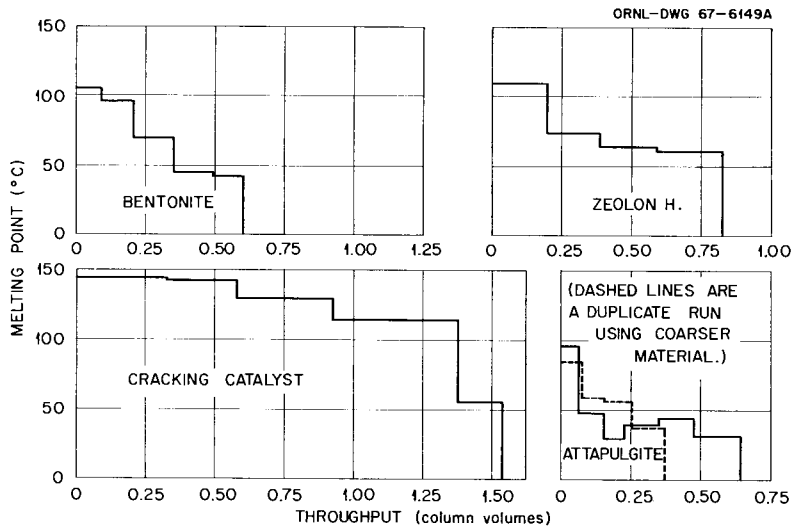

Fig. 4.4. Melting Point of Slow Percolation Effluents.

Table 4.2. Results of Flow Tests

Molecular weight of untreated coolant = 267 ± 3
Percolation tests are 350°C runs

Material	Surface Area (m^2/g)	Temperature (°C)	Molecular Weight of Succeeding Fractions[a]							
			1	2	3	4	5	6	7	8
Cracking catalyst		310	271	270	253	250	251			
Alumina	172	310	252	261	264	267	268			
$CaSiO_3$	125	310	264	262	262	257	270			
Attapulgite	117	309	257	264	262	259	264			
Linde 13X	449	308	262	282?	260	255	263			
Bentonite	23.4	309	264	263	266	272	272			
Spent cracking catalyst	125	313	253	261	259	251	225			
Cracking catalyst[b]	463	350	232	228	230	238	232	226		
Zeolon H[b]	~600	350	255	239	208	238				
Attapulgite[b]	117	350	239	220	250	249	241	235		
Alumina[b]	172	350	254	234	256	246	254	256	242	234

[a]Fifteen-milliliter fractions for flow tests.

[b]Percolation tests.

Flow tests were made on bentonite, activated bauxite, cracking catalyst, calcium silicate, and Linde 13X molecular sieve. Upflow was used at 300 to 310°C, 0.92 cm^3/min. After the test the column was drained, divided into a top and bottom, and treated further.

The most noticeable characteristic of the percolation tests is that the coolant emerges from the column looking as bad as it did going in. Optical absorption measurements of benzene aliquots at the maximum (3525 A) and the minimum (5500 A) showed no changes of color or turbidity. The effluent did not solidify.

The molecular weight of the effluent fractions was measured by the Rast method (freezing point depression) using phenanthrene as the solvent. The results from the flow tests, as well as those from some of the slow percolation tests, are summarized in Table 4.2. Based on these results, it is concluded that alumina, bentonite, and attapulgite soon lose their ability to remove high-molecular-weight materials from the impure coolant.

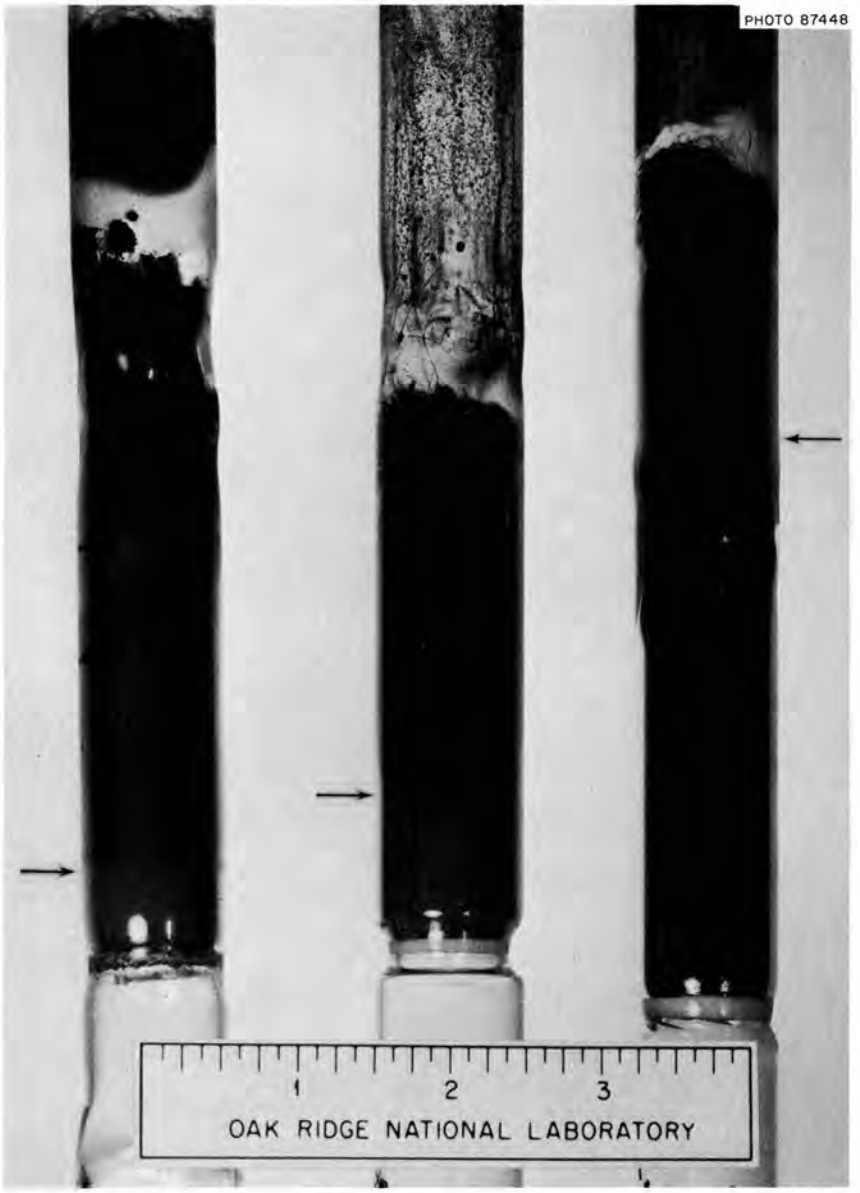

Fig. 4.5. Purification by Slow Percolation Due to Filtration.

On this basis the cracking catalyst appears to be the most promising material. Cracking of the coolant (molecular weight <231) does not seem to occur to any great extent.

Finally, the various columns were tested to see how much organic matter was adsorbed. Since one could hardly hope for complete and uniform drainage from the adsorbent, various washing procedures (benzene, CCl_4) were first used, followed by determination of the exchange capacity and of the amount of organic matter oxidizable by chromate. (These are standard procedures used in the analysis of soils and clays.[9]) The oxidizable organic determination is subject to a blank correction; the values in Table 4.3 are already corrected.

On the basis of these data, attapulgite and the cracking catalyst are the most effective in removing organic matter, although both are inferior to Linde 13X (which is prohibitively expensive). It must be remembered, however, that the organic matter determination does not distinguish pure coolant from contaminant particles and that, as carried out, it is partially a measure of the competition between the adsorbent and the washing solvent.

[9]M. J. Jackson, *Soil Chemical Analysis*, pp. 57, 205, Prentice-Hall, Englewood Cliffs, N.J., 1958.

Table 4.3. Degree of Use of the Adsorbents[a]

Sample	Exchange Capacity (meq/100 g)	Oxidizable Organic Matter (mg per gram of adsorbent)
Linde 13X		
Blank	Not measured	1
Top of column	Not measured	247
Bottom of column	Not measured	242
Bentonite		
Blank	91	15.3
Top of column		33
Bottom of column	88	40
Attapulgite		
Blank	37	6.2
Top of column		90
Bottom of column	29	123
Alumina		
Blank	6	8.5
Top of column		54
Bottom of column	5	81
Cracking catalyst		
Blank	48	2.3
Top of column		66
Bottom of column	30	116

[a]For surface area comparisons, each milligram of adsorbent covers about 3.1 m^2.

5. Engineering, Economic, and Safety Evaluations

K. E. Cowser
Jacob Tadmor[1]
D. G. Jacobs
F. L. Parker
W. J. Boegly, Jr.
G. H. Llewellyn[2]
D. A. Dyslin[2]

KRYPTON-85 AND TRITIUM IN AN EXPANDING WORLD NUCLEAR POWER ECONOMY

The complete release of ^{85}Kr and ^{3}H during the reprocessing of spent reactor fuel may impose unacceptable radiation exposures to man and his environment as nuclear power production increases. Study indicates that the worldwide distribution of these radionuclides in the year 2000 may result in a total body dose rate of 1.8 millirems/year from ^{85}Kr and a body tissue dose rate of 2.1×10^{-3} millirem/year from ^{3}H (ref. 3). However, the limits of permissible discharge and the requirements for treatment of effluent must be determined for local environments in which the reprocessing plants are sited.

Procedures for Estimating Permissible Release

Acceptable rates of ^{85}Kr and ^{3}H release are now being investigated for a hypothetical fuel-reprocessing plant located in Oak Ridge. All critical pathways of internal and external exposure are being considered both for the hypothetical fuel-reprocessing plant and for current Oak Ridge operations that result in the release of radionuclides.

Average annual downwind air concentrations are calculated by a modified Gaussian plume formula as follows:

$$X(\theta x) = \sum^{S} \sum_{i=1}^{R} \frac{2.032 F(\theta S)_i Q_0}{\sigma(Sx)_z \, \overline{\mu}(\theta S)_i x} \times \exp\left[-\frac{h^2}{2\sigma(Sx)_z^2}\right], \quad (1)$$

where

$X(\theta x)$ = average annual concentration along 22.5° arc at distance x in direction θ (curies/m^3),

$F(\theta S)_i$ = fraction of time wind is in direction θ for stability S and wind speed group i,

Q_0 = initial emission rate (curies/sec),

$\sigma(Sx)_z$ = vertical dispersion coefficient at distance x for stability S (m),

$\overline{\mu}(\theta S)_i$ = average wind speed in direction θ, for stability S and speed group i (m/sec),

h = stack height (m),

R = index denoting wind speed groups,

S = index denoting stability parameter.

This expression is obtained by integrating the Gaussian plume formula over the crosswind direction and distributing the results uniformly along the entire arc. Since the average wind speed vector and its frequency of occurrence are used,

[1]Visiting scientist on leave from Israel AEC.

[2]General Engineering and Construction Division.

[3]K. E. Cowser, W. J. Boegly, Jr., and D. G. Jacobs, *Health Phys. Div. Ann. Progr. Rept. July 31, 1966*, ORNL-4007, pp. 35–57.

calculations yield average annual air concentrations. Applications of this technique have been demonstrated previously by Culkowski.[4]

Equation (1) is modified to include washout and fallout by multiplying by the appropriate correction factors. Corrections for washout and fallout are based on the work of Chamberlain and Slade respectively.[5,6] These corrections are as follows:

$$Q_{\text{washout}} = \exp\left[-\frac{\Lambda x}{\bar{\mu}(\theta S)_i}\right], \qquad (2)$$

where Λ is washout coefficient (sec^{-1}); and

$$Q_{\text{fallout}} = \exp\left\{-(2/\pi)^{1/2}\frac{V_g}{\bar{\mu}(\theta S)_i} \times \int_0^x \frac{1}{\sigma(Sx)_z}\exp\left[-\frac{h^2}{2\sigma(Sx)^2}\right]dx\right\}, \qquad (3)$$

where V_g is deposition velocity (m/sec). Equations (1) to (3) are coded for the CDC 1604-A computer. Equation (3) can be evaluated numerically, based on curves of σ_z values given by Hilsmeier and Gifford.[7]

Figure 5.1 shows the calculated air concentrations at the ground surface for a 1 part/sec release from a 100-m stack. The most recent meteorological data reported by Hilsmeier are used in these calculations.[8] Concentrations shown in Fig. 5.1 can be compared with others that include fallout, washout, and changes in stack height; by this process average annual doses can be estimated for a variety of conditions.

[4]W. M. Culkowski, "Estimates of Accumulated Exposures and Environmental Buildup of Radioactivity," *Sixth Air Cleaning Conference, July 7–9, 1959*, TID-7593, pp. 89–99 (October 1960).

[5]A. C. Chamberlain, *Aspects of Travel and Deposition tion of Aerosol and Vapor Clouds*, AERE-HP/R-1261 (1955)

[6]D. H. Slade, *Dispersion Estimates from Pollutant Releases of a Few Seconds to 8 Hours in Duration*, Technical Note 2-ARL-1 (August 1965).

[7]W. F. Hilsmeier and F. A. Gifford, Jr., *Graphs for Estimating Atmospheric Dispersion*, ORO-545 (July 1962).

[8]W. F. Hilsmeier, *Supplementary Meteorological Data for Oak Ridge*, ORO-199 (Mar. 15, 1963).

Washout and Fallout Corrections

Dose-equivalent estimates have been projected for a 6-ton/day fuel-reprocessing plant located in Oak Ridge.[9] These preliminary estimates of dose are being reevaluated by incorporating in the computer program the most recent meteorological data and the best estimates of washout and fallout coefficients.

Washout. – Washout coefficients for soluble gases have been calculated by Chamberlain, using the assumption that the rate of absorption is controlled by the rate of gas diffusion to the raindrop.[5,10] Since the solubility of krypton in water is small (1.85×10^{-10} g of krypton per gram of water at equilibrium),[11] it was assumed that the solubility limit controls the amount of krypton absorbed. The solubility of ^{85}Kr in rainwater, even when released at 1 curie/sec, would be limited by the stable krypton in the atmosphere (about 4×10^{-3} g/m^3 near sea level).[12] It was further assumed that krypton is washed out of the atmosphere, beginning at an average height of 1 mile. This assumption is based on the height of rain-bearing cumulus clouds and the extent of vertical development of radioactive clouds released as a point source. The average intensity of rainfall is about 4 mm/hr in the Oak Ridge area,[13] and, at equilibrium, 2×10^{-14} g of krypton per second could be absorbed in a column of the atmosphere 1 mile high and 1 cm^2 in area. About 5×10^{-4} g/cm^2 of stable krypton is contained in the atmosphere to a height of 1 mile. Based on these considerations, the average washout coefficient was calculated to be

$$\Lambda = \frac{2 \times 10^{-14}\ \text{g Kr/sec/cm}^2}{5 \times 10^{-4}\ \text{g Kr/cm}^2} = 4 \times 10^{-11}\ \text{sec}^{-1}.$$

The washout coefficient of tritiated water vapor (HTO) has been estimated from Chamberlain's calculations for SO_2 deposition in rainwater.[5]

[9]R. E. Blanco *et al.* (July 29, 1966), internal memorandum.

[10]A. C. Chamberlain, *Intern. J. Air Pollution* 3, 63 (1960).

[11]H. Hintenberger *et al.*, *Z. Naturforsch.* **19a**, 1227 (1966).

[12]E. Glueckauf and G. P. Kitt, *Proc. Roy. Soc. (London)* **A234**, 557 (1956).

[13]A. S. Rogowski, ORNL, personal communication, December 1966.

ORNL-DWG 66-10211

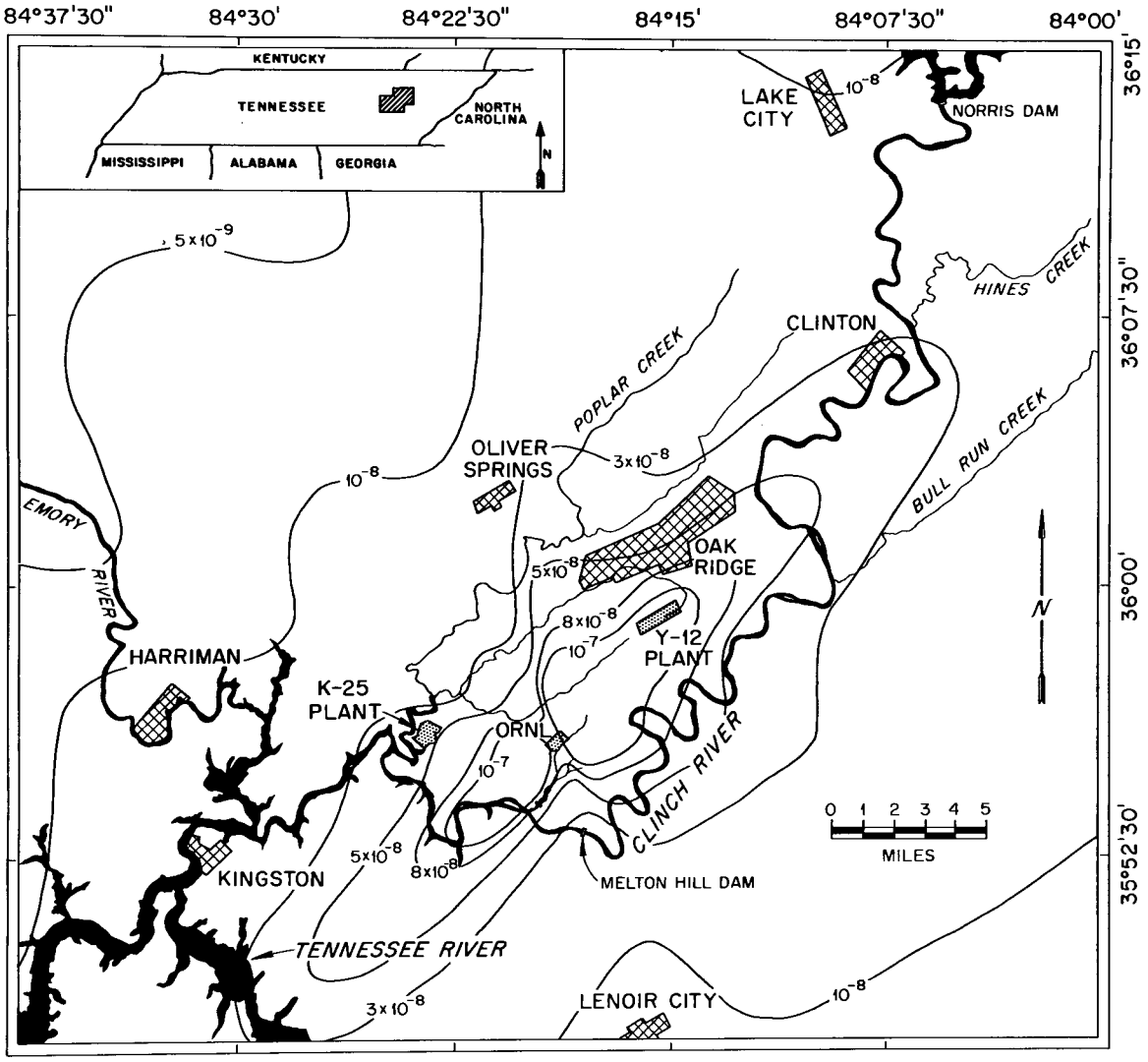

Fig. 5.1. Average Annual Air Concentrations at Ground Surface Concentrations, Parts per Cubic Meter. (Source height $h = 100$ m; source strength $Q = 1$ part/sec.)

The washout coefficient was considered to be proportional to the diffusion coefficient of the vapor in air. Therefore, the following expression was used to calculate Λ_{HTO} for a 4-mm/hr rainfall:

$$\Lambda_{HTO} = \Lambda_{SO_2} \frac{D_{HTO}}{D_{SO_2}} = 4 \times 10^{-4}\ \text{sec}^{-1} ,$$

where

Λ_{HTO} = washout coefficient of HTO vapor (sec^{-1}),

Λ_{SO_2} = washout coefficient of SO_2 ($2 \times 10^{-4}\ \text{sec}^{-1}$),[5]

D_{HTO} = diffusion coefficient of HTO vapor in air (0.23 cm^2/sec),[14]

D_{SO_2} = diffusion coefficient of SO_2 in air (0.115 cm^2/sec).[5]

Loss of HTO from the raindrop to the atmosphere was assumed to be negligible. This assumption is valid if the distance the raindrop falls below the

[14] P. J. Barry, *The Use of Radioactive Trace Gases to Study the Rate of Exchange of Water Vapour Between Air and Natural Surfaces*, AECL-2576 (1966).

contaminated cloud is small as compared with the relaxation length.[15]

A washout coefficient of 4×10^{-4} sec^{-1} for HTO vapor is consistent with that indicated by Chamberlain and Eggleton.[16] Similar values can also be deduced from published data on the concentration of tritium in the atmosphere and in rainwater. For example, the maximum concentration of tritium, in tritium units (TU), was reported to be 10^6 in hydrogen,[17] 10^3 in water vapor,[17] 2×10^4 in methane,[18] and 1.4×10^3 in rainwater.[19] Assuming an average content of water vapor of 8.6 g/m^3 (at 50% relative humidity and 20°C) and using the values of TU listed above, the concentration of tritium in the atmosphere is estimated to be 2.9×10^{-11} curie/m^3. The tritium content in a column of the atmosphere 1 mile high and 1 m^2 in area is 4.7×10^{-8} curie. The rate of tritium removal by a 4-mm/hr rainfall on an area of 1 m^2 would be 5.1×10^{-12} curie/sec. Therefore, the washout coefficient is calculated to be

$$\Lambda = \frac{5.1 \times 10^{-12} \text{ curie/sec}}{4.7 \times 10^{-8} \text{ curie}} = 1.1 \times 10^{-4} \text{sec}^{-1} .$$

Fallout. – If the sorption of a radionuclide by the ground surface is irreversible, the flux of the radionuclide to the surface does not depend on the amount already deposited.[20] Chamberlain describes the rate of deposition for such a system in terms of a deposition velocity. The following equation is used to estimate the deposition velocity of gases or very small particles:[10]

$$V_g(Z_1) = \frac{ku^*}{\ln (ku^* Z_1 D^{-1})} , \qquad (4)$$

where

V_g = deposition velocity (cm/sec),

k = von Karman's constant (0.4),

u^* = friction velocity (cm/sec),

Z_1 = reference height above ground surface at which the concentration of the radionuclide is measured (cm),

D = molecular diffusivity (cm^2/sec).

By assuming $u^* = 40$ cm/sec (appropriate to the Oak Ridge area),[21] $Z_1 = 100$ cm and $D = 0.15$ cm^2/sec (diffusion coefficient of krypton in nitrogen),[22] the deposition velocity of krypton is 1.7 cm/sec. For tritiated water vapor, with $D = 0.23$ cm^2/sec, the deposition velocity is 1.8 cm/sec.[14]

Retention of krypton by the soil is assumed to be limited by the adsorption capacity of the soil for krypton. Krypton retention by soil can be estimated assuming that the amount of krypton adsorbed is proportional to the surface area of the soil. From measurements of krypton adsorption on charcoal (2×10^{-6} g of krypton per gram of charcoal at 25°C and 10^{-3} mm Hg partial pressure)[23] and the ratio of soil to charcoal surface area, 50 m^2/g/1000 m^2/g,[24] the adsorption of krypton by soil is estimated to be 10^{-7} g per gram of soil (or 1.2×10^{-7} g/cm^3 for a soil density of 1.2 g/cm^3). The rate of krypton deposition to the soil is estimated as the product of the deposition velocity ($V_g = 0.017$ m/sec) and the krypton concentration in the atmosphere ($X = 4 \times 10^{-3}$ g/m^3), or 6.8×10^{-5} g m^{-2} sec^{-1}. At this rate of deposition throughout geologic time, soil is probably saturated with krypton and may not act as a perfect sink for the addition of ^{85}Kr. The amount of ^{85}Kr adsorbed on the soil at equilibrium is assumed to be directly proportional to the ratio of radioactive and stable krypton in the atmosphere. For a ^{85}Kr release rate of 1 curie/sec, the soil load (at equilibrium) at the point of maximum ground-level air concentration would be 1.2×10^{-7} g/cm^3 (soil) $\times 4 \times 10^{-9}$ g/m^3/4 $\times$

[15] Relaxation length is the distance in which the isotopic composition of the raindrop decreases by 1/e.

[16] A. C. Chamberlain and A. E. J. Eggleton, *Washout of Tritiated Water Vapour by Rain*, AERE-R3970 (1962).

[17] A. Doury, "Risques Presentes far la Diffusion de Grandes Quantites de Tritium dans l'Atmosphere," *Seminaire sur la Protection Contre les Daniers du Tritium, Le Vesinet, April 16–18, 1964.*

[18] J. Roulin, "Contamination par le Tritium Partir de l'Atmosphere," *Seminaire sur la Protection Contre les Daniers du Tritium, Le Vesinet, April 16–18, 1964.*

[19] R. Bibron, *Detection Atmospherique du Tritium*, CEA-R2629, p. 70 (1965).

[20] A. C. Chamberlain, "Aspects of the Deposition of Radioactive and Other Gases and Particles," in *Aerodynamic Capture of Particles*, Pergamon, New York, 1960.

[21] W. M. Culkowski, personal communication, May 31, 1967.

[22] G. A. Cook (ed.), *Argon, Helium, and the Rare Gases*, vol. 1, p. 38, Interscience, New York, 1961.

[23] W. E. Browning, personal communication, November 1966.

[24] L. D. Baver, *Soil Physics*, 3d ed., p. 14, Wiley, New York, 1956.

10^{-3} g/m^3 (air) $\times$ 397 curies per gram of ^{85}Kr = 4.8×10^{-11}curie/cm^3.

Since the adsorption of ^{85}Kr by the soil may not be an irreversible process, the net flux of ^{85}Kr to the soil (g m^{-2} sec^{-1}) may change as the soil approaches saturation. The deposition velocity calculated from Eq. (2) can be used to estimate only the initial flux of ^{85}Kr to the soil (and cloud depletion by fallout). The flux to the soil would be expected to diminish with time until steady-state conditions are attained.

The mechanisms by which HTO vapor may be retained by the soil would probably include adsorption, condensation, and exchange with soil moisture. Evaporation, evapotranspiration, and soil drainage would act to redistribute the deposited material. Water vapor (H_2O) in the atmosphere would also be acted upon by these mechanisms and would compete with HTO vapor for retention by the soil. In the absence of isotopic fractionation, the ratio at equilibrium of the deposition rate of HTO vapor to H_2O vapor would be directly proportional to the ratio of their respective concentrations in air. A deposition velocity of 0.018 in./sec can be used to estimate the flux when the soil acts as a perfect sink. Assuming an average water vapor content in the atmosphere of 8.6 g/m^3, the flux of water vapor to the soil due to fallout would be 0.15 g m^{-2} sec^{-1} (4.7×10^6 g m^{-2} year^{-1}). The average rate of rainfall in Oak Ridge is 1.1 g m^{-2} sec^{-1}. For a frequency of rainfall of 0.037, the quantity of rainwater deposited each year is 1.3×10^6 g/m^2. These rates imply that if the soil acts as a perfect sink for water vapor fallout, the soil would receive an amount of water equivalent to a continuous rainfall of about 0.4 mm/hr. Obviously this does not occur, and the soil would not act as a perfect sink for either HTO or H_2O vapor. Therefore, the flux of HTO vapor to soil would be expected to vary with time. Only a free water surface, such as the Clinch River, can be assumed to act as a perfect sink for HTO vapor released from a stack. Further studies are necessary to evaluate the flux of both ^{3}H and ^{85}Kr to the soil during transient and steady-state conditions.

Krypton and H_2O vapor might be adsorbed on particulates in the atmosphere and be deposited on the ground with these particles. The quantity of krypton associated with particles is estimated by assuming that the air contains 1.4×10^{-4} g/m^3 of particulates (average of city atmosphere)[25] and, as an upper limit, that the particles can adsorb as much krypton as charcoal (2×10^{-6} g of krypton per gram of particles). Adsorption of krypton on particulates is estimated to be 3×10^{-10} g per cubic meter of air, which is negligible compared with the krypton in the atmosphere (4×10^{-3} g/m^3). Assuming that the particulates (charcoal) can retain two layers of water vapor, the adsorption of water vapor by the particulates is estimated to be 7×10^{-5} g per cubic meter of air. This value is negligible compared with that of water vapor in the atmosphere (8.6 g/m^3).

UNDERGROUND DISPOSAL OF ^{85}Kr

Continuous disposal of ^{85}Kr to suitable geologic formations is one possible means of reducing or avoiding atmospheric release. Although the apparent advantages of underground disposal are its relative simplicity and its effectiveness, one severe requirement imposed on any disposal formation is that it must be essentially free of vertical channels.

The mechanisms considered by which ^{85}Kr may be retained underground include containment and adsorption. In the absence of connective transport, movement is influenced only by molecular diffusion. These mechanisms are evaluated for quantities of ^{85}Kr and volumes of off-gas assumed to be produced at a 10 metric ton/day reprocessing plant (i.e., a continuous release of 1 curie/sec of ^{85}Kr in an off-gas stream at 80 ft^3/min).[26]

Containment

Complete containment of the off-gas in a permeable layer requires an annual storage volume of about 4×10^7 ft^3. In addition, the material overlying the disposal formation must be sufficiently impermeable to prevent the permeation of the gas.

Dynamic Adsorption

Although the adsorption capacity of underground material for krypton is very low, adsorption may

[25] H. E. Landberg and J. van Mieghen (eds.), *Advances in Geophysics*, vol. 4, pp. 39, 97, Academic, New York, 1958.

[26] Jacob Tadmor and K. E. Cowser, *Safety Evaluation of the Release and Removal of Krypton-85 from Nuclear Fuel Reprocessing Plant*, ORNL report (in preparation).

be important in the delay of ^{85}Kr breakthrough because of the large mass of material available underground.

The following relation[27] expresses the retention time t (min) of a gas in the process of dynamic adsorption in a permeable disposal formation:

$$t = \frac{km}{F} , \qquad (5)$$

where

k = adsorption coefficient $\left[\frac{\text{cm}^3\ (\text{STP})}{\text{g}}\right]$,

m = amount of adsorbent (g),

F = flow rate of the carrier gas (cm^3/min).

Assuming an adsorption coefficient of 3 cm^3/g (the basis for this assumption is detailed in ref. 26) and isotropic movement of ^{85}Kr, the required thickness of the disposal formation overlying the point of gas injection for a retention time of about 250 years (decay factor of 10^{-7}) is 250 m.

Molecular Diffusion

Vertical movement of ^{85}Kr is assumed to occur in a relatively impermeable formation (e.g., shale) overlying the disposal formation, in which convective flow is negligible as compared with molecular diffusion. Steady-state conditions are assumed as a first approximation. The average travel time t (sec) of a gas moving by molecular diffusion over a distance L (cm) and having an initial concentration much larger than the concentration at distance L can be expressed by a derivation of Fick's diffusion law:[28]

$$t = \frac{L^2}{2D} , \qquad (6)$$

where D is diffusion coefficient of the gas in the underground formation (cm^2/sec). It is assumed that the diffusion coefficient of krypton is 0.015 cm^2/sec. The thickness of the relatively impermeable formation required to reduce the initial radioactivity of the ^{85}Kr by a factor of 10^7 is computed to be 150 m.

Simultaneous Diffusion and Adsorption

The vertical flow of ^{85}Kr through a relatively impermeable formation in which both molecular diffusion and adsorption take place is assumed to be analogous to the flow of a contaminant in groundwater.[29]

The following equation gives an estimate of the rate of ^{85}Kr movement:

$$\frac{v_a}{v_d} = \frac{1}{1 + (QS/PC_0)} , \qquad (7)$$

where

v_a = velocity of flow of ^{85}Kr retarded by adsorption,

v_d = velocity of flow of ^{85}Kr moving by molecular diffusion (1.5 m),

Q = sorption capacity of ground material (10^{-7} g of krypton per gram of adsorbent) at C_0,

S = bulk density of medium (1.5 g/cm^3),

P = porosity of medium (0.2),

C_0 = initial concentration of ^{85}Kr (1.3×10^{-7} g/cm^3).

The thickness of a relatively impermeable formation required to reduce the initial radioactivity of the ^{85}Kr by a factor of 10^7 is computed to be 55 m.

Comparison Between Stack and Ground Level Releases

Some ^{85}Kr might reach the ground surface following underground disposal and be dispersed into the atmosphere as a ground-level volume source. Since the radioactivity of the ^{85}Kr is assumed to be reduced by a factor of 10^7 as the gas moves underground, air concentrations would be up to 7 orders of magnitude lower than those following a release from a 100-m stack.

---

[27] W. E. Browning, R. E. Adams, and R. D. Ackley, *Removal of Fission Product Gases from Reactor Off-Gas Streams by Adsorption*, ORNL-CF-59-6-47.

[28] P. C. Reist, *Krypton Disposal Studies*, Internal Report, Department of Industrial Hygiene, Harvard School of Public Health, Boston, Mass. (June 10, 1964).

[29] W. J. Kaufman and G. T. Orlob, *J. Am. Water Works Assoc.* **48**, 559 (1956).

Conclusions

The present evaluation indicates that, considering adsorption and molecular diffusion of ^{85}Kr, underground disposal of ^{85}Kr from reprocessing plants may be feasible, provided the right geologic setting is available at the plant site. Requirements for the complete containment of ^{85}Kr in a permeable layer are severe, and finding a suitable site for this operation would be extremely difficult.

EXPERIMENTAL STUDIES ON THE SORPTION AND DIFFUSION OF KRYPTON AND XENON IN SOIL AND UNDERGROUND MATERIALS

Experimental studies were initiated for the measurement of the equilibrium and dynamic adsorption of krypton and xenon as well as of their diffusion coefficients in soil and underground materials. The materials tested were Idaho Falls regolith, vermiculite, limestone, and argillaceous sandstone, including shale.

Preliminary results indicate a definite sorption of both krypton and xenon on all the tested materials. The equilibrium sorption experiments indicate that the sorption capacity of the soil and underground materials is linearly proportional to the partial pressure of the gases (within the range tested of 0.15 to 15 mm Hg). The sorption capacity of Idaho Falls regolith for xenon at a partial pressure of 1.4 mm Hg was found to be $(5.5 \pm 0.7) \times 10^{-6}$ g of xenon per gram of soil. The sorption capacity of the ground materials for xenon is higher than for krypton by a factor of 3 to 4, similar to that found on other adsorbent materials.[30] No appreciable difference was found between the sorption of the gases on the natural ground materials and the materials heated at 450°C for 3 hr.

These experimental results show that the diffusion coefficient of krypton in air is equal (0.15 cm^2/sec) to that assumed in the theoretical evaluations. They also indicate a delay in the breakthrough of the gases eluted in columns filled with ground materials, as compared with empty columns or columns filled with nonsorbent materials (e.g., Lucite).

[30] S. Kitani and J. Takada, *J. Nucl. Sci. Technol.* 2, 51 (1965).

LONG-RANGE WASTE MANAGEMENT STUDY

A more detailed analysis of the projected growth of nuclear power indicates that previous long-range estimates are probably low for the period between 1970 and 2000.[3] As a result a new power projection has been made which takes into account the recent increase in orders for power reactors. Also included in the new estimates are estimates of reactor capacity required for process heat sources and water desalination. The revised estimates are shown in Table 5.1.

In order to develop estimates of waste volumes, it is necessary to predict nuclear reactor characteristics for the period 1970 to 2000. Three assumptions have been followed in developing these predictions:

1. Nearly all reactors installed prior to 1975 will be light-water-moderated (PWR or BWR).
2. Fissile ore cost may increase considerably early in the 21st century unless breeders are introduced.
3. High-thermal-efficiency reactor concepts can be expected to displace the light-water concepts when the associated technological advances have been made.

Many complicating factors must be considered in projecting which reactor concepts will be used. For example, technological advances could come about which would allow a molten-salt concept to be the most economical and displace others.

Table 5.1. Installed Nuclear Electrical Capacity (Mw) by Region in the United States, 1970 to 2000

Region[a]	1970	1980	1990	2000
	$\times 10^3$	$\times 10^3$	$\times 10^3$	$\times 10^3$
I	5.0	20	65	175
II	1.0	15	62	162
III	2.6	18	68	163
IV	4.0	12	39	96
V	0	0	3	26
VI	0.2	2	6	18
VII	0.8	6	21	60
VIII	1.0	12	46	150
Total	14.6	85	310	850

[a] Regions are those defined by the Federal Power Commission (*National Power Survey*, vols. I and II, Federal Power Commission, October 1964.)

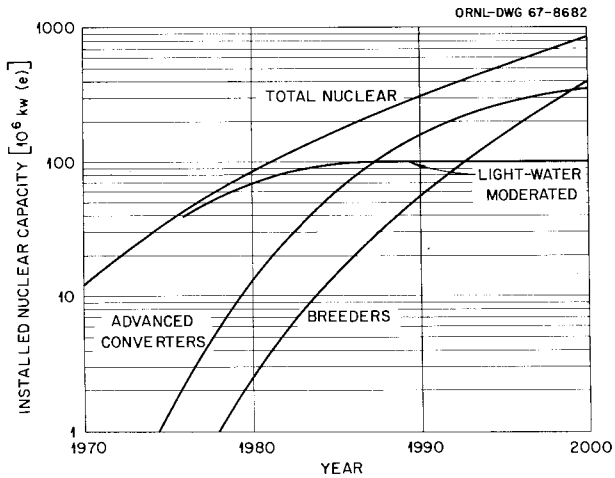

Fig. 5.2. Projected Distribution of Reactor Capacity by Primary Type.

Prior reactor installations and availability of fabrication and processing facilities may influence selection of reactor type for new installations in one area or even in one system. Power cost depends on financial structure so that the optimum for a public facility may not necessarily be the same as for an investor operation.

It is postulated that breeder reactors will be installed as rapidly as breeder fuel can be made available after a given date. It is assumed that thereafter there will be three predominant types of reactors: breeders, advanced converters fueled with ^{235}U and producing breeder fuel, and light-water-moderated reactors. The advanced converters may be of several types, including fast reactors.

The projection of total installed nuclear capacity by primary type is shown in Fig. 5.2. It was assumed that advanced converters would operate at a load factor of about 0.8 and breeders at 0.85; older plants would be expected to operate at a load factor of less than 0.7. Water-moderated plants are expected to operate at a thermal efficiency of 0.32 or higher, while advanced concepts should achieve 0.44.

Prediction of the distribution by region of different reactor types is difficult. There is expected to be some demand for special applications, for example, process heat for desalination purposes, making low-temperature systems attractive. Proximity of suitable fabrication and processing facilities may also be an influencing factor. At this time adequate information is not available to allow significant geographic differentiation of reactor type.

SAFETY EVALUATION OF TANK STORAGE

In the event of a leak of radioactive liquids from a high-level waste storage tank or pipeline into the surrounding soil, localized "hot" spots, exterior to the primary container, are likely to develop. The consequences of such a leak are directly related to the temperature rise in, and adjacent to, the contaminated zone. Since tank leaks have occurred in actual practice, the probability of such a failure is finite. Fortunately, these leaks did not result in a major release of radioactivity.[31,32]

Tank studies for the Oak Ridge environment have thus far characterized hypothetical high-level wastes in storage, considered the loss-of-cooling accident and the resultant atmosphere transport and dose equivalents associated with the vented material, and estimated the underground movement of several radionuclides.[33,34] This study is concerned with the temperature rise in Conasauga shale resulting from fission products that may leak from a tank.

Information developed previously on the construction details and contents of a 1,000,000-gal acid waste storage tank was used as the starting point for the study. The tank, 85 ft in diameter by 35 ft high, is made of stainless steel and is contained within a steel-lined concrete vault. When filled, the tank contains 6,800,000,000 curies of fission products in a 5.7 *M* HNO_3 solution and produces heat at 72,000,000 Btu/hr. Decay heat is removed to maintain the solution temperature at 140°F.

---

[31] R. E. Tomlinson, "Hanford High-Level Waste Management," p. 93 in *Proceedings of the Symposium on Treatment and Storage of High-Level Radioactive Wastes, Vienna, October 8–13, 1962*, IAEA, Vienna, 1963.

[32] B. F. Campbell, E. Doud, and R. E. Tomlinson, "Current Practice in the Management of High-Level Radioactive Wastes in the United States of America," p. 23 in *Proceedings of the Symposium on Treatment and Storage of High-Level Radioactive Wastes, Vienna, October 8–13, 1962*, IAEA, Vienna, 1963.

[33] D. G. Jacobs *et al.*, *Health Phys. Div. Ann. Progr. Rept. July 31*, 1964, ORNL-3697, pp. 56–59.

[34] L. C. Emerson and J. O. Blomeke, "A Safety Analysis of Tank Storage," paper presented at Tenth Annual Meeting, Health Physics Society, Los Angeles, California, June 14–17, 1965.

Steady-State Approximation

Spherical shell geometry and thermal equilibrium were assumed as a first approximation to estimate the magnitude of the thermal problem in contaminated Conasauga shale. Figure 5.3 shows the simplified model and the heat-generating capacity of the contaminated shale by zones. A solution to the spherical shell geometry has been described by Etherington.[35] In the present study the tank has been ignored as a heat sink, and a heat sink was assumed to be located at the edge of a variable-sized non-heat-generating region. To define the limits of temperature rise, two cases were considered. The first assumes that liquid waste is retained in the shale pore volume, and the second assumes that liquid is not retained in this way. The source strength is listed for each zone, and the volume occupied by each zone is normalized to 1 gal of waste. For example, if a leak of 1000 gal occurs and liquid waste is retained by the shale pores, then the volume of zone 1 is 150 ft^3 and the heat-generating rate in this zone is 30,000 Btu/hr.

When acid waste leaks from a tank, it will be neutralized by the buffering action of the shale (260 meq of H^+ per 100 g).[33] Zone 1 depicts the acid zone; the remaining zones are neutralized. Soil loadings were estimated from studies conducted at ambient temperatures and from judicious application of these results to the analysis.[33,36] Values of thermal conductivity of unweathered Conasauga shale range from 1 to 2 Btu min^{-1} ft^{-1} $(°F)^{-1}$ when measured at 30 to 33°C.[37] Similar data do not exist for elevated temperatures. Therefore, it was assumed that the thermal conductivity of shale increases gradually with increasing temperature and follows the pattern observed in metal systems.[38] In all likelihood the thermal conductivity of shale will decrease as temperature increases, especially when water is lost from the shale. Thus, the temperature rise estimated in this analysis is likely to be lower than that which may actually occur.

[35] H. Etherington, *Nuclear Engineering Handbook*, pp. 1–53, McGraw-Hill, New York, 1958.

[36] D. G. Jacobs, *Health Phys.* **4**, 157 (1960).

[37] W. H. Diment and E. C. Robertson, *J. Geophys. Res.* **68**(17), 5035–47 (Sept. 1, 1963).

[38] L. R. Ingersall, O. J. Zobel, and A. C. Ingersall, *Heat Conduction*, p. 288, Univ. of Wisconsin Press, Madison, Wis. 1954.

ORNL-DWG 66-10860A

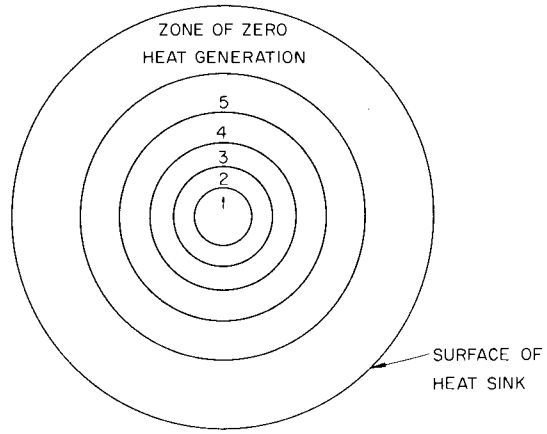

ZONE	LIQUID RETAINED		LIQUID NOT RETAINED	
	Btu ft^{-3} hr^{-1}	ft^3/gal	Btu ft^{-3} hr^{-1}	ft^3/gal
1	200	0.15	61	0.15
2	280	0.05	220	0.06
3	250	0.09	140	0.25
4	33	0.18	4.7	2.80
5	0.45	0.01	0.05	0.73

Fig. 5.3. Configuration and Characteristics of Contaminated Soil Zones.

Figure 5.4 shows the temperature attained in the center of the spherical system as a function of leak volume. Maximum temperatures increase with the volume of leak, the retention of liquid in pore spaces, and the absence of a heat sink. For a leak of 1000 gal, temperatures range from 870 to 1250°F.

Transient Solution

Transient temperatures are now being investigated as a function of time and space in a system that includes a variable-sized cylindrical geometry representing the contaminated zone, and variably spaced heat sinks located at the tank, at the groundwater table, and at the ground surface.

A digital computer program, TOSS, contains many of the requisites for solving the transient problem for a multivariate system.[39] This program, modified to suit the needs of the present study, has the capability of calculating the temperature distribution for a three-dimensional, multiregional problem having internal heat generation. A number of cases are now being analyzed. Studies are also under way to evaluate the diffusivity, or specific heat, and the thermal conductivity of Conasauga shale as functions of temperature.

[39]D. Bagwell, *TOSS, an IBM-7090 Code for Computing Transient or Steady-State Temperature Distributions*, K-1494 (December 1961).

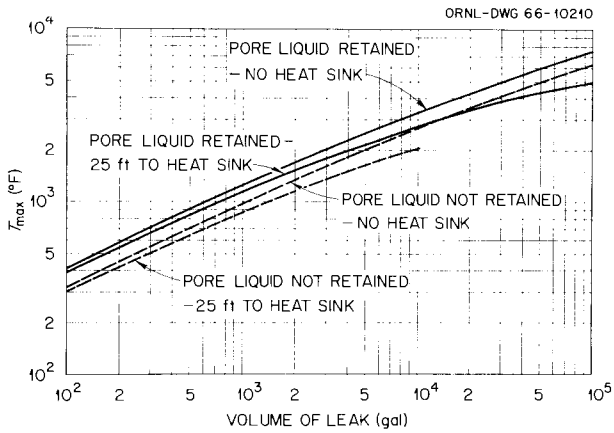

Fig. 5.4. Steady-State Temperature for Spherical Geometry.

6. Earthquakes and Reactor Design[1]

T. F. Lomenick

GENERAL

The problem of the siting and design of reactors to circumvent or withstand transient ground motions and differential ground displacements associated with earthquakes in seismically active areas is one of the most perplexing problems that faces the nuclear power industry today. In general, the problem of earthquakes and reactor design can be divided into two rather distinct phases. First, there are problems associated with prediction of the expected ground vibrations and displacements, and second, there are questions concerning the design of reactor structures to withstand these movements. Ideally, the expected ground motions and permanent displacements at potential sites would be described and defined, and then the structures would be designed accordingly. Recently, however, there has been considerable controversy concerning the expected ground motions and especially the expected differential ground displacements at some sites. Also, suggested structural designs to accommodate differential displacements have not yet been proven. The recent controversies over both the Bodega Bay and Malibu sites attest to this. For many parts of the country where seismic activity is very low and even within some stable areas of California and Nevada, which are states having a high degree of seismic activity, earthquake effects may not be critical with respect to the siting and design of reactors. By contrast there are other well-defined sites, such as those astride the San Andreas fault trace, where reactor structures would most certainly have to be designed to withstand maximum shaking and very great horizontal and perhaps even vertical ground displacements. These extreme cases, however, do not present a problem, since in the former case the structure could be constructed with little or no modifications to accommodate earthquake effects, while in the latter case, reactor structures would simply not be located in such areas. The main problem then is to define and describe the expected earthquake ground effects and design the structures accordingly in those areas that lie near major faults, where movements are likely to occur, or even in those areas where it cannot be reasonably determined whether surface faulting will occur or not. It appears that in most cases the principal surface breaks can be defined in siting, but, in general, it is much more difficult to define the location and extent of the so-called subsidiary or minor faults that may move or develop as a result of the major fault movement.

FAULTS

The exact mechanisms for generating earthquakes are not known; however, it is generally agreed that faulting is the cause of most of the large shallow earthquakes in California and tectonically similar areas of the world.[2] For the continental United States, historic faulting has been confined to the area west of the Rocky Mountains, with the possible exception of a small local area near New Madrid, Missouri. There is good reason to believe

[1]This state-of-the-art paper is a joint venture with the Reactor Division. The Health Physics Division has responsibility for the earth science portion of the review paper, which is summarized here, while the Reactor Division is concerned with structural aspects.

[2]C. R. Allen, "Geologic Relationships of Faults and Earthquakes," 1966 National Meeting of the Association of Engineering Geologists, October 18–23, 1966.

that faulting in the foreseeable future will be restricted primarily to those general regions that have experienced historic faulting; however, there is certainly no guarantee of this. The San Andreas system of faults, which extends from northern California to the Gulf of California, is the most important zone of active faulting in the western United States. However, historic surface ruptures have also occurred along other fault systems in California, Nevada, and Montana.

Through observations of major historic surface breaks, a general evaluation of the length of faulting and the amount of displacement that may be associated with a specific magnitude earthquake along a major active fault can be made. However, little is known about the nature and extent of minor or subsidiary faulting that is associated with the major breaks. In general, the bands of minor displacements are more narrow for strike-slip faults than for normal, reverse, and thrust faults, and the frequency of fractures and the amounts of displacement along the fractures generally decrease away from the main break.[3,4] Also, the surface displacement of faults is more likely to be a straight-line, single fracture in hard massive rocks than in soft alluvial materials.[3] The determination of the nature and extent of minor or subsidiary faulting is one of the principal problems in the siting and design of reactors in seismically active areas. This stems from the fact that the major fault traces are usually, but by no means always, easily recognizable; and, since they are generally quite narrow, they would not be considered as suitable for reactor sites. It should be emphasized here that single or narrow fault traces do not occur for all major faults; there are many where major faulting may extend over a rather wide area. However, since minor fracturing may extend several hundred to several thousand feet on either side of the major break, many potential sites would be included in or near these areas of minor displacements associated with the major faults, especially in seismically active areas like California, where active faults may lie relatively close to one another.

Another important and controversial problem in reactor siting concerns the degree of activity of faults. Many faults in the western part of the United States can be clearly labeled as active, while others have been determined to be unquestionably inactive. However, a great number of faults lie between these two extremes, and these probably are of greatest concern, since they inject further uncertainty as to their likelihood of breaking. The difficulty then lies in the present inability to determine the date of the latest activity along faults and to define an elapsed period of time since the last movement along a fault that would give assurance that the fault was indeed "dead" and that no further movement would occur in the foreseeable future.

Slippage or creep has been noted along several faults in California and may be a rather common phenomenon. Through the establishment of additional small-scale triangulation nets and displacement-meter-type devices along selective faults, some further knowledge of slippage may be obtained that would be useful in an evaluation of faults at reactor sites.

The evaluation of faulting at reactor sites usually entails geological and geophysical investigations, seismological studies, and a review of historic evidence of breaks. These studies all provide data on the activity of nearby faults and, to a lesser degree, on the extent and nature of minor fractures. Undoubtedly, the best indicator of recent fault activity is historic movement along a fault; however, the great majority of faults have not moved in historic times. Seismological evidence often provides useful information on the tectonic activity of many faults, but since the seismological record is relatively short and many shocks are not clearly related to any specific surface fault, seismological information of the activity of faults at many sites is inconclusive.

Geological and geophysical investigations of faults and fault zones provide information on the activity of faults and on the location, distribution, and extent of surface ruptures. Detailed geologic mapping is extremely useful for the evaluation of faults; however, because of the large areal extent of faults, detailed mapping is usually confined to small specific sites. Techniques for defining faults, such as the new remote sensing techniques of multispectral photography, radar imagery, and infrared imagery, as well as the more proven geophysical methods of seismic reflection and refraction, gravity, magnetics, and electrical resistivity, are important in defining the general location

[3] L. S. Cluff, Woodward, Clyde, Sherard, and Associates, Consulting Engineers and Geologists, San Francisco, Calif., personal communication, January 1967.

[4] M. G. Bonilla, U.S. Geological Survey, Menlo Park, Calif., personal communication, December 1966.

of faults in remote and inaccessible areas, under bodies of water (off-shore seismic reflection methods) and in areas where thick covers of alluvium (such as in deep alluvial valleys) or other unconsolidated materials may conceal ruptures in the underlying hard rock. However, these techniques are of limited value in defining the extent and nature of strike-slip faulting and minor fractures in fault zones.

Sensitive seismographs, tiltmeters, strainmeters, and precise surveying techniques on triangulation nets are extremely useful in estimating the activity of faults. Strain buildup or creep in rocks adjacent to faults may be measured by surveys along triangulation nets that cross faults and/or by the installation of strainmeters in rocks. Tectonic uplift or subsidence in the vicinity of faults is commonly measured by precise leveling, tiltmeters, and tide gages.

The two most important problems of faulting in regard to reactor siting and design are exemplified in the evaluation of faulting at the Bodega Bay and Corral Canyon (Malibu) sites. These problems concern: (1) the uncertainty in determining the nature and extent of minor or subsidiary faulting at a specified distance from a known major fault and (2) the uncertainty in determining the activity and, therefore, the likelihood of future breaking along major faults or perhaps fault zones that cannot be classified clearly as active or inactive.

GROUND MOTION

Since ground motions are generated by all earthquakes, some shaking occurs over all parts of the earth's crust. During strong shocks, extremely large areas (hundreds or thousands of square miles) may be subjected to severe shaking. The strong earth motions associated with these larger shocks are of great importance to reactor siting and design. However, at the present time, there is considerable uncertainty in defining the characteristics of the motions that may be expected at particular sites.

Strong-motion accelerameters are commonly used to record severe shaking; however, currently there are only about 140 of these instruments located throughout the United States.[5] Ground accelerations have been recorded for a relatively large number of small shocks, but only four large earthquakes have been recorded on strong-motion instruments. The characteristics of these ground accelerations have been thoroughly analyzed, and this information is commonly used along with other seismic and geologic data for estimating the amount and nature of expected ground motions at other sites. There is, of course, a great need for determining and defining strong shaking for many larger earthquakes at various distances from the epicentral locations of the shocks and under a wide variety of rock and soil conditions.

Even though there is considerable uncertainty about the nature and extent of shaking that might be experienced at many locations in California, it is agreed by many (at least up until the time of the Parkfield, California, earthquake of June 27, 1966) that the maximum shaking within about 12 miles of the surface fault of a large earthquake probably will not exceed 60 sec and will have alternating pulses of acceleration of 0.50*g* for periods of 0.1 to 0.5 sec. The duration of ground motion at greater distances from the fault will increase, while the peak accelerations will be less.

Earthquake-induced ground motions in soils usually result in some amplification of the oscillations as compared with that in hard rock; however, it is not possible to state precisely the magnitude of the difference. Most studies that reveal the intensity of shaking in various types of rock and soil have been conducted with small shocks, and it is difficult to extrapolate ground motions from small to large shocks.

Maximum ground accelerations and ground motions may be estimated from the modified Mercalli intensity rating of earthquakes; however, because this measure of earthquake intensity is a purely subjective one, the true shaking at some locations, especially in alluviated areas, will not be defined adequately in this manner. Strong ground motions have not been recorded for the largest earthquakes, like the 1966 San Francisco (magnitude 8.2) shock; however, from measurements of shocks, such as the 1940 El Centro (magnitude 7), and from observations of other faults and ground motions, estimates of the intensity of shaking to be expected from these large shocks have been made.

A review of the derivations of the expected ground motions at several reactor sites illustrates vividly the lack of strong-motion records for defining the essential characteristics of shaking

[5] W. K. Cloud, "Strong-Motion Seismology," *ESSA Symposium on Earthquake Prediction, February 1966.*

under various combinations of earthquake intensities, soil and rock conditions, and distances from faults or epicentral locations. The limitations of the relatively short seismic record for predicting earthquake occurrence and magnitudes are also pointed out by these examples.

TSUNAMIS (SEISMIC SEA WAVES)

Tsunamis and tsunami-generated oscillations are potentially dangerous to reactor installations at coastal sites. Prediction of maximum runup height is difficult because of relatively obscure coastal and submarine features that tend to amplify waves. The best guidelines for prediction appear to be previous local experience with tsunamis, since some sites have consistently high waves, whereas most locations along the West Coast have consistently low waves, regardless of the direction of approach.

Tsunamis are thought to be generated by vertical displacement of the subsea bottom.[6] About 62% of all recorded tsunamis originate in the Pacific Ocean, where large earthquakes occur along deep bordering trenches.[7] Runup heights in Japan, Kamchatka, Chile, Peru, Alaska, and the Hawaiian Islands have often exceeded 30 ft. However, the West Coast of the United States has not been subjected to runup heights much greater than 16 ft. The 50-ft tsunami wave at Gaviata, California, in 1812 was not accurately documented, and there is considerable doubt that the wave actually exceeded a few feet. The relatively low runup along the West Coast of the United States is attributed to the coastal shelf. Chances of a tsunami off the West Coast are generally thought to be limited, mainly because there have been no local damaging tsunamis in the past and the earthquake of 1906 on the San Andreas fault did not cause a tsunami, even though differential movement probably occurred along the submarine extension. It appears that an earthquake of at least magnitude 6.3 at a shallow depth is needed to cause tsunami runups of 0.5 m, and a magnitude 7.75 earthquake is needed to cause a disastrous tsunami having runups exceeding 30 ft.[7,8] The greatest tsunami runups occur where the coastal shelf is very steep. Where the coastal shelf is not steep, coastal physiographic features that favor high runups include cliffs, triangular-shaped bays, headlands, and submarine ridges. Features that favor low runup include wide fringing reefs, low-lying coasts, and protected coasts.[6,8] In addition, beamed tsunami waves that are normal to the dipole strike of the generating fault are usually higher than the waves along the strike of the fault. Landslides are also sources of local tsunamis.

Only five large tsunamis [Aleutians (2), Kamchatka (1), Chile (1), and Alaska (1)] have been recorded along the West Coast of the United States since 1946. Runup data indicate that, regardless of direction of approach, Crescent City and Avila Beach, California, have experienced higher runup than other stations along the West Coast.[9] Except for the Alaskan tsunami of March 28, 1964, which was beamed toward northern California, most runup heights recorded at West Coast sites have not exceeded the tidal range of about 6 ft; however, Crescent City and Avila Beach have recorded runup heights exceeding 6 ft for tsunamis that were not beamed toward northern California.

INSTRUMENTATION

Seismic instruments for operating scram systems are available; however, they are not being generally considered for power reactors, because it is believed, at least by some, that reactors should remain operable during large earthquakes to provide electrical power for recovery operations. This approach, however, may not be realistic, since power lines are commonly severed during large earthquakes, causing fires.

---

[6] R. L. Wiegel, *Oceanographical Engineering*, p. 532, Prentice-Hall, Englewood Cliffs, N.J., 1964.

[7] B. W. Wilson, L. M. Webb, and V. A. Hendrickson, *The Nature of Tsunamis; Their Generation and Dispersion in Water at Finite Depth*, National Engineering Science Co. Report No. SN-57-2, p. 150.

[8] W. G. Van Dorn, "Tsunamis," *Advances in Hydroscience*, vol. 2, pp. 1–48, Academic, New York, 1965.

[9] M. G. Spaeth and S. C. Berkman, *The Tsunami of March 28, 1964, as Recorded at Tide Stations*, U.S. Department of Commerce, Coast and Geodetic Survey, 59 pp.

7. Dose-Estimation Studies Related to Proposed Construction of an Atlantic-Pacific Interoceanic Canal with Nuclear Explosives

K. E. Cowser P. S. Rohwer
S. V. Kaye W. S. Snyder
E. G. Struxness

In Public Law 88-609, the Congress of the United States authorized an investigation and study of sites for construction of a sea-level canal connecting the Atlantic and Pacific oceans.

Battelle Memorial Institute (BMI), as a principal AEC contractor, is responsible for the management of studies to determine the radiological safety of using nuclear explosives to excavate the proposed canal through southern Panama or northern Colombia. Battelle has awarded subcontracts for studies in ecology (including human, agricultural, terrestrial, marine, and freshwater ecology), in physiochemical oceanography and hydrology, and in dose estimation. The Health Physics Division has the subcontract to make estimates of dose to man and to compare these estimates with appropriate radiological safety standards.

The phase I dose-estimation studies (or tasks) to be performed under the ORNL contract were delineated as follows:

1. Identification of the radionuclides that may contribute the largest dose equivalents to man from both external and internal doses,
2. Development of methods for estimating the potential external and internal doses,
3. Identification, interpretation, and description of the radiation protection guidelines applicable to the radiological-safety feasibility study.

A report was issued in March 1967 which deals in detail with the following major topics:[1] (1) methods for estimating external and internal dose equivalents, for quantifying the transfer of radionuclides through critical exposure pathways, and for identifying the radionuclides likely to be critical; (2) criteria for evaluating the radiological safety of the operation; and (3) lists of radionuclides arranged according to the dose commitment which results from exposure to a unit quantity of each radionuclide.

MODELS FOR DOSE ESTIMATION

External Dose

In the case of external exposure from radionuclide i at location k, an expression $Y_i f_{ij} P_{ijk}(t)$ is a measure of the level of contamination (μc/g or μc/cm^2, dependent upon the pathway of exposure j) present at post-detonation time t. In this expression, Y_i is the yield (μc) of radionuclide i, f_{ij} is the fraction of Y_i entering or available to pathway j, and $P_{ijk}(t)$ is the concentration (μc/g per microcurie released or μc/cm^2 per microcurie released) of radionuclide i present in pathway j for location k at time t per unit activity of radionuclide i initially available to pathway j. The dose

[1] K. E. Cowser *et al.*, *Dose-Estimation Studies Related to Proposed Construction of an Atlantic-Pacific Interoceanic Canal with Nuclear Explosives: Phase I*, ORNL-4101 (March 1967).

rate via pathway j at time t to an individual of age γ (years) at location k would be $Y_i f_{ij} P_{ijk}(t) C_{ij}(\gamma)$ in rems/day. The dose rate term $C_{ij}(\gamma)$ is the dose rate to the reference tissue of an individual of age γ exposed to a unit concentration of radionuclide i in the mode of exposure appropriate for pathway j, and thus includes all necessary factors which account for the habits and characteristics of the individual, including occupancy factors. The total dose, $D^{\text{ext.}}_{ijk}[t_1, t_2, \gamma(t_1)]$, due to radionuclide i in pathway j at location k, accumulated from time t_1 to time t_2 for an individual of age $\gamma(t_1)$ at the beginning of the exposure period is given by

$$D^{\text{ext.}}_{ijk}[t_1, t_2, \gamma(t_1)] = Y_i f_{ij} \int_{t_1}^{t_2} P_{ijk}(t)\, C_{ij}[\gamma(t)]\, dt \text{ (rems)} .$$

The modes of exposure considered were irradiation from a contaminated surface, submersion in contaminated water, and submersion in contaminated air. By use of appropriate expressions for C_{ij}, dose rates and total dose were calculated for an initial unit amount of 176 radionuclides. To permit adaptations to future dose estimates, dose rates were calculated at times of 0, 13 weeks, 1 year, 30 years, and 50 years; accumulated doses were calculated at times of 13 weeks, 1 year, 30 years, 50 years, and infinity.

Internal Dose

The level of contamination $[Y_1 f_{ij} P_{ijk}(t)]$ at post-detonation time t is as defined in "External Dose," although the concentrations considered here would be those in materials which may be ingested or inhaled. The expression $C_{ij}[\gamma(t), t_2 - t]$ denotes the dose commitment in the $t_2 - t$ days following a one-day exposure of an individual then of age $\gamma(t)$ in an environment containing a unit concentration of radionuclide i in the mode appropriate for pathway j. This expression is considered to include all factors which account for habits and characteristics of the individual, including occupancy factors. The total dose accumulated to time t_2 for an exposure beginning at time t_1 is given then by

$$D^{\text{int.}}_{ijk}[t_1, t_2, \gamma(t_1)] = Y_i f_{ij} \int_{t_1}^{t_2} P_{ijk}(t) \times C_{ij}[\gamma(t), t_2 - t]\, dt \text{ (rems)}. \quad (2.2)$$

The dose commitment $C_{ij}[\gamma(t), t_2 - t]$ is considered as a function of time, because the time interval t_1 to t_2 may extend over years and the dose commitment may vary as a function of age. This is particularly important for assessing exposure of fetuses and infants.

Internal dose models for exposure by ingestion and inhalation of radioactive materials were based on a modified version of the "standard man" concept.[2] A single intake of 1 μc was assumed for "standard man." The "standard man" concept was modified to include the age dependence of radionuclide intake and organ mass for the Caucasian, assuming that the age-dependent intake of radionuclides by ingestion and intake by inhalation were directly proportional to water and air intakes respectively.[3–5] The effective absorbed energy, the effective half-time in the organ of interest, and the fraction of radionuclide taken into the body that arrives in the organ of interest were fixed at "standard man" values. Field studies by other subcontractors are expected to furnish information describing the habits and characteristics of the population under consideration.

Radionuclides and body organs selected for analyses were based on the availability of detailed information in ICRP Publication 2.[2] Ages at time of intake were chosen as 0.5, 3.5, 10.5, and 20.5 years. Post-detonation intake times were selected at 60 days, 1 year, and 5 years, and post-intake times for which accumulated doses have been computed were 1 year, 30 years, and 70 years.

---

[2] International Commission on Radiological Protection, *Report of Committee No. 2 on Permissible Dose for Internal Radiation*, ICRP Publication 2, Pergamon, London, 1959; *Health Phys.* 3 (June 1960).

[3] *Report of ICRP Task Group on the Revision of Standard Man* (in preparation).

[4] E. Boyd, *Outline of Physical Growth and Development*, Burgess, Minneapolis, Minn., 1941.

[5] Y. Mochizuki, R. Mowafy, and B. Pasternack, *Health Phys.* 9, 1299 (1963).

Radionuclide Dose Commitment List

Radionuclides were arranged according to (1) external dose commitment from 1 μc per gram of water, per gram of air, and per square centimeter of ground surface; and (2) internal dose commitment from a 1-μc single intake by inhalation and ingestion. A Radionuclide Dose Commitment List does not consider production, venting, or environmental exposure pathways.

Refinements of Internal Dose Calculations for Critical Radionuclides

The internal dose calculations used in the search for critical radionuclides will be reviewed for possible further refinement. Results of preliminary work with ^{131}I illustrate refinements which can be made if the necessary information is available.

A considerable amount of information is available describing ^{131}I metabolism. Figures 7.1 and 7.2

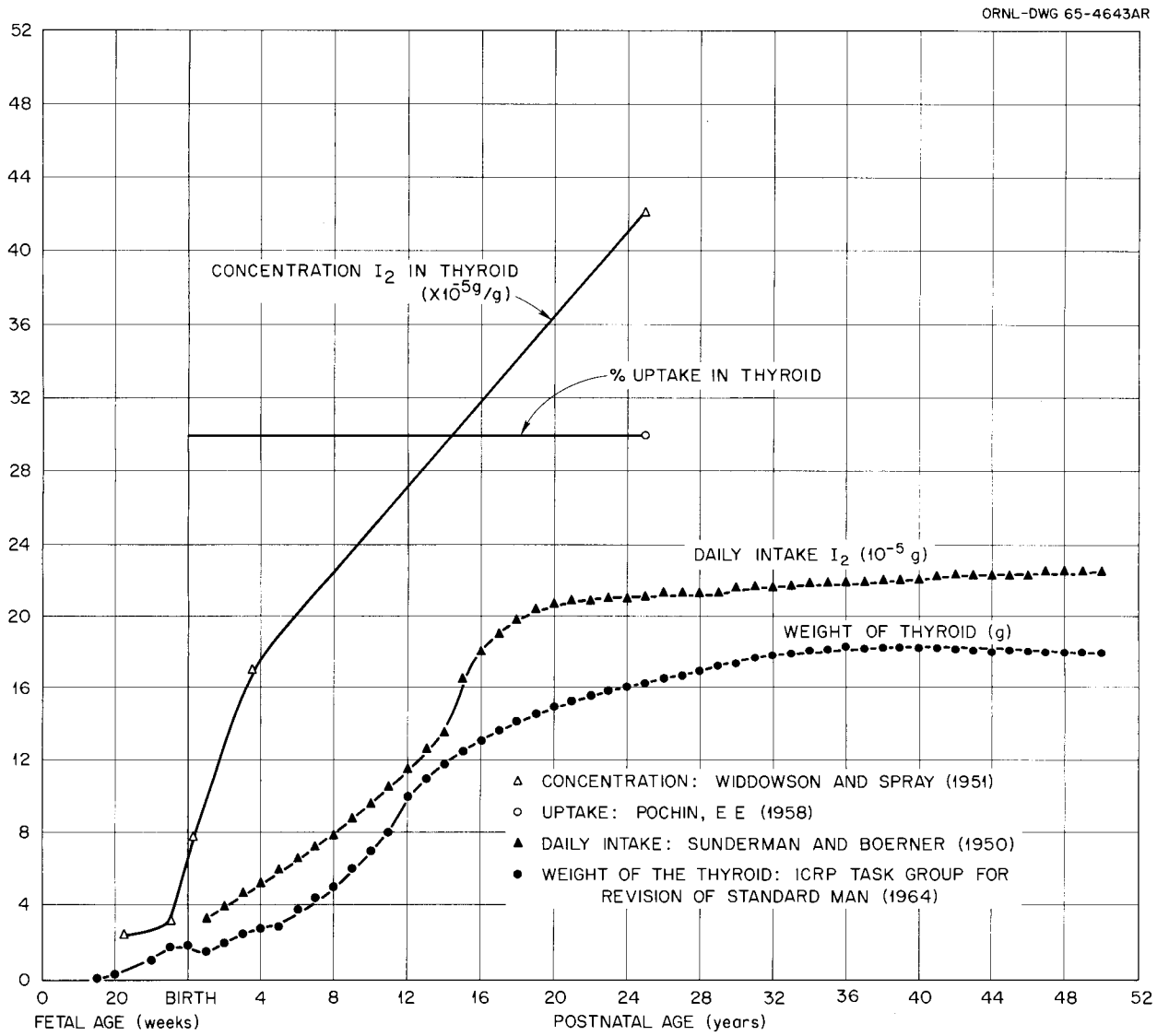

Fig. 7.1. Change in Metabolic Rate of Iodine as a Function of Age.

present some of these data. Thyroid uptake of iodine is the only parameter presented which does not seem to vary significantly with age. These data were used to calculate the infinite rem dose to the thyroid as a function of age at time of ^{131}I intake. Intake was set at 1 μc. The results of

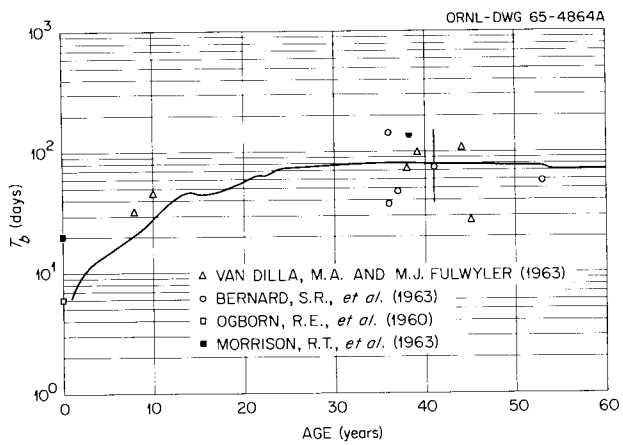

Fig. 7.2. Variation of Biological Half-Time of Iodine as a Function of Age.

these calculations are given in Fig. 7.3. Mass of the thyroid was the only age-dependent variable evaluated in the uppermost curve; all others were fixed at their "standard man" values. Mass of the thyroid and effective half-time of iodine in the thyroid were varied with age in generating the middle curve. Mass of the thyroid, effective half-time of iodine in the thyroid, and daily intake were varied with age in the bottom curve, leaving the energy term as the only age-dependent parameter uncorrected. This intake adjustment, based on daily iodine intake rather than daily water or air intake, assumes the same pathway to man for all iodine. Radionuclides released to the environment by nuclear excavation could follow pathways to man different from those followed by their normal dietary counterparts.[6] The curves in Fig. 7.3 illustrate the importance of evaluating each of the age-dependent parameters. Unfortunately, the data required for such adjustments are either scarce or nonexistent for most other radionuclides. Ideal calculations would use data specific for the populations living in the canal area.

[6]H. N. Wellman *et al.*, *Health Phys.* **12**, 1791 (1966).

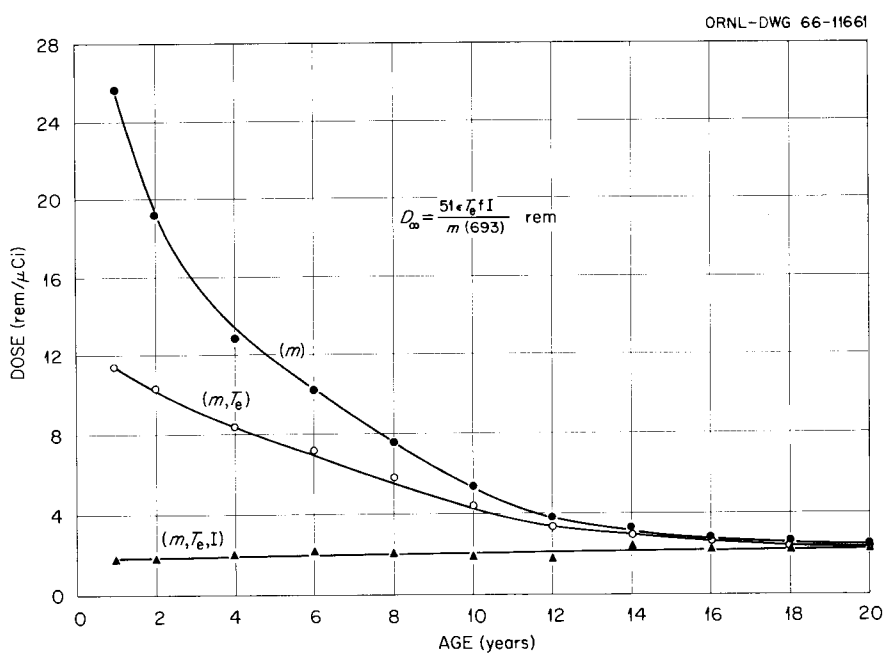

Fig. 7.3. Dose to the Thyroid from 1 μc of ^{131}I as a Function of Age at Time of Intake.

Environmental Pathways

The principal objective of the on-site canal studies is to gather environmental data that will be used to identify the pathways of radionuclide transfer to man, in order to estimate the radiation doses from radionuclides released by nuclear devices. A useful way of dealing with environmental pathways for analytical purposes is the diagrammatic representation of the environment by a network of coupled compartments. Each compartment represents an environmental unit (e.g., grasses and herbs, surface water, sea turtles, etc.). Each has income and loss flux (via environmental pathways) which together alter the inventory of material within the compartment. The types of inventory of interest include stable element, radionuclide, and in some cases biomass. The aspect of biomass of most interest is the flux of food to man, since food is the vehicle for transfer of radionuclides and stable elements. Amounts of food must be considered, along with activity per gram of food or per gram of element, to estimate nuclide intake in the terms needed for internal-dose models.

A preliminary general diagram of a coupled compartmental model of coupled pathways is shown in Fig. 7.4. A general purpose of the entire field program is to define the compartments, pathways, and transfer coefficients involved in the food chains leading to indigenous man. The model diagrammed in Fig. 7.4 is based only on preliminary information, and it is presented here only to illustrate the method of tracing radioactivity through the food web from point of entry to man. As pertinent data become available, the model can be modified to provide a more detailed, more realistic representation of the important compartments and critical

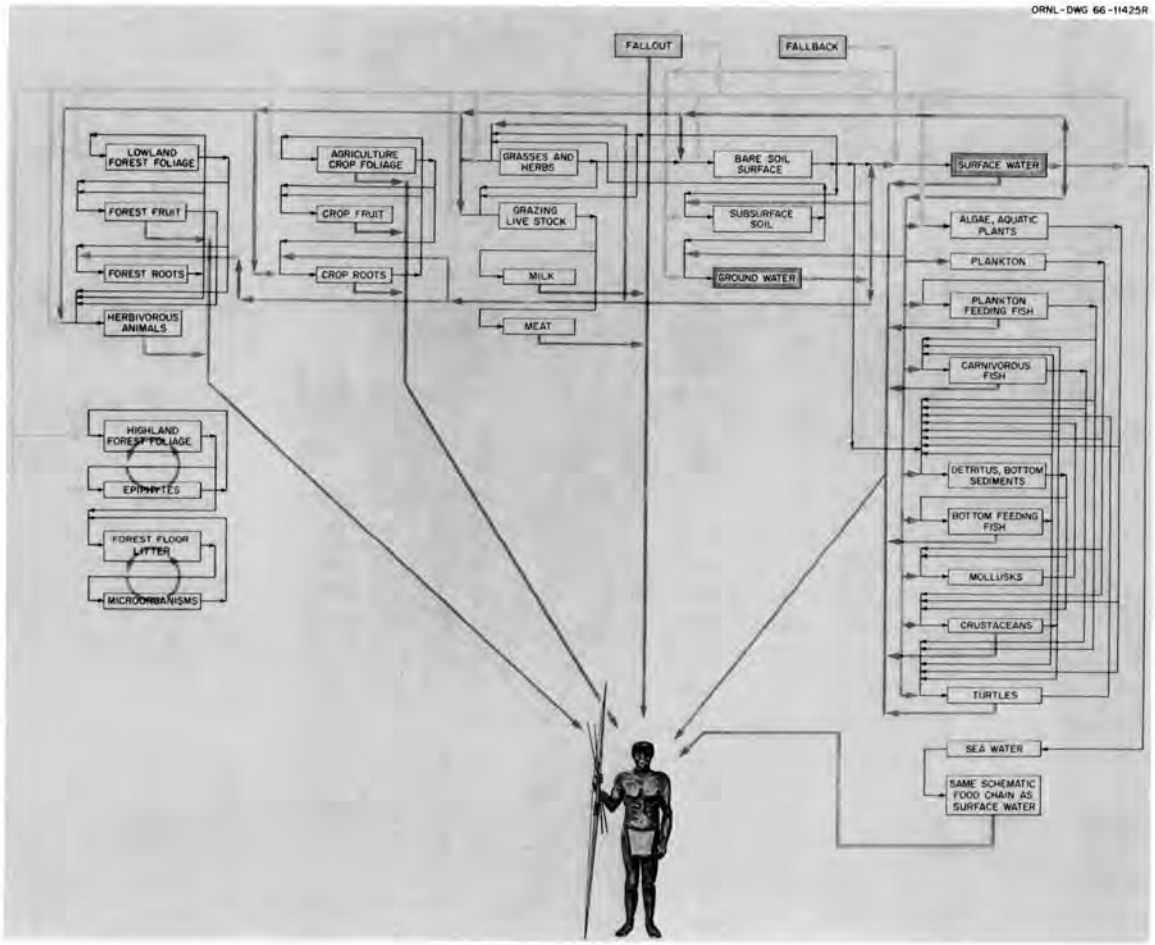

Fig. 7.4. Coupled Compartment Diagram of the Tropical Environment.

food-chain pathways. Proper implementation of this model may help to start bridging the large gap in knowledge between radioactivity entering the environment and that small fraction of the total which could contribute to the internal radiation dose received by man.

The left side of each compartment is the income side, and the right side is the loss side. Compartments that have direct food-chain inputs to man show an arrow leaving the bottom side of the compartment box.

A nuclear detonation results in a radioactive cloud, fallback material, and ejected material that is too heavy to be carried away by the cloud and is blown too far laterally to fall back into the excavation. Figure 7.4 shows only the transfer of radionuclides from fallout and fallback, which comprise two source compartments for the model. This does not imply that the ejecta compartment is a sink, because it is not. Losses from the ejecta compartment have simply not been considered at this time. The loss arrow from the fallout compartment can be followed to see where it becomes income for the primary interceptor compartments. Visualize the fallout descending on the environment and falling on forests, agricultural crops, grasses and herbs, bare soil, surface water, aquatic plants, and seawater. There may even be inhalation by livestock and man. The other source compartment, fallback, has inputs to subsurface soil, groundwater, and surface water. The income to any primary receptor compartment from the two source compartments is proportioned out as loss from the primary receptor compartments to arrive as income to other compartments in the coupled system.

Forests have been arbitrarily divided into a highland ecosystem (~300 m elevation, or ecologically similar to the El Verde forest in Puerto Rico) and a lowland ecosystem (<300 m elevation). The highland forest may be subject to runoff and possible erosion, and the lowland ecosystem may accumulate water or sediments from the uplands. Recent research by Kline and Odum has shown that epiphytes on foliage were apparent accumulators of fallout radionuclides in tropical forests[7] and that when radionuclide tracers (^{134}Cs, ^{85}Sr, and ^{54}Mn) were sprayed on the forest floor at El Verde, there was negligible uptake by roots.[8] Canopy and understory leaves in lower montane tropical forests might get many of their nutrients by aerial interception, including interception by epiphytic organisms, but chemical budget studies to determine this have been started only recently.[8,9] The fraction of the fallout initially washed from the leaves to the forest floor in Fig. 7.4 was cycled between the forest floor microorganisms and the litter, because studies in the El Verde forest have shown that radionuclides reaching the forest floor may not be available as income to the underlying soil and groundwater.[8] However, a small fraction of some radionuclides may be taken up by the roots, which form a thick mat in the litter layer.[10] Witkamp has shown that there is a high year-round activity of microorganisms in the forest floor litter at El Verde.[11] This observation may account for the apparent retention of some radionuclides with the forest floor ecosystem of the lower montane forest.

Provisionally, assume that the forest canopy and the forest floor litter function as ecosystem sinks, as shown by the model, and that there is no loss to compartments outside the highland forest ecosystem (e.g., by erosion of litter and soil to the lowlands). Thus, in this hypothetical situation, the fraction of the total fallout that falls in the highland ecosystem would be isolated from any direct inputs to man (unless man foraged there for food). If this ecosystem were to become a sink, it would be of significant importance, because it would apply to the area of the continental divide in Panama where the elevation is about 300 m. Whether or not these broad generalizations and extrapolations between El Verde and Panama can be made remains to be determined from field observations.

Reference is frequently made to the specific activity concept as a method for evaluating the hazards to man from radionuclides in the environment. Some assumptions for applying various specific activity models are:

---

[7] J. R. Kline and H. T. Odum, *Bull. Ecol. Soc. Am.* **47**, 121 (1966).

[8] J. R. Kline, *Bull. Ecol. Soc. Am.* **47**, 119 (1966).

[9] M. Witkamp, "Mineral Retention by Epiphyllic Organisms," in *A Tropical Rainforest* (in manuscript).

[10] J. R. Kline, "Retention of Fallout Radionuclides of Stratospheric Origin by Tropical Forest Vegetation," in *A Tropical Rainforest* (in manuscript).

[11] M. Witkamp, "Aspects of Soil Microflora in a Gamma Irradiated Rainforest," in *A Tropical Rainforest* (in manuscript).

1. stable and radioactive atoms of the element are completely mixed and behave similarly,
2. biological half-time is known,
3. organisms are in equilibrium with their environment,
4. concentrations of the stable element are known,
5. rates of growth of the organisms are known,
6. rates of input of radioactive atoms are constant.

This concept was evaluated in a way that reveals its limitations, considering the time-dependent relative importance of radioactive half-life, biological half-time, and biological growth. The concept may be useful for the marine environment and possibly for parts of the freshwater environment. Application to the terrestrial environment is likely to be limited, principally because there may not be uniform mixing of radioactive atoms with stable atoms of the same element.

Radiation Safety Criteria

Criteria for evaluating radiological safety were developed from the recommendations of recognized authorities which might reasonably apply in an operation of this magnitude, taking account of the principle of balancing the possible benefits against the potential risks. Reports of five national and international authorities (ICRP, IAEA, NCRP, FRC, and MRC) were considered in developing the criteria listed in Table 7.1.

Table 7.1. Radiation Safety Criteria for the Bioenvironmental and Radiological-Safety Feasibility Study

Critical Organ	Currently Accepted Dose Limit or Dose Commitment for Individuals in the General Population Requiring No Special Evaluation[a] (rems/year)	Projected Dose Commitments Requiring Special Evaluation of Risks vs Benefits[b]	
		Maximum Dose Commitment in Any 1 Year Following the Contaminating Events[c] (rems/year)	Maximum Dose Commitment in 70 Years Following the Contaminating Events[d] (rems/70 years)
Red bone marrow	0.5	3	10
Gonads	0.5	3	10
Whole body	0.5	3	10
Lenses of eyes	0.5	8	15
Other single organs	1.5	8	15
Skin, bone, thyroid[e]	3.0	15	30
Hands, forearms, feet, and ankles	7.5	38	75

[a]Values listed are from ICRP, FRC, and IAEA and are for individuals in the general population. They should be reduced to one-third of these numerical values when applied to the average of a critical group in the population. These dose limits, or dose commitments, are permissible for the lifetime of an individual in the general population without undue risk. Any situation leading to exposure in excess of these limits should be evaluated appropriately, and efforts should be made to reduce them accordingly.

[b]Considering all exposure situations judged to be important in the construction of routes 17 and 25 with nuclear explosives, dose commitments will be estimated (projected) for each radionuclide and each exposure pathway (as a function of time following each contaminating event and distance from the two canal alignments) for several different age groups in the contiguous populations, and summed. If the estimated dose commitments exceed the levels in column 2, special considerations (including cost estimates) will be required to assess the feasibility of methods to reduce the potential exposures, balancing the benefits against the risks. Generally, the higher the projected dose commitments, the greater will be the effort required to reduce potential exposures.

[c]Maximum dose commitment for any one year is the estimated (projected) dose which would be received in one year for individuals in the general population from the contaminating events if no action were taken to avert it.

[d]Maximum dose commitment in 70 years is the estimated lifetime dose which would be received by individuals in the general population from the contaminating events if no action were taken to avert it.

[e]ICRP and FRC recommended that the annual dose for the thyroid gland of children be limited to 1.5 rems.

8. Related Cooperative Projects

COOPERATION OF OTHER AGENCIES IN ORNL STUDIES

The research and development program of the Radioactive Waste Disposal Section is of special interest to various public and private agencies. Several study projects provide an opportunity for others to participate, both to supplement the Laboratory's research effort and to gain information and experience of value to the other agency. The ways in which another agency may cooperate include assignment of on-loan personnel as temporary additions to the ORNL staff, performance of specific work under cooperative agreements to augment ORNL programs, work authorized under ORNL subcontracts and performed by the contracting agency, and coordination of related work projects with ORNL projects for mutual benefit.

Disposal in Salt Formations

Agencies participating in this program during the past year have included the Carey Salt Company of Hutchinson, Kansas, an ORNL subcontractor. The results of this cooperative program are given in the section headed "Disposal in Natural Salt Formations," Chap. 3 of this report.

VISITING INVESTIGATORS FROM ABROAD

During the year, three noncitizen guests participated as temporary members of the research staff of the section. They are Roger Rzekiecki (France), Jacob Tadmor (Israel), and Joseph Shalhevet (Israel).

NUCLEAR SAFETY REVIEW

During the year, several individuals in the section contributed review articles which were published under the category "Consequences of Activity Release."

COMMITTEE WORK

American Standards Association

Three members of the section continued in their assignments under ASA Subcommittee 2 on Radioactive Waste Disposal during the first six months of the present report. This subcommittee and its parent committee, ASA N5 on Nuclear Fuel Cycle Engineering, were discontinued, and the subcommittee program was turned back to the Nuclear Standards Board of ASA in February 1967.

ASCE – Committee on Sanitary Engineering Aspects of Nuclear Energy

The Section Leader served as a member of the Committee on Sanitary Engineering Aspects of Nuclear Energy of the American Society of Civil Engineers.

PARTICIPATION IN EDUCATIONAL PROGRAMS

Two members of the section participated in the cooperative program with the University of Tennessee. One taught a course on Radioactive Waste Disposal and the other a course on Health Physics Aspects of Radioactive Waste Disposal.

During the ten weeks of field training of the AEC Fellowship course in applied radiation physics at ORNL, two students were assigned to work five weeks in the section under the supervision of a staff member.

Part II. Radiation Ecology

S. I. Auerbach

9. Responses of Animal Populations to Ionizing Radiation

C. E. Baker
B. G. Blaylock[1]
D. A. Crossley, Jr.[1]
Gladys J. Dodson[1]
P. B. Dunaway
J. T. Kitchings III
C. Koh[2]
Lovell L. Lewis[3]
C. M. McConnell
Margaret F. Miller
D. E. Reichle[1]
J. D. Story
L. E. Tucker

RADIATION EFFECTS IN BLOOD OF INDIGENOUS SMALL MAMMALS

P. B. Dunaway
J. D. Story
J. T. Kitchings III
L. E. Tucker
L. L. Lewis
C. Koh
C. M. McConnell

Prior studies established basic hematological values for native small mammals, and effects of certain endogenous and exogenous factors were described.[4,5] Hematology is of interest because hematopoietic tissues are relatively radiosensitive, and sampling of peripheral blood permits diagnosis of radiation effects and other pathologies without sacrificing animals, which is advantageous in population studies. Radiation responses in peripheral blood of four species of indigenous rodents were measured after whole-body irradiation. Species used were: rice rat, *Oryzomys palustris;* cotton rat, *Sigmodon hispidus;* white-footed mouse, *Peromyscus leucopus;* and house mouse, *Mus musculus.* Five individuals of each species received 0, 200, or 400 rads. Blood samples were taken from each animal 11 days before irradiation, and 1, 10, and 20 days postirradiation.

Total leukocyte number in all irradiated groups dropped sharply by one day postirradiation. Decreases in number of lymphocytes primarily accounted for the decrease in total number of leukocytes. Even by day 10, leukocyte count was still low. The rice rat exhibited the greatest decreases in leukocyte number (81 and 85% at postirradiation days 1 and 10 respectively); decrease in the other three species ranged from 49 to 71% on days 1 and 10. By day 20, recovery in leukocyte number was evident for all species (49 to 82% of original values). Erythrocyte count and associated values (hemoglobin concentrations and hematocrit percentages) decreased by day 20 in the rice rat, but these values were not significantly lower in the other species. This evidence indicates that the extreme radiosensitivity of the rice rat[6] may be attributable to radiosensitivity of the hemopoietic system of this species.

Cotton rats were irradiated with 200 and 600 rads, and blood samples were taken from two specimens each of the controls and the treatment groups on day 14 preirradiation, every day for the first nine days postirradiation, and thereafter on days 11, 13, 15, 17, 20, 24, and 30. All animals of each group at each sampling period were sacrificed after bleeding, and radiosensitive tissues of one of each group were removed for pathological examination by G. E. Cosgrove, Biology Division, ORNL. As in the previous experiment, the most severe depression was in total leukocyte number, which was caused primarily by a decrease

[1]Dual capacity.

[2]Foreign student.

[3]Deceased.

[4]S. I. Auerbach *et al.*, *Health Phys. Div. Ann. Progr. Rept. July 31, 1964*, ORNL-3697, p. 79.

[5]P. B. Dunaway and L. L. Lewis, *Nature* **205**, 481–84 (1965).

[6]P. B. Dunaway *et al.*, to be published in Proc. 2nd National Symposium Radioecology, May 15–17, 1967.

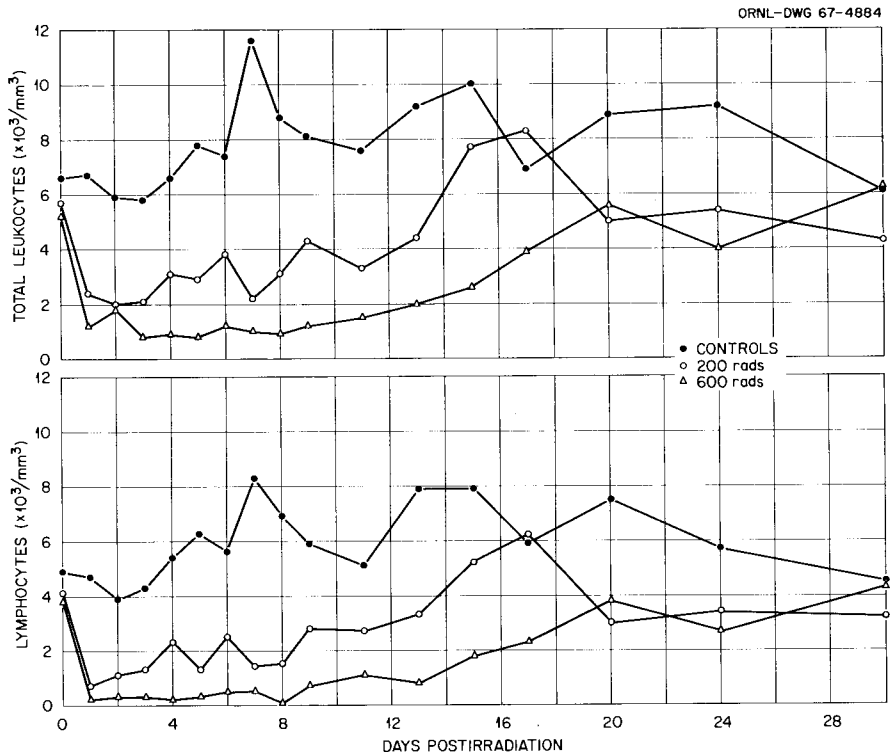

Fig. 9.1. Irradiation Response of Total Leukocyte Number and Lymphocyte Number in Cotton Rats.

in lymphocyte number (Fig. 9.1). Recovery in lymphocyte number in the 600-rad animals did not begin until about day 9, but there is evidence of recovery within the first few days in the 200-rad animals. The peaks in lymphocyte recovery at day 17 for the 200-rad group and at day 20 for the 600-rad group are not explicable at this time but may represent an "overrun" phenomenon or a reflection of cellular proliferation cycles. Similarly, the general increase in lymphocytes after day 3 in controls cannot be explained at present.

Erythrocyte number, hematocrit percentage, and hemoglobin concentration were consistently lower than controls in the 600-rad rats for the first 11 days; these values also were lower than controls in the 200-rad animals for the first four days, but were slightly higher than controls from day 5 to day 13. From day 15 to 30, erythrocyte count and associated values for the 0-, 200-, and 600-rad groups were similar. Histological examinations of radiosensitive tissues substantiated the findings in the peripheral blood samples; damage in lymphatic tissues was especially severe during the first week.

RADIONUCLIDE EXCRETION IN INDIGENOUS SMALL MAMMALS

P. B. Dunaway C. E. Baker
J. D. Story J. T. Kitchings III
L. E. Tucker

Projected studies of irradiated small mammals living in field enclosures require techniques for measuring metabolism, blood responses, and radionuclide incorporation. Disturbances to the experimental animals in the field must be kept to a minimum, and serial sacrifices of the animals will not be practicable in most experiments. Methods utilizing radionuclides and radioactive compounds may solve some of these problems.

A previous laboratory study[7] indicated that a thymidine analog, 5-iodo-2′-deoxyuridine (IUDR), will be useful in measuring gastrointestinal damage and general metabolism in free-ranging

[7]T. P. O'Farrell, S. I. Auerbach, and P. B. Dunaway, *Incorporation of a Thymidine Analog by Indigenous Rodents*, ORNL-3907 (1966).

animals, but it was necessary to develop a field technique for blocking uptake of catabolized radioiodine by the thyroid and extrathyroidal pools. An intraperitonal injection of 10 mg of stable NaI in cotton rats (450 mg/kg) 2 hr before administration of $Na^{131}I$ provided an effective blocking dose for the radioiodide; 0.1 mg was not adequate, and 20, 30, 50 mg were no more effective than 10 mg.

Future research with cotton rats in ^{137}Cs-contaminated field enclosures requires advance knowledge of the behavior of cesium in these animals in response to environmental factors. The objective of a recent laboratory study was to test for a correlation between cesium retention and general metabolism in the cotton rat. Retention of intraperitoneally injected ^{134}Cs after three weeks at 5, 15, and 25°C was 2.9, 4.1, and 4.8%, respectively, of the initial activity. Slopes of the regression lines differed significantly ($P < 0.01$), indicating that the three groups of cotton rats had different cesium-retention rates. Oxygen consumption was 3.2, 2.2, and 1.5 $cm^3\ hr^{-1}\ g^{-1}$ at 5, 15, and 25°C respectively. Therefore, there was an inverse relationship between oxygen consumption and cesium retention. Oxygen consumption rates also were related inversely to increasing body weights at the three temperatures, but no relation between cesium retention and body weight was evident. Results of this study suggest that cesium may be used as an index of thermoregulation but not as an index of general metabolism.

Loss rates of ^{59}Fe at 25°C were determined in seven species of native rodents in an effort to establish a suitable index of radiation damage in erythropoietic tissues and hemoglobin synthesis in free-ranging animals. Four specimens of each species were injected intraperitoneally with ^{59}Fe, and whole-body counts were made until postinjection day 114. Excretion rates of the ^{59}Fe were low. Eleven days were required to reach a constant elimination rate in *P. leucopus, O. palustris, S. hispidus,* and *M. musculus;* the golden mouse, *Peromyscus nuttalli,* and the harvest mouse, *Reithrodontomys humulis,* eliminated at a constant rate after day 15; and the Norway rat, *Rattus norvegicus,* required 22 days to reach a constant rate. The biological elimination constants and half-lives of ^{59}Fe for these species are listed in Table 9.1. Two species (*P. nuttalli* and *O. palustris*) deviated from the expected pattern of decreasing excretion rates with increasing body weight.

Table 9.1. Elimination Constants (λ_b) and Biological Half-Lives (T_b) of ^{59}Fe in Seven Species of Indigenous Rodents

Taxon	Average Weight[a] (g)	λ_b (%/day)	T_b (days)
Cricetidae			
R. humulis	8.9	0.34	204
P. leucopus	19.3	0.30	231
P. nuttalli	23.4	0.17	408
O. palustris	48.0	0.14	495
S. hispidus	110.0	0.21	330
Muridae			
M. musculus	16.5	0.34	204
R. norvegicus	218.6	0.22	315

[a]Average weight from time of injection to day of irradiation.

Whole-body irradiation of two animals of each species with 400 rads produced a 1.2% decrease from the established λ_b in the radiosensitive rice rat by postirradiation day 5, but slight increases (0.2 to 1.3%) were measured in the other species. The remaining two individuals in each species then were given a dose about 150 rads below the previously established $LD_{50\text{-}30}$ estimates for each species.[8] Decreases in all species ranged from 1.9 to 4.4% by day 5 except in *M. musculus,* in which no change occurred. It appears that radiation effects on iron metabolism cannot be detected with this technique, on a short-term basis at least, in animals irradiated at relatively low levels.

SURVIVAL OF IRRADIATED INSECTS IN FIELD ENVIRONMENTS

D. A. Crossley, Jr. M. H. Shanks

The ability of insect populations to survive a nuclear attack is an important factor in planning for postattack agricultural procedures. Analyses of postattack insect problems are currently hampered by insufficient data on the radiation sensi-

[8]P. B. Dunaway *et al.*, Proc. 2nd National Symposium Radioecology, May 15–17, 1967.

Fig. 9.2. Field Enclosure for Irradiated Crickets Released into a Fescue Meadow, September 1966.

tivity of insect populations in their natural environments. Recent laboratory studies have shown that insects are more radiosensitive than had been previously supposed.[9] The extrapolation of these laboratory results to field areas must be done cautiously, since radiation damage may be intensified or ameliorated by interaction with environmental factors.

The postirradiation survival of brown crickets (*Acheta domesticus*) in a grassland habitat was analyzed and compared with the results of laboratory experiments. This insect, easily maintained for laboratory studies, has been the subject of detailed studies on the mortality response of several life history stages to various radiation doses.[10] Enclosures were erected which consisted of sheet-metal walls sealed with cold tar at their unions and bases (Fig. 9.2). Plastic shields on the tops of the walls prevented crickets from crawling over them. Crickets released into these pens were recaptured with pitfall traps[11] around the inner periphery of the pens. Up to 50% of the population could be recaptured in one night.

An initial experiment in September 1966 evaluated survival of adult *Acheta* following irradiation with 4000 rads from a ^{60}Co source. Irradiated crickets (250 adults) were released into a pen and then recaptured nightly in traps. Captured crickets were returned to the pen. In the laboratory, 50 similarly irradiated crickets from the same stock were held at the optimum rearing temperature[12] of 85°F, and their survival was recorded. An additional group of 50 crickets was similarly irradiated and then maintained in a controlled environment chamber, programmed daily to duplicate the temperature regimen recorded in the field pen.

Results of the experiment are illustrated in Fig. 9.3. Crickets held at 85°F had a 50% survival time of 8.5 days, which agrees with previous find-

[9] S. I. Auerbach *et al.*, *Health Phys. Div. Ann. Progr. Rept. July 31, 1965*, ORNL-3849, pp. 53–56.

[10] E. F. Menhinick and D. A. Crossley, Jr., unpublished data.

[11] D. E. Reichle and D. A. Crossley, Jr., *Health Phys.* 11, 1375–84 (1965).

[12] L. M. Sparks, Clemson Agr. Coll. Extension Serv. Circ. 464, 14 pp., 1960.

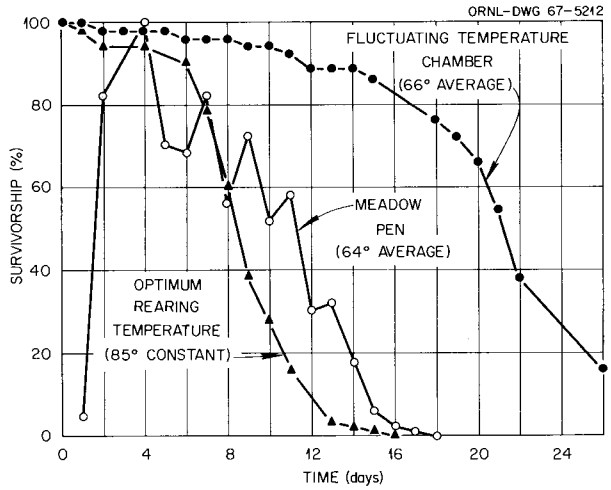

Fig. 9.3. Survivorship of Crickets (*Acheta domesticus*) Irradiated with 4000 rads and then Maintained Under Three Different Environmental Regimes. Lower curve shows survivorship of crickets held at a constant 850°F (the optimum rearing temperature) in a controlled environment chamber. Middle curve illustrates survivorship in a meadow pen, estimated from trapping recaptures. Upper curve shows survivorship in a controlled environment chamber programmed to duplicate temperatures recorded in the meadow pen.

ings for an acute radiation dose of 4000 rads.[10] (Unirradiated controls had a 50% survival time of about 25 days.) Irradiated crickets maintained in the programmed environmental chamber had a 50% survival time of 21 days (Fig. 9.3). This prolonged survival is produced by the lower effective temperatures (mean daily temperature, 66°F).

Recaptures of irradiated crickets from the pen suggest a 50% survival time of about 11 days in the meadow environment. Figure 9.3 shows that the largest recapture was obtained on the fourth day after release. Such a lag in trap response is typical for *Acheta*. Recaptures on the fourth day amounted to 40% of the population released (100 out of 250), suggesting that little or no mortality had occurred during the first four days. Decline in recaptures after day 4 resembles a typical survivorship curve, if random fluctuation in daily estimates is assumed.

The decreased survival time of crickets in the meadow pens indicates that additional mortality factors were operating there which do not affect survival in laboratory cultures. One obvious factor is predation in the field pens. Wolf spiders (*Lycosa* spp.) were captured in the pitfall traps and were observed feeding on these crickets. Further experimentation will attempt to measure the magnitude of predation by using transfer of a radioisotope tag from crickets to lycosid spiders.

LIFE HISTORY RADIATION SENSITIVITY OF BAGWORMS (LEPIDOPTERA: PSYCHIDAE)

D. E. Reichle Gladys J. Dodson

The effects of radiation on natural ecological systems depend upon many biological, environmental, and time-dependent phenomena which may affect individual population responses as well as total ecosystem interactions. One important parameter is the differential radiosensitivity of organisms between immature and adult developmental stages. The time at which a population is subjected to radiation stress can affect both the population structure and number. In insects with high intrinsic rates of reproduction and population growth, adult survival and maturation – barring possible genetic damage– are critical factors determining the capacity for population recovery.

The evergreen bagworm is a voracious feeder upon many coniferous and deciduous trees. Approximately 60% of its life cycle (October through April) is spent in the egg stage attached to branches of the host plant. Embryonic development and hatching occur in early May, and the active larvae predominate until autumn. Both life history stages were irradiated in a ^{60}Co gamma source (exposure dose rate of 14.4 rads/sec). Eggs were irradiated at successive intervals after breaking dormancy (postdiapause) and larvae at four size (age) stages (Fig. 9.4). The radiation response compared was 50% mortality at 20 days (LD_{50-20}) following treatment. For eggs, this time interval included hatching as well as subsequent larval survival. These data are summarized in Fig. 9.5.

The mean LD_{50-20} for one-day postdiapause eggs was 420 rads, but it progressively increased during embryonic development to approximately 14,600 rads for eight- and ten-day eggs. Immediately before hatching (12.5 days) egg sensitivity increased, showing a mean LD_{50-20} of only 4600 rads. Other parameters, such as maximum mortality doses and minimal tolerances, have previously been reported for developing bagworm

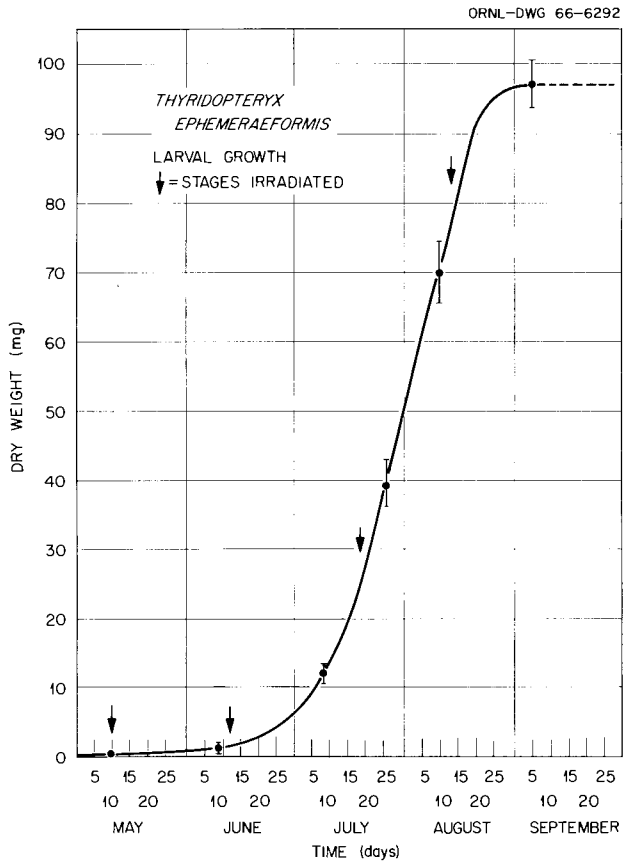

Fig. 9.4. Growth Curve for Bagworm Larvae, Showing Size (Age) Classes Irradiated. Mean ± 2 S.E.

eggs.[13] At hatching the larva weighs about 0.5 mg. During the first few days, the larva displays an intricate behavior pattern during construction of its protective case. Radiation doses as low as 1600 to 3200 rads were found to disrupt this behavior and prevent case construction. This compares with an LD_{50-20} of 9300 rads for day-old larvae, and only 15% mortality at 20 days resulting from exposure to 6400 rads. By early June, larvae enter a phase of intensive feeding and rapid growth. During July and August larvae double in size about every 12 days (Fig. 9.4). However, there was no correlation between radiation sensitivity and larval size (or age). The LD_{50-20} values plotted in Fig. 9.5 were, respectively, 13,180, 9550, and 10,470 rads for 33-, 70-, and 95-day-old larvae. The size of these instars ranged from 12 to 97 mg dry body weight.

For a single radiation end point (LD_{50-20}), sensitivities between egg and larval stages varied by a factor of nearly 35. Even greater ranges in radiosensitivity may be expected when more information is available on behavioral and genetic effects. Current research is examining aspects of fertility, fecundity, and environment (tempera-

[13] S. I. Auerbach *et al.*, *Health Phys. Div. Ann. Progr. Rept. July 31, 1965*, ORNL-3849, pp. 56–58.

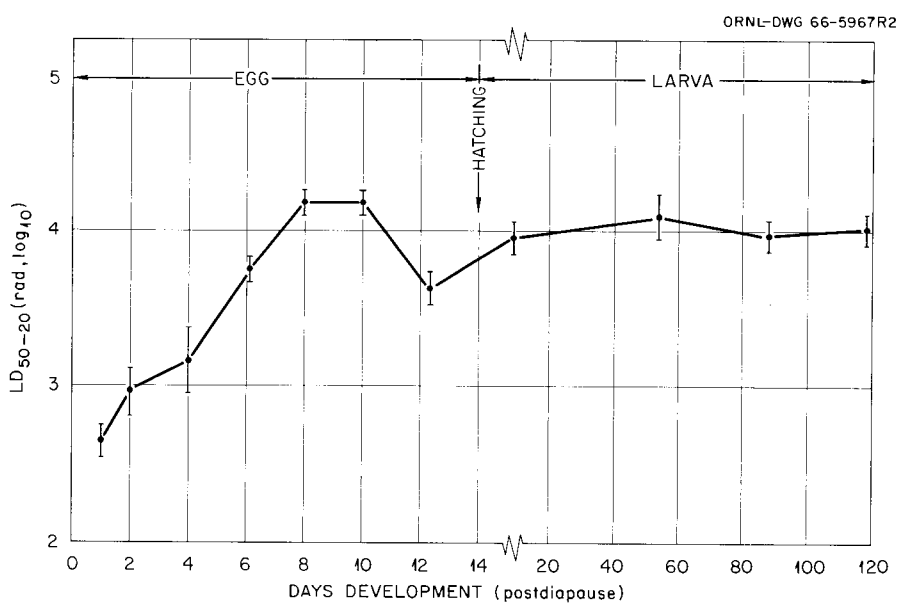

Fig. 9.5. Radiation Sensitivity of the Evergreen Bagworm *Thyridopteryx ephemeraeformis* at Various Life History Stages. Mean ± 2 S.E.

ture influence on metabolism) in relation to the population responses of irradiated insects.

POPULATION GENETICS AND RADIATION EFFECTS STUDIES

B. G. Blaylock Margaret F. Miller

The detection of an increased frequency of chromosomal aberrations in the natural population of *Chironomus tentans* inhabiting White Oak Lake[14] has led to related field and laboratory investigations. The genetic damage suffered by irradiated populations may be expressed as the fitness of an organism, or its ability to leave surviving offspring. In contrast to the studies with *Chironomus*, a dipteran, one of the important components of fitness, fecundity, was studied in the mosquito fish, *Gambusia affinis affinis*, a vertebrate.

The *Gambusia* in White Oak Lake may receive approximately 130 rads/year from the internal emitters they have accumulated while living in the radioactive contaminated area and may receive as much as 10 rads/day from the bottom sediments of White Oak Lake. Fish having well-developed embryos were dissected, and the viable embryos, dead embryos, and embryonic abnormalities were scored. Fecundity, or brood size, was found to be greater in *Gambusia* from White Oak Lake than in a control population. In 99 fish from White Oak Lake and 98 from a control area (Swan Pond), 4672 and 3257 embryos, respectively, were examined (Table 9.2). The average number of viable embryos per fish from White Oak Lake was 44.4 ± 1.83; the average number from the control area was 32.1 ± 1.49. Besides the brood size, the percent of dead embryos and abnormalities was greater in the White Oak Lake population. The increase in embryonic mortality and abnormalities can be attributed to the high background radiation to which the fish are exposed, but the brood size would be expected to be decreased by the exposure to ionizing radiation. However, many environmental and physiological factors can affect egg production and the percent of offspring reaching maturity. Natural selection and genetic variability enable populations of fecund species with a short generation time to adjust rapidly to the different environmental pressures. In this way a population can adjust to the increased mortality produced by ionizing radiation.

Effects of acute and chronic radiation on interspecific competition were studied in the laboratory. The relative fitness of *Drosophila* populations was measured by the competition between different species. Populations started with 50% *Drosophila melanogaster* and 50% *Drosophila simulans*, which are similar both morphologically and genetically, were exposed to different doses of radiation. *Drosophila simulans* was the superior species for 30 weeks in the control populations, but was eliminated by *D. melanogaster* when the populations were exposed to a chronic dose of 4.3 rads/hr (Fig. 9.6). After an acute dose of 2000 rads, *D. melanogaster* was the superior species for approximately 12 weeks. However, the opposite effect was found when the populations were given 10,000 rads; *D. melanogaster* was eliminated in 6 weeks. The number of irradiated *D. melanogaster* or irradiated *D. simulans* (2000 rads) decreased rapidly when placed in competition with nonirradiated flies of the opposite species. Irradiated *D. melanogaster* were able to recover under these conditions, but the number of irradiated *D. simulans* continued to decrease, and they were eliminated in one population after 24 weeks.

These experiments show that the exposure to ionizing radiation can influence the outcome of competition between closely related species. The success of these species was dose dependent. Apparently the components that contribute to the fitness of these closely related species have

Table 9.2. Embryo Production and Abnormalities in *Gambusia affinis affinis*

	White Oak Lake	Swan Pond
Number of females examined	99	98
Average number of embryos	47.2 ± 1.89	33.2 ± 1.55
Average number of viable embryos	44.4 ± 1.83	32.1 ± 1.49
Total number of dead embryos	258	108
Phenotypic abnormalities	16	2

[14] S. I. Auerbach *et al.*, *Health Phys. Div. Ann. Progr. Rept. July 31, 1966*, ORNL-4007, pp. 48–49.

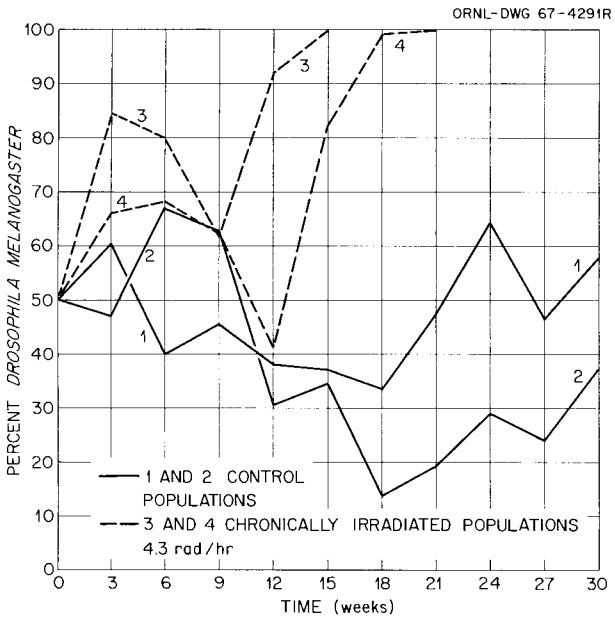

Fig. 9.6. Effect of Chronic Radiation on Interspecific Competition Between *Drosophila melanogaster* and *Drosophila simulans* in Laboratory Populations Started with Equal Numbers of Each Species Is Shown by the Change in Frequency of *D. melanogaster*.

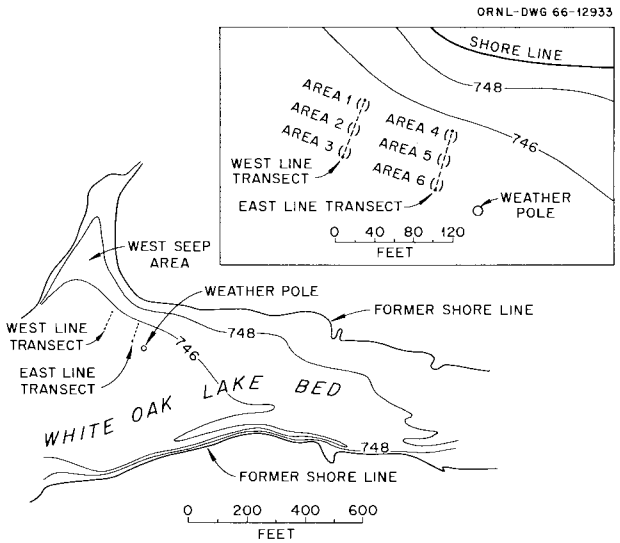

Fig. 9.7. Locations of Line Transects and Sampling Areas on Upper White Oak Lake Bed, Summer 1964.

different sensitivities to radiation. Ionizing radiation was an additional stress on these populations, but unlike environmental factors which select only the present genotype, radiation may influence future generations by adding new genetic combinations to their gene pools.

MOVEMENT OF ^{106}Ru, ^{60}Co, AND ^{137}Cs IN ARTHROPOD FOOD CHAINS ON WHITE OAK LAKE BED

D. A. Crossley, Jr. M. H. Shanks

The behavior of ^{137}Cs and ^{90}Sr in food chains has been documented previously for herbaceous vegetation and associated arthropods on the White Oak Lake bed sediments.[15,16] Ruthenium-106 was neglected in earlier studies because of its variable distribution on the lake bed and losses during ashing of samples. A sampling program conducted in the summer of 1964 was designed to take advantage of the high ^{106}Ru content of soils in the vicinity of the waste seepage pits nearby.[17] Location of the study area on White Oak Lake bed is shown in Fig. 9.7. Two replicate line transects were laid out. Each week for eight consecutive weeks, a sweep net sample of insects was taken in each transect. A sample unit consisted of all insects captured in 50 strokes of the net. Three samples of the herbaceous vegetation and three soil samples also were taken in each transect per week. All samples were air-dried on laboratory benches, without artificial heat, to avoid volatilization losses of ^{106}Ru. Counting for radioactivity utilized an automatic multichannel analyzer system together with a computerized spectral analysis program ("RESAP"), for estimation of gamma-emitting radionuclides.

Comparative distribution of the three radionuclides along food chains is indicated by the data of Table 9.3. Distribution of ^{137}Cs among biota in the seep area was similar to that previously reported for White Oak Lake bed. Compared with ^{137}Cs, more efficient food chain movement is suggested by the data for ^{106}Ru and ^{60}Co. Uptake from soil was greater for these latter radioisotopes than for radiocesium (concentration factors of 0.06 vs 0.02). Transfers from

[15] S. I. Auerbach *et al.*, *Health Phys. Div. Ann. Progr. Rept. July 31, 1962*, ORNL-3347, pp. 47–48.

[16] D. A. Crossley, Jr., and H. F. Howden, *Ecology* **42**, 302–17 (1961).

[17] T. F. Lomenick and D. A. Gardiner, *Health Phys.* **11**, 567–77 (1965).

Table 9.3. Distribution of Radioisotopes Along Arthropod Food Chains on White Oak Lake Bed (West Seep Area)

Samples from two line transects during an eight-week period, summer 1964

Trophic Level	^{106}Ru		^{60}Co		^{137}Cs	
	picocuries/mg	Conc. Factor[a]	picocuries/mg	Conc. Factor[a]	picocuries/mg	Conc. Factor[a]
Soil	28.3		4.57		14.13	
Vegetation	1.74	0.062	0.265	0.058	0.377	0.027
Herbivore	0.721	0.41	0.114	0.43	0.110	0.29
Predator	2.06	2.86	0.122	1.07	0.101	0.92

[a]Concentration factor = $\frac{\text{grand mean for trophic level}}{\text{grand mean for preceding level}}$.

vegetation to herbivores and from herbivores to predators also appeared more efficient for ^{106}Ru and ^{60}Co than for ^{137}Cs. In particular, ^{106}Ru concentrations in predators were almost three times higher than those in herbivores. Consequently, the relative abundances of the three radioisotopes became rearranged by the food chain processes. Ruthenium-106 had twice the concentration of ^{137}Cs in soils; in predators, ^{106}Ru was 20 times more abundant than ^{137}Cs. Similar increases of ^{106}Ru relative to ^{137}Cs in plant to insect transfers are evident in data recently published by Bourdeau *et al.*,[18] for irrigated ecosystems in the Po Valley of Italy.

For each radionuclide, concentration factors always increased during progression along this soil-vegetation-arthropod food chain. Actual concentrations (picocuries per milligram) usually decreased (except for two herbivore-predator transfers). The increasing concentration factors imply that differences in actual concentration became reduced at each transfer until predator concentrations equaled or exceeded herbivore concentrations. The significance of these increasing concentration factors may lie in an increasing need for mineral or ion conservation at the higher trophic levels, if the food items do not contain a surplus quantity. In future studies it would be desirable to segregate the predator trophic level into "primary" predators and "top" predators to determine whether the increase in concentration factors actually continues at still higher trophic exchanges. If so, then the minimal concentration of a given radionuclide would not be found at the terminus of a food chain, but rather in members of some intermediate trophic level.

[18]P. Bourdeau *et al.*, *Health Phys.* 11, 1429–44 (1965).

10. Responses of Plants to Ionizing Radiation

Leslie Fraley, Jr.[1]
H. L. Ragsdale[2]
F. G. Taylor, Jr.
J. P. Witherspoon
D. R. Johnson[3]

RADIOSENSITIVITY OF FOREST TREE SPECIES TO ACUTE FAST-NEUTRON RADIATION

J. P. Witherspoon F. G. Taylor, Jr.

Radiation studies on the responses of experimental plant populations have been in progress for the past two years. These studies have employed potted forest tree species, which were subjected to acute fast-neutron radiation at the HPRR and then maintained in greenhouse or growth-chamber facilities for observations. Responses in terms of growth, morphological, or mortality criteria have been measured for locally important tree species. This information may be compared with data on effects of other types of ionizing radiation. In addition, methods of predicting radiosensitivity of plants, such as chromosome volume comparisons, can be evaluated for fast-neutron radiation.

Plants were irradiated as potted seedlings or rooted cuttings two to three years old at the time of exposure. Exposure times were 5 to 10 min, and irradiations were performed during periods of active growth. All irradiations were performed in the HPRR building within 4 m of the unshielded reactor core. To reduce exposure to radiation scattered from the floor, plants were placed on racks 1 to 2 m high. The number of plants per exposure varied between 10 and 50. The elapsed time between the end of an irradiation and scoring for effect varied, depending upon the life cycles and growth rates of species. The main end points used were lethality and degree of growth inhibition. In order to yield results comparable with other studies, "severe growth inhibition" was considered to be growth reduction to 15% of the control, and "slight growth inhibition" was growth reduction to about 85% of the control.

Tolerance data for three biological end points are given in Table 10.1 for 13 species of trees. These species represent ten families that are widely distributed taxonomically. The extreme radiosensitivity of the conifers (*Pinus*) is apparent, with lethal doses being about 12 times less than the average lethal dose for the deciduous species. The most sensitive deciduous trees tested were dogwood (*Cornus florida*), sassafras (*Sassafras albidum*), and sweetgum (*Liquidambar styraciflua*). Doses required to produce lethality and severe growth effects in these species averaged 33 and 35% lower, respectively, than those required to produce these end points in the other deciduous trees. The most resistant species tested were mimosa (*Albizzia julibrissin*) and red oak (*Quercus rubra*). Doses producing lethality and severe growth effects in these species averaged 40 to 57% higher, respectively, than those for other deciduous species. Severe growth inhibition of shoots occurred after exposure to doses averaging 49% of the lethal doses, and slight shoot-growth inhibition occurred at doses averaging 17% of the lethal dose.

Although not enumerated here, fast neutrons induced morphological abnormalities such as altered leaf shape and size, stem malformations, and disarrangement of leaf sequence. These abnormalities were observed in plants of all species that survived irradiation, and both their extent and frequency increased with dose.

[1]ORAU summer participant.
[2]ORAU Predoctoral Fellow.
[3]Radiation Dosimetry Section.

Table 10.1. Acute Fast-Neutron Doses Producing Lethality and Shoot-Growth Inhibition in Forest Tree Species

Species	LD_{100}/one year (rads)	Doses Producing Shoot-Growth Inhibition (rads)		Average Interphase Chromosome Volume in June 1966 ($\mu^3 \pm$ standard error)
		Severe	Slight	
Acer rubrum	1000	500	200	5.7 ± 0.19
Albizzia julibrissin	2000	1350	420	4.5 ± 0.21
Cornus florida	900	350	100	10.1 ± 0.48
Diospyros virginiana	1350	510	140	5.6 ± 0.22
Liquidambar styraciflua	850	450	175	4.2 ± 0.24
Liriodendron tulipifera	1000	400	160	6.5 ± 0.22
Pinus echinata	100	50	25	39.8 ± 3.54
P. strobus	<75	50	25	64.4 ± 3.16
P. virginiana	75	50	25	35.9 ± 1.88
Populus deltoides (A-21 clone)	1200	575	150	3.1 ± 0.12
Quercus alba	1150	600	275	6.4 ± 0.40
Q. rubra	1500	1000	400	5.3 ± 0.31
Sassafras albidum	900	580	150	6.0 ± 0.14

The linear relationship between interphase chromosome volumes in plant meristematic tissue and gamma-ray exposures necessary to produce various biological end points has been demonstrated by Sparrow[4] for woody and herbaceous plants. This relationship also holds true in the case of fast-neutron radiation. From the data in Table 10.1, the regression of LD_{100}'s and 85% shoot-growth inhibitions on interphase chromosome volumes were calculated. For the LD_{100} end point, the relationship is

$$\log_{10} Y = 3.78 - 1.08 \log_{10} X ,$$

where Y is fast-neutron exposure in rads and X is interphase chromosome volume in μ^3. For the 85% growth inhibition, the relationship is

$$\log_{10} Y = 1.29 - 1.09 \log_{10} X .$$

These regressions are shown in Fig. 10.1. Also shown are regressions for acute gamma-radiation exposures necessary to produce the same end points in tree species as given by Sparrow.[4] A comparison of the fast-neutron and gamma-radiation

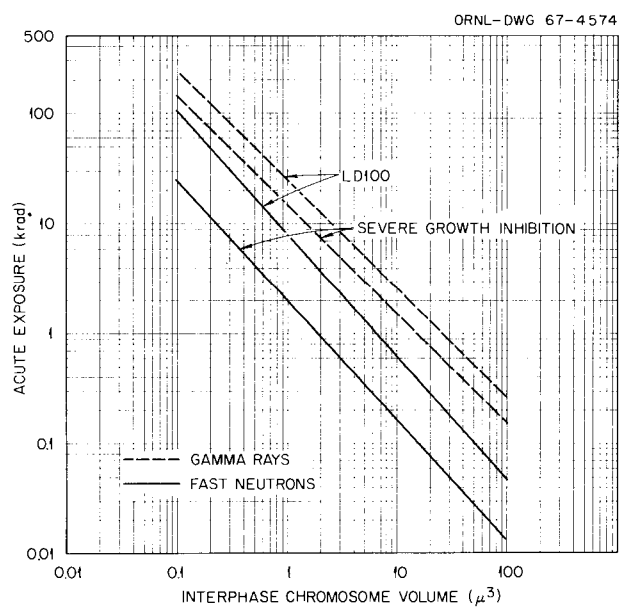

Fig. 10.1. Regressions of Exposures Necessary to Produce Lethality and Severe Growth Inhibitions on Interphase Chromosome Volume for Woody Species. Regressions for ^{60}Co gamma rays are from A. H. Sparrow, *Japan J. Genetics* 40, 12 (1964).

[4]A. H. Sparrow, *Nippon Idengaku Zasshi* 40, 12 (1964).

regressions serves to illustrate the relative biological effectiveness (RBE) of these two radiation types. For lethality, the fast neutrons are three to four times more effective than ^{60}Co gamma rays. For severe growth inhibitions, they are seven to nine times more effective. Of course, this is not exactly a true RBE, since the two radiations were not delivered at the same dose rate. However, an acute mode was used in both cases, and the differences in dose rate may not be important for these particular biological end points. Also, the fast-neutron radiation employed here was not monoenergetic, but comprised a spectrum of energies with an average of 1 Mev. However, the range of RBE values found in this study seems reasonable when compared with other work.

GENETIC MODIFICATION OF RADIOSENSITIVITY

J. P. Witherspoon F. G. Taylor, Jr.

Studies reported last year[5] showed that genetic factors other than degree of ploidy and chromosome size affect plant responses to ionizing radiation. Nuclear criteria for genotypes of *Populus deltoides* (Eastern cottonwood) grown in a field nursery were investigated to establish whether chromosome volume differences existed in the experimental population. Figure 10.2 shows the frequency in size class distribution of estimated average chromosome volumes for 30 clones representing ecotypes from six states. All clones had the diploid (38) number of chromosomes. The range of the interphase chromosome volumes with their associated standard errors was from 2.38 ± 0.07 to 4.24 μ^3 ± 0.16. These two extreme values suggest that a difference in radiosensitivity may exist between these clones due to this 1.8 factor of increase in chromosome size. However, the other clones tested had chromosome volumes differing from one another only by a factor of 1.4 or less. Past work has shown that size differences of this magnitude are not likely to correlate well with exposure predictions for growth or mortality end points.

Genotypic control of growth rate may influence apparent radiosensitivity when growth inhibition or biomass production is used as end point. Table 10.2 shows growth responses of four clones of Eastern cottonwood (*Populus deltoides*) following exposure to fast-neutron radiation. Dormant cuttings, 20 per clone per treatment, of equal age and size were irradiated and then placed, with controls, in aerated nutrient solution in a plant-growth chamber. After 20 days all plants were harvested, and shoot and root biomass (new growth) was determined.

Both the A-8 and C-1 clones produced more growth (1.7 times the biomass) of shoots and roots than did the A-6 and K-4 clones (Table 10.2). Under the environmental conditions maintained during this experiment, cellular divisions related to growth were proceeding at a faster rate in the former than in the latter. Growth inhibition of both shoots and roots from the highest dose (950 rads) was 3 to 4 times greater in the more rapidly growing clones. Greater inhibition also was found at the lower doses in the case of A-8 and C-1 but only by a factor of about 1.4. These responses probably corresponded to differences in cell division rate,

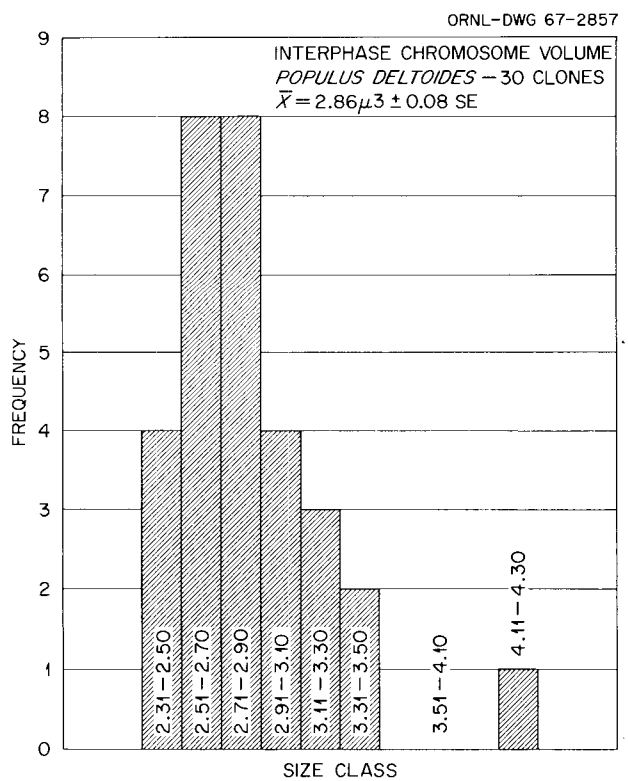

Fig. 10.2. Frequency in Size Class Distribution of Estimated Average Chromosome Volumes for 30 Genotypes of Eastern Cottonwood.

[5] J. P. Witherspoon, J. W. Curlin, and F. G. Taylor, Jr., *Health Phys. Div. Ann. Progr. Rept. July 31, 1966*, ORNL-4007, pp. 55–56.

Table 10.2. Growth Responses of *Populus deltoides* Clones to Acute Fast-Neutron Irradiation

Clone and Source	Shoot Biomass (% of controls ± standard error)			Root Biomass (% of controls ± standard error)			Chromosome Volume (μ^3 ± standard error)	Control Biomass per Plant (g dry wt)	
	950 Rads	400 Rads	130 Rads	950 Rads	400 Rads	130 Rads		Shoot	Roots
A-8, Alabama	7.8 ± 2.1	40.4 ± 15.3	76.0 ± 10.0	17.2 ± 3.6	33.0 ± 5.8	44.8 ± 3.0	3.3 ± 0.16	6.93	1.18
A-6, Alabama	18.2 ± 4.0	51.6 ± 13.0	84.2 ± 7.7	40.0 ± 6.9	43.0 ± 4.7	65.0 ± 12.0	2.9 ± 0.11	3.82	0.71
K-4, Kentucky	29.6 ± 5.2	73.1 ± 8.9	90.6 ± 14.5	74.3 ± 5.7	70.9 ± 9.1	68.3 ± 9.5	2.8 ± 0.06	4.26	0.70
C-1, Mississippi	5.6 ± 1.8	45.0 ± 6.3	94.3 ± 7.0	11.1 ± 2.0	44.7 ± 3.4	48.0 ± 3.8	3.0 ± 0.20	6.82	1.28

and those tissues with more mitotic activity exhibited greater radiosensitivity. Since the growth rates here are under genotypic control, a genetic basis for differential radiosensitivity that is not related to ploidy or chromosome volume was demonstrated. Future work on other clones is planned in order to quantify this variation in growth and radiosensitivity within a population.

DOSIMETRY IN FORESTS AROUND THE HPRR

J. P. Witherspoon D. R. Johnson

Previous estimates of cumulated fast-neutron dose delivered to components of forests surrounding the HPRR were made by multiplying values from a dose-distance curve, obtained at a 1-kw reactor power level, by cumulated kilowatt-hours of reactor operation. This year a dosimetry study was carried out in which both fast-neutron and gamma-radiation doses in the forest were normalized to initial count rates (ICR's) of activated sulfur pellets attached to the reactor core. Since sulfur pellets are attached in a standard position on the core during each reactor operation, ICR data, which are routinely recorded in a log book, can be used to determine dose delivered to various forest components from any reactor operation – burst or steady state. Moreover, this dosimetry study was designed to obtain additional information on fast-neutron-to-gamma ratios and shielding effects of vegetation and topographic features.

Two Phillips (No. 18509) micro G-M counters and two Radsan fast-neutron dosimeters were positioned at various stations in the forest. With the reactor operating at approximately 60 w, three count-rate determinations were made on each dosimeter at each station. These data were normalized with sulfur-pellet counts for each run, and dose values in millirads per ICR were obtained for fast-neutron and gamma radiation at each station.

Metal conduits outside the reactor building were found to shield out 36% of the fast-neutron dose delivered to portions of several small trees, thus explaining differential biological effects observed in these plants. Small shrubs and foliage offered little shielding of fast neutrons, but tree trunks (1 dm in diameter) reduced tissue dose in air values by a factor of 3 at 35 m from the reactor. Gamma rays were found to be nearly isotropic at this distance. Fast-neutron-to-gamma ratios were between 3 and 4 at 20 to 35 m but approached 1 when directional neutrons and isotropic gamma rays were measured in back of tree trunks. Dose-vs-distance curves have been prepared utilizing these data, and correlations are being made with existing biological effects observed in vegetation.

EFFECTS OF INTERNAL EMITTERS ON NATIVE PLANT SPECIES

J. P. Witherspoon Leslie Fraley, Jr.

Quantitative studies on the levels of internal radionuclide that are necessary to produce radiation effects on growth or reproductive processes

of plants are relatively few in number. Yet such information is important in determining practical levels of radionuclide to be used in ecological tagging experiments. Moreover, the ecological effects of internal emitters need to be studied in relation to changes in reproductive capacity of a species or population of plants. Two studies that utilized low-level internal radiation were completed this year. Vegetative cuttings of a *Tradescantia* hybrid (*T. occidentalis* × *T. ohiensis*) were rooted in a potting medium. This clone is heterozygous for flower color, and somatic mutations produced during floral development appear as individual red cells or multicellular red sections in otherwise purple petals and stamen hairs. Plant roots were placed in aerated ^{32}P solution (0.5 $\mu c/ml$) for 2, 4, or 6 hr, and then transplanted into pots and maintained under controlled environmental conditions. Meristematic tissue was harvested periodically to ascertain ^{32}P concentrations for dose calculations. Additional plants were scored for frequency of color sector mutations and morphological anomalies of floral parts after 30 days. Total beta-radiation dose to buds ranged between 57 and 199 rads for the 30-day period. From 69 to 81% of the flowers produced by these buds were abnormal, either in size, shape, or number of parts. The number of mutant (red) sectors on petals increased by a factor of 8 to 11 over controls, with a spontaneous mutation rate of 0.9 sector per flower. Mutation rates in stamen hairs were increased 9 to 17 times over controls with 1.1 mutant sectors per hair. The frequency of mutant-sector occurrence in this plant has been previously related to external gamma radiation, and the extreme radiosensitivity of this clone has been established at Brookhaven National Laboratory. The effects induced by relatively small total doses of an internal beta emitter emphasize the fact that tracer levels of radionuclide may be damaging to some plants. Therefore, caution should be used in interpreting physiological studies in which radiosensitive plants are tagged.

Mature yellow poplar trees from the ^{137}Cs-tagged *Liriodendron* forest served as sources of tagged seed for a study on effects of an internal emitter on reproductive capacity. Trees of similar age and size growing adjacent to the tagged forest area served as control seed sources. Mature cones were collected in October from six tagged trees and three control trees. All cones were selected from upper crown positions to minimize differences in seed quality due to location on the tree. Seed production within cones was calculated on the basis of percentage of filled ovules. This was determined by examination of 200 fruit from each tree.

Seeds for germination tests were soaked for 12 hr in tap water, placed wet in plastic bags, and stratified for 120 days at 2 to 7°C. After stratification, 1000 seeds from each tree were planted in topsoil of the Bolton series in wooden flats. Each flat contained 500 seeds planted approximately 0.5 cm deep. Flats were maintained in a greenhouse with 30°C maximum daily temperatures and 22°C nightly temperatures. Germination percentages were recorded for 31 days.

Germination expressed on the basis of planted seed without estimates of seed viability or soundness can be misleading. Table 10.3 gives seed production, expressed as percentage of filled ovules, for each tree. Percent germination corrected for seed soundness also is shown. An analysis of covariance showed germination to be related to seed production and not to treatments. There was no significant difference in germination of tagged vs control seeds when mean germination

Table 10.3. Production and Germination of *Liriodendron* Seed from ^{137}Cs-Tagged and Control Trees

Tree	Seed Production (% of ovules filled)	Germination	
		Percent of Planted Seed	Percent of Viable Seed
Control 1	34	5.3	15.6
Control 2	24	4.5	18.7
Control 3	56	7.5	13.4
Average ± standard error	38.0 ± 11.0	5.8 ± 0.8	15.9 ± 1.9
Tagged 1	20	4.3	21.5
Tagged 2	10	0.9	9.0
Tagged 3	23	6.4	27.8
Tagged 4	13	2.8	21.5
Tagged 5	17	3.3	19.4
Tagged 6	14	1.4	10.0
Average ± standard error	16.1 ± 2.1	3.2 ± 0.9	18.2 ± 3.0

was adjusted for seed soundness. There was, however, a significant difference ($p = 0.10$) in seed soundness between control and tagged trees.

Examination of fruit showed 2.3 times more seeds in the fruits of control trees. Yellow poplar fruit are one-winged woody carpels with two ovules. The percentage of filled ovules in these fruits usually averages 50 to 60%. Control-tree values in this study averaged 38 ± 11% of ovules filled, while tagged trees averaged 16.1 ± 2.1%.

Internal dose rates were estimated from radiocesium concentrations in mature seed at 136 millirads/day (122 millirads beta). Since seed abortion or failure to set occurred in earlier developmental stages representing structures of different shapes and radionuclide content, this dose estimate serves only to indicate the possible magnitude of exposure levels. Also, it is not known to what extent chronic radiation exposures affected cytological and chemical processes prior to floral formation. The ^{137}Cs concentrations in components of tagged parent trees were about three times less than concentrations present the year prior to the formation of seeds used in this study.

The significant decrease in seed production of tagged trees reported here and of trees subjected to chronic gamma radiation from external sources indicates that significant effects of ionizing radiation on reproductive potential of forest trees may be caused at exposure rates much less than those necessary to produce visible growth inhibitions or mortality.

RADIONUCLIDE UPTAKE AS A MEASURE OF RADIATION STRESS IN SINGLE-COMPONENT MICROCOSMS

H. L. Ragsdale

Assessment of radiation damage to biological communities has been made on the basis of productivity, mortality, diversity, and phenology. While these measurements are useful and lead to valid conclusions concerning the radiation effects, they do not provide information concerning the significance of radiation stress on mineral cycling in a biological community. In order to determine the feasibility of mineral cycling as an index of radiation stress, the uptake and concentration of ^{137}Cs and ^{60}Co was followed in "simple" aquatic microcosms having the single living plant component *Elodea*.

Replicate microcosms were tagged with 1 μc each of ^{60}Co and ^{137}Cs. The microcosms were then irradiated with acute fast-neutron doses of 95, 380, and 950 rads. Growth and elongation, morphological differentiation, and radionuclide uptake were then followed for 828 hr.

The processes of growth and elongation in *Elodea* resulted in an average length increase of 0.05 mm/day. Up to 440 hr after irradiation, the growth of *Elodea* is an arithmetic function of time for controls and treated plants. Under the conditions of this experiment, a normal morphological development is the formation of adventitious shoots and roots along the major plant axis. This occurs with loss of apical dominance and hence with a decrease in the growth rate of the major plant axis. This development occurred at 348 hr after the irradiation and tagging of the microcosms. Measurements of growth made 120 hr later revealed a decline in the growth rates of the controls and of those treated with 95 rads, while those treated with 380 and 950 rads continued growth.

Observations of adventitious shoot formation showed that the plants receiving 95 rads formed the same number of shoots as the control plants. Shoot formation in the 380- and 950-rad-treated plants was inhibited early in the experiment, but later these plants developed almost as many lateral shoots as the controls. Root development was inhibited by the 95-rad irradiation, these plants developing approximately one-half the number of roots as the controls. Both the 380- and 950-rad irradiations inhibited root formation for the entire experiment.

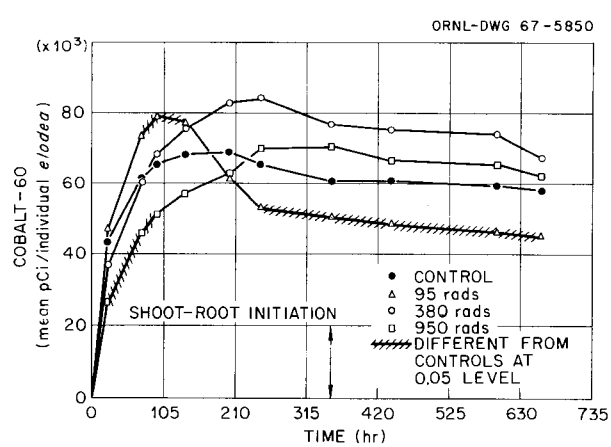

Fig. 10.3. Uptake of ^{60}Co by Aquatic Plants (*Elodea*) Following Exposure to Acute Fast-Neutron Radiation.

Cobalt-60 concentration by *Elodea* (Fig. 10.3) resulted in similar end points for the controls and the 380- and 950-rad-treated plants, while the 95-rad-treated plants showed a statistically lower concentration compared with that of the controls. The earliest maximum concentration occurred in the 95-rad-treated plants, and the concentration at this time was statistically higher than in the controls. The initial uptake of ^{60}Co by the 380-rad treated plants was similar to that of the controls, but the maximum concentration was higher and occurred later than in the controls. The 950-rad dose resulted in a lag in cobalt uptake initially, but the maximum concentration value was similar to that of the controls and occurred at a later time. While no statistical significance can be attributed to the end-point concentrations of ^{60}Co (except for the 95-rad treatment), it is significant that the same ranking of concentrations at 380, 950, 0, and 95 rads occurred in a similar experiment. These results suggest that the effect of higher doses of radiation can enhance the concentration of radionuclides, while lower doses result in a decreased concentration compared with controls.

Cesium-137 uptake (Fig. 10.4) shows a pattern of decreasing concentration with increasing dose from fast-neutron exposure. This relationship is suggested during the initial phases of the experiment and becomes quite evident in the later observations. The difference in concentration of radiocesium is correlated with the delay in shoot-root formation and subsequent growth of lateral structures. In this respect, the differences in concentration may represent a difference in surface area and mitotic activity. The concentration differences also may be explained on the basis of differential leaching rates among the treatments, possibly resulting from differential membrane damage caused by the radiation treatments.

This study demonstrates that the effects of sublethal radiation doses (95 rads), which can be observed only on the basis of slight differences in morphology, are quite significant when analyzed on the basis of radionuclide uptake and concentration. Based on these results, experiments are now in progress to further delineate radiation effects in terms of mineral cycling. The influence of radiation stress on several aquatic microcosm components, considered singly and in various combinations, is being analyzed in terms of ^{60}Co and ^{137}Cs uptake and concentration. Experiments are now in progress to determine how microcosm complexity (species diversity) affects the manner in which an ecological system responds to radiation stress. System responses will be measured in terms of cycling rates of ^{60}Co and ^{137}Cs within systems containing one plant species, soil, and water; two plant species, soil, and water; and two plant species, one animal species, soil, and water.

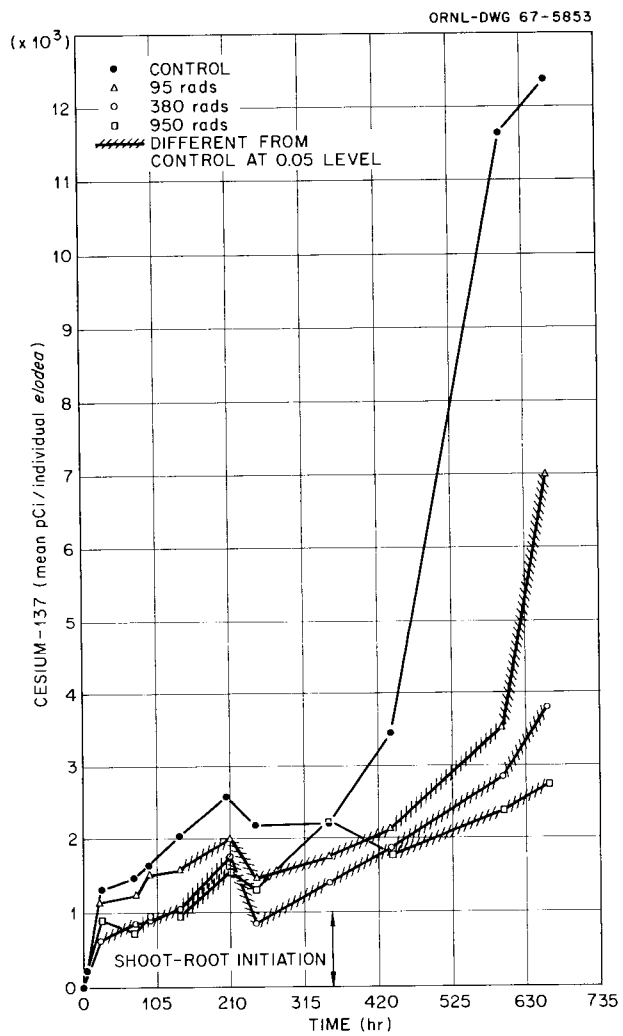

Fig. 10.4. Uptake of ^{137}Cs by Aquatic Plants (*Elodea*) Following Exposure to Acute Fast-Neutron Radiation.

11. Radionuclide Cycling in Terrestrial Ecosystems

Regina M. Anderson
Barbara Barzansky[1]
L. J. Bledsoe[2]
D. A. Crossley, Jr.[3]
Gladys J. Dodson
Marilyn L. Frank
S. V. Kaye
B. C. Moulder[4]
J. S. Olson[3]
L. N. Peters
D. E. Reichle[3]
M. H. Shanks
R. L. Tabor
W. A. Thomas
H. D. Waller
Martin Witkamp
P. B. Whitford[5]

SUMMARY OF RADIOCESIUM MOVEMENT IN A FOREST LANDSCAPE

J. S. Olson
D. A. Crossley, Jr.
D. E. Reichle
Martin Witkamp
H. D. Waller
Regina M. Anderson

Early transfer of radiocesium from dominant plants to the soil led ecologists to predict that there would be less activity in the tree leaves, and in all the animal food chains which depended on leaves, in the second and later years. Glass rod dosimeters and repeated increment boring of trunks and roots throughout the second growing season confirmed the idea that some of the radiocesium which had moved down to roots for storage over winter moved up again when the sap rose in the spring and was available for the new crop of leaves. As predicted, however, the maximum foliage cesium was less than in the previous year (81 $\mu c/m^2$ in Fig. 11.1). In the second and later years, as in the first, there was a loss of about one-half of this radioactivity during each growing season and a corresponding decrease in absolute loss rates from the canopy. Almost all the radioactivity in the ground vegetation appeared to be due to contamination from rain leaching from the overhanging canopy of tree leaves.

Five years of research, including laboratory experiments on insect feeding, have clarified many problems related to the animal food chains which depend either on live tree foliage or on the tree litter which falls each year, mostly in the autumn. Some gaps in the numerical data of Fig. 11.1 are scheduled for study in the second five years. Over 2 $\mu c/m^2$ of foliage consumption was necessary to maintain radioactivity levels in canopy insect populations, even though the total activity represented in them was very small (about 0.004 $\mu c/m^2$) at any one time. Likewise, the contributions of insects, and probably of other animals, to the export of radioactivity from the plot by animals appeared small (less than 0.1 $\mu c/m^2$) by comparison with the measured export in blowing leaves which fell outside the plot boundaries in autumn (5.3 $\mu c/m^2$ in 1963; less in later years). Litter falling inside the plot contributed about 5 $\mu c/m^2$ to animal food chains (especially ground insects and millipedes), which eventually return their absorbed cesium to the litter layer or underlying soil. Fungi and bacteria may immobilize cesium temporarily within their own tissues, but they work jointly with soil animals to hasten the general movement of cesium toward the ultimate reservoir in the soil.

Equations that were used previously in mathematical models for accumulations of nutrients in soils, plants, and animals were extended to an overall analysis and to a prediction of radiocesium movement in and around the tagged forest. The continued decreases in radioactivity of tree foliage imply readjustment toward lower

[1]ORAU Undergraduate summer trainee.
[2]Consultant.
[3]Dual capacity.
[4]ORAU Predoctoral Fellow.
[5]ORAU summer participant.

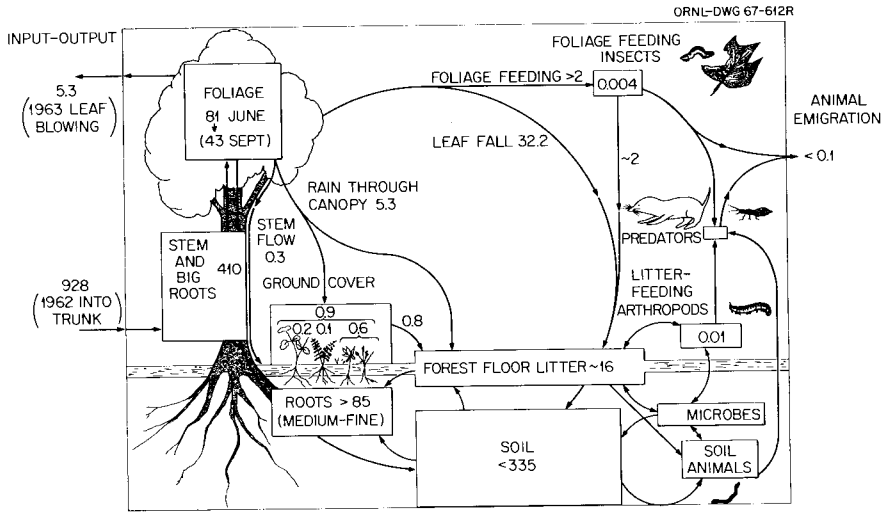

Fig. 11.1. Radiocesium Cycle in a Tagged Forest Ecosystem (*Liriodendron tulipifera*) at ORNL. This forest (20 × 25 m) was originally tagged with ^{137}Cs in May 1962. Continuous inventory has followed the seasonal and annual distribution of radiocesium between components of the forest ecosystem. Numbers in boxes are microcuries per square meter of ground surface area in summer 1963. Arrows indicate the pathways of radiocesium transfer between compartments. Numbers by these arrows are estimates of total transfer during the 1963 growing season.

levels of activity throughout the animal food webs. In spite of the tendency of soil minerals to fix cesium ions, recycling into plant roots may lead to an almost steady state, at levels less than 1% of the first year levels of activity, between the fifth and tenth year of the experiment. One model prediction indicates that continued input of activity to the soil may be balanced by radioactive decay in approximately seven years, but improvements in the model's assumptions and in field data can be expected to revise any such estimate.

Predictions about export from the plot also follow, since blowing of leaves away from the plot should carry negligible radioactivity after ten years. Export in stream runoff is excluded by plot location in an undrained sinkhole. Leaching through the deep colluvial soil appears to be negligible, as expected from the outset.

Such efforts to model the internal and external exchanges of radiocesium have broader implications for the dispersal of other nuclides and of other kinds of contaminants over the landscape. Similar models help to comprehend the natural processes of nutrient circulation, which are important for sound management of extensive forests and rangelands. Knowledge of budgets of organic matter (and its food energy) and of nutrient cycles is essential for understanding productive efficiency of ecosystems as converters of solar energy into life.

ACCUMULATION OF ^{137}Cs IN SOILS OF THE TAGGED *LIRIODENDRON* FOREST

J. S. Olson R. L. Tabor
L. N. Peters H. D. Waller
Regina M. Anderson

Early sampling of ^{137}Cs in forest compartments after tagging dominant *Liriodendron* trees[6] and compartment models based on these results[7] led to predictions of continuing transfer of ^{137}Cs into the soils. The 1965 autumn sampling indicates that over 50% of the initial radioactivity had reached the soils within the 20- by 25-m tagged area. Contamination outside the plot diminished abruptly, from near 500 $\mu c/m^2$ inside the plot to near 1 $\mu c/m^2$ in a fringe area 5 to 15 m outside the plot boundary (Fig. 11.2). The details of this fringe pattern and especially the transition between high and low activity were still highly variable owing

[6]H. D. Waller and J. S. Olson, *Ecology* 48(1), 15–25 (1967).

[7]J. S. Olson, *Health Phys.* 11(12), 1385–92 (1965).

to contributions such as the roots of tagged trees and the position of tagged tree canopy overhanging the plot edge. However, results to date warrant further prediction that accumulation will continue into the soil and into the area around the tagged plot at diminishing rates. A further survey was conducted on the fifth anniversary of the tagging in order to provide an empirical check on the longer-range trends of nuclide redistribution and to provide further information on compartment models.

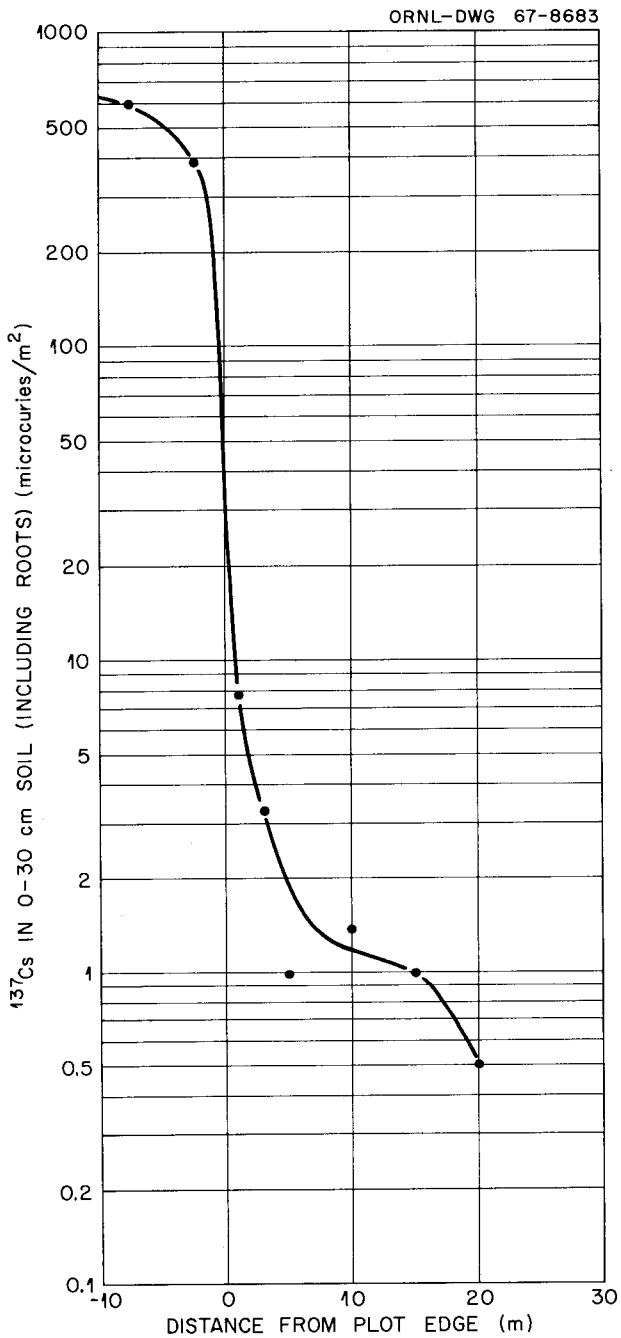

Fig. 11.2. Radiocesium Concentrations Inside the Tagged *Liriodendron* Forest Plot (Left) and Successively Greater Distance Outside (Right).

MICROBIAL IMMOBILIZATION OF RADIONUCLIDES IN THE FIELD

Martin Witkamp Marilyn L. Frank
Barbara Barzansky

Microbial immobilization of ^{137}Cs on decaying leaf litter has been demonstrated in the laboratory comparing ^{137}Cs leaching from sterile and decaying litter.[8] Difficulty in using sterile litter outside the laboratory hampered evaluation of microbial immobilization in the forest floor until the following experiment was performed.

Ninety-six individually weighed and numbered leaves of tulip poplar (*Liriodendron tulipifera*) were exposed on threads in the forest floor inside and outside the ^{137}Cs-tagged tulip poplar stand. Forty-eight of the leaves contained known amounts of ^{137}Cs and were exposed outside the tagged forest after half had been rinsed in 1% $HgCl_2$ for sterilization and the other half had been rinsed in distilled water. This series was to compare loss of ^{137}Cs and weight by sterile and decaying leaves. A parallel series with untagged leaves was exposed in the tagged forest to compare ^{137}Cs uptake by sterile and decaying leaves. In similar series, individually marked pieces of cellophane (1 by 2 in.) which had been soaked for two days in water or water with ^{137}Cs and then treated with 1% $HgCl_2$ or distilled water were exposed on the same sites. Duplicate leaves and pieces of cellophane from both sites and with and without $HgCl_2$ were collected twice a week, and weights, ^{137}Cs contents, and microbial activity (O_2 uptake) were measured.

After three weeks, microscopic examination as well as the Warburg measurements of O_2 consumption indicated loss of sterility of the $HgCl_2$-treated series. A second rinse of this series in 1% $HgCl_2$ and of the parallel series in water was required.

Averages of all measurements (Table 11.1) show that significantly more ^{137}Cs was taken up per

[8] S. I. Auerbach *et al.*, *Health Phys. Div. Ann. Progr. Rept. July 31, 1962*, ORNL-3347, pp. 64–65.

Table 11.1. Accumulation of ^{137}Cs by Sterile and Decaying Untagged Leaves and Cellophane on Tagged Soil and Percent of Initial ^{137}Cs Remaining in Percent of Initial Dry Weight in Sterile and Decaying Tagged Leaves and Cellophane on Untagged Soil During Six Weeks of Incubation in the Forest Floor

	Average ^{137}Cs Content and Significance of Difference			Average O_2 Uptake by Two Leaves or Two Pieces of Cellophane (μl/hr)	
	Decaying		Sterile	Decaying	Sterile
Leaves					
Untagged					
(dis/min per mg of dry weight)	8.2	$2\% < P < 5\%$	3.6	891	41
Tagged					
(% Cs/% wt)	0.69	$P < 0.1\%$	0.48	591	17
Cellophane					
Untagged					
(dis/min per mg of dry weight)	184	$0.1\% < P < 1\%$	52	340	13
Tagged					
(% Cs/% wt)	0.062	$20\% < P$	0.078	278	25

gram of decaying leaves and cellophane than of sterilized ones. Similarly, significantly more ^{137}Cs (percent of initial) remained on the tissue of decaying leaves (percent of initial) than on sterile leaves. Corresponding data for cellophane showed no significant difference, presumably because over 90% of the ^{137}Cs had already leached out after three days of exposure in the field. The rates of loss of weight and O_2 consumption for both leaves and cellophane were also significantly higher ($P < 5\%$) for decaying than for sterile series. Thus, for the first time, microbial immobilization of a mineral on decaying litter was experimentally demonstrated in the field.

^{137}Cs TRANSFER IN TERRESTRIAL MICROCOSMS

Martin Witkamp Marilyn L. Frank

A series of terrestrial microcosms consisting of litter, millipedes, soil, and soil leachate was incubated for 14 weeks at 5, 15, and 25°C. Each series consisted of nine microcosms receiving biweekly one, two, or four times simulated rain and having three, six, or nine millipedes.

There was a rapid loss of ^{137}Cs from the tagged litter during the first two weeks. Subsequent loss rates and concurrent rates of accumulation of ^{137}Cs in soil and soil leachate were significantly slower and near constant. Average loss rates of ^{137}Cs from litter at 5, 15, and 25°C were 1.0, 1.9, and 2.3%/week. Corresponding loss rates for systems with three, six, and nine millipedes were 1.4, 1.8, and 1.9%/week. The effects of different rates of leaching were less evident because of interactions between temperature and moisture. At 5°C, all litter remained wet, and the loss rate of ^{137}Cs increased 2.2 times as the rate of leaching quadrupled. In contrast, at 25°C there was a significant decrease with an increasing rate of leaching. Systems receiving rain only once every two weeks dried out between leaching, and subsequent leaching removed ^{137}Cs from dead microbial tissue. On litter with rain twice a week, ^{137}Cs remained immobilized by the microbes on the permanently moist litter. The average weekly loss of ^{137}Cs from litter was 1.7%. Of this, 1.4% was absorbed onto soil and 0.3% moved through soil into the soil leachate. Millipedes accumulated an average of 1% of the ^{137}Cs during the first four weeks, after which their contents

Table 11.2. Average Percent Losses ($N = 9$) of ^{137}Cs, K, Mg, Weight, and Caloric Content of Tulip Poplar Litter After 14 Weeks of Incubation as Affected by Differences in Temperature, Faunal Density, and Moisture Regime

	^{137}Cs	K	Mg	Weight	Caloric Content
Temperature, °C					
5	22	27	18	16	16
15	35	53	27	26	28
25	45	63	30	41	44
Number of millipedes					
3	27	49	19	23	*a*
6	34	48	27	29	*a*
9	40	48	25	29	*a*
Number of biweekly leachings					
1	32	46	23	29	*a*
2	33	47	24	27	*a*
4	37	51	24	25	*a*

[a]Not yet completed.

decreased as a result of declining ^{137}Cs in the litter substrate. Multiple regression equations were calculated for the ^{137}Cs content of the various compartments as functions of temperature, rate of leaching, faunal density, and time.

In addition to the biweekly measurements of ^{137}Cs, initial and final distributions of potassium and magnesium in the various systems were measured using flame photometry. Average losses for ^{137}Cs, K, Mg, organic matter, and caloric content of all litters were 34, 47, 25, 27, and 29% respectively. Thus, concentrations of K, and less rapidly of ^{137}Cs and caloric values, decreased, whereas magnesium concentrations increased.

Increasing temperatures from 5° to 25°C almost doubled the losses of Mg (Table 11.2) and more than doubled the losses of K and ^{137}Cs; losses of weight and caloric contents increased almost threefold; and overall metabolism, measured by the CO_2 evolved, increased almost by a factor of 3.3. Millipedes increased ^{137}Cs turnover but did not greatly affect the loss of K. Leaching, on the other hand, increased the loss of K more than that of ^{137}Cs. Whereas almost all the ^{137}Cs lost from litter was adsorbed on soil, most of the K was recovered in leachate, especially in the systems with millipedes.

This work provides new and useful information concerning the differences in turnover of various minerals and matter and quantifies the effects of temperature, moisture, and biological activity on these turnovers.

TROPHIC LEVEL CONCENTRATION OF ^{137}Cs, SODIUM, AND POTASSIUM IN FOREST ARTHROPODS

D. E. Reichle
D. A. Crossley, Jr.
Gladys J. Dodson
M. H. Shanks

Radioactive tracers have proved valuable in defining nutrient transfers between ecosystem components. The movement and ultimate distribution of radionuclides in ecosystems can provide information on food chain pathways, nutrient budgets, and nutrient turnover by biota at various trophic levels in the system. Assessment of the fate of radionuclides in the environment can often be made, if radionuclide mobility bears a relationship to the stable chemistry of the exchange pathways (e.g., food chains). Summarized here are data on the ^{137}Cs, K, and Na levels in forest floor detritus food chains consisting of leaf litter base, arthropod consumers (saprovores), and primary predators.[9]

During decomposition, K and Na content of detritus remains relatively stable (Table 11.3). Both ^{137}Cs and stable cesium concentrations increase through the litter profile. Sodium and potassium are readily leachable in organic and upper soil horizons; cesium, however, is more tightly bound on mineral soil.[10] Increased ^{137}Cs and Cs concentrations in lower litter layers were due to soil mixing. For comparison with various arthropod trophic levels, mean element concentrations of the L and F_1 litter horizons for September 1964 to March 1965 were used. Cesium-137 concentrations decreased by a factor of 0.67 from litter (17.94 pc per milligram of dry weight) to saprovores (5.95 pc per milligram of dry weight);

[9]D. E. Reichle and D. A. Crossley, Jr., "Trophic Level Concentrations of Cesium-137, Sodium, and Potassium in Forest Arthropods" in *Proc. 2nd Natl. Symp. Radioecology, Ann Arbor, Mich., May 15–17, 1967* (in press).

[10]H. D. Waller and J. S. Olson, *Ecology* 48(1), 15–25 (1967).

Table 11.3. Nutrient Attributes of *Liriodendron tulipifera* Leaf Litter at Various Stages of Decay, Based upon Assays of February 1966 Collections

Data illustrate the general distribution in organic horizons of radiocesium, total cesium, potassium, and sodium; upper litter horizons typically comprise the food base of saprovorous arthropods considered in this study

Litter Layer	Percent Ash	^{137}Cs (picocuries per milligram of dry weight)	Cs (micrograms per gram of dry weight)	K (milligrams per gram of dry weight)	Na (milligrams per gram of dry weight)
L	14.8	13.2	0.62	1.58	0.20
F_1	16.7	19.6	0.60	1.40	0.21
F_2	25.3	25.7	0.95	1.29	0.20
H	36.5	42.5	1.56	1.60	0.30

the predator trophic level (3.00 pc per milligram of dry weight) showed a further decrease, by a factor of 0.50. Mean K concentrations in saprovores (4.42 μg/mg), were a factor of 3.5 higher than in detritus (1.26 μg/mg) but thereafter dropped similar to ^{137}Cs by a factor of 0.47 to 2.35 μg/mg in predators. Mean sodium concentrations progressively increased through all trophic levels: 0.20 μg/mg in detritus, 3.57 μg/mg in saprovores, and 5.38 μg/mg in predators.

Biological half-lives and assimilation efficiencies for ^{134}Cs and ^{42}K in one insect species, the cricket *Acheta domesticus*, were used for comparison of the uptake and turnover of these elements by arthropods. Considerable information was already available on the ^{134}Cs turnover by a variety of different arthropod species. Change in the ^{137}Cs-to-K ratio between litter and saprovores was primarily the result of differential exchangeability from litter (Table 11.4). Nineteen percent of L layer ^{137}Cs was exchangeable (24 hr contact with 1 *N* $MgCl_2$) opposed to 83% for K. A discrimination factor of 0.75 for ^{134}Cs to ^{42}K digestive assimilation also affected successive trophic level ratios of ^{137}Cs to K. No adjustment of data for turnover of ^{137}Cs and K was made, since there was no significant difference between biological half-lives in *Acheta* (^{42}K $T_b = 69.2 \pm 6.4$ hr; ^{134}Cs $T_b = 76.6 \pm 9.9$ hr). The ^{137}Cs-to-K ratio decreased with each trophic exchange (Table 11.4). When appropriate corrections were made for availability of each element to consumer trophic levels, experimental predictions were not statistically different from the ratios obtained from independent chemical analyses.

Table 11.4. ^{137}Cs to K Ratios in Trophic Levels of a Forest Floor Arthropod Community, Expressed as Picocuries of ^{137}Cs per Microgram of K ± S.E.

Litter ratio adjusted to the exchangeable cation ratio; assimilative ratios represent further adjustment for differential assimilation of each element by the next trophic level

Food Base	Total	Exchangeable	Assimilative
Leaf litter ($N = 4$)[a]	14.25 ± 4.12	2.58 ± 0.80	2.08 ± 0.65
Saprovores ($N = 11$)[a]	1.49 ± 0.21		1.20 ± 0.17
Predators ($N = 7$)[a]	1.22 ± 0.36		0.98 ± 0.30

[a]Number of samples.

These data on the distribution of three alkali metals in arthropod food chains show that trophic processes do not result in increased concentration of ^{137}Cs and K between arthropod links in the food chains. Since fallout ^{137}Cs has often been reported to be accumulated in vertebrate food chains, it is apparent that the faunistic composition of environmental pathways must be considered before the fate of ^{137}Cs in trophic levels of ecosystems can be assessed.

BODY SIZE AND BIOENERGETIC RELATIONS IN FOREST ARTHROPODS

D. E. Reichle Gladys J. Dodson

Food intake and respiratory heat loss are the major pathways of energy flow through animal communities. The faunistic complexity of many ecosystems makes absolute measurement of each parameter for all species impractical. Of distinct advantage, therefore, are functions which can relate these energetic parameters to basic and easily measurable interspecies characteristics (e.g., body size). For a given temperature gradient between an animal and its environment, the rate of heat transfer is proportional to its body surface area. Different-sized bodies of similar shape and density have surface areas proportional to the $\frac{2}{3}$ power of their weights. Metabolic parameters (Y) of arthropods from the floor of a *Liriodendron tulipifera* forest were correlated with size (X) of species: $Y = aX^b$. The species examined ranged in size from 2.1 mg to 1.6 g live weight and spanned a diversity of food habits and taxonomic categories.

Food consumption (Fig. 11.3) was proportional to the 0.68 power of body weight:

$$Y = 0.063X^{0.68 \pm 0.129} .$$

The value assumed by b (0.68 ± 0.129) is not statistically different from $b = 0.67$ of the body surface model. Using similar power function relationships, metabolic parameters are usually correlated with higher powers of body weight[11] intermediate between a simple weight ($b = 1$) or surface area ($b = 0.67$) response. Metabolism (μl of O_2 per hour) varied with the 0.84 power of body weight (Fig. 11.4):

$$Y = 0.32X^{0.84 \pm 0.071} .$$

Metabolic rate (μl of O_2 per gram per hour) was inversely proportional ($b = -0.16$) to body size, indicating higher metabolisms for smaller species with higher surface-to-volume ratios. The biological

[11] D. E. Reichle, "Relation of Body Size with Food Intake, Oxygen Consumption, and Trace Element Metabolism in Forest Floor Arthropods," *Ecology* (in press).

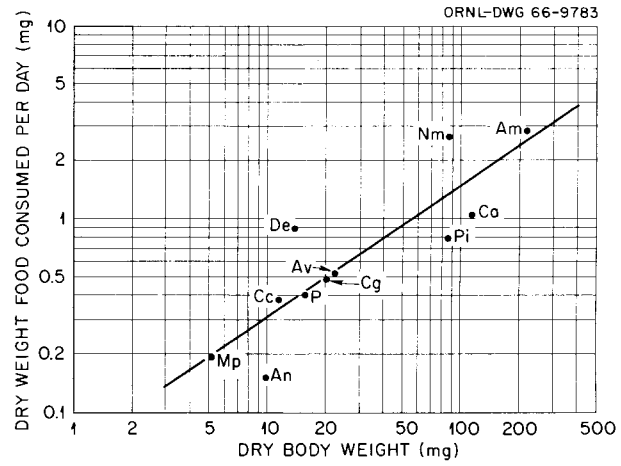

Fig. 11.3. Relationship Between Arthropod Body Size and Food Consumption: Am (*Apheloria montana*), An (*A. nasatum*), Av (*Armadillidium vulgare*), Ca (*Cambala annulata*), Cc (*Cylisticus convexus*), Cg (*Ceuthophilus gracilipes*), De (*Dixidesmus erasus*), Mp (*Metoponorthus pruinosus*), Nm (*Nemobius maculatus*), P (*Parcoblatta sp.*), Pi (*Ptyoiulus impressus*).

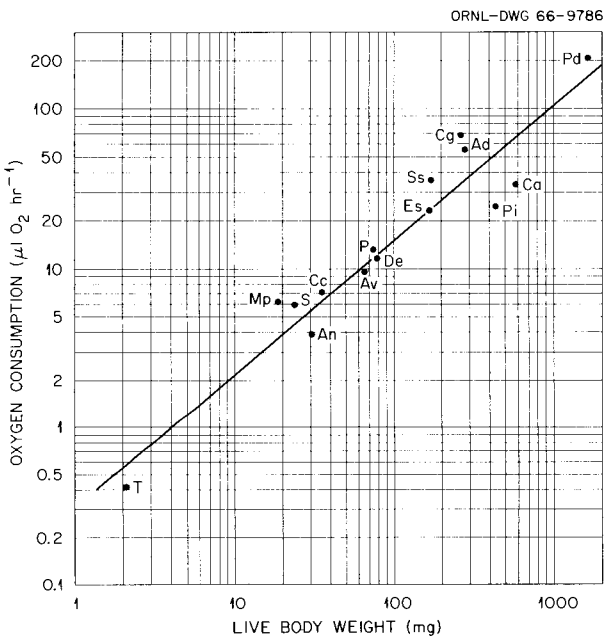

Fig. 11.4. Resting Metabolism (Microliters of O_2 per hour) of Forest Floor Arthropods Plotted as a Function of Live Body Weight. Ad (*Acheta domesticus*), Es (*Evarthrus sodalis*), Pd (*Popilius disjunctus*), S (*Schizocosa sp.*), Ss (*Sphaeroderus stenostomus*), T (unidentified termite species); see Fig. 11.3 for explanation of remaining species codes.

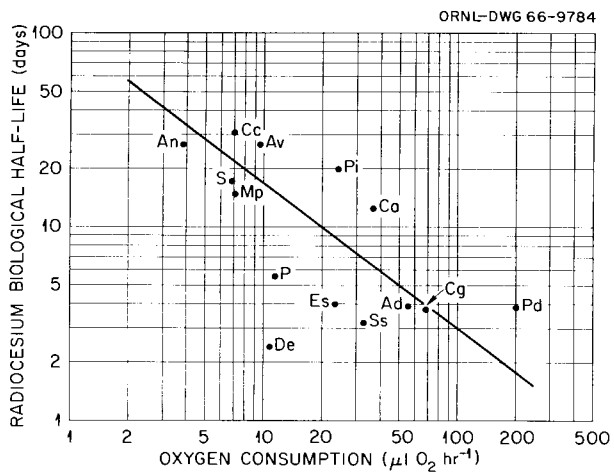

Fig. 11.5. Correlation Between Biological Half-Life of Radiocesium and Metabolism (Microliters of O_2 per hour) of Different Forest Floor Arthropods. See Figs. 11.3 and 11.4 for explanation of symbols.

half-life of radiocesium has been shown previously[12,13] to be related to body size in insects, with smaller species exhibiting more rapid turnover rates. A significant correlation ($P < 0.02$) also existed (Fig. 11.5) between the biological half-life of ^{134}Cs and oxygen consumption (μl of O_2 per hour) for certain forest floor arthropods:

$$Y = 94.4X^{-0.75 \pm 0.273} .$$

Although the error associated with b makes precise interspecies estimates of metabolism from ^{134}Cs biological half-lives somewhat tenuous, closer within-species correlations offer unique advantages. The biological turnover of radiocesium by certain species[14] has been demonstrated to be influenced by some of the same physiological and environmental parameters which also affect metabolism. In such cases, radioisotope retention by free-ranging field populations may serve as metabolic indices for species subjected to the environmental fluctuations of their natural habitats.

ELIMINATION RATES OF RADIOCESIUM BY SPIDERS AS A FUNCTION OF TEMPERATURE AND BODY SIZE

B. C. Moulder Gladys J. Dodson

Studies have been initiated on the predatory energy drain of spiders on the saprovore trophic level in the litter stratum of the ^{137}Cs-tagged *Liriodendron* forest. Bioelimination of ^{134}Cs by various groups of spiders (Lycosidae, Gnaphosidae, and Thomisidae) has been measured in the laboratory to provide an estimate of isotope turnover rates in the field.

Spiders collected in the field were kept in the laboratory in separate small plastic or glass containers to prevent cannibalism. After accumulating sufficient ^{134}Cs, administered by feeding the spiders crickets containing the isotope, the spiders were weighed and transferred to clean cages and placed in constant-temperature cabinets. Spiders were fed cesium-free fruit flies (*Drosophila*) or crickets (*Acheta*) during the elimination study. Measurements of ^{134}Cs were made by use of a series 410A Packard Auto-Gamma spectrometer with a small well-type crystal.

Bioelimination by these spider species occurred in two exponential phases, as exemplified in Fig. 11.6, where the log of the percent initial activity is plotted as a function of time. The more rapid initial phase probably represents the elimination of an unassimilated fraction of isotope voided from the gut in feces. The longer straight portion of the line represents the rate of elimination of assimilated isotope. Extrapolating the longer component back to $t = 0$ and subtracting the contribution of this portion (a_2) from the total apparent activity gives the contribution of the first component (a_1). The biological half-life of the assimilated fraction (T_{b2}) is very slow compared with half-lives of most insect species but approximates the values reported by Reichle and Crossley[15] for other terrestrial arthropod species.

[12] D. A. Crossley, Jr., "Use of Radioactive Tracers in the Study of Insect-Plant Relationships," pp. 43–54 in *Proc. Radiation and Radioisotopes Applied to Insects of Agricultural Importance*, IAEA, 1963.

[13] D. E. Reichle and D. A. Crossley, Jr., "Investigations on Heterotrophic Productivity in Forest Insect Communities" in *Proc. Working Meeting on the Principles and Methods of Secondary Productivity in Terrestrial Ecosystems*, Warsaw, Poland, 1966.

[14] S. I. Auerbach *et al.*, *Health Phys. Div. Ann. Progr. Rept. July 31, 1966*, ORNL-4007, pp. 67–68.

[15] D. E. Reichle and D. A. Crossley, Jr., *Health Phys.* 11, 1375–84 (1965).

Groups of spiders maintained at three different temperatures (15, 20, and 25°C) exhibited significantly different average biological half-lives (T_{b2}), as shown in Table 11.5. Shorter average half-lives reflect higher rates of metabolism at higher temperatures. The fraction of isotope assimilated fluctuated only slightly with change in temperature. The various species show little difference in ability to assimilate ^{134}Cs from their ingested food, although the values for crab spiders (Thomisidae) appear to be somewhat higher than the others.

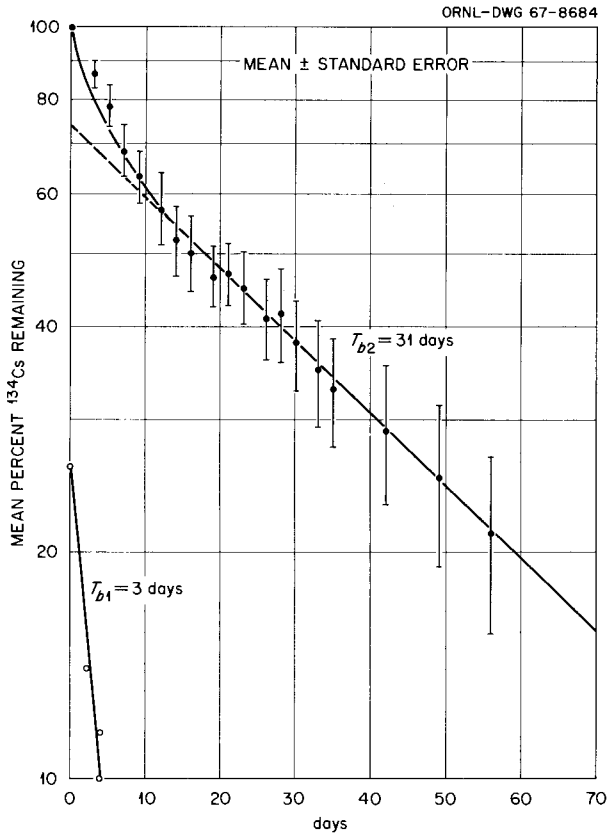

Fig. 11.6. Elimination of ^{134}Cs by *Lycosa punctulata* Hentz, Based on Four Individuals Maintained at 25°C.

If the above data are interpreted in view of the feeding habits of spiders, two interesting observations can be noted. First, spiders are predaceous and therefore should have higher metabolic rates than arthropods on the detritus-feeding trophic level. These higher rates should be reflected by shorter biological half-lives, which instead are much longer than those for detritus-feeding insects. A possible explanation may be that spiders are efficient users of energy, accomplishing metabolic work with low energy expenditure. In isolated cages in the laboratory, spiders are observed to sit motionless for long periods of time unless disturbed. Field elimination studies are under way to determine whether spiders eliminate radioisotopes more rapidly under more nearly normal circumstances.

Second, since spiders ingest only the predigested tissues of their victims, they are essentially fluid feeders. Fluid-feeding arthropods and predators in general tend to show a high percent of ^{134}Cs assimilation; in fact, fluid feeders or animals ingesting the isotope in drinking water usually show no trace of the initial gut component in their loss curve. Spiders do exhibit a significantly larger assimilation fraction than arthropods feeding

Table 11.5. Biological Half-Lives (T_{b2}), Fraction of ^{134}Cs Assimilated (a_2), and Mean Body Weight for Various Spider Species Cultured in the Laboratory

Species	15°C		20°C		25°C		Mean Body Weight (mg)
	T_{b2} (days)	a_2	T_{b2} (days)	a_2	T_{b2} (days)	a_2	
Lycosidae							
Lycosa punctulata	51.0	0.84			31.0	0.74	252.8
Schizocosa sp.	42.0	0.85	33.0	0.85	30.5	0.82	22.2
Gnaphosidae							
Gnaphosa sp. and *Drassyllus* sp.	42.0	0.87	32.5	0.88	17.0	0.89	22.2
Thomisidae							
Xysticus sp.	35.0	0.94			11.5	1.00	15.4

on solid matter but a smaller fraction than such fluid feeders as *Sphaeroderus*. This suggests that spiders, contrary to current belief, may actually ingest a considerable percent of their food in the form of undigested or partly digested particulate matter.

RADIOACTIVE TUNGSTEN RETENTION BY INSECTS

D. A. Crossley, Jr. S. V. Kaye

Radioisotopes of tungsten are among the most abundantly produced radionuclides from Plowshare-type nuclear explosives, including the type that would be used to excavate the proposed Atlantic-Pacific Interoceanic Canal. Significant quantities of ^{181}W, ^{185}W, ^{187}W, and ^{188}W were released into the desert environment by the Sedan detonation.[16] During a three-year cropping study, both native and domestic plants concentrated radiotungsten through root uptake from Sedan ejecta soil.[17] Radiotungsten is known to localize in bone of mammals, with a relatively long retention time.[18] However, tungsten distribution in ecosystems – its utilization, retention, and distribution among trophic levels – remains relatively unknown. Specifically, there is no information published on tungsten metabolism by insects, although these animals might constitute an important pathway for environmental redistribution of tungsten. Laboratory studies of ^{187}W retention were performed with two species of insects to determine what magnitude of food chain transfer might be expected in tungsten-tagged environments.

Twenty adults of the brown cricket *Acheta domesticus* and ten adults of the large milkweed bug *Oncopeltus fasciatus* were given access to tagged drinking water. A 25-ml Erlenmeyer flask fitted with a cellulose sponge wick and containing 120 μc of ^{187}W in 20 ml of water was used as a watering vessel. Within 24 hr, 11 of 20 *Acheta* and 8 of 10 *Oncopeltus* had accumulated sufficient radioactivity for retention studies. These insects were then confined singly and counted for radioactivity periodically during the next two days.

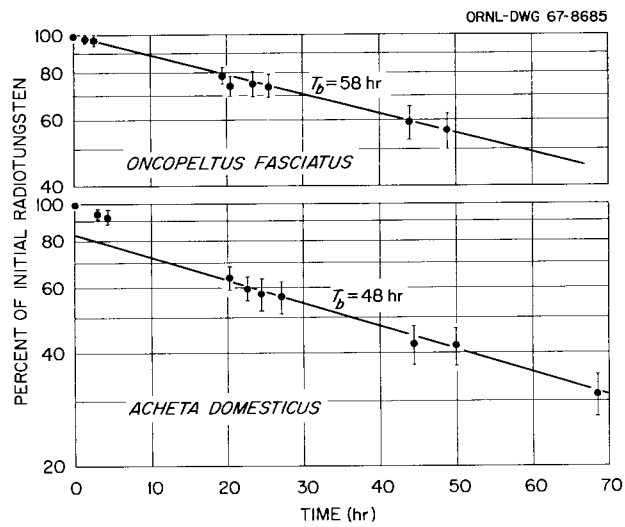

Fig. 11.7. Retention of ^{187}W by Adults of the Large Milkweed Bug (*Oncopeltus fasciatus*) and the Brown Cricket (*Acheta domesticus*). Each determination based on 8 individuals of *Oncopeltus* or 11 of *Acheta*. Range indicated for points equals two standard errors. Lines fitted by least-squares regression analyses.

Between counting periods, insects were maintained in a controlled-environment chamber at 83°F and 50% relative humidity and were supplied with food and water *ad libitum*.

The pattern of ^{187}W retention in *Acheta* and *Oncopeltus* is illustrated in Fig. 11.7, which shows the mean retention at each counting period. For *Oncopeltus*, the intercept of the least-squares regression line with the ordinate is 99.9%, suggesting complete absorption of the radiotungsten. The curve for *Acheta* in Fig. 11.7 was estimated without reference to the first three points. Its intercept is at 83%. For both species, absorption from drinking water appears to be nearly complete.

The biological half-lives for tungsten, based on the mean retention estimates at each counting time (Fig. 11.7), were 48 hr for *Acheta* and 58 hr for *Oncopeltus*. Biological half-lives were computed for the individual insects as well, to obtain an estimate of the error in these values. In both insect species, the distribution of biological half-lives was found to be strongly skewed to the right. Biological elimination coefficients (log $2/t_{1/2}$), however, had symmetrical distributions. By converting half-lives to elimination coefficients, errors could be estimated. Percentage error was found to be about 20%.

[16] E. H. Essington *et al.*, *Health Phys.* 11, 689 (1965).

[17] E. M. Romney *et al.*, *Radioecological Concentration Processes*, p. 391, Pergamon, Oxford, 1967.

[18] S. V. Kaye, *Distribution and Retention of Orally Administered Radiotungsten in the Rat*, Ph.D. thesis, University of Rochester, 1966.

Radiotungsten absorption and retention parameters appear similar to those for radiocesium in *Acheta* and *Oncopeltus*. Radiocesium absorption in insects typically is high, approaching 100%.[19] Biological half-lives for radiocesium (62 hr for *Acheta*, 35 hr for *Oncopeltus*) also resemble those for radiotungsten. From these measurements it is inferred that radiotungsten movements through the arthropod portions of food chains may approximate movement of radiocesium. Previous work on the White Oak Lake bed[20] has demonstrated that ^{137}Cs had slightly reduced, or virtually unchanged, concentrations during food chain transfers. Such efficient movement of radiotungsten appears unlikely, since radioisotopes of tungsten have more rapid radioactive decay rates.

CYCLING OF ^{45}Ca BY DOGWOOD TREES

W. A. Thomas

Flowering dogwood (*Cornus florida* L.) has been cited as a nutritionally beneficial understory tree due to accumulation of calcium in its leaves, thus keeping this essential element in circulation in upper soil layers. Results reported here are from one experiment in a comprehensive investigation of the accumulation and cycling of calcium by this species.

Twelve trees (4.4 to 7.1 cm in diameter at ground level and 3.3 to 5.2 m in height) in a pine plantation were stem-tagged with $^{45}CaCl_2$ (0.67 to 2.51 mc, proportional to estimated tree weight) on 4 May 1966. Radiocalcium in foliage was estimated monthly, and foliar leachate under all trees and stemflow samples from four trees were collected after every period of precipitation. The amount of ^{45}Ca removed from foliage by insects was estimated monthly from data for leaf area removed by insects and distribution of ^{45}Ca in leaves.

On 4 November, six months after inoculation, eight tagged trees were harvested and analyzed for radiocalcium. Total leaf number was estimated with a regression equation which related number of leaves to branch diameter.

On 5 June, one month after inoculation, 73% ± 6 of total inoculum was in leaves. Calcium-45 concentrations (absolute amount or percentage of total) steadily decreased during the remainder of the season due to physical decay, foliar leaching, and leaf fall. Radiocalcium lost from the tree by leaf fall was 64% ± 1 of total inoculum.

Radiocalcium loss due to insect damage was 4% of maximum ^{45}Ca in foliage although only 1.8% of leaf area had been removed by insects through October. This loss represented 3% of total inoculum.

All samples of throughfall and stemflow, collected 15 times during the experiment, contained ^{45}Ca. It was impossible to ascertain the percentage of radiocalcium in foliage that was removed by precipitation since leaf samples were not collected immediately prior to every period of precipitation. The equivalent of 8% of maximum radiocalcium in foliage (June) was removed by precipitation during the entire experiment. This amounted to 6% ± 1 of total inoculum. Although stemflow volume was appreciable (usually from 100 to 3500 ml, depending upon the tree and amount of precipitation), it accounted for only 0.20% ± 0.01 of total volume and 0.17% ± 0.02 ($n = 60$) of total ^{45}Ca which reached the forest floor under trees. Radiocalcium in stemflow was only 0.01% ± 0.01 of total inoculum.

Two litter and soil samples were collected under each tree on 12 October. Soil samples were taken to a depth of 6 cm (soil at greater depths did not contain ^{45}Ca), and ^{45}Ca was extracted with 1.0 *N* HCl. Of total ^{45}Ca found, 88% ± 1 ($n = 24$) was in litter. Radiocalcium was found in aboveground portions of ground vegetation, but this transfer of ^{45}Ca represented a negligible amount of the inoculum due to paucity of ground vegetation under the trees. Of radiocalcium remaining in nonfoliar organs of the eight harvested trees on 4 November, 97% ± 2 was in aboveground tissues.

The estimated amount of ^{45}Ca accounted for at the end of the experiment (106% ± 5 of inoculum remaining after physical decay) was well within limits of sampling error for a weak beta emitter in a tree-soil system for six months.

Sample data and known pathways of calcium transfer were used to prepare a diagrammatic summary of the results (Fig. 11.8). Stem and branches retained 26% of the inoculum, most of which was probably bound on exchange sites in

[19] S. I. Auerbach *et al.*, *Health Phys. Div. Ann. Progr. Rept. July 31, 1965*, ORNL-3849, pp. 53–54.

[20] D. A. Crossley, Jr., and H. F. Howden, *Ecology* 42, 302–17 (1961).

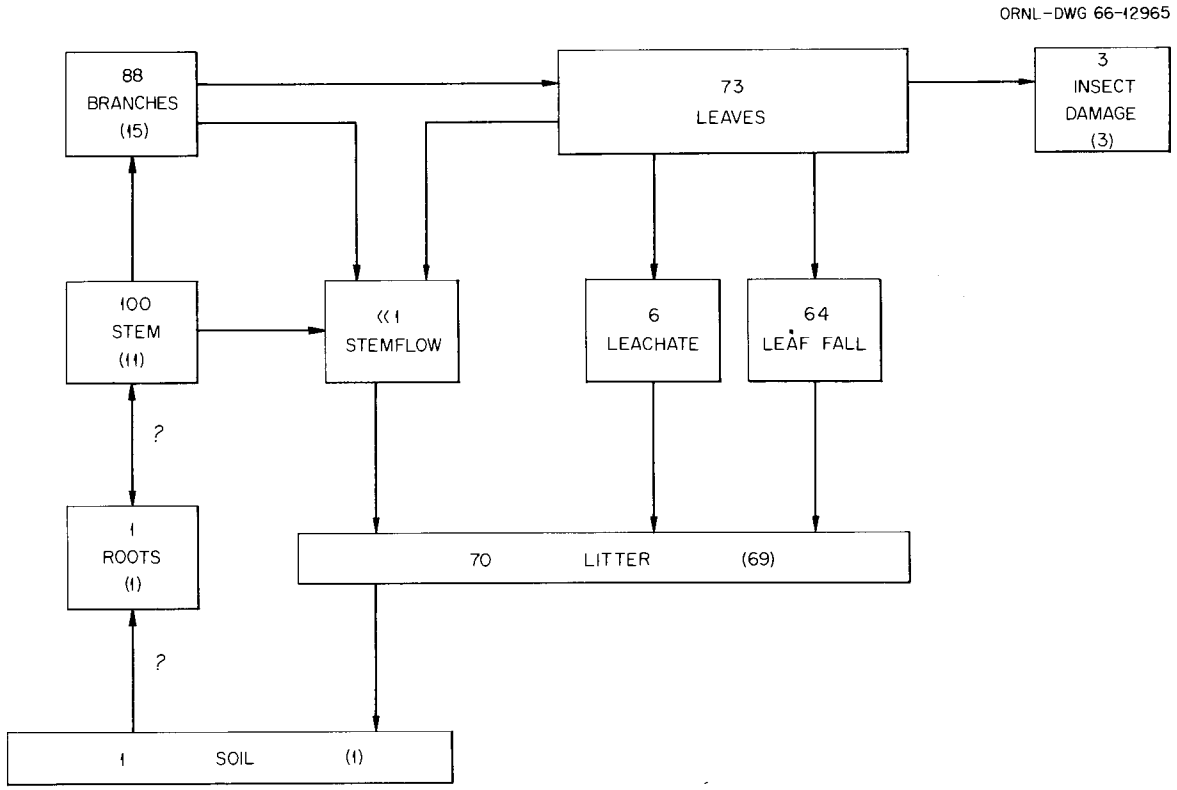

Fig. 11.8. Distribution of ^{45}Ca After Stem Inoculation of Dogwood Trees. Numbers in parentheses are percentages of inoculum found after leaf abscission. Numbers not in parentheses represent maximum percentages of inoculum in components during the growing season. Trees were tagged on 4 May and harvested on 4 November 1966.

xylem.[21] The large percentage of total ^{45}Ca which reached foliage (73%) was due to rapid uptake of inoculum and polarity of calcium in plants, which limits calcium to acropetal movement.[22] Because calcium is not returned to woody tissues prior to leaf abscission, as are several other elements,[23] a large fraction of foliar calcium was lost from the tree in leaf fall.

The appreciable role of precipitation in removal of calcium from foliage is to be expected,[24] while the role of stemflow will normally be minimal due to its small contribution to total precipitation reaching the forest floor under trees.[25]

Much of the ^{45}Ca in litter will be subsequently transferred to soil due to leaf decomposition and leaching by precipitation, although a sizable fraction of it will probably remain in the litter layer due to abundance of exchange sites on dead pine needles.

It is not clear how ^{45}Ca entered roots, but it probably descended from the stem since the amount of radiocalcium in roots greater than 4 cm in diameter was 4.4 times that in roots less than 4 cm in diameter and since there was so little radiocalcium available for absorption by roots in litter and soil. This does not refute the concept of polarity for calcium movement since trees were inoculated so close to the roots that some radiocalcium could have diffused downward in bark (as opposed to translocation).

Rapid turnover of inoculated calcium by these trees is further evidence that dogwoods are beneficial in keeping calcium in circulation in the upper layers of soil, thus keeping it available for use by other species.

---

[21] C. W. Bell and O. Biddulph, *Plant Physiol.* **38**, 610–14 (1963).

[22] H. B. Tukey, S. H. Wittwer, and M. J. Bukovac, *Agrochimica* **7**, 1–28 (1962).

[23] G. Stenlid, *Encyclopedia of Plant Physiology*, vol. 4, pp. 615–37, Springer-Verlag, New York, 1958.

[24] P. M. Attiwill, *Plant Soil* **24**, 390–406 (1966).

[25] J. D. Helvey and J. H. Patric, *Water Resources Res.* **1**, 193–206 (1965).

BIOMASS REGRESSION RELATIONS FOR THE EL VERDE RAIN FOREST IN PUERTO RICO

J. S. Olson L. J. Bledsoe

At the request of the Puerto Rico Nuclear Center (PRNC), a visit to the El Verde rain forest provided advice on the continuing PRNC study of secondary succession following massive gamma irradiation which killed part of this forest.[26] Also ORNL computer programs were used to calculate appropriate regression parameters relating tree diameter and/or height to the mass of several tree parts in order to compute the forest biomass. Early steps included the conversion of fresh weights to dry weights on the basis of sampling that was initiated by J. D. Ovington in November 1963 and completed by the PRNC staff during several months following. Preliminary regression analyses then were made for the few individual species and genera for which sufficient numbers of trees were available for individual regressions.

For many species there were only one to three individuals represented, but fortunately these appeared to fit the same mass-diameter-height relations as were found for the more thoroughly sampled groups. Diameter was generally a much better predictor for mass than was tree height. Simple, usable bases for predicting mass of major components could therefore be made on the basis of diameter alone for certain broad species groups shown in Table 11.6. These linear regressions were made using the formula

$$\ln(\text{mass}) = A - B \ln(\text{diameter at 137 cm height}) , \quad (1)$$

which is equivalent to the power expression

$$m = e^A d^B , \quad (2)$$

where d is diameter (cm) and m is mass (g).

Table 11.6. Regression of Mass on Diameter for Several Tree Components of the El Verde Rain Forest, Puerto Rico

Component	Species Group[a,b]			
	C		D	
	e^A	B	e^A	B
Leaves	45.925	1.400	21.867	1.930
Branches	47.656	1.629	15.518	2.493
Bole	194.416	1.816	95.297	2.416
Branch plus bole	254.68	1.831	115.123	2.413
Large and butt roots	52.300	2.095	22.646	2.578
All roots (estd)	65.170	1.950	27.113	2.512

[a]Group C includes miscellaneous species: *Alchorneopsis portoricensis, Cecropia peltata, Calycogonium squamulosum, Drypetes glauca, Didymopanax morototoni, Eugenia stahlii, Hirtella rugosa, Myrcia spendens, Ocotea portoricensis, Psychotria berteriana,* and *Tetramogastris balsamifera.*

[b]Group D includes major species in two subgroups – namely, A: *Dacryodes excelsa, Palicourea riparia, Cordia borinquensis, Cordia sulcata, Cyrilla recemiflora, Ocotea leucoxylon, Micropholis garciniaefolia, Ocotea spathulata,* and *Tabebuia heterophylla* (or *pallida*); and B: *Ormosia krugii, Inga vera, Inga laurina, Miconia tetrandra, Miconia prasina, Matayba domingensis, Buchenayia capitata, Casearia arborea, Casearia sylvestris, Sloanea berteriana,* and *Manilkara bidentata* (or *nitida*).

FOLIAR APPLICATION OF ^{137}Cs ON UNDERSTORY SPECIES OF MESIC FOREST

P. B. Whitford J. S. Olson

Earlier studies on a 20- by 25-m plot of *Liriodendron* forest used ^{137}Cs injected in trunks of canopy trees at the rate of 936 μc per square meter of plot area to trace the movement of this nuclide in the forest ecosystem.[27] Results indicated that a small portion (<0.5%) was absorbed by understory species from rainout during the first growing season, while major portions of the isotope remained in the woody parts of the injected trees or moved into litter, fine roots, and soil.[28] The present study was planned to clarify the relative absorption of the rainout fraction by foliage of understory species and to check previous estimates of movement to litter and soil through understory species which may have been obscured by the much larger activities remaining in other parts of

[26]H. T. Odum, ed., *The Rain Forest Project Annual Report FY-65*, PRNC-61 (Mar. 1, 1965).

[27]J. S. Olson, *Health Phys.* 11(12), 1385–92 (1965).

[28]H. D. Waller and J. S. Olson, *Ecology* 48(1), 15–25 (1967).

the system. On June 27, 1966, the same isotope was applied as a foliar spray at the rate of 35 $\mu c/m^2$ to vegetation up to 1 m high on a plot 2 by 5 m about 10 m from the original plot. The isotope was diluted in 10 liters of tap water and applied with a garden sprinkling can to simulate a rainout effect equivalent to about 0.04 in. of rain through the canopy.

Figure 11.9 shows 18% retention of the isotope on foliage after 2 hr and 9, 8, and 7% after two, four, and six weeks; the major part of the applied solution dripped onto the litter layer. Approximately 22 cm of rain during the test period accounted for most of the reduction in isotope in the foliage as well as for transfer through the litter to the top 5 cm of soil (3% of application) by the end of the sixth week. Less than 5% was absorbed and translocated to stem and roots. Differences between species are probably related to leaf surface structure, mass/area ratio, and leaf orientation.

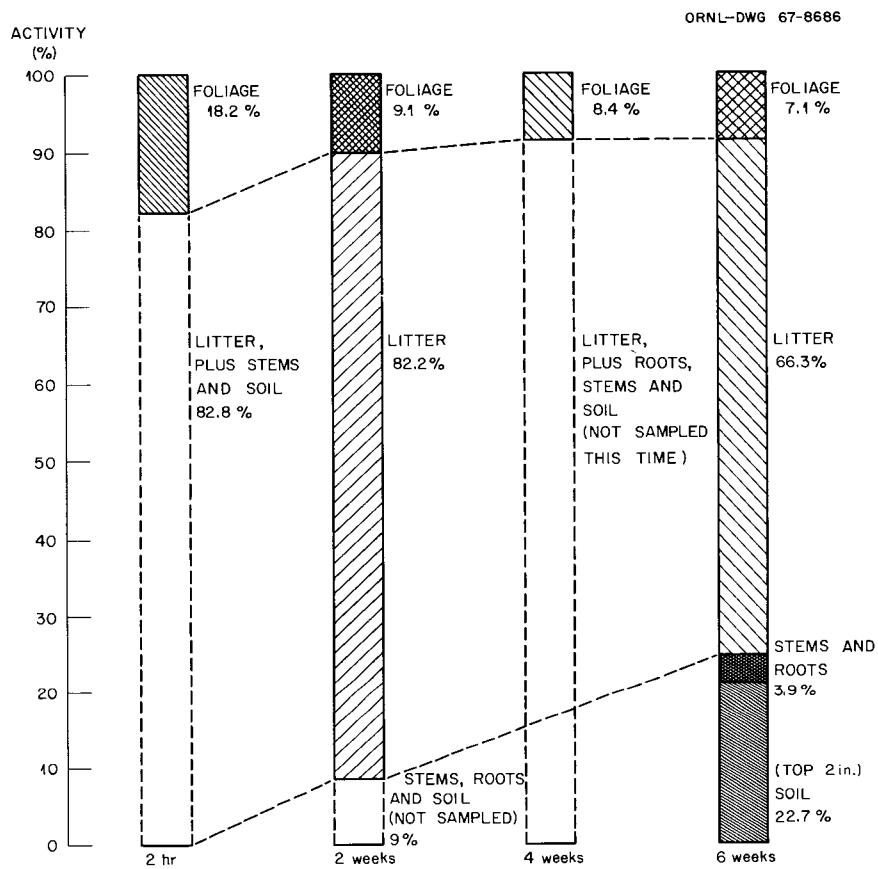

Fig. 11.9. Distribution of ^{137}Cs After Foliage Application.

12. Radionuclide Cycling in Aquatic Ecosystems

B. G. Blaylock[1]
C. E. DePoe[2]
N. A. Griffith
N. R. Kevern
E. C. Neal
D. J. Nelson
B. C. Patten[1]
J. R. Reed
J. L. Wilhm

UPTAKE AND METABOLISM OF STRONTIUM IN BLUEGILL FLESH AND BLOOD

J. R. Reed D. J. Nelson
N. A. Griffith

Studies of Sr uptake and turnover by fish were continued,[3] with emphasis on the role of flesh and blood. These soft tissues contain much less Sr than do the calcareous tissues, but they are a major pathway by which humans might obtain radionuclides of Sr from aquatic habitats.[4] The objectives of the research were to determine (1) the effect of different environmental Sr concentrations on the uptake of Sr in fish flesh and (2) the quantitative importance of fish flesh and blood in the uptake and turnover of Sr.

Several different types of experiments were used to clarify the respective roles of fish flesh and blood in Sr uptake and turnover. The different experiments were necessary because of the high concentrations and rapid rate of deposition of Sr in scales and bone, which literally masked Sr uptake in flesh and other soft tissues. The biological half-life of Sr was studied using both whole-body counting and dissection methods to delineate the role of individual tissues in Sr excretion.

Bluegills (*Lepomis macrochirus* Rafinesque) were selected for the study on the basis of previous work with the closely related white crappie. In the uptake studies bluegills were subjected to waters with various stable Sr concentrations ranging from 0.3 to 30,000 ppb and containing ^{85}Sr as a tracer. After 24 hr in test solutions the fish were sacrificed and blood and flesh samples processed for chemical analysis. Another aspect of the uptake study was concerned with the response of bluegills to a continuous radiostrontium exposure for 35 days. Fish were removed at 1, 2, 4, 8, 16, and 35 days during the test period, and samples of blood and flesh were processed for analysis. The biological half-life of Sr in bluegills was measured by using ^{85}Sr as a tracer and counting the whole fish in a small-animal whole-body counter.

Specific activities or radiostrontium-to-total-Sr ratios were used to determine whether the Sr in flesh and blood was in equilibrium with that in water. At equilibrium the specific activities in water and fish tissue will be equal, while at non-equilibrium conditions the specific activity indicates the proportion of Sr in tissue which was exchanged. Concentration factors, or the amount of radiostrontium in fish flesh or blood relative to the amount in the test water, were formulated in some cases for ease of calculation.

Uptake and Turnover of Radiostrontium by Flesh and Blood

The blood incorporated radiostrontium rapidly, reaching about two-thirds of the maximum activity

[1]Dual capacity.

[2]ORAU summer research participant.

[3]S. I. Auerbach *et al.*, *Health Phys. Div. Ann. Progr. Rept. July 31, 1964*, ORNL-3697, p. 95.

[4]K. E. Cowser and W. S. Snyder, *Safety Analysis of Radionuclide Release to the Clinch River*, ORNL-3721, Suppl. 3 (1966).

level in 24 hr (Fig. 12.1). The concentration factor rose from 0.124 at 1 day to 0.194 at 35 days. A second component of the blood uptake curve was very long, but sufficient data were not available for accurate extrapolation. On the basis of stable Sr concentration factors in the blood in fish from natural waters, radiostrontium concentration factors of between 3.26 and 6.23 should be reached (Table 12.1).

The specific activity ($\mu\mu c$ $^{89}Sr/\mu g \times 10^{-3}$ Sr) in the blood did not change appreciably in the test period, rising from 0.47 at 1 day to 0.74 at 35 days. The specific activity expected at equilibrium was 24.1. In the rapidly exchanged component of the soft tissues, blood accounted for 2% of the activity in 24 hr, and in the longer component blood accounted for 3% of the activity in 35 days. Since blood represents about 3% of the body weight in fish, the radiostrontium present in the blood was a very small fraction of that present in the whole fish. The blood was a compartment which rapidly exchanged radiostrontium but which comprised very little of the total Sr in flesh.

The greatest rate of ^{89}Sr uptake by the flesh occurred in the first four days. The second component of the uptake curve was faster for flesh than

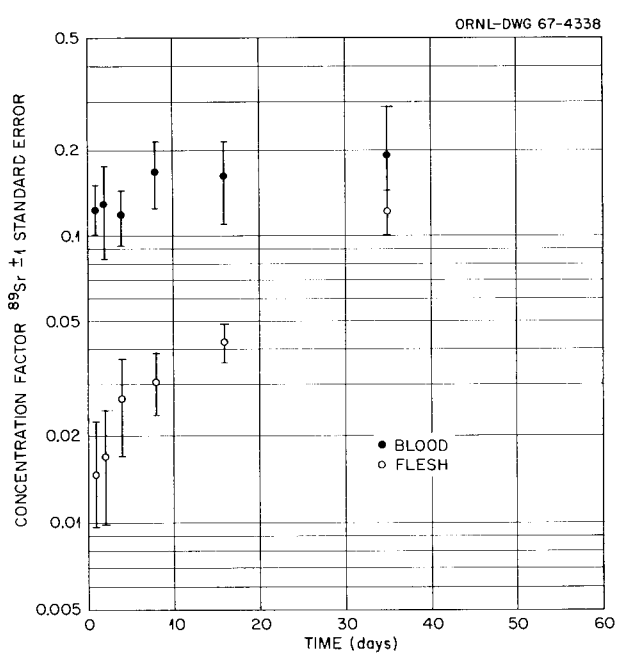

Fig. 12.1. Concentration Factors of ^{89}Sr in Bluegill Flesh and Blood During a 35-day Exposure Period.

for blood (Fig. 12.1), and the maximum concentration factor reached after 35 days was 0.121. Extrapolation of the second component indicates that approximately 72 days are necessary for bluegill flesh to reach a concentration factor of 1, which may be expected from stable Sr analyses (Table 12.1).

The specific activity in the flesh rose from 0.28 in 1 day to 2.4 in 35 days, while again the expected specific activity ratio was 24.1 ($\mu\mu c$ $^{89}Sr/\mu g \times 10^{-3}$ Sr). Approximately 1% of the activity in the soft tissues was present in the flesh in 24 hr, increasing to 10% in 35 days. Thus, the short components measured for flesh and blood represented only 1% of the activity in the soft tissues in 24 hr, while the longer components represented 9% of the activity in 35 days. The remaining activity (90%) probably was in a compartment which did not readily exchange Sr.

The turnover of Sr in bluegills was studied in a series of excretion experiments. Various combinations of live and dead fish were tagged with ^{85}Sr and counted in a whole-body counter to study short-term excretion patterns. The results showed a rapid rate of ^{85}Sr loss during the initial 40 min (Fig. 12.2). The rate slowed somewhat in those fish which were tagged while alive, whereas those tagged when dead declined steadily. The curve for fish tagged alive but counted dead was similar to that for fish tagged alive and counted alive. This indicated that ^{85}Sr was incorporated into the body of the live fish, but that early losses were due to physical processes rather than biological excretion. This physical loss, attributed to the flushing action of the water, occurred despite the rinsing of fish in uncontaminated water prior to placing them in the excretion chamber. The excretion curves of fish which were tagged alive show evidence of a "biological sink" which prevented ^{85}Sr losses, since the majority of the isotope was bound in the sink. Fish which were tagged when dead lost ^{85}Sr rapidly and lacked the "sink" aspect in the excretion curve.

An experiment lasting several days was performed to determine if the flesh was actually losing ^{85}Sr via excretion. The initial phase was like that described above. After 2 hr the fish still retained 70% of the initial activity (Fig. 12.2). However, after one day the loss of activity was greater, and after seven days of excretion only 50% of the initial whole-body activity remained. At that point, the curve flattened, and the value for 14

Table 12.1. Stable Strontium in Bluegill Flesh and Blood

	Number of Fish	Stable Strontium Concentration (ppb) ±2 Times Standard Error	Concentration Factor
Blood			
Pond	5	196 ±62	3.26
Spring	5	187 ±50	6.23
Flesh			
Pond	5	45 ±3	0.75
Spring	5	35 ±4	1.17
Water			
Pond		60	
Spring		30	

days was also 50%. Rosenthal[5] stated that for ^{90}Sr in *Poecilia* (=*Lebistes*) the first rapidly disappearing component, with a biological half-life of eight days, was due to losses from viscera. Current experiments with bluegills, employing dissections immediately following a short tag with ^{85}Sr and after 2 hr of excretion, indicate that blood is also an important factor in early losses of activity and may comprise a portion of the losses attributed to viscera. The blood lost 75% of its initial activity in 2 hr. Results from dissections of bluegills as described above for blood excretion showed that the flesh lost 46% of its initial activity in 2 hr. Nelson[6] reported a biological half-life of 12 to 48 min for ^{85}Sr in flesh of white crappies.

The bluegill excretion curve was comprised of three components. The initial rapid component of 2 hr was due to blood and flesh excretion and, to some extent, physical losses. A slower component of 2 hr to nine days represented the long blood component and viscera and muscle excretion. The very long third component reached at approximately nine days may be attributed to flesh excretion and possibly to turnover of Sr in connective tissue. On the basis of previous estimates of the flesh turnover of radiostrontium and from the current study, it appears that there are at least three compartments in flesh excretion.

Uptake Responses to Different Environmental Sr Concentrations

Since comparisons of uptake at different stable Sr concentrations were made on a uniform 24-hr exposure time, these results should be related only to the quickly exchanged fraction of Sr in flesh and blood. Concentration factors of radiostrontium (Fig. 12.3) indicate that about 1% of the Sr in flesh was exchanged in 24 hr.

The concentration factor for radiostrontium was virtually constant within the range from 0.3 to 30,000 ppb stable Sr in the test solutions (Fig. 12.3). Since the concentration factors remained constant over the wide range of stable Sr concentrations, the readily exchanged Sr fraction was accumulating Sr in direct proportion to that in the environment. Results of the stable Sr analyses (Fig. 12.3 and Table 12.2) indicated that concentration factors of stable Sr were inversely proportional to the Sr concentration in test waters, except at the two highest environmental Sr concentrations, 3000 and 30,000 ppb. Otherwise, the inverse relationship showed that concentration factors calculated on the basis of stable Sr concentrations were highly dependent upon the environmental Sr

[5]H. L. Rosenthal, *Ann. N. Y. Acad. Sci.* **109**, 278–93 (1963).

[6]D. J. Nelson, "The Prediction of ^{90}Sr Uptake in Fish Using Data on Specific Activities and Biological Half-Lives," pp. 843–51 in *Radioecological Concentration Processes*, ed. by B. Åberg and F. P. Hungate, Pergamon, New York, 1967.

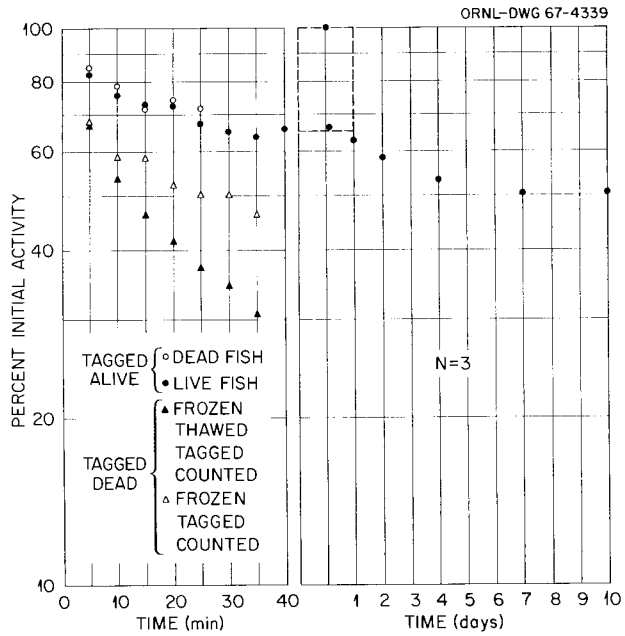

Fig. 12.2. Comparative Whole-Body Excretion of ^{85}Sr in Bluegills Which Had Been Tagged Either While Living or After Having Been Killed by Freezing. The initial excretion in the left portion of the figure is included within the dotted box in the right portion of the figure. Note difference in time scales.

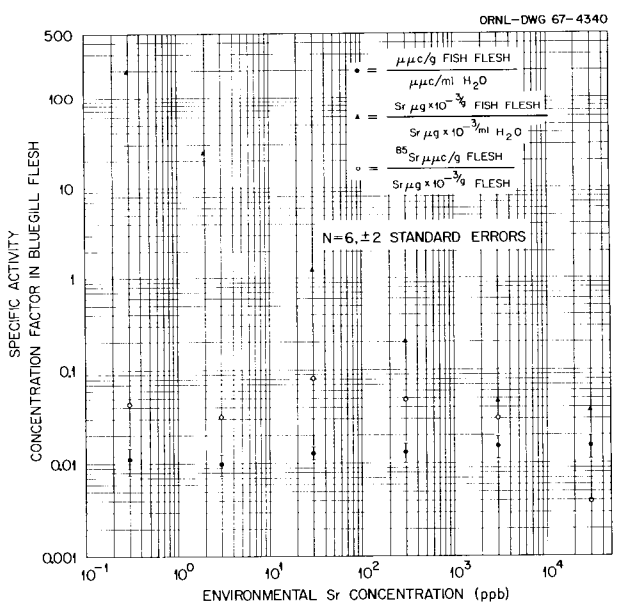

Fig. 12.3. Concentration Factors of Stable Sr and ^{85}Sr and Specific Activities of ^{85}Sr in Bluegill Flesh at the End of a 24-hr Uptake Experiment.

Table 12.2. Strontium in Bluegill Flesh from Waters with Different Sr Concentrations

Water Sr (ppb)	Number of Fish Analyzed	Flesh Sr (ppb)
30,000	6	1017 ± 230[a]
3,000	5	132 ± 36
300	6	57 ± 16
30	6	37 ± 9.4
3	5	44 ± 12.2
0.3	6	36.7 ± 2.6

[a]Mean ± 2 standard errors.

concentration. The levels of stable Sr in the flesh of the experimental fish did not change significantly. These results showed that the quickly exchanged fraction of Sr in bluegill flesh was a small proportion of the total Sr in flesh.

At 3000 and 30,000 ppb Sr concentrations the fish flesh contained approximately 2 and 20 times, respectively, as much Sr as those fish at the lower environmental concentrations (Table 12.2). These results suggested the lack of an ability by bluegills to discriminate against the uptake of Sr from waters containing abnormally high concentrations. At environmental concentrations of 300 ppb and below, the fish had similar concentrations of Sr in flesh which ranged from 37 to 57 ppb. The constancy of these flesh values was due, in part, to a lack of sufficient time for test fish to equilibrate with the test solutions. However, at these lower concentrations it was evident that active regulation of the Sr content in flesh occurred and that it did not occur at the two higher concentrations.

The specific activity in flesh (Fig. 12.3) reflected the relative constancy of ^{85}Sr and stable Sr concentrations in fish at all concentrations except 30,000 ppb. At the 30,000 ppb Sr concentration, the specific activity was reduced because of a diluent effect of stable Sr which might be expected at exceedingly high concentrations.

Strontium Relationships in Flesh and Blood

Strontium concentrations in fish flesh and blood are a minor fraction of the total quantity in fish.

Flesh and blood appeared to have short components in both uptake and excretion experiments. However, the flesh contribution to these quickly exchanged components is of greater significance. Blood is about 3% of the body weight of bluegills, and the 35-day uptake experiment demonstrated that 2% of the blood Sr was exchanged in 1 day and 3% was exchanged at 35 days. The remaining 97% of the Sr in blood consists of a component with a long biological half-life. Since organs such as the kidney, heart, liver, and spleen contain most of the blood, the contribution of blood Sr to the turnover of Sr in flesh is minor ($<0.09\%$).

The three separate experiments showed the presence of a quickly exchanged Sr fraction in flesh. The specific activity at the end of 1 day in the 35-day uptake study was about 1% of the expected equilibrium value, and the 24-hr experiments also suggested that about 1% of the Sr in flesh was exchanged. The excretion studies showed the biological half-life of this fraction to be approximately 2 hr. The 35-day experiment and the excretion study also showed that an additional 9% of the Sr in flesh was turned over with a half-life of 9 days. Since five biological half-lives are required for exchange reactions to reach 97% of equilibrium values, the 9% value for Sr exchanged within 35 days is slightly low. Nevertheless, about 90% of the Sr in flesh is in a component having a long biological half-life.

These experiments, in addition to clarifying our knowledge regarding quantitative aspects of Sr uptake and turnover by fish flesh and blood, demonstrated a new application for specific activity data. Conventional extrapolations of excretion curves by the "peel-off" method assume that 100% of the pool of an element in the tissues is available for exchange. By determining specific activities the proportion of the total Sr pool involved in excretion in fish flesh was determined.

CESIUM AND POTASSIUM IN AQUATIC FOOD CHAINS

D. J. Nelson N. R. Kevern
N. A. Griffith

The previous chemical analyses[7] of white crappie and other Clinch River fish for their cesium and potassium concentrations were supplemented with investigations of food-chain relationships. The comparative retention and metabolism of cesium and potassium have been associated with an "increase ratio,"[8] implying that cesium to potassium ratios will increase at succeeding trophic levels in the food chain. The primary reason for the higher ratio was related to a more tenacious retention of cesium in the body. Since the chemical data on cesium and potassium gave no concise evidence on the "increase ratio," the biological half-lives of cesium and potassium in white crappie were compared.

Crappies were tagged either with ^{134}Cs or ^{42}K by feeding them goldfish that had been injected with isotope solutions. Thus, the experimental feedings simulated as nearly as possible the passage of radionuclides through the food chain. Following tagging, the fish were counted initially and thereafter at intervals in a whole-body counter to determine remaining radioactivity.

Two components were distinguished in the excretion curve for ^{134}Cs. A short component having a T_b of 3 days accounted for 26% of the activity, while a component of about 280 days included the remaining 74% of the ^{134}Cs activity. Because of the short physical half-life of ^{42}K (12.46 hr), the crappie could be counted only for 5 days. During this period no excretion of ^{42}K was observed. If, as Pendleton *et al.*[8] suggested, K is excreted more rapidly than Cs, at least a short component of a ^{42}K excretion curve should have been identified. However, if K excretion was of a single-component curve with a T_b approximating that of Cs, detection would have been impossible over a five-day period. Our results suggest that K was retained more efficiently than Cs under identical dietary conditions.

A trophic-level increase of ^{137}Cs in aquatic food chains has been observed by several investigators.[8,9,10] Pendleton *et al.*[8] reported

---

[7] S. I. Auerbach *et al.*, *Health Phys. Div. Ann. Progr. Rept. July 31, 1966*, ORNL-4007, pp. 84–87.

[8] R. C. Pendleton *et al.*, *Health Phys.* 11, 1503–10 (1965).

[9] P. A. Gustafson, "Comments on Radionuclides in Aquatic Ecosystems," pp. 853–58 in *Radioecological Concentration Processes*, ed. by B. Åberg and F. P. Hungate, Pergamon, New York, 1967.

[10] S. Kolehmainen, E. Häsänen, and J. K. Miettinen, "^{137}Cs in Fish, Plankton and Plants in Finnish Lakes During 1964–1965," pp. 913–19 in *Radioecological Concentration Processes*, ed. by B. Åberg and F. P. Hungate, Pergamon, New York, 1967.

Table 12.3. Concentration Factors of Stable Cesium and Potassium in Clinch River and Cesium Concentration Factors for White Oak Lake Fish

The concentration factor is the ratio of the concentration of the element per gram of fresh tissue to the concentration per milliliter of water

Species	Clinch River		White Oak Lake
	Cs	K	Cs
White crappie (*Pomoxis annularis*)	516	2677	
Freshwater drum (*Aplodinotus grunniens*)	349	2508	
White bass (*Roccus chrysops*)	640	2707	
Channel catfish (*Ictalurus punctatus*)	163	2615	
Bluegill (*Lepomis macrochirus*)	138	2523	407
Gizzard shad (*Dorosoma cepedianum*)			514
Black bullhead (*Ictalurus melas*)			272
Largemouth bass (*Micropterus salmoides*)			400

that bluegills contained 3.3 times as much ^{137}Cs as the young pumpkin seeds (*Lepomis gibbosus*) being eaten. In contrast, the bluegills from the Clinch River had the lowest concentration factor for Cs of the five species analyzed (Table 12.3).

The Clinch River bluegills are carnivores, and examination of stomach contents suggested bottom organisms were the primary food source. Kolehmainen *et al.*[10] found less ^{137}Cs in fish consuming bottom organisms in Finnish lakes and also observed higher ^{137}Cs concentrations in pike (*Esox lucius*) and perch (*Perca fluviatilis*), which are primarily piscivorous. Gustafson's[9] analyses of Red Lake, Minnesota, fish showed that the pike contained 4.81 times as much ^{137}Cs as perch (*Perca flavescens* in this case) which they were eating. While the perch were also eating fish, their ^{137}Cs content was only 1.85 times greater than their food base. Although pike and perch are always considered carnivores, their relative ^{137}Cs concentrations varied in different habitats. The white crappie and white bass were the most piscivorous of the Clinch River fish analyzed and also had the highest concentration factors for Cs.

Analyses of four White Oak Lake fish for stable Cs showed no consistent pattern of Cs content with respect to trophic level (Table 12.3). The black bullhead had a Cs concentration factor noticeably less than the other species and in this respect was similar to the closely related channel catfish. Gizzard shad, which are primarily algae and detritus feeders, concentrated Cs as much as the piscivorous largemouth bass. Bluegills in White Oak Lake have food habits similar to bluegills from the Clinch River, but the Cs concentration factor of the White Oak Lake bluegills was comparable with those in largemouth bass.

Trophic-level increases in Cs concentrations do not appear to be a general rule in aquatic environments. In comparing the results of Cs and ^{137}Cs analyses from the Clinch River, Finnish lakes, and Red Lake, it was apparent that trophic-level increases occurred only part of the time. These differences may be the results of different food chains in different habitats, which in turn affect Cs concentration at succeeding trophic levels. Data available at present do not warrant the general application of trophic-level increases to Cs in food chains.

RADIATION EFFECTS ON CARP REPRODUCTION

B. G. Blaylock J. R. Reed
N. A. Griffith

Study of the reproductive capabilities of carp from White Oak Lake and Fort Loudon Reservoir

has continued. The hatchability of fertilized carp eggs from White Oak Lake, where the gonads of a five-year-old carp may accumulate a dose of approximately 800 rads, was compared with the hatchability of eggs of fish from Fort Loudon Reservoir. Spawning fish from the natural populations inhabiting these study areas were collected and artifically spawned in the laboratory. The spawning season of carp is controlled by the water temperature and may vary from April to June in East Tennessee; thus spawning, which may last for only a few days, can occur at different times in the two study areas.

Five pairs of carp were collected from Fort Loudon Reservoir and at least 1200 eggs taken from each pair. The mean percent hatch for these five pairs of carp was 95.1%, which compared favorably with the 95.7% observed in 1966 for four pairs of carp taken from the same area.[11] The highest percent egg hatchability from White Oak Lake was 80.8; however, observations have been made only on three pairs of fish. These data indicate that the percent of egg hatchability was reduced by the exposure to chronic radiation received by the carp living in the radioactive contaminated environment of White Oak Lake. Additional observations are needed on White Oak Lake fish, and crosses between the two populations should be made to test for intermediate effects.

PERIPHYTON GROWTH AND RADIONUCLIDE ACCUMULATION

B. C. Patten E. C. Neal
C. E. DePoe

Periphyton colonization, biomass development, and radionuclide accumulation were studied by suspending 6-ft polyethylene tape vertically for as long as nine weeks in White Oak Lake. After two weeks biomass growth was nearly complete on the upper tape sections, but full development on the deeper sections took longer (Fig. 12.4). Maximum biomass occurred at 6- to 20-in. depths. Bacterial colonization and slime formation went unobserved. Blue-greens were the initial algal dominants, succeeded by diatoms and filamentous greens. Species succession continued beyond biomass equilibrium, with blue-greens tending to maintain importance in the deeper zones and greens developing best in the upper, lighted regions. Animals were minor constituents.

Radioisotope concentrations equilibrated rapidly in both the artificial substrates and the periphyton biomass. Ambient concentrations of ^{65}Zn in water and periphyton were below detection. The other isotopes contributed about equally (*ca.* 10 to 20 dis min^{-1} mg^{-1}) to biomass radioactivity. Biomass activity densities of ^{106}Ru and ^{137}Cs increased slightly with depth; this pattern was pronounced for ^{60}Co (Fig. 12.4). Factors considered to account for observed vertical distributions include: different radioisotope concentrations in surface and deep water; a hyperbolic rather than linear relationship between activity density and biomass; and, in the case of ^{60}Co, concentration by blue-green algae as an essential element, or by microbiota for use in cobalamin synthesis.

COMMUNITY STRUCTURE AND FUNCTION OF BENTHIC MACROINVERTEBRATES IN A CONSTANT TEMPERATURE SPRING

J. L. Wilhm

Populations of benthic macroinvertebrates have been studied extensively because they are important in aquatic food chains and in polluted bodies of water are useful as indicators of the degree and severity of organic pollution. The objectives of this research were to analyze community structure and to determine the function of the benthic macroinvertebrates in a spring pool.

The populations of organisms sampled inhabited a small spring pool having an area of 93 m^2. The maximum pool length was 15 m and maximum width was 10 m. Depth increased from several centimeters near the margin to 0.6 m in the middle. The bottom was covered with mud. Water entered the pool near the upper end and flowed into a spring brook, which was about 1 m wide and was choked with watercress (*Nasturtium officinale*). Average discharge was 0.0028 m^3/sec.

Bottom samples were taken at monthly intervals and included four samples from the watercress-choked littoral areas and three samples from the open-water area in the center of the spring pool. Organisms were separated from sediments and debris by washing them in sieves. Organisms were

[11] S. I. Auerbach *et al.*, *Health Phys. Div. Ann. Progr. Rept. July 31, 1966*, ORNL-4007, p. 48.

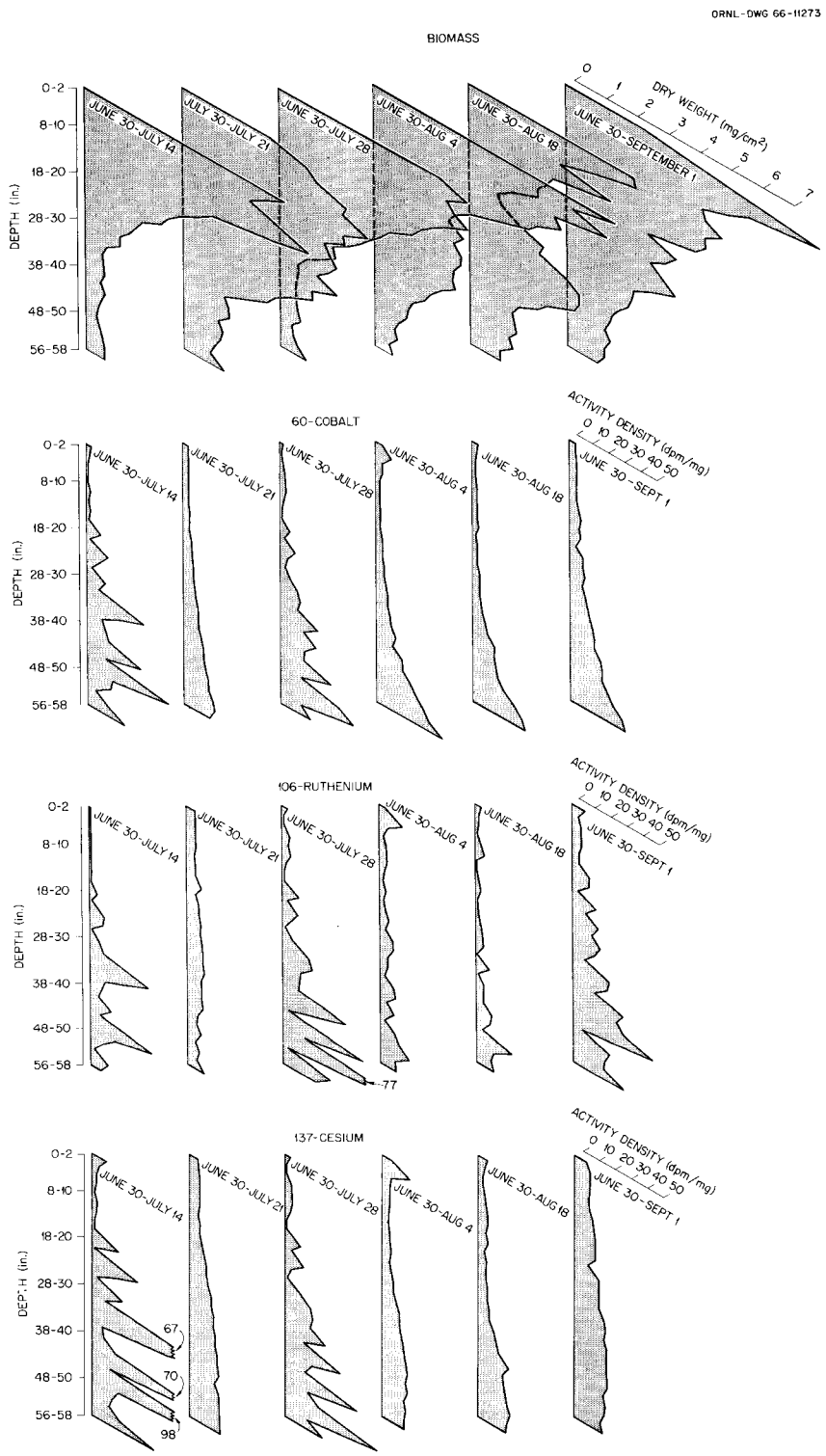

Fig. 12.4. Vertical Profiles of Biomass and Three Radionuclides in Periphyton Scraped from Polyethylene Substrates 2, 3, 4, 5, 7 and 9 weeks After Placement in White Oak Lake.

counted, and those not analyzed were returned to the spring. Gravimetric analyses were conducted monthly on abundant organisms and at least once during the study on the rarer invertebrates. Energy content of the principal organisms, vegetation, and detritus was determined in a bomb calorimeter, and rates of respiration were determined in a Warburg apparatus. Primary productivity and community respiration were determined in situ, with light and dark Plexiglas cylinders pushed into the sediment to seal the bottom and covered on top with a Plexiglas lid.

A greater variety of species was obtained in the vegetated area, but more individuals were taken in the open area. *Stictochironomus annulicius* and *Limnodrilus* sp. comprised 93% of the individuals and of the biomass in the open area and 78% of the individuals and 73% of the biomass in the vegetation. Other common species included *Procladius, Physa,* and *Lymnaea.* A comparison of diversity indices using data on either numbers of individuals or biomass units suggested that biomass units were more appropriate. The biomass units reflected seasonal changes in the average size of organisms. Diversity was greater in the vegetated portions of the spring pool than in the open area.

Watercress was important in influencing the structure and diversity of the benthic community but was unimportant as a direct energy source. The mean monthly standing crop of algae in the entire spring was 3500 kcal, while detritus averaged 15,900 kcal. Most of the detritus was derived from watercress. The average standing crop of benthic herbivores was 3800 kcal. The size of the benthic community was probably limited by space but not by food.

Detritus and algae from White Oak Lake were used to verify trophic relationships among the more abundant organisms. The food materials were naturally contaminated with ^{106}Ru, ^{60}Co, and ^{137}Cs. *Limnodrilus, Stictochironomus,* and *Physa* accumulated the radionuclides within several days, indicating that they were primary consumers. *Procladius*, a carnivore, had a delayed uptake until maximum activity was attained in about two weeks.

13. Watershed Aquatic Habitat Interactions

J. W. Curlin[1]
D. J. Nelson[1]
Tom Grizzard
E. L. Norman
F. G. Taylor, Jr.[1]
C. H. Abner[2]
R. H. Boyett[1]
E. E. C. Clebsch[3]
W. F. Johnson[2]
B. R. Fish[1]
T. Tamura[1]
W. M. Snyder[4]

LAND-WATER INTERACTIONS

The biotic productivity and water quality of tertiary streams are determined by the landscape from which the stream originates and through which it flows. From the time water enters an ecosystem as precipitation until it ultimately reaches the sea, it is continually accruing minerals and energy from the biogeochemical cycle. The biotic life of the aquatic system is closely coupled with the terrestrial system in juxtaposition.

Chemical solutes and particulate matter, in the surface water or in deep seepage water, represent an irreversible loss to the terrestrial-aquatic ecosystem, whereas dynamic processes of weathering, biological uptake, fixation, and decomposition tend to replenish the supply and to cycle the elements within the system. Water received as precipitation contains chemical elements and also acts as solvent and carrier for nutrients; thus rate and volume of precipitation are major factors in determining the chemical flux of terrestrial-aquatic ecosystems. The climatic and microclimatic regime is thus an integral part of the total system which establishes, to a great degree, the rate of biotic production, decomposition, net energy input, and nutrient loss.

Within the stream itself a similar intrasystem cycle operates. Dissolved nutrients and decomposition products from particulate organic matter carried into the stream are taken up directly by biota and thus enter the food chain of fishes, aquatic insects, and bottom-feeding organisms. Mineral fixation by periphyton, uptake of dissolved nutrients by phytoplankton, and precipitation as insoluble compounds act as resistors to chemical loss by the flow of surface water.

A watershed, therefore, defines a practical ecosystem – a system which reacts to the climate of the atmosphere above, depends upon the regolith below for nutrition, and is subject to irreversible loss through surface stream flow and deep seepage, but which resists such loss by constant recycling and biosynthesis.

By studying the watershed unit as a system, one can relate the productivity of a natural forested landscape to the productivity and nutrient balance of the stream. Chemical mass balance data collected from individual components of the system can be synthesized into a model for determining empirical input, transfer, and loss rates. Inferences from such a model can help explain the mechanisms involved in maintaining terrestrial-aquatic productivity. Bench-mark data of this type are virtually nonexistent – yet, they are the key to the natural maintenance of productivity and are a measure of the natural entropy of the ecosystem. Comparison of the stability of an undisturbed system with the dynamics of one altered by man's cultural practices and abuse is a gage of environmental degradation.

Degradation of landscapes is a major problem associated with increasing human activity. The effects of environmental pollution are particularly noticeable in both ground and surface water resources. Problems arising from land abuse or applications of noxious chemicals to the terrestrial system, in turn, result in reduced water quality and disturbance of stream biota. Maltreatment of the water resource at its source (the watershed),

[1]Dual capacity.
[2]ORNL engineering support.
[3]Consultant, University of Tennessee.
[4]Consultant, Georgia Institute of Technology.

further augmented by industrial and domestic pollution, is a major national problem today.

A program was initiated this year which unifies the terrestrial, aquatic, and environmental studies in an effort to gain further understanding of the intimate relationship between land and water. Four drainage basins, ranging in size from 200 to 1000 acres, which have potential for future watershed studies, have been reserved on the Oak Ridge Reservation. These occur on contrasting geology and varying antecedent land-use pattern. Such areas will provide ample opportunity for comparing the effects of land management, waste disposal, and other cultural treatments on water quality and productivity under a variety of ecological conditions.

WALKER BRANCH WATERSHED FACILITY

Description and Objectives

This year, preliminary work was begun on a project designed to obtain bench-mark data of water quality and stream productivity from a relatively undisturbed forested watershed (Fig. 13.1).

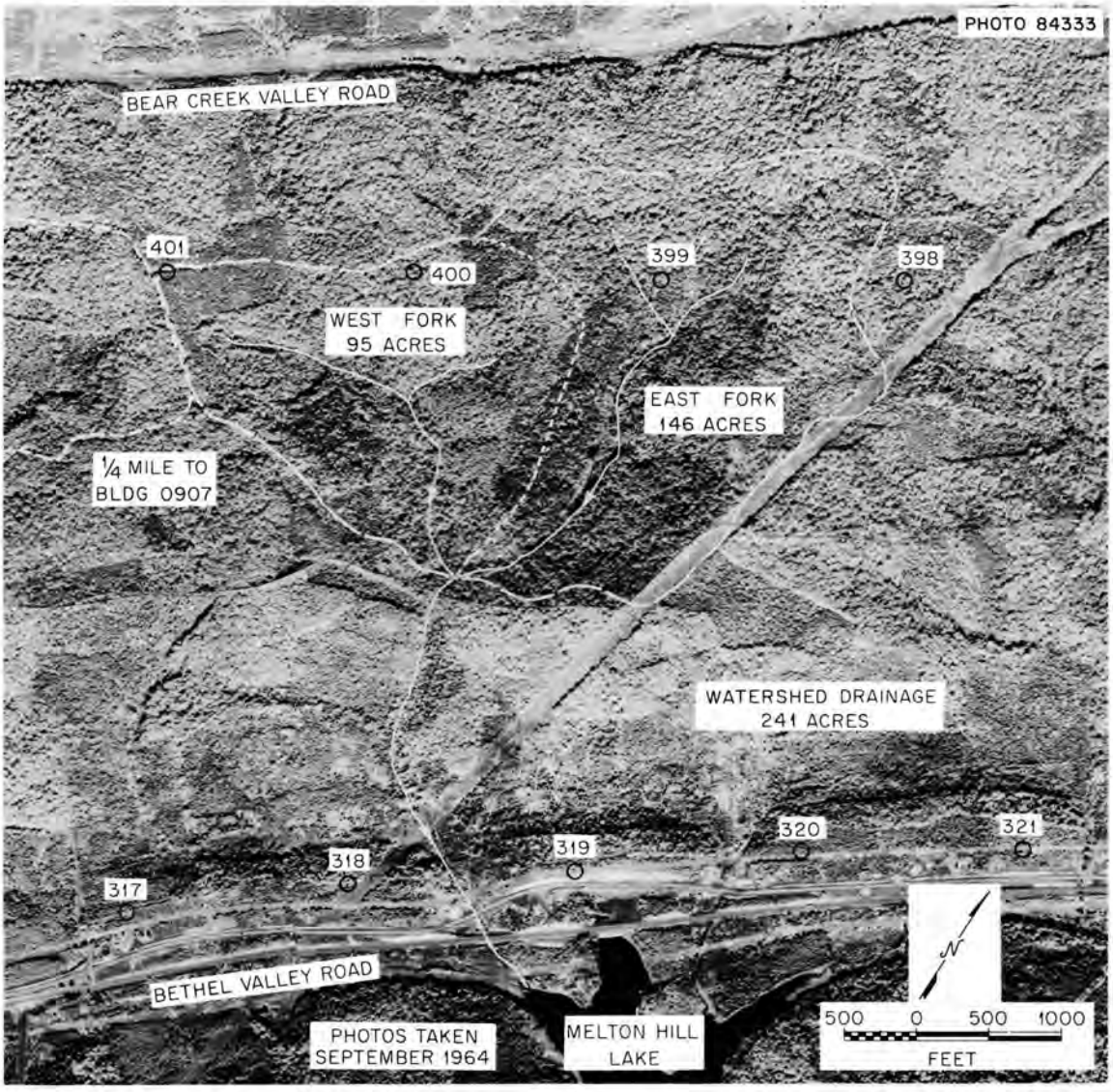

Fig. 13.1. Photo Map of Walker Branch Watershed.

The catchment basin covers a total area of 241 acres situated over limestone geology of the lower Ordovician age (Knox dolomite). This geological formation represents a major aquifer in the Ridge and Valley physiographic province of the Appalachian region.

Topography of the watershed is highly dissected by well-defined drainageways and water courses (Fig. 13.2). The drainage basin is divided into two subwatersheds separated by a sharp-crested ridge. Elevations range from 875 ft above mean datum at the confluence of the two forks to 1180 ft at the highest point on the northern crest. The area of the west fork subwatershed is 95 acres, and that of the east is 146 acres. For practical purposes the entire watershed is forested. The two streams emerge as springs in the upper reaches and are complemented by numerous small springs and intermittent seeps along the watercourse. Stable base flows during summer and fall dry seasons maintain a rich aquatic population.

Research objectives at Walker Branch are aimed at the construction of an empirical watershed model which will (1) relate the water quality and productivity of the stream to the productivity and chemical budget of the adjacent terrestrial ecosystem, (2) equate the net loss of chemical elements to the rate of mineral cycling, (3) establish the relationship between the hydrologic cycle and the mineral cycle, and (4) provide bench-mark information of natural terrestrial-aquatic ecosystems for comparison with those modified by man's cultural practices.

Stream Gages and Environmental Monitoring

Measurement of stream flow volume will be made at weirs on each fork just above the confluence of the streams. The weirs will have a 120° V-notch cross section capable of measuring rates up to 63 cfs (Fig. 13.3). Stage height to the nearest one-thousandth foot above the apex of the notch will be recorded at 5-min intervals on punched tape by an automatic data recorder.

Automatic water samplers at each weir will continuously siphon a sample proportional to flow. On sensing a critical rise in stream flow, the sampling units will commence a fast sampling mode which will fractionate the sample into 250-ml subsamples at intervals throughout the storm peak and into the recession curve. Analysis of water samples collected in this manner will provide information on chemical movement as a function of flow rate and volume.

Five precipitation gages located on triangular coordinates will automatically record incoming precipitation at 5-min intervals. Rainfall collectors, in association with these gages, will provide the basis for estimates of chemical input from precipitation and dry fallout.

Computer programs will summarize and reduce the large amount of data into integrated flow volumes, flow rates, and runoff components.

Vegetational Survey

A 264-ft square grid system has been superimposed over the watershed. Grid lines are surveyed on the ground and referenced to the ORNL geographical grid system. The surveyed lines are painted yellow, and the intersection of each line is assigned a north-south and east-west coordinate number. This grid system forms the basis for vegetational surveys, soil surveys, and positional reference of experimental facilities. The coordinate system is adaptable to computer processing, since the position of any two coordinates can be related in azimuth and distance.

Overstory vegetation was mapped in April 1967. Stratification was based on three vegetational characteristics – species composition (forest type), density, and average stand height (Fig. 13.4). This stratification will serve as the basis for additional vegetation analysis which will quantify floristic characteristics, aerial biomass, and chemical budget. An inventory system based on concentric plot sampling is being installed. The sampling intensity in each species-density-height stratum is proportional to its contribution to the total area on each subwatershed. Plots are located on random coordinates within strata. Random assignment was done with a computer program from a computer-generated vegetation type map (Fig. 13.5). Each tree on the sample plots will be tagged and recorded for permanent reference. Radial line transects radiating from plot center will estimate the understory shrub and herbaceous cover.

Individual tree and plot data will be used to generate population diameter frequencies by species within each stratum. These data will later be expanded to total biomass and chemical content. Periodic remeasurement of the same plots will provide an estimate of biomass production and expansion. The plots will also serve as sampling units for associated studies of litter fall, foliar leaching loss, and mortality.

ORNL-DWG 67-6873

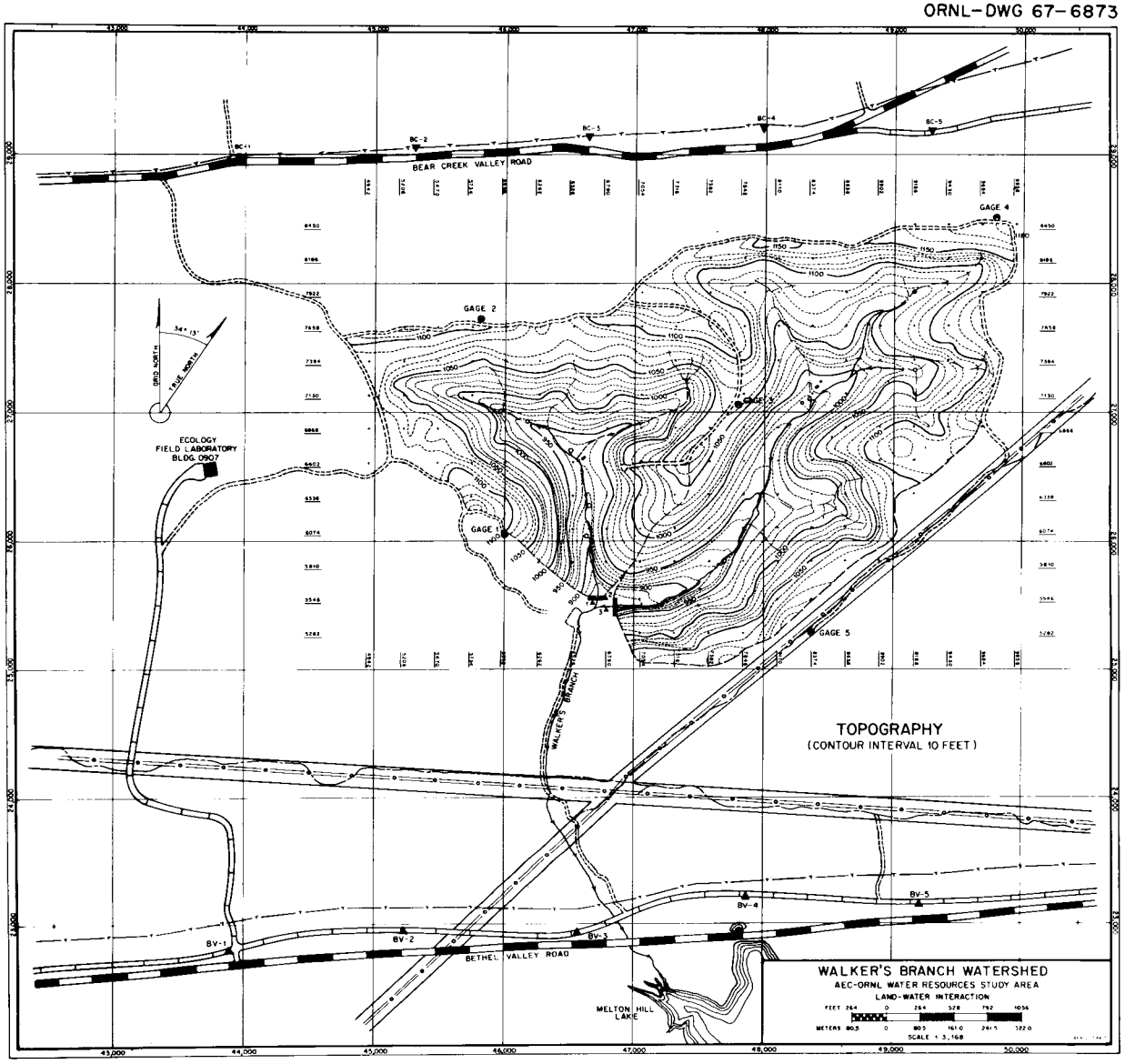

Fig. 13.2. Topography of Walker Branch Watershed.

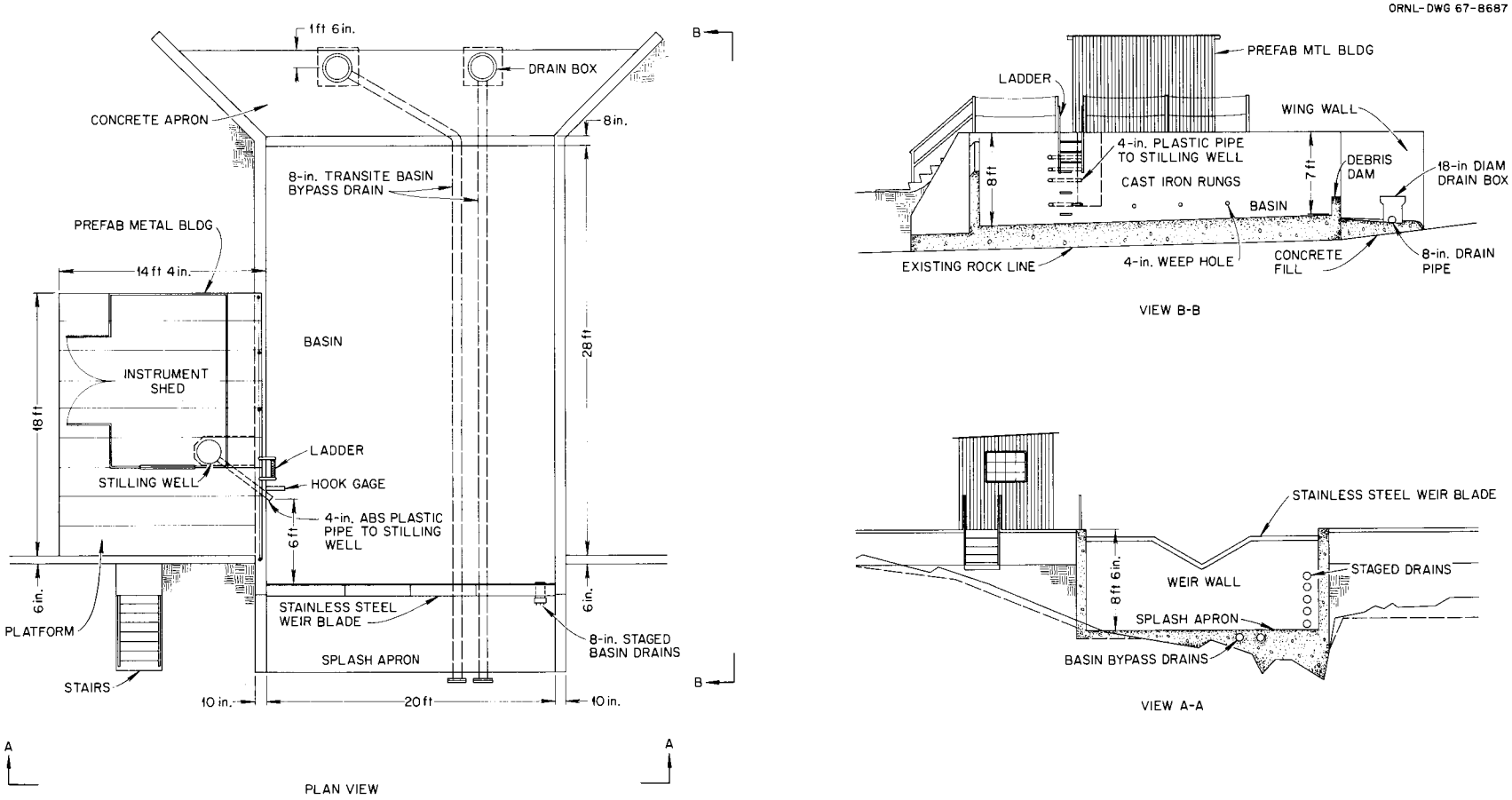

Fig. 13.3. Details of Weir Construction.

ORNL-DWG 67-8759

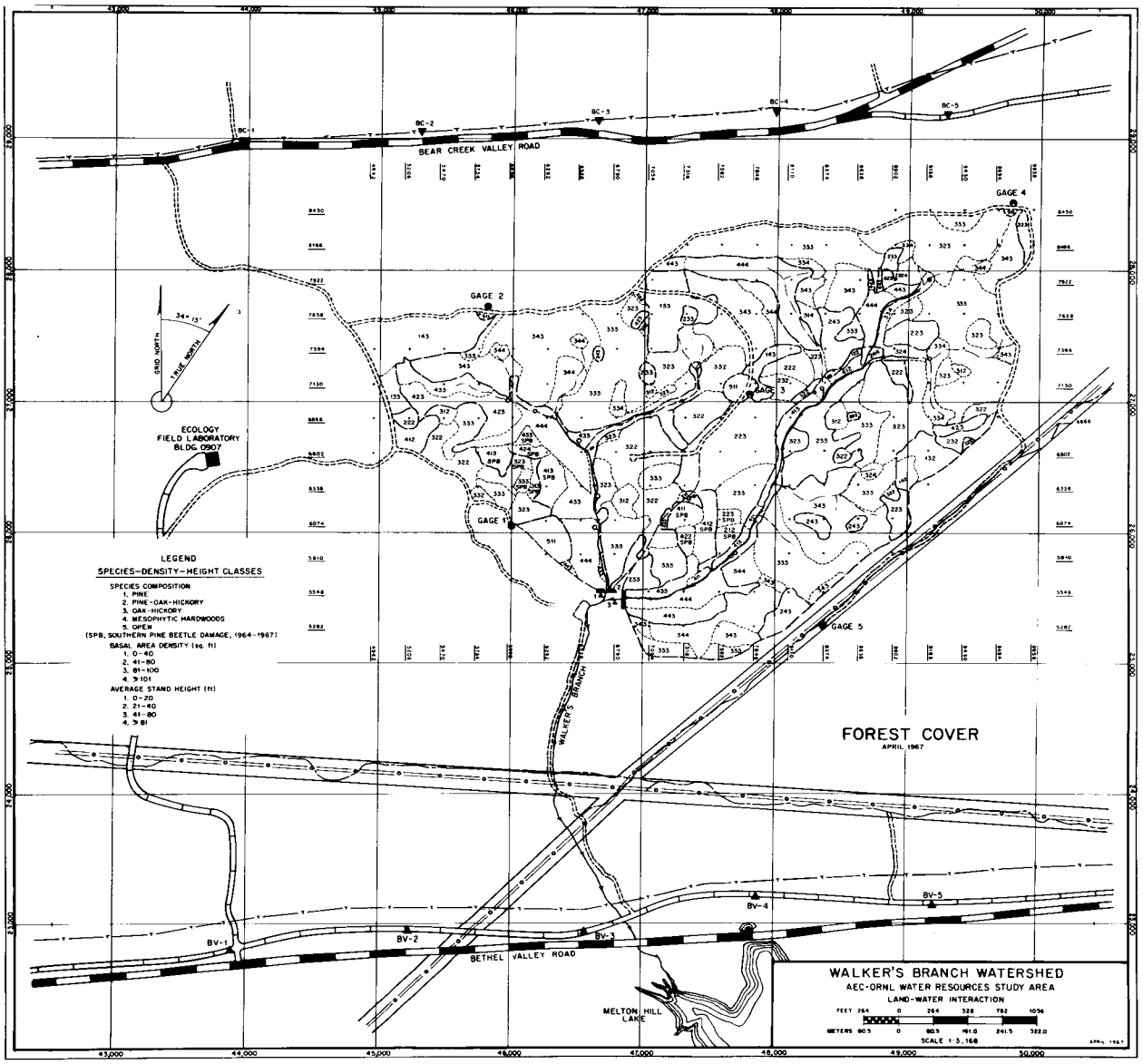

Fig. 13.4. Vegetational Map of Walker Branch Watershed.

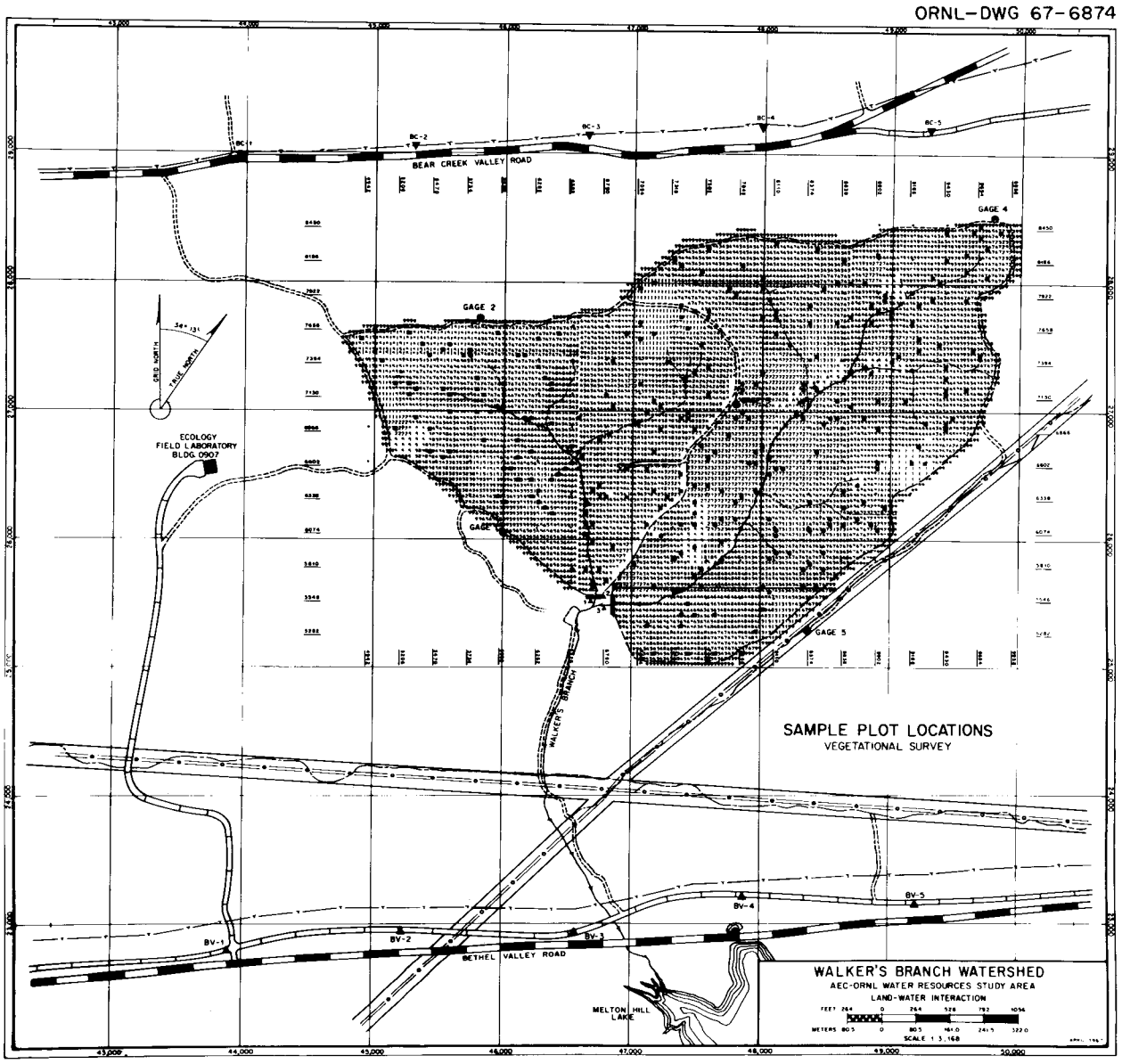

Fig. 13.5. Computer Map and Randomized Plot Locations for the Detailed Vegetational Survey.

CONCENTRATION AND TRANSPORT OF SUSPENDED AND DISSOLVED MATERIAL BY RIVER WATER

D. J. Nelson

Surface water streams receive a chronic influx of material from the watershed which alters water quality. The influent material (allochthonous) consists of dissolved and particulate fractions and includes organic and inorganic matter. Particulate allochthonous organic material was demonstrated as being important for the heterotrophic nutrition of stream-living organisms.[5] Data were obtained on both the dissolved organic and inorganic matter as well as on the particulate inorganic matter. These results were never summarized but are of considerable interest because of the significant interaction between the watershed and the river draining it.

[5]D. J. Nelson and D. C. Scott, *Limnol. Oceanog.* 7, 396–413 (1962).

Study Area and Methods

The Middle Oconee River is in the piedmont of Georgia; upstream from the sampling area it has a watershed area of 398 square miles (9.86×10^8 m^2). Of this 44% was woodland, 30% cropland, 22% pasture, and 4% other uses such as roads, house sites, and fallow. The Middle Oconee River is a typical muddy piedmont stream with a shifting sand bottom, except in restricted reaches where rock outcrops occur. Because of the nature of the stream, it was assumed that very little primary productivity occurred either from the flowing water or from periphyton growing on the bottom. Analyses of diel oxygen determinations showed that the river was in a negative oxygen balance, further confirming the lack of photosynthetic activity in the stream.

Water samples were obtained by holding the mouth of a gallon jug about 1 in. below the surface. Three 1-liter aliquots of this sample were passed through a Foerst continuous flow centrifuge ($4400 \times g$) at the rate of 1 liter each 7 min. The material retained in the centrifuge cup was termed particulate; however, it was recognized that distinction between dissolved and particulate matter was somewhat arbitrary. The supernatant liquid was evaporated to dryness. Both the particulate and dissolved fractions were dried at 103°C, weighed, ashed at 550°C, and reweighed to obtain dry weight, ash weight, and loss on ignition. Loss on ignition was considered organic material, and the ash weight was inorganic material.

Previous analyses of the particulate organic fraction showed a seasonal difference in its occurrence. During the period from May through September (summer samples), the levels of particulate organic in water were higher than during the October through April period (winter conditions). No seasonal differences were noted in the dissolved fractions.

The quantity of material transported downstream annually in the four fractions was estimated by multiplying the average discharge by the average concentration. For the particular organic matter the average discharge for summer conditions was 217 cfs and during winter was 365 cfs. Sixty-nine samples were collected in the summer period, and 44 were collected in the winter. The mean content of dissolved organic matter was multiplied by the average annual discharge (285 cfs). Total inorganic material transported downstream from the sampling point was obtained in a manner which paralleled that for the organic materials.

Total Material Transported

Summary data for the concentrations of the several fractions and their transport downstream from the sampling point are given in Table 13.1. While the concentrations of both particulate organic and inorganic materials were higher under summer conditions, the quantities of particulate material transported in the winter conditions were approximately equal. This was due to the higher river discharge during the winter. Under all circumstances the movement of inorganic matter, both dissolved and particulate, was greater than that of organic matter. About 83% of the dissolved and particulate material carried was of the inorganic fraction. However, about 29% of the dissolved fraction consisted of organic matter, while about 13% of the particulate fraction was organic.

These materials transported by the stream are loss from the watershed upstream. Since an insignificant proportion of the organic matter in the stream could be attributed to autochthonous primary productivity, this organic matter was considered to be of allochthonous origin. The quantity of organic matter estimated as being derived from the catchment basin may actually be an underestimate since mineralization of this material commences as soon as it enters the water. However, the organic matter, if considered to have been derived evenly from the entire watershed, represents a loss of about 0.57 g per square meter of watershed (Table 13.1). This is a small quantity of organic material as far as the land is concerned. Annual leaf fall in forested areas is in the range of 200 to 400 g m^{-2} $year^{-1}$.[6] This quantity of organic material in the river represents a significant input of a food source for heterotrophic aquatic organisms.

The materials in solution represent the rate of chemical denudation of the watershed. Inorganic

[6] J. D. Helvey, "Rainfall Interception by Hardwood Forest Litter in Southern Appalachians," U.S. Forest Serv., Res. Paper SE-8, 1964.

matter in streams in eastern United States amounts to a quantity equal to about 100 tons/mile^2 (35 g/m^2).[7] The denudation rate for the Middle Oconee River watershed (including particulate matter) was only 2.72 g/m^2, which reflects the softness of the waters draining the crystalline rocks in the piedmont.

[7] W. A. Durum, S. G. Heidel, and L. J. Tison, "World-wide Runoff of Dissolved Solids," Intern. Assoc. Sci. Hydrol.: Publ. 51, 618–28 (1960).

Table 13.1. Particulate and Dissolved Fractions of Organic and Inorganic Material in Middle Oconee River Water

Results are expressed as mg/liter and total material transported

Concentrations

	Number of Samples	Organic (mg/liter)	Inorganic (mg/liter)	Discharge (cfs)
Particulate material				
Summer	69	11.5	88.8	217
Winter	44	4.25	32.8	365
Dissolved material				
Annual	113	15.3	52.8	285

Transport

	Organic (g)	Inorganic (g)
	$\times 10^8$	$\times 10^8$
Particulate material		
Summer	0.933	7.20
Winter	0.803	6.20
Annual	1.736	13.4
Dissolved material		
Annual	3.89	13.4
Grand total	5.63	26.8

Rate of Transport (g per square meter of watershed)

Organic	Inorganic
0.571	2.72

14. Theoretical and Systems Ecology

J. S. Olson[1]
B. C. Patten[1]

THE SYSTEM IDENTIFICATION PROBLEM

B. C. Patten

Mathematical definition of a system precedes analysis of its performance characteristics such as stability, sensitivity, or optimality. In the past year this has become recognized as a bottleneck in the evaluation of ecological systems by systems analysis techniques. The problem belongs to a class variously referred to as system identification, black box, or inverse problems.

Typically in experiments a time series of noisy observations is obtained. From these data, representing a solution of system equations, the task is to (1) determine an appropriate set of equations from which a meaningful systems analysis can proceed and (2) estimate the parameters. A twofold approach is now being taken within limitations of available project support.

First, attention is being restricted to the set of linear autonomous equations

$$\frac{dx_i}{dt} = \sum_{j \neq i} a_{ij} x_i \,, \qquad i = 1, 2, \ldots, n \,,$$

representing an n-compartment ecosystem. With experimental data represented by $x_i(t)$ and the initial conditions by $x_i(0)$, values of the constant parameters a_{ij} which give the best square-integral fit to the sum of the integrated form of the system equations are sought. Programs have been written[2] to obtain a_{ij} by an iterative linear least-squares method, and also by a direct search method incorporating the constraints $a_{ij} \geqq 0$. The two have also been combined, using the linear method to provide initial estimates for the search program. Results have been mixed, possibly because experiments involve some of the parameters weakly, enabling equally good fits to be obtained by different parameter sets.

Second, to minimize problems from noisy data, experimental precision is being stressed in radionuclide cycling studies with laboratory microcosms. With careful attention to details of technique, low variability can be obtained with few replications in systems of limited complexity ($n \leqq 10$). A typical example of precision now obtainable is shown in Fig. 14.1, depicting ^{85}Sr and ^{137}Cs uptake by a water fern (three replications).

RADIANT ENERGY BUDGET OF DECIDUOUS FOREST

J. S. Olson

For the years 1957–65, solar radiation records from the ESSA Atmospheric Turbulence and Diffusion Laboratory in Oak Ridge (Fig. 14.2) indicate that May averaged slightly higher mean daily solar radiation than June: 537 vs 533 langleys. Daily means averaged for a whole month varied considerably: from 479 to 587 langleys/day for June (1963 and 1958 respectively) and from 140 to 198 for December (1964 and 1958). Variations in spring and autumn cloudiness also contribute wide variations in the pattern of monthly totals. Totals near 16,000 langleys (160,000 kcal/m^2) for the highest month thus seem typical of wide areas of the eastern deciduous forest, yet the

[1]Dual capacity.

[2]A. S. Householder *et al.*, *Math. Div. Ann. Progr. Rept. Apr. 30, 1967*, ORNL-4083, pp. 15–16.

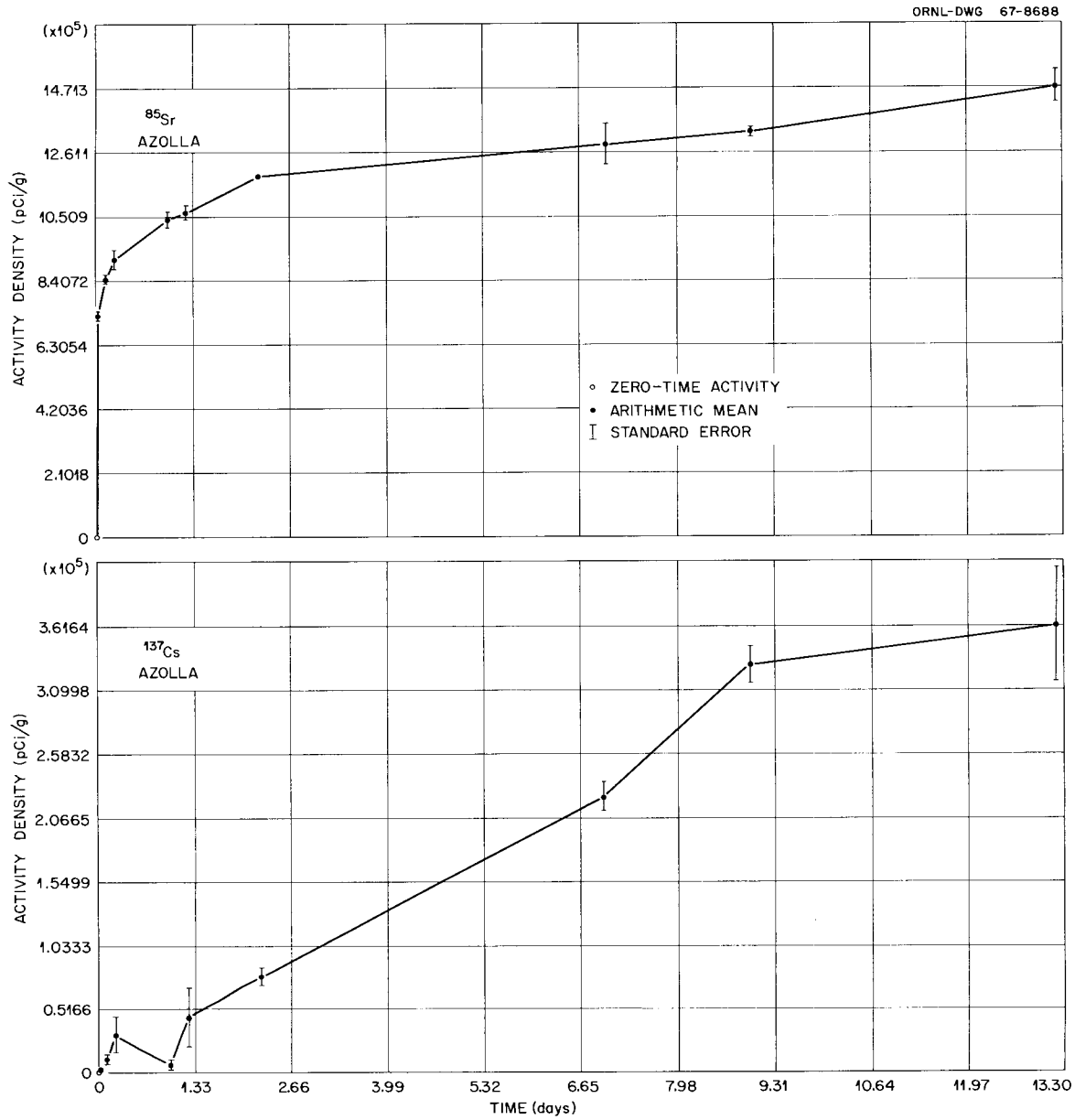

Fig. 14.1. Uptake of ^{85}Sr and ^{137}Cs by *Azolla caroliniana*; Means and Standard Errors Based on Three Replications.

considerable variations among months in different years indicate the need for localized radiometer data if broad averages are not sufficient for meteorological or productivity studies.

Outside a Branford, Connecticut, forest dominated by black oak, total downward hemispheric radiation on a clear July day, between 1052 and 1328 hours, averaged 1.92 langleys/min. This flux included 1.14 langleys/min as direct radiometer reading, which slightly underestimates 0.3-μ solar radiation. The additional 0.78 langley/min is the correction for thermal (black-body) radiation (3 to 30 μ). Under the black oak forest canopy, thermal radiation correction was 0.70 langley/min. Short-wave radiation was approximately 0.21, and net downward radiation flux onto the blueberry-sedge ground cover (*Vaccinium vacillans* Torr. and *Carex pensylvanica* L.) was 0.14 langley/min (Fig. 14.3).

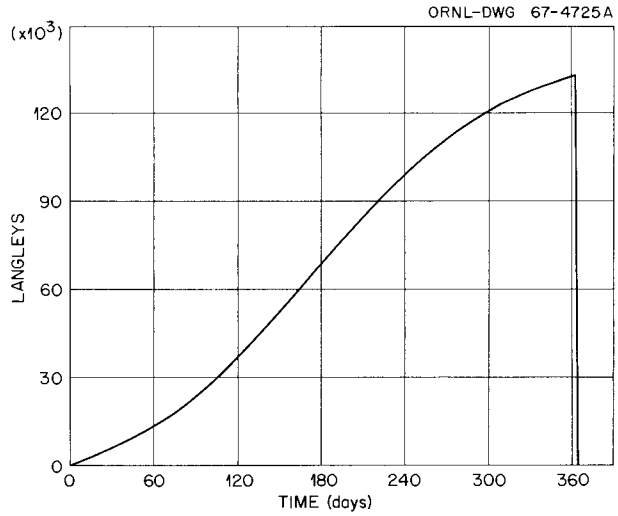

Fig. 14.2. Average Cumulative Curve of Solar Radiation at Oak Ridge, Tennessee, for 1957 to 1965 with Tentative Adjustments for Change in Eppley Pyroheliometer Calibration During this Period.

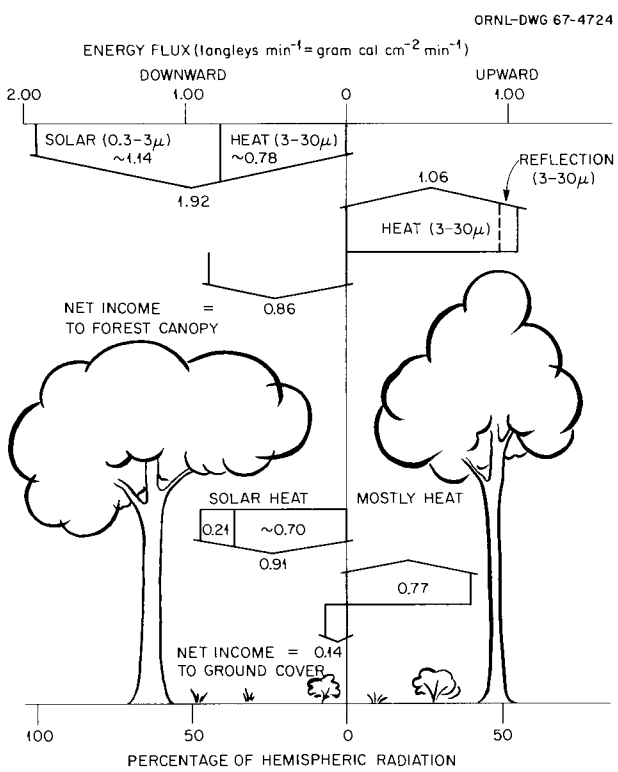

Fig. 14.3. Budget of Solar and Thermal Radiation for a Black Oak Forest (*Quercus velutina*) on a Hot July Day.

INITIAL MODEL FOR ENERGY FLOW IN *LIRIODENDRON* FOREST

J. S. Olson

The foregoing data on radiant energy input and preliminary data on productivity[3,4] and energetics[5] of *Liriodendron* forests are combined in a model which is intended to guide continuing field research. Details may change in the light of new data and efforts to remove simplifying assumptions. Principles governing this model are explained in earlier reports and are formalized here in equations representing parts of a general matrix multiplication model.[6]

Whittaker[4] estimated higher aboveground annual production (2408 g m^{-2} $year^{-1}$ = 2400 for trees and shrubs) for *Liriodendron* than for 24 other forest and heath stands in the Great Smoky Mountains–Oak Ridge area. He estimated almost 2000 g m^{-2} $year^{-1}$ as stem production and 410 g m^{-2} $year^{-1}$ as foliage production (tree plus shrub). Our Oak Ridge litter production included 339 g m^{-2} $year^{-1}$ of nonwoody parts in a favorable year.[5] Clebsch's preliminary caloric values for stems (averaging 4.59 kcal/g, personal communication) times stem production mass gives about 9000 kcal m^{-2} $year^{-1}$. His and our late spring caloric values for leaves (about 4.75 kcal/g, which is higher than our summer values) would indicate 1950 kcal/m^2 as a maximum estimate for nonwoody canopy.

A more conservative and perhaps typical assumption for production-model exploration for this paper was 1600 and 8000 kcal m^{-2} $year^{-1}$ for leaves and stems, respectively, with 1600 (annual tentatively) for roots. These correspond to 0.12, 0.6, and 0.12% of the annual (all wavelength) solar energy input to leaves, stems, and roots respectively. In Table 14.1, these values are 0.0012, p_{13} = 0.006, and p_{14} = 0.0012 as fractions of the "input" compartment (No. 1) converted to these plant compartments.

The values of p_{jk} just given determine the first row of the matrix in Table 14.1, except for p_{11}. The latter is left as 1.0 in order to fit

[3] R. H. Whittaker, N. Cohen, and J. S. Olson, *Ecology* **44**(4), 806–10 (1963).

[4] R. H. Whittaker, *Ecology* **47**, 103–21 (1966).

[5] S. I. Auerbach *et al.*, *Health Phys. Div. Ann. Progr. Rept. July 31, 1966*, ORNL-4007, pp. 57–60.

[6] *Ibid.*, pp. 104–5.

the assumption of the artificial compartment 1 as an "input," which is constant from time step $t-1$ to time t. The general equation following as part of (3) and this particularly simple case are:

$$v_1^{(t)} = \{v_1 p_{11} + v_2 p_{21} + \ldots + v_j p_{j1} + p_n p_{n1}\}^{(t-1)}$$
$$= 1{,}330{,}000 \times 1 + 0 + \ldots + 0 + 0 \ . \qquad (1)$$

Foliage (compartment 2) has an input from the sun, $v_1 p_{12}$. In an ideal deciduous forest, carryover from one year to the next $p_{22} = 0$. There may be input from stored foods in stem or root, but no attempt is made to model these here. Hence the general and specific equations for leaves are:

$$v_2^{(t)} = \{v_1 p_{12} + v_2 p_{22} + \ldots + v_j p_{j2} + \ldots + v_n p_{n2}\}^{(t-1)}$$
$$= 1{,}330{,}000 \times 0.0012 + \ldots + 0 + 0 \qquad (2)$$
$$\cong 1600 \text{ for all time from one year onward} \ .$$

Table 14.1. Matrix of Probable Average Rates of Transfer of Energy for a Model *Liriodendron* Forest[a]

	1	2	3	4	5	6
1	1.0	0.0012	0.006	0.0012	0	0
2	0	0	0	0	0.9	0.1
3	0	0	0.95	0	0.05	0
4	0	0	0	0.94	0	0
5	0	0	0	0	0.5	0
6	0	0	0	0	0	0

[a]Except for p_{11}, which is arbitrarily set at 1 to provide for constant energy input, the diagonal elements of this matrix are "carryover fractions" or probable fractions of retention of material from one year to another in the remaining compartments. Nondiagonal terms p_{jk} are assumed transfers from source (rows) to destination (columns).

In the case assumed in Table 14.1 and Fig. 14.4 with turnover $= f_{33} = -0.05$, carryover $= p_{33} = 0.95$ and $t_{0.5} = 14$ years. General and specific equations for stem growth are:

$$v_3^{(t)} = \{v_1 p_{13} + v_2 p_{23} + v_3 p_{33} + \ldots + v_n p_{n3}\}^{(t-1)}$$
$$= 1{,}330{,}000 \times 0.006 + 0 + v_3(0.95) + 0 \ . \qquad (3)$$

Fractional loss rates of roots are presumably higher than for stems, because they include similar losses from death of whole trees and perhaps a relatively high turnover of small roots:

$$v_4^{(t)} = \{v_1 p_{14} + \ldots + v_4 p_{44} + \ldots + v_n p_{n4}\}^{(t-1)}$$
$$= 1{,}330{,}000 p_{14} + 0 + v_4(0.94) \ . \qquad (4)$$

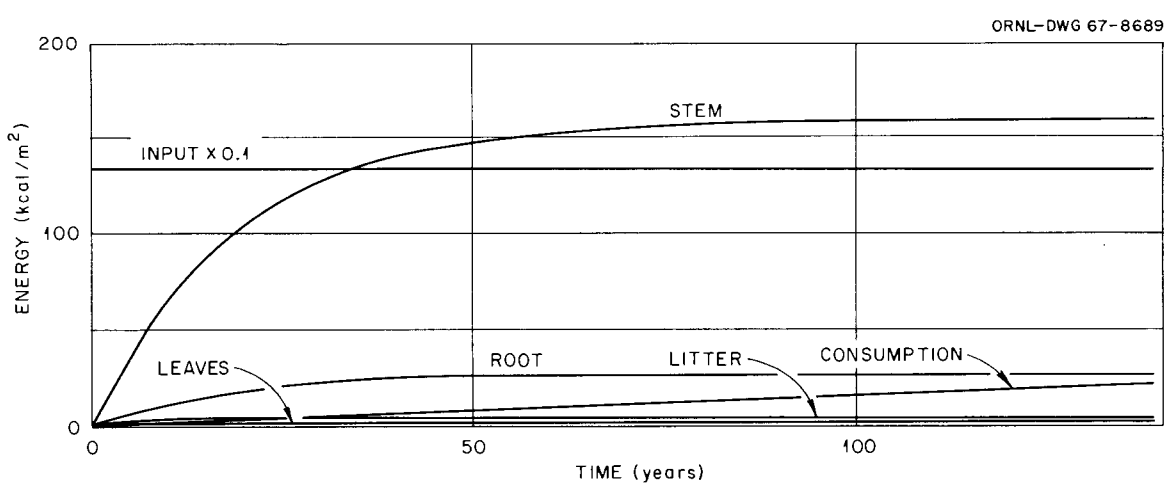

Fig. 14.4. Simulation of Buildup of Organic Matter in Major Components of a Model Forest, Suggested by Preliminary Data on Tulip Poplar (*Liriodendron tulipifera*) Productivity in Eastern Tennessee.

VERTICAL PERIPHYTON GROWTH

B. C. Patten

Figure 12.4 indicates that autotrophic growth of periphyton in the euphotic zone was faster than heterotrophic development in deeper layers of White Oak Lake. However, continuation of heterotrophic growth ultimately could produce a uniform vertical distribution of periphyton biomass instead of the distributions shown. This hypothesis was evaluated through the logic of a simple model.

At any depth, growth of biomass, $B(z,t)$, is a balance of income and loss processes:

$$\frac{\partial B}{\partial t} = [f_1 \text{ (colonization)} + f_2 \text{ (photosynthesis)} + f_3 \text{ (animal invasion)}] - [f_4 \text{ (respiration)} + f_5 \text{ (secretion, excretion)} + f_6 \text{ (sloughing)} + f_7 \text{ (grazing)}] \,. \quad (1)$$

In general, the loss processes, $f_4, \ldots, f_7$, are dependent on the amount of biomass present, B. Thus, $f_i = \phi_i B$, where ϕ_i is the transfer function of the ith loss process. Biomass equilibrates at any depth when $\partial B/\partial t = 0$, that is,

$$\sum_{i=1}^{3} f_i = \sum_{i=4}^{7} f_i = B \sum_{i=4}^{7} \phi_i \,,$$

so that equilibrium biomass is

$$B_{(\mathrm{eq})} = \frac{\sum_{i=1}^{3} f_i}{\sum_{i=4}^{7} \phi_i} \,. \quad (2)$$

The equilibrium periphyton mass at each depth is the ratio of input fluxes (dimensions $ML^{-2}T^{-1}$) to rates of loss (dimensions $L^{-2}T^{-1}$).

The improbability of this ratio being equal at every depth is generally obvious, but a specific example is helpful. Compare in Fig. 12.4 the 8- to 10-in. interval with the 48- to 50-in. interval. Decreased photosynthesis f_2 at the deeper level would have to be compensated by decreased *rates* (not fluxes) of one or more of the loss processes. Changes of sufficient magnitude to offset the dimensional difference between a rate and a flux are highly unlikely, and it is concluded that in general uniform vertical biomass distributions are not the expected steady state of periphyton communities.

RATES OF GEOCHEMICAL DENUDATION OF THE CONTINENTS

J. S. Olson

A literature review has shown differences (Table 14.2) among geochemists' estimates of abundance of 65 major and minor elements in crystalline and sedimentary rock types, and more especially in their inferences from these data concerning the cumulative denudation of the continents over geologic time. For example, computer-derived geochemical balances of Horn and Adams[7] lead to estimates of 2×10^{18} metric tons of igneous rocks weathered on the continents – more than twice the estimates of several earlier geochemists. Even this new estimate is admittedly biased on the low side because of metamorphic and metasomatic recycling of sediments in the rock cycle; Barth[8] deduces weathering rates many times this

[7] M. K. Horn and J. A. S. Adams, *Geochim. Cosmochim. Acta* **30**, 279–97 (1966).

[8] T. F. W. Barth, *Geochim. Cosmochim. Acta* **23**, 1–8 (1961).

Table 14.2. Different Estimates of Cumulative Erosion over Geologic Times

Author	Geochemical Data	Tons in Geologic Time
		$\times 10^{18}$
Goldschmidt	Na, Ca, Mg	0.82
Conway	Na, Si	0.74
Wickman	Al, Fe, Na, K, Si, Ca, Mg	0.99
Goldberg and Arrhenius	Na, K, Ca, Mn	0.94
Barth (1961)	Ca, Na, Mg	41
Horn and Adams (1966)	55 elements	2
Plausible minimum	(half the sediments recrystallized)	4
Plausible maximum	(half the crystallines sedimentary)	8
Plausible compromise		6

high from a steady-state model of Na, K, and Ca in the ocean.

On geologic grounds it may be excessive to assume that more than half the earth's crust (8×10^{18} tons) has passed through the sedimentary cycle, but a volume at least twice that presently recognized as sediments may have done so (over 4×10^{18} tons). The compromise estimate is 6×10^{18} tons of denuded rock, which is almost an order of magnitude higher than the estimates of early geochemists that were based on a model that neglected recycling from the oceans to the sediments and crystalline rock compartments of the earth.

With Barth's assumed duration of 3,000,000,000 years for erosional history of the earth, this implies 2,000,000,000 metric tons per "average year." This geochemical estimate was made before discovering Alekin and Brazhnikova's[9] present hydrological estimate of 2,310,000,000 metric tons to undrained interior seas of the continent. The matching in order of magnitude seems remarkably close, in view of several (partially canceling) tendencies which might have led us to expect present erosion rates markedly higher or markedly lower than the average over geologic time.

---

[9]O. A. Alekin and L. V. Brazhinkova, "Chemistry of the Earth's Crust," ed. by A. P. Vinogradov, transl. by N. Kaner and R. Amoils from *Proc. Geochem. Conf. Commemorating Centenary of Academician V. I. Vernadskii's Birth*, vol. 1, pp. 291–303, Israel Program for Scientific Translations (1966).

15. Forest Management

W. C. Cate E. L. Norman[2]
W. M. Ciesla[1] E. H. Rosenbalm
J. W. Curlin[2]

FOREST MANAGEMENT

J. W. Curlin W. C. Cate
E. H. Rosenbalm

Southern pine beetle control (*Dendroctonus frontalis*) again dominated the land management operations this year. Success of the control program during the past two years is manifest in the results of a recent survey by the U.S. Forest Service. Infestation levels of the destructive insect have decreased from 21.7 ± 6.4 infested spots per thousand acres in September 1966 to 13.1 ± 2.2 in January 1967. Threat of the epidemic continued to diminish in the spring of 1967.

Since inception of the forest management program in 1964, 645,000 board feet of sawtimber and 11,000 cords of pine pulpwood have been sold to local industries on competitive bid. Timber harvesting is conducted in a manner compatible with the ecology research program.

AEC has pledged participation with TVA in an effort to establish a forest-based industry in the Oak Ridge area. The plan calls for cooperative marketing of 8,600,000 board feet of timber annually from five federal, state, municipal, and private landowners. Pooled stumpage of this magnitude would assure an adequate resource base for establishment of a sizable permanent wood-using industry in the area which will provide jobs, stable markets, and improved prices for timber products.

[1]U.S. Forest Service.

[2]Dual capacity.

USE OF LINEAR PROGRAMMING IN FOREST REGULATION

E. L. Norman J. W. Curlin

In cooperation with the University of Georgia, School of Forestry, work has begun on the development of a computerized system of optimum cut allocation using linear programming techniques. The primary objective of forest management at ORNL is to maximize present net worth of the forest resource in connection with the primary research and production mission. To accomplish this, decisions on where, when, and how much to cut must be made. Such decisions are presently based on subjective data or judgment and often do not represent the optimum solutions of the problem. Few attempts have been made to apply the techniques of linear programming for forest regulation – none have dealt with all-aged multispecies stand of upland hardwood.

The linear programming regulation technique attempts to maximize a linear objective function Q, of a number of variables (V_{ik}), which are combinations of stand volumes by tree condition classes obtained from diagnostic stand surveys. Certain management constraints are placed on the V_{ik}'s, in the objective function. In matrix notation this problem can be stated as follows:

$$A\mathbf{v} = \mathbf{b}, \tag{1}$$

where

- $\mathbf{v}$ is a column vector of the V_{ik}'s,
- A is the matrix of constraint coefficients on the on the V_{ik}'s,
- $\mathbf{b}$ is the column vector of quantified levels of the various constraints.

Equation (1) is solved for **v** in a manner which maximizes Eq. (2):

$$Q(\text{maximum}) = \sum_{i=1}^{m} \sum_{k=1}^{n} \text{PNW}_{ik} , \qquad (2)$$

where PNW_{ik} is the present net worth of stand i under management alternative k.

Constraints imposed on Q are: (1) minimum acceptable stumpage value, (2) total maximum cut, (3) minimum income required, and (4) minimum permissible volume for economical operations within stands.

A unique feature of this approach is that the cutting intensity and silvicultural treatment are allocated and scheduled by the computer from field data compiled by the forester. The forest manager has complete control of the decision through use of constraint coefficients and, therefore, may impose the use of certain silvicultural systems for biologic rather than economic reasons. The computer, in turn, guides the manager in making proper economic decisions, which are often more obscure than the biological principles.

Part III. Radiation Physics

G. S. Hurst

16. Theoretical Radiation Physics

Jacob Neufeld R. H. Ritchie

V. E. Anderson[1]
J. C. Ashley
Julian Crowell[2]
Mary Feezell[1]
Kenneth Fox[2]
W. R. Garrett
R. N. Hamm
Larry Johnson[3]
J. W. McKeever[3]
H. C. Schweinler
W. S. Snyder
J. E. Turner
R. E. Wilems[3]
H. A. Wright

DOUBLE PLASMON EXCITATION BY CHARGED PARTICLES

A calculation of the mean free path for the second-order process in which an incident charged particle excites two plasmons in an electron plasma has been reported earlier.[4] This problem is being reconsidered in a different theoretical framework which allows for damping of the intermediate state due to competing processes such as electron-hole excitation. The transition rate from the initial state $|0\rangle$ to final state $|F\rangle$ through intermediate states $|I\rangle$ for terms "on the energy shell" is given by

$$W_{F0} = \frac{2\pi}{\hbar} |H_{FI} H_{I0}|^2 \frac{\pi}{2\gamma} \delta(\hbar\omega_{I0}) \delta(\hbar\omega_{F0}) ,$$

where H_{AB} is the A,B matrix element of the interaction Hamiltonian H, $\hbar\omega_{AB}$ is the energy difference between states A and B, and γ gives the damping of the intermediate state. The inverse mean free path for the double-plasmon excitation process is obtained by summing the transition rate over final states and dividing by $v_0 = \hbar p_0/m$, where v_0 is the velocity of the charged particle of wave vector $\mathbf{p}_0$. The result is

$$\frac{1}{\gamma_{2p}} = \left(\frac{\omega_p e^2}{\hbar}\right)^2 \frac{1}{2\gamma} \frac{1}{v_0^2 \sqrt{v_0^2 - (2\hbar\omega p/m)}} \cdot \ln\left[\frac{(\sqrt{p_0^2 - \alpha} + \sqrt{p_0^2 - 2\alpha};\ k_c)}{\sqrt{p_0^2 - \alpha} - \sqrt{p_0^2 - 2\alpha}}\right] \cdot \ln\left[\frac{(p_0 + \sqrt{p_0^2 - \alpha};\ k_c)}{p_0 - \sqrt{p_0^2 - \alpha}}\right]$$

for an incident particle of mass m and charge e. Also, $\hbar\omega_p$ is the plasmon energy, $\alpha \equiv 2m\,\omega_p/\hbar$, and k_c is the cutoff wave vector for plasma oscillations. The notation $(x;\ y)$ indicates that the smaller of x and y is taken. When values of γ are calculated, then λ_{2p} will be completely determined.

CALCULATION OF THE MINIMUM DIPOLE MOMENT REQUIRED TO BIND AN ELECTRON TO A FINITE ELECTRIC DIPOLE

The existence of a minimum dipole moment required to bind an electron to a finite permanent electric dipole has been established rigorously, and its value has been calculated to be $D_{min} = 1.625 \times 10^{-18}$ esu-cm.[5] This confirms earlier

[1] On loan from Central Data Processing Facility (ORGDP).

[2] Consultant.

[3] Oak Ridge Graduate Fellow.

[4] Jacob Neufeld *et al.*, *Health Phys. Div. Ann. Progr. Rept. July 31, 1966*, ORNL-4007, p. 129.

[5] J. E. Turner and K. Fox, *Phys. Letters* **23**, 547 (1966).

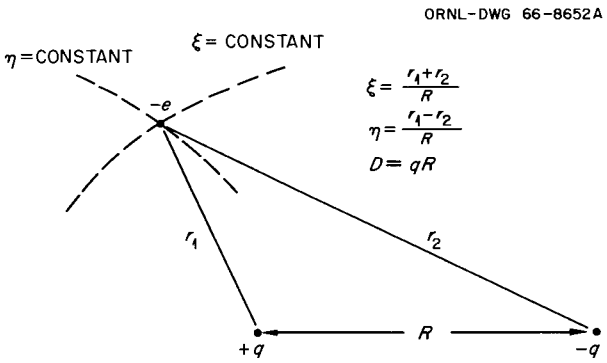

Fig. 16.1. Electron-Dipole System.

indications of the existence of a nonzero value of D_{min}.[6,7] The exact value differs by less than 2% from an approximate value obtained by using a simple variational function.[6,8] Several independent calculations, with a variety of techniques, have corroborated the numerical value of D_{min}.[9–14]

The method[5] of calculating D_{min} is now described. The dipole is represented by charges $\pm q$ separated by a distance R, the dipole moment being $D = qR$. The Schrödinger wave equation for the motion of the electron of charge $-e$ and mass m in the dipole field is separable in elliptic coordinates defined by $\xi = (r_1 + r_2)/R$ and $\eta = (r_1 - r_2)/R$, where r_1 and r_2 are the distances of the electron from the charges $+q$ and $-q$. (The azimuthal angle ϕ about the line connecting the charges $\pm q$ is a cyclic variable.) The geometry is indicated in Fig. 16.1.

The Schrödinger equation for the energy eigenfunctions Ψ and eigenvalues E is $H\Psi = (T + V)\Psi = E\Psi$ with

$$T = \frac{-2\hbar^2}{mR^2(\xi^2 - \eta^2)}\left\{\frac{\partial}{\partial\xi}\left[(\xi^2 - \xi)\frac{\partial}{\partial\xi}\right] + \frac{\partial}{\partial\eta}\left[(1 - \eta^2)\frac{\partial}{\partial\eta}\right]\right\},$$

$$V = \frac{4De\eta}{R^2(\xi^2 - \eta^2)}.$$

The wave function is represented in the form

$$\Psi(\xi,\eta) = \sum_{p,q=0}^{\infty} C_{pq}\phi_{pq},$$

where $\phi_{pq} = \exp(-\frac{1}{2}\alpha\xi^t)\xi^p\eta^q$. In the variational calculation to follow, α, t, and the C_{pq} are adjustable constants.

The energy and normalization matrices are

$$H_{pq,ij} \equiv \int \phi_{pq} H \phi_{ij}\, d\tau = \frac{1}{2}\pi R a_0^2 Ry(t_{pq,ij} + Dv_{pq,ij}),$$

$$N_{pq,ij} \equiv \int \phi_{pq}\phi_{ij} d\tau = \frac{1}{2}\pi R^3 n_{pq,ij}.$$

Here $d\tau = \frac{1}{4}\pi R^3(\xi^2 - \eta^2)\, d\xi\, d\eta$; $Ry \equiv e^2/2a_0$ is the Rydberg energy; $a_0 = \hbar^2/me^2$.

$$t_{pq,ij} = \left\{\frac{2e^{-\alpha} + [-(p-i)^2 + 1 + t(p+i+1)]\, I_{p+i} + [(p-i)^2 - 1 - t(p+i-1)]\, I_{p+i-2}}{q+j+1} + \frac{8qj\, I_{p+i}}{(q+j)^2 - 1}\right\}\frac{1 + (-1)^{q+j}}{2},$$

$$v_{pq,ij} = \left\{\frac{8I_{q+i}}{q+j+2}\right\}\frac{1 - (-1)^{q+j}}{2},$$

$$n_{pq,ij} = \left\{\frac{I_{p+i+2}}{q+j+1} - \frac{I_{p+i}}{q+j+3}\right\}\frac{1 + (-1)^{q+j}}{2}.$$

[6] J. E. Turner and K. Fox, *On the Bound States of an Electron in the Field of a Permanent Electric Dipole*, ORNL-3895 (1965).

[7] K. Fox and J. E. Turner, *Am. J. Phys.* **34**, 606 (1966).

[8] K. Fox and J. E. Turner, *J. Chem. Phys.* **45**, 1142 (1966).

[9] M. H. Mittleman and V. P. Myerscough, *Phys. Letters* **23**, 545 (1966).

[10] J-M. Lévy-Leblond, *Phys. Rev.* **153**, 1 (1967).

[11] W. B. Brown and R. E. Roberts, *J. Chem. Phys.* **46**, 2006 (1967).

[12] O. H. Crawford and A. Dalgarno, *Chem. Phys. Letters* **1**, 23 (1967).

[13] C. A. Coulson and M. Walmsley, *Proc. Phys. Soc.* **91**, 31 (1967).

[14] O. H. Crawford, *Proc. Phys. Soc.* (to be published).

Table 16.1. Smallest Dipole Moment D Needed to Obtain Zero Ground-State Binding Energy with Trial Function Having K Terms

$$\psi(\xi,\eta) = e^{-\alpha\xi^t/2} \sum_{p,q=0}^{\infty} C_{pq}\, \xi^p \eta^q$$

Rank K	$D(ea_0)$
2	0.649520
3	0.639370
4	0.639316
5	0.639316
.	.
.	.
.	.
20	0.639312
30	0.639309
40	0.639307
70	$D_{min} = 0.639307$

The dipole moment D is now expressed in units of ea_0. The quantities I_r are defined by

$$I_r \equiv \int_1^{\infty} \xi^r \exp(-\alpha\xi^t)\, d\xi .$$

In principle, when a given number K of terms ϕ_{pq} is used in the trial function Ψ, the determinantal equation $|H - \lambda N| = 0$ could be solved for the lowest value of λ obtainable by adjusting α and t. One would then obtain, by virtue of the variational theorem, an upper bound to the binding energy for a given value D of dipole moment. The actual calculation employed an equivalent but simpler procedure for obtaining the numerical value of D_{min}. Since by definition $\lambda = 0$ when $D = D_{min}$, the simpler equation $|H| = 0$ can be solved for D when α and t have arbitrary fixed values. By using a larger and larger number K of terms ϕ_{pq} in the trial function Ψ, the sequence of values of D thus obtained approaches the value D_{min} from above. Furthermore, by adjusting α and t this sequence can be made to converge with varying rapidity. The most rapid convergence was found in the limit of α and t approaching zero. Apparently this limit best describes the very gradual falloff of the wave function Ψ with increasing ξ as characteristic of a state having zero binding energy. In this limit the determinant $|H|$ can be factored,[5] and the convergence of values of D to D_{min} as more terms are taken is found to be rapid. This procedure was carried out in integral steps from $K = 2$ to 20 and thereafter for other values shown in Table 16.1, which summarizes the results. No change in the value of $D_{min} = 0.6393\ ea_0 = 1.625 \times 10^{-18}$ esu-cm was found after $K = 40$.

ELECTRON SCATTERING FROM ATOMS OF $1s^2 2s^2 2p^q$ CONFIGURATION

The series of elements possessing $1s^2 2s^2 2p^q$ atomic configurations exhibit physical and chemical characteristics which are generally quite dissimilar for the various members of the series. However, experimental data on elastic scattering of electrons on nitrogen, oxygen, and neon indicate that the elastic scattering cross sections are quite similar over the range of energies from about 1 to 20 ev. A study was made previously[15] of elastic scattering of electrons from atomic oxygen in which detailed calculations were made of the adiabatic distortion of the target atom by the incident electron, utilizing the method of polarized orbitals. Since the calculation of target distortion or the polarization potential which describes the distortion is quite tedious, it is worth while investigating whether one might find a simpler procedure by which the polarization of other members of the sequence might be described in terms of that calculated for oxygen.

In the present investigation the polarization potential in the total interaction potential for electrons scattering from nitrogen and neon was obtained from that previously calculated for oxygen and from the experimental dipole polarizabilities.

First we note that the asymptotic form of the polarization potential $V_p(r)$ for any atomic system should be $V_p(r) \xrightarrow[r\to\infty]{} -\alpha/r^4$, where α is the dipole polarizability of the target atom in question. These quantities are known for a large number of atomic systems.[16] Since the same type of atomic orbitals is involved, it is also reasonable that the form of $V_p(r)$ should be similar for all members of the $2p^q$ series, being, to a first approximation, only scaled by the relative atomic size of the particular species

[15] W. R. Garrett and H. T. Jackson, Jr., *Phys. Rev.* **153**, 28 (1967).

[16] A. Dalgarno, *Advan. Phys.* 11, 281 (1962).

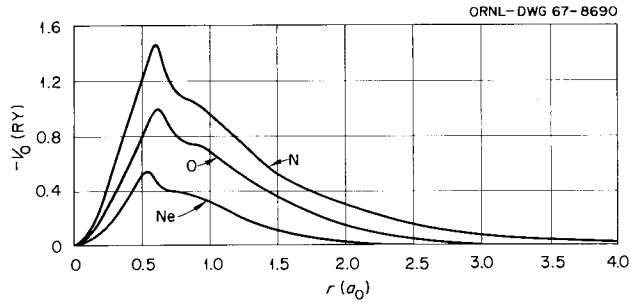

Fig. 16.2. Dipole Polarization Potential for Atomic Nitrogen, Oxygen, and Neon.

in the sequence. Thus in this investigation the polarization potentials describing the distortion of nitrogen and neon were derived from that for oxygen by defining the familiar Thomas-Fermi-type coordinate $r' = aZ^{1/3}r$, where a is a constant, and writing $V_p(r') = V_p^{\text{oxygen}}(r) \cdot \alpha/\alpha_{\text{oxygen}}$, where α is the dipole polarizability of nitrogen or neon ($\alpha = 1.13$ A^3 for nitrogen and $\alpha = 0.395$ A^3 for neon). The polarization potentials thus defined are shown in Fig. 16.2, along with that of oxygen from ref. 15.

With the term $V_p(r')$ thus defined, the elastic scattering cross section was derived by the usual partial wave analysis where the lth partial wave satisfies

$$\left[\frac{d^2}{dr'^2} - \frac{l(l+1)}{r'^2} + V_{\text{HF}}(r') + V_p(r') + k^2\right] F_l(r') = 0$$

for an electron of energy k^2 rydbergs. The term $V_{\text{HF}}(r)$ is the modified Hartree-Fock-Slater atomic potential as described in ref. 15.

Figures 16.3 and 16.4 show the elastic scattering cross sections for nitrogen and neon compared with the experimental data of Ramsauer and Kollath,[17] Bruche,[18] and Phelps *et al.*[19] for neon and of Neynaber *et al.*[20] for nitrogen. The agreement with experiment is rather good for a procedure as simple as that proposed herein.

The present results indicate that the determination of the polarization potential for one member

[17]C. Ramsauer and R. Kollath, *Ann. der Phys.* **5**, 536 (1929).

[18]S. Bruche, *Ann. der Phys.* **4**, 283 (1927).

[19]A. V. Phelps, O. T. Fundingsland, and S. C. Brown, *Phys. Rev.* **84**, 559 (1951).

[20]R. H. Neynaber *et al.*, *Phys. Rev.* **129**, 2069 (1963).

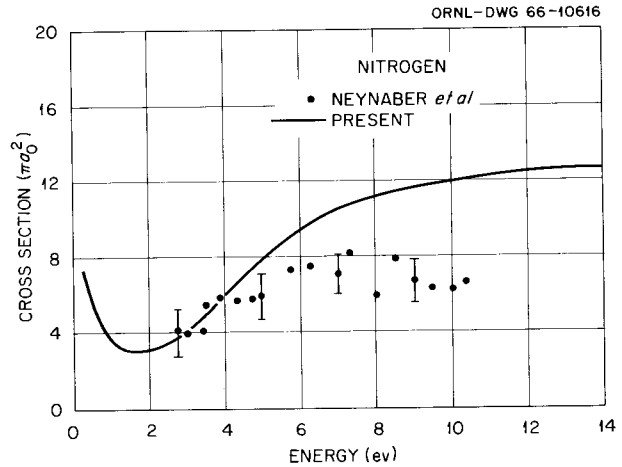

Fig. 16.3. Elastic Scattering Cross Section for Atomic Nitrogen Compared with Experimental Values of Neynaber *et al.*

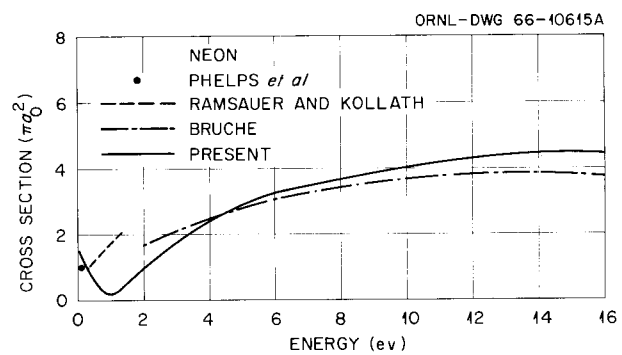

Fig. 16.4. Elastic Scattering Cross Section for Neon. Experimental values are those of Phelps *et al.*, Ramsauer and Kollath, and Bruche.

of an atomic series of a given type of configuration provides an adequate representation of target distortion for other atoms of the same series. Since distortion effects are relatively difficult to determine, this could be particularly convenient for more complicated systems, for example, heavy atoms or simple molecules.

NONADIABATIC TARGET DISTORTION IN LOW-ENERGY ATOMIC SCATTERING

One of the central questions in the treatment of low-energy electron or positron scattering from atomic and molecular systems concerns the importance of dynamic effects on the distortion of

the target system by the incident charged particle. In the present investigation a perturbation method is used to obtain equations for the dynamic distortion of the target system, and the important question of the velocity dependence of the interaction potential describing the scattering process is investigated for the positron-hydrogen problem.

In Rydberg units ($\hbar = 1$, $m_e = \frac{1}{2}$, unit of energy = 13.6 ev) the spin-free Hamiltonian for the positron-hydrogen scattering problem can be written

$$H = -\nabla_1^2 - \frac{2}{r_1} - \nabla_p^2 + \frac{2}{r_p} - \frac{2}{r_{1p}} = H_0 - \nabla_p^2 + \frac{2}{r_p} + W , \tag{1}$$

where r_1 is the electron coordinate, and r_p is the positron coordinate. For convenience we introduce $W = -2/r_{1p}$ and H_0, the Hamiltonian of the hydrogen atom, whose wave functions $\phi_0(r)$ satisfy

$$H_0\phi_n(\mathbf{r}_1) = \mathcal{E}_n\phi_n(\mathbf{r}_1) . \tag{2}$$

Without loss of generality we choose to write the total wave function satisfying the time-independent Schrödinger equation in the form

$$\Psi(\mathbf{r}_1,\mathbf{r}_p) = \psi(\mathbf{r}_p)\,[\phi_0(\mathbf{r}_1) + \chi(\mathbf{r}_1,\mathbf{r}_p)] . \tag{3}$$

Here $\psi(\mathbf{r}_p)$ is the scattered wave for the positron, which has the asymptotic behavior

$$\psi(r_p) \xrightarrow[kr_p \to \infty]{} \frac{\sin}{kr_p}\left(kr_p - \frac{l\pi}{2} + \delta_l\right) ;$$

$\chi(\mathbf{r}_1,\mathbf{r}_p)$ represents the correlation between the positron and electron and is chosen to satisfy $\langle \phi_0, \chi\rangle = 0$. We now employ the variational method in order to obtain an equation for the scattered wave $\psi(\mathbf{r}_p)$. Thus,

$$\delta \int \Psi(\mathbf{r}_1,\mathbf{r}_p)\,(H - E)\,\Psi(\mathbf{r}_1,\mathbf{r}_p)\,d\tau = 0 . \tag{4}$$

With $\Psi(\mathbf{r}_1,\mathbf{r}_p)$ of the form of Eq. (3), the variation principle yields an equation for $\psi(\mathbf{r}_p)$ which, through second order in the correlation function χ, is

$$\begin{aligned} &-\nabla_p^2\,\psi(\mathbf{r}_p) + [(2/r_p) - V_c(r_p) - k^2]\,\psi(\mathbf{r}_p) \\ &+ \langle \phi_0, W\chi\rangle\,\psi(\mathbf{r}_p) + \psi(\mathbf{r}_p)\Big[\langle \chi, (H_0 - E_0 - \nabla_p^2)\chi\rangle \\ &- \langle \chi, (V_c - W)\phi_0\rangle\Big] - 2\langle \chi, \nabla_p\psi\cdot\nabla_p\chi\rangle = 0 . \end{aligned} \tag{5}$$

The integration in the matrix elements is over $\mathbf{r}_1$, and k^2 and E_0 are the kinetic energy of the positron and the ground-state energy of hydrogen respectively.

Now in order to obtain an equation for the correlation χ, we used a perturbation method. To this end we write the total Schrödinger equation in the form

$$(H_0 + H_p + W)\,(\phi_0 + \chi)\psi = E_t(\phi_0 + \chi)\psi , \tag{6}$$

where the notation is as before with $H_p = -\nabla_p^2 + 2/r_p$, and E_t is the total energy. If we perform a scalar multiplication on this equation with $\phi_0\psi$ and impose $\delta E \to 0$, we get

$$E_t\psi = E_0\psi + \langle H_p + V_c + V_p\rangle\psi , \tag{7}$$

where $V_c = \langle \phi_0, W\phi_0\rangle$, and $V_p = \langle \phi_0, W\chi\rangle$. Putting this Eq. (6) and retaining terms through first order in the correlation χ, we get an equation for the correlation function or distortion term $\chi(\mathbf{r}_1,\mathbf{r}_p)$:

$$\begin{aligned} \psi(H_0 - E_0 - \nabla_p^2)\,\chi(\mathbf{r}_1,\mathbf{r}_p) &= \psi(V_c - W)\phi_0 \\ &+ 2\nabla_p\psi\cdot\nabla_p\chi\,(\mathbf{r}_1,\mathbf{r}_p) . \end{aligned} \tag{8}$$

This equation determines the distortion of the atomic system by the incident particle. We note that with Eq. (8) the second line of the scattering equation [Eq. (5)] vanishes. The scattering equation then becomes

$$\begin{aligned} -\nabla_p^2\,\psi(\mathbf{r}_p) + \Big[(2/r_p) - V_c(r_p) - k^2 \\ + \langle \phi_0, W\chi\rangle\Big]\,\psi(r_p) = 0 , \end{aligned} \tag{9}$$

which contains all terms through second order in χ. Thus the solutions to Eqs. (8) and (9) describe the scattering. However, these equations are coupled and not amenable to solution in their present form. We must resort to some approximation in order to solve the above. First we note the identity

$$\nabla^2\,\psi\chi = \chi\nabla^2\psi + \psi\nabla^2\chi + 2\nabla\psi\cdot\nabla\chi$$

and write Eq. (8) as

$$\psi(H_0 - E_0)\,\chi - \nabla_p^2\chi + \chi\nabla_p^2\psi - \psi(V_c - W)\phi_0 = 0 . \tag{10}$$

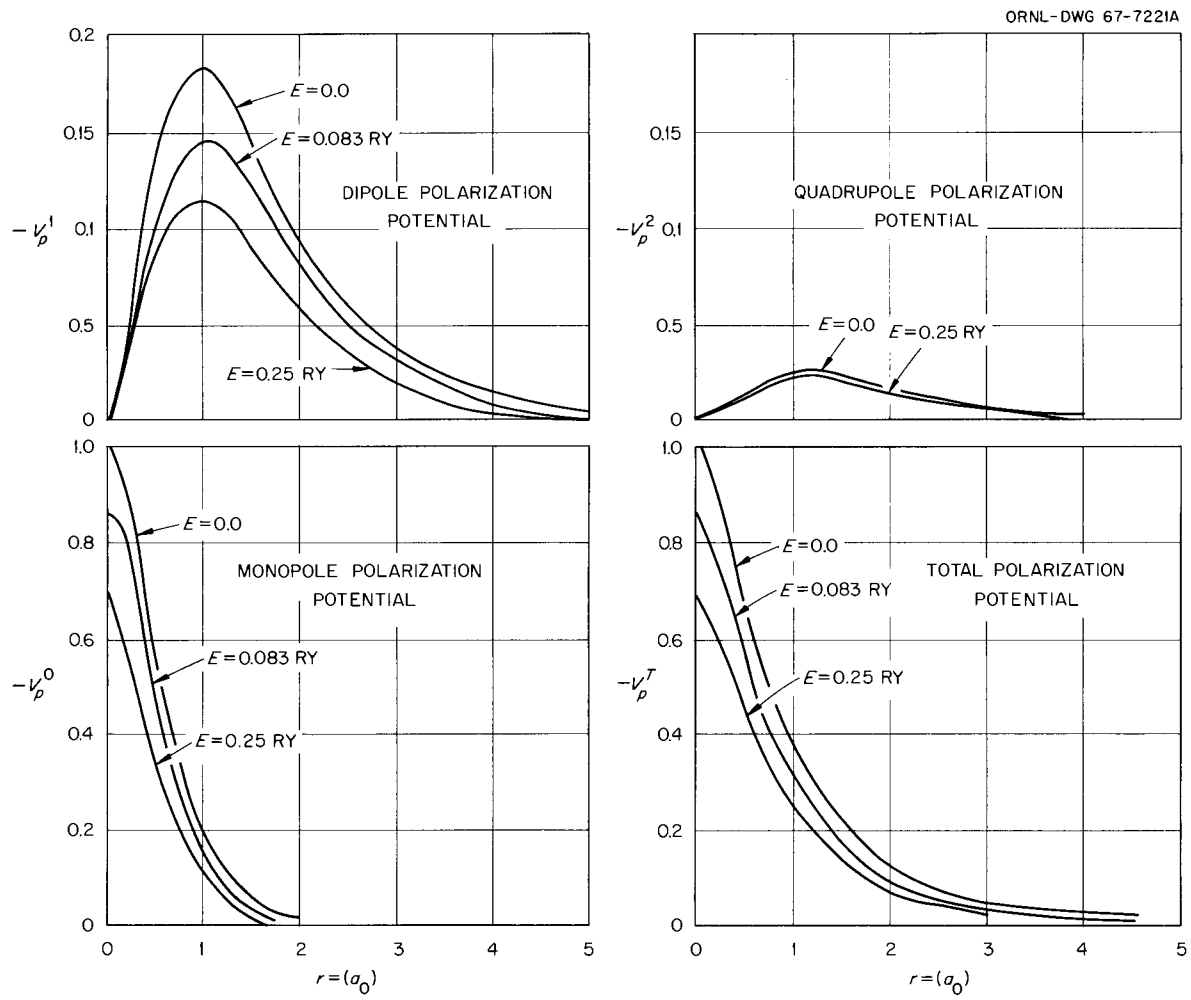

Fig. 16.5. Various Multipole Contributions to the Polarization Potential of the Hydrogen Atom as a Function of Positron Energy.

Since the above contains the operators ∇_1^2 and ∇_p^2, it is an equation in six dimensions and entirely too complex for solution. In order to simplify the equation, we will make an approximation for the dynamic terms, that is, the terms which contain the kinetic-energy operator $-\nabla_p^2$ of the incident positron. The ordinary adiabatic approximation[21] to χ results if these two terms are dropped in Eq. (10).

The operator ∇_p^2 influences the above equation through its operation $-\nabla_p^2\psi$ on the continuum function ψ and $\nabla_p^2\chi$ on the correlation function χ. We first note that asymptotically the first term behaves as $\nabla_p^2\psi \cong -k^2\psi$ with solution $\psi \sim e^{\pm i\mathbf{k}\cdot\mathbf{r}}$. We then note that it is possible to write the correlation function $\chi(\mathbf{r}_1,\mathbf{r}_p)$ in terms of a double sum over the complete set of plane-wave continuum functions for the positron, denoted by $\zeta_\nu(\mathbf{r}_p)$, and the complete set of hydrogen atom wave functions $\phi_j(r_1)$. That is, we could write the expansion

$$\chi(\mathbf{r}_1,\mathbf{r}_p) = \int \sum_j a_{\nu j}\zeta_\nu(\mathbf{r}_p)\,\phi_j(\mathbf{r}_1)\,d\nu\,. \qquad (11)$$

Thus the correlation function can be formed from a wave packet in $\mathbf{r}_p$ space centered about k^2, and a set of hydrogen solutions $\phi_j(\mathbf{r}_1)$ in $\mathbf{r}_1$ coordinates. We now choose to represent χ in the dynamic term $\nabla_p^2\chi$ by a wave packet centered about k^2 but of zero width; that is,

[21] W. R. Garrett, *Phys. Rev.* **140**, A705 (1965).

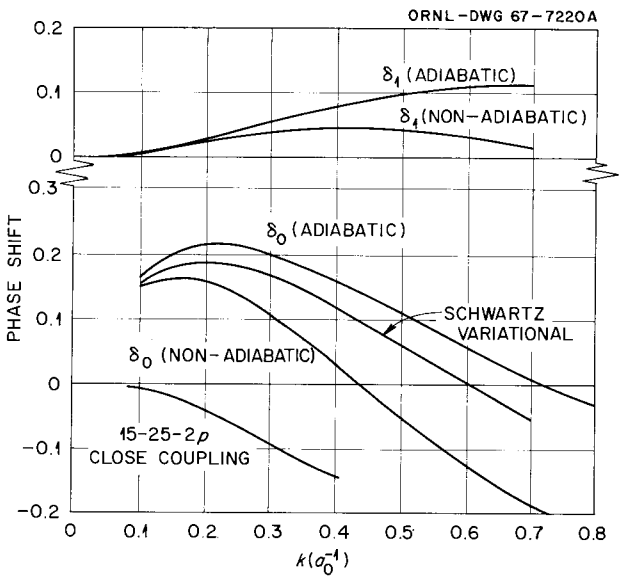

Fig. 16.6. Partial Phase Shifts for Positron Scattering on a Hydrogen Atom as a Function of Positron Energy.

$$\chi(\mathbf{r}_1,\mathbf{r}_p) = \int \sum a_{\nu j}\, \delta(\nu - k^2)\, \zeta_\nu(\mathbf{r}_p)\, \phi_j(\mathbf{r}_1)\, d\nu$$

$$= \sum_j a_j e^{\pm i\mathbf{k}\cdot\mathbf{r}_p}\, \phi_j(\mathbf{r}_1)\,. \qquad (12)$$

Thus in the two dynamic terms of Eq. (10) we make an "asymptotic" approximation and replace the terms by the approximate form which they assume when the positron is "outside" the atomic system. The equation then partially separates and becomes

$$\psi(H_0 - E_0)\,\chi + 3k^2\,\psi\chi - \psi(V_c + W)\phi_0 = 0 \quad (13)$$

or

$$(H_0 - E_0 + 3k^2)\,\chi - (V_c + W)\,\phi_0 = 0\,. \qquad (14)$$

This last equation is of the form of the polarized orbital equation investigated earlier,[21] with an additional term $3k^2$ which depends on the energy of the incident particle. Equation (14) may be solved by expanding $W = 2/r_{1p}$ in a multipole expansion, thus yielding the correlation or distortion term $\chi(\mathbf{r}_1,\mathbf{r}_p)$ and the resultant polarization potential $V_p(r_p) = \langle \phi_0, W\chi \rangle$ of Eq. (9).

The various contributions to the polarization potential of hydrogen are shown in Fig. 16.5 for a few incident energies. As expected, the distortion of the atomic system by the incident particle decreases with increasing incident energy. The effect on the phase shifts is shown in Fig. 16.6, where the adiabatic phase shift, obtained by neglecting the kinetic effects on the polarization potential, is shown for comparison. The importance of the dynamic effects is dramatic for low-energy collisions.

Additional aspects of the dynamic effects mentioned here are being investigated along two lines. First, the effect of virtual positronium formation on the scattering phase shifts is being studied. Second, the method outlined above is being applied to more complicated atomic systems, where essentially no work has been done along these lines.

POTENTIAL ENERGY SHIFT AT THE ATOMIC NUCLEUS

The charge distributions and corresponding potential energy functions for atomic systems find application to problems in various branches of physics. One particularly simple physical parameter, which is very useful in certain studies of nuclear beta decay, is the potential energy at the nucleus due to all the atomic electrons of an atomic system. This potential energy shift V_0 is utilized in determining the Fermi function $F(\pm Z,W)$ for the decay of a nucleus of charge Z decaying with energy W. If the total beta energy W is in mc^2 units and momentum p is in mc units, the Fermi function is defined as

$$F(\pm Z,W) = (f_1^2 + g_{-1}^2)/2p^2\,, \qquad (1)$$

where f_1 and g_{-1} are the two components of the radial wave functions of the emitted particle, evaluated at the nuclear surface. (The positive sign is for electrons; the negative is for positron emission.) Rose[22] has shown how the function $F(\pm Z,W)$ may be easily evaluated in a very good approximation by utilizing pure Coulomb functions for f_1 and g_{-1} in the above expression and replacing F by a shifted function $F_s^{\pm}$ defined as

$$F_s^{\pm} \equiv F(\pm Z,W)\,[\{(W \mp V_0)^2 - 1\}/(W^2 - 1)]^{1/2} \times (W \mp V_0)/W\,, \qquad (2)$$

[22] M. E. Rose, *Phys. Rev.* **49**, 727 (1936).

where V_0 is the potential energy shift at the nucleus due to the atomic electrons.

Due to its ready utility, the quantity V_0 has been approximated in various ways by different investigators. One simple estimate may be obtained from the statistical models of the atom, either the Thomas-Fermi (TF) model or the Thomas-Fermi-Dirac (TFD) model. The TF equation yields a single solution which is applicable, by simple scaling, to any atom of the periodic table. This solution gives $V_0 = 1.795Z^{4/3}$ in atomic units, where the unit of energy is 27.2 ev; or in mc^2 units $V_0 = 1.795\alpha^2 Z^{4/3}$, where α is the fine-structure constant. The TFD model, which differs from the TF method through the inclusion of electron exchange, yields V_0 over a range from $V_0 \cong 1.9\alpha^2 Z^{4/3}$ for light atoms to $V_0 = 1.81\alpha^2 Z^{4/3}$ for heavy elements.

Estimates of V_0 have also been obtained by comparing the experimental binding energy of K electrons with the theoretical values from the hydrogen-like model for the K shell.[23] These estimates are somewhat lower than the true value, since the K electron spends much of its time some distance from the nucleus.

A great improvement in the accuracy of V_0 may be achieved by solving the Hartree-Fock (HF) equations for a particular atomic system and subsequently using the HF wave functions to determine the potential at the nucleus. For calculations which involve a large number of atoms, the Slater approximation to the HF equations forms a very convenient, and for most purposes reliable and accurate, representation of the complete HF equations.[24] In the Hartree-Fock-Slater (HFS) method, self-consistent field wave functions are obtained for each of the atomic electrons where ψ_i for the ith electron satisfies

$$\left[-\frac{1}{2}\nabla_1^2 - (Z/r_1) + V_c(\mathbf{r}_1) - A_s(\mathbf{r}_1) \right] \psi_i(\mathbf{r}_1) = \epsilon_i \psi_i(\mathbf{r}_1) . \quad (3)$$

Here $V_c(r_1)$ is the electrostatic potential of the electron charge distribution

Table 16.2. Potential Energy Shift at the Nucleus V_0 and Thomas-Fermi Parameter a from HFS Wave Functions

Z	V_0 (kev)	a	Z	V_0 (kev)	a
7	0.510	1.399	39	5.589	1.553
8	0.618	1.420	45	6.803	1.561
9	0.735	1.444	49	7.641	1.566
10	0.863	1.471	52	8.277	1.567
11	0.982	1.476	53	8.492	1.568
12	1.105	1.474	54	8.707	1.568
14	1.359	1.481	55	8.919	1.567
15	1.495	1.484	60	10.05	1.572
16	1.633	1.488	64	10.98	1.577
17	1.776	1.494	66	11.48	1.579
18	1.921	1.496	68	11.98	1.586
20	2.208	1.495	70	12.48	1.590
23	2.677	1.504	74	13.47	1.593
25	3.009	1.513	76	13.97	1.595
27	3.358	1.518			
30	3.907	1.540	80	15.00	1.599
32	4.264	1.556	86	16.53	1.600
35	4.830	1.550			
36	5.016	1.551	92	18.09	1.601
38	5.396	1.552	94	18.64	1.603

$$V_c(r_1) = \sum_j \int \psi_j^*(\mathbf{r}_2)\,(1/r_{12})\,\psi_j(\mathbf{r}_2)\,d\mathbf{r}_2 , \quad (4)$$

and $A_s(r_1)$ is the Slater exchange potential

$$A_s(r_1) = 3\,[(3/8\pi) \sum_j \psi_j^*(\mathbf{r}_1)\psi_j(\mathbf{r}_1)]^{1/3} . \quad (5)$$

Atomic units are used in Eqs. (3), (4), and (5), where $e = m = \hbar = 1$ and the unit of energy is 27.21 ev. The value of the electrostatic potential at the nucleus due to the atomic electrons is just the term $V_c(r)$ of Eq. (4) evaluated at $r = 0$.

In order to establish reliable values of V_0 for any atomic system, the HF equations have been solved and the potential shift V_0 evaluated from Eq. (4) for a large number of atoms scattered throughout the periodic table.[25] The results for V_0 as a function of Z are given in Table 16.2 and are shown in Fig. 16.7, where they are compared with estimates from K-binding energy data. As is

[23] U. Fano, *Natl. Bur. Std. Monograph, Appl. Math. Series No. 13*, 12 (1962).

[24] J. C. Slater, *Phys. Rev.* **81**, 545 (1951).

[25] W. R. Garrett and C. P. Bhalla, *Z. Physik* **198**, 453 (1967).

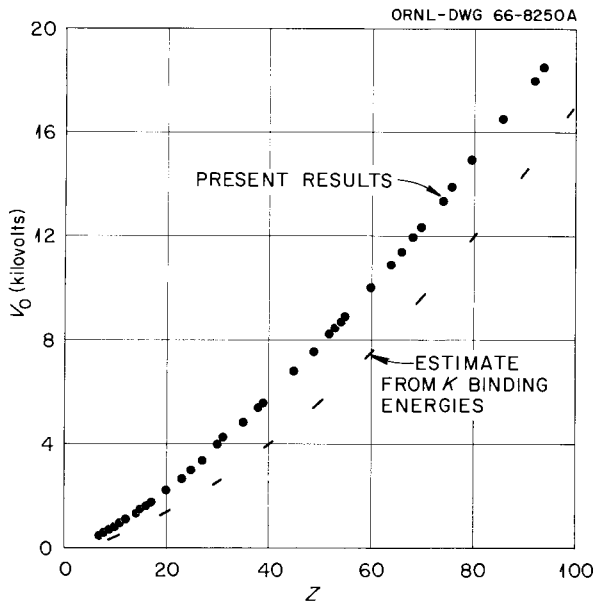

Fig. 16.7. Comparison of Potential Energy Shift at the Nucleus Obtained from Hartree-Fock Wave Functions with Estimate from K-Binding Energy Data (in kev).

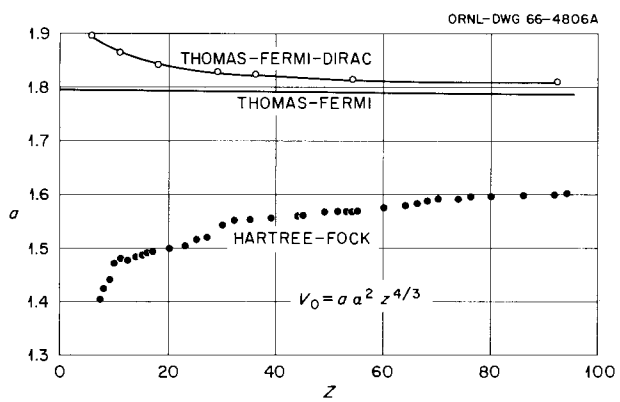

Fig. 16.8. Z Dependence of the Thomas-Fermi Potential Energy Parameter a as Obtained from Thomas-Fermi, Thomas-Fermi-Dirac, and Hartree-Fock Results.

to be expected, the estimate from binding energy data is somewhat lower than the actual value of V_0.

Returning to the statistical model of the atom, we note that V_0 is proportional to $Z^{4/3}$. The present results can be utilized to check the deviation of the true potential from that yielded by the statistical models. This can be done most conveniently by writing the present results in the form $V_0 = a\alpha^2 Z^{4/3}$, where a is chosen to give V_0 as determined from the HF calculations. These numbers are also shown in Table 16.2. We note that the screening is not proportional to $Z^{4/3}$, since a varies from 1.4 for light Z to 1.6 for heavy Z. Thus the statistical models are seriously in error, especially for light Z, as shown in Fig. 16.8, where the value of a is plotted as a function of Z.

With the values obtained in the present investigation, accurate numerical values for the potential energy shift V_0 are available for any element in the periodic table.

ELECTRON MEAN FREE PATHS IN A FREE ELECTRON GAS

The mean free path of low-energy electrons in a free electron gas has been calculated using the expression reported previously[26,27] which takes explicit account of the exclusion principle in intermediate states. The results, which have been obtained thus far for special cases, give a lower scattering cross section with the exclusive-principle correction when compared with previous calculations and thus bring the calculated values into better agreement with experiment. More general calculations are in progress.

EFFECTS OF PHANTOM GEOMETRY ON DOSE DISTRIBUTION

Calculations have been made of the spatial distribution of dose and dose equivalent due to protons of energies 250 and 400 Mev incident on a tissue phantom, which has dimensions approximating those of a human torso and has the form of a right elliptical cylinder with a height of 70 cm and with semiaxes of the elliptical base as 20 and 10 cm. The results obtained have been compared with the corresponding data previously obtained for a tissue slab having thickness of 30 cm.[28] It is shown that within the limits of accuracy due to statistical fluctuations the distributions of dose and dose equivalent are not substantially different in a cylindrical phantom from the corresponding values in a slab phantom.

---

[26] Jacob Neufeld *et al.*, *Health Phys. Div. Ann. Progr. Rept. July 31, 1966*, ORNL-4007, p. 127.

[27] R. N. Hamm, R. H. Ritchie, and J. C. Ashley, *Bull. Am. Phys. Soc.* 11, 738 (1966).

[28] Jacob Neufeld *et al.*, "Effects of Phantom Geometry on Dose Distribution," in *Proc. Intern. Congr. Intern. Radiation Protection Assoc., 1st, Rome, Italy, Sept. 5–10, 1966* (to be published).

REFORMULATION OF THE DIELECTRIC CONSTANT AND OF OHM'S LAW IN AN ABSORBING MEDIUM

It is proposed that a fundamental revision of the formulation of the dielectric constant and of the conductivity of an absorbing medium be considered. In the conventional formulation the dielectric constant is represented by a real quantity ϵ when the medium is nonabsorbing and by a complex quantity $\epsilon = \epsilon_1 + i\epsilon_2$ when the medium is absorbing. In case of an absorbing medium, both ϵ_1 and ϵ_2 depend on the mechanism which controls the energy absorption, and, therefore, in the conventional representation ϵ_1 as well as ϵ_2 is expressed in terms of a frictional parameter γ which is used in the microscopic description of the medium. Such a representation, although widely accepted in the current literature, is not consistent with Maxwell's formulation of the principle of conservation of energy, and more particularly is not consistent with the physical meaning of the expression $\frac{1}{4}\pi(\mathbf{E} \cdot d\mathbf{D}/dt)$, where $\mathbf{E}$ is the electrical intensity, and $\mathbf{D}$ is the displacement.[29] Because of this inconsistency the formulation $\epsilon = \epsilon_1 + i\epsilon_2$ is not adapted to the analysis of the energetic behavior of absorbing media. For instance, the equivalence of the velocity of energy flow and of the group velocity in dispersive media has been shown to exist only if one neglects absorption.[30]

The above inconsistency does not occur in the proposed formulation in which the dielectric constant of an absorbing medium is always real and is independent of the absorption mechanism.

The conventional formulation for an idealized atomic medium is based on the equality $m(\ddot{\mathbf{r}} + \gamma\dot{\mathbf{r}} + \omega_b^2\mathbf{r}) = e\mathbf{F}$, representing the motion of an oscillating dipole, where m and e are the mass and charge of an electron respectively; $\mathbf{r}$ is the perturbed position of the electron due to the driving force $e\mathbf{F}$; $m\gamma\dot{\mathbf{r}}$ is the frictional force; and ω_b is the binding frequency. In order to determine the motion of the electron, the driving force $e\mathbf{F}$ must be defined. The departure of the proposed formulation from the conventional lies in the assumptions used to arrive at a suitable definition of the driving force.

In the conventional formulation it is assumed that the driving force is due entirely to the electrical intensity, that is, that $e\mathbf{F} = e\mathbf{E}$. Consequently, $\ddot{\mathbf{P}} + \gamma\dot{\mathbf{P}} + \omega_b\mathbf{P} = \omega_e^2\mathbf{E}$, where $\mathbf{P} = Ne\mathbf{r}$ is the polarization of the medium, $\omega_e^2 = 4\pi Ne^2/m$, and N is the number of atoms per unit volume. Applying the relationship $\mathbf{D} = \epsilon\mathbf{E} = \mathbf{E} + 4\pi\mathbf{P}$, the well-known expression for the dielectric constant is obtained and has the complex form $\epsilon = \epsilon_1 + i\epsilon_2$, in which ϵ_1 and ϵ_2 are functions of ω, ω_b, ω_e, and γ.

The novelty of the proposed formulation is based on the introduction of the concept of an "extraneous" (nonelectrical) force. It is assumed here that the driving force $e\mathbf{F}$ does not depend entirely on the "electrical" force $e\mathbf{E}$ but rather on the "electrical" force $e\mathbf{E}$ and the "extraneous" force $e\mathbf{E}^{(\mathrm{extr})}$. Thus, the equality $e\mathbf{F} = e\mathbf{E}$ should be replaced by the equality $e\mathbf{F} = e\mathbf{E} + e\mathbf{E}^{(\mathrm{extr})}$. The "electrical" force is used to represent the storage of the energy of an electric field per se and, more particularly, the mechanism which is effective in storing the polarization energy. The "extraneous" force is involved in the dissipative process in which the polarization energy is transformed into dissipated energy such as heat.

The formulation of the dissipative process in terms of a frictional force of the type $m\gamma\dot{\mathbf{r}}$ (analogous to that of a viscous fluid) is not always applicable. Therefore, using a formulation which is not dependent on a particular model, the frictional force will be expressed as $\boldsymbol{\varphi} = \boldsymbol{\varphi}(\dot{\mathbf{r}}, \omega_0, \lambda_1, \lambda_2, \ldots, \lambda_n)$, where $\boldsymbol{\varphi}$ represents a function of $\dot{\mathbf{r}}$, ω_0, and of the parameters $\lambda_1, \lambda_2, \ldots, \lambda_n$ which are necessary for the complete description of the dissipation mechanism.

Applying the concept of the "extraneous" force, the motion of an oscillating electron can be described by two equalities as follows: $m(\ddot{\mathbf{r}} + \omega_b^2\mathbf{r}) = e\mathbf{E}$ and $\phi(\dot{\mathbf{r}}, \omega_0, \lambda_1, \lambda_2, \ldots, \lambda_n) = e\mathbf{E}^{(\mathrm{extr})}$. The concept of the "extraneous" force is related to the concept of the "impressed" force $e\mathbf{E}^{(\mathrm{impr})}$ used in the customary representation of Ohm's law. The "extraneous" force is associated with a transformation of an electrical into a nonelectrical form of energy (energy sink), whereas the "impressed" force represents an inverse process (energy source). Thus, in the case of Ohm's law, one has $\mathbf{j} = \sigma[\mathbf{E} + \mathbf{E}^{(\mathrm{impr})}]$, where $\mathbf{j}$ is the electrical current density, and σ is the conductivity.[31]

---

[29] V. L. Ginzburg, *The Propagation of Electromagnetic Waves in Plasmas*, pp. 477–95, Pergamon, New York, 1964.

[30] L. Brillouin, *Wave Propagation and Group Velocity*, p. 98, Academic, New York, 1960.

[31] R. Becker, *Electrodynamic Fields and Interactions*, vol. I – *Electromagnetic Theory and Relativity*, p. 217, Blaisdell, New York, 1964.

Using the relationship $m(\ddot{\mathbf{r}} + \omega_b^2\mathbf{r}) = e\mathbf{E}$, which, as stated above, is applicable to both absorbing and nonabsorbing media, and applying the equalities $\mathbf{P} = Ne\mathbf{r}$ and $\mathbf{D} = \epsilon\mathbf{E}$, we obtain for the dielectric constant the expression

$$\epsilon = 1 + \omega_e^2/(\omega_b^2 - \omega^2) , \qquad (1)$$

which is valid for *both* absorbing and nonabsorbing media.

In order to formulate the conductivity σ of the medium, we represent the rate of dissipated energy Q (for an oscillating field having frequency ω) as

$$Q = [Ne\mathbf{E}^{(\mathrm{extr})} \cdot \mathbf{r}]_{\mathrm{average}} = \sigma E^2 . \qquad (2)$$

The averaging process is extended over a time interval which is large when compared with $1/\omega$. In the expression $(n + 4\pi i\sigma/\omega)$ for the index of refraction, the terms ϵ and σ are represented by (1) and (2) respectively.

The representation of ϵ as a complex quantity has caused considerable difficulties. Thus, the mean energy density $U^{(e)}$ stored in a dispersive and absorbing medium by an oscillating electric field $\mathbf{E} = \mathbf{E}_0 \sin \omega t$ has not as yet been formulated in terms of the dielectric constant. It is well known that the expression $U^{(e)} = (1/16\pi)d/d\omega (\omega\epsilon)E_0^2$ is valid for a nonabsorbing medium ($\epsilon =$ real), but it does not give physically acceptable results if ϵ is complex (absorbing medium).[29] Since in the proposed formulation ϵ is the same for absorbing and nonabsorbing media and since in both cases ϵ is real, the difficulties referred to above do not occur. The same expression $U^{(e)}$ is applicable to both absorbing and nonabsorbing media.

CHARACTERISTIC ENERGY GAIN BY FAST ELECTRONS IN SOLIDS

It has been predicted that Coulomb-stimulated plasmons in thin films may undergo radiative decay.[32] That this phenomenon can be viewed alternatively as a special case of transition radiation[33] was pointed out by others.[34] Considerable experimental work on this phenomenon has been carried out subsequently. This work, together with measurements on characteristic energy losses by fast electrons, has been useful in investigating the valence electron dynamics of many different solids.

It may be possible to observe the inverse of the plasmon decay process in a characteristic energy-loss experiment. This phenomenon involves the photoexcitation of a plasmon, which de-excites by delivering its energy to a fast electron. Thus, energetic electrons passing through a thin foil which is irradiated simultaneously by an intense light beam of the proper frequency should exhibit energy gain in quanta of the plasmon field. An estimate of the probability of this process shows that it appears feasible to attempt observation of such "characteristic energy gains" using a pulsed laser source and suitable frequency discrimination techniques.

A more detailed account of this work is given in *Phys. Letters* **24A**, 348 (1967).

PLASMON EXCHANGE SCATTERING BY FAST ELECTRONS

The basic Møller cross section for the scattering of two free electrons upon one another has been tested experimentally over a wide energy range. Agreement with theory to within a few percent has been found from 50 kev to 250 Mev.[35] The cross section, or equivalently the mean free path for plasmon creation by a fast electron in several metals, has been determined experimentally over a much narrower range.[36]

A related process of some interest, which has not been observed experimentally to date, is one in which two fast electrons scatter on one another through the plasmon field. This exchange of a virtual plasmon should evince itself in the gain of the plasmon quantum of energy by one electron at the expense of the other. The experiment would require two beams of electrons with slightly different energies which are focused on the same area of a thin foil of a metal which possesses a well-defined plasmon state. For best results the

[32] R. A. Ferrell, *Phys. Rev.* **111**, 1214 (1958).

[33] V. L. Ginsburg and I. M. Frank, *J. Phys. USSR* **9**, 353 (1954).

[34] R. H. Ritchie and H. B. Eldridge, *Bull. Am. Phys. Soc.* **4**, 384 (1959); *Phys. Rev.* **126**, 1935 (1962); E. A. Stern, *Phys. Rev. Letters* **8**, 7 (1962).

[35] For a review of the experimental situation, see R. D. Birkhoff, in *Handbuch der Physik*, vol. 34, pp. 55–61 (ed. by S. Flügge), Springer-Verlag, Berlin, 1958.

[36] R. H. Ritchie, M. Y. Nakai, and R. D. Birkhoff, "Low-Energy Electron Mean Free Path in Solids," in *Advances in Radiobiology*, vol. 3 (in press).

beams should be nearly colinear. Energy analysis of one of the beams after interacting in the foil should show a characteristic energy-gain peak corresponding to the plasmon energy $\hbar\omega_p$.

An estimate of the probability for this process has been made. For the case of two colinear beams of electrons (1) and (2) with energies E_1 and E_2 respectively, we find that P, the probability per electron of energy E_1 that an electron of energy E_2 will undergo an energy gain in interacting with an electron of energy E_1 in a foil of thickness a, is

$$P = 4\pi^2 \frac{Ry}{\hbar\Gamma}\left(\frac{v_1}{\omega_p}\right)^2 \frac{an_2}{(1+\delta)^2},$$

where Ry is the Rydberg energy (13.60 ev), Γ is the damping rate of the plasmon, v_1 is the velocity of an electron with energy E_1, n_2 is the density of electrons in beam (2), and δ is defined by the equation

$$E_1 - E_2 = (1+\delta)(\hbar\omega_p) .$$

The quantity δ is assumed to be of order unity and is taken to be positive definite.

If one assumes that beam (2) consists of 5-kev electrons at a current of 10 μa normally incident on an aluminum foil 2000 A thick, that $\delta = 0.5$, and that the beam area is 10^{-2} cm^2, then one estimates that there will be $\sim 10^{-9}$ electron/sec experiencing energy gain in beam (2) per electron/sec incident in beam (1) if the beams intercept the same area on the foil surface.

Even though this is quite a small efficiency for the process, one may be able to use frequency-discrimination techniques; for example, beam (2) might be pulsed while beam (1) is maintained constant. In this case, only frequency components of the energy analyzer output at the pulse rate of beam (2) would be accepted.

SURFACE SECONDARY ELECTRON EMISSION FROM SOLIDS

Similarities between secondary electron emission from metals and the photoelectric effect in metals have been discussed theoretically.[37,38] Important differences between these two processes appear when one takes into account the dynamic response characteristics of a metal to disturbances which vary appreciably in a time comparable with the inverse plasma frequency of the metal. The surface photoemission phenomenon involves the creation of a radiative plasmon which decays causing electron emission from the metal. A theory of this process is given which leads to the prediction of periodic fluctuations in the yield with foil thickness analogous to fluctuations observed in transition radiation yield with foil thickness.[39] The surface secondary emission process may occur through "Auger" decay of either radiative or nonradiative surface plasmons created by energetic charged particles. It is predicted that such decays may be responsible for a steep rise in the spectrum of secondary electrons at an energy equal to the surface plasmon energy minus the metal work function. This process may have been observed already in the secondary electron spectrum of magnesium.[40] It is proposed that experiments using fast primaries at grazing incidence may make such features of the spectrum readily observable.

GROUP THEORY OF NORMAL MODES AND MOLECULAR ORBITALS

The motion of nuclei in a molecule can be described in terms of normal modes formed from linear combinations of the vector displacements of the nuclei from their equilibrium positions. It is advantageous to choose the normal modes so that, when subjected to a symmetry operation of the point group of the molecule, they form bases for irreducible representations of the point group.

The distribution of electrons in a molecule can be described in terms of molecular orbitals formed from linear combinations of atomic orbitals about the several nuclei. It is advantageous to choose the molecular orbitals so that, when subjected to a symmetry operation of the point group of the molecule, they form bases for irreducible representations of the point group.

[37] H. Frölich, *Proc. Phys. Soc. (London)* **B68**, 657 (1955).

[38] I. Adami, *Phys. Rev.* **134**, A1649 (1964).

[39] E. T. Arakawa, N. O. Davis, and R. D. Birkhoff, *Phys. Rev.* **135**, 224 (1964).

[40] O. H. Zinke, *Phys. Rev.* **106**, 1163 (1957).

The problem in each case is to find the appropriate linear combinations, and the problems have similar structures. This structure is: (1) under the symmetry operation, equivalent nuclei are permuted, and this permutation provides a representation of the group; (2) under the symmetry operation, the coordinates of the vector are bases for a vector representation in the first case, and the degenerate atomic orbitals are the bases for a representation in the second case. An appropriate ordering of the basis elements (displacement coordinates in the first case and atomic orbitals in the second) provides a representation of the symmetry operations which is the direct product of a permutation representation and another representation. The complete reduction of each of these representations is much simpler than the original problem and leads to a representation of the group by matrices which are the direct sum of direct products of irreducible representations. The latter direct products are reduced to direct sums of irreducible representations by transformation by Wigner matrices, which are known for all the point groups of molecular physics. The composite transformation thus provides the normal mode coordinates in the first case and the symmetry orbitals in the second case, which form the desired bases for irreducible representations of the point group of the molecule.

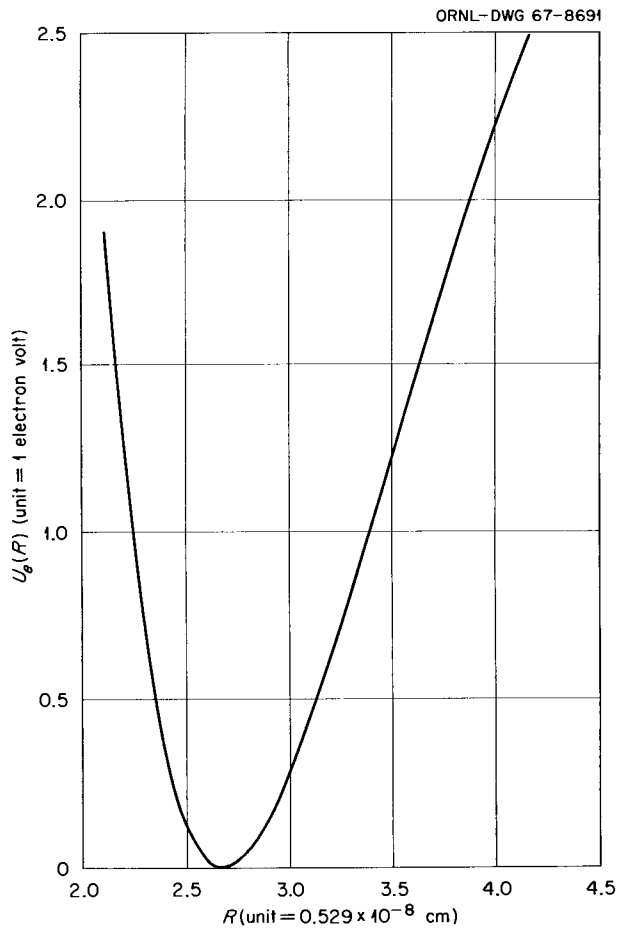

Fig. 16.9. Electronic Potential Energy of $H^{81}Br$ as a Function of Internuclear Distance.

POTENTIAL ENERGY CURVES FOR DIATOMIC MOLECULES

Klein's[41] semiclassical method for obtaining the potential energy U_e as a function of internuclear distance R was modified to take into account the difference between old and new quantum theories and was programmed for high-speed computation. For two problems which are completely soluble analytically (Coulomb plus centrifugal potential and harmonic plus centrifugal potential), the numerical output $U_e(R)$ agrees with the analytical input to 1 part in 10^7. The electronic potential energy of $H^{81}Br$ has been computed from experimental term values; the result is shown in Fig. 16.9.

[41] O. Klein, *Z. Physik* **76**, 226 (1932).

OSCILLATOR STRENGTHS IN MAGNESIUM PORPHIN

Magnesium porphin, $MgN_4C_{20}H_{12}$, is essentially the kernel of the chlorophyll molecule. Orthonormalized molecular orbitals of D_{4h} symmetry were formed from linear combinations of nitrogen and carbon $2s$ and $2p$ atomic orbitals, magnesium $3s$ and $3p$ orbitals, and hydrogen $1s$ orbitals; the oscillator strength was computed for many transitions from high-lying filled to low-lying empty orbitals. The conclusions are: (1) the oscillator strengths vary greatly even for transitions between states of the same symmetry close together in energy; (2) the largest oscillator strengths occurred when the electric vector of the light was parallel to the plane of the molecule; and (3) two prominent strong absorptions were found near the experimental values.

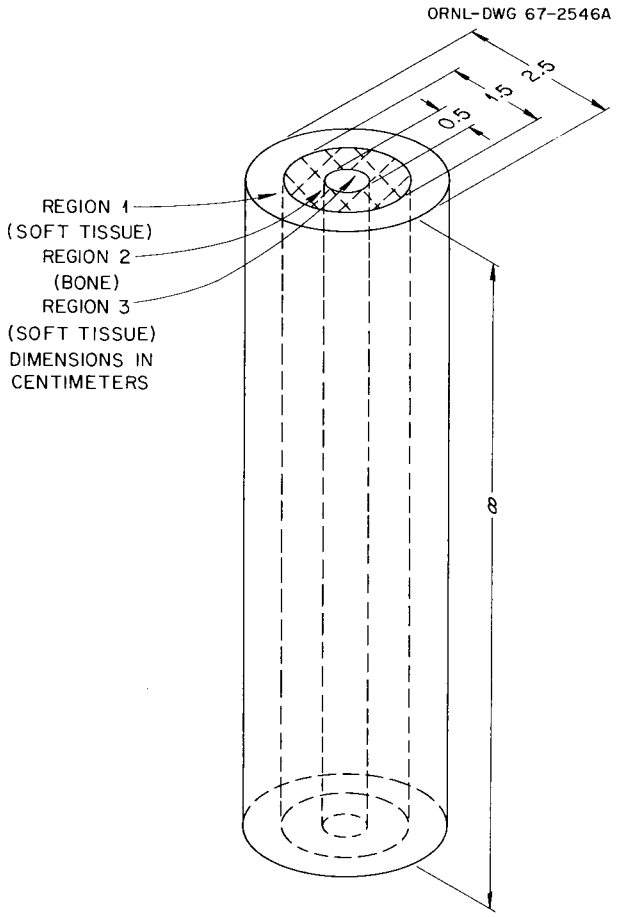

Fig. 16.10. Cylinder of Soft Tissue Surrounded by Concentric Annular Cylinders of Bone and Soft Tissue. Dimensions are in centimeters.

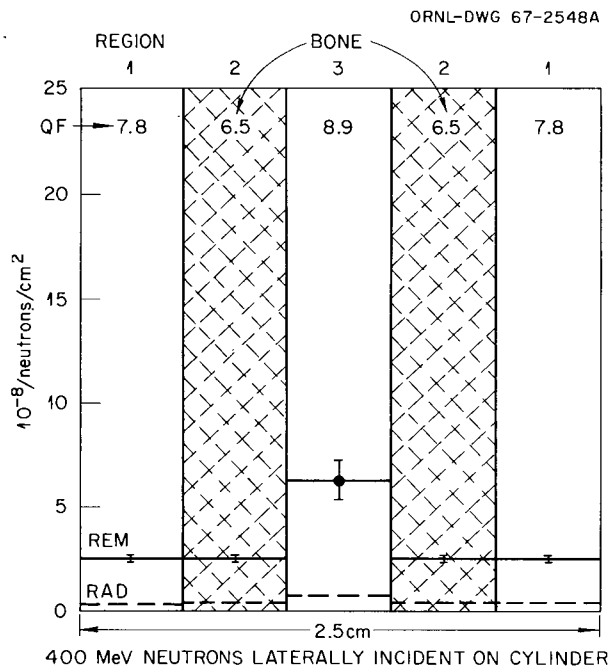

Fig. 16.11. Absorbed Dose and Dose Equivalent in Cylinder with Bone from Broad Beam of Laterally Incident 400-Mev Neutrons. The spread in rem values wos that obtained from two calculations, each using 10,000 incident neutrons.

HIGH-ENERGY DOSIMETRY

Studies of the passage of high-energy nucleons through multiregion phantoms, consisting of soft tissue and bone parts, have been made for protons and neutrons with energies up through 400 Mev. These studies employ the Monte Carlo method previously described[42] for nucleon interaction and transport. Both large and small phantoms have been used. The presence of bone in a target irradiated by protons appears to make little difference in the dose equivalent in different regions. In contrast, when the target is irradiated by neutrons the dose equivalent in bone appears to be affected when compared with that in neighboring regions of soft tissue. Figure 16.10 shows a cylinder approximately the size of a limb of a small primate. When irradiated laterally by a broad beam of 400-Mev neutrons, the average values of dose and dose equivalent in the three regions indicated are shown in Fig. 16.11. The quality factor QF given in each region is the ratio of the dose equivalent and the absorbed dose in that region. It appears that the QF in the bone is substantially lower than that in the two soft tissue parts. Possible reasons for this behavior have not yet been fully analyzed. Additional details are given elsewhere.[43]

[42] J. E. Turner *et al.*, *Health Phys.* 10, 783 (1964).

[43] J. E. Turner *et al.*, "Dose from High Energy Radiations in an Interface Between Two Media," AEC Symposium on Biological Interpretation of Dose from Accelerator-Produced Radiation, Berkeley, California, Mar. 13–16, 1967.

17. Interaction of Radiation with Liquids and Solids

E. T. Arakawa R. D. Birkhoff

Ada E. Carter
J. G. Carter
L. C. Emerson
F. W. Garber[1]
J. A. Harter
J. D. Hayes[2]
A. G. Kenerly[3]
R. A. MacRae[4]
W. J. McConnell
M. Y. Nakai[5]
S. J. Nalley[6]
Margaret S. Riedinger[2]
Linda R. Painter[2]
J. C. Sutherland[1]
L. H. Toburen[1]
R. C. Vehse[2]
Mary W. Williams[4]
E. K. Yeargers[7]

PHOTON EXCITATION OF SURFACE PLASMONS: ANALYSIS OF ALUMINUM DATA

Data on the normal-incidence reflectance of aluminum films in the wavelength region 800 to 2000 A have been reported previously.[8] Evidence was seen of a mode of absorption around 1250 A (10 ev), which we have now attempted to analyze.

Reflectance data for oxide-free aluminum in the energy range 0 to 22 ev are presented in Fig. 17.1. Ehrenreich *et al.*[9] give an interpretation in terms of an interband transition at 1.5 ev and a volume plasma resonance at 15.2 ev but do not interpret the minimum[8–12] in the region of 10 ev.

The energy-dependent refractive index, $n(E)$, and the extinction coefficient, $k(E)$, were obtained by Kramers-Kronig analysis of the reflectance vs energy as outlined by Ehrenreich *et al.*[9] The real and imaginary parts of the dielectric constant, $\epsilon(E) = \epsilon_1(E) + i\,\epsilon_2(E)$, were then calculated from $\epsilon_1(E) = n^2 - k^2$ and $\epsilon_2(E) = 2nk$. These values of ϵ_1 and ϵ_2 yield the energy-loss function $-\mathrm{Im}\,[\,1/(\epsilon + 1)\,]$, which is plotted as a function of energy in Fig. 17.2. This function[13] describes the probability that fast electrons traversing the material will lose energy due to induced surface collective electron oscillations. Ritchie predicts that this surface plasma loss should occur at $E_p/\sqrt{2}$ for a plane film, where E_p is the observed volume plasma loss. In aluminum[9] the volume plasma loss occurs at 15.2 ev, and thus the surface plasma loss should occur at 10.7 ev. A sharp maximum in the energy-loss function for surface plasmons is seen to occur at 10.7 ev as predicted.

Ritchie[14] has made a theoretical estimate of the probability that a photon incident normally on a thick metal foil will be absorbed in a second-order process in which a surface plasmon is excited through the intermediary of an intraband electronic transition. This probability increases linearly with photon energy, E, above its threshold at the surface-plasmon energy. Thus if surface plasmons are excited by incident photons, there should be a corresponding decrease in the reflectance, ΔR, given in aluminum by $\Delta R \cong 8 \times 10^{-4}(E - 10.7)$

[1]Oak Ridge Graduate Fellow.

[2]USAEC Special Health Physics Fellow.

[3]On loan from Instrumentation and Controls Division.

[4]Consultant.

[5]On loan from Thermonuclear Division.

[6]U. S. Public Health Service Fellow.

[7]Postdoctoral Fellow.

[8]E. T. Arakawa *et al.*, *Health Phys. Div. Ann. Progr. Rept. July 31, 1966*, ORNL-4007, pp. 150–51.

[9]H. Ehrenreich, H. R. Philipp, and B. Segall, *Phys. Rev.* **132**, 1918 (1963).

[10]R. P. Madden, L. R. Canfield, and G. Hass, *J. Opt. Soc. Am.* **53**, 620 (1963).

[11]W. R. Hunter, *J. Phys. Radium* **25**, 154 (1964).

[12]R. C. Vehse, E. T. Arakawa, and J. L. Stanford, *J. Opt. Soc. Am.* **57**, 551 (1967).

[13]R. H. Ritchie, *Phys. Rev.* **106**, 874 (1957).

[14]R. H. Ritchie, *Surface Sci.* **3**, 497 (1965).

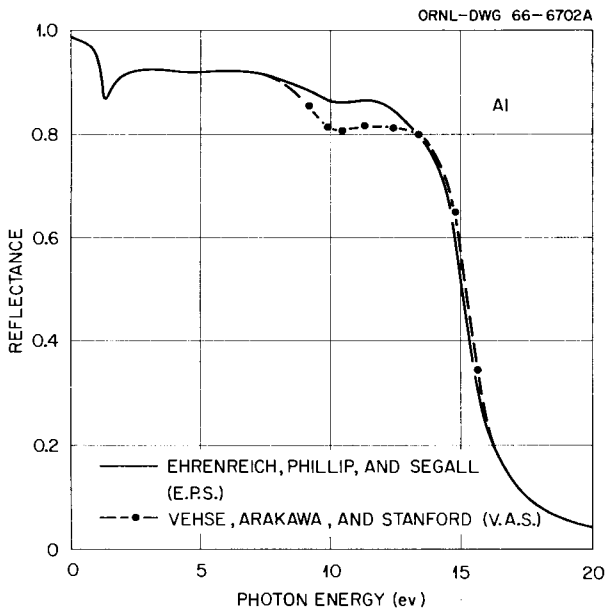

Fig. 17.1. Reflectance of Vacuum-Evaporated Al vs Photon Energy. E. P. S. data are from ref. 9 and V. A. S. from refs. 8 and 12.

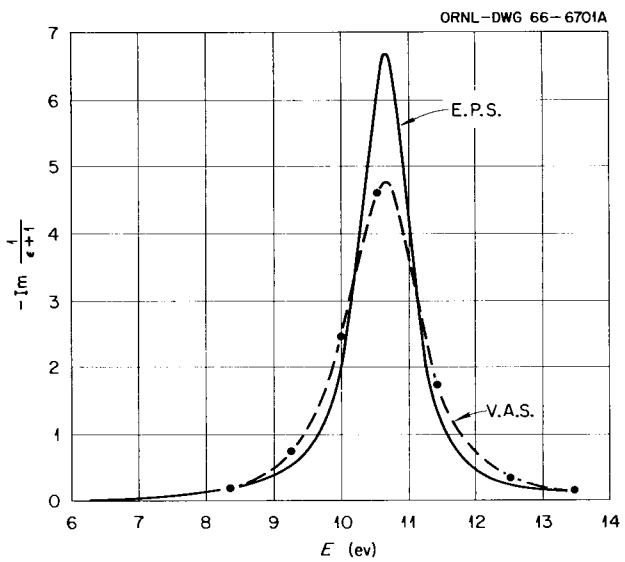

Fig. 17.2. The Energy Loss Function $-\mathrm{Im}[1/(\epsilon+1)]$ for Surface Plasmons in Al.

with E in electron volts. It is seen by examination of Fig. 17.1 that optical surface plasma resonance absorption may occur, but Ritchie's expression for ΔR does not account for all of the observed structure in the reflectance data in the region of 10 ev. Another possible cause of a decrease of reflectance in this energy region is photon-induced interband transitions. It has been shown[9,15] that $\epsilon(E)$ can be represented as the sum of a free-electron contribution $\epsilon^{(f)}(E)$ and a contribution due to bound electrons $\delta\epsilon^{(b)}(E)$. Thus

$$\epsilon_2(\exp) = \epsilon_2^{(f)}(E) + \delta\epsilon_2^{(b)}(E)$$

$$= \frac{\hbar}{\tau E}\left[\frac{E_{pa}^2}{E^2 + (\hbar/\tau)^2}\right] + \delta\epsilon_2^{(b)}(E) \ , \quad (1)$$

where E_{pa} is the free-electron volume plasma energy and τ is the relaxation time. Figure 17.3 shows $\delta\epsilon_2^{(b)}(E)$ calculated using the experimental values of ϵ_2 in Eq. (1) and on the assumption[9] that $E_{pa} = 12.7$ ev and $\tau = 5.12 \times 10^{-15}$ sec. The value of $\delta\epsilon_2^{(b)}(E)$ contains contributions from two interband transitions: the 1.5-ev transition identified by Ehrenreich *et al.* (see Fig. 4, ref. 9) and

[15]E. T. Arakawa *et al.*, *Health Phys. Div. Ann. Progr. Rept. July 31, 1966*, ORNL-4007, pp. 153–55.

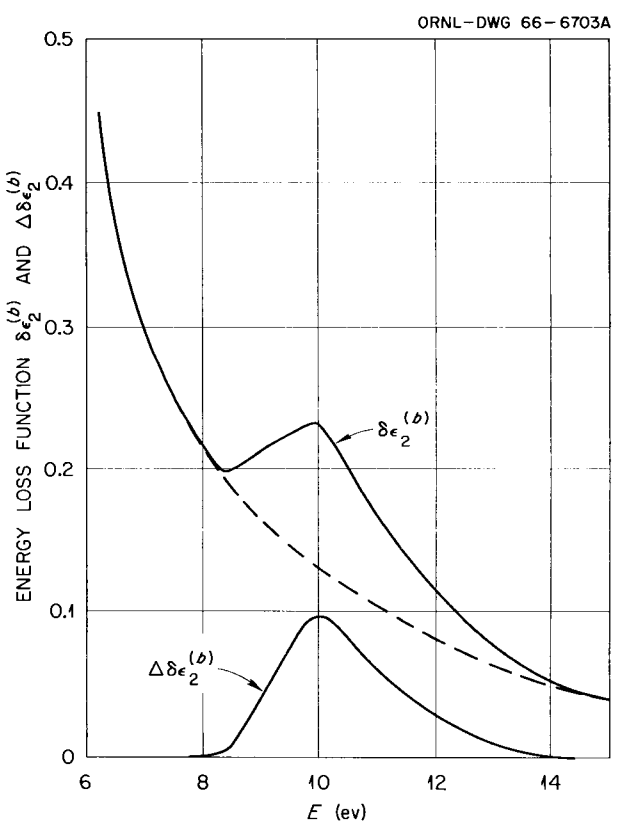

Fig. 17.3. The Total Contribution to ϵ_2 Due to Bound Electrons, $\delta\epsilon_2^{(b)}(E)$, and the Contribution $\Delta\delta\epsilon_2^{(b)}(E)$ Due to the Transition at 10.0 ev (V. A. S. Data).

a higher transition at about 10 ev. The contribution due to this higher transition has been plotted as $\Delta\delta\epsilon_2^{(b)}(E)$ in Fig. 17.3 and is seen to peak at 10.0 ev. Thus the structure in the reflectance is seen to be at least partially due to an interband transition at 10.0 ev, identified by a relative maximum[16] in ϵ_2 at this energy. The identification of this transition on an energy-band diagram is not so clear. Energy-band calculations[9] for aluminum show that interband transitions associated with critical points at the X symmetry point should occur from $X_1 \rightarrow X_{5'}$ at 7.9 ev and from $X_{4'} \rightarrow X_1$ at 12.0 ev. The present analysis leads to the conclusion that the observed interband transition at 10.0 ev may represent these two unresolved transitions. If this is so, the $X_1 \rightarrow X_{5'}$ transition would have to be higher than the 7.9 ev predicted from band calculations. Ehrenreich *et al.*[9] estimate the relative intensities of the various interband transitions. Compared with unity for the 1.5-ev transition, the value for the $X_1 \rightarrow X_{5'}$ transition is 0.008 and for the $X_{4'} \rightarrow X_1$ transition, 0.004. The experimentally obtained peak value of $\delta\epsilon_2^{(b)}$ for the 1.5-ev transition is about 40 (see Fig. 4, ref. 9), and for the 10.0-ev transition it is 0.1 (Fig. 17.3). Thus the ratio of these two quantities is 0.0025, which is of the correct order of magnitude.

We thus conclude that the photon excitation of surface plasmons, as predicted by Ritchie, may occur in aluminum. However, interband transitions in the neighborhood of 10.0 ev, in close proximity to the surface-plasmon resonance energy of 10.7 ev, mask any small variation in reflectance that would be due to this effect.

OPTICAL PROPERTIES OF CERTAIN INSULATING MATERIALS

Fundamental properties associated with a solid can be obtained from an analysis of reflectance as a function of incident photon energy. In addition, the properties of insulating materials are of interest in connection with their possible use as windows or as reflective coatings for mirrors and gratings in vacuum ultraviolet spectrometers.[17]

Reflectance measurements, shown in Figs. 17.4 and 17.5, have been made from just below the fundamental absorption edge up to 29 ev for single crystals of MgF_2 and MgO. The MgF_2 crystals were polished, and the MgO crystals cleaved in the 100 plane. For MgF_2, the measurements were made at 20, 70, and 75°, and for MgO at 15°. In addition, transmission measurements were made in the region of the fundamental absorption edge, and the reflectances shown have been corrected for multiple reflections in the transmitting regions. No previous measurements were available for MgF_2 single crystals over the whole energy range or for

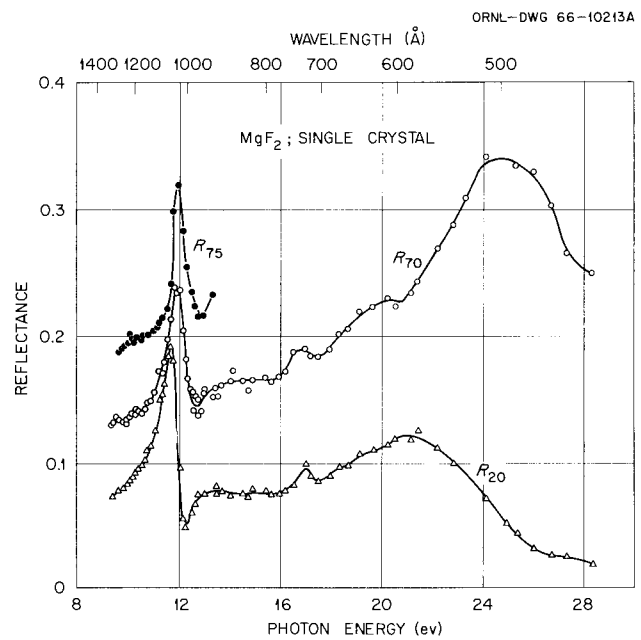

Fig. 17.4. Reflectance vs Incident Photon for MgF_2.

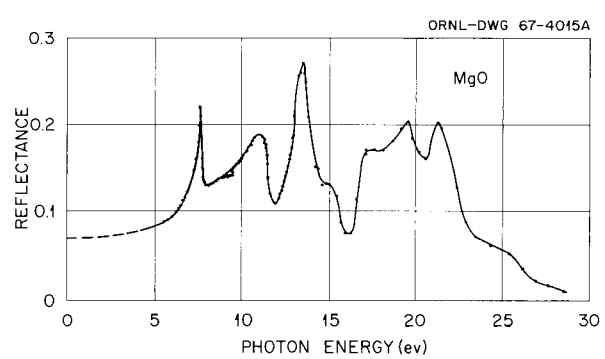

Fig. 17.5. Reflectance vs Incident Photon Energy for MgO.

[16] H. Fröhlich and H. Pelzer, *Proc. Phys. Soc. (London)* **A68**, 525 (1955).

[17] M. W. Williams, R. A. MacRae, and E. T. Arakawa, *J. Appl. Phys.* **38**, 1701 (1967).

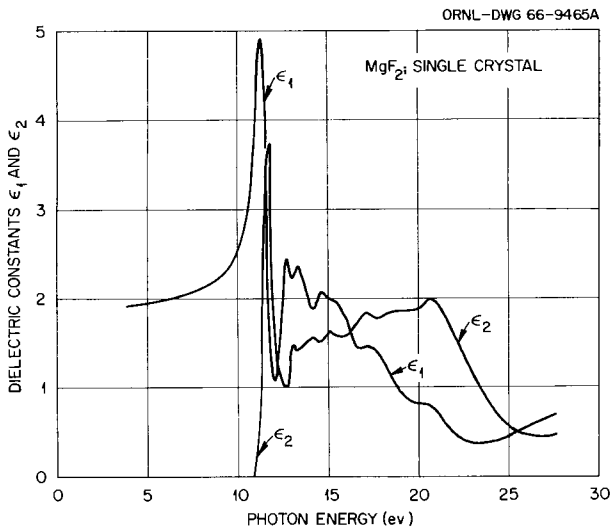

Fig. 17.6. Dielectric Constants vs Incident Photon Energy for MgF_2.

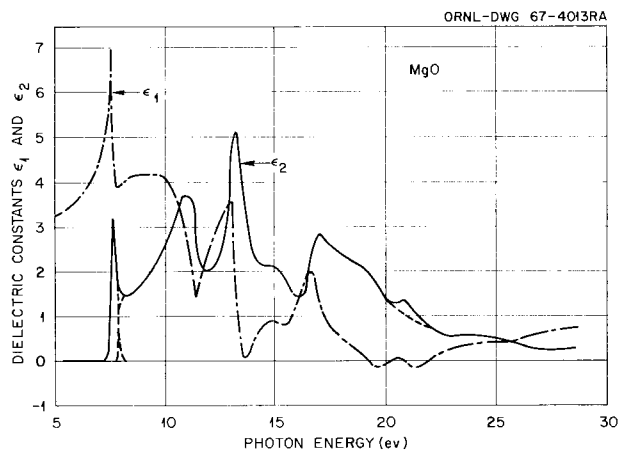

Fig. 17.7. Dielectric Constants vs Incident Photon Energy for MgO.

MgO single crystals above 14.5 ev. The real and imaginary parts, $\epsilon_1(E)$ and $\epsilon_2(E)$, respectively, of the energy-dependent complex dielectric constant $\epsilon(E)$ were obtained for MgF_2 by the two-angle method[17] and for MgO by means of a Kramers-Kronig analysis.[18] These are shown in Figs. 17.6 and 17.7. The calculated energy-loss functions $-\mathrm{Im}\,[\,\epsilon(E)+1\,]^{-1}$ and $-\mathrm{Im}\,[\,\epsilon(E)\,]^{-1}$ are shown in Figs. 17.8 and 17.9.

Structure in the ultraviolet reflectance spectra of semiconductors and insulators has been interpreted

[18]See, for example, F. C. Jahoda, *Phys. Rev.* **107**, 1261 (1957); F. Stern, p. 299 in *Solid State Physics*, vol. 15, ed. by F. Seitz and D. Turnbull, Academic, New York, 1963.

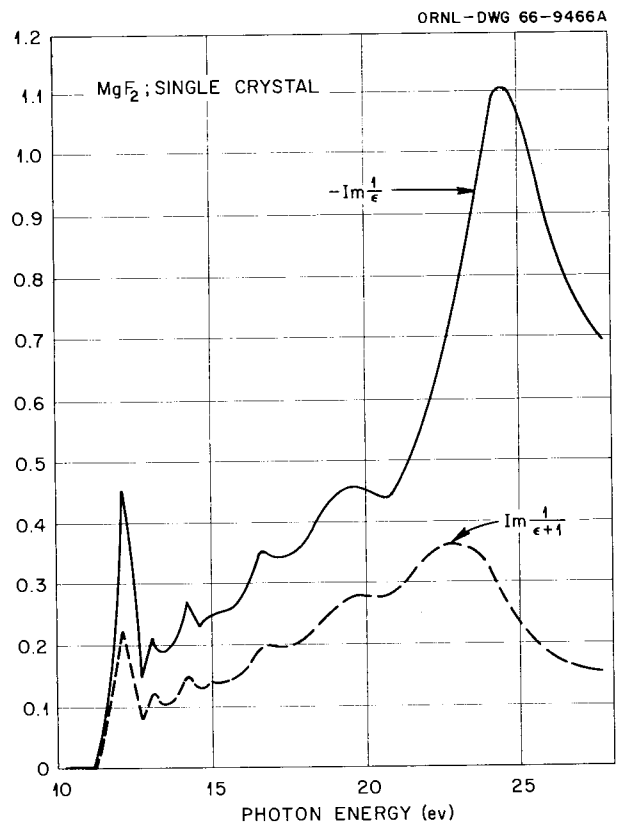

Fig. 17.8. Energy Loss Functions vs Incident Photon Energy for MgF_2.

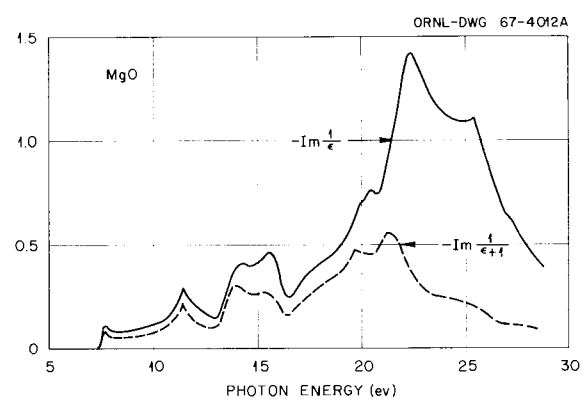

Fig. 17.9. Energy Loss Functions vs Incident Photon Energy for MgO.

mainly in terms of excitons, interband transitions, and volume plasma resonances.[17] Single-electron transitions are characterized[16] by peaks in ϵ_2, whereas collective oscillations, or plasma resonances, are characterized by prominent peaks in the loss functions unassociated with structure in

ϵ_2. We have identified the sharp oscillator-like structure in ϵ_2 at 11.8 ev for MgF_2 and at 7.65 ev for MgO with excitons and the broader peaks at 20.8 ev for MgF_2 and at 11.0, 13.3, 17.3, and 20.9 ev for MgO with interband transitions. The exciton peak in both cases obscures the edge for band-to-band transitions, which we have estimated to be at about 13 ev in MgF_2 and at 7.9 ev in MgO.

The energy-loss functions $-\mathrm{Im}\,(\epsilon+1)^{-1}$ and $-\mathrm{Im}\,(\epsilon)^{-1}$ describe the probability that fast electrons traversing the material will lose energy by inducing surface and volume collective electron oscillations respectively.[13] In a free-electron gas, with $\epsilon_2 \sim 0$, $-\mathrm{Im}\,(\epsilon)^{-1}$ has a maximum at the plasma energy E_p, given by

$$E_p = \hbar(4\pi N n e^2/m_{\mathrm{eff}})^{1/2}\,, \qquad (2)$$

where N is the number of molecules per unit volume, m_{eff} the effective mass of the electrons, and n the number of electrons per molecule that would participate in volume plasma oscillations induced by fast electrons traversing the material. For insulators, such as MgF_2 and MgO in the energy range covered by these observations, Nn is the particle density in the filled valence band. Furthermore, we can assume m_{eff} is the free-electron mass.[19] The total number of valence electrons per MgF_2 molecule is 16. Equation (2) with $n = 16$ and m_{eff} made equal to the free-electron mass yields a calculated free-electron plasma energy of 25.8 ev. The observed maximum in $-\mathrm{Im}\,(\epsilon)^{-1}$ is seen in Fig. 17.8 to be at 24.5 ev. This plasma resonance involves all 16 valence electrons per MgF_2 molecule, but is shifted from the free-electron value because of the presence of interband transitions. Similarly in MgO, maxima are seen in $-\mathrm{Im}\,(\epsilon)^{-1}$ at 22.4 and 25.4 ev (Fig. 17.9), corresponding to plasma resonances involving 6 and 8 valence electrons per MgO molecule respectively. These values are shifted from the free-electron values of 21 and 24 ev, respectively, due to interband transitions.

In view of the fact that the behavior is not free-electron-like in the vicinity of the plasma resonances, the closeness of the observed resonances to the values calculated from Eq. (2) may seem surprising. However, this is explained by use of

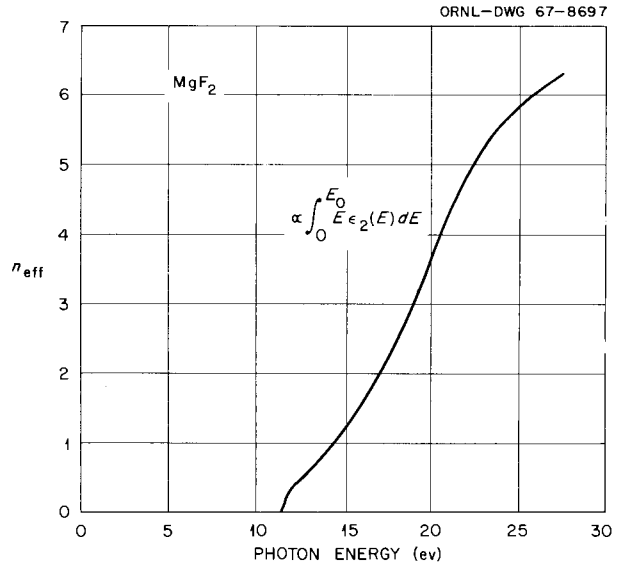

Fig. 17.10. Effective Numbers of Electrons per Molecule vs Incident Photon Energy Obtained by Numerical Integration of the Experimental Value of ϵ_2 for MgF_2.

the sum rule[20]

$$\int_0^{E_0} E\;\epsilon_2(E)\;dE = \frac{2\hbar^2\pi^2 N e^2}{m_{\mathrm{eff}}}\;n_{\mathrm{eff}}\,. \qquad (3)$$

Equation (3) yields an $n_{\mathrm{eff}}(E_0)$ that is the effective number of electrons per molecule contributing to optical transitions in the energy range up to E_0. Values of $n_{\mathrm{eff}}(E_0)$ are plotted in Figs. 17.10 and 17.11 and should saturate at the number of valence electrons per molecule: 16 for MgF_2 and 8 for MgO. The fact that $n_{\mathrm{eff}}(E_0)$ does not saturate at these values means that the oscillator strengths have not been completely exhausted even at 29 ev. This means that for both MgF_2 and MgO an interband transition, or transitions, above 29 ev must involve valence electrons and contribute to the sum rules. Interband transitions below the free-electron plasma energy raise the observed value of the volume plasma energy above the free-electron value, while interband transitions above the free-electron plasma energy lower the observed value of the plasma energy.[21] For MgF_2,

[19] H. R. Philipp and H. Ehrenreich, *Phys. Rev.* **129**, 1550 (1963).

[20] See, for example, H. Ehrenreich, H. R. Philipp, and B. Segall, *Phys. Rev.* **132**, 1918 (1963); P. Nozieres and D. Pines, *Phys. Rev.* **113**, 1254 (1959).

[21] H. Raether, *Springer Tracts Mod. Phys.* **38**, 84 (1965).

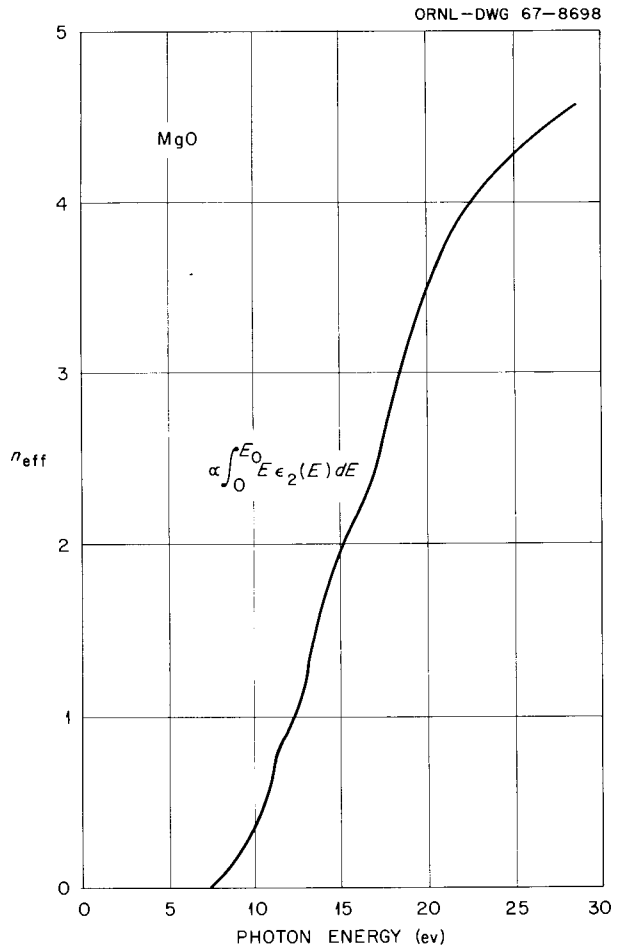

Fig. 17.11. Effective Numbers of Electrons per Molecules vs Incident Photon Energy Obtained by Numerical Integration of the Experimental Value of ϵ_2 for MgO.

the value of $n_{eff}(E_0)$ in Fig. 17.10 at 25.8 ev (the value of the free-electron plasma energy) is 6, which is less than half the saturation value of 16. This explains why the observed plasma energy of 24.5 ev is less than the free-electron value. Similar inspection of Fig. 17.11 for MgO explains why the observed plasma energies are slightly higher than the free-electron values.

Finally, there are no characteristic electron-energy-loss measurements available for MgF_2, but those for MgO[22] show losses that agree well with our predicted values. In fact, it is possible to identify unambiguously the characteristic electron energy losses as due to single-electron transitions or to collective losses by means of our optical data.

[22]C. J. Powell and J. B. Swan, *Phys. Rev.* **118**, 640 (1960).

A NEW METHOD OF KRAMERS-KRONIG ANALYSIS

Reflectance measurements, $R(E)$, at near-normal incidence can be interpreted by means of a Kramers-Kronig analysis to yield the real and imaginary parts of the energy-dependent complex refractive index, $N(E) = n(E) - i\,k(E)$. Assuming that the complex reflectance amplitude $\tilde{r}(E) = r(E)\,e^{i\,\theta(E)}$, where $|r(E)|^2 = R(E)$ and the phase change on reflection, $\theta(E)$, is restricted to $-\pi < \theta(E) < 0$, then

$$\theta(E) = \frac{E}{\pi}\int_0^{\infty} \frac{\ln R(E')}{(E')^2 - E^2}\,dE' . \qquad (4)$$

Then $\theta(E)$ and $R(E)$ yield $n(E)$ and $k(E)$ from

$$n = (1 - r^2)/(1 + r^2 - 2r\cos\theta)$$

and (5)

$$k = (-2r\sin\theta)/(1 + r^2 - 2r\cos\theta) .$$

The main difficulty with this method is that the integral in Eq. (4) must be performed over the whole energy spectrum, whereas, experimentally, the reflectance is only known over a limited range. The method usually used[18] is to make some reasonable smooth extrapolations in the energy regions outside the experimental region. Assuming that the values of $n(E_0)$ and $k(E_0)$ are known from independent experiments for some energy E_0 (usually in the low-energy region), the upper limit of the integration in Eq. (4) is adjusted so that Eqs. (5) then yield the correct values of $n(E_0)$ and $k(E_0)$. However, the form used for the extrapolation to high energies can influence considerably the values obtained for $n(E)$ and $k(E)$ within the experimental region ($E \neq E_0$).

We consider that the following method overcomes this difficulty when $n(E)$ and $k(E)$ are known in two separate energy ranges and are to be calculated in the intermediate energy range.

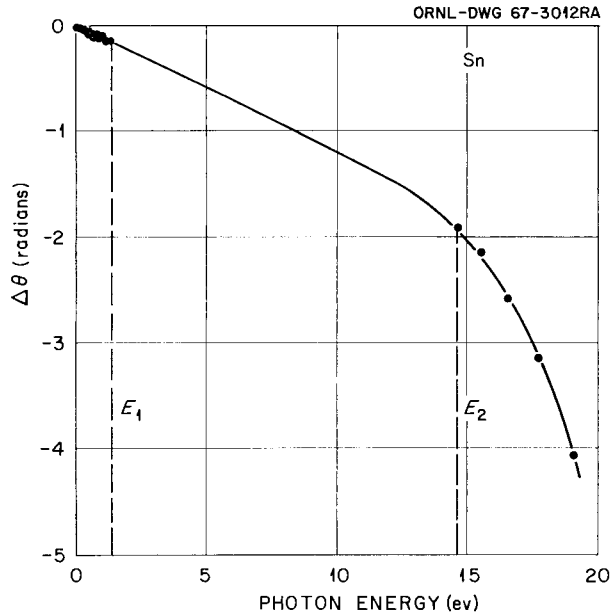

Fig. 17.12. Contribution to the Phase Angle Due to Absorption Above E_m (20.5 ev) for White Tin As a Function of Incident Photon Energy (x, Calculated Values).

When $n(E)$ and $k(E)$ are known, $\theta(E)$ can be calculated from

$$\theta(E) = \tan^{-1} 2k/(1 - n^2 - k^2) \; ; \qquad (6)$$

$\theta(E)$ can also be written, according to Eq. (4), as

$$\theta(E) = \frac{E}{\pi}\int_0^{E_m} \frac{\ln R(E')}{(E')^2 - E^2}\, dE' + \frac{E}{\pi}\int_{E_m}^{\infty} \frac{\ln R(E')}{(E')^2 - E^2}\, dE' , \qquad (7)$$

where E_m is the maximum energy for which reflectance has been measured. The integral from 0 to E_m can be calculated from the known reflectance together with a low-energy extrapolation, which usually extends over a very small energy range. Hence, in the energy region where $\theta(E)$ is known from Eq. (6), the integral from E_m to infinite energy can be calculated from Eq. (7). Values of this second integral, calculated in this way for white tin,[23] are plotted as $\Delta\theta$ in Fig. 17.12 from 0 to the energy E_1 and from E_2 to E_m, which are the energy regions where independent values of $n(E)$ and $k(E)$ are known for tin; $\Delta\theta$ is the contribution to the phase change on reflection due to absorption in the energy region above E_m and should be a smoothly varying function of the energy within the experimental range. Thus $\Delta\theta$ is interpolated in the intermediate energy range from E_1 to E_2 by a smoothly varying function as shown by the curve in Fig. 17.12. Knowing $\Delta\theta(E)$ in the intermediate energy range, $\theta(E)$ can be obtained from Eq. (7), and hence $n(E)$ and $k(E)$ from Eqs. (5).

[23]R. A. MacRae, E. T. Arakawa, and M. W. Williams, "Optical Properties of Vacuum-Evaporated White Tin," to be published in the *Physical Review*.

OPTICAL PROPERTIES OF EVAPORATED FILMS OF AMORPHOUS SELENIUM

The optical constants $n(E)$ and $k(E)$ have been determined from reflectance measurements in the energy region between 5 and 27 ev for films of amorphous selenium evaporated in situ. The optical constants are shown in Fig. 17.13. The real and imaginary parts of the complex energy-dependent dielectric constant, $\epsilon(E) = \epsilon_1(E) + i\,\epsilon_2(E)$, and the charged-particle energy-loss functions, $-\mathrm{Im}\,(\epsilon)^{-1}$ and $-\mathrm{Im}\,(\epsilon + 1)^{-1}$, have been calculated from the constants $n(E)$ and $k(E)$. These are shown in Figs. 17.14 and 17.15.

A peak in $\epsilon_2(E)$ at 8.25 ev is attributed to interband transitions. The volume loss function has maxima at 5.25 and 18.8 ev. These maxima agree well with the characteristic electron energy loss

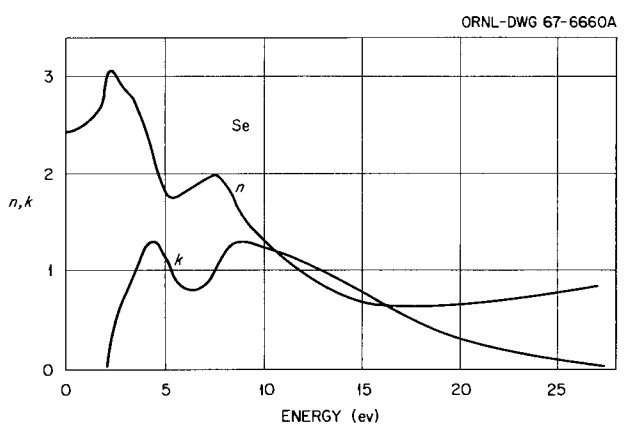

Fig. 17.13. Optical Constants of Selenium.

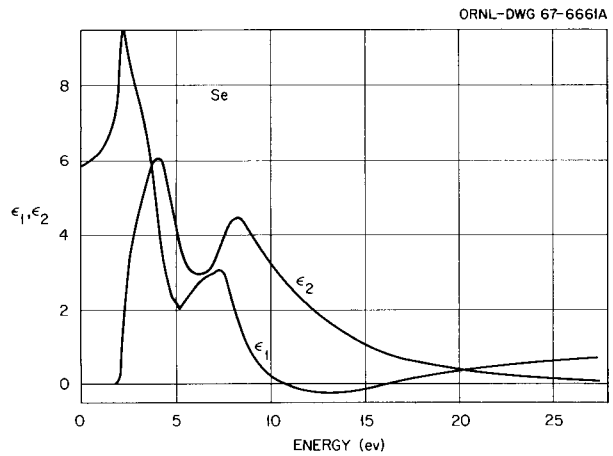

Fig. 17.14. Dielectric Constants of Selenium.

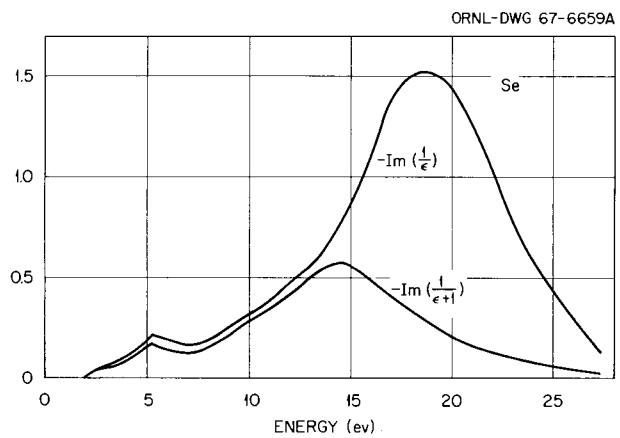

Fig. 17.15. Energy Loss Function for Selenium.

data of Robins.[24] We attribute the loss at 5.25 ev to volume plasma oscillations involving the electrons in the uppermost valence band and the loss at 18.8 ev to volume plasma oscillations involving all six valence electrons.

A similar analysis is being carried out for evaporated films of tellurium.

REFRACTIVE INDEX OF POTASSIUM

The refractive index of metallic potassium was measured for photon energies from 3.96 to 8.30 ev by the critical-angle method. Potassium films were

[24] J. L. Robins, *Proc. Phys. Soc. (London)* **79**, 119 (1962).

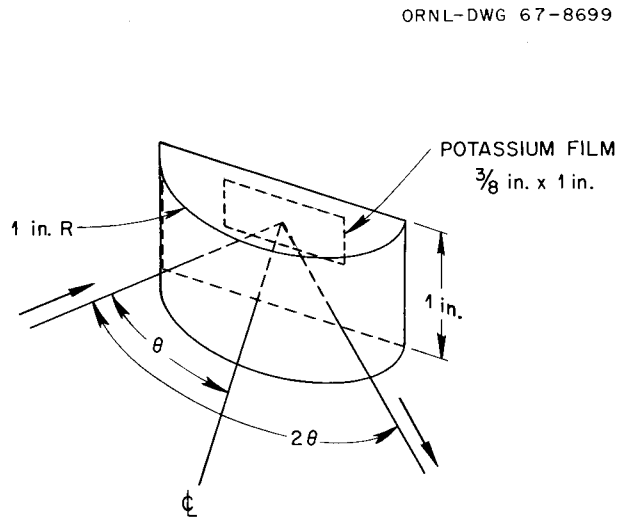

Fig. 17.16. Hemicylinder Showing Position of the Potassium Film and Path of the Beam as It Enters the Hemicylinder and Is Reflected from the Film.

deposited in situ by thermal evaporation on the flat surface of a quartz or calcium fluoride hemicylinder as shown in Fig. 17.16. The hemicylindrical shape was chosen because the beam enters and leaves normal to the curved surface. Thus the angle θ is not affected by refraction. Also, losses due to the reflections at the curved surface and absorption inside the hemicylinder are the same for all angles θ.

The refractive index of the hemicylinder, designated by $n(\mathrm{hc})$, was found by measuring the reflectance of the hemicylinder-vacuum interface from the hemicylinder side as a function of θ. Since $n(\mathrm{hc})$ is greater than 1.0, this is a dense-to-rare reflection, and there is a critical angle $\theta_c(\mathrm{hc{:}vac})$ marking the start of the region of total reflection as shown in Fig. 17.17. The slope of the reflectance curve is discontinuous at the critical angle, and

$$n(\mathrm{hc}) = [\sin \theta_c(\mathrm{hc{:}vac})]^{-1} . \qquad (8)$$

For photon energies greater than the plasma energy of potassium, the extinction coefficient of potassium is small, and the refractive index of potassium is less than 1.0. Thus the reflectance of the hemicylinder-potassium interface is also dense-to-rare and resembles the situation described above. The finite extinction coefficient of the metal removes the discontinuity in the slope of the reflectance (see Fig. 17.17), but if the extinction

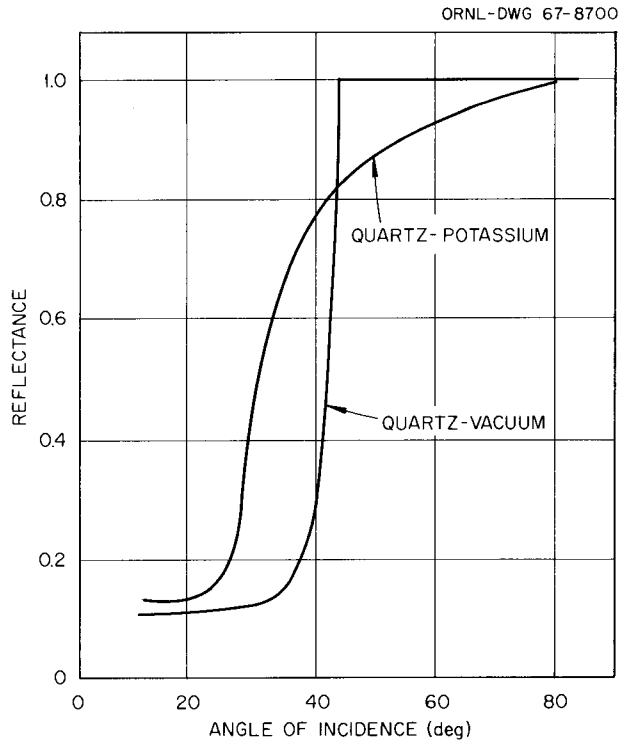

Fig. 17.17. Reflectance of Quartz:Vacuum and Quartz:Patassium Interfaces Measured Through the Hemicylinder with 2537-A Radiation.

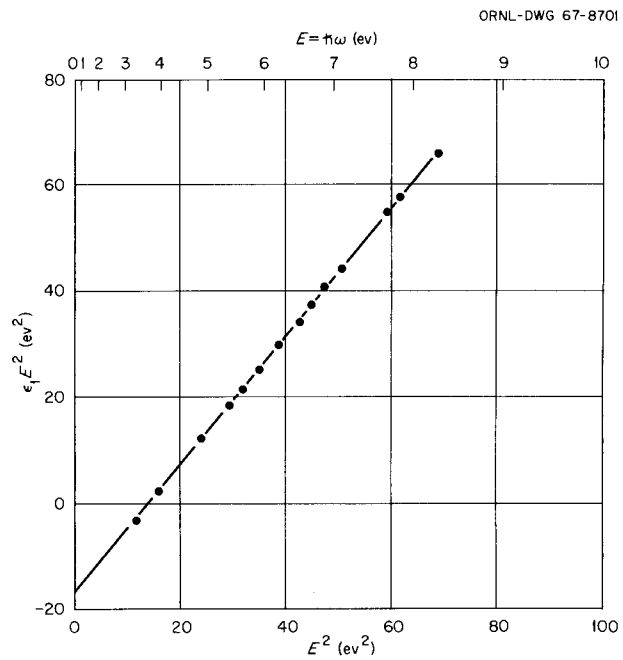

Fig. 17.18. $\epsilon_1 E^2$ vs E^2. The line fitted to the experimental data is used to calculate the plasma energy, ion-core polarization, and optical-effective mass of the conduction band electrons of potassium.

coefficient is small, the critical angle can be replaced by the angle for which the slope of the reflectance is a maximum, θ_m.[25] The refractive index of the metal is given by

$$n(\mathrm{K}) = n(\mathrm{hc}) \sin \theta_m(\mathrm{hc{:}K}) \ . \tag{9}$$

Critical-angle measurements made on the vacuum surface of the metal film give values of $n(\mathrm{K})$ in agreement with the values determined from Eq. (9). The vacuum surface of a reactive metal like potassium is oxidized slightly in a few seconds after the film is deposited. Thus it was shown experimentally that the critical-angle method is unaffected by oxidation of the surface of the metal being investigated.

The extinction coefficient of potassium is very small in the metal's transparent region, and thus ϵ_1, the real part of the complex dielectric constant, is to a good approximation equal to n^2. According to the nearly-free-electron model,

$$\epsilon_1 = A - B/E^2 \ , \tag{10}$$

where E $(=\hbar\omega)$ is the energy of the incident photons. Arakawa *et al.*[26] have pointed out that the ability of the nearly-free-electron model to describe the optical properties of a given metal can be tested by plotting the experimental values of $\epsilon_1 E^2$ as a function of E^2. If the experimental points lie on a straight line, the nearly-free-electron model is adequate, since Eq. (10) may be rewritten

$$\epsilon_1 E^2 = AE^2 - B \ . \tag{11}$$

The experimental values of $\epsilon_1 E^2$ are shown as a function of E^2 in Fig. 17.18. The points lie on a straight line and thus indicate the adequacy of the simple model for this metal. The solid line was fitted to the experimental points by the method of least squares. The plasma energy of potassium was found from the intersection of the line and the

[25] W. R. Hunter, *J. Opt. Soc. Am.* **54**, 15 (1964).

[26] E. T. Arakawa, R. N. Hamm, W. F. Hanson, and T. M. Jelinek, pp. 374–85 in *Optical Properties and Electronic Structure of Metals and Alloys, Proc. Intern. Colloq., Paris, Sept. 1965*, ed. by F. Abeles, North-Holland, Amsterdam, 1966.

abscissa to be 3.74 ev. The intersection of the line and the ordinate was used to determine the optical effective mass of the conduction electrons to be 1.1 times the rest mass of a free electron. Finally, the slope of the line gave the ion-core polarization of potassium to be 0.2.

MEASUREMENT OF OPTICAL PROPERTIES AT LONG WAVELENGTHS

The method routinely used to determine optical properties of solids in the vacuum ultraviolet spectral region involves the analysis of reflectance data obtained at several angles of incidence.[27] However, at wavelengths longer than about 3500 A the small difference in reflectance, for metals in particular, leads to large uncertainties in the determination of the optical constants n and k.

To circumvent this difficulty, an apparatus was constructed to permit direct measurements of the optical constants by analysis of the ellipticity of the light reflected from a flat surface. The surface under study is prepared within an ultrahigh vacuum chamber held at a pressure of 1 to 2×10^{-9} torr. The maintenance of this low pressure throughout the study prevents the growth of surface films that would otherwise introduce errors in the measurements.

The initial studies using this apparatus have been carried out with palladium samples. The values found for n and k are shown in Fig. 17.19. The data for between 3500 and 6500 A were obtained using a standard photomultiplier with an S-II response. A lead sulfide detector was used to obtain the data at wavelengths longer than 8800 A. For comparison, the measurements obtained by Lostis[28] also are shown. The measurements obtained at ORNL are consistently higher than those of Lostis throughout the entire wavelength region.

Further studies are now being carried out using a photomultiplier with an improved infrared response in an effort to include the region between 6500 and 8800 A.

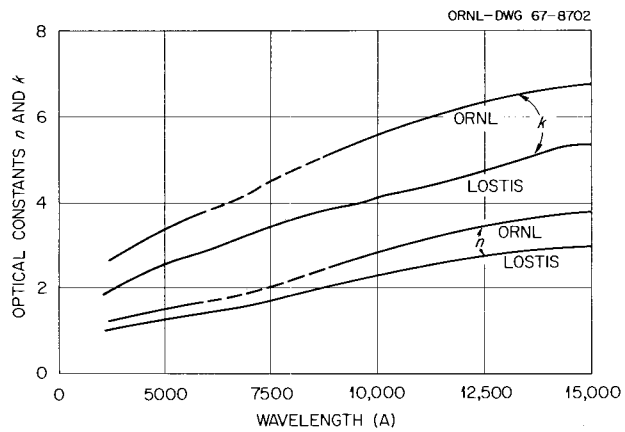

Fig. 17.19. Optical Properties of Palladium Between 3500 and 15,000 A.

AN ANGLE DOUBLER FOR REFLECTANCE MEASUREMENTS IN EVACUATED SYSTEMS

The measurement of the optical reflectance from a planar sample as a function of the angle of incidence has proved to be a very useful method for the determination of the optical constants of solids in the vacuum ultraviolet.[29] If a continuous scan of reflectance vs angle of incidence is desirable, as in the critical-angle method[25] for the determination of the index of refraction, an angle-doubling technique is required to move the detector at twice the angular velocity of the sample. For work in the vacuum ultraviolet, it would be desirable to be able to align the angle doubler external to the vacuum system in the wavelength region to be used. An angle doubler of a new design, shown schematically in Fig. 17.20, meets this requirement and has the added feature not found in existing models[30,31] that full 360° rotation is possible.

The shafts that support the photomultiplier and sample holder are connected to a common external shaft by toothed polyurethane timing belts and toothed pulleys supplied by Precision Instrument

[27] R. D. Birkhoff *et al.*, *Health Phys. Div. Ann. Progr. Rept. July 31, 1964*, ORNL-3697, p. 139.

[28] P. Lostis, *J. Phys. (Paris)* **25**, 118 (1964).

[29] O. S. Heavens, *Physics of Thin Films*, vol. 2, ed. by G. Hass and R. E. Thun, Academic, New York, 1964.

[30] G. Hass, W. R. Hunter, and R. Tousey, *J. Opt. Soc. Am.* **46**, 1009 (1956).

[31] R. P. Madden and L. R. Canfield, *J. Opt. Soc. Am.* **51**, 838 (1961).

ORNL-DWG 66-12108

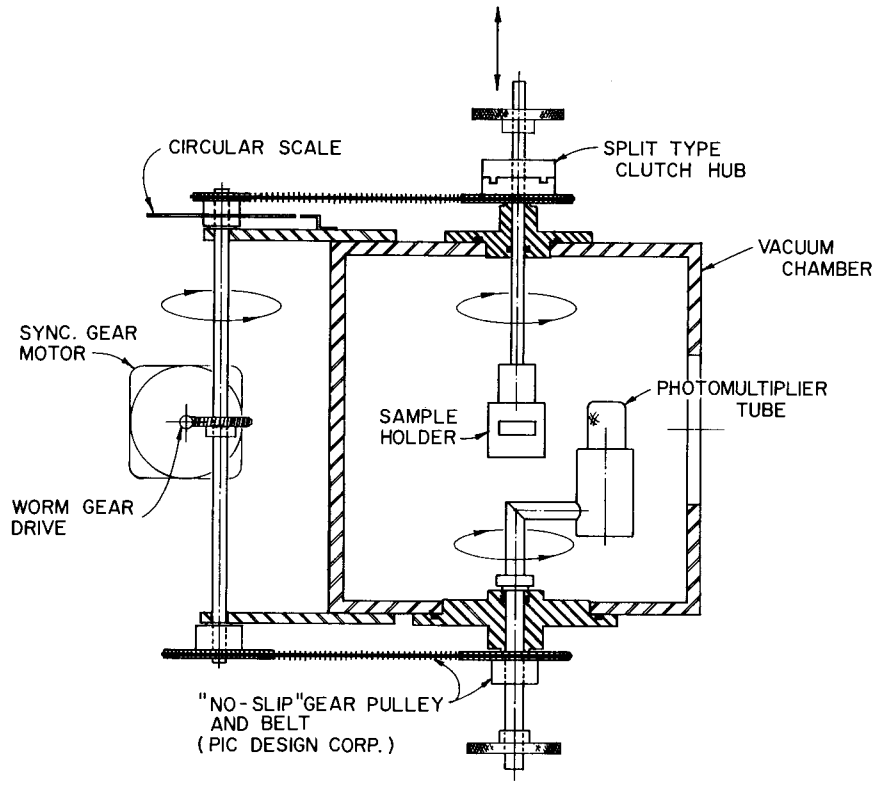

Fig. 17.20. Schematic Diagram of Reflectance Chamber and Angle Doubler.

Corporation, East Rockaway, L. I., New York 11518. The external shaft is driven by a five-speed synchronous motor, and the sample-holder shaft is connected to its pulley by a split-type clutch hub to facilitate withdrawal of the sample from the incident beam. The angle at which radiation is incident on the sample can be read within ±0.25° from a vernier scale mounted on the external shaft. In use, the angular velocity of the detector is maintained at twice that of the sample holder with no apparent backlash.

The effectiveness of the angle doubler is illustrated in Fig. 17.21, where the tracing of a chart-recorder plot shows the reflectance from the quartz-vacuum interface of a Suprasil-quartz hemicylinder as a function of incident angle (the sign of the angle denotes the left-right horizontal position of the reflected beam with respect to the incident-beam direction in the plane of incidence). The incident beam passes through the curved surface of the hemicylinder, is reflected at the quartz-vacuum interface, and emerges from the photomultiplier. Thus the optical path length within the quartz and the reflectances at the curved surface are independent of the angle of incidence.

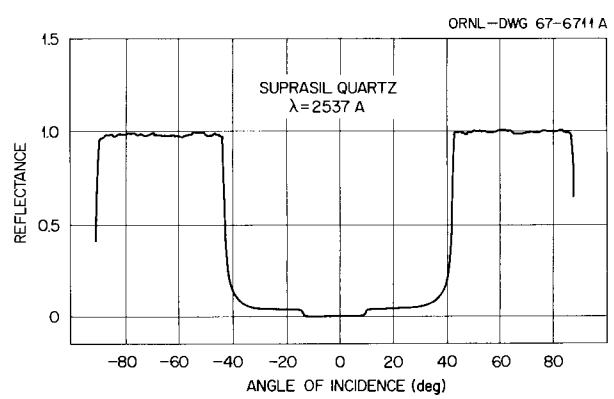

Fig. 17.21. Reflectance of 2357-A Radiation from a Quartz-Vacuum Interface Measured as a Function of Angle of Incidence.

The radiation used in the example is the emission from mercury at 2537 A, and from the figure we see that the critical angle is reached at 43°; thus the index of refraction for Suprasil quartz at this wavelength is 1.467, the reciprocal of the sine of the critical angle. Good alignment and proper adjustment of the angle doubler are reflected in the symmetry of the plot with respect to the position of normal incidence and the flatness of the portions of the plot for angles of incidence greater than the critical angle, for which the reflectance is expected to be 100%. Finally, the reader will note that the effective range of operation of the angle doubler covers angles of incidence from 13 to 87°. The large-angle cutoff occurs when the effective sample area becomes smaller than the incident beam, and the low-angle cutoff occurs when the photomultiplier-tube housing intercepts the beam. The low-angle cutoff points will not necessarily lie at symmetrical points with respect to normal incidence unless the sensitive portion of the phototube is precisely centered along the geometrical axis of the housing.

PHOTOEMISSION MEASUREMENTS FOR SILVER, PALLADIUM, AND NICKEL IN THE VACUUM ULTRAVIOLET

It has been suggested recently[32] that an "anomalous" peak appearing in the density of electronic states of nickel and cobalt is related to the ferromagnetism of the 3*d* transition metals. The method of determining density of states from photoemission measurements as developed by Berglund and Spicer [33,34] is dominated by the energy distribution of photoelectrons that emerge from the metal surface for a given incident photon energy. In the case of nickel and cobalt, Yu and Spicer have observed a strong peak in the electron energy distribution curves for incident-photon energies up to 10.2 ev that corresponds to the "anomalous" structure at about 5 ev below the Fermi level in the density of states; however, no such structure was found in palladium. We have extended these measurements for photon energies up to 22.4 ev for nickel and palladium and have correlated these results with previous results on silver.[35] These data reveal structure in the photoelectron energy distribution curves that suggests that the excited photoelectrons, emerging from within the metal, suffer losses of discrete amounts of energy prior to emission.

Samples were prepared by the rapid evaporation of high-purity nickel or palladium wire from a two- or three-strand helical tungsten filament onto a clean glass microscope slide. Evaporation took place in vacua of about 6×10^{-9} torr, and the film thicknesses ranged from 1500 to 2500 A. The sample was electrically connected to a Keithley model 409 picoammeter in order that the photoelectric currents could be measured. The energies of the emitted electrons were measured by a retarding-voltage technique using cylindrical symmetry for the collector, and the distributions were obtained by the direct graphical measurement of the photoelectron-current curve plotted continuously as a function of the scanning retarding potential. It was possible to achieve sufficient stability in the electronic system to obtain an energy resolution of the order of 0.5 ev.

The families of photoelectron energy distributions for silver, palladium, and nickel are shown in Figs. 17.22 to 17.24. Each curve represents the average behavior of at least three samples prepared under identical conditions. The curves are plotted so that the energy scale is relative to the Fermi level E_F and represents the energy state from which the electron is emitted; that is, $E^* = E - h\nu + \phi$, where E is the energy of the emitted electron, $h\nu$ is the energy of the incident photon, and ϕ is the work function, taken to be 4.7 ev, 4.2 ev, and 4.6 ev for silver, palladium, and nickel respectively. In silver (Fig. 17.22), the sharp peak arising from the *d*-band electrons is observed at about 4.5 ev below the Fermi level. This is in agreement with the findings of Berglund and Spicer;[34] however, at $h\nu = 10.2$ ev, where comparison between the two sets of data is possible, there is considerable disagreement at the low-energy end of the emitted-electron distribution in that the contribution due to electron-electron scattering is not so dominant in our data. It has been shown[35] that the effect of

[32] A. Y.-C. Yu and W. E. Spicer, *Phys. Rev. Letters* **17**, 1171 (1966).

[33] C. N. Berglund and W. E. Spicer, *Phys. Rev.* **136**, A1030 (1964).

[34] C. N. Berglund and W. E. Spicer, *Phys. Rev.* **136**, A1044 (1964).

[35] F. Wooten and T. Huen, *J. Opt. Soc. Am.* **57**, 102 (1967).

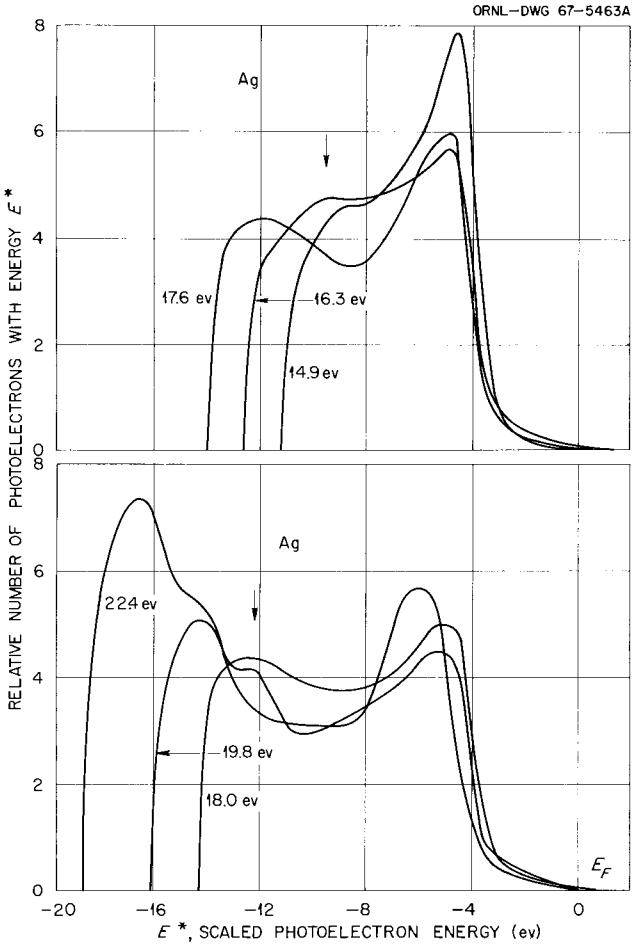

Fig. 17.22. Normalized Photoelectron Energy Distributions in Silver for Photon Energies from 14.9 to 22.4 ev.

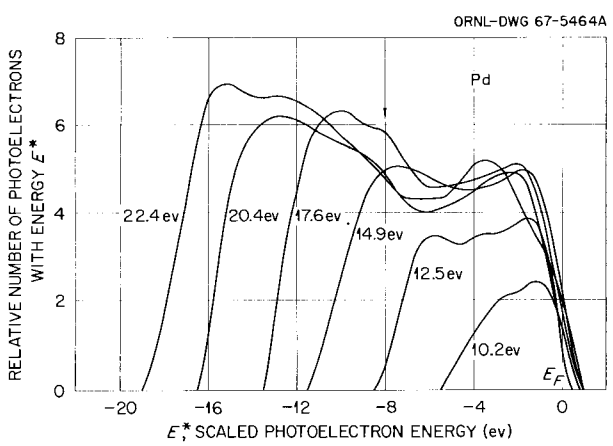

Fig. 17.23. Normalized Photoelectron Energy Distributions in Palladium for Photon Energies from 10.2 to 22.4 ev.

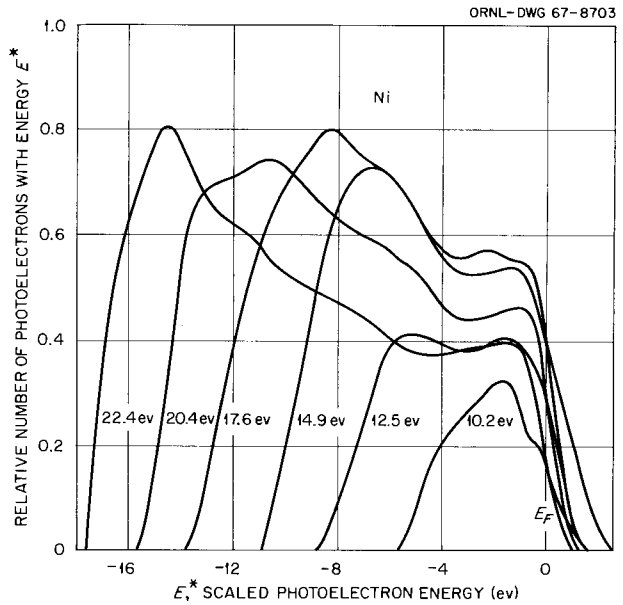

Fig. 17.24. Normalized Photoelectron Energy Distributions in Nickel for Photon Energies from 14.9 to 22.4 ev.

cesium or other forms of contamination on aluminum films produces an enormous change in the general shape of the energy distribution curves; likewise, in the case of nickel, Breen[36] has demonstrated the gross changes brought about during the cleaning of the metal surface. In both cases, the result of contaminants on the surface is that a very large peak appears in the low-energy portion of the distribution that tends to mask all other structure. We have also observed these characteristics in samples of palladium that were allowed to age in vacuum for 24 hr. This is shown in Fig. 17.25.

A sharp energy loss of 3.8 ev in silver has been observed in electron energy loss experiments. If nascent photoelectrons also suffer discrete losses within the metal, this effect should manifest itself as structure in the distribution curves 3.8 ev below the *d*-band peak. Although the structure is weak, it does appear in the upper set of curves in Fig. 17.22 (shown by the downward arrow), but it is superimposed on the electron-electron scattering peak, which appears at the low-energy end of the

[36] W. M. Breen, *Photoemission Investigation of the Band Structure of Ferromagnetic Ni-Al Alloys*, UCRL-50118 (1966) (unpublished).

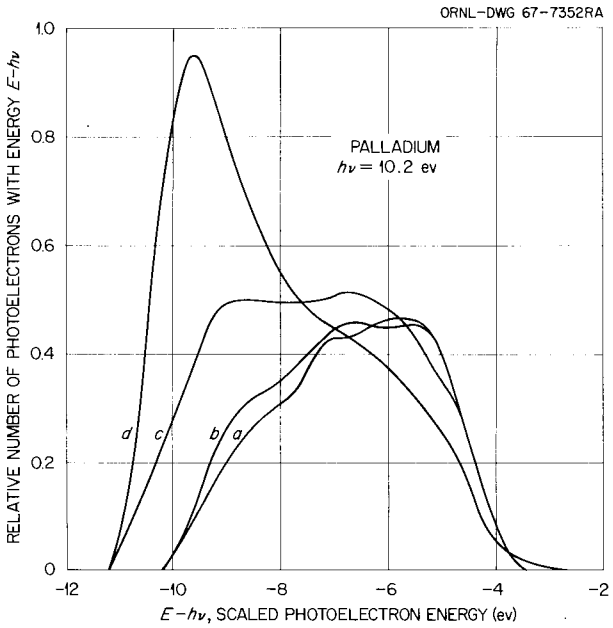

Fig. 17.25. Temporal Behavior of Photoelectron Energy Distributions in Palladium for $h\nu$ = 10.2 ev. Curves *a*, *b*, *c*, and *d* were obtained 3 min, 45 min, 4 hr, and 24 hr, respectively, after preparation of surface.

distribution. This structure begins to appear at $h\nu$ = 14.87 ev and emerges clearly for $h\nu$ = 16.3 ev. At $h\nu$ = 17.6 ev, the structure exhibits itself as a broad tail on the electron-electron scattering peak.

In the lower curves of Fig. 17.22, structure appears at about 7 ev below the *d*-band peak. It begins to emerge for $h\nu$ = 18.0 ev and is clearly evident for $h\nu$ = 19.8 ev, but it is broadened considerably by scattering when the photon energy is increased to 22.4 ev. This structure is attributed to interband transitions in accordance with the optical data of Ehrenreich and Philipp[37] and the characteristic energy loss measurements of Robins[38] and Powell.[39]

Figure 17.23 shows the family of energy distribution curves for palladium using incident-photon energies ranging from 10.2 to 22.4 ev. In these curves, there appears structure that maintains a fixed position at about 3.5, 8.0, and 12.5 ev below the Fermi level. The structure at −8.0 ev makes its first appearance for $h\nu$ = 17.6 ev and appears again for the higher photon energies, although it is not so pronounced owing to the broadening produced by scattering. From optical studies on samples prepared in the same manner as described, we have confirmed[40] the results of Stephan, Lemonnier, and Robin[41] and Seignac, Stephan, and Robin[42] as to the evidence of electron-plasma resonance behavior in palladium at 7.4 ev. The contribution to the energy distribution curves by the creation of a plasmon by an excited electron would be the appearance of a distribution of the same general shape as the unscattered electron energy distribution but shifted lower in energy by an amount equal to the excitation threshold for plasmon creation. This is precisely what appears in the curves for the higher values of the incident-photon energies, but the exact shape of the shifted distribution is masked by the contribution from the electron-electron scattering. As in the case of silver, there is also good agreement with characteristic energy loss experiments.[38] The peaks at −3.5 ev and −12.5 ev can be attributed to interband transitions.

As in the case of palladium, the electron energy distribution in nickel (Fig. 17.24) is characterized by a sharp rise just below the Fermi level. Structure is apparent at about −2, −5, and −10.5 ev. On the basis of the optical data of Ehrenreich, Philipp, and Olechna[43] and of the characteristic energy loss data of Robins and Swan,[44] the peaks at −2 and −5 ev can be attributed to interband transitions and the peak at −10.5 ev to plasmon excitation.

By the preceding analyses, we suggest that structure appearing in the photoelectron energy distribution curves may arise from the discrete loss of energy by the photoexcited electrons as they escape from within the metal. It is, therefore, possible that the "anomalous" peaks reported by Yu and Spicer do not arise from peaks in the density of states but that they are energy-loss peaks instead.

---

[37] H. Ehrenreich and H. R. Philipp, *Phys. Rev.* **128**, 1622 (1962).

[38] J. L. Robins, *Proc. Roy. Soc. (London)* **78**, 1177 (1961).

[39] C. J. Powell, *Proc. Roy. Soc. (London)* **76**, 593 (1960).

[40] R. C. Vehse and E. T. Arakawa, *Bull. Am. Phys. Soc.* **11**, 830 (1966).

[41] G. Stephan, J. C. Lemonnier, and S. Robin, *Compt. Rend.* **260**, 6819 (1965).

[42] A. Seignac, D. Stephan, and S. Robin, *Compt. Rend.* **260**, 3587 (1965).

[43] H. Ehrenreich, H. R. Philipp, and D. J. Olechna, *Phys. Rev.* **131**, 2469 (1963).

[44] J. L. Robins and J. B. Swan, *Proc. Roy. Soc. (London)* **76**, 857 (1960).

18. Atomic and Molecular Radiation Physics

L. G. Christophorou

M-E. M. Abu-Zeid[1]
R. P. Blaunstein[2]
D. Q. Brown[3]
J. F. Burns[3]
Ada E. Carter
J. G. Carter
R. N. Compton
J. T. Cox
F. J. Davis
H. W. Dickson[4]
Kenneth Fox[3]
W. R. Garrett
J. A. Harter
R. H. Huebner[2]
G. S. Hurst
A. G. Kenerly[5]
C. E. Klots
D. R. Nelson
DeVaughn Pittman
P. W. Reinhardt
R. H. Ritchie
H. C. Schweinler
J. A. Stockdale
J. E. Turner

MOLECULAR SCATTERING OF THERMAL ELECTRONS

The drift velocity, w, of an electron swarm moving through a gas at pressure P under the action of a constant electric field E may be related to the cross section for electron momentum transfer $\sigma(v)$ by the relation

$$w = -\frac{4\pi}{3}\frac{e}{mN}\frac{E}{P}\int_0^\infty \frac{v^2}{\sigma(v)}\frac{df_0}{dv}\,dv\,. \qquad (1)$$

For values of $E/P < 0.1$ v cm^{-1} torr^{-1} in ethylene gas or mixtures of organic vapors with ethylene, the electron velocity distribution $f_0(v)$ is Maxwellian:

$$f_0(v) = \left(\frac{m}{2\pi kT}\right)^{3/2} e^{-mv^2/2kT}\,. \qquad (2)$$

In Eqs. (1) and (2) v, m, and e are the electron velocity, mass, and charge, respectively, and N is the number of gas molecules per cubic centimeter when $P = 1$ torr and the temperature $T = 298°$K.

For a gas mixture we may write

$$\sigma(v) = \frac{P_x}{P}\sigma_x(v) + \frac{P_E}{P}\sigma_E\,, \qquad (3)$$

where P_x/P, P_E/P are the concentrations of additive gas and ethylene, respectively, and σ_E is the known constant[6] momentum transfer cross section in pure ethylene.

The values of undetermined coefficients in an assumed form of $\sigma_x(v)$ may be obtained by using Eqs. (1), (2), and (3) to calculate drift velocities for comparison with the experimental values. A static polarizability potential results in the form $\sigma_x = B'/v$, and the coefficients B' have been obtained using this procedure for a number of molecules which do not possess permanent electric dipole moments.[7] Figure 18.1 shows $\langle\sigma\rangle$, the momentum transfer cross section averaged over the Maxwell velocity distribution at 298°K for these molecules, plotted against the atomic polarizability α. The apparent nonlinear increase

[1]Student from the University of Tennessee.

[2]Radiological Health Physics Fellow.

[3]Consultant.

[4]USAEC Health Physics Fellow.

[5]On loan from Instrumentation and Controls Division.

[6]L. G. Christophorou, G. S. Hurst, and W. G. Hendrick, *J. Chem. Phys.* **45**, 1081 (1966).

[7]L. G. Christophorou, G. S. Hurst, and A. Hadjiantoniou, *J. Chem. Phys.* **44**, 3506 (1966).

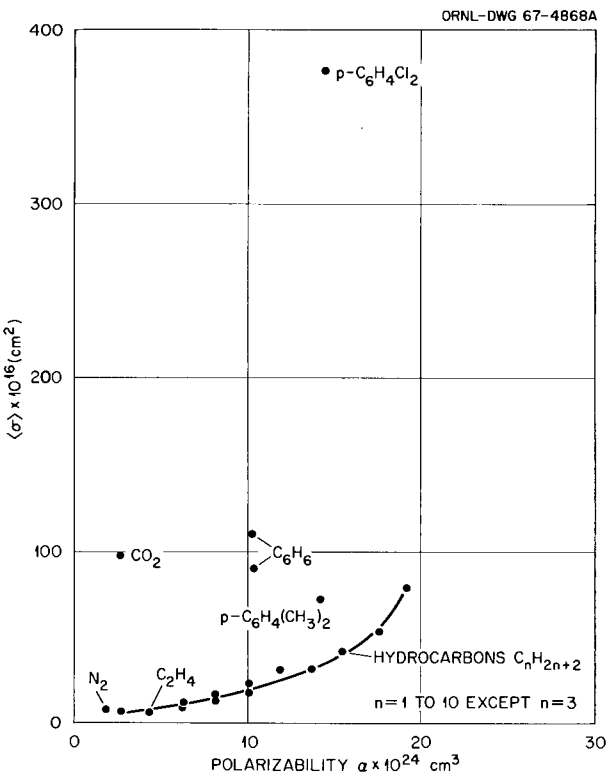

Fig. 18.1. Average Momentum Transfer Cross Sections for Polarizable Molecules at 295°K vs Polarizability.

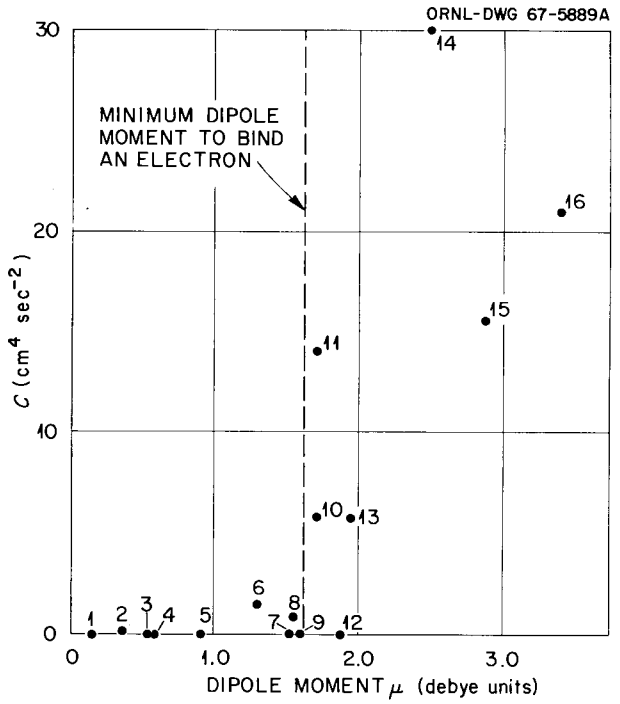

Fig. 18.2. Coefficient C vs μ for Polar Molecules: (1) N_2O; (2) $C_6H_5CH_3$ and m-$C_6H_4(CH_3)_2$; (3) o-$C_6H_4(CH_3)_2$; (4) $C_6H_5C_2H_5$; (5) H_2S and $(C_2H_5)_2NH$; (6) $(CH_3)_2O$; (7) C_6H_5Br; (8) NH_3; (9) CH_2Cl_2; (10) CH_3OH; (11) C_6H_5Cl; (12) H_2O; (13) $C_2H_2(NH_2)_2$; (14) CH_3CHO; (15) CH_3COCH_3; (16) CH_3NO_2.

in $\langle\sigma\rangle$ with α for the straight-chain hydrocarbons is of interest, as is the very high value of $\langle\sigma\rangle$ for *p*-dichlorobenzene, the latter being associated with the formation of a temporary negative ion.[8] There are no adequate theoretical estimates available for comparison with these results.

For molecules with a permanent electric dipole moment, the form $\sigma_x = B/v + C/v^2$ is suggested as a trial function. Application of this form to previously reported drift velocity data[9] and further new measurements for molecules with large dipole moments have resulted in improved agreement between calculated and experimental drift velocities. Figure 18.2 shows a plot of the coefficient C associated with the dipole term of the trial function against the dipole moment μ. There is a striking change in the values of C in the vicinity of μ = 1.6 Debye units. This appears to be the first experimental finding related to recent theoretical demonstrations[10] that μ = 1.64 Debye units – independent of the dipole extension – is the minimum dipole moment necessary to bind an electron. For a point dipole there suddenly become available at this value of μ, infinitely many bound states of infinite binding energy. (For finite dipole extensions the binding energy is inversely proportional to the extension.) Since the wavelength of a thermal electron extends over many molecular diameters, it is reasonable to expect that this behavior will be reflected in the form of the interaction potential.

[8]R. N. Compton, L. G. Christophorou, and R. H. Huebner, *Phys. Letters* **23**, 656 (1966).

[9]L. G. Christophorou, G. S. Hurst, and A. Hadjiantoniou, *J. Chem. Phys.* **44**, 3506 (1966); G. S. Hurst, J. A. Stockdale, and L. B. O'Kelly, *J. Chem. Phys.* **38**, 2472 (1963); N. Hamilton and J. A. Stockdale, *Australian J. Phys.* **19**, 813 (1961).

[10]See, for example, J. E. Turner and K. Fox, *Phys. Letters* **23**, 547 (1966); M. H. Mittleman and K. Myerscough, *Phys. Letters* **23**, 545 (1966).

ELECTRON CAPTURE BY HYDROGEN HALIDES AND THEIR DEUTERATED ANALOGS

In endeavoring an understanding of the detailed mechanisms of electron attachment to molecules, a study of the hydrogen halide molecules offers some advantages. One hopes to understand the interaction of an electron with a diatomic molecule better than its interaction with a polyatomic molecule. Electron capture in diatomic molecules may serve as a guide to the understanding of processes which occur in polyatomic molecules, just as atomic orbitals have been used as a basis for the more complex molecular orbitals.

The swarm-beam method,[11] which combines information from electron swarm and electron beam experiments to establish an independent energy scale calibration and to allow determination of capture cross sections as a function of electron energy, has been employed to study the electron capture processes in HX and DX (X = halogen) molecules.

Figure 18.3 shows the absolute rates of electron attachment to HCl, DCl, HBr, and DBr in the carrier gas N_2 and to HI and DI in the carrier gas Ar.

[11] L. G. Christophorou *et al.*, *J. Chem. Phys.* **43**, 4273 (1965).

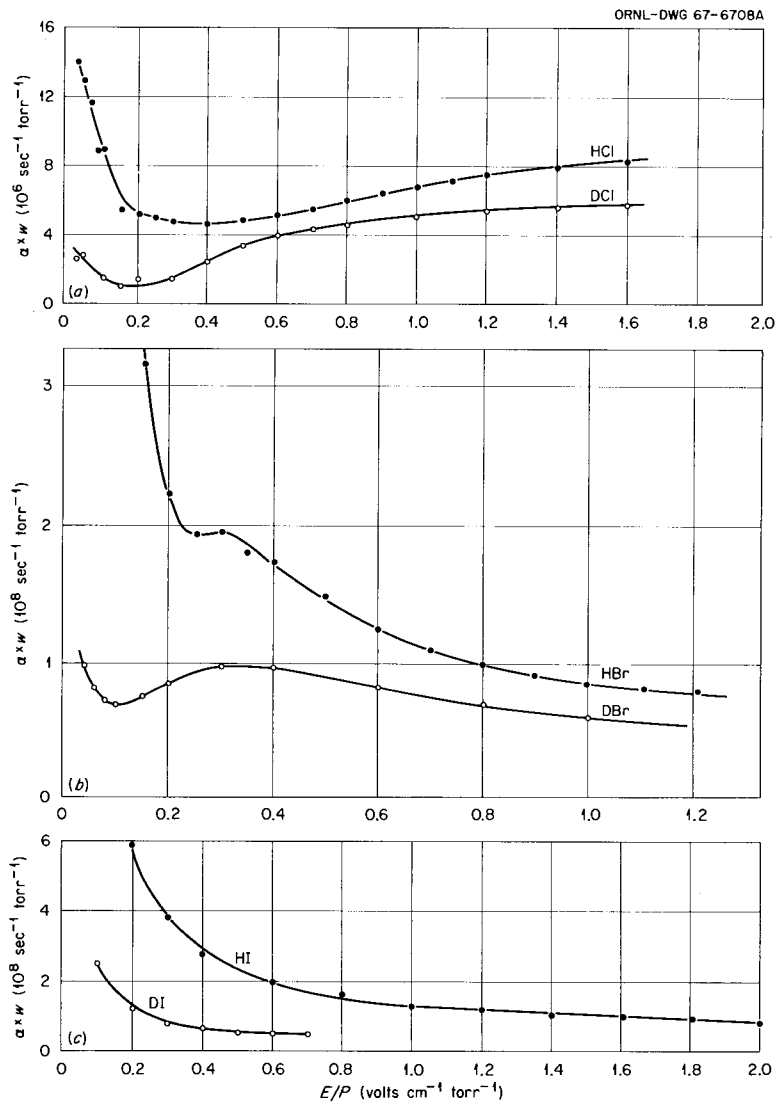

Fig. 18.3. Rates of Capture vs E/P for Hydrogen Halides and Their Deuterated Analogs.

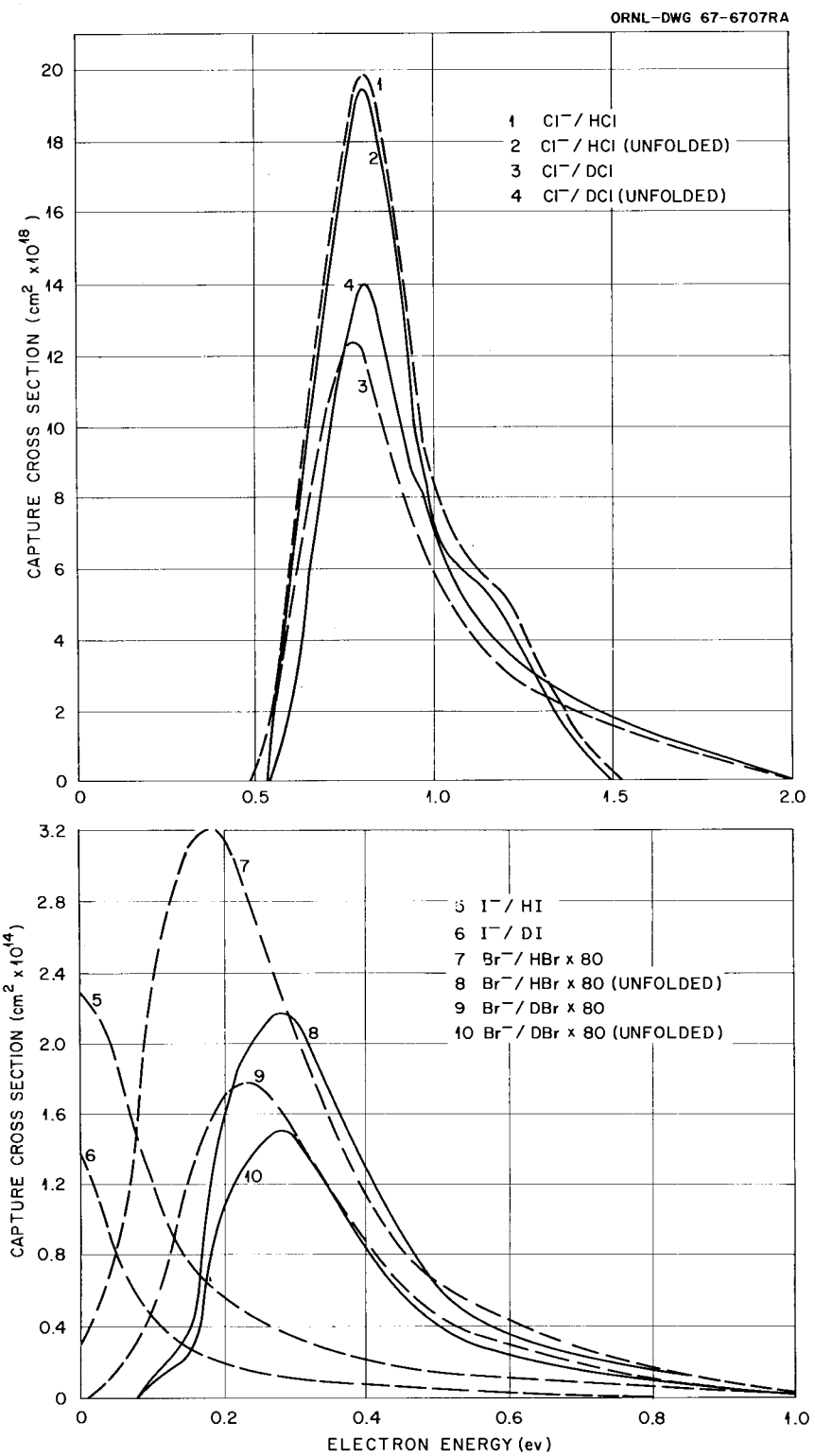

Fig. 18.4. Electron Capture Cross Sections for Hydrogen Halides and Their Deuterated Analogs. Curves 2, 4, 8, and 10 were obtained from curves 1, 3, 7, and 9, respectively, through an unfolding procedure which corrects for the finite width of the electron pulse. From L. G. Christophorou, R. N. Compton, and H. W. Dickson, *Phys. Rev.*, submitted for publication.

These results strongly suggest that in addition to the direct dissociative electron attachment to these molecules [i.e., HX (or DX) + e → H (or D) + X^-] another negative ion is formed at very low energies. The rate of formation of this ion at low energies increases linearly with the HX (or DX) pressure (1 to 20 μ) and is independent of the carrier gas pressure (200 to 800 torrs). It has been concluded that the low-energy capture process in HX and DX molecules cannot be due to double [$(HX)_2$ or $(DX)_2$] molecules, or to dissociation of HX (or DX) molecules from a higher vibrational state or to the formation of HX (or DX) parent negative ions. It is believed that the negative ion produced is a complex involving more than one HX (or DX) molecule.

Figure 18.4 shows the capture cross section, $\sigma_c(\epsilon)$, as a function of electron energy, ϵ, for the direct dissociative attachment process. There is a strong increase in $\sigma_c(\epsilon)$ with decreasing energy of the dissociative attachment peak. Interesting isotope effects are also observed. The ratio of $\sigma_c(\epsilon)$ for isotopic species is very nearly equal to the square root of the inverse ratio of the reduced masses of the products.

A detailed analysis of these results has been completed and will appear in a forthcoming publication.

The importance of combining electron swarm and electron beam techniques to obtain a more complete picture of the electron-molecule interaction is clearly indicated from these studies.

ELECTRON CAPTURE BY O_2 (O_2-C_2H_4 AND O_2-C_2H_4-H_2O MIXTURES)

Permanent capture of thermal electrons by O_2 to form O_2^- ions requires the participation of a third body in the collision process to provide a dynamical channel for stabilization. The effectiveness of H_2O and C_2H_4 as stabilizing agents in three-component (C_2H_4-O_2-H_2O) and two-component (C_2H_4-O_2) mixtures has been investigated using the Bortner-Hurst swarm technique.[12] The results are consistent with the following three-body reaction scheme:

$$e + O_2 + O_2 \xrightarrow{k_1} O_2^- + O_2 + \text{energy} ,$$

$$e + O_2 + H_2O \xrightarrow{k_2} O_2^- + H_2O + \text{energy},$$

$$e + O_2 + C_2H_4 \xrightarrow{k_3} O_2^- + C_2H_4 + \text{energy} .$$

Table 18.1 lists the values of the rate constants k_1, k_2, and k_3 obtained from this work and other investigations.[13,14] The present results remove the anomalous behavior of the data reported by Hurst and Bortner[13] for O_2-C_2H_4 mixtures.

[12] T. E. Bortner and G. S. Hurst, *Health Phys.* 1, 39 (1958).

[13] G. S. Hurst and T. E. Bortner, *Phys. Rev.* 114, 116 (1959).

[14] J. L. Pack and A. V. Phelps, *J. Chem. Phys.* 44, 1870 (1966); *J. Chem. Phys.* 45, 4316 (1966).

Table 18.1. Electron-Oxygen Attachment Rates at 300°K

Three-body attachment processes

Investigator	Rate Constant (cm^6/sec)		
	k_1	k_2	k_3
	$\times 10^{-29}$	$\times 10^{-29}$	$\times 10^{-29}$
This work			
Three-component mixtures		1.4 ± 0.5	0.34 ± 0.04
Two-component mixtures			0.31 ± 0.02
Pack and Phelps[a]	0.20 ± 0.02	1.4 ± 0.2	
Hurst and Bortner[b]	0.26 ± 0.10		0.23 ± 0.10

[a] J. L. Pack and A. V. Phelps, *J. Chem. Phys.* 44, 1860 (1966); *J. Chem. Phys.* 45, 4316 (1966).

[b] G. S. Hurst and T. E. Bortner, *Phys. Rev.* 114, 116 (1959).

ELECTRON CAPTURE BY AROMATIC MOLECULES

The investigation of low-energy electron attachment to aromatic molecules has been extended from the halogenated benzene derivatives[15] to benzene itself, and to naphthalene.

The benzene molecule was found to capture thermal electrons at a rate $\lesssim 3 \times 10^3$ torr^{-1} sec^{-1}. At electron energies greater than thermal the capture rates were greatly reduced, suggesting that the benzene temporary negative ion observed in the beam experiments[8] at 1.4 ev has a very short lifetime. No benzene parent negative ion was observed in the mass spectrometer. From beam studies it is concluded that the electron affinity of the benzene molecule is $\gtrsim -1.4$ ev.

Thermal electron attachment to naphthalene has been studied at 80°C. Thermal electrons were found to attach to the naphthalene molecule at a rate of 5×10^4 torr^{-1} sec^{-1}. Electron attachment decreased at higher energies, indicating that the temporary negative ion observed in naphthalene at 0.8 ev has an extremely short lifetime. The temporary negative ion observed in naphthalene at 0.8 ev puts a lower limit to the electron affinity of naphthalene equal to -0.8 ev.

In view of the fact that various characterizations of electron attachment to molecules have been invoked to explain the action of biologically important molecules, such as the carcinogenic properties of aromatic hydrocarbons, any information on the interaction of low-energy electrons with these molecules is of extreme significance. Very little, if any, is known on the subject. Special equipment has been designed, built, and tested which allows a study of the interaction of low-energy electrons with higher aromatic molecules including carcinogenic molecular agents. This special arrangement is now in operation.

ELECTRON CAPTURE OF TOXIC CHLORINATED COMPOUNDS

There are numerous halogenated organic compounds of major toxicological importance whose potency is believed to be associated with their ability to react readily with low-energy electrons. A program has been initiated to study more systematically the electron transport properties of a number of such toxic compounds.

Among the important toxic compounds are the aromatic halogenated hydrocarbons. Halogenated benzene derivatives were found to capture electrons dissociatively, and both absolute rates for electron attachment and capture cross sections have been reported.[15] These results tend to refute suggestions made in the past that the toxicity of these compounds can be attributed to their electron affinity. On the contrary, these results suggest that the radicals formed following electron capture by these molecules may be more important to their toxic effects.

Absolute rates of electron attachment have been measured for several chlorine-substituted aliphatic hydrocarbons at room temperature. Table 18.2 lists the absolute capture rate, $\alpha \times w$, at thermal energies for the compounds studied. Figure 18.5 shows the dependence of $\alpha \times w$ with increasing E/P in nitrogen. Preliminary analysis indicated the possibility of increasing toxicity with a corresponding increase in the electron capture ability of these molecules at low energies.

Measurements of the temperature dependence of the capture rates of the compounds and other toxic compounds of biological importance such as halogenated naphthalene derivatives and other halogenated substituted aliphatic hydrocarbons are in progress. These measurements will be combined with beam studies to get $\sigma_\epsilon(\epsilon)$. Also, further attention will be given to the possible role of radicals produced upon dissociative attachment to molecules.

Table 18.2. Thermal Electron Capture Rate for CH_2Cl_2, $CHCl_3$, and CCl_4

Compound	Thermal Capture Rate, $\alpha \times w$ (cm^{-1} sec^{-1})
Dichloromethane (CH_2Cl_2)	5.1×10^5
Chloroform ($CHCl_3$)	12.6×10^7
Carbon tetrachloride (CCl_4)	$>9.0 \times 10^9$

[15] L. G. Christophorou *et al.*, *J. Chem. Phys.* **45**, 536 (1966).

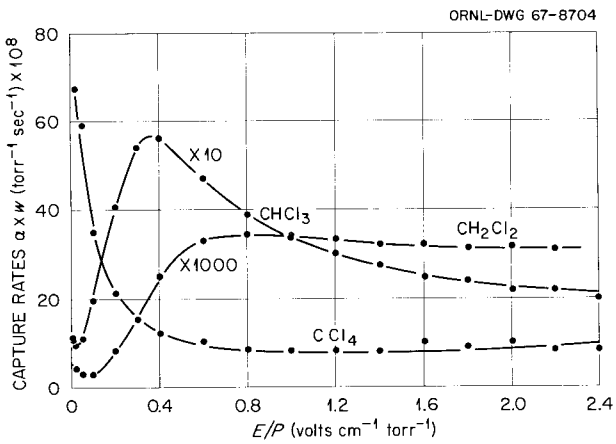

Fig. 18.5. Electron Capture Rate $\alpha \times w$ vs E/P in Nitrogen for Chlorine-Substituted Aliphatic Compounds.

TEMPORARY NEGATIVE ION LIFETIMES

The nondissociative attachment of low-energy electrons to polyatomic molecules is of particular experimental and theoretical interest. A greatly expanding number of organic molecules has been found to possess extremely large cross sections and long lifetimes for unimolecular electron attachment. The rates of attachment and autoionization of a few of these have been determined.[16] A model has been proposed to explain the large cross sections and long lifetimes whereby the excess energy of negative ion formation is distributed among the various vibrational degrees of freedom of the molecule. Under the assumption, the lifetime of a negative ion possessing N vibrational degrees of freedom is related to the attachment cross section $\sigma(v)$ by

$$\tau = \frac{2\pi^2\hbar^3}{W_m m^2 v} \frac{(\epsilon_e + \epsilon_a + a\epsilon_z)^{N-1}}{\Gamma(N) \prod_i^N h\nu_e} \frac{1}{v\sigma_{(v)}}, \qquad (4)$$

where ϵ_e and v are the energy and velocity of the incident electron, ϵ_z is the zero-point energy of the ion, ϵ_a is the electron affinity of the molecule, W_m is the number of states available to the molecule after electron ejection, $\Gamma(N)$ is the gamma function of N, and a is a parameter to be evaluated for each molecule and each value of $(\epsilon_e + \epsilon_a)/\epsilon_z$. Equation (4) shows that the product $\tau \times \sigma$ is extremely sensitive to ϵ_a, which suggests the interesting possibility of calculating electron affinities from measurements of lifetimes and cross sections. Measurements of τ and σ for SF_6 allowed determination of the electron affinity of SF_6, which was found equal to ~ 1.15 ev, as compared with an experimental measurement of 1.49 ev. Similar electron affinity calculations have been carried out for nitrobenzene (0.4 ev), diacetyl (1.1 ev), and glyoxal (1.6 ev).

[16] R. N. Compton *et al.*, *J. Chem. Phys.* **45**, 4634 (1966).

TEMPORARY NEGATIVE ION RESONANCES IN ORGANIC MOLECULES

Short-lived negative ion resonances have been previously invoked to explain the unusually large energy-loss resonances for electron scattering in nitrogen[17] at ~ 2 ev. The SF_6 scavenger technique was employed to observe temporary negative ion resonances in benzene and six of its derivatives.[18] The first singlet peak in the energy-loss spectrum of each compound was used to calibrate the corresponding electron energy scale. Figure 18.6 shows the energy-loss spectra at low energy for the seven benzenes. The peak energies (in electron volts) for the observed resonances are 1.55, 1.45, 1.35, 0.93, 0.85, and 0.36 for C_6H_6, $C_6H_5CH_3$, C_6H_5F, o-$C_6H_4CH_3Cl$, C_6H_5Cl, C_6H_5Br, and o-$C_6H_4Cl_2$ respectively. There is a consistent displacement of the observed negative ion resonances to lower energy with increasing resonance interaction of the substituent with the benzene ring. The energy-loss peak in the benzene spectrum at 1.55 ev requires the electron affinity of benzene to be $\geqq -1.55$ ev, consistent with theoretical calculations ranging from -1.63 to -1.4 ev.

In Fig. 18.6, also, the inelastic energy-loss resonances for o-$C_6H_4CH_3Cl$, C_6H_5Cl, C_6H_5Br, and o-$C_6H_4Cl_2$ are compared with the dissociative negative ion resonances observed previously.[15] Both the peak and shape of the two resonances coincide, suggesting that dissociative attachment is in competition with autoionization as a decay channel of the temporary negative ion.

[17] G. J. Schulz, *Phys. Rev.* **116**, 1141 (1959).

[18] R. N. Compton, L. G. Christophorou, and R. H. Huebner, *Phys. Letters* **23**, 656 (1966).

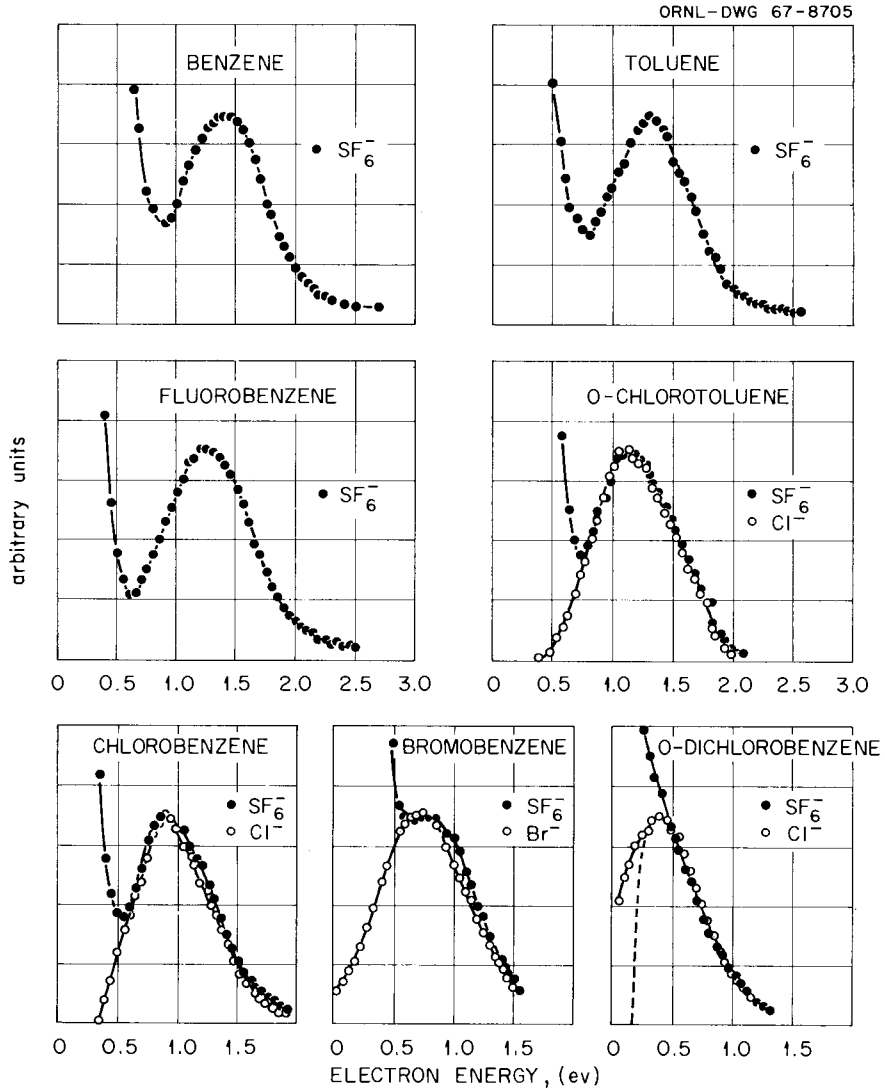

Fig. 18.6. Electron Energy Loss Resonances in Benzene and Benzene Derivatives and Comparison with the Dissociative Attachment Resonances for Severol Halogenated Benzenes. The dotted curve represents a subtraction of the primary SF_6^- current from the total SF_6^- current with both SF_6 and *o*-dichlorobenzene in the mass spectrometer.

Further inelastic energy-loss measurements suggested the existence of a temporary negative ion state in naphthalene at 0.80 ev. The width of this resonance is approximately half that of the benzene negative ion resonance, suggesting a longer lifetime for the naphthalene temporary negative ion.

A high-resolution electron spectrometer employing a 127° electrostatic analyzer has been constructed and will be employed to determine the cross sections in absolute units for the observed temporary negative resonances.

THERMAL (FIELD FREE) ELECTRON CAPTURE RATE AND THERMAL ELECTRON DIFFUSION COEFFICIENT DETERMINATIONS FROM TIME-OF-FLIGHT (TOF) STUDIES USING ELECTRON MULTIPLIER TECHNIQUES

The reaction chamber of the electron time-of-flight apparatus using electron multiplier techniques, described previously,[19] has been altered

[19] G. S. Hurst *et al.*, *Health Phys. Div. Ann. Progr. Rept. July 31, 1965*, ORNL-3849, p. 112.

ORNL-DWG 67-6668

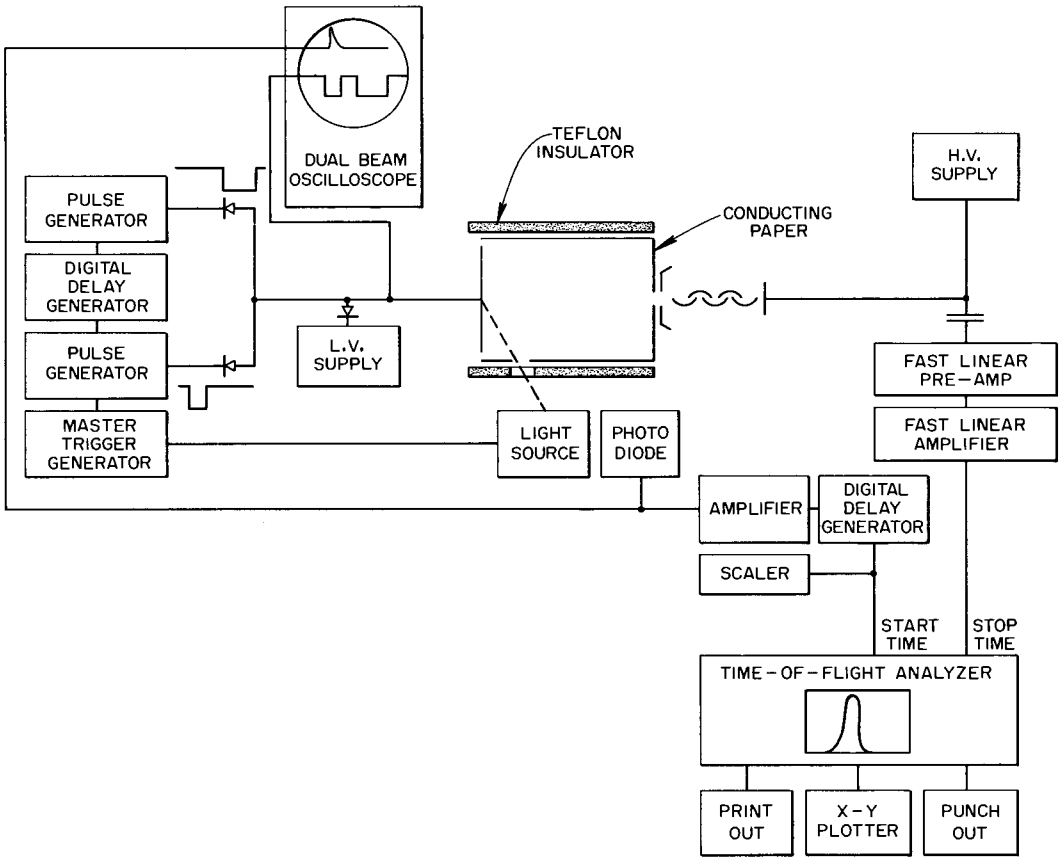

Fig. 18.7. Electronic Logic of Pulse TOF Swarm Experiment.

in order to facilitate the measurement of zero electric field thermal electron attachment and diffusion. The swarm region was modified by replacing the field rings with a cylinder of semiconducting paper. A 0.125-in.-thick cylinder of Teflon was first fitted snugly inside the 10-in.-diam reaction chamber. The conducting paper cylinder (CPC) ($\sim$1500 ohms/square) was then made to fit inside the Teflon insulator. A narrow ($\sim 1/32$ in.) strip of silver conducting paint was applied to the ends of the CPC to determine the cathode and anode boundary planes. The photocathode and anode (25 cm apart) were also made from the semiconducting paper. The important advantages of the modified reaction chamber are: (1) increased swarm region by removing the physical boundary to a larger lateral distance, and (2) a more uniform field (especially at $E/P \cong 0$) is obtained by the removal of the finite-thickness field rings with their associated spacing, alignment, and construction tolerance imperfections. Probably most important in this regard was the elimination of small inadvertent stray fields caused by charging of the field ring insulators or by spurious contact potentials.

A technique was devised for rapidly and accurately pulsing the electron swarm from the photocathode to the center of the CPC, where the electrons are left in a zero electric field where they attach and diffuse for accurately measured periods of dwell time (DwT) before being pulsed out to the detector at the anode. Figure 18.7 shows the block diagram of the electronic logic. Success of this pulse technique depends on (1) an accurate and stable DwT between the input and takeout pulses, which is determined by the digital delay generator, and (2) the rise and fall times of the input and takeout pulses which are produced by the pulse generators.

Determination of thermal electron capture rates (αw) by the pulse technique has two distinct advantages over previous methods. First, the capture

rate (αw) is measured directly instead of determining α and w independently and then calculating their product. Second, αw is measured for thermal (zero field) electrons and is not obtained from an extrapolation of near-thermal or low-E/P data. The value αw is determined by measuring the number of electron counts (C) per number of light flashes (F) as a function of DwT. The slope of a semilogarithmic C/F vs DwT plot gives αw directly. Except for oxygen, all the gases studied have such high capture cross sections that they were mixed (15 to 300 ppm) with a carrier gas. Methane was chosen as a carrier gas since it has a high drift velocity and correspondingly short equilibration period. An SF_6-CH_4 mixture (17.0 ppm) gave thermal αw's of 0.60, 0.60, and 0.59×10^{10} sec^{-1} $torr^{-1}$ for three total pressures of 1, 2, and 5 torrs respectively. Thermal αw measurements for TeF_6, C_6F_6, C_7F_{14}, O_2, and others are in progress.

Determination of a thermal electron diffusion coefficient [$D_t(0)$] is accomplished with the same experimental pulse technique as used for the αw measurements. The value of D_t is determined from the slope of a $(\delta t)^2$ vs t(DwT) plot, where δt is the time-of-flight distribution full width at $1/e$ of the peak. From the field-free, no-boundary solution of the transport equation, it is easily shown that $(\delta t)^2 = (16D_t/w^2)t$, where w is the takeout pulse drift velocity. The value of D_t is found by solving the $(16D_t/w^2)$ expression after equating it to the slope of the experimental $(\delta t)^2$ vs t(DwT) curve.

Figure 18.8 shows some representative data for argon, methane, and nitrogen. The ordinate is in arbitrary units and the abscissa gives the total time t[t = drift time (DrT) + DwT]. The first point for each curve gives the full width squared and the DrT of the electron swarm for its traversing straight through the CPC at the input and takeout E/P with zero DwT. Since the extrapolated intercepts of the $(\delta t)^2$ vs t plots generally do not pass through the origin, this simply means that the value of the diffusion coefficient [$D(E/P)$] for the electron swarm during its input and takeout motion at some E/P is not equal to the thermal diffusion coefficient [$D_t(0)$]. The argon data show a marked deviation from the typical curves of methane and nitrogen. Two factors are responsible for this deviation. First, the average energy loss per collision by an electron with an argon molecule is very small compared with a polyatomic molecule such as

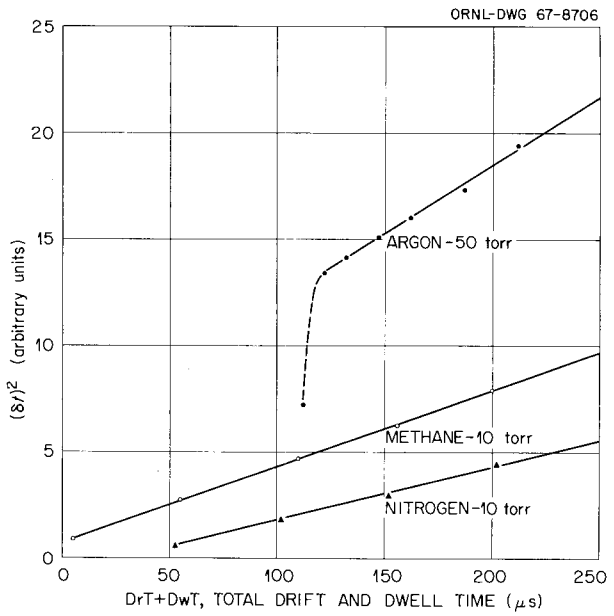

Fig. 18.8. Comparison of $(\delta t)^2$ vs DrT + DwT Curves for Argon, Nitrogen, and Methane.

methane. Therefore, the time required for the electrons to reach thermal equilibrium may be quite large, especially at low pressure. Second, argon has the well-known Ramsauer-Townsend window; low-energy electrons (~0.25 ev) do not seem to see the argon atoms due to a narrow transparency in the scattering cross section. Thus the mean free path between collisions becomes quite large at the window, and correspondingly the diffusion coefficient increases. Since most of the swarm electrons have energies above 0.25 ev for the input E/P (~0.06) pulse used, the passage of these electrons through the window while equilibrating to the thermal energy distribution produces a marked deviation in the $(\delta t)^2$ vs t curve.

Preliminary thermal diffusion-pressure coefficients (D_tP) for several gases are: $D_tP = 0.25$ $cm^2/\mu sec$ (CH_4); 0.27 $cm^2/\mu sec$ (C_2H_4); 0.18 $cm^2/\mu sec$ (CO); 0.15 $cm^2/\mu sec$ (H_2); 0.33 $cm^2/\mu sec$ (N_2). Estimates of D_tP can be obtained from sufficiently low E/P drift velocity data, where its extrapolation to $E/P = 0$ yields an initial slope of μP ($wP/E = \mu P$) value. This μP can then be substituted into the Einstein relation, $D_t/\mu = D_tP/\mu P = 0.025$ ev, to yield a D_tP estimate. Such D_tP estimates for neon

calculated from open-literature[20–22] drift velocity data show about ±5% agreement with those measured here. The D_tP measurements for He, Ne, Ar, D_2, O_2, CO, and CO_2 are in progress.

EXCITATION OF ATOMS AND MOLECULES BY ELECTRON IMPACT

Threshold excitation spectra were obtained for the hydrogen halide molecules (HCl, HBr, and HI), benzene, seven benzene derivatives, and naphthalene by the SF_6 electron scavenger technique described previously.[18,23] This technique has provided unique information regarding the energy position of the triplet and singlet states of molecules and the location of temporary negative ion resonances for a number of aromatic hydrocarbons.

In Fig. 18.9 the threshold excitation spectrum of HCl is shown. Calibration of the energy scale (to within 0.05 ev) for HCl, benzene, and naphthalene was obtained by using the energy maximum of the Cl^- negative ion dissociation peak, which has been determined accurately by the use of the swarm-beam technique and found to occur at 0.82 ± 0.05 ev.[24] No electron energy-loss processes were observed below 6 ev. The features of the HCl spectrum closely resemble the atomic-like optical absorption spectrum measured by Price.[25] In fact, all of the electronic levels, including the vibrational spacings of the $C\ ^1\pi$ state, are the same as observed by Price to within 0.05 ev. A clearly defined Rydberg series is evident above 10 ev, which converges to an ionization potential of 12.6 ± 0.2 ev (determined from the Rydberg formula). Threshold excitation of HBr and HI by the electron scavenger method also showed general agreement with the optical studies by Price.[25]

[20] A. V. Phelps, O. T. Fundingsland, and S. C. Brown, *Phys. Rev.* **84**, 559 (1951).

[21] G. Cavalleri, E. Gatti, and A. M. Interlenghi, *Nuovo Cimento* **40B**, 450 (1965).

[22] J. L. Loyd, *Proc. Phys. Soc. (London)* **75**, 387 (1960).

[23] R. K. Curran, *J. Chem. Phys.* **38**, 780 (1963).

[24] L. G. Christophorou, R. N. Compton, and H. W. Dickson, *Phys. Rev.* (submitted for publication).

[25] W. C. Price, *Proc. Roy. Soc. (London)* **167**, 216 (1938).

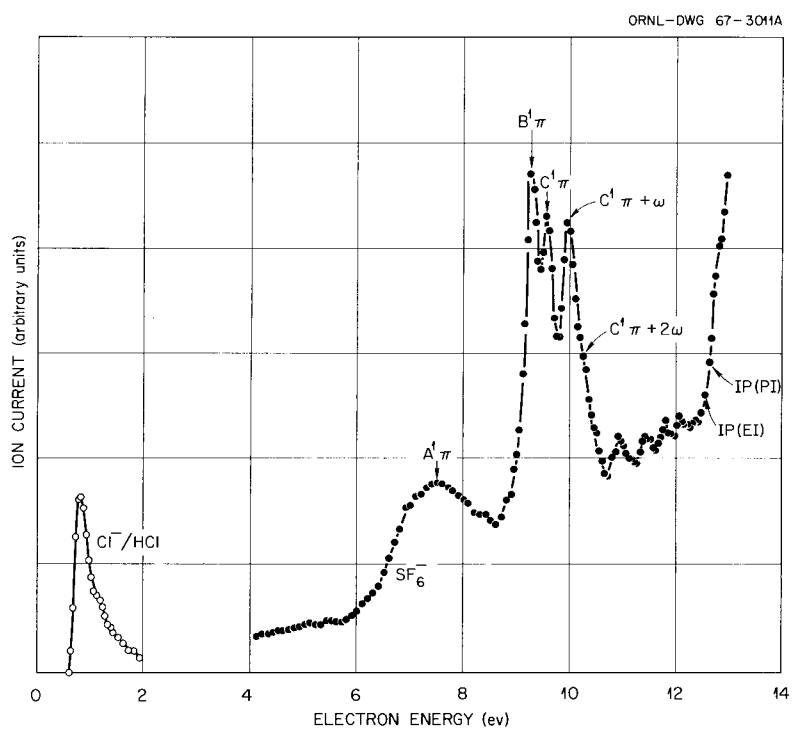

Fig. 18.9. Electron Impact Excitation Spectrum of Hydrogen Chloride.

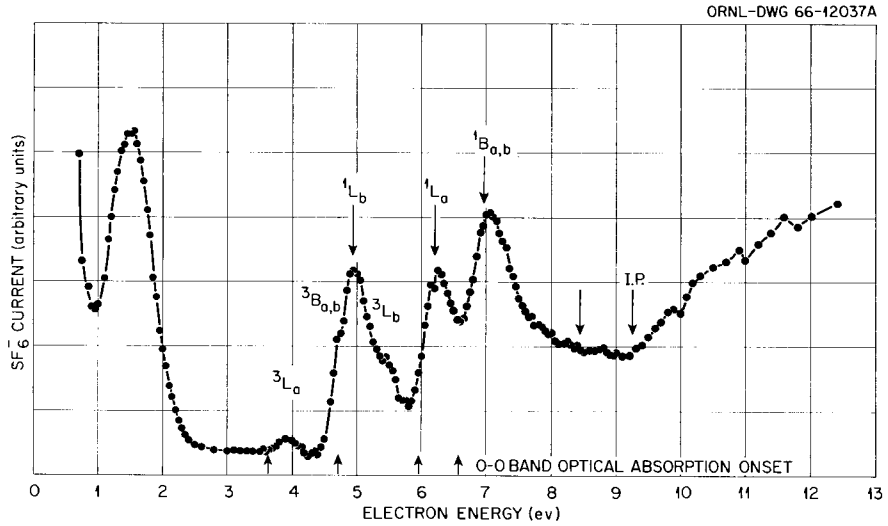

Fig. 18.10. Electron Impact Excitation Spectrum of Benzene.

Electron impact excitation of benzene (C_6H_6), however, exhibits features uniquely different from the usual optical absorption spectrum. In Fig. 18.10 the peak at 1.6 ev, which lies below the lowest electronic state of benzene, is attributed to the formation of a temporary negative ion state. Apparently the benzene negative ion autoionizes quickly after formation, releasing a thermal energy electron and leaving the parent molecule in a vibrationally excited state. A detailed study of the temporary negative ion resonances in benzene and six of its derivatives is presented elsewhere in this report. In addition to the three optically allowed transitions, which peak at 4.8, 6.2, and 7.0 ev, the spin "forbidden" lowest triplet state ($^3B_{1u}$ or ^3L_a in Platt's notation) is observed to peak at 3.9 ev. Furthermore, the shoulder observed at 4.7 ev is attributed to excitation of the second triplet state ($^3E_{1u}$ or ^3B in Platt's notation), which has been observed optically by Colson and Bernstein[26] using a low-temperature NO or O_2 perturbation technique. The abrupt rise of the SF_6^- current beginning at 9.2 ev corresponds to the first ionization potential of benzene.

In the naphthalene spectra shown in Fig. 18.11 the closed and open circles indicate spectra obtained under different degrees of electron beam

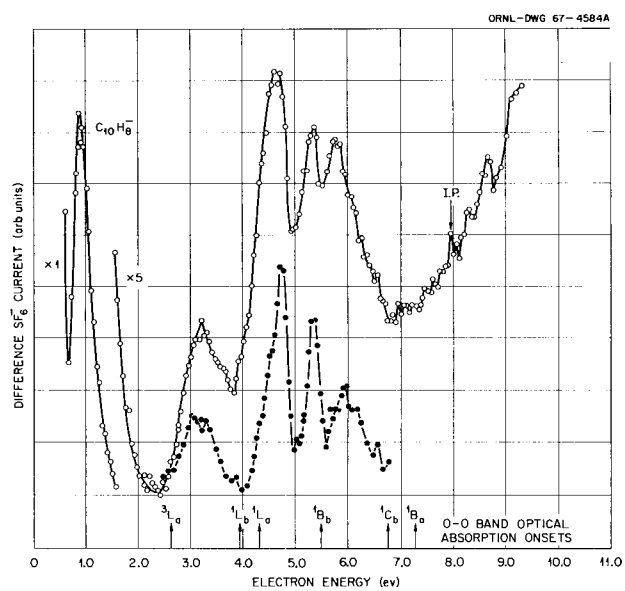

Fig. 18.11. Electron Impact Excitation Spectrum of Naphthalene.

[26]S. D. Colson and E. R. Bernstein, *J. Chem. Phys.* **43**, 2661 (1965); *J. Chem. Phys.* **45**, 3873 (1966).

resolution. Temporary negative ion formation is indicated by the narrow resonance peaking at 0.8 ev. The broad peak that begins at 2.6 ev and peaks about 3.2 ev is identified as the lowest triplet state (^3L_a in the Platt notation) with possible contribution from the second triplet state. A number of singlet states are observed, but the peak at 5.4 ev does not correspond to any known excited states of naphthalene.

EMISSION FROM ORGANIC LIQUIDS EXCITED BY ELECTRON IMPACT

The usual emission spectra which are characteristic of the monomeric $S_{1,0} \rightarrow S_{0,n}$ transitions in organic molecules ($S_{1,0}$ and $S_{0,n}$ being the first excited and ground electronic π singlet states respectively) were completely absent when liquid benzene (B), toluene (T), and 2-ethylnaphthalene (2-EN) were excited by an intense electron beam with average energies ranging from 4 to 36 kev. Instead, the emission from the three liquids was in all cases totally excimeric. When the same liquids (B, T, and 2-EN) were excited by a weak and diffused x-ray beam, the emission spectra were similar to those obtained under ultraviolet excitation of the same system, mostly characteristic of the $S_{1,0} \rightarrow S_{0,n}$ monomeric radiative transition.

Figures 18.12 and 18.13 show the emission spectra of liquid benzene and liquid toluene excited by ultraviolet light,[27] x rays,[28–30] and monoenergetic electrons. It is seen that the emission for ultraviolet and x-ray excitation is similar and corresponds to the usual $S_{1,0} \rightarrow S_{0,n}$ radiative transition in M^* (where M^* is an excited monomer molecule) with some excimer emission on the long-wavelength portion of the spectrum. The emission from the same liquids under electron bombardment is seen to be totally excimeric. Figure 18.14 shows the emission spectra from 2-EN in solution (curve 3) and from the pure liquid under x ray (curve 1) and electron (curve 2) excitation. For 2-EN in the liquid state and under x-ray excitation there is a small residual monomer emission which is completely absent under electron bombardment. The integrated emission intensity I_{int} [$\equiv \int I(\lambda)\, d\lambda$, where $I(\lambda)$ is the relative emission intensity at the wavelength λ] for benzene varied linearly with electron beam intensity I_e and electron beam energy E_e. For ease of comparison, the emission spectra from liquid benzene, toluene, and 2-ethylnaphthalene excited by electron impact are shown in Fig. 18.15 together with the prompt excimer fluorescence spectrum[31] originating from excimers, $^1M_2^*$, in a singlet excited state. All spectra are normalized at their peak intensities. It is clearly seen that the electron-impact-induced emission from the three liquids studied coincides with the $^1M_2^*$ emission.

The linear dependence of I_{int} on I_e and E_e suggests that ion recombination rather than biphotonic processes is responsible for the observed emission, since the number of ion pairs produced is proportional to E_e. Thus, neglecting intermediate steps and alternative processes to radiative emission, we may write

$$M^+ + e + M \longrightarrow {}^{1,3}M_2^* \begin{cases} \nearrow M_S + M_S + h\nu_{(\text{excimer})} \\ \searrow M_S^* + M_S \longrightarrow M_S + M_S + h\nu_{(\text{monomer})} \end{cases} \tag{5}$$

where M^+, M_S, M_S^*, $^1M_2^*$, and $^3M_2^*$ are positive ions of M, M molecules in their singlet ground state, M molecules in their first excited π singlet state, singlet state excimers, and triplet state excimers respectively.

Let us denote by k_{fD}, k_{iD}, k_{MD}, k_{DM}, k_{fM}, k_{iM}, $k_{qD}[Q]$, $k_{qM}[Q]$ the rate constants for excimer fluorescence, excimer internal quenching, excimer dissociation to produce M_S^* and M_S, excimer formation from M_S^* and M_S association, monomer (M_S^*) fluorescence, monomer internal quenching, excimer quenching by an ionization-produced quencher Q, and monomer quenching by Q. Then assuming that

[27] I. B. Berlman, *Handbook of Fluorescence Spectra of Aromatic Molecules*, Academic, New York, 1965.

[28] L. G. Christophorou and J. G. Carter, *Nature* **209**, 568 (1966).

[29] L. G. Christophorou and J. G. Carter, *Nature* **212**, 816 (1966).

[30] J. G. Carter and L. G. Christophorou, *J. Chem. Phys.* **46**, 1883 (1967).

[31] J. G. Birks, C. L. Braga, and M. D. Lumb, *Proc. Roy. Soc. (London)* **283A**, 83 (1965).

M_2^* is initially formed under electron bombardment, we have the following expression for the ratio of the integrated excimer to monomer emission, $(I_D/I_M)_e$:

$$\left(\frac{I_D}{I_M}\right)_e = \frac{k_{fD}(k_{fM} + k_{DM} + k_{iM} + k_{qM}[Q])}{k_{fM}\, k_{MD}} . \qquad (6)$$

It is seen that k_{iD} and $k_{qD}[Q]$ do not enter into Eq. (6) and thus do not affect the ratio $(I_D/I_M)_e$. This is exactly the opposite of what has been observed earlier[28] for pyrene solutions in cyclohexane under x-ray excitation, where M_S^* was initially formed and the corresponding ratio $(I_D/I_M)_{x\ ray}$ was

$$\left(\frac{I_D}{I_M}\right)_{x\ ray} = \frac{k_{fD}\, k_{DM} c}{k_{fM}(k_{fD} + k_{iD} + k_{MD} + k_{qD}[Q])} . \qquad (7)$$

In Eq. (7) k_{iM} and $k_{iD}[Q]$ do not enter and thus do not affect $(I_D/I_M)_{x\ ray}$. Since no monomer emission is observed under electron bombardment, $(I_D/I_M)_e >> 1$, and this may be due to a large value of the quenching rate constant $k_{qM}[Q]$, that is, due to strong ionization quenching of M_S^*. The fact that $(I_D/I_M)_e >>$

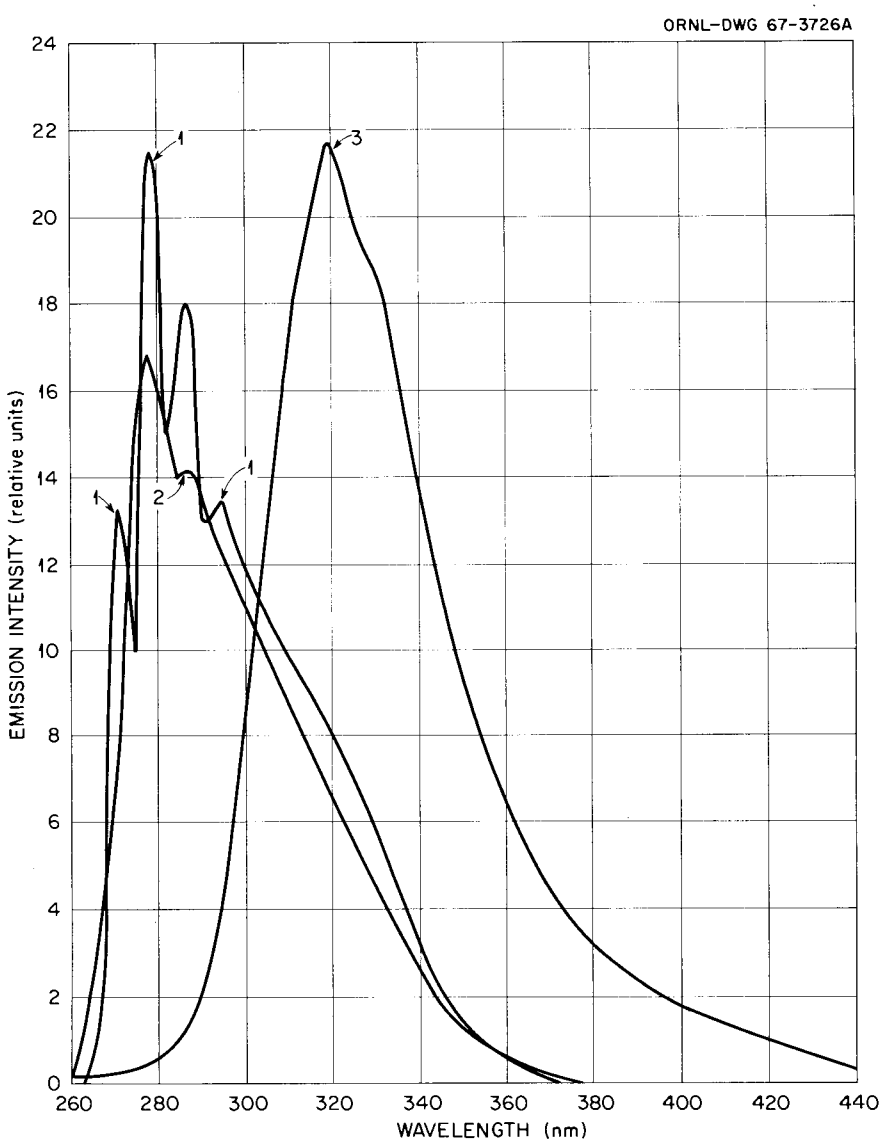

Fig. 18.12. Emission from Liquid Benzene Excited by (1) Ultraviolet, (2) X Rays, and (3) Electrons.

$(I_D/I_M)_{x\ ray}$ suggests that $(k_{qM}[Q])_e >> (k_{qD}[Q])_{x\ ray}$ The singlet state excimer M_2^* also was found[29,30] to be less susceptible to collisional quenching than M_S^*. It has to be noted further, that for large ionization densities ion recombination not only leads to M_2^{**} but also competes with static quenching.

The difference between the scintillation spectra excited by x rays and by electrons for the three liquids studied may be due to differences in the excitation and ionization densities under the two modes of excitation. Thus, the scintillation emission, $I(\lambda)$, may be dependent in intensity and energy distribution on the intensity of exciting radiation.

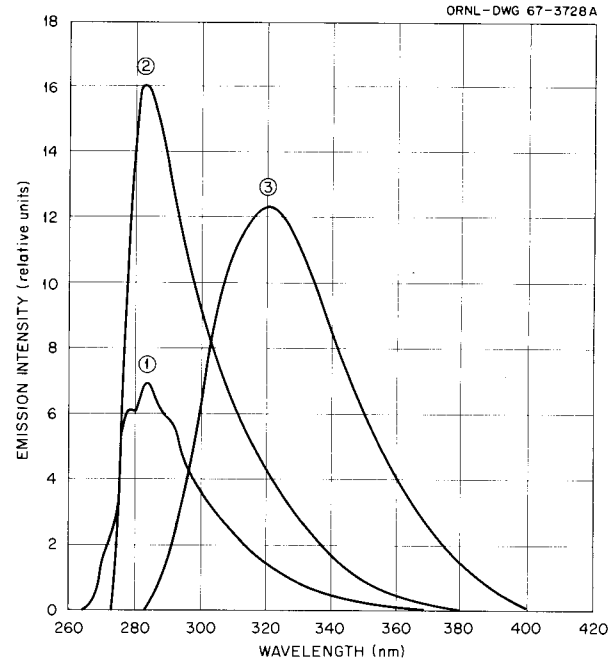

Fig. 18.13. Emission from Liquid Toluene Excited by (1) Ultraviolet, (2) X Rays, (3) Electrons.

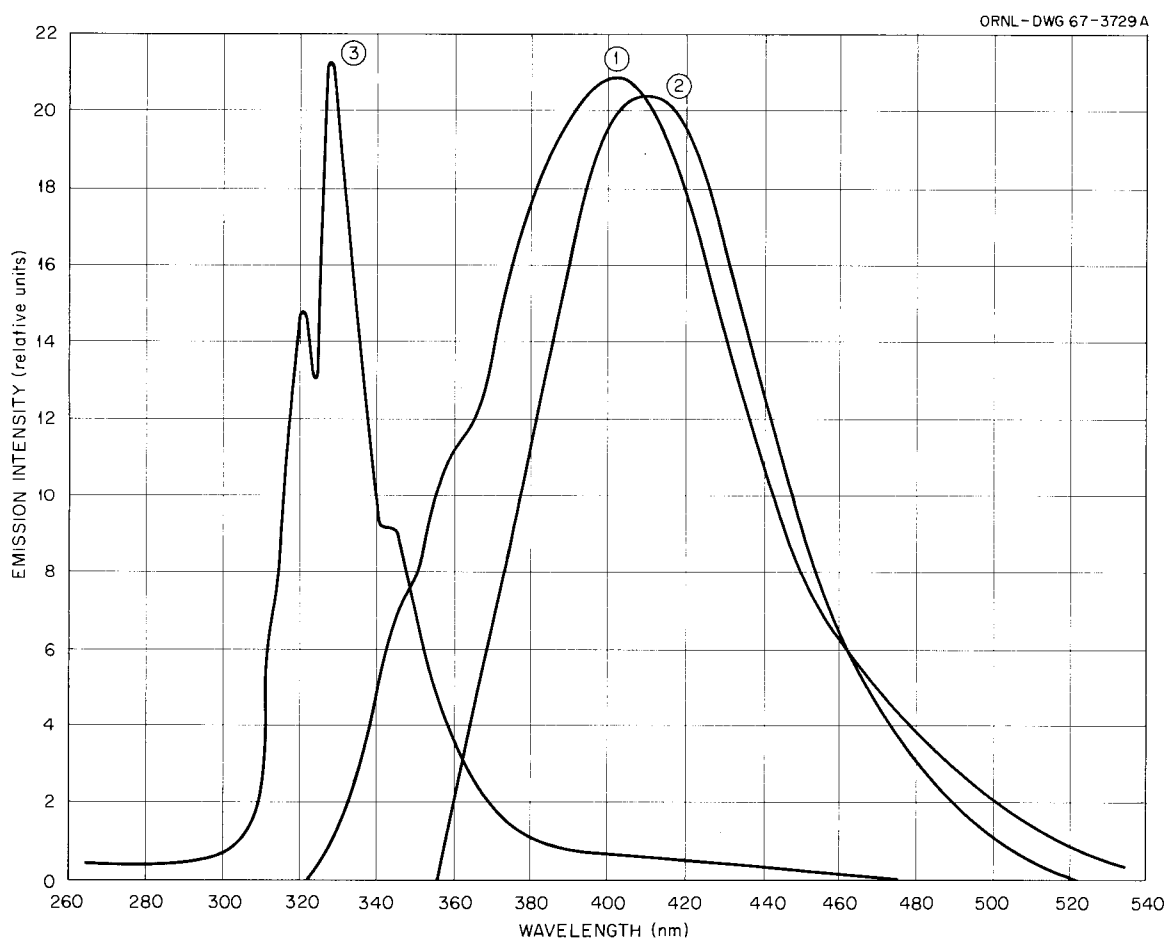

Fig. 18.14. Emission from Liquid 2-Ethylnaphthalene Excited by (1) X Rays, (2) Electrons, (3) X Rays, 5×10^{-3} M/L 2-Ethylnaphthalene in Cyclohexane.

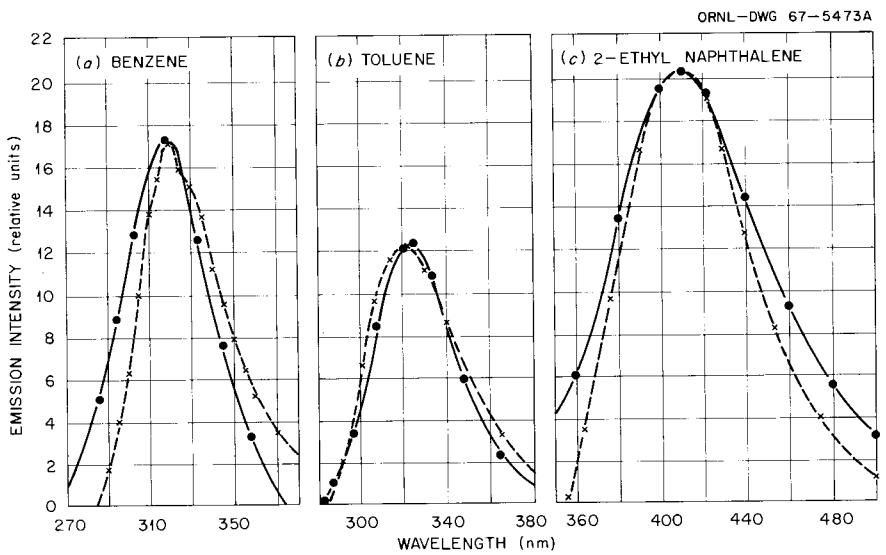

Fig. 18.15. Comparison of the Emission from Organic Liquids Excited by Electron Impact (x---x---x) with $^1M_2^*$ Emission from the Same Systems Excited by Ultraviolet Light (--•--•).

A basic difference between the emission spectra observed under optical excitation and under electron impact excitation with electron energies greater than the ionization potential of the molecules involved is that in the second mode of excitation, species such as M_T^{**}, M_T^*, M^+, e^-, and M_2^{**} are more abundant (M_T^{**} and M_T^* are M molecules in higher and lowest excited π triplet states respectively). Thus these species should be responsible for the differences between the optical and electron-impact-induced scintillation spectra. If again we assume that M_S^* is strongly quenched under high ionization densities, then Eq. (5) can account for the observed differences.

It is concluded that since the use of different modes and intensities of excitation changes the relative abundance of the emitting excited species M_S^*, M_T^*, $^1M_2^*$, and $^5M_2^*$ (and possibly $^3M_2^*$), where $^5M_2^*$ is a quintet state excimer, the emission spectra depend on the mode and intensity of the exciting radiation.

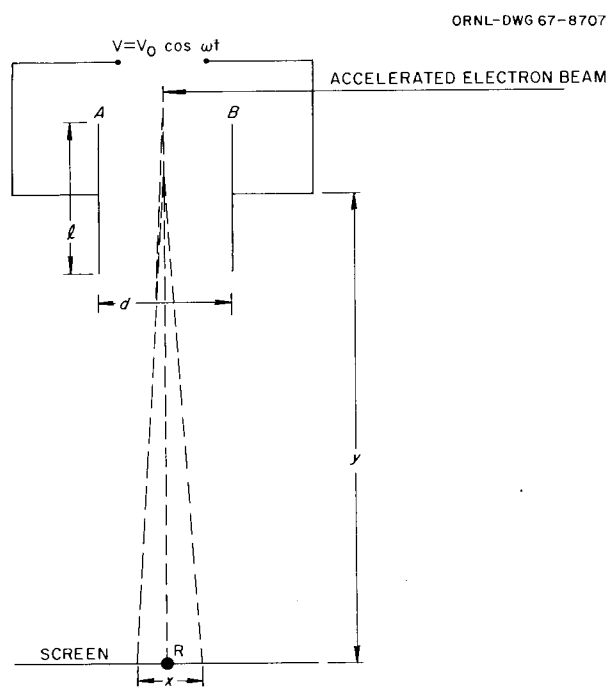

Fig. 18.16. Schematic Diagram Illustrating the Principle of the Pulsed Electron Source.

DEVELOPMENT OF A NANOSECOND PULSED SOURCE FOR SCINTILLATION DECAY TIME MEASUREMENTS

Scintillation decay times and energy-transfer processes among molecules will be investigated using a nanosecond pulsed electron source for excitation. Such studies will aid considerably our understanding of molecular structure, luminescence properties of molecules, and energy-transfer processes between molecules. Figure 18.16 shows the principle of the method. A beam of electrons with

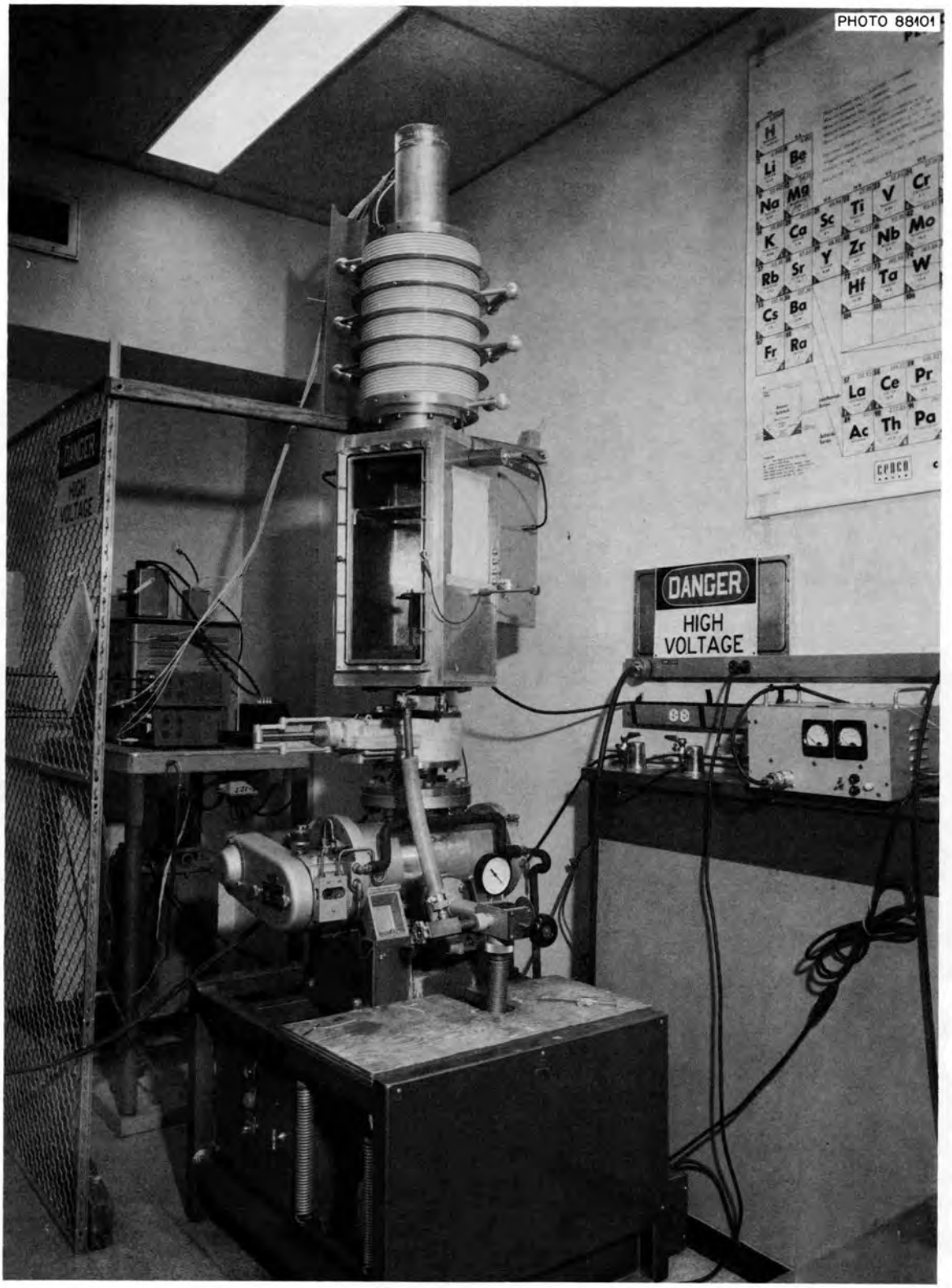

Fig. 18.17. Overall Arrangement of the Pulsed Electron Source.

energy E passes between two parallel deflection plates A and B, which are connected to an alternating voltage $V = V_0 \cos \omega t$. A fluorescent screen is placed in a plane perpendicular to the common axis of the two deflection plates. If the separation distance, d, between the two deflection plates is 1.5 cm, the length, l, of the deflection plates is 10 cm, and the distance, y, from the center of the plate to the screen is 35 cm, the sweep velocity of the final spot of the beam on the screen is given by

$$\frac{dx}{dt} = \frac{1}{2} y \frac{l}{d} \frac{V_0 \omega}{E} . \tag{8}$$

For a slit width of 0.05 cm, centered at the point R (see Fig. 18.16), and for values of E, V_0, and $\omega/2\pi$ equal to 50 kv, 1.25 kev, and 2.3 megahertz, respectively, an electron pulse of about 1 nsec duration can be obtained as the beam sweeps across the slit. The apparatus is in the final stages of testing. Figure 18.17 shows the overall arrangement.

NEGATIVE-ION–MOLECULE REACTIONS[28]

The importance of negative-ion–neutral-molecule reactions far outweighs the present experimental efforts devoted to their study. An experimental technique, previously employed to study positive-ion–molecule reactions, is presently being used to determine rate constants for negative-ion–molecule reactions and charge-transfer collisions. The feasibility of such measurements is based on the observation[32] that for the reactions

$$H^- + H_2O \longrightarrow OH^- + OH \tag{9}$$

and

$$H^- + O_2 \longrightarrow O_2^- + H \tag{10}$$

the yield for OH^- and O_2^- increases with the time delay between the electron gate pulse and the ion-pusher pulse in a time-of-flight mass spectrometer. A plot of

$$-\ln\left(1 - \frac{[OH^-]}{[H^-]}\right),$$

where $[OH^-]$ is the concentration of hydroxyl negative ions and $[H^-]$ is the initial concentration of hydrogen negative ions, vs the delay time (reaction time) yields a straight line (see Fig. 18.18) whose slope can be used to calculate the rate constants for reactions.

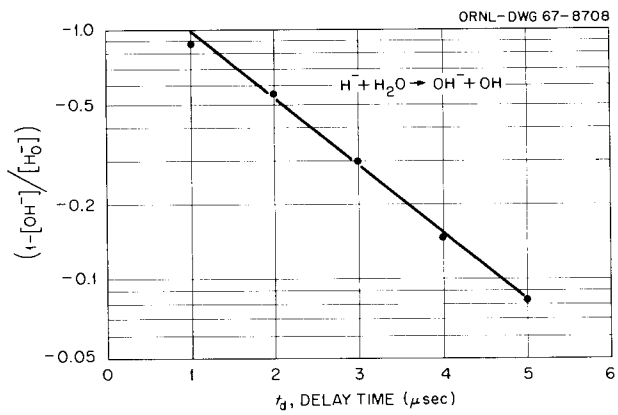

Fig. 18.18. $-\ln\left[1 - \frac{[OH^-]}{[H^-]}\right]$ vs Reaction Time.

COLLISIONAL DETACHMENT EXPERIMENTS

Cross sections and thresholds for detachment of electrons from negative ions by collisional processes such as

$$XY^- + e \longrightarrow XY + 2e \tag{11}$$

or

$$XY^- + A \longrightarrow XY + A + e \tag{12}$$

(where XY^- is a stable negative ion and A a neutral atom or molecule) are of great interest. These processes may permit more accurate evaluation of molecular electron affinities. Such results would complement electron affinity estimates already obtained from negative-ion lifetime measurements.[33]

A simple electron collision negative-ion source employing magnetic mass analysis of the emerging beam has been constructed and is being tested.

[32] R. N. Compton and L. G. Christophorou, *Phys. Rev.* **154**, 110 (1967).

[33] R. N. Compton *et al.*, *J. Chem. Phys.* **45**, 4634 (1966).

This will be used with a time-of-flight mass spectrometer to study reactions (11) and (12). In the case of (11), crossed ion and modulated electron beams will be used with subsequent detection of neutral particles. In case (12) the target gas, A, will be helium containing a small concentration of SF_6. It is hoped to use the large SF_6 resonance electron capture cross section at zero energy to detect the onset of the collisional detachment reaction.

SENSITIZED IONIZATION OF MOLECULES

A photoionization apparatus has been constructed which will provide data allowing a considerable insight into the mechanics of highly excited molecules. An argon resonance lamp, emitting almost exclusively 1170-A radiation, will be used to photoionize various molecules, M:

$$h\nu + M \longrightarrow M^* \longrightarrow M^+ + e$$
$$M^* \longrightarrow \text{decomposition}$$

and to measure the photoionization efficiency for each such molecule. These results will be compared with efficiencies for indirect sensitization:

$$h\nu + \mathrm{Ar} \longrightarrow \mathrm{Ar}^* ,$$

$$\mathrm{Ar}^* + M \longrightarrow M^* + \mathrm{Ar} ,$$

$$M^* \longrightarrow M^+ + e$$
$$\longrightarrow \text{decomposition} ,$$

which can also be followed in the same apparatus. Comparison will be made also with the apparent efficiencies associated with the excited argon atoms produced by alpha-particle irradiation.[34] The comparison will afford a definitive test of the assignment of the alpha-induced excitations.

YIELDS OF RESOLVED TRANSITIONS IN GASES

A fundamental objective of radiation physics is to devise techniques for enumerating the yields with which a given electronic transition is induced in matter when exposed to high-energy radiation. A realistic, yet accurate, formulation with which this might be accomplished is given by

$$G_n = \frac{\int \sigma_n(T)\, y(T)\, dT}{\int Q_i(T)\, y(T)\, dT} \times \frac{100}{W} , \qquad (13)$$

wherein G_n is the desired yield (per 100 ev deposited), a function of the W value of the medium, σ_n and Q_i (the cross section for the desired transition and for total ionization – each a function of particle energy T), and $y(T)$, the prevailing degradation spectrum.

A crucial factor in the construction of degradation spectra is the need for cross-section formulas for fast secondary electrons. Correction factors to the usual free-electron Rutherford formula have thus been evaluated, in the Born approximation, from hydrogen-like wave functions. These are illustrated in Fig. 18.19 as universal functions of two variables, $K = \epsilon/I_k$ and $\eta = 2mv^2/I_k$, where ϵ is the energy of the ejected electron, v the projectile velocity, and I_k its binding energy. Similar "correction terms" have been obtained using Gryzinski's classical collision model. With these, degradation spectra have been constructed for 5-Mev alpha particles in a number of gases; yields of several unimportant transitions then have been deduced. The calculated yields are insensitive

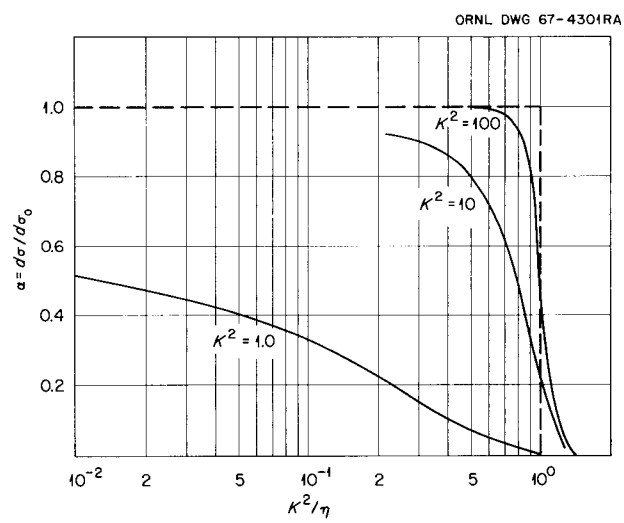

Fig. 18.19. Correction Factors to the Rutherford Formula for Calculating Secondary Electron Yields.

[34] G. S. Hurst, T. E. Bortner, and R. E. Glick, *J. Chem. Phys.* **42**, 713 (1965).

to small variations in $y(T)$ and thus, presumably, to the remaining errors in these degradation spectra. Serious departures from the prediction of the "optical approximation" are noted.

UNIMOLECULAR DECOMPOSITIONS

In conjunction with experiments currently in progress in the Chemistry Division, calculations are being made on the rates of unimolecular decompositions of the general type:

$$NH_3BF_3^* \longrightarrow NH_3 + BF_3 .$$

The experimental technique employs crossed molecular beams to create the activated species through just the reverse of the above-indicated reaction. Preliminary calculations have delineated the conditions under which the postulated decomposition should be observable. The extent to which experiment reproduces the calculations will reflect directly on theories of unimolecular decomposition and of intramolecular energy transfer.

19. Graduate Education and Vocational Training

K. Z. Morgan
J. C. Ashley
R. D. Birkhoff
L. G. Christophorou
L. C. Emerson
M. F. Fair
C. E. Klots
R. H. Ritchie
H. C. Schweinler
J. E. Turner

GRADUATE EDUCATION AND VOCATIONAL TRAINING

Thirteen USAEC Fellows in Health Physics reported to the Division in June for summer training. Four came from the University of Tennessee, eight from Vanderbilt University, and one from the University of Rochester. The summer program is open to Fellows from all participating universities. The first week was spent in the ORAU Special Training Division doing health physics experiments. The second week was spent at ORNL in a program of orientation. The remainder of the training period included five weeks with the research groups and five weeks in applied health physics.

In the applied health physics training, the student gains practical experience in all phases of radiation protection under the supervision of a senior health physicist. The student learns the radiation protection services that are provided for the Physics Division, Reactor Chemistry Division, Metals and Ceramics Division, Solid State Division, Chemical Technology Division, Rolling Mill, Tracer Facilities, High Level Radiochemical Development Laboratory, Fission Products Pilot Plant, Waste Disposal Group, Isolation Laboratory, Pilot Plant Operations, transuranium facilities, and the Ecology Research Group. In addition, he learns of personnel monitoring, instrument calibration, counting facilities, bioassay techniques, and whole-body counters.

In health physics research, the students are first given a brief summary of all the research projects which are in progress in the Division. They then choose the group in which they will remain for the five-week period of basic research under senior scientist supervision. The fields of investigation include: interaction of radiation with gases, solids, and matter; theoretical radiation physics; Health Physics Research Reactor; dosimetry; radioactive waste disposal; and radiation ecology.

The summer program gives the student sufficient experience in applied health physics to enable him to take a position in this field. Also, he learns of the tremendous breadth in research health physics and is made aware of the diverse problems available for thesis work should he decide to continue his education for the M.S. or Ph.D. degree under the fellowship.

Four AEC Fellows, four physics majors, and one student from Cyprus completed the course in General Health Physics (Physics 4710-20-30), taught by Division members at the University of Tennessee. This was a three-quarter course which met 3 hr/week. A course in Applied Radiation Physics (Physics 234) at Vanderbilt University was completed by nine AEC Fellows and one physics major. This was a one-semester course which met 4 hr/week. Students were selected for the 1967–68 Fellowship Program.

The book "Principles of Radiation Protection: A Textbook in Health Physics," for which proofs and page proofs have been received and corrected, is expected to be published by September 1967. This book should be widely used in health physics education and particularly in the UT and Vanderbilt courses listed above.

Universities and colleges at which ORNL health physics research and educational activities were discussed are listed below:

Catawba College	Womens College of Georgia
Clinch Valley College	Clemson College
George Peabody College	Emory and Henry College
Muskingum College	Georgia Institute of Technology
Tennessee Technological University	Indiana State University
University of Georgia	Ohio University
Vanderbilt University	University of Missouri
Western Carolina College	University of Tennessee
Winthrop College	Virginia Military Institute
Western Maryland College	

Many of these visits were made under the Traveling Lecture Program. As an added bonus the Division staff members who visited these schools were able to acquaint the staff members with the work and facilities of this Division.

There were a number of Oak Ridge Graduate Fellows, AEC Fellows, and USPHS students in the Division working on theses as partial requirements for advanced degrees. Their thesis titles and universities are listed below.

1. M-E. M. Abu-Zeid, "Optical Emission and Lifetimes of Organic Molecules Excited by Electron Impact" (UT)
2. R. P. Blaunstein, "Electron Transport in Carcinogens" (UT)
3. W. G. Connor, "Semi-Classical Model of the Photoelectric Effect in Metals" (Vanderbilt)
4. L. S. Cram, "Investigation of the 'Surface Plasma' Radiation from Electron-Bombarded Ag" (Vanderbilt)
5. Julian Crowell, "Positron Annihilation in an Electron Gas" (Vanderbilt)
6. Patricia Dalton, "Mean Excitation Energies Calculated from Stopping Power and Range Data" (Vanderbilt)
7. H. W. Dickson, "Measurement of Electron Attachment Coefficients in Hydrogen Halides and Water-Bromobenzene Mixtures" (UT)
8. F. W. Garber, "Transmission of Low-Energy Electrons Through Thin Alkali Metal Films" (UT)
9. R. N. Hamm, "The Mean Free Path of Low Energy Electrons in an Electron Gas" (UT)
10. J. D. Hayes, "Optical Properties of Selenium and Tellurium in the Vacuum Ultraviolet" (Vanderbilt)
11. R. H. Huebner, "Electron Impact Investigation of Aromatic Hydrocarbons and Other Complex Molecules" (UT)
12. S. J. Nalley, "Low-Energy Electron Studies on Thin Metallic Films" (UT)
13. D. R. Nelson, "Lifetimes of Electrons on Polyatomic Molecules" (UT)
14. H. L. Pray, "Low-Energy Electron Studies on Tl, Mg, and In" (UT)
15. M. S. Reidinger, "A Study of the Optical Properties of Sodium by Ellipsometry" (Vanderbilt)
16. Linda L. Robinson, "Optical Reflectivity of Water in the Vacuum Ultraviolet" (UT)
17. J. L. Stanford, "Photoelectric and Optical Properties of Commercial Pt, Au, and Pd Foils and Evaporated Al and Ag Films in the Extreme Ultraviolet" (UT)
18. J. C. Sutherland, "The Optical Properties of Sodium in the Vacuum Ultraviolet" (Georgia Institute of Technology)
19. L. H. Toburen, "Charge Exchange Cross Sections for Mev Protons in Various Gases" (Vanderbilt)
20. R. C. Vehse, "Reflectance of Evaporated Al Films in the Wavelength Region 800 to 2000 A" (UT)
21. R. E. Wilems, "Collective Interactions in Solids" (UT)
22. H. A. Wright, "Differentiability of Set Functions" (UT)

Seven research participants, eight ORAU undergraduate students, and ten undergraduate research participants in ecology worked with the Division during the summer. At the same time, 18 summer technical students and 4 students from the Youth Opportunity Program assisted the Division.

Mr. H. O. Mohamed, a citizen of Egypt, completed a five-month training period in Applied Health Physics.

Several Health Physics Division staff members assisted members of the University of Tennessee Physics Department in preparing proposals for research support. These were:

1. an application to the National Science Foundation for a Center of Excellence award;
2. a proposal to the Division of Biology and Medicine of the USAEC for a contract entitled "An Investigation of Excitation and Energy Transfer Processes in Atoms and Molecules";
3. a request for support under Project Themis to the Department of Defense entitled "Optical Aspects of Interactions of Radiation and Matter."

Several members of the Division assisted the University of Tennessee in setting up a new undergraduate curriculum leading to the B.S. degree with a major in health physics. This type of assistance and consultation is available to any school desiring to set up a health physics program or institute courses in this field. Queries pertaining to setting up such courses have been received from Central Florida Junior College, Georgia Institute of Technology, Montgomery Junior College (Md.), Rose Polytechnic Institute, and University of Arkansas.

One member of the Radiation Physics Section served as a judge for a session of papers on plasma physics at the Sixth Annual Student Conference of the American Nuclear Society held in Gatlinburg in April 1967. Another member of the section helped screen applicants for the 1967–68 USAEC Fellowship Program. This work was done at the Oak Ridge Associated Universities.

The Division participated in a three-day conference entitled "Principles of Radiation Protection" sponsored by ORAU and DNET (Division of Nuclear Education and Training). Approximately 100 college and university faculty members attended the conference. Several members of the Division participated in the Traveling Lecture Program, the ORNL Orientation Program, and various other community activities.

The Division, in cooperation with ORAU, presented for state personnel a ten-week course in health physics sponsored by the Atomic Energy Commission. This was part of the overall AEC program to turn over to the individual states the responsibility for regulation and control of radioactive materials. Twenty students completed the course, which was followed several months later by an advanced three-week course taken by 12 students from various state health departments.

One-week lecture and tour programs were arranged for the University of Arkansas Radiological Health Course and the University of North Carolina Radiological Health Course. Lectures were also given at ORAU during four Medical Radioisotopes Courses attended by approximately 60 physicians.

Division personnel participated in the presentation of a two-week course in Radiation Safety for ORNL staff. The Division also assisted in the presentation of an eight-week course in Health Physics offered by ORAU during the summer of 1967 for college and university staff members who have responsibility for campus radiation safety.

The demands for education in health physics have continued to rise. Emphasis will be on education to the Ph.D. level to provide personnel for positions of leadership in industrial, academic, and medical institutions. Although the advanced program will be emphasized, education will continue to be offered during the summer at the master's level to provide vocational training which includes a knowledge of health physics principles and procedures. The needs of the reactor industry must be met.

20. Physics of Tissue Damage

R. D. Birkhoff

M-E. M. Abu-Zeid[1]
Ada E. Carter
J. G. Carter
L. G. Christophorou
M. Y. Nakai[2]
W. J. McConnell
Linda R. Painter[3]
E. K. Yeargers[4]

LOW-ENERGY ELECTRON TRANSMISSION IN SOLIDS

A new electron gun and ultrahigh vacuum preparation and irradiation chamber have been constructed and put into use this year to measure electron transmission in solids. In these experiments an aluminum substrate is vacuum-evaporated onto a glass slide and then oxidized to a depth of 75 A. The slide is placed in an ultrahigh vacuum system and pumped down to a pressure of the order of 10^{-9} torr. Another metallic layer of the order of 200 A in thickness is then vacuum-evaporated on top of the oxide. The electron beam from a low-energy electron gun is directed at the target sandwich at various angles of incidence, and the currents to the top layer and the bottom layer are amplified by Philbrick P2 amplifiers and their ratio measured with a Vidar digital ratiometer. The ratio of the top current to the incident current is proportional to the absorption in the film. These experiments differ from those reported previously (ORNL-TM-1153 and -1565) in that they are carried out under ultrahigh vacuum conditions (thus guaranteeing atomically clean surfaces), the electron beam angle is variable, and the electron gun is capable of operation at as little as 1 ev, compared with the minimum operating voltage of about 7 ev for the gun employed previously.

Typical data as determined with a 200-A aluminum top layer are shown in Fig. 20.1. Proceeding from 1 ev toward higher energies one notices the following features: in the region of 1 to 7 ev, the current decreases with energy, implying a decreasing scattering cross section between incident electrons and conduction electrons. At oblique

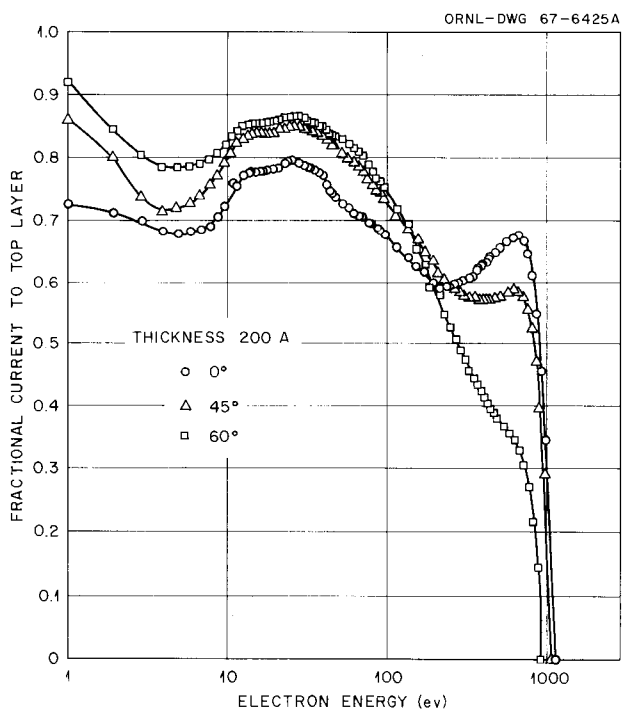

Fig. 20.1. Ratio of Current to Top Layer and Incident Beam Current. Layer is 200 A thick and electrons are incident at angles of 0, 45, and 60° to the normal direction.

[1]Student from the University of Tennessee.
[2]On loan from Thermonuclear Division.
[3]USAEC Health Physics Fellow.
[4]Postdoctoral Fellowship.

angles of incidence, the absorption is more complete, due to the longer path lengths required to traverse the top layer.

At about 7 ev above the vacuum level, the absorption begins to increase, due to onset of surface-plasmon excitation. This cross section then declines subsequently in the region above 20 ev, but its decline is matched by an enhancement of the volume-plasmon excitation cross section. Thus, a fairly constant transmission is noted between about 15 ev and about 50 ev.

All three of the above cross sections decline as the energy is increased until the onset of *L*-shell ionization at around 100 ev. The transmission curves taken at various electron angles cross in the vicinity of 200 ev, with a strong *L*-shell absorption being noted for normally incident electrons and a declining absorption being seen as the electron angle is increased to 45° and finally 60°. The cross section for *L*-shell ionization computed from the normal incidence data is in reasonable agreement with a theoretical calculation by Ritchie (unpublished) in first Born approximation, if one assumes that only single collisions in the top layer are responsible for the absorption. The absorption in the *L* shell should thus increase as the electron angle moves toward the oblique direction, but this is contrary to what we have noted experimentally. The reasons for this disparity in prediction and in fulfillment are not understood but may involve the angular distribution of the electrons after scattering on the *L* shell.

Further experiments with other metals are in progress, as is an extension of Monte Carlo transmission studies to higher electron energies. Also, a multicollision theory is being developed for *L*-shell interactions which occur as the electron passes through the top layer.

EXCITATION OF AMINO ACIDS BY ELECTRON BOMBARDMENT

In the course of designing an experiment to bombard amino acids in the solid state with low-energy electrons in order to measure their optical emissions, it became apparent that the incident electron beam could cause a charge buildup on the sample surface, since the amino acids are poor electrical conductors. To investigate this possibility, sandwiches of amino acids were constructed consisting of an aluminum electrode, a variable thickness of sublimed amino acid, and another electrode. The conductivity of the amino acid was then measured as a function of temperature and voltage across the sample. The results near room temperature may be stated as follows: The amino acid films are semiconductors, with a band gap of 2.7 ev and a resistivity of about 10^{16} ohm-cm. They undergo a dielectric breakdown at field strengths of the order of 10^5 v/cm. It is the breakdown phenomenon which permits the films to be used in the irradiation work described below. That is, the films do not charge up appreciably, nor are the electrons conducted through the film in the normal ohmic fashion, but rather by the more efficient method of avalanching.

In order to prevent charge buildup on the surface of the poorly conducting biochemicals, they were sublimed onto a substrate to a thickness between 100 and 1000 A. The sample holder was attached to a cryostat for temperature regulation and control.

An electron gun was constructed containing a parallel-plate deflecting device which bent the electron beam on emergence from the gun by approximately 90°. This parallel-plate bender acted as a light trap for the light emitted by the filament of the electron gun; that is, the electrons emerging from the exit slit of the bender were incident on a dark sample. Thus any light emitted from the sample could be attributed to the fluorescence or phosphorescence of the sample and not to light from the gun reflected by the sample. The electron beam struck the sample film at 45° to the normal, and the emitted light then passed through a quartz window at 90° from the electron beam direction. The light was dispersed by a monochromator and monitored by a photomultiplier.

Emission data from tryptophan and tyrosine films at 100°K indicated no substantial differences in the ratio of phosphorescence to fluorescence for excitation by 500 ev electrons and 30 ev electrons. This is corroborated by the observation that the P/F ratios for 500 ev and 30 ev excitation are about the same for radiation by 100 kev electrons and by x rays. This implies that the emission properties in all of the above cases must be governed completely by the slow secondary electron spectrum.

The conclusion that x-ray effects on emission spectrum may depend entirely on slow electrons is somewhat unexpected and makes accurate slow-electron inactivation work on enzymes very desirable. That is, the ionization from high-energy

electrons on cells has long been held to be more important than that from low-energy excitation. If these results are correct, then previous optical studies on these systems may have to be reevaluated. That is, subionization excitation may be much more important than previously expected.

Considerable difficulty was experienced in preventing the deposition of residual gases in the vacuum system upon the targets when the latter were maintained at low temperature. Although the pressure in the sample container was about 10^{-7} torr before the sample was cooled, upon cooling a pressure change of the order of 10^{-8} torr was noted. Assuming the ideal gas law to hold in a differential form, one finds that a pressure change of 10^{-8} torr corresponds to about 10^{-11} mole of gas being bound to the 1-cm^2 target surface, this corresponding to the order of 10^{13} molecules. The thickness of this layer depends upon the molecular weight of the material absorbed and is unknown. It is clear that future studies of this kind should be performed in an ultrahigh vacuum system so that this complicating absorption effect may be eliminated.

RADIATION INTERACTIONS WITH LIQUIDS

The reflectance method of determining optical and electronic properties of solids has been extended to the study of liquids. Liquid water, one of the most important and abundant of all substances, is currently being studied.

Despite the prevalence of water and its importance, very little is known about its electronic properties. Electronic properties determine how liquid water responds to light and how it behaves in biological systems, including those exposed to nuclear radiation. A knowledge of the electron transport properties of water will be useful in understanding electron transfer in biological processes. The only electronic property of water which is known and has been studied to any degree is that due to the generation and presence of polarons or hydrated electrons. The polaron is an electron in water bound with approximately 2 ev energy. Information on the electronic behavior of water above this energy is unavailable. It has been speculated that there may be two resonance energies in liquid water at somewhat higher energies, one at about 12.5 ev due to ionization of individual molecules in liquid water and the other about 17 ev due to plasmon generation.

To determine the optical and electronic properties of liquid water in the spectral region below 2000 A, a method has been devised to measure the reflectances of the liquid as a function of wavelength and angle of incidence. These reflectances may be used to evaluate the dielectric constants of water and subsequently to evaluate the electronic energy levels to determine which levels are excited by ionizing radiation.

The experimental apparatus consists of a vacuum ultraviolet Seya-Namioka monochromator, a light source, and a double-jacketed water cell. Light from the monochromator enters horizontally into the cell, where water in an open dish is in equilibrium with its vapor at a pressure just above that of the triple point of water. Incident light reflects downward from a mirror onto either the water or a reference surface of known optical properties. The light is then specularly reflected onto a photomultiplier coated with the nonhygroscopic phosphor coronene.

Several difficulties are encountered in reducing the pressure in the cell by means of vacuum pumping without violently disrupting the water sample. The temperature of the cell and the sample must be lowered as the pressure is reduced so that the sample remains in the liquid state and in equilibrium with its vapor. The state of the sample is controlled by regulating the temperature of the cell, controlling the vapor leak through the optical slits, and assuring that the state of aeration of the sample and temperature of the sample itself are right for the liquid state. Vaporization from the liquid surface is controlled by use of an auxiliary heated water reservoir.

By minimizing the vapor pressure and path length to a few torr-centimeters, it is possible (at wavelengths corresponding to minimum absorption by the vapor) for light of sufficient intensity to reach the photomultiplier. Comparison of the spectral reflectance from the water surface with that of a reference gold surface gives the reflectance of liquid water.

Preliminary reflectance measurements at 20, 45, and 70° indicate an increase in reflectance with decrease in wavelength below 2000 A. There are indications of peaks in the reflectance curves at 1250, 1700, and 2100 A, as shown in Fig. 20.2.

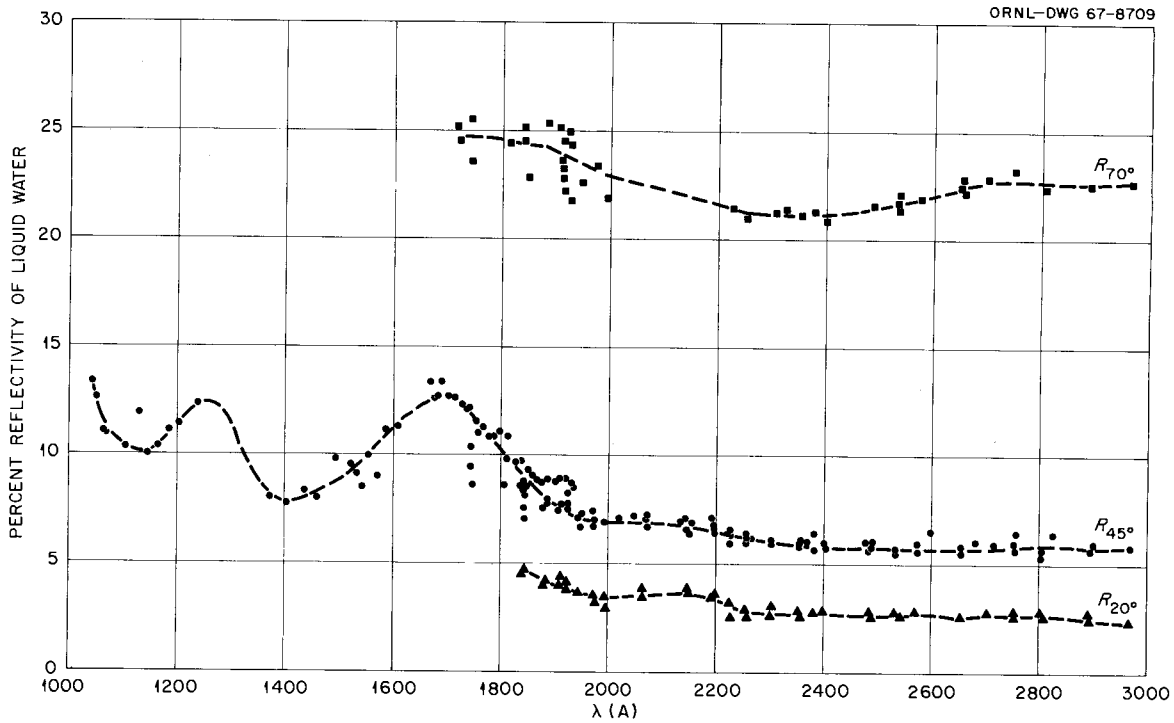

Fig. 20.2. Reflectance of Liquid Water as a Function of Wavelength at Angles of 20, 45, and 70° to the Normal Direction.

ORGANIC SCINTILLATORS WITH 2-ETHYLNAPHTHALENE AS A SOLVENT

The work on excimer scintillators reported previously (ORNL-4007) has continued with the investigation of the emission intensities, quenching effect, and pulse heights of 11 efficient scintillator solutes in 2-ethylnaphthalene (2-EN).

For 2-EN, excimer emission dominates at room temperature. This liquid also has a higher density than commonly used scintillator solvents (e.g., 19% higher density than toluene). The scintillation spectra for 11 of the most efficient scintillator solutes in 2-EN are given in Fig. 20.3B and C. The spectra were taken at room temperature, in oxygen-free solutions, and under identical conditions, so that they could be compared directly. The intensity under x-ray excitation is referred to that of a standard solution [TP (5 g/liter) + POPOP (0.5 g/liter) in toluene, Fig 20.3A] with the same volume and same geometrical arrangement as those of the sample solutions. All results were reproducible to within a few percent.

Table 20.1 compares the integrated emission intensities at approximately optimum concentration for the various scintillators studied. It should be kept in mind, however, that because the index of refraction for the 2-EN solutions is higher than that of toluene and quartz, the actual integrated emission intensity, I_{int}, for the 2-EN solutions is larger than that measured due to total internal reflection. In Table 20.1 the ratio of the reflectivity of TiO_2 to that of Al is also given for λ_{max}, that is, the wavelength λ at which the emission intensity, $I(\bar{\nu})$, reaches a peak for each scintillator. For most of the scintillators studied, the improved reflectivity of TiO_2 at $\lambda > 4000$ A can be employed. The integrated emission intensities from 2-EN containing DPA or α-NPO, PPO, DPH, and POPOP compare well with those of the best liquid scintillators. It is worth noting also that the emission from these systems matches ideally the S-II photocathode spectral response. When the improved reflectivity of TiO_2 is considered, the mixture DPA (12 g/liter) in 2-EN is 0.91 as efficient as system I [TP (8 g/liter) in toluene] and 0.86 as efficient as system II (Table 20.1).

Scintillator loading materials in the past varied in quenching effect from weak to strong; that is, the fluorescence intensity of the liquid scintillator

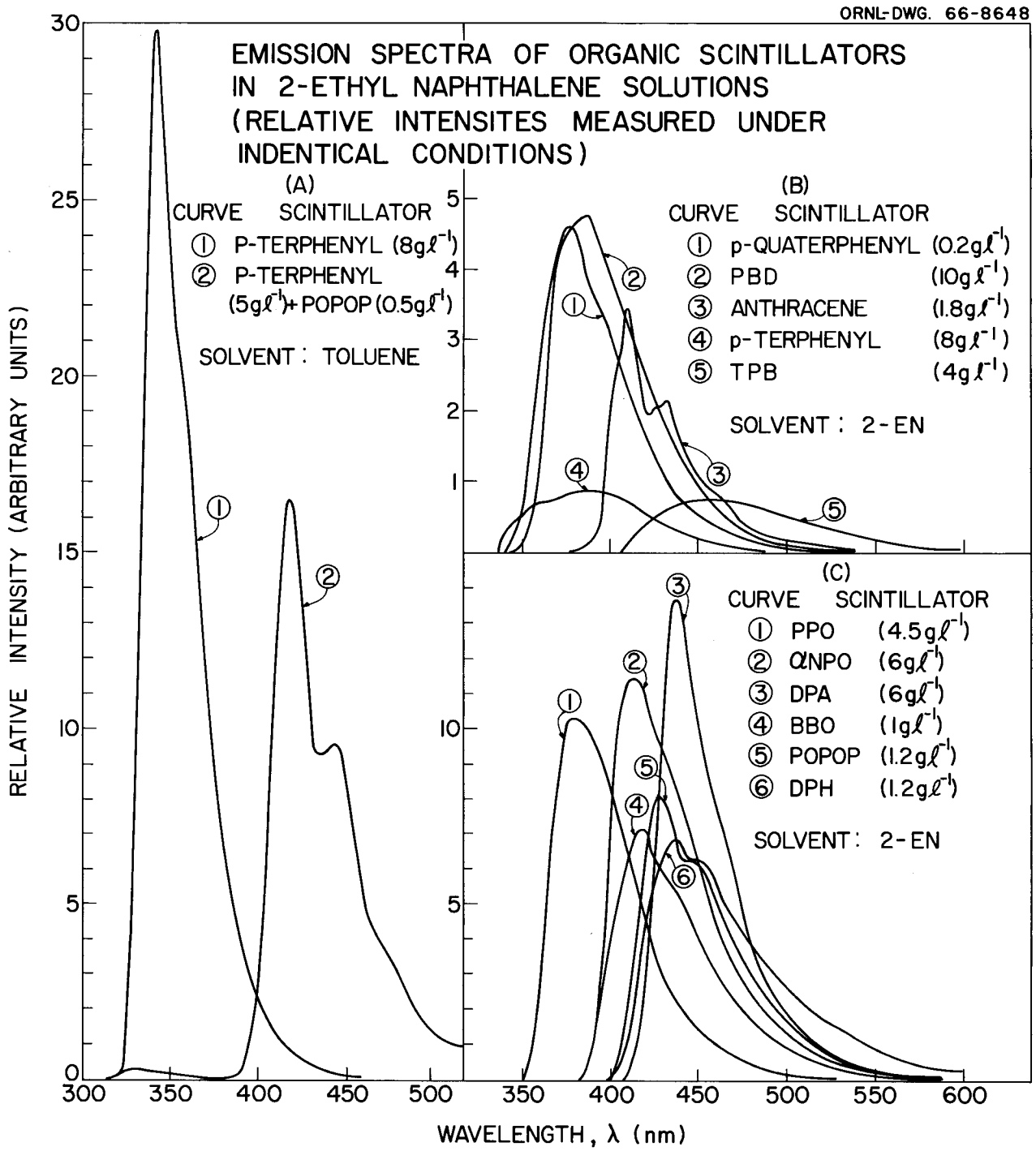

Fig. 20.3. Emission Spectra of Organic Scintillators in Toluene and 2-EN. Relative intensities measured under identical conditions.

Table 20.1. Data for Organic Scintillators in 2-EN Solutions

Scintillator	$\int_0^\infty I(\bar{\nu})\,d\bar{\nu}$	λ_{max}	$\frac{TiO_2}{Al}$	Concentration (g/liter)
TP (8 g/liter) in toluene[a]	1.38	340	0.86	
TP (5 g/liter) + POPOP (0.5 g/liter) in toluene[b]	1.00	420	1.23	
DPA	0.81	448	1.38	12
α-NPO	0.71	413	1.21	6
PPO	0.70	382	1.03	4
DPH	0.68	448	1.38	1.2
POPOP	0.63	416	1.21	1.2
BBO	0.56	418	1.22	1
PBD	0.4	388	1.03	10
Anthracene	0.18	410	1.18	1.8
TPB	Very small	461		4

[a]Reference system I.

[b]Reference system II.

Table 20.2. Integrated Emission Intensities for Organic Scintillators in Solutions of 2-EN Containing Quenching Materials

Scintillator Solute	Quencher	Percent of Quencher (by mass)	Integrated Emission Intensity Compared with Standard[a]
9, 10-DPA (12 g/liter)	DBM	7	358
9, 10-DPA (12 g/liter)	Thiophene	85	225
α-NPO (5 g/liter)	DBM	7	209
9, 10-DPA (12 g/liter)	Triphenyl bismuthene	0.5	114
9, 10-DPA (12 g/liter)	Tri-*n*-butyl phosphate	49	103

[a]TP (5 g/liter) + POPOP (0.5 g/liter) in toluene taken as 100.

decreased with increasing concentration of the loading material. An apparent negative quenching was discovered for a number of quenchers (see Table 20.2) when 2-EN was used as a scintillator solvent.[5]

Pulse height distributions were taken for the following systems: II, *p*-terphenyl [TP] 5 g/liter + POPOP [2,2′-*p*-phenylenebis(5-phenyloxazole)] 0.5 g/liter in toluene; III, DPA 12 g/liter in 2-EN + DBM [di-*n*-butylmercury] 7%; and IV, DPA [diphenylanthracene] 12 g/liter in 2-EN. Table 20.3 lists the maximum pulse heights obtained for the three systems. Under all conditions except ^{32}P excitation with large solution thicknesses, system IV gave appreciably higher pulse heights than the reference system II. The pulse heights from system III were lower than those of the reference system II, but still high compared with the data of Furst and Kallman,[6] who found that the integrated emission intensity from α-NPO (5 g/liter) in xylene decreased to only 9% of its original value on addition of 10% by mass of DBM. This supports the argument that quenchers in scintillating 2-EN solutions are less effective than in other systems. The pulse heights for the systems III and IV would have been even higher than their present values had the differences in the indices of refraction in these solutions and those of system II and the photomultiplier window been considered.

In a solvent such as 2-EN, electronic excitation energy transfer from M_S^* (M molecules in their first excited π-singlet state) to another molecule S may occur predominantly through the photoassociated M_2^*, that is,

$$M_2^* + S \longrightarrow S^* + M + M\,. \qquad (1)$$

Process (1) may be more efficient than the corresponding one for M_S^*. Furthermore, in an excimer-

[5]J. G. Carter and L. G. Christophorou, *J. Chem. Phys.* **46**, 1883 (1967).

[6]M. Furst and H. P. Kallmann, *Phys. Rev.* **97**, 583 (1955).

Table 20.3. Maximum Pulse Heights for Various Scintillators

Scintillator Thickness (cm)	Radioactive Source	Maximum Pulse Height		
		TP (5 g/liter) + POPOP (0.5 g/liter) in Toluene[a]	DPA (12 g/liter) in 2-EN[b]	DPA (12 g/liter) in 2-EN + DBM (7%)[c]
0.088	^{32}P (E_β = 1.7 Mev)	100	136	84
	^{22}Na (E_γ = 1.3 Mev)	100	129	84
	^{137}Cs (E_γ = 0.66 Mev)	100	114	96
0.2	^{32}P	100	181	108
	^{22}Na	100	122	74
	^{137}Cs			
0.6	^{32}P	100	106	60
	^{22}Na	100	118	74
	^{137}Cs	100	136	100
1.0	^{32}P	100	96	55
	^{22}Na	100	105	71
	^{137}Cs	100	104	91
1.4	^{32}P	100	96	54
	^{22}Na	100	119	69
	^{137}Cs	100	107	67
1.6	^{32}P	100	95	54
	^{22}Na	100	122	68
	^{137}Cs	100		68

[a]System II.
[b]System IV.
[c]System III.

forming solvent the quenching of the solvent by a quencher Q must also be visualized as

$$M_2^* + Q \longrightarrow M_s + M_s + Q \ . \qquad (2)$$

If process (1) is fast and process (2) is slow, it is possible in a loaded scintillator to observe increased emission due to energy transfer from Q* to S.

Since in our experiments with 2-EN as a solvent we observed less quenching of the emission of organic scintillators by Q than in other cases,[6] process (1) may be faster and/or process (2) may be slower than the corresponding ones for M_s^* (the lowest energy level of M_2^* lies below the corresponding one of M_s^*).

It is important to point out the role of the solvent excimer as an "intermediate solvent" or "secondary solute." Thus, instead of using a three-component liquid scintillator, and limiting the solubility in some cases, a two-component system may be used with the solvent excimer serving as a "secondary solute," shifting the M_s^* emission to that of M_2^*.

EXCITATION OF VOLUME PLASMONS WITH LOW-ENERGY ELECTRONS

Much experimental work has been done on the excitation of plasmons by electrons, but the work has been confined to electron energies above 10

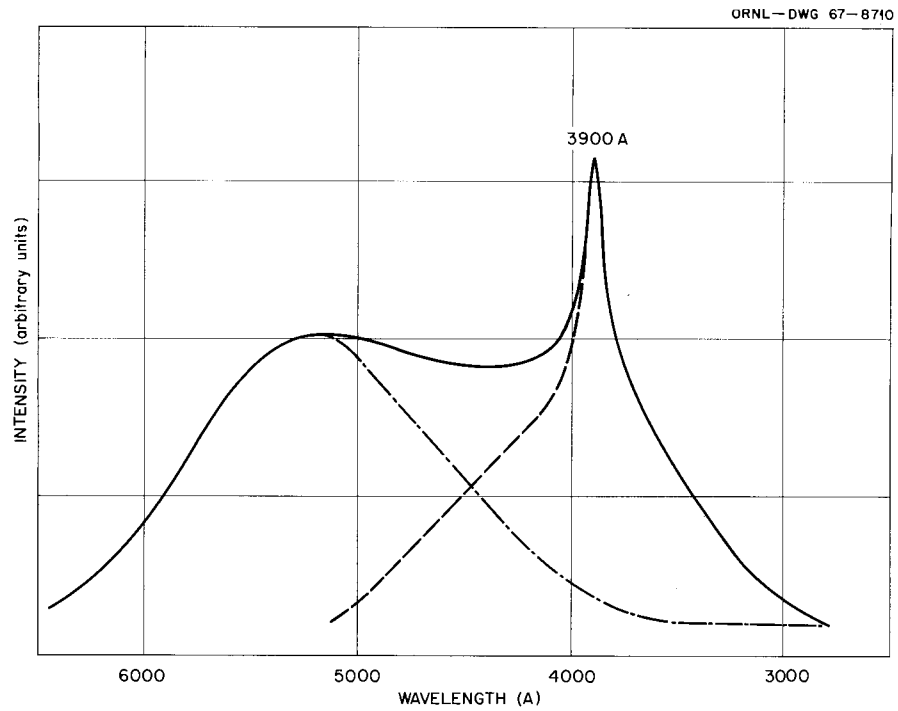

Fig. 20.4. Spectrum of Light Emitted by Silver Foil Bombarded by 200-ev Electrons.

kev. Preliminary results have been obtained for Ag using 200-ev and 700-ev electrons incident normally on an Ag foil. The photons are viewed at 45° from the normal to the foil. The spectra show a peak at 3900 A, as illustrated in Fig. 20.4 using 200-ev electrons. The broad peak at 5200 A is light from the electron gun filament. Further work is required before identification of the 3900-A peak with plasmon decay is possible.

EXCITATION AND IONIZATION YIELDS IN Al

Electron flux spectra[7] from ^{198}Au and ^{64}Cu beta rays slowing down in Al were analyzed to obtain the number of interactions/cm^3 per primary electron/cm^3 for K-shell ionization, L-shell ionization, volume-plasmon excitation, and electron-electron collisions. The number, N, of interactions/cm^3 per primary electron/cm^3 is given by

$$N = \int_{T_{th}}^{T_{max}} y(T)\, \lambda^{-1}(T)\, dT\ , \qquad (3)$$

where y is the electron flux in units of electrons cm^{-2} ev^{-1} per primary electron/cm^3, λ^{-1} is the inverse mean free path or macroscopic cross section in cm^{-1}, and T_{th} is the threshold energy for the interaction. Equation (3) can be put into more convenient form by multiplying and dividing by T to get

$$N = \int_{T_{th}}^{T_{max}} T\, y(T)\, \lambda^{-1}(T)\, d \ln T\ . \qquad (4)$$

Further, if $T\, y(T)\, \lambda^{-1}(T)$ is plotted vs ln T, an area under this curve between any two energies T_1 and T_2 is equal to the number of events occurring within the energy range $T_2 - T_1$. The inverse mean free paths used in the calculations[8] are shown in Fig. 20.5 as the solid lines. Values of N given in Table 20.4 were determined by graphical methods from plots of $T\, y(T)\, \lambda^{-1}(T)$ as a function of log T as shown in Figs. 20.6–20.8. A plot of $T\, y(T)\, \lambda^{-1}(T)$ as a function of log T for electron-electron interactions is shown in Fig. 20.9. The excitation of a volume plasmon in aluminum requires 15 ev; thus the amount of energy expended in exciting volume plasmons was 260 kev for the ^{64}Cu source and 275 kev for the ^{198}Au source. These can be compared with the average

[7] *Health Phys. Div. Ann. Progr. Rept. July 31, 1966*, ORNL-4007, pp. 157–60.

[8] R. H. Ritchie, unpublished.

energies of the beta spectra, which are 230 kev for ^{64}Cu and 315 kev for ^{198}Au. Thus when an electron slows down in a metal, nearly all of the energy goes ultimately into volume-plasma excitation.

Due to the large discrepancy between theoretical and experimental flux at low energies, an electron gun has been constructed to extend the calibration of the Keplertron above 3 kev. The electron gun will be used to obtain line profiles to determine if the ratio of the height of the spurious low-energy tail to the height of the central peak retains the same constant value (0.0015), independent of the electron energy, above 3 kev. The electron gun also will be used to determine if the line profiles are affected by the azimuthal angle at which electrons emerge from the source.

Table 20.4. Excitation and Ionization Yields in Aluminum from ^{64}Cu and ^{198}Au Beta Rays

Interaction	Interactions/cm^3 per Primary Electron/cm^3	
	^{64}Cu	^{198}Au
K-shell ionization	2.6	4.0
L-shell ionization	266	324
Volume-plasmon excitation	17,420	18,320

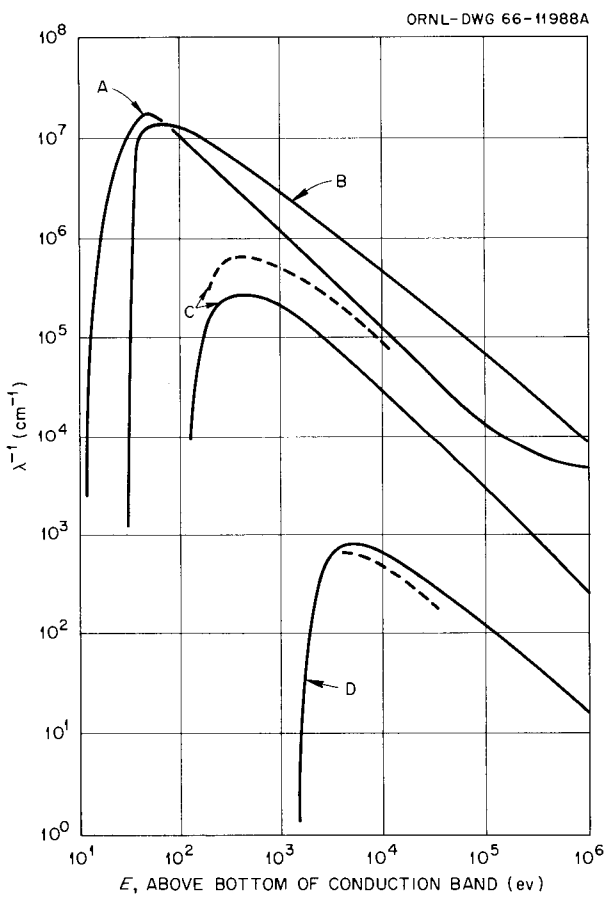

Fig. 20.5. Inverse Mean Free Paths in Aluminum. (*A*) Electron-electron interactions in the conduction band, (*B*) volume-plasmon excitation, (*C*) *L*-shell ionization, (*D*) *K*-shell ionization. The solid lines are theory by Ritchie; the dashed line for *L*-shell ionization is a Gryzinski-type calculation [M. Gryzinski, *Phys. Rev.* 138, A305, A322, A336 (1965)]; the dashed line for *K*-shell ionization is the theory of A. M. Arthurs and B. L. Moiseiwitsch, [*Proc. Roy. Soc.* **A247**, 550 (1958)].

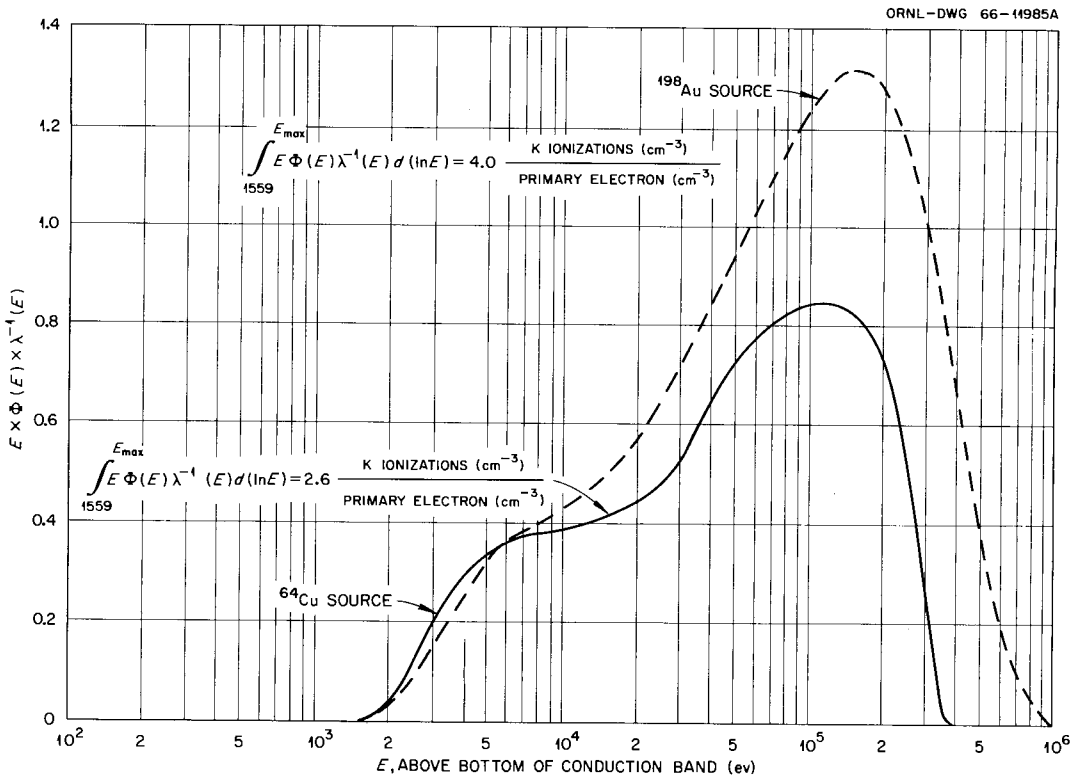

Fig. 20.6. K-Shell Ionization in Aluminum. Solid line, ^{64}Cu source; dashed line, ^{198}Au source.

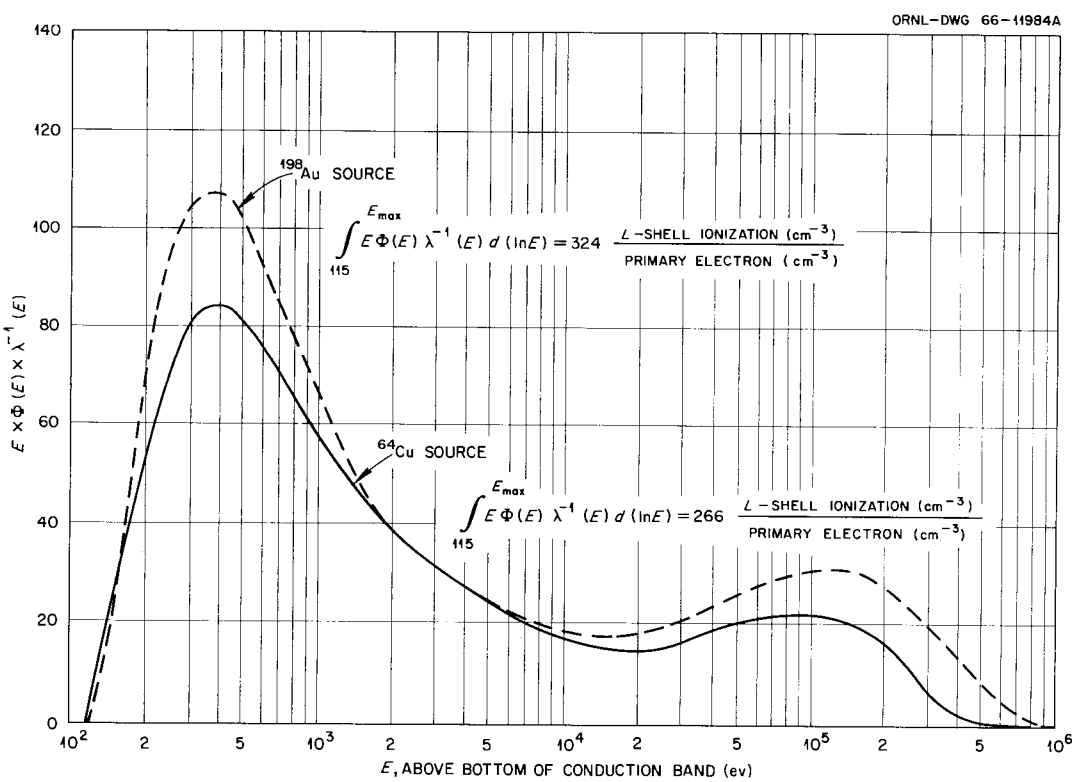

Fig. 20.7. L-Shell Ionization in Aluminum. Solid line, ^{64}Cu source; dashed line, ^{198}Au source.

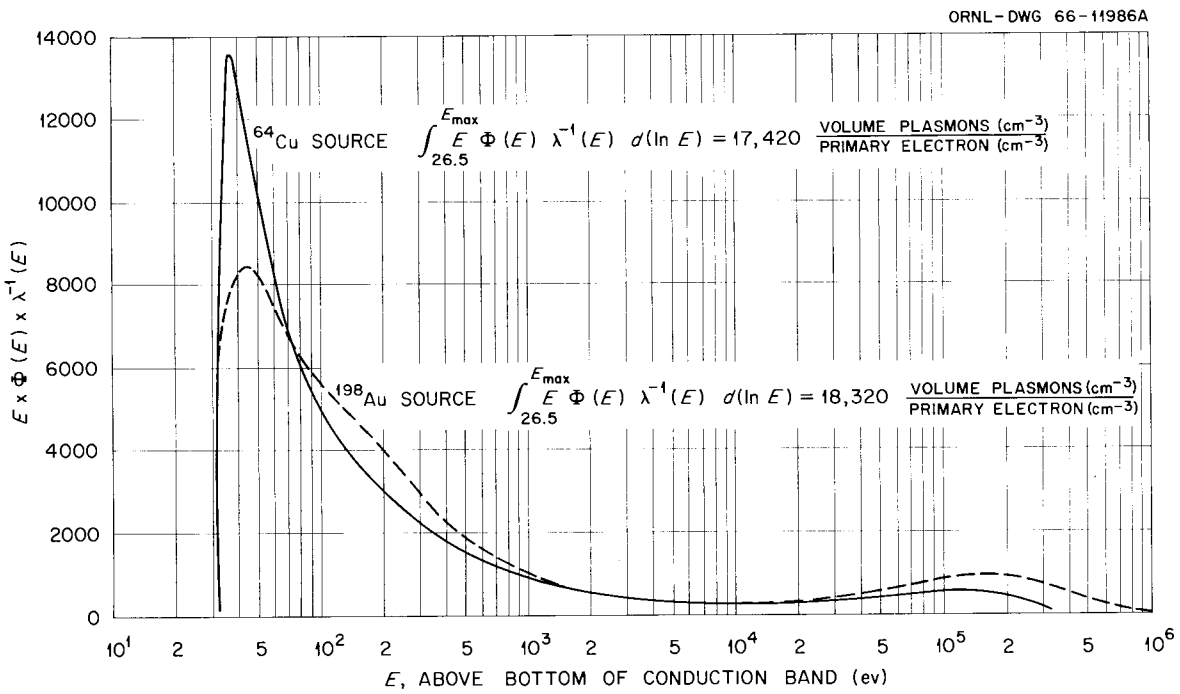

Fig. 20.8. Volume Plasmons Excited in Aluminum. Solid line, ^{64}Cu source; dashed line, ^{198}Au source.

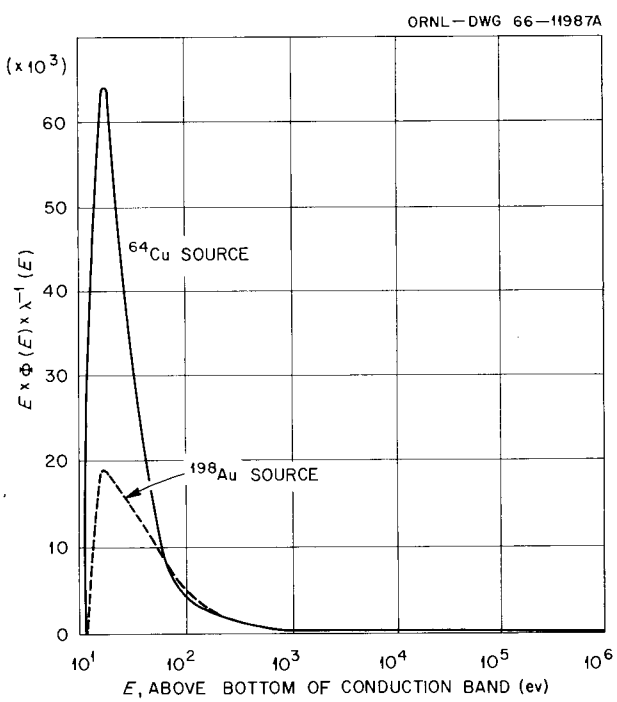

Fig. 20.9. Electron-Electron Interactions in the Conduction Band of Aluminum. Solid line, ^{64}Cu source; dashed line, ^{198}Au source.

Part IV. Radiation Dosimetry

J. A. Auxier

21. Ichiban Studies

J. A. Auxier

J. S. Cheka H. H. Hubbell, Jr.
F. F. Haywood T. D. Jones
D. R. Johnson

ICHIBAN LIAISON

Two visits were made to the Atomic Bomb Casualty Commission (ABCC) in Japan, one from February 4 to March 3, 1967, and one from June 3 to June 28, 1967. Assistance was rendered to ABCC on various problems that have arisen in computing the present estimates (T65D) of radiation doses to the survivors of the wartime bombings.

The survivors may be classified according to the method by which it is possible to assign doses to each of them,[1] as follows: (1) globe,[2] (2) nine-parameter formulas,[3] (3) air dose,[4] and (4) no method applicable.

The types of shielding environments and the number of persons constituting category 4 are shown in Table 21.1. The Ichiban group is currently conducting studies which will permit the estimation of doses for the survivors inside concrete buildings, for survivors shielded by combinations of factors (including terrain shielding), and for several cases in the miscellaneous class. Most persons surviving the nuclear explosions inside cave-type air-raid shelters were sufficiently far from the hypocenter and shielded by enough earth that the exposure level was nearly zero. With a small amount of additional study, it should be possible to estimate the doses for the survivors inside army barracks and those inside railway passenger coaches. The estimation of exposure level for the survivors inside streetcars represents a nearly impossible task if one attempts to obtain a degree of accuracy which will permit any correlation of biological effects (at 8:15 AM the streetcars were packed with people; thus no high level of reliability can be assigned to the survivors' locations or their mutual shielding effects).

Table 21.1. Numbers of Japanese Survivors for Whom No Shielding Calculation Is Applicable at Present

Position of Survivors	Number of Survivors	
	Hiroshima	Nagasaki
Inside concrete building	332	610
Inside cave-type air-raid shelter	31	108
Shielded by combination of factors, including terrain shielding		262
Inside streetcar	155	
Inside railway passenger coach	47	
Inside army barracks	74	
Miscellaneous	160	79
Total	799	1069

[1] J. A. Auxier *et al.*, *Health Phys. Div. Ann. Progr. Rept. July 31, 1966*, ORNL-4007, p. 173.

[2] J. S. Cheka, ORNL-CF-66-5-31 (internal memorandum).

[3] J. S. Cheka *et al.*, *Distribution of Weapons Radiation in Japanese Residential Structures*, CEX-62.11 (August 1965).

[4] J. A. Auxier *et al.*, *Health Phys.* **12**, 425–29 (1966).

Of these 1868 shielding histories, the liaison correspondent studied 650 in Hiroshima (including 140 high-dose cases for people whose calculated doses exceeded 800 rads) and about 241 cases in Nagasaki (including 66 high-dose cases). Those histories yielding an estimated dose of more than 800 rads are being given special attention, case by case. In many instances, these high-dose cases died on August 6, 1945, or a few days later and should not be included as "survivors." There are also a number of apparent mistakes or false claims because some survivors claim they were within 600 yd of the hypocenter, totally unshielded, not burned by the flash, and showed no permanent radiation-induced trauma even up to the present. Such a combination of circumstances is manifestly impossible. Permanent copies of the shielding histories of the 206 high-dose cases have been sent to ORNL for further investigation. The ABCC has estimated T65 doses for about 19,500 survivors, or about 91% of the total number of cases under study in Hiroshima, and about 73,000, or about 88% of the total, in Nagasaki; so these 206 high-dose cases represent only about 0.8% of the completed T65D.

Now that the ABCC has finished the T65 estimates, it is possible to start the correlation of the biological response functions to dose. Since these T65D estimates for Hiroshima are significantly lower than the earlier T57D estimates in nearly all cases, it is felt that the biological effects observed in the two cities will show closer correlation to exposure level than was indicated in the past.

RADIATION ATTENUATION BY CONCRETE

In order to calculate exposures to survivors in heavily shielded locations such as concrete buildings, additional data are needed on the attenuation by concrete for weapons-type radiation at long distances from the burst point. Since weapons tests are no longer conducted, measurements of attenuation of similar radiation were undertaken at the DOSAR. Dose rates were measured separately for fast neutrons with a Hurst proportional counter and a Radsan pulse integrator and for gamma rays with a Phil counter,[5] under various thicknesses of concrete slabs. The measurements were made near the DOSAR control building, where the source was the air-scattered radiation from the HPRR. The direct radiation was completely shielded by a hill. Measurements were also made directly beneath the HPRR, which was at an elevation of 6 m.

The first runs were made with a 1-in.-diam (phantom) proportional counter for fast neutrons and a miniature G-M counter (Phil), shielded by ^{6}Li, for gamma rays. These proved to be too insensitive for measuring the scattered radiation, giving poor statistical reliability after a few 3-in. slabs were added. However, they were adequate for measurements of the direct radiation from the HPRR.

The phantom counter and the Phil counter were, consequently, replaced by the standard-sized Hurst counter and a larger G-M tube, having sensitivities greater by factors of ~20 and ~45 respectively.

[5] E. B. Wagner and G. S. Hurst, *Health Phys.* 5, 20 (1961).

Table 21.2. Neutron Fluence Spectra from Various Sources as Observed by Threshold Detector Systems

Tabulated numbers are fractions of the total fluence between the energy thresholds of the elements listed

Source	Energy Range			
	Pu-Np, 1 kev–0.75 Mev	Np-U, 0.75–1.5 Mev	U-S, 1.5–2.5 Mev	S, >2.5 Mev
HPRR leakage	0.242	0.385	0.157	0.216
Weapons (total at 1000 yd)	0.566	0.240	0.097	0.097
Weapons (0° at 1000 yd)[a]	0.232	0.236	0.212	0.319
Weapons (90° at 1000 yd)[b]	0.729	0.152	0.062	0.056

[a] This is the fluence spectrum as observed by a threshold detector system in a collimator at a 1000-yd slant range from the weapon burst point (for air bursts), with the collimator aimed at the burst.

[b] This fluence spectrum is obtained with a similar arrangement, but with the collimator aimed in a direction 90° to the line to the burst point and above the horizon.

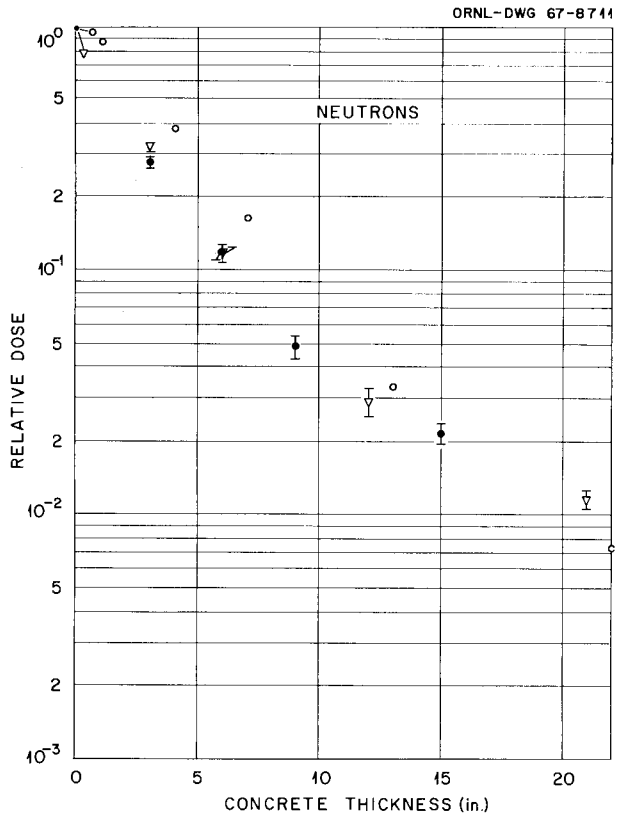

Fig. 21.1. Attenuation by Concrete of Direct and Scattered Neutron Doses from the HPRR. ⊙ Slabs placed horizontally on concrete floor 20 ft directly below reactor so that direct radiation was incident normally. Δ Slabs placed vertically against wall of building 7712 1000 ft from reactor with slab surface normal to a line to the reactor. Direct radiation completely shielded by a hill; scattered radiation only was incident. ▮ Slabs placed horizontally on a concrete ramp outside building 7710 1000 ft from reactor. Direct radiation completely shielded by a hill and a building; scattered radiation only was incident.

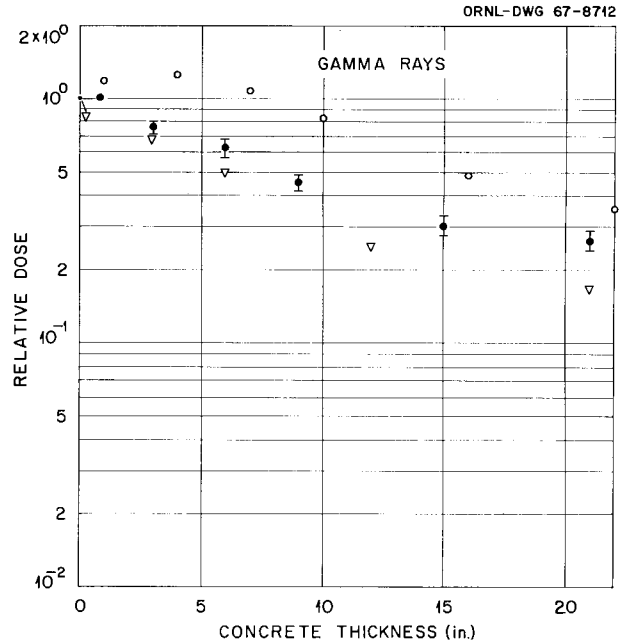

Fig. 21.2. Attenuation by Concrete of Direct and Scattered Gamma-Ray Doses from the HPRR. Experimental arrangements and point symbols same as for Fig. 21.1.

Measurements of the scattered radiation were made with the slabs in a vertical position against a thick concrete wall that faced the direction of the HPRR and also with the slabs in a horizontal position on a concrete runway at the DOSAR control building. The results of the neutron and gamma-ray measurements are given in Figs. 21.1 and 21.2 respectively.

The attenuation curves differ at the various locations, as expected, because of spectral differences; the differences in spectra are indicated by fluence data from threshold detector dosimeters, as shown in Table 21.2.

The gamma-ray spectra also differ; the scattered radiation near the DOSAR control building is harder, principally because of (n, γ) reactions of the fast neutrons from the reactor with oxygen and nitrogen in the air.

The dose attenuation lengths as determined with HPRR radiation are to be corrected to the values to be expected for weapons radiation, using fluence spectra such as those in Table 21.2. From these data the shielding of Japanese survivors in concrete buildings may be calculated using the "globe" (spherical coordinate projector) in models of the survivors' surroundings at the time of the bomb burst plus the known angular distributions of dose components reaching the survivors.

OPERATION HENRE – GENERAL OPERATIONS

The design, fabrication, and testing of a high-yield 14-Mev neutron generator have been reported earlier.[1,6] This generator is a positive-ion accelerator utilizing the low-energy reaction $T(d,n)^4He$ with an accelerating potential of 150

[6] T. G. Provenzano *et al.*, *Feasibility Study: Intense 14-Mev Neutron Source for Operation HENRE*, CEX-65.01 (May 1966).

kv and a beam current of 400 ma. The accelerator was put in normal operation at the Nevada Test Site on October 12, 1966. It is supported at several heights on a 1527-ft tower and operated for periods of 3 to 4 hr. Measurements in the mixed radiation field are designed to furnish data that may be used to test the validity of assumptions employed in shielding and transport calculations.

The postulated neutron yield for this accelerator at the time of design was 10^{13} neutrons/sec for 4-hr periods. A yield of approximately 5×10^{11} neutrons/sec was realized from the first target. This low yield precluded neutron and gamma-ray measurements at large distances from the tower; however, valuable information was obtained at distances to 500 ft. Two successive changes were made in the target preparation procedures. It was noted that each change produced a marked improvement in the neutron yield and resulted finally in surpassing the design yield of 10^{13} neutrons/sec. One target had an average yield of 1.5×10^{13} neutrons/sec for 4 hr and for a second 4-hr period yielded an average of 5×10^{12} neutrons/sec, nearly doubling the expected lifetime of this target. Although neutron yield and target lifetime are critical functions of the quality of the target, an average yield of 8×10^{12} to 1.1×10^{13} neutrons/sec for 4 hr can be realized routinely through rigorous control of the target preparation parameters.

Accelerator systems designed and fabricated at ORNL have rendered trouble-free operation. However, the commercially obtained 150-kv, 0.5-amp high-voltage power supply has failed to operate satisfactorily on several occasions. Because of these malfunctions, field operations at the Nevada Test Site were suspended during December 1966 and from February through mid-June 1967. During this latter period, repairs were made and the circuit components that protect the transformers and rectifier bridges in the power supply were redesigned. Short-circuit and load tests performed after the power supply was reassembled indicated that these design changes were sufficient to provide the protection required for the power supply. Field operations were resumed in late June and are expected to be completed in September.

ORNL Participation

The Division is conducting an experiment designed to (1) determine the angular distribution of neutron and gamma-ray dose and energy spectra (each independently) as a function of distance from the source, (2) study the effect of the presence of the ground on the propagation of neutrons and gamma rays by determining boundary correction factors for dose as a function of source height and distance from the source, and (3) study the interaction of the components of a mixed radiation field with materials having a wide range of atomic weights.

Effect of the Air-Ground Interface on the Spatial Distribution of Dose

Since only a small portion of the field experiment has been completed, most of the experimental results will be reported later. However, a measurement of neutron and gamma-ray dose has been made as a function of distance from the source with the detectors supported from a helicopter at heights to 1000 ft above the ground. Detector height was indicated by the aircraft's altimeter, and horizontal distance was indicated by radar beamed at the tower. A comparison of dose as a function of distance for two detector heights reveals a marked lengthening in the relaxation length for gamma-ray dose as the detector is raised above the air-ground interface. This is shown in Fig. 21.3 (ref. 7), where neutron and gamma-ray dose multiplied by R^2 (slant range squared) is plotted as a function of R. The air density was 1.08 g/liter.

The greater relaxation length for 14-Mev neutrons compared with fission neutrons (from the HPRR) is shown in Fig. 21.4, where neutron dose multiplied by R^2 is plotted as a function of source height; the detector was positioned on the ground at a slant range of 1800 ft. For this slant range, it is seen that, relative to a fission spectrum, 14-Mev neutrons produce 30 and 50% higher neutron dose rates for source heights of 300 and 1125 ft respectively.

One of the most important aspects in the study of the radiation field in an air-over-ground geometry is to determine experimentally the boundary correction factors for radiation sources as a function of their height above the ground. By measuring the dose distribution in an infinite medium

[7] Z. G. Burson, Edgerton, Germeshausen and Grier, Inc., private communication.

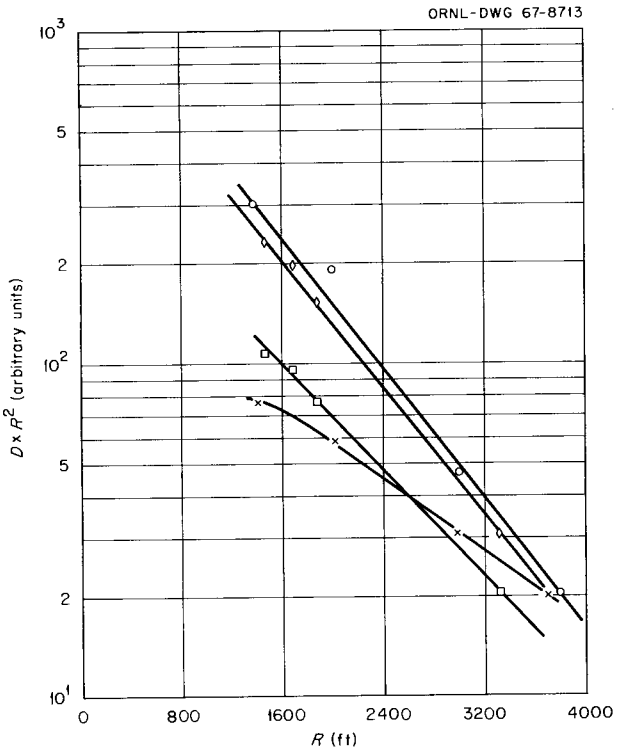

Fig. 21.3. Neutron and Gamma-Ray Dose as a Function of Slant Range and Detector Height for a Source Height of 1125 ft. ⊙ Detector height 700 ft, neutron dose; ◇ detector height 3 ft, neutron dose; ⊡ detector height 3 ft, gamma-ray dose; X detector height 700 ft, gamma-ray dose.

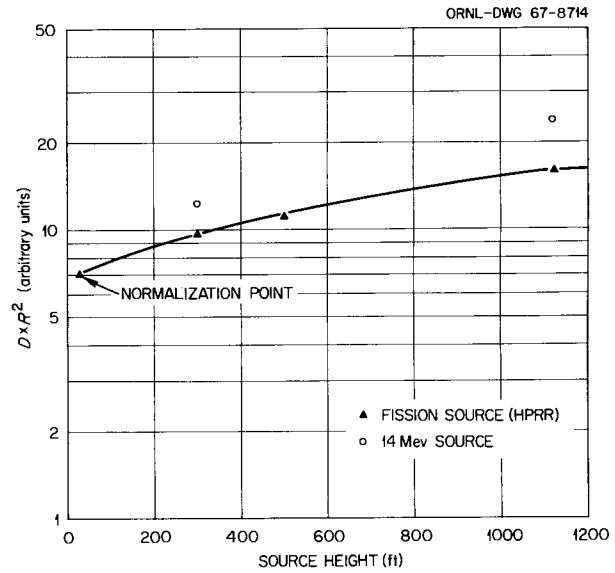

Fig. 21.4. Comparison of Neutron Dose from HENRE Accelerator to That of HPRR as a Function of Source Height with Dosimeter on the Air-Ground Interface at 1800 ft Slant Range.

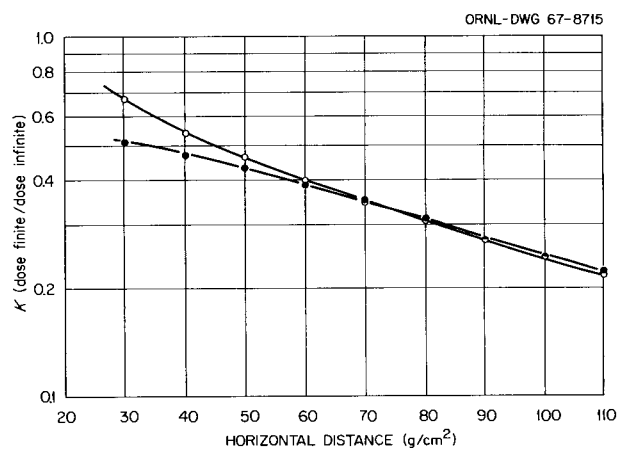

Fig. 21.5. The Ratio of Dose in the Finite Medium (with Ground) to the Dose in an Infinite Air Medium for Fast Neutrons as a Function of Horizontal Distance from the Source as Calculated by Ritchie and as Measured During Operation HENRE. ○ K (theoretical) ORNL-Ritchie, $H_s = 10$ m, $H_D = 0$ m; ● K (experimental) HENRE 1.4, $H_s = 8.2$ m, $H_D = 1.0$ m.

of air and in a finite medium (in air near the ground), it is possible to obtain these correction factors. The boundary correction factor K is defined as the ratio of the dose in the finite medium to the dose in an infinite medium. Once this has been done, a significant reduction in computer time may be realized by utilizing these factors in the more elementary case of calculating the dose in an infinite air medium instead of in the finite medium. As an example: dose in finite medium = $K \times$ calculated dose in infinite medium.

Data from weapon tests,[8] Operation BREN,[9] and Operation HENRE indicate that measurements made at 1000 to 1500 ft above the ground for both source and detector may be considered to be in an infinite air medium. A comparison between experimental and theoretical values of K is shown in Fig. 21.5, where K is plotted as a function of distance from

[8] J. A. Auxier, J. S. Cheka, and F. W. Sanders, WT-1725 (March 1961) (classified).

[9] F. F. Haywood, J. A. Auxier, and E. T. Loy, *An Experimental Investigation of the Spatial Distribution of Dose in an Air-over-Ground Geometry*, CEX-62.14 (October 1964).

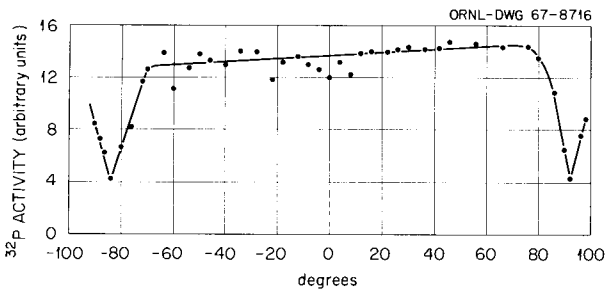

Fig. 21.6. Angular Distribution of Neutron Fluence Around HENRE Target at 1 m from Center of Target. 0° is direction of beam, positive angles toward front of tower.

the source in grams per square centimeter. The divergence is probably due to the fact that measurements in the finite medium were low because of anisotropy of the source caused by a thick rim of copper around the target circumference. This rim of copper is responsible for a depression in the neutron flux around the target, as seen in Fig. 21.6 (ref. 10). In order that the shadow of this material not interfere with the radiation field near the ground, a new accelerator tube has been fabricated which holds the target at an angle of 25° from horizontal. It is expected that better agreement between the experimental value of K and Ritchie's theoretical value[11] will be obtained in all subsequent measurements.

PRELIMINARY RESULTS OF ANGULAR DOSE AND NEUTRON ENERGY SPECTRUM MEASUREMENTS MADE DURING OPERATION HENRE

There were a total of four useful accelerator runs during the period January 17 to 31, 1967. The first two runs, at a 400-ft source elevation, were utilized primarily for measurements inside a simple shelter system for civil defense applications (see Fig. 21.7) located approximately 300 ft from the tower. There was 3 ft of earth on top of the shelter, and the resulting neutron spectrum data were marginal due to poor counting statistics.

[10]J. K. Morrow, U.S. Air Force Weapons Laboratory, private communication.

[11]R. H. Ritchie and V. E. Anderson, ORNL-3116 (July 1962) (classified).

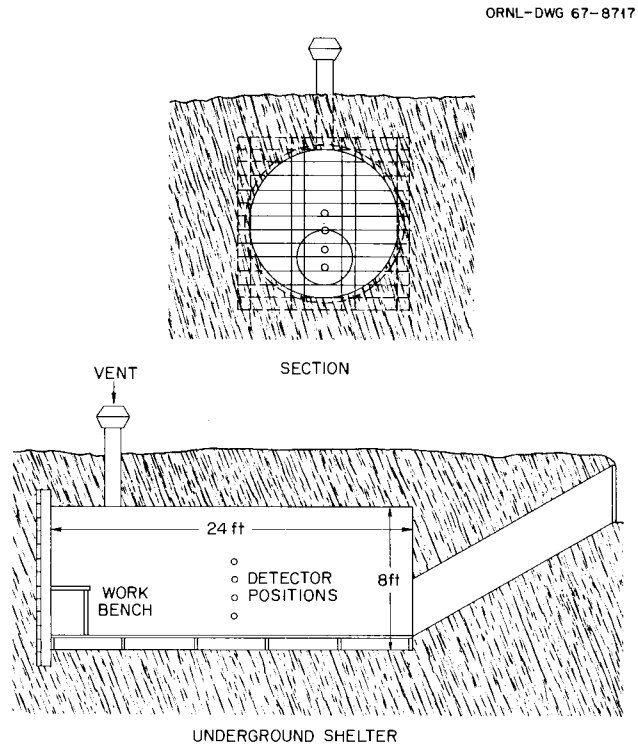

Fig. 21.7. Sectional Views of Cylindrical Pipe Shelter Used During Operation HENRE for Earth Attenuation Studies.

The second operation consisted of three runs with earth covers of approximately 2, 1, and 0 ft, respectively, on top of the shelter. For these cases, a substantial amount of spectral data was obtained with the ^{6}LiI spectrometer (discussed elsewhere in this report). After all earth had been removed, a prominent peak occurred at 4 Mev with a full width at half maximum height (FWHM) of about 1.5 Mev. In magnitude the 4-Mev differential neutron flux was about 13 times that at the 14-Mev primary energy. Minor peaks near 6 and 9 Mev also occurred in the case with no earth cover, while the 4-Mev peak showed up in the 1- and 2-ft thicknesses but with reduced magnitudes. The results for the case with no earth cover are presented graphically in Fig. 21.8.

The neutron energy spectrum as measured at 750 yd from the base of the tower for a source elevation of 1125 ft is shown in Fig. 21.9. Energy increments of 1 Mev were used in the data reduction to allow for the finite resolution of the spectrometer. In addition to the 14-Mev primary energy, there are distinct peaks at 4 and 9 Mev that

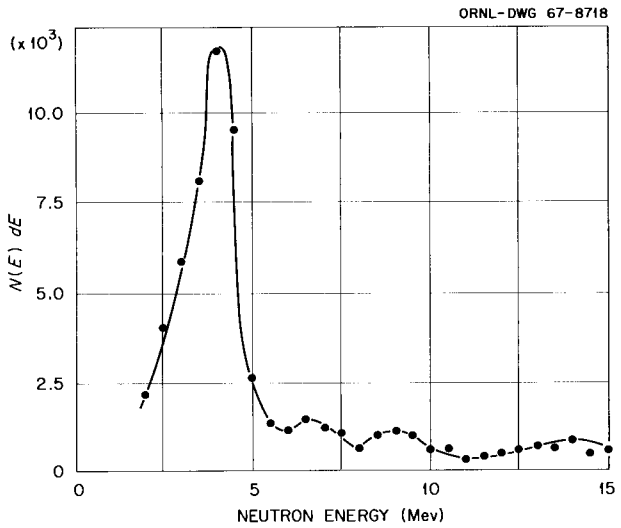

Fig. 21.8. Neutron Energy Spectrum Measured Inside the Pipe Shelter (No Earth Covering) During Operation HENRE. $H_s = 300$ ft.

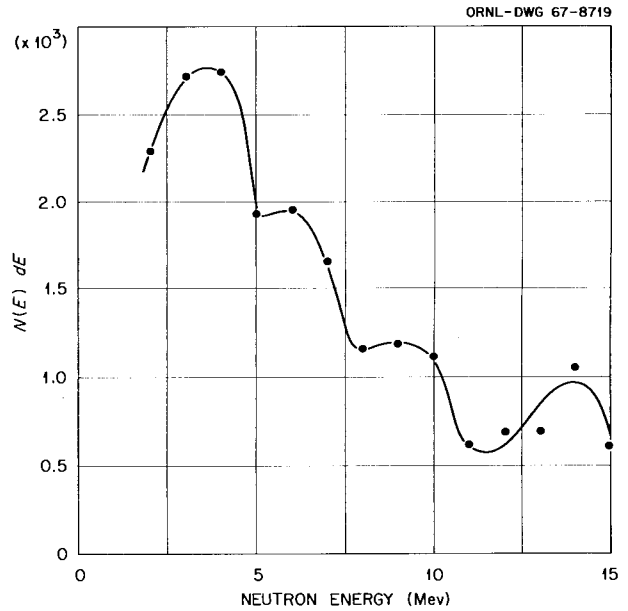

Fig. 21.9. Neutron Energy Spectrum Measured "In Air" with ^{6}LiI Spectrometer During Operation HENRE. $D =$ 750 yd, $H_s = 1125$ ft.

are presumably due to inelastic scattering reactions. Substantial agreement has been noted between these results and those of Trubey[12] based on a "moment" type of calculation.

A computer code was written and used to calculate the recoil particle energies for 14-Mev neutrons incident on nitrogen, utilizing the Q energy values for known excited states. About eight levels in nitrogen with energies between 8.71 and 10.05 Mev could scatter 14-Mev neutrons into the 4-Mev range, and about four levels between 3.945 and 5.685 Mev could give 9-Mev neutrons. It is not evident why peaks should appear rather than broad distributions. These levels are presumed to be responsible for the intense high-energy gamma rays observed at long distances from the HPRR and certain types of weapons.

At the same distance and source height, angular dose measurements were made at 0, 30, 60, and 90°, all with collimator openings of 30°. These measurements were made using the Hurst proportional counter–Radsan system for neutrons and the RCL 10-60 G-M tube for gamma rays (described in the section entitled "High-Sensitivity G-M-Type Gamma-Ray Dosimeter for Operation HENRE"). On the next run, further measurements were made at 15, 45, 330 (3.5° below the horizon), and 300° (in this case the collimators had 45° acceptance cones). After deduction of appropriate background, the "angular" dose rates were normalized and compared with the 0° data to get the percent dose at each angular inclination. Standard deviations based on total counts for each measurement were calculated, and error propagation calculations were carried through the background subtractions and the two divisions. Except for the 300° point, the neutron results had probable errors ranging from ±7 to 8.5%, while the gamma-ray results were better, with a range of ±2 to 3.4%. These results are compared with BREN results[13] in Figs. 21.10 and 21.11. There is good agreement in the neutron angular dose results for BREN and HENRE, whereas the gamma-ray results are somewhat different for the two cases. The gamma-ray angular results for HENRE seem more sharply peaked in the forward direction.

[12] E. A. Straker, *Calculations of the Transport of Neutrons from Fission and 14-Mev Point Sources in an Infinite Medium of Air*, ORNL-TM-1547 (Aug. 9, 1966).

[13] J. H. Thorngate *et al.*, *Energy and Angular Distribution of Neutrons and Gamma Rays – Operation BREN*, CEX-62.12 (February 1967).

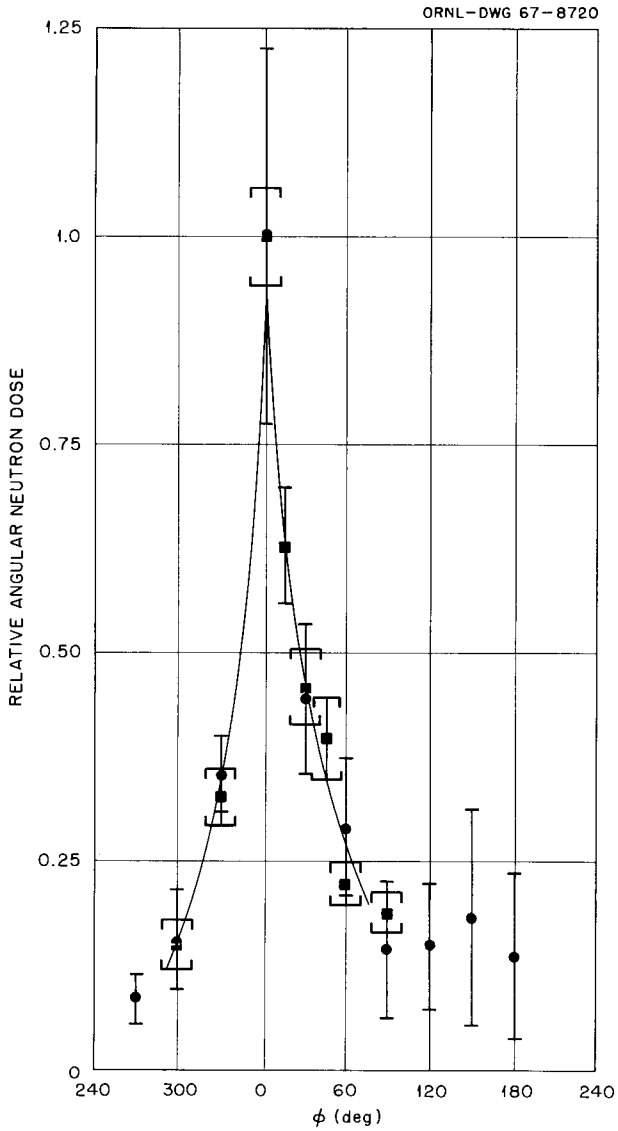

Fig. 21.10. Relative Angular Neutron Dose Distributions for Operations BREN and HENRE (Normalized at 0°). $H = 1125$ ft, $D = 750$ yd, acceptance cone = 30°. ● BREN results, ■ HENRE results.

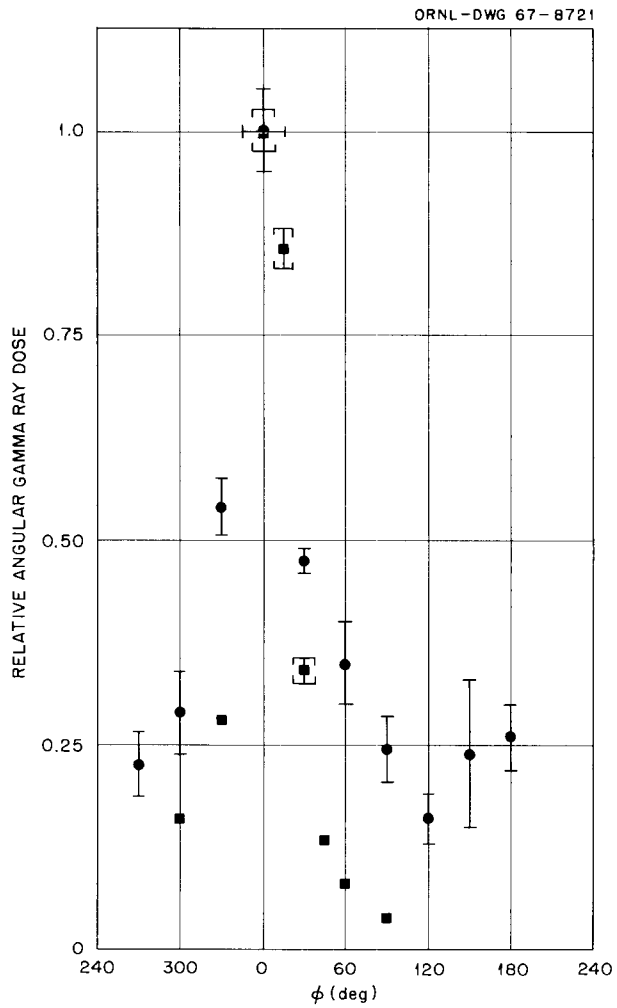

Fig. 21.11. Relative Angular Gamma-Ray Dose Distributions for Operations BREN and HENRE (Normalized at 0°). $H = 1125$ ft, $D = 750$ yd, acceptance cone = 30°. ● BREN results, ■ HENRE results.

22. Spectrometry and Dosimetry Research

J. H. Thorngate

M. D. Brown[1] P. T. Perdue
D. R. Davy[2] T. Saigusa[2]
D. R. Johnson E. B. Wagner

A POSSIBLE NUCLEAR-ACCIDENT DOSIMETER BASED ON ^{103}Rh[3]

Nuclear installations for which the threshold detector system is too complicated or expensive need a simple personnel nuclear-accident dosimeter. Rhodium foils can fill this need; the 100%-abundant stable ^{103}Rh forms three isotopes under neutron irradiation. Thermal and epithermal neutron activation leads to ^{104}Rh and ^{104m}Rh, with half-lives of 44 sec and 4.4 min, respectively, and fast-neutron irradiations excite the 40-kev nuclear level by inelastic scattering to give ^{103m}Rh, with a half-life of 56 min.

In a nuclear-accident dosimeter, the thermal and epithermal reactions are unwanted. Their significance can be considerably reduced by employing thick (0.050-in.) cadmium and indium shields (the ^{115}In resonance at 1.5 ev substantially overlaps the ^{104m}Rh resonance at 1.25 ev); but, in any case, they can be ignored after ~40 min decay.

The cross section for the ^{103}Rh(n,n') reaction is shown in Fig. 22.1. For comparison, the variation of surface multicollision dose (SMCD) with incident neutron energy is also shown. The choice of SMCD is somewhat arbitrary; it does, however, give a consistent set of units since the auto-integral gamma dose arising from neutron irradiation is always measured with surface dosimeters.

An indication of the extent to which the ^{103m}Rh activity is directly proportional to the incident neutron dose is given by Figs. 22.2 and 22.3 for the neutron spectra from the Y-12 and Vinca accidents respectively.[4,5] As a further check on this direct proportionality, rhodium foils were exposed both directly to the neutron spectrum from the HPRR and to the same spectrum after moderation with either an 8-in.-thick slab of graphite or polyethylene. The 20-kev x ray was detected with a 2-in.-diam, 0.050-in.-thick bare CsI(Tl) crystal optically coupled to an EMI 9524 "S" photomultiplier.

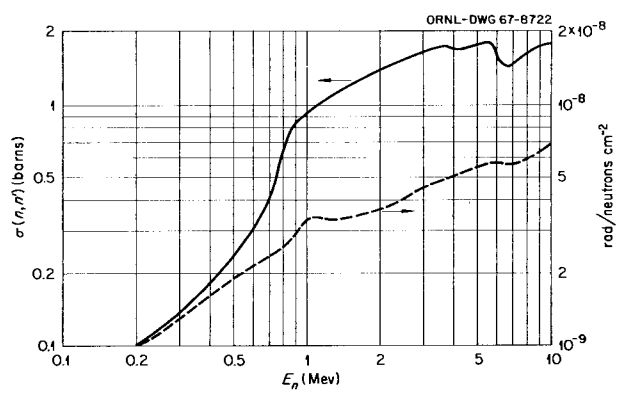

Fig. 22.1. Cross Section for ^{103}Rh(n,n') Reaction in barns as a Function of Neutron Energy in Mev and Surface Multicollision Dose in rads neutron^{-1} cm^2 as a Function of Neutron Energy in Mev. — Cross section for ^{103}Rh(n,n') reaction; — — surface multicollision dose.

[1] Part time.

[2] Alien guest.

[3] These data were intended for publication in the preceding annual report but were delayed by international patent considerations.

[4] G. S. Hurst *et al.*, *Health Phys.* **2**, 121 (1959).

[5] G. S. Hurst *et al.*, *Health Phys.* **5**, 179 (1961).

Table 22.1. Instantaneous ^{103m}Rh Activity Following Irradiation by Different Neutron Spectra

Primary Neutron Source	Moderator	SMCD (rads neutron^{-1} cm^2)	^{103m}Rh Activity (counts min^{-1} rad^{-1})
		$\times 10^{-9}$	
HPRR	None	3.4	22
HPRR	8-in. graphite	2.9	21
HPRR	8-in. polyethylene	2.8	22

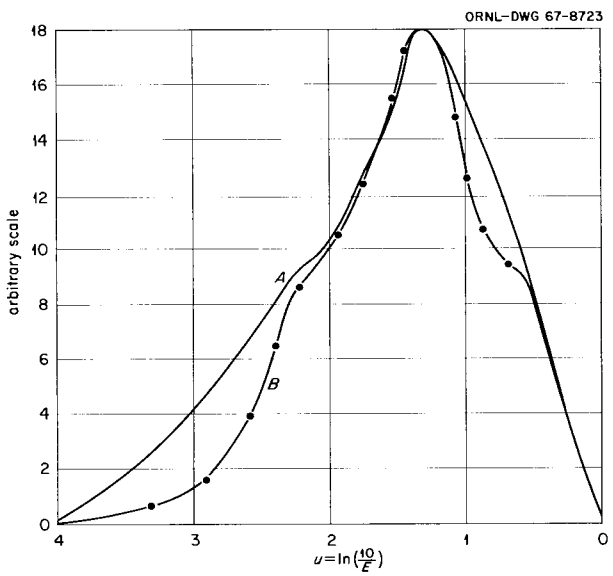

Fig. 22.2. Dose Response $D(E)E\phi(E)$ and Rh Activation $\sigma(E)E\phi(E)$ in Arbitrary Units as a Function of ln $10/E$ When the Incident Spectrum Is like That Resulting from the Y-12 Nuclear Accident. Curve A, dose response $D(E)E\phi(E)$; curve B, Rh response $\sigma(E)E\phi(E)$.

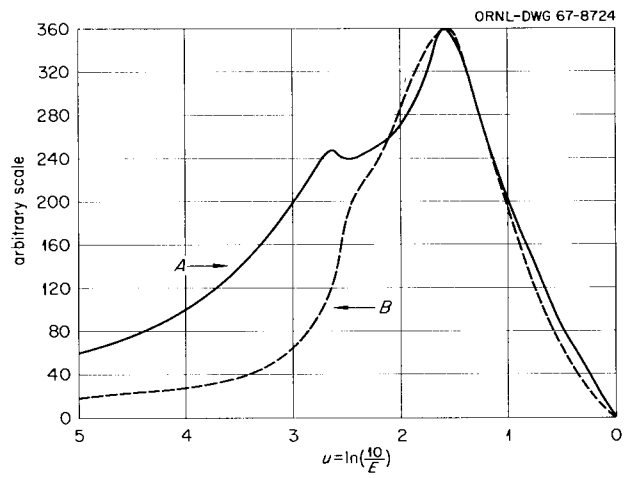

Fig. 22.3. Dose Response $D(E)E\phi(E)$ and Rh Activation $\sigma(E)E\phi(E)$ in Arbitrary Units as a Function of ln $10/E$ When the Incident Spectrum Is like That Resulting from the Vinca Nuclear Accident. Curve A, dose response $D(E)E\phi(E)$; curve B, Rh response $\sigma(E)E\phi(E)$.

Resolution for the 20-kev photopeak was ~65% and was summed between the energy limits of 11 and 34 kev. For these settings the background was ~100 counts/min and originated mainly from thermal emission at the photocathode. The results obtained for the three classes of exposure are summarized in Table 22.1.

Although certain aspects of a dosimeter based on this reaction are appealing, it is likely to find more acceptance when spontaneous fission sources become sufficiently available to provide an absolute "in-house" calibration of the counting system.

EXPERIMENTALLY DETERMINED RECOIL-PARTICLE ENERGY SPECTRA PRODUCED IN TISSUE-EQUIVALENT MATERIAL BY 3- AND 15-Mev NEUTRONS

An experiment was performed to measure the energy spectrum of recoil particles produced when a tissue-equivalent phantom is irradiated with neutrons. The phantom used was a cylinder 30 cm in diameter by 60 cm high filled with a water solution of sugar and urea which closely approximated the composition of wet tissue. It was placed 100 cm from the target of the DOSAR low-energy accelerator (see section entitled "DOSAR Low-Energy Accelerator Modifications and Applications"), which

provided monoenergetic 3- or 15-Mev neutrons. Recoil particles were measured with semiconductor detectors. For the 3-Mev irradiations, a 200-μ-thick surface-barrier diode with a sensitive area of 3 cm^2 was used. A lithium-drifted silicon detector in the shape of a cube 1.5 mm on a side was used for measurements with 15-Mev neutrons. Since the diodes were immersed in the tissue-equivalent liquid for measurement, they had to be protected to prevent excessive surface leakage that would result in high noise levels. A thin coating of Marvethane provided adequate protection of the diodes without unduly perturbing the tissue-equivalent environment. Both diodes were mounted on rods of tissue-equivalent plastic to further reduce the perturbation caused by inserting the detector in the phantom.

Measurements were made at axial depths of 2.5, 7.5, 12.5, 17.5, 22.5, and 27.5 cm from the front of the phantom, at normal depths of 2.5, 7.5, and 12.5 cm from the side, and at a constant height of 30 cm. These results are shown in Figs. 22.4 and 22.5 for 3-Mev neutrons and in Figs. 22.6 and 22.7 for 15-Mev neutrons. The front gold layer and rear aluminum layer of the 200-μ detector prevented the low-energy carbon, nitrogen, and oxygen ions from entering the sensitive volume; but the cube detector had four sides without a dead layer, which, coupled with the higher energy of the incident neutrons, resulted in a significant number of the heavy ions being recorded. These ions result in the upturn of the recorded spectra at low energies as shown in Figs. 22.6 and 22.7. Unfortunately high noise levels limited the low-energy measurements.

Careful measurements were made to determine the contribution made to the spectra by (n,p) and (n,α) reactions in the silicon and by neutrons scattered from the floor and walls around the experimental setup. For the worst case, these resulted in a 10% increase in the measured spectra.

A computer program has been developed and is being run which mathematically simulates this experiment. If agreement is obtained, it will give added confidence to other computational programs that have been or will be run.

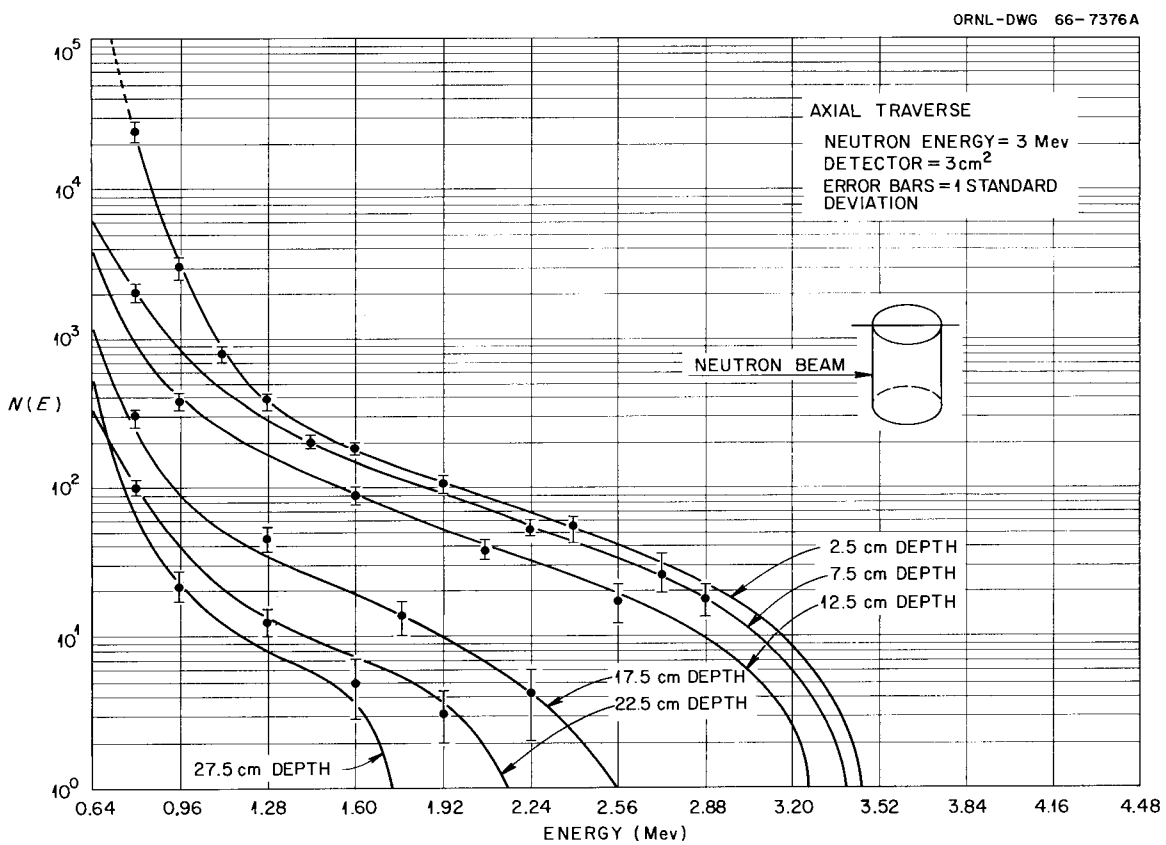

Fig. 22.4. Charged-Particle Spectra as a Function of Depth into a Cylindrical Phantom for Incident 3-Mev Neutrons.

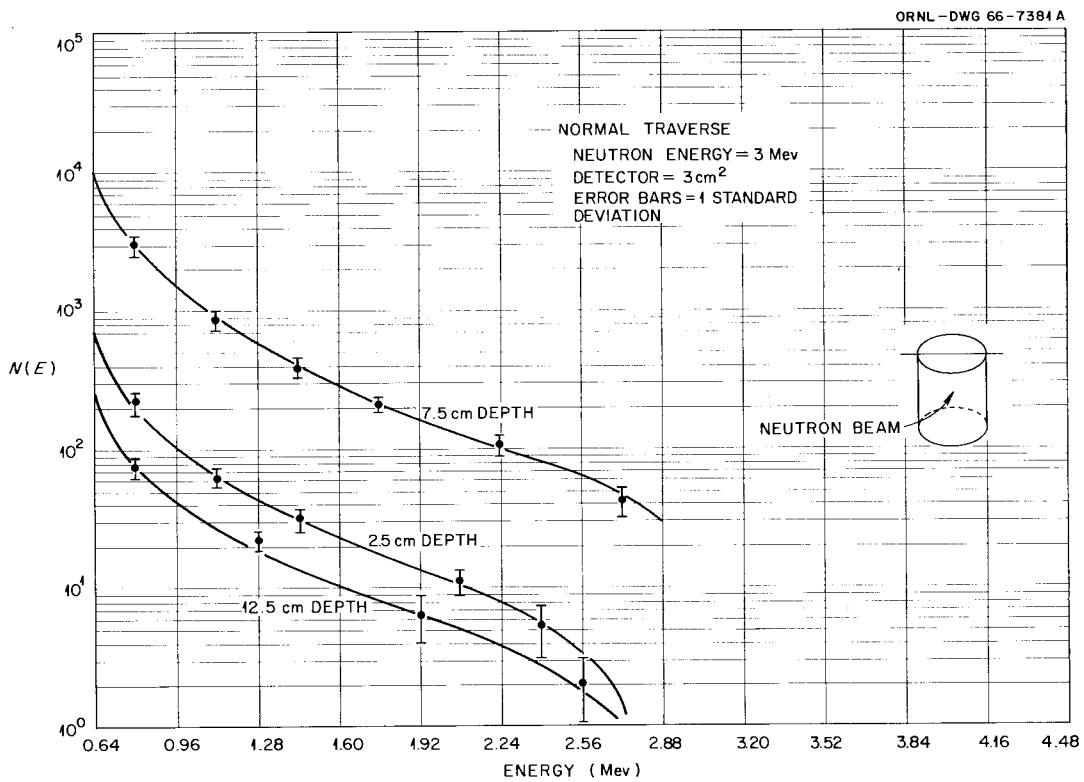

Fig. 22.5. Charged-Particle Spectra as a Function of Depth into a Cylindrical Phantom in the Midplane Perpendicular to an Incident Beam of 3-Mev Neutrons.

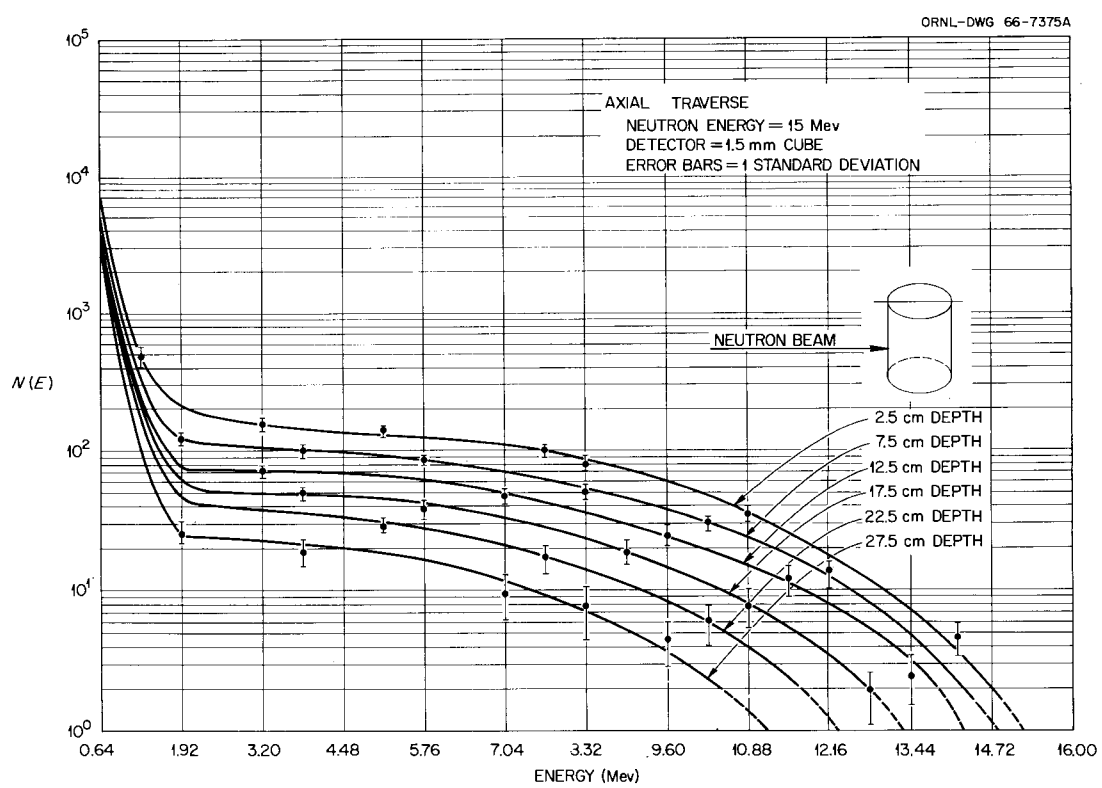

Fig. 22.6. Charged-Particle Spectra as a Function of Depth into a Cylindrical Phantom for Incident 15-Mev Neutrons.

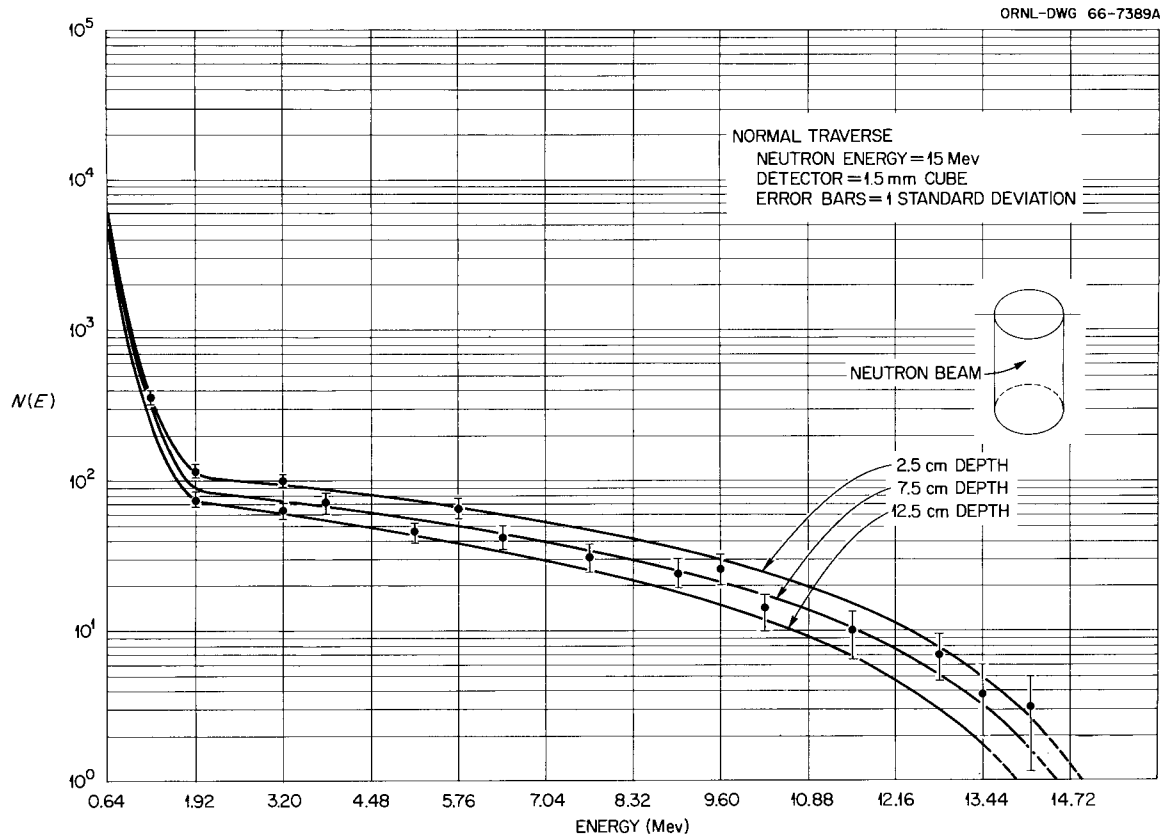

Fig. 22.7. Charged-Particle Spectra as a Function of Depth into a Cylindrical Phantom in the Midplane Perpendicular to an Incident Beam of 15-Mev Neutrons.

AN INTERMEDIATE-ENERGY NEUTRON SPECTROMETER USING MAGNETIC ANALYSIS OF RECOIL PROTONS

As part of a continuing effort to develop a neutron spectrometer to make measurements in wide energy ranges, a unit was designed for measurements in the energy range below 1 Mev. Although this range has considerable importance in the dosimetry for reactor installations, it is a particularly difficult region in which to make spectrum measurements. The problems are largely associated with noise in the detection system, particularly when the detector must supply energy information. To overcome this problem, a spectrometer was designed which uses a magnetic field to measure the momentum of the proton recoils produced when a collimated beam of neutrons strikes a hydrogenous target. Since the particle detector is no longer required to measure energy, an electron multiplier may be used. By proper selection of dynode materials, ions from a few kev to as much as 3 Mev will produce a secondary electron yield of 2 or greater. Figure 22.8 shows the device. A 60° magnetic deflection was required owing to the maximum field obtainable from the available electromagnet. This design provides other advantages in neutron collimation and detector shielding, since these goals may be accomplished without enclosing the magnet. A Hall-effect device is used to regulate and control the magnetic field.

^{6}LiI SPECTROMETRY

Lithium Iodide Spectrometer

Even with the high neutron yield of the HENRE accelerator, the neutron flux available for dose and spectrum measurements at distances of several hundred yards from the tower is marginal. Thus a

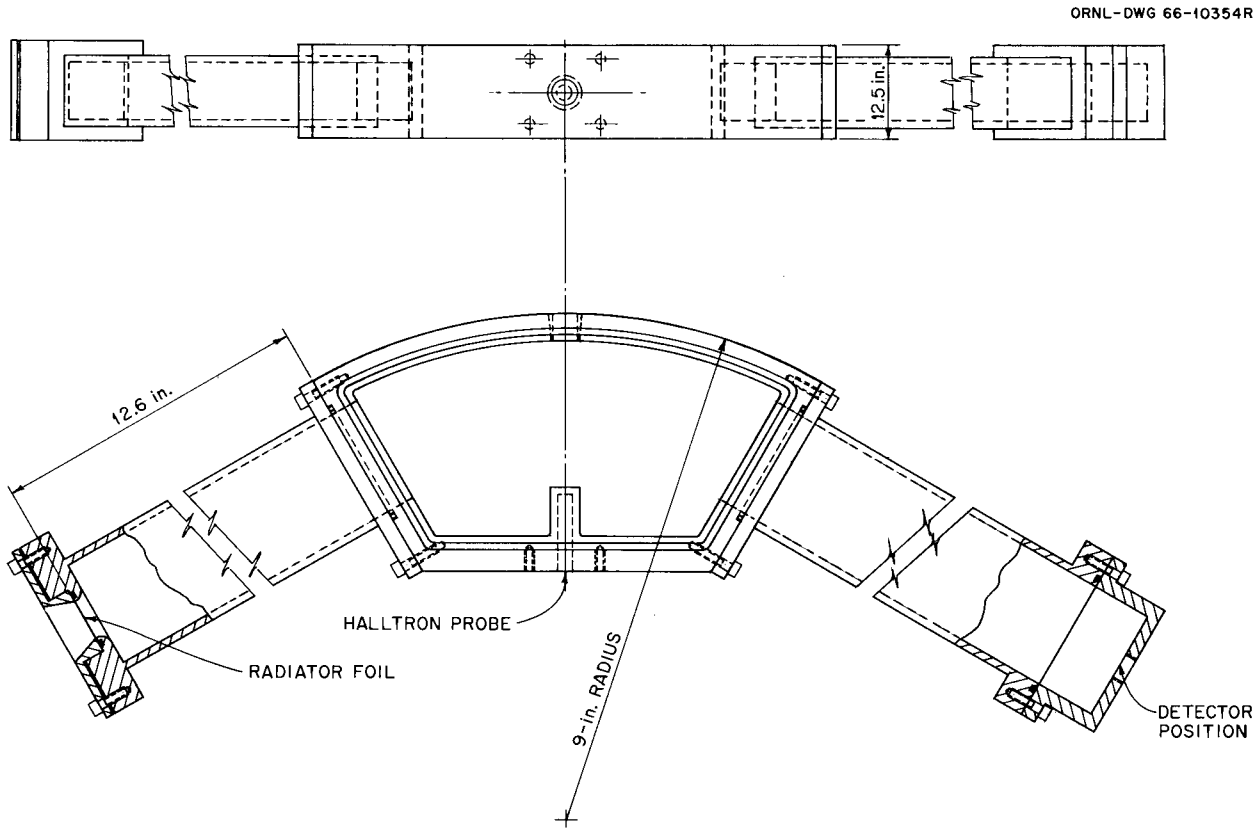

Fig. 22.8. Schematic Sectional Views of the Magnetic Analyzer Used for Recoil Protons as a Part of the Neutron Spectrometry for Intermediate-Energy Neutrons.

sensitive neutron spectrometer is required in order to make measurements at distances of 750 yd or greater.

After an extensive literature search, it was concluded that a good choice for such an application was an ^{6}LiI(Eu) spectrometer as described by Murray in 1958.[6] The advantages were: (1) high efficiency, 10^{-2} to 10^{-3} counts neutron^{-1} cm^2; (2) acceptable neutron energy resolution when cooled to less than 150°K; and (3) simplicity of electronics. The main disadvantage, other than cooling it to low temperatures, was the competing reactions which become significant when a considerable fraction of the neutrons have energies near 15 Mev. An approximate solution to the competing reactions problem involves subtracting the response of an identically sized ^{7}LiI crystal from the response of the ^{6}LiI unit. The primary competing reaction expected in ^{6}LiI is ^{6}Li$(n,dn')\alpha$, which has a Q value of -1.47 Mev. The corresponding reaction in ^{7}Li is ^{7}Li$(n,tn')\alpha$, with a Q of -2.57 Mev, thus requiring approximately 1.1 Mev more input neutron energy than in ^{6}Li. Cross sections for both these competing reactions are similar in shape and size, particularly above E_n = 8 to 9 Mev, where the (n,dn') reaction begins to compete with the ^{6}Li$(n,t)\alpha$ reaction. If it is assumed that these competing reactions are the dominant ones, then the response of ^{7}LiI for 14.7-Mev neutrons would be similar to that of ^{6}LiI except for about a 1-Mev difference in the high-energy cutoff due to the higher Q for the ^{7}Li reaction.

Three LiI(Eu) spectrometer units were purchased, two enriched in ^{6}Li and the other in ^{7}Li. The 2-mm-thick, 5-cm-diam scintillators are attached to 15-cm-long quartz light pipes equipped with copper bellows to permit thermal expansion and contraction during cooling operations. Quartz was selected in preference to Lucite to reduce neutron

[6] R. B. Murray, *Nucl. Instr.* **2**, 237–48 (1958).

scattering from the light pipe; the 15-cm length was chosen because the difference in neutron energy resolution is not a sensitive function of light-pipe length between 7.5 and 15 cm. It was assumed that the additional 7.5 cm would eliminate the necessity of considering the temperature of the photocathode of the photomultiplier tubes used.

Owing to the harsh environment at the Nevada Test Site, the spectrometer and its associated electronics and the cooling apparatus were engineered to be as simple and rugged as possible. The photomultiplier tubes were attached to the light pipes with silicon grease and centered firmly in place with a length of rubber tubing. Aluminum foil was used as a reflector for the 7.5 cm of exposed quartz, and a magnetic shield enclosed the photomultiplier tube and the first 1.75 cm of the light pipe. An emitter-follower preamplifier housed in the photomultiplier socket transmitted signals to a double-differentiating linear amplifier with 4-μsec delay lines, the output of which was analyzed by a 256-channel analyzer. The cooling apparatus consisted of a stainless steel cooling jacket attached to the spectrometer bellows. A nitrogen Dewar with an internal cold trap was used to provide N_2 gas at temperatures near 77°K, although the lowest steady-state temperature obtained at the detector was about 140°K. After filling the Dewar with liquid N_2, a 100-w Nichrome wire heater was energized, and the resulting nitrogen vapor passed through the internal cold trap and out through the spectrometer cooling jacket. Liberal use of polystyrene foam at all exposed surfaces permitted stable operation at 140 to 150°K for periods of about 4 hr. The Dewar could be refilled during use with negligible effect on the equilibrium temperature.

According to Eaton and Walker,[7] the pulse-height resolution for neutrons may be improved by a factor of about 2 by cooling the crystals from room temperature to 77°K; however, about 90% of the improvement is obtained by cooling to 140°K, so not much is gained by additional temperature reduction. For this reason and because it was undesirable to have more "air" between the source and detector than already existed at distances of several hundred meters, cooling the crystals directly with liquid N_2 was not attempted.

[7] J. Eaton and J. Walker, *Proc. Phys. Soc.* **83**, 301–9 (1964).

Checkout Calibration

Preliminary checkout of the spectrometer was made using thermal and (d,T) neutrons. The Dewar was filled with liquid N_2 and allowed to cool until reduced gaseous evolution indicated that the Dewar insulation temperature had equilibrated. After replacing the evolved coolant, the spectrometer assembly with cooling jacket, photomultiplier, and socket attached was connected to the outlet tube of the Dewar and supported firmly with a large ring stand. Upon closing the Dewar fill tube and turning on the 100-w heater, N_2 gas started flowing through the spectrometer cooling jacket and slowly reduced the temperature of the detector end of the apparatus to approximately 140°K. This seemed to be an optimum with the existing equipment.

Once equilibrium temperature was reached, a thermal-neutron calibration was performed to establish the proper high-voltage and amplifier gain settings consistent with the dynamic range of the analyzer. A ^{137}Cs calibration was also made at a factor of 10 higher amplifier gain to facilitate setting up the ^{7}LiI crystal at the same equivalent gain. For the (d,T) runs the spectrometer crystal was positioned approximately 1.4 m from the accelerator target and at an angle of about 30° (14.3 Mev), since the operational height of the spectrometer was higher than the target. The resolution of the ^{6}LiI spectrometer for thermal neutrons both at room temperature and at 140°K was about 13%, which agrees fairly well with published values for a 3.75-cm-diam crystal. The pulse-height resolution at 140°K for (d,T) neutrons was approximately 10% full width at half maximum, which corresponds to a neutron energy resolution of 13%. According to Eaton and Walker, the improvement in pulse-height resolution at 77°K results in a neutron energy resolution of 7% for 14.7-Mev neutrons, considerably better than the present results. This difference is probably attributable not only to their use of a lower temperature but also to their use of a smaller diameter crystal and a shorter light pipe.

Upon integrating the number of counts under the peak, an efficiency of approximately 10^{-3} counts neutron^{-1} cm^{2} for (d,T) neutrons was obtained, a value that is consistent with calculations based on a cross section of 25 mb at 14.7 Mev. In the 3-to-6-Mev region, where a substantial fraction of scattered neutrons at large distance from the HENRE accelerator were expected, the ^{6}LiI spectrometer efficiency should be approximately ten times better than at 14.7 Mev or 10^{-2}.

After running both ^{6}LiI spectrometer units and establishing that they were essentially identical with respect to neutron energy resolution, the ^{7}LiI unit was investigated, using (d,T) neutrons to determine the feasibility of correcting for competing reactions in ^{6}LiI by the subtraction technique. The ^{7}LiI response had an upper energy cutoff approximately 1 Mev lower than the response of the ^{6}LiI due to competing reactions, as expected. The main problem was the compensation for this slight discrepancy in the two crystals so that the subtraction technique of eliminating the ambiguous ^{6}LiI response to competing reactions could be used with confidence. A gain increase in the ^{7}LiI unit was considered but discarded, since a fixed ΔE of about 1 Mev is to be added to all ^{7}LiI pulses. The approach chosen was to shift the ^{7}LiI response up by 1 Mev by using the low-energy bias of the analyzer.

Use During HENRE

The spectrometer was set up and allowed to equilibrate thermally at approximately 140°K, a thermal-neutron calibration was performed to establish operating high-voltage and gain settings, and a ^{137}Cs gamma-ray photopeak was determined at a factor of 10 higher amplifier gain to facilitate making gain settings for the ^{7}LiI unit. The gains of both were equalized by adjusting the ^{7}LiI gain until the ^{137}Cs photopeak was in the same channel as for the ^{6}LiI unit. Analyzer bias was used to add 1.1 Mev to each pulse from the ^{7}LiI unit to compensate for the lower Q values for competing reactions. Thus a bias setting of 0.50 was used for ^{6}LiI and 0.70 for ^{7}LiI, since the zero-energy suppression per 0.10 bias setting is seven channels; this difference, coupled with the usual gain setting of 0.078 Mev/channel, had the desired effect of adding approximately 1.1 Mev to the ^{7}LiI results. The 0.50 setting provided more dynamic range on the analyzer, since it shifted the entire spectrum down by 35 channels, which placed the thermal-neutron peak in the relatively low position of channel 16 to 18 and the 15-Mev peak in the region of channels 200 to 230.

The ^{6}LiI data were taken generally for 2-hr periods, whereupon the socket-preamplifier assembly was switched to the ^{7}LiI unit for the final 2 hr of each scheduled operation. Since the Dewar consumed about 2 liters of N_2 per hour, 4 liters were added routinely at each detector changeover.

Data were normalized via a BF_3 normalization counter, the purpose being to subtract the appropriate amount of ^{7}LiI "background" from the ^{6}LiI results and to allow comparisons of measurements made with different accelerator targets.

Data reduction was simplified by the limited energy resolution of the detectors. In addition, the data in individual channels were frequently not statistically significant, so that analysis was performed by summing data in groups of seven channels centered at integral energy units. Thus, channel numbers corresponding to energies of 1, 2, . . . , 15 Mev were marked, data three channels above and below each energy were summed, and the corresponding ^{7}LiI background was subtracted. Finally, each data point was divided by the ^{6}Li(n,α) ^{3}H cross section to arrive at differential neutron energy spectra.

23. Dosimetry Applications

J. A. Auxier

J. S. Cheka
Mary P. Haydon[1]
H. H. Hubbell, Jr.
D. R. Johnson
T. D. Jones
G. D. Kerr
J. W. Poston
W. S. Snyder

SILVER-ACTIVATED PHOSPHATE GLASS DOSIMETRY

During the past several years, silver-activated phosphate glass detectors have been developed with greater sensitivity, less energy dependence, and lower inherent fluorescence.[2,3] These improvements have been made by modifying the composition of the glass, improving the processing of the glass, increasing the size of the detector element, forming it into the shape of a block, and developing better fluorometers.

As an example, an FD-P6-1 detector (fluorescent dosimeter, size $6 \times 6 \times 3.3$ mm, formula 1) available from the Toshiba Company, Japan, can be used to detect 25 mr and measure 100 mr of ^{60}Co gamma rays with a fractional standard deviation of ±3%. Predose fluorescent readings are approximately 500 mr. An FD-P8-1 glass-block detector ($8 \times 8 \times 4.7$ mm) manufactured by the same company can detect 10 mr and measure 50 mr of ^{60}Co gamma rays to ±3%.

Use of a low-Z base mix of $Al(PO_3)_3$ and $LiPO_3$ has reduced the enhanced response per roentgen of these detectors to low-energy quantum radiation. However, the response at 50 kev is still high by a factor of approximately 7.5 for the unshielded FD-P6-1 detectors and 7.2 for the unshielded FD-P8-1 detectors, as shown in Figs. 23.1 and 23.2 respectively. Also shown in the figures are calculated response curves for monoenergetic beams of x or gamma rays and the experimentally determined response to x-ray spectra; the experimental values were normalized to the response at 1 Mev.

For dosimetric applications, shields can be used to modify or to flatten the response to low-energy radiation. Figure 23.3 shows the response of FD-P6-1 detectors shielded with 1 mm of aluminum, copper, or tin. Liners of 0.25 mm of Teflon were used in the shields to prevent mechanical damage to the glass detectors.

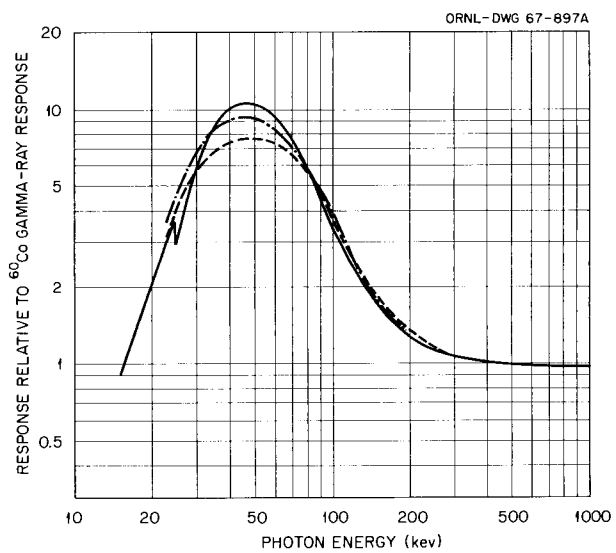

Fig. 23.1. The Response per roentgen of the Toshiba FD-P6-1 Detectors as a Function of Photon Energy.
—— Calculated response assuming monoenergetic x rays; –·– calculated response correcting for x-ray spectrum; – – – experimental response.

[1]Part time.

[2]R. Yokota and S. Nakajima, *Health Phys.* **12**, 241 (1965).

[3]K. Becker, *Nucl. Instr. Methods* **36**, 323 (1965).

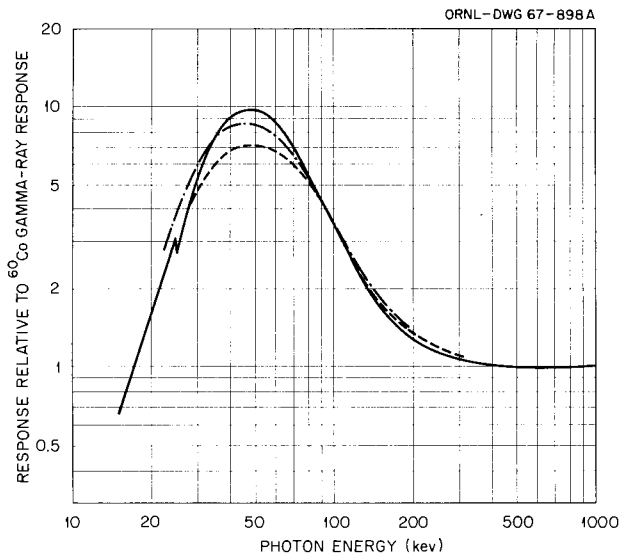

Fig. 23.2. The Response per roentgen of the Toshiba FD-P8-1 Detectors as a Function of Photon Energy. —— Calculated response assuming monoenergetic photons; – · – calculated response correcting for x-ray spectrum; – – – experimental response.

These data show that a 1-mm tin shield will flatten the response to within ±25% above 80 kev. With a 1.2-mm tin shield the response is flat to within 10% above 100 kev. An exposure-equivalent response to low-energy quantum radiation can be obtained with these filters by the use of conical bores in the faces.[4]

Use of two or more detectors with shields such as aluminum or copper can provide a method of personnel dosimetry at medical x-ray facilities. As an example, ratios of the readings from several glasses with different shields can be used to provide information on the effective energy of the exposures and provide a correction factor for the enhanced sensitivity in the low-energy region.

One problem associated with the use of these highly lithiated glasses is their high sensitivity to thermal neutrons. Investigations using the thermal pile at the HPRR have shown that a fluence of thermal neutrons equal to a "first-

[4]K. Becker, *Nukleonik* **5**, 154 (1963).

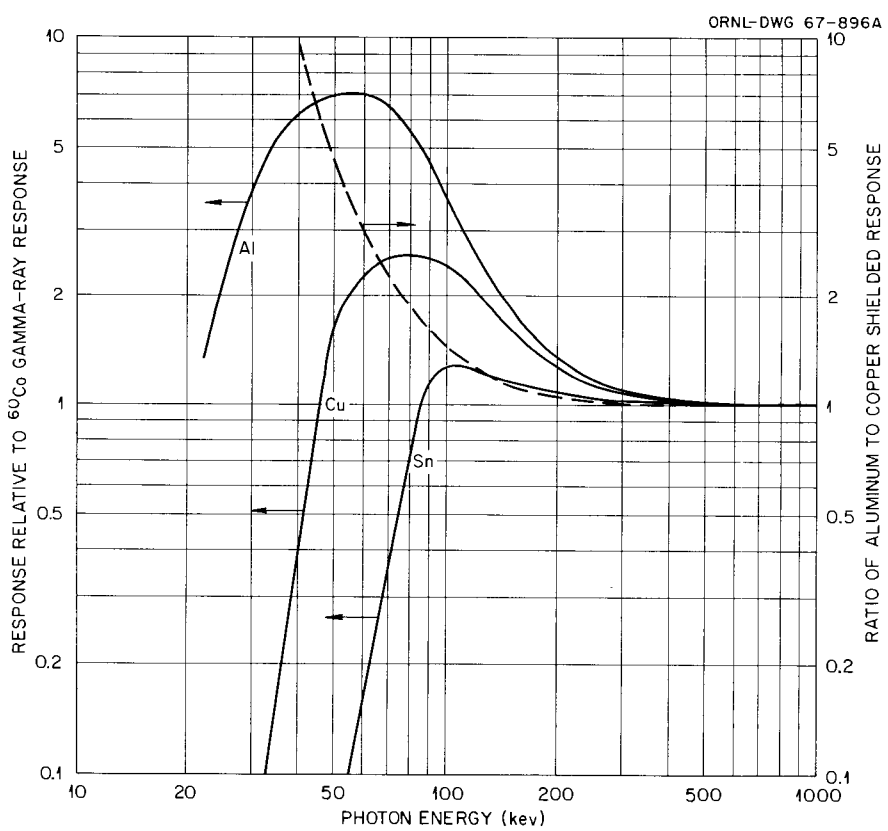

Fig. 23.3. The Response per roentgen of Toshiba FD-P6-1 Detectors as a Function of Photon Energy When Shielded by 1 mm of Al, Cu, or Sn.

collision" dose of 1 rad gives the same response in a Toshiba FD-P8-1 detector as a ^{60}Co gamma-ray exposure of 135 r (±10%).

Glass detectors of the Toshiba FD-3 formulation have been fabricated at our request with isotopic ^{7}Li in the $LiPO_3$. Formula 3 differs from formula 1 chiefly by containing 4% activating $AgPO_3$ instead of 7%. Measurements indicated that the thermal-neutron sensitivity of these detectors is lower than the normal lithium phosphate glass by a factor of 14.

Experimental investigations of these detectors, designated as FD-P8-3S (fluorescent dosimeter, 8 × 8 × 4.7 mm, formula 3, special), showed that the response to quantum radiation was the same as that of the FD-P8-1 detectors within the inherent experimental errors. Sensitivity to ^{60}Co gamma rays was 1.06 times that of the FD-P8-1 detectors.

Sensitivities of both types of detector elements to 14.6-Mev neutrons were measured to be 0.04 ± 0.02 r gamma equivalent per rad of dose to tissue. Calculations of energy deposited in the glass detectors per rad of dose to tissue indicate that response to fast fission spectrum neutrons would be less than the above value for 14.6-Mev neutrons.

A method to overcome the adverse response to thermal neutrons was to use the differential response of the FD-P8-1 and FD-P8-3S detectors. In a mixed neutron and gamma-ray field, the response (Y) of a detector can be written as

$$Y = C[X + (\mathrm{RNS})_{n_f} D_{n_f} + (\mathrm{RNS})_{n_{\mathrm{th}}} D_{\mathrm{th}}] ,$$

where C is the calibration factor of the fluorometer, X is the gamma-ray exposure, D is the neutron dose, and RNS is the relative neutron sensitivity expressed in roentgens gamma equivalent per rad of neutron dose to tissue. By ignoring the small fast-neutron response, two simultaneous equations can be solved to give a relationship for calculating the gamma-ray exposure, which is

$$X = \frac{GY_2 - (C_2/C_1)Y_1}{C_2(G-1)} ,$$

where $G = \mathrm{RNS}_1/\mathrm{RNS}_2$ is the ratio of the relative thermal-neutron sensitivities. In our case, subscripts 1 and 2 refer to the FD-P8-1 and FD-P8-3S detectors respectively. Using experimental values from our investigations, the equation becomes

$$X = \frac{14Y_2 - 1.06Y_1}{13C_2} = \frac{1.08Y_2 - 0.082Y_1}{C_2} .$$

This equation shows that the FD-P8-1 detector is used only as a device to make a small correction to the reading obtained from the FD-P8-3S detector. The standard error in X calculated in this method is essentially the same as that of the FD-P8-3S because of the large ratio of the relative thermal-neutron sensitivities. In addition, the fast-neutron response with the two detector systems is the same as that for either of the separate detectors.

Comparison of this system with the Phil gamma-ray dosimeter and with Toshiba microdosimeter rods exposed in ^{6}Li shields in the fast fission spectrum (HPRR) and the fission spectrum moderated by 13 cm of steel gave agreement to within ±10%. In all experimental exposures the glasses were exposed in shields which were equivalent to approximately 1.2 mm of tin.

SOLID-STATE TRACK DETECTORS

The term "solid-state track detectors" has been applied to insulating solids in which the damaged region along a charged particle track can be exposed by a chemical etch.[5] Tracks of many charged particles, especially fission fragments, are of a convenient size to be observed at 400× with an optical microscope. Figure 23.4 shows fission fragment tracks in Lexan plastic etched with a 25 wt % NaOH solution at 60°C for 1 hr.

Use of these detectors with fissile radiators has made conventional neutron threshold detector units more suitable for nuclear accident dosimetry[6] by eliminating (1) the special counting system needed for accurate evaluation of the encapsulated fissile foils, (2) the necessity of immediate retrieval because of the fast decay of fission products, and (3) the need for gram quantities of fissile materials.

Components of a threshold detector system employing nuclear track detectors are shown in Fig. 23.5. Thin spacer rings are used to separate the fissile radiators and Lexan track detectors to pre-

[5] R. L. Fleisher *et al.*, *Phys. Rev.* **133**, A1443 (1964).

[6] G. D. Kerr and T. D. Strickler, *Health Phys.* **12**, 1141 (1966).

Fig. 23.4. Fission Fragment Tracks in Lexan Etched with a 25% by Weight NaOH Solution at 60°C for 1 hr.

vent abrasion of the foil surface. These three detector units, one each of ^{239}Pu, ^{237}Np, and ^{238}U, can be placed inside the boron and cadmium shields presently used with conventional threshold detector units (TDU's).

Track registration efficiency of the Lexan is 100%, since the rate of energy loss of the fission fragments from thin foils used with this system is above the critical rate of energy loss for track formation.[5] However, the detection efficiency is less than 100%, because it depends upon track registration geometry, as shown in Fig. 23.6.[7] If the rate of etch along the track is T and the rate of surface etch of the detector is S, the critical angle θ_c for observing a track is arc cos (S/T).

The critical angle for Lexan has been measured to be 86°.[5] If track counting is limited to a central region of the detector, the detection efficiency ϵ is just the solid angle Ω over which tracks will be observed or

$$\epsilon = \frac{d\Omega}{2\pi} = \frac{\int_0^{2\pi} \int_0^{\theta_c} \sin\theta \, d\theta \, d\phi}{2\pi}$$

$$= 1 - \cos\theta_c \, .$$

With 1.9-cm-diam fissile radiators, a 0.25-mm-thick spacer can be used to provide a 1-cm^2 circular area about the detector's center which is free of edge effects. Smaller fissile radiators have been used with Corning microsheet glass No. 0211, which has a critical angle of approximately 58°. A disadvantage of this method was that HF was required to expose the fission fragment tracks. With Lexan, either NaOH or KOH solutions can be used, which are safer to handle.

Etching times of Lexan detectors using a 25% by weight solution at 60°C range from 15 min with 10^6 tracks/cm^2 to 1 hr with 10^3 tracks/cm^2. First, detectors are etched for 15 min, and the approximate track density is determined. Etching is then continued to obtain optimum track sizes without overlapping of tracks, which makes positive track identification difficult.

The track density N of the detector is related to neutron fluence ϕ above the threshold energy of the fissile material by the equation

$$N = \phi n \sigma \epsilon P \, ,$$

where n is the number of fissile atoms per unit area, σ is the effective cross section of the fissile material enclosed by the ^{10}B shield,[8] p is a correction factor for perturbation of neutron fluence by the boron shield,[8] and ϵ is the detection efficiency. First-collision dose to tissue can be calculated from these fluence measurements in the normal manner.[8]

A fast-neutron dose of 10 to 10^4 rads can be measured by the use of ^{239}Pu, ^{237}Np, and ^{238}U radiators of 30, 50, and 30 μg/cm^2 respectively. A source of foils with the above specifications and having a uniform distribution of fissile material is now available. Fractional standard deviations in track counting of ±10% at 10 rads to less than ±1% at 100 rads can be obtained. In general, high track densities are counted by viewing individual fields, and low track densities are counted by scanning the surface.

Calculations of tracks produced by spontaneous fission in foils of the above size indicate that the detectors should be changed once per year. In this case, the accumulated "background" dose from spontaneous fission would be less than 1 rad.

Some attention has been given to the feasibility of using a small, thin ^{238}U fissile radiator in contact with a track detector in personnel meters and orientation belts. These would extend the lower range of detectability in the way that small sulfur

[7] R. L. Fleischer and P. B. Price, *J. Geophys. Res.* **69**, 331 (1964).

[8] D. R. Johnson *et al.*, *Health Phys.* 11, 759 (1965).

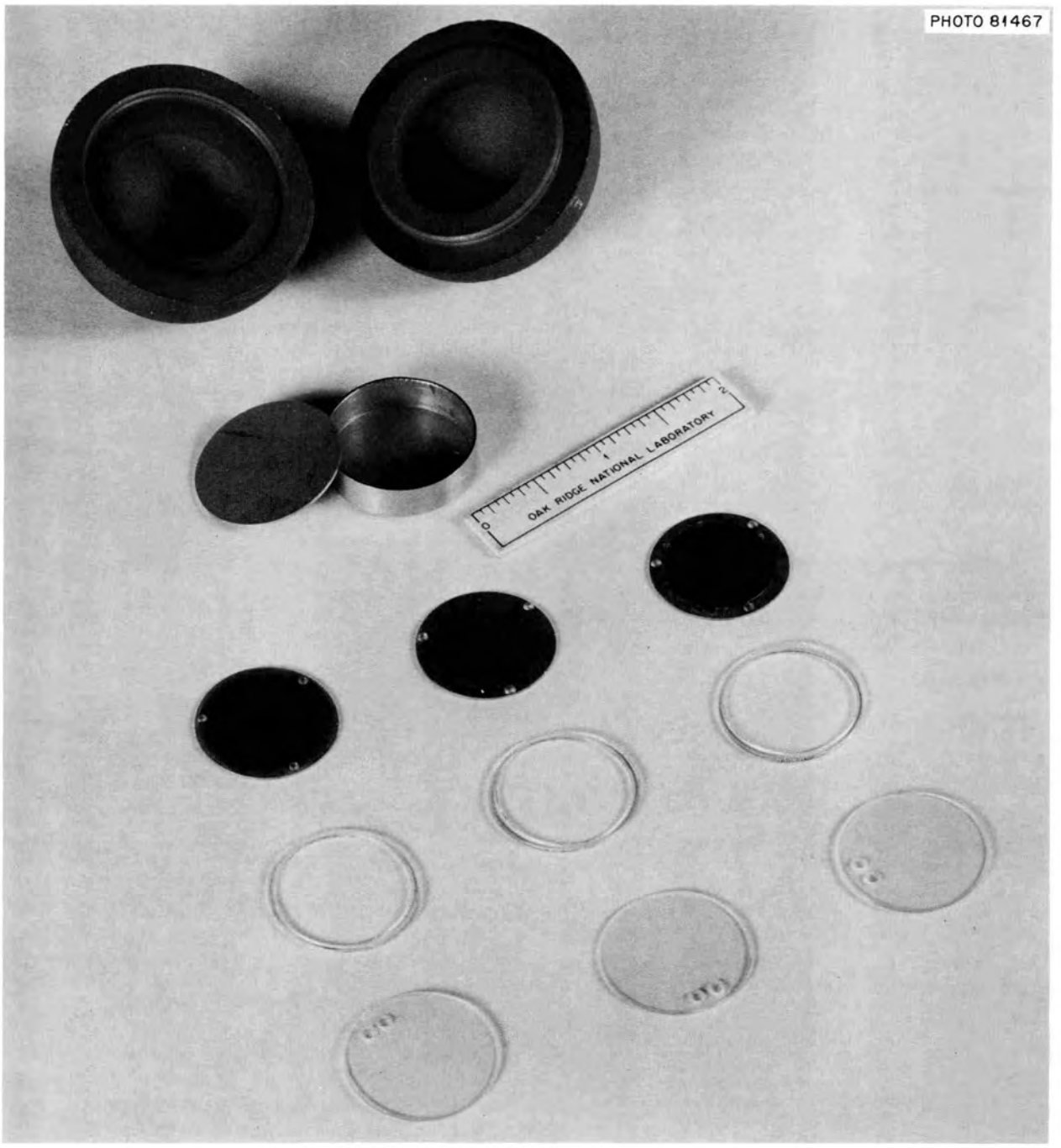

Fig. 23.5. Components of a Neutron Energy Threshold Detector System Employing Track Detectors. Boron shield (top), cadmium shield (upper center), fissile radiators (center), spacer rings (lower center), and Lexan track detectors (bottom).

foils are used at present in such dosimetric devices. Preliminary investigations of dose rates from a 1.9-cm-diam, 1-mm-thick uranium foil shielded with different metals is shown in Fig. 23.7. Although this foil is much larger than those which would be used in personnel nuclear accident dosimeters, results indicate that more information is needed before use of such detectors can be considered in devices worn on the body of a person.

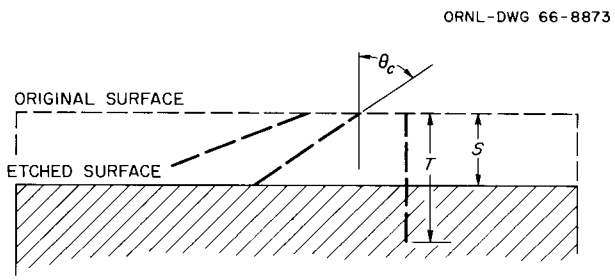

Fig. 23.6. Track Registration Geometry. Tracks are observed at angles less than θ_c after etching detector. Those incident at angles larger than θ_c are etched away when detector is processed.

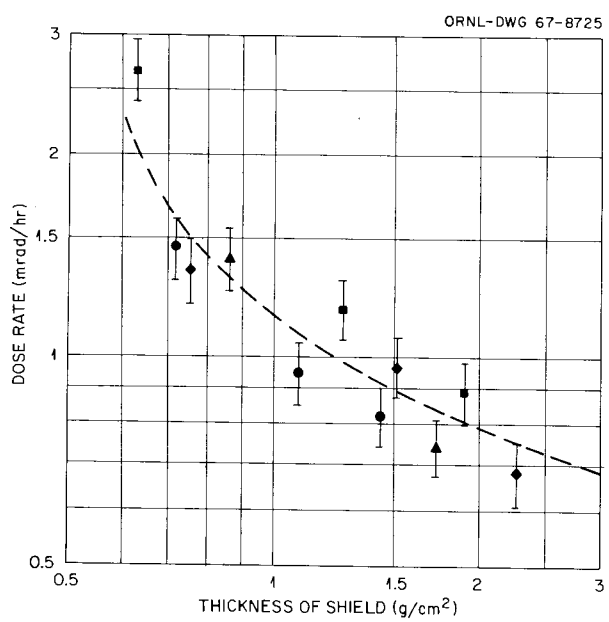

Fig. 23.7. Dose Rate at Center Surface of Various Metal Shields of Different Thickness Surrounding a 1.9-cm- by 1-mm Thick ^{238}U Foil. ■ Stainless steel, ● tin, ▲ cadmium, ◆ lead.

DOSIMETRY INTERCOMPARISONS WITH CERN (EUROPEAN ORGANIZATION FOR NUCLEAR RESEARCH, GENEVA, SWITZERLAND)

During fiscal year 1967, a personnel exchange of one year was completed between the ORNL Radiation Dosimetry Research Section and the Health Physics Group at CERN. During this exchange, two ORNL dosimeters were calibrated against standardized neutron and gamma-ray sources at CERN and at ORNL, and excellent agreement was obtained, as indicated below. Stray radiation fields were measured with these dosimeters and with the customary array of CERN dosimeters at the CERN 600-Mev synchrocyclotron and the 28-Gev proton synchrotron.

For fast neutrons, the ORNL system used a Hurst proportional counter,[9] a linear amplifier, and a multichannel analyzer. The dose was obtained by summing the number of pulses per channel times the energy per channel, with an appropriate calibration factor. Counts in the low-energy channels were obtained by extrapolation of the counts per channel vs channel number curve to zero energy, in order to compensate for the counts lost under the bias or obscured by the large number of noise pulses in the low-energy channels. Only the counter and the preamplifier were used at both laboratories. The main amplifier, analyzer, and high-voltage supply were obtained locally.

For gamma rays the ORNL Phil system was used.[10] This consists of a small Geiger counter used as a single ion detector and shielded with lead, tin, and fluorothene to give a response independent of gamma and x-ray energy. Again, only the counter, shield, and preamplifier were used in both laboratories. Associated scalers and high-voltage supplies were those in common use in each laboratory. The ^{6}Li thermal-neutron shield often used with this dosimeter was not available, but the thermal-neutron components of the radiation fields measured were known to be small.

Calibrations were performed at CERN with a PuBe neutron source and an Ra gamma source which were certified by the National Physical Laboratory in England. Similar calibrations of

[9] E. B. Wagner and G. S. Hurst, *Rev. Sci. Instr.* **29**, 153 (1958).

[10] E. B. Wagner and G. S. Hurst, *Health Phys.* **5**, 20 (1961).

the same instruments were done at ORNL with a PuBe source and a ^{60}Co source, both certified by the U.S. National Bureau of Standards. The two calibrations for each instrument agreed well within the probable errors of about 5%, as shown by Table 23.1.

The CERN array of instruments was essentially that described by Baarli and Sullivan[11,12] and consisted of ionization chambers with various fillings to give different neutron and gamma-ray sensitivities, fast- and thermal-neutron counters, and activation detectors. These were routinely calibrated at CERN with the same two sources.

Measurements of stray radiation outside the shields at the two large accelerators gave less good agreement on fast-neutron and gamma-ray doses. This is indicated in Table 23.2, where the ratios are given between neutron doses as measured by the two CERN techniques, namely ionization chambers and neutron counters, and between the Hurst counter results and the CERN instrument results. The Phil gamma doses are also compared with the ion chamber results. In some cases the agreement is good, but in many there is considerable difference, and the ratios are far from unity. Several factors may explain the discrepancies. In the first place, the radiation spectra are very complex, containing broad energy ranges of neutrons, electrons, hyperons, mesons, gamma rays, etc. The sensitivities of the different instruments to different radiations and different radiation energies vary; therefore they may respond differently to the various components of the field. Second, the ORNL instruments were used as integrating dosimeters over relatively long periods of time, and the accelerator beam intensities varied markedly with time, including some short shutdowns for which allowances are hard to make. The neutron counters were not always operated over the same time spans as the ORNL instruments, because several people speaking different languages were operating the various instruments. Also, the ion chambers were dose-rate instruments and did not integrate beyond fractions of a minute, though strip-chart recording was used in some cases. Third, a great deal of trouble was experienced with electrical noise pulses arising both within

Table 23.1. Calibration of Hurst Proportional Counter as a Fast-Neutron Dosimeter[a]

	Hurst Counter (millirads/count)	Phil Geiger Counter (millirads/count)
CERN	$7.13 \times 10^{-4} \pm 0.38$	$1.598 \times 10^{-4} \pm 0.040$
ORNL	$7.31 \times 10^{-4} \pm 0.22$	$1.593 \times 10^{-4} \pm 0.037$
Average	$7.23 \times 10^{-4} \pm 0.30$	$1.595 \times 10^{-4} \pm 0.038$

[a]The errors quoted are standard deviations of the series of measurements. The CERN sources had National Physical Laboratory (U.K.) calibrations; the ORNL sources had U.S. National Bureau of Standards calibrations. The CERN gamma source was 10 mg Ra; the ORNL one was ^{60}Co. The neutron sources were PuBe.

[11]J. Baarli, K. Goebel, and A. H. Sullivan, *Health Phys.* **9**, 1057 (1963).

[12]J. Baarli and A. H. Sullivan, *Health Phys.* **11**, 353 (1965).

Table 23.2. Ratios of Stray Radiation Doses as Measured at CERN by the Hurst Proportional Counter for Fast Neutrons, by the Phil Geiger Counter for Gamma Rays, and by the CERN Ion Chambers and Neutron Counters[a]

Fast-Neutron Dose Ratio			Gamma Dose Ratio,
Hurst / Ion Chambers	Hurst / Neutron Counters	Ion Chambers / Neutron Counters	Phil / Ion Chambers
1.12 ± 0.42	1.04 ± 0.47	0.95 ± 0.21	1.20 ± 0.50

[a]Stated errors are standard deviations of the ratios from a series of measurements using the various dosimeters together. The "ion chambers" were a tissue-equivalent chamber filled with tissue-equivalent gas and a CO_2-filled chamber. The "neutron counters" were a Hansen-McKibben "long counter" and a Moyer "proton recoil" counter.

the ORNL systems and from the large pulsed radio-frequency fields and spark chambers associated with the accelerators. Finally, the radiation was always pulsed, especially at the 28-Gev machine, so that the instantaneous dose rate during a pulse was sometimes much too large for resolving times of the counters though the average rate was quite low.

The conclusion was drawn that the Hurst proportional counter and the Phil gamma dosimeter were potentially satisfactory for use at large accelerators only if the instantaneous dose rates were within their useful ranges and if the noise problems could be eliminated; it now appears practical to eliminate the noise for this application.

THIRD ANNUAL INTERCOMPARISON STUDY

The third annual intercomparison study of nuclear accident dosimetry (NAD) systems was conducted at the DOSAR facility during the two-week period from May 15 to 26, 1967. Eleven laboratories, nine domestic and two European, were represented by a total of 22 participants. Several discussion sessions served to familiarize participants with response characteristics of all NAD systems tested. In addition to the HPRR, the DOSAR low-energy accelerator (DLEA) was used to provide monoenergetic neutrons for fiduciary studies.

Two "in-air" bursts were run during the first week with dosimeters arranged on a 3-m radius around the HPRR. A Bomab phantom filled with saline solution (1.5 mg of Na per milliliter of solution) was also placed at 3 m and instrumented by several participants. During the second week, two "moderated" bursts were run, again with the dosimeters arranged in a 3-m radius around the HPRR but with a 13-cm-thick steel shield positioned between the detectors and the reactor. Due to lack of space behind the shield, Bomab was placed at a distance of 4 m during the moderated exposures.

A critique was held May 26 in which preliminary results were presented. Final results, received approximately one month after the study, are shown in Tables 23.3 to 23.6. In general, the preliminary results were encouraging, particularly for the "in-air" studies, in which the overall average of the measured values for each irradiation had a standard deviation of only ±17% for neutron dose and ±10% for gamma-ray dose (see Table 23.7). For the "moderated" cases the gamma-ray results were less consistent, and the neutron results showed a considerably wider range of values (about a factor of 5 to 7), with a standard deviation of about ±40%. A small part of this spread was probably due to dose variations depending on position on the 3-m radius (i.e., DOSAR personnel exposed several dosimeters at various locations on the experimental radius, and the observed spread in neutron dose results was about 11% for both moderated tests). The variations were slightly less (8 to 10%) for the "in-air" tests.

"TOTAL" AND "EXCHANGEABLE" SODIUM STUDIES IN SWINE AND SHEEP USING ACTIVATION ANALYSIS AND ISOTOPIC DILUTION

In a recent publication, Smith *et al.*[13] questioned the accuracy of 105 g of sodium per 70 kg "standard man" as reported by ICRP (1961).[14] They report that (1) exchangeable sodium (within 24 hr) is approximately 75 to 80 g per 70 kg of body weight, in good agreement with other literature values;[15] and (2) total body sodium is essentially the same as exchangeable sodium (i.e., all body sodium is exchangeable, and total body sodium is probably 75 to 80 g instead of 105 g per 70 kg). If these lower values are correct, the neutron dose estimates for survivors of the Yugoslav criticality accident at Vinca were low, by approximately 40%.[16]

Elemental composition of body tissues as reported by the ICRP is usually determined by spectrographic analysis of samples taken from adult cadavers. However, the work of Smith *et al.* employed neutron activation of the sodium present in two human volunteers. In essence, two men and a man phantom filled with an aqueous solution containing 105 g of sodium were irradiated with partially moderated 14-Mev neutrons and analyzed for the resulting ^{24}Na using a whole-body counter.

---

[13] J. S. Smith *et al.*, *Personnel Dosimetry for Radiation Accidents*, p. 369, IAEA, Vienna, 1965.

[14] "Elements in the Body Organs of Standard Man," Report of ICRP Committee II on Permissible Dose for Internal Radiation (1959), with Bibliography for Biological, Mathematical, and Physical Data, *Health Phys.* 3 (1960).

[15] G. J. Hine *et al.*, *Whole Body Counting*, IAEA, Vienna, 1962.

[16] G. S. Hurst *et al.*, *Health Phys.* 5, 179–202 (1961).

Table 23.3. NAD Intercomparison Data, "In Air" Burst, May 17, 1967

Burst yield = 7.2×10^{16} fissions

Study Group	D_n (rads)	D_γ[a] (rads)	n/γ Dose Ratio	Neutron Fluence (neutrons/cm^2) Φ_{th} (neutrons/cm^2)	Φ_{Pu} or >1 kev	Φ_{Np} or >0.75 Mev	Φ_U or >1.5 Mev	Φ_S or >2.5 Mev	Φ_{Al}	Φ_{Mg}	Φ_{Cu}	Φ_{In}	Bomab ^{24}Na (μc/ml)	Bomab Dose Based on ^{24}Na, Badges, TDU, etc.[b]	Neutron Dosimetry System	Gamma Dosimetry System
				$\times 10^{10}$	$\times 10^{10}$	$\times 10^{10}$	$\times 10^{10}$	$\times 10^{10}$	$\times 10^{10}$	$\times 10^{10}$	$\times 10^{10}$	$\times 10^{10}$				
AFWL	316	45	7.0	0.817	13.7[c]	7.23	4.34	2.59							TDU	TLD
ANL	360	44	8.2	0.56	15.1[d]	10.7	4.93	1.86[e]			1.82[f]		9.87×10^{-4}	304/37	TDU (modified)	TLD
CEA (France)	255	43–53		0.73	13.1	6.3	4.1	2.22							SNAC	RPL
		55–70		0.80											Film	Film
DOSAR	295	41	7.2	0.60	12.2	8.54	3.94	2.22	0.12[g]				8.3×10^{-4}		TDU	RPL
EG&G	355	29	12.2	0.52	15.5[h]	10.9[i]	4.48	1.55[j]	0.074[k]	0.146[l]					TDU and other foils	TLD
K-25	349	43.5	8.0	0.61	13.4	9.6	4.4	2.2			0.412[m]	5.08[n]	9.91×10^{-4}	320/40	TDU	RPL
	317		7.3					2.18						296	ORGDP	
LASL	320	40	8.0	0.625				2.12							Activation foils	RPL
LRL	288[o]	50	5.8	0.52[p]	12.8[h]	7.8[i]	4.0	1.5[r]	0.062[s]			8.0[t]	8.4×10^{-4}		TDU	TLD
	390			0.46			4.7[q]	1.6								
	350			0.59				1.5								
REECO	408			0.52	17.6			1.57[j]			4.49[t]				Hanford activation foils	RPL
	281			0.64	10.7[u]											
UKAEA	183	54	3.4	0.78[v]	17.6[w]			1.56[x]					6.6×10^{-4}	258/89[y]	Activation foils	Film
				0.69												
USNRDL	293				13.2[d]	10.3	3.96	1.67[j]							TDU-Lexan	TLD
DOSAR (Expt.)	305	40	7.6		13.2	7.8	3.95	2.3							TDU-Lexan	RPL

[a] 0.87 rad/roentgen conversion used.
[b] Neutron dose/gamma dose.
[c] >4 kev.
[d] ^{235}U, >0.4 kev.
[e] >2.9 Mev.
[f] 0.17 to 400 ev.
[g] >6.6 Mev.
[h] >10 kev.
[i] >0.6 Mev.
[j] >3.0 Mev.
[k] >7.5 Mev.
[l] >6.3 Mev.
[m] Fluence per unit ln E evaluated at 580 ev.
[n] >1.5 Mev.
[o] Foils, REM meter, and Phylatron dosimeter respectively.
[p] Au, In, and Cu respectively.
[q] Double U foils.
[r] Sulfur >3.0 Mev, nickel >3.0 Mev, hair sulfur respectively.
[s] >7.3 Mev.
[t] >1 Mev.
[u] Mn epithermal correction.
[v] Maxwellian and Westcott convention respectively.
[w] Estimated from combined results of activation foils.
[x] >2.8 Mev.
[y] Front of phantom.

Table 23.4. NAD Intercomparison Data, "In Air" Burst, May 18, 1967

Burst yield = 6.9×10^{16} fissions

Study Group	D_n (rads)	D_γ[a] (rads)	n/γ Dose Ratio	Neutron Fluence (neutrons/cm^2) Φ_{th} (neutrons/cm^2)	Φ_{Pu} or >1 kev	Φ_{Np} or >0.75 Mev	Φ_U or >1.5 Mev	Φ_S or >2.5 Mev	Φ_{Al}	Φ_{Mg}	Φ_{Cu}	Φ_{In}	Bomab ^{24}Na (μc/ml)	Bomab Dose Based on ^{24}Na, Badges, TDU, etc.[b]	Neutron Dosimetry System	Gamma Dosimetry System
				$\times 10^{10}$	$\times 10^{10}$	$\times 10^{10}$	$\times 10^{10}$	$\times 10^{10}$	$\times 10^{10}$	$\times 10^{10}$	$\times 10^{10}$	$\times 10^{10}$				
AFWL	323	40	8.1	0.82	13.7[c]	7.23	4.34	2.59							TDU	TLD
ANL	338	45	7.5	0.55	14.4[d]	9.97	4.57	1.81[e]			1.79[f]		1.01×10^{-4}	305/40	TDU (modified)	TLD
CEA (France)	252	43.5–52		0.72	13.0	6.21	4.04	2.20							SNAC	RPL
		52–70		0.68											Film	Film
DOSAR	285	41	7.0	0.54	11.7	8.29	3.84	2.13					7.8×10^{-4}		TDU	RPL
EG&G	348			0.51	15.8[g]	10.0[h]	4.20	1.5[i]							TDU and other foils	TLD
K-25	308	42.6	7.2	0.72	12.5	8.5	4.0	2.1			0.401[j]	4.75[k]	9.73×10^{-4}	293/41	TDU	RPL
	299		7.0	0.59				2.06						287	ORGDP	
LASL	Did Not Participate															
LRL	275[l]	60[m]	4.6	0.48[n]	12.6[g]	7.0[h]	3.8	1.4[o]	0.048[p]				8.6×10^{-4}		TDU	TLD
	385			0.54				1.6								
	320							1.4								
REECO	365			0.36	15.6			1.48[i]				4.16[q]			Hanford activation foils	RPL
UKAEA	187	54	3.5	0.64[r]	18.2[s]			1.57[t]					6.5×10^{-4}	244/87[u]	Activation foils	Film
				0.56												
USNRDL	2.69				11.8[d]	9.43	3.91	1.53[i]							TDU-Lexan	TLD
DOSAR (Expt.)	Did Not Participate															

[a] 0.87 rad/roentgen conversion used.
[b] Neutron dose/gamma dose.
[c] >4 kev.
[d] ^{235}U, >0.4 kev.
[e] >2.9 Mev.
[f] 0.17 to 400 ev.
[g] >10 kev.
[h] >0.6 Mev.
[i] >3.0 Mev.
[j] Fluence per unit ln E evaluated at 580 ev.
[k] >1.5 Mev.
[l] Foils, REM meter, and Phylatron dosimeter respectively.
[m] Film, no TLD-700 for this exposure.
[n] Au and In respectively.
[o] Sulfur >3.0 Mev, nickel >3.0 Mev, hair sulfur respectively.
[p] >7.3 Mev.
[q] >1 Mev.
[r] Maxwellian and Westcott convention respectively.
[s] Estimated from combined results of activation foils.
[t] >2.8 Mev.
[u] Front of phantom.

Table 23.5. NAD Intercomparison Data, "Shielded" Burst, May 23, 1967

Burst yield = 6.9×10^{16} fissions

Study Group	D_n (rads)	D_γ[a] (rads)	n/γ Dose Ratio	Neutron Fluence (neutrons/cm^2) Φ_{th} (neutrons/cm^2)	Φ_{Pu} or >1 kev	Φ_{Np} or >0.75 Mev	Φ_U or >1.5 Mev	Φ_S or >2.5 Mev	Φ_{Al}	Φ_{Mg}	Φ_{Cu}	Φ_{In}	Bomab ^{24}Na (μc/ml)	Bomab Dose Based on ^{24}Na, Badges, TDU, etc.[b]	Neutron Dosimetry System	Gamma Dosimetry System
				$\times 10^{10}$	$\times 10^{10}$	$\times 10^{10}$	$\times 10^{10}$	$\times 10^{10}$	$\times 10^{10}$	$\times 10^{10}$	$\times 10^{10}$	$\times 10^{10}$				
AFWL	101	7.1	14.2	0.44	5.1[c]	2.8	0.89	0.37							TDU	TLD
ANL	146	11	13.3	0.33	7.83[d]	3.86	1.03	0.27[e]			1.17[f]		3.30×10^{-4}	83/6	TDU (modified)	TLD
CEA (France)	50	10.9–13.9 15.5–8.7		0.38 0.31–0.23	4.2	1.0	0.59	0.31							SNAC Film	RPL Film
DOSAR	119	11	10.8	0.31	5.64	2.99	0.84	0.33					2.6×10^{-4}	61/– –	TDU	RPL
EG&G	145	5.3	27.4	0.17	8.17[g]	3.51[h]	0.86	0.26[i]							TDU and other foils	TLD
K-25	95 93	10.4	9.1 8.9	0.21	6.0	3.1	0.88	0.34 0.34			0.249[j]	1.18[k]	3.33×10^{-4}	71/– –	TDU ORGDP	RPL
LASL	98[l]	<30						0.29							Activation foils	RPL
LRL	108[m] 142	12	9.0	0.27[n] 0.23 0.26	6.6[g]	2.4[h]	0.80 0.60[o]	0.22[p] 0.22[i]				2.0[q]	2.6×10^{-4}		TDU	TLD
REECO	154			0.09	7.2			0.30[i]				1.26[q]			Hanford activation foils	RPL
UKAEA	30	14.5	2.1	0.26[r] 0.23	9.82[s]			0.235[t]					2.2×10^{-4}	63/20[u]	Activation foils	Film
USNRDL	115				6.95[d]	3.95	1.01	0.235[i]							TDU-Lexan	TLD
DOSAR (Expt.)	124	10.9	11.4		6.2	2.9	0.90	0.34							TDU-Lexan	RPL

[a] 0.87 rad/roentgen conversion used.
[b] Neutron dose/gamma dose.
[c] >4 kev.
[d] ^{235}U, >0.4 kev.
[e] >2.9 Mev.
[f] 0.17 to 400 ev.
[g] >10 kev.
[h] >0.6 Mev.
[i] >3.0 Mev.
[j] Fluence per unit ln E evaluated at 580 ev.
[k] >1.5 Mev.
[l] Phylatron dosimeter.
[m] Foils and REM meter respectively.
[n] Au, In, and Cu respectively.
[o] Double U foils.
[p] Sulfur foil and hair sulfur respectively.
[q] >1 Mev.
[r] Maxwellian and Westcott convention respectively.
[s] Estimated from combined results of activation foils.
[t] >2.8 Mev.
[u] Front of phantom.

Table 23.6. NAD Intercomparison Data, "Shielded" Burst, May 24, 1967

Burst yield = 7.3×10^{16} fissions

Study Group	D_n (rads)	D_γ[a] (rads)	n/γ Dose Ratio	Neutron Fluence (neutrons/cm^2) Φ_{th} (neutrons/cm^2)	Φ_{Pu} or >1 kev	Φ_{Np} or >0.75 Mev	Φ_U or >1.5 Mev	Φ_S or >2.5 Mev	Φ_{Al}	Φ_{Mg}	Φ_{Cu}	Φ_{In}	Bomab ^{24}Na (μc/ml)	Bomab Dose Based on ^{24}Na, Badges, TDU, etc.[b]	Neutron Dosimetry System	Gamma Dosimetry System
				$\times 10^{10}$	$\times 10^{10}$	$\times 10^{10}$	$\times 10^{10}$	$\times 10^{10}$	$\times 10^{10}$	$\times 10^{10}$	$\times 10^{10}$	$\times 10^{10}$				
AFWL	110	7.0	15.7	0.362	5.27[c]	2.74	0.864	0.352							TDU	TLD
ANL	140	11	12.7	0.30	7.32[d]	3.76	0.97	0.26[e]			1.07[f]		3.05×10^{-4}	78/6	TDU (modified)	TLD
CEA (France)	47	11.3–13 15.3–8.3		0.33 0.3–0.19	4.05	0.91	0.54	0.29							SNAC Film	RPL Film
DOSAR	108	10.7	10.1	0.29	5.33	2.69	0.79	0.30					2.59×10^{-4}	57/– –	TDU	RPL
EG&G	125			0.166	7.10[g]	2.89[h]	0.802	0.257[i]	0.0057[j]	0.025[k]					TDU and other foils	TLD
K-25	88 86	9.6	9.2 9.0	0.25 0.21	5.7	2.8	0.76	0.33 0.329			0.232[l]	1.11[m]	2.59×10^{-4}	64/7.9	TDU ORGDP	RPL
LASL	Did Not Participate															
LRL	90[n] 120 140	11.6	7.8	0.26[o] 0.30 0.25	5.2[g]	2.2[h]	0.75 0.93[p]	0.20[i] 0.25[q]				1.5[r]	2.5×10^{-4}		TDU	TLD
REECO	227			0.08	11.8			0.18[i]				0.64[r]			Hanford activation foils	RPL
UKAEA	30	11.5	2.6	0.27[s] 0.24	8.91[t]			0.242[v]						58/19[v]	Activation foils	Film
USNRDL	101				5.96[d]	3.53	0.77	0.22[i]							TDU-Lexan	TLD
DOSAR (Expt.)	118	10.6	11.1		6.1	2.5	0.82	0.31							TDU-Lexan	RPL

[a] 0.87 rad/roentgen conversion used.
[b] Neutron dose/gamma dose.
[c] >4 kev.
[d] ^{235}U, >0.4 kev.
[e] >2.9 Mev.
[f] 0.17 to 400 ev.
[g] >10 kev.
[h] >0.6 Mev.
[i] >3.0 Mev.
[j] >7.5 Mev.
[k] >6.3 Mev.
[l] Fluence per unit ln E evaluated at 580 ev.
[m] >1.5 Mev.
[n] Foils, REM meter, and Phylatron dosimeter respectively.
[o] Au, In, and Cu respectively.
[p] Double U foils.
[q] Hair sulfur.
[r] >1 Mev.
[s] Maxwellian and Westcott convention respectively.
[t] Estimated from combined results of activation foils.
[u] >2.8 Mev.
[v] Front of phantom.

Table 23.7. Neutron and Gamma-Ray Dose Results

Burst No.	Yield	Neutron Dose (rads)		Gamma Dose (rads)	
		Range	Average	Range	Average
	$\times 10^{16}$				
B303	7.2	183 to 390	317 ± 54[a]	29 to 63	45 ± 8.6
B304	6.9	187 to 385	304 ± 41	40 to 61	48 ± 7.3
B305	7.1	30 to 154	109 ± 36	7 to 15	11 ± 2.9
B306	6.6	30 to 227	109 ± 46	7 to 12	11 ± 1.6

[a] $\sigma = \sqrt{\frac{\Sigma(x_i - x)^2}{n-1}}$.

After normalization to the neutron fluences and other corrections, the ^{24}Na activities per 70 kg of the men were some 20 to 25% less than that of the phantom; hence the conclusion that sodium content of man is less than 105 g per 70 kg. Because of this uncertainty, a study was undertaken by this section in collaboration with the UT-AEC Agricultural Research Laboratory and Oak Ridge Associated Universities (ORAU) to investigate "exchangeable" and "total" body sodium in large animals with the hope of learning more about the sodium content of standard man.

The use of animals instead of humans permitted a different method of determining total body sodium. Although this method also involved whole-body neutron irradiation and subsequent whole-body counts to ascertain the quantity of ^{24}Na formed, much larger neutron doses were delivered, thus improving counting statistics in the whole-body counting as well as permitting the analysis for ^{24}Na in the blood serum. After irradiation, blood samples were taken, and the equilibrium activities of ^{24}Na per milligram of sodium in the serum were obtained by conventional techniques. Since the ^{24}Na activity per milligram of sodium in blood serum is representative of that present throughout the whole body,[17] the simple quotient of microcuries formed divided by microcuries per milligram of sodium in blood serum yielded a reasonable estimate of total body sodium.

There are numerous variables which may cause errors when assaying for radioactive elements in vivo using a whole-body counter. Some of these factors are:

1. nonuniformity of isotope distribution in the body,
2. variable body size and bone/tissue ratio,
3. self-absorption of gamma rays being analyzed,
4. geometry of whole-body counter.

The ORAU whole-body counter is comprised of an array of eight 4- by 4-in. NaI(Tl) crystals, four above and four below the stretcher. The crystals are arranged such that a point source yields the same net counting rate regardless of its location on the stretcher; therefore, neither nonuniformity of ^{24}Na distribution in the animals nor the exact position of the animals in the whole-body counter should affect the results appreciably. The relatively high-energy gamma ray from ^{24}Na (2.76 Mev) minimizes errors due to self-absorption; therefore the efficiency of the whole-body counter does not vary rapidly as a function of animal weight.

The whole-body counter was calibrated by assaying sheep and swine that had been injected with known amounts of ^{24}Na solution. Counter efficiency was determined in units of net counts per minute under the 2.76-Mev photopeak of ^{24}Na per microcurie injected. The first group of animals were sacrificed and assayed only a few minutes after injection. Later, two anesthetized animals were injected and assayed live after allowing several hours for equilibration of ^{24}Na. Results of these two calibrations were in close agreement. The actual shape of the efficiency-vs-weight curve was determined using known ^{24}Na activities in various-sized polyethylene bottles; however, for

[17] F. W. Sanders and J. A. Auxier, *Health Phys.* 8, 371–79 (1962).

given weights the bottle technique gave efficiencies that were in error by 4% for swine and 14% for sheep. Thus, the animal injection experiments were necessary to assure an accurate whole-body counter calibration.

The total sodium experiments involved irradiating groups of sheep and swine to neutrons from the HPRR. After irradiation, blood samples were taken, and the animals were sacrificed and assayed for ^{24}Na in the whole-body counter. Blood serum samples were analyzed for ^{24}Na (μc) and total Na (mg) per milliter to arrive at microcuries per milligram of sodium in the serum. Finally, total body sodium was obtained by dividing total ^{24}Na formed in the animals by the activities per milligram of sodium in the serum. The results were 119 and 139 g of Na per 70 kg of body weight for swine and sheep respectively.

For determining "exchangeable" sodium, isotopic dilution seemed to be the only practical method. Four swine and four sheep were each injected with approximately 1 mc of ^{24}Na solution. Blood samples were taken from all animals at 1, 4, and 24 hr after injection. In addition, samples were taken from one of the swine at 5-min intervals during the first hour and samples were taken from one sheep at 10-min intervals for the first 2 hr in order to measure the equilibration rate of the ^{24}Na in the animals. The blood samples were allowed to coagulate and were centrifuged to obtain serum. Five-milliliter serum samples were assayed for ^{24}Na activities using conventional NaI techniques. After correcting for radioactive decay, the ^{24}Na activities of the serum samples were plotted as a function of sampling time, and the resulting curve showed that equilibrium was probably reached after 4 hr and certainly by 24 hr, assuming negligible loss by excretion. The serum samples were also analyzed for sodium content by flame photometry. Then, the "equilibrium" ^{24}Na activity in units of millicuries per milliliter of serum was divided by the average sodium content in milligrams per milliliter to obtain the equilibrium concentration of ^{24}Na per milligram of sodium. Finally, the quotient of microcuries injected divided by the equilibrium activity in the blood serum (mc/mg) yielded exchangeable sodium contents of 80 and 69 g per 70 kg of body weight for swine and sheep respectively. These results are consistent with published results.[13,15]

The results of these studies certainly suggest that not all body sodium is exchangeable. They also suggest that, at least for swine and sheep, total body sodium content is more than 105 g per 70 kg. Recently published data for standard man include a value for sodium of 140 g per 70 kg of body weight;[18] however, this number is only tentative.[19]

HIGH-SENSITIVITY G-M-TYPE GAMMA-RAY DOSIMETER FOR OPERATION HENRE

To measure gamma-ray dose as a function of angle during Operation BREN, the Phil dosimeter was used.[20] However, due to the small size and relative insensitivity of the Phil (approximately 80 counts min^{-1} millirad^{-1} hr), the gamma-ray angular dose results for Operation BREN were limited by poor counting statistics. For Operation HENRE the Phil was replaced with a more sensitive gamma-ray dosimeter to improve the angular dose-rate statistics. The low neutron sensitivity and favorable photon energy response as well as the simplicity inherent in the Phil G-M counter led to the selection of the RCL 10-60 G-M tube for the angular dose measurements during HENRE.

Development

A suitable photon energy shield for an RCL G-M tube was designed and experimentally tested.[21] However, when design was begun of a thermal-neutron shield, it became apparent that, due to the large size of the RCL counters and the relatively high cost of enriched ^{6}LiF powder, it would be cheaper to place the thermal-neutron shield inside the energy shield next to the glass wall of the counters. When this was done, each shield held about 31 g of ^{6}LiF (worth $60) in a 3.2-mm thickness that provided a thermal-neutron shielding factor of approximately 200. Several 1-mm-thick tin energy shields were made to fit snugly over the thermal-neutron shields and were perforated according to the specifications of Fukuda. The completely assembled detectors,

---

[18] J. A. Auxier *et al.*, *Health Phys. Div. Ann. Progr. Rept. July 31, 1966*, ORNL-4007, p. 242.

[19] I. H. Tipton, University of Tennessee, private communication.

[20] J. H. Thorngate *et al.*, *Energy and Angular Distribution of Neutrons and Gamma Rays — Operation BREN*, CEX-62.12 (February 1967).

[21] J. A. Auxier *et al.*, *Health Phys. Div. Ann. Progr. Rept. July 31, 1962*, ORNL-3347, p. 85.

including the inner ^{6}LiF thermal-neutron shields and the outer perforated tin energy shields, were subjected to an energy response study using a 250-kvp x-ray machine and several isotopic sources of gamma rays of various energies.

The energy response of the counter in the original, Fukuda-designed, energy shield was redetermined. This was done in two steps at each x-ray energy: (1) A 250-mr Victoreen chamber was exposed at high beam currents alongside a small Phil (equipped with a perforated energy shield for fairly flat response down to about 50 kev), which also provided a recalibration of the Phil energy response. (2) Then the responses of the RCL and Phil counters were compared at lower dose rates consistent with the dead-time limitations of the larger counter. A simple ratio provided the calibration factor of counts min^{-1} mr^{-1} hr for the large counter.

The energy response of an identical G-M counter with the new shields was then studied relative to the Fukuda-type "standard" counter by taking response ratios for the various x-ray energies. The "end" response of the new design was also studied for application to collimated beams during Operation HENRE. The results of these studies are summarized in Fig. 23.8.

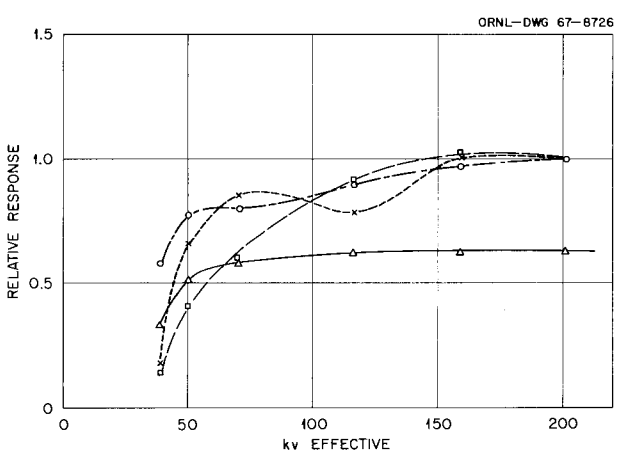

Fig. 23.8. Response of RCL 10-60 and Phil per Unit Exposure as a Function of Photon Energy for Several Shield Configurations. ⊙ RCL 10-60 Fukuda energy shield; ⊡ new energy and thermal neutron shields (normalized to 1.0 at 201 kev effective energy); △ new energy and thermal neutron shields, end response (HENRE); X Phil with standard perforated energy shield normalized to side response of 1.0 at 200 kev.

Angular response studies were carried out on the RCL 10-60 counter with the new energy and thermal-neutron shields in place. These studies were performed using a ^{60}Co source at a distance of about 5 m to minimize uncertainties in the location of the effective center of the counter. A detector and source height of 1.5 m was used to minimize scattered radiation. Measurements were made on an asphalt pad located outdoors and away from any scattering media other than air. Response was determined at angles from 0 to −150° at 15° increments after a preliminary check showed that the counter response was essentially symmetrical around its sides. The results of this study are shown in Fig. 23.9 and are in good agreement with previously published data.[21]

Finally, with the new thermal-neutron and energy correction shields in place, the response of the RCL 10-60 counter was studied using higher-energy photons and fast neutrons. The sources of gamma rays used included ^{60}Co, ^{137}Cs, and the high-energy gamma rays formed by neutron capture in air; a source of sufficient intensity is observed outside the DOSAR control building when the HPRR is operating. A neutron response study was conducted using neutrons from a 5-curie AmBe source surrounded with 0.3 mm of lead to decrease the response due to the ^{241}Am x rays. For this case, the neutron to gamma-ray dose ratio was approximately 1.4. Since it is virtually impossible to obtain fast neutrons without coexistent gamma rays, it was difficult to determine how much of the counter's response was actually due to neutrons from the AmBe source. As an approximate solution to this problem, the response of the RCL counter with its ^{6}LiF and energy shields in place was compared with that of a Phil with a perforated energy shield and LiF thermal-neutron shield, the assumption being that any appreciable increase in the ratio of RCL to Phil response represented an overresponse of the RCL counter. Previous theoretical and experimental studies of the Phil response indicated an effective fast-neutron response of less than 2% and a gamma-ray response that is proportional to the tissue rads from 100 kev to 8 Mev with an accuracy of ±20%.

The ratio of RCL to Phil response was determined for all radiation fields studied, including the x-ray work, and the results are shown in Table 23.8. All measurements were made at low counting rates such that dead-time losses in the RCL counter were less than 3%. Above 100 kev photon energy,

the average RCL/Phil ratio was 44.5 with a probable error of about ±7%, which is well within the ±20% accuracy of the Phil for measuring tissue rads of pure gamma rays. Therefore it is concluded that, when properly shielded for low-energy photons and thermal neutrons, the RCL 10-60 has response characteristics similar to those of the Phil and is acceptable for gamma-dose measurements during Operation HENRE. The added sensitivity, compared with the Phil, considerably improved counting statistics during HENRE angular dose studies.

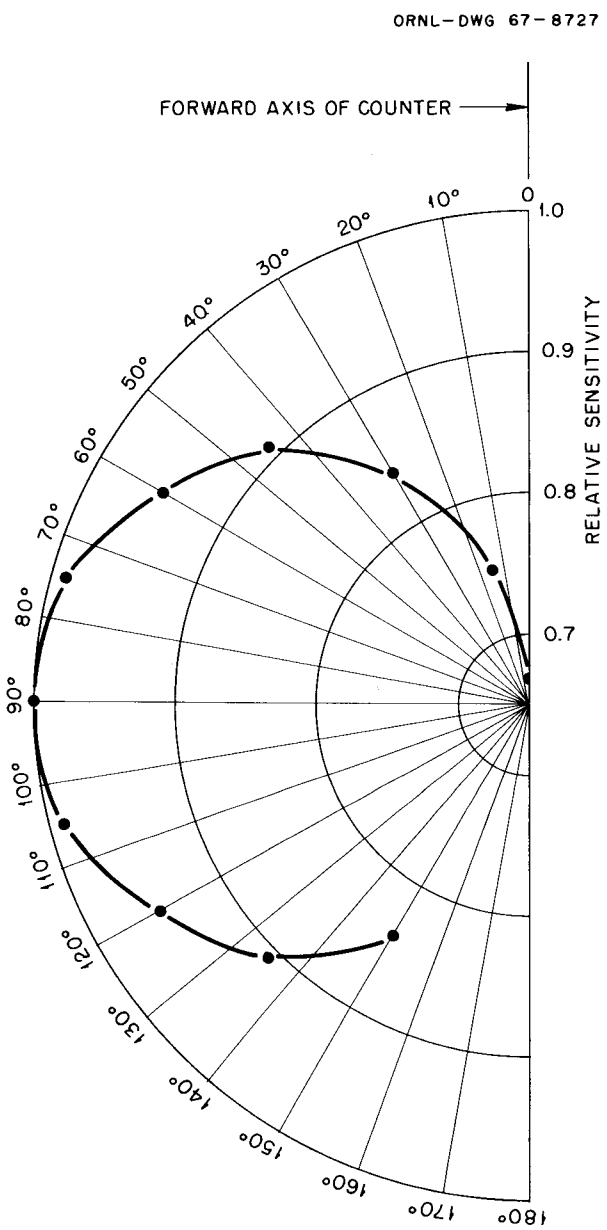

Fig. 23.9. Dependence of the Response of the RCL 10-60 in Its Improved Shield on the Angle of Incidence of the Radiation Relative to Its Axis, Where 0° Represents Radiation Incident upon the Exposed End of the Counter.

Table 23.8. Relative Response of the RCL and Phil Counters as a Function of Photon Energy

Effective Energy	RCL/Phil Ratio
39 kev	30.1
50 kev	24.0
70 kev	27.1
116 kev	45.2
159 kev	39.5
201 kev	38.3
0.662 Mev (^{137}Cs)	42.8
1.25 Mev (^{60}Co)	50.8
AmBe plus 0.33 mm Pb	47.8
HPRR scattered radiation	47.1

YIELD, ENERGY, AND ANGULAR DISTRIBUTIONS OF NEUTRONS PRODUCED IN GRAPHITE, COPPER, AND TANTALUM TARGETS IRRADIATED WITH 63-Mev PROTONS

A series of experiments were performed at the Oak Ridge Isochronous Cyclotron (ORIC) to determine the yield as well as the energy and angular distributions of neutrons produced by 63-Mev protons on various target materials. Carbon (graphite), copper, and tantalum were chosen as target materials, not only because they are frequently used as such but because they represent a wide range in atomic number. Data presented herein should be of value in designing appropriate shielding for future experiments in which this problem is encountered [e.g., for the "inject" stage of the proposed Separated Orbit Cyclotron (SOC), which will use rather large currents of protons in this energy region].

Materials and Methods

Threshold detector techniques were used in this study. Activation reactions used included ^{58}Ni(n, p)^{58}Co, ^{32}S(n,p)^{32}P, ^{27}Al(n,α)^{24}Na, and ^{12}C(n, $2n$)^{11}C, with approximate threshold energies of 1.1,

Table 23.9. Relative Angular Distribution of Neutron Yield for 63-Mev Protons on Graphite

Angle (deg)	$^{32}S(n,p)^{32}P$	$^{58}Ni(n,p)^{58}Co$	$^{27}Al(n,\alpha)^{24}Na$	$^{12}C(n,2n)^{11}C$
0	1.00	1.00	1.00	1.00
45	0.54	0.45	0.47	0.30
90	0.33	0.28	0.25	0.04
180	0.18			

1.8, 7, and 20 Mev respectively. In addition, ^{239}Pu, ^{237}Np, and ^{238}U fission foils were used to estimate total neutron yields on the assumption that nearly all neutrons produced were above about 1 Mev. Packets containing sulfur, aluminum, nickel, and carbon (plastic scintillators) detectors were exposed on a 30-cm arc at 0, 45, and 90°, while fission foils were exposed only in the forward direction (0°). Since ^{11}C has a 20-min half-life, the plastic scintillator detectors were assayed shortly after irradiation using a 2-in. photomultiplier.[22] Fission and aluminum foil activities were determined next using standard NaI crystal techniques.[23,24] Sulfur pellets were assayed on a 2-in.-diam plastic scintillator at least 24 hr after irradiation to allow for decay of ^{31}Si and any other short-lived contaminants.[23] Finally, the nickel foils were analyzed using a 3- by 3-in. NaI crystal and a multichannel analyzer after a delay of several days for decay of ^{58m}Co.

Cross sections were taken from BNL-325[25] and McElroy *et al.*[26] Data reduction utilized an iterative type of procedure in which a neutron energy spectrum was inferred from foil activities based on average cross sections above the various threshold energies. Total neutron yields were estimated from fission foil results, whereas yields above 10 and 20 Mev were obtained from aluminum foil and plastic scintillator results respectively. Coarse differential neutron energy spectra were obtained by taking differences in these total values and dividing by the number of Mev in each interval. After plotting these spectra in block diagram form, a best-fit smooth curve was drawn through the center of each block, and this spectral information was used to "weight" the foil cross sections for repeated fluence calculations. The best resulting data fit seemed to be a "peak-with-$1/E$-tail" type of approximation as suggested by Wadman.[27] Depending upon where the peak is placed, this type of curve fitting permits a wide variation in the relative "hardness" of assumed neutron energy spectra. This technique is somewhat coarse and leads to ambiguous answers if carried to extremes; however, the spectra generated for this series of experiments seem consistent with previously published results.

Results

1. *63-Mev Protons on Graphite*
   a) Neutron yield: 1.5×10^{10} neutrons sec^{-1} μa^{-1} $steradian^{-1}$ (calculated from 0° data although output is not isotropic).
   b) Neutron energy spectrum: peaked at 3 to 4 Mev with $1/E$ tail upward in energy to undetermined cutoff energy.
   c) Angular distribution of neutron yield: see Table 23.9.
2. *63-Mev Protons on Copper*
   a) Neutron yield: 2.2×10^{10} neutrons sec^{-1} μa^{-1} $steradian^{-1}$ (0° data).
   b) Neutron energy spectrum (0°): peaked at about 2 Mev with $1/E$ tail upward in energy to undetermined cutoff energy.
   c) Angular distribution of neutron yield: see Table 23.10.

[22] J. Baarli and A. H. Sullivan, *Health Phys.* 11, 353–61 (1965).

[23] G. S. Hurst and R. H. Ritchie, *Radiation Accidents: Dosimetric Aspects of Neutron and Gamma-Ray Exposures*, ORNL-2748 (Part A) (1959).

[24] R. L. Heath, *Scintillation Spectrometry Gamma-Ray Spectrum Catalogue*, IDO-16408 (1957).

[25] *Neutron Cross Sections*, BNL-325, 2d ed., TID-4500 (May 1964).

[26] D. Ewing and W. N. McElroy, *Neutron Flux Spectra Determination by Foil Activation*, AFWL TR-65-34, vols. I, II, and III (1965).

[27] W. W. Wadman, *Health Phys.* 11, 659–65 (1965).

Table 23.10. Relative Angular Distribution of Neutron Yield for 63-Mev Protons on Copper

Angle (deg)	$^{32}S(n,p)^{32}P$	$^{58}Ni(n,p)^{58}Co$	$^{27}Al(n,\alpha)^{24}Na$	$^{12}C(n,2n)^{11}C$
0	1.00	1.00	1.00	1.00
45	0.98	0.94	0.69	0.50
90	0.66	0.56	0.37	0.090

Table 23.11. Relative Angular Distribution of Neutron Yield for 63-Mev Protons on Tantalum

Angle (deg)	$^{32}S(n,p)^{32}P$	$^{58}Ni(n,p)^{58}Co$	$^{27}Al(n,\alpha)^{24}Na$	$^{12}C(n,2n)^{11}C$
0	1.00	1.00	1.00	1.00
45	1.08	1.10	0.86	0.60
90	1.06	1.10	0.57	0.21
180	0.79			

3. *63-Mev Protons on Tantalum*

   a) Neutron yield: 5.0×10^{10} neutrons sec^{-1} μa^{-1} $steradian^{-1}$ (0°); output nearly isotropic.

   b) Neutron energy spectrum: peaked near 1 Mev with $1/E$ tail upward in energy, much "softer" than in either copper or graphite studies.

   c) Angular distribution of neutron yield: see Table 23.11.

Discussion

Apparent neutron yields based on forward-direction measurements are shown as a function of atomic weight in Fig. 23.10. While neutron yield seems to increase exponentially with atomic weight, the energy spectra become progressively softer and the angular distributions become more nearly isotropic.

In an attempt to corroborate the neutron energy spectra reported herein, a separate experiment was performed using an ^{6}LiI neutron spectrometer after the design of Murray.[28] Unfortunately, during the allotted work shift, difficulties with the cyclotron prevented successful extraction of 63-Mev protons as planned. As a substitute, 68-Mev alpha particles were used with a graphite target, and neutron en-

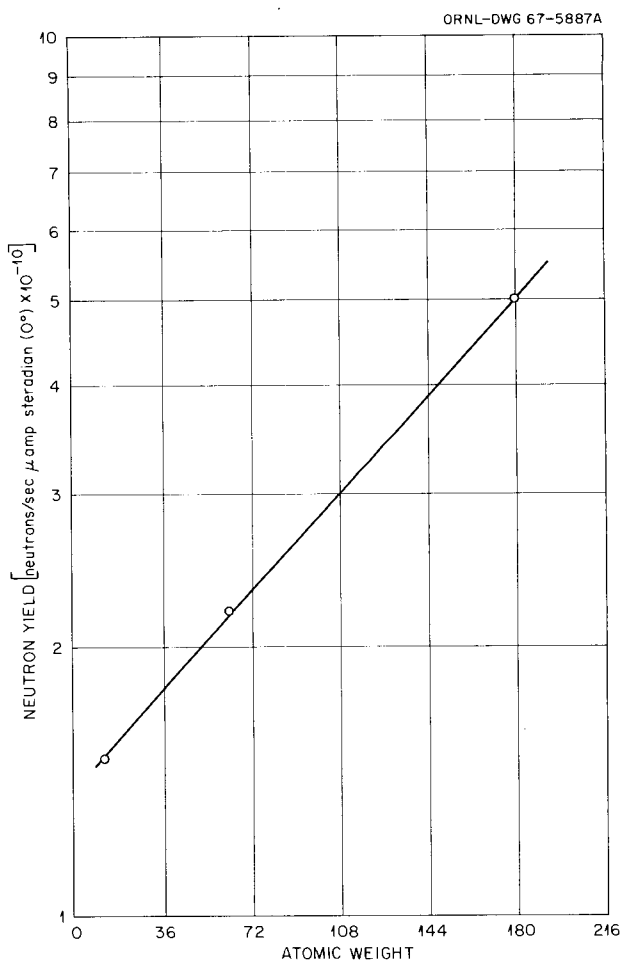

Fig. 23.10. Neutron Yield for 63-Mev Protons on C, Cu, and Ta Targets as a Function of Atomic Weight.

[28] R. B. Murray, *Nucl. Instr.* 2, 237–48 (1958).

ergy spectral measurements were made with the ^{6}LiI spectrometer. For comparison, threshold foil measurements for this case predicted a neutron yield of approximately 1.6×10^9 neutrons sec^{-1} μa^{-1} steradian^{-1} with an energy spectrum peaked at about 3 Mev with a $1/E$ tail upward to an undetermined cutoff energy (see Fig. 23.11). Although the ^{6}LiI spectrometer results corroborated the existence of a peak near 3 to 4 Mev, the upward slope seemed to fall less rapidly than 1/E, and a second broad peak occurred near 16 Mev. Low counting statistics and lack of cross-section data for ^{6}Li above 20 Mev prevented any further conclusions from the spectrometer work. However, the fair agreement between the two systems seems sufficient to permit the use of these threshold detector results for 63-Mev protons on carbon, copper, and tantalum in calculating shielding requirements for future experiments of this type.

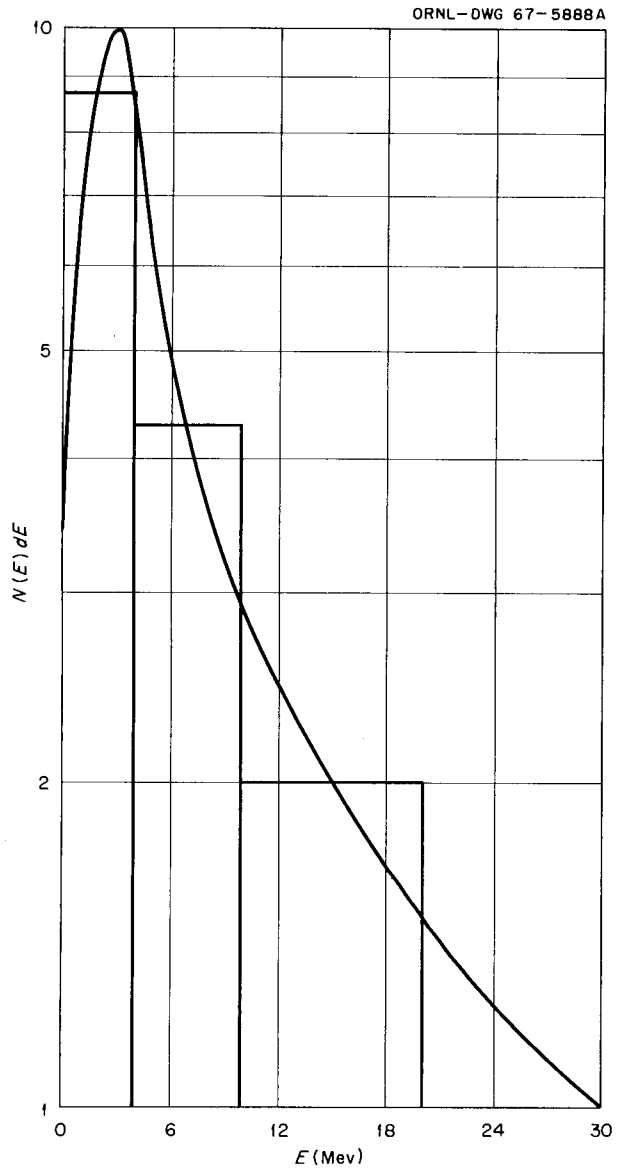

Fig. 23.11. Neutron Energy Spectrum for 68-Mev Alpha Particles Incident on Graphite. Smooth curve, assumed spectrum peaked at 3 Mev + $1/E$ tail upward; blocks, resulting experimental spectrum from threshold detectors (σ's weighted to smooth curves).

THE EFFECT OF SLANT INCIDENCE OF A BROAD PARALLEL BEAM OF NEUTRONS ON THE DISTRIBUTION OF DOSE IN A CYLINDRICAL TISSUE PHANTOM

The exploration of the behavior of the depth-dose curve when the direction of the neutron beam makes an acute angle to the face of the slab and to the top truncation of the cylinder was begun. Since only a few cases have been studied thus far, the results presented here are preliminary in the sense that only a few angles, neutron energies, and phantom shapes have been tried.

First, consider a volume element at depth x in the slab (see Fig. 23.12) and a neutron beam making an angle θ with the normal to the slab surface. We take an infinitesimal volume element as a parallelepiped with the two ends having dimensions of $dl \times dl$ cm and the four sides each having an area of dA cm^2. The orientation is such that two of the sides are parallel and the remaining two are normal to the flight paths of the incident particles. The volume of the parallelepiped is then $(\cos\theta)\, dA\, dl$ cm^3. If the beam has intensity of 1 neutron/cm^2, there are $dA \times \cos\theta \times e^{-\lambda x \sec\theta}$ neutrons entering the front face of the parallelepiped which have had no previous interaction in the slab, λ being the total macroscopic cross section. The expected number of interactions in the parallelepiped is $\lambda\, dl\, dA \times \cos\theta \times e^{-\lambda x \sec\theta}$. If the energy absorbed locally is E_{ab} (Mev/disintegration), then the dose due to energy absorbed locally as a result of first collisions of the neutrons (so-called "first-collision dose") is given by

$$D_1(x) = \lambda E_{ab} \times 1.6 \times 10^{-8} \times e^{-\lambda x \sec\theta} \text{ (rads)} . \qquad (1)$$

Thus the dose at the surface of the slab is independent of the beam direction, specified by θ, and

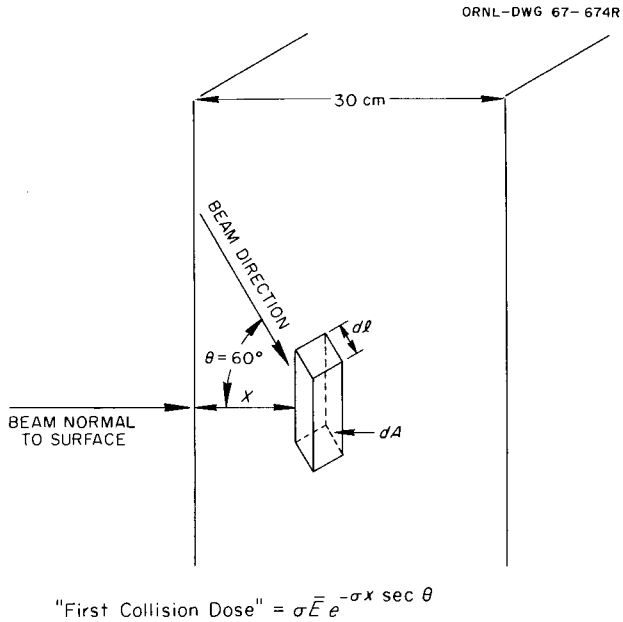

Fig. 23.12. An Infinitesimal Volume Element for the Calculation of the Distribution of Dose in a Semi-infinite Slab.

the slope of the line representing Eq. (1) on semi-log paper varies directly with sec θ. For neutrons of 0.5 to 5 Mev, this first-collision dose is a major portion of the total dose near the irradiated surface, and one might expect to see somewhat the same behavior of the depth-dose curve as that indicated above.

One cannot expect that the variation with θ indicated by Eq. (1) will be closely similar for the total dose curve or that this type of variation will be valid at large depths below the irradiated surface, since the dose due to "buildup" (i.e., subsequent interactions of the neutrons and of capture photons) probably will not show the same type of dependence on θ. It is difficult to state any precise rules concerning the variation of "buildup" dose as θ varies. One would expect that the larger the angle θ, the less would be the penetration of neutrons, on the average, and that escape might therefore be more probable. Thus the average depth at which interactions occur might be less for large values of θ than for small angles of incidence and thus would tend to increase the dose near the surface. These tendencies seem to be present in the data presented below.

The dose from a neutron beam in a tissue slab of 30 cm thickness is shown in Figs. 23.13 and 23.14. In both cases the beam makes an angle of 60° with the normal to the slab surface, and the results are shown for neutrons of energies 1 Mev and 10 kev respectively. The dose from photons and the dose from protons and particles of higher LET are shown separately. For comparison the corresponding dose curves for neutrons of 1 Mev and 5 kev from *NBS Handbook* **63** (ref. 29) are shown. The data suggest that there is additional buildup of dose near the irradiated surface and that the surface dose from particles of high LET (i.e., protons and recoil nuclei) may be higher for a beam of slant incidence than for a beam normal to the surface. The excess is by about a factor of 2 in both cases if one makes the comparison only for the dose of high-LET radiation. However, the dose due to photons is less for the beam of slant incidence than for the normal beam, and this more than offsets the increase for the neutron beam of energy 10 kev, although the comparison is not entirely firm. For neutrons of energy 1 Mev, the increase in total dose due to slant incidence of the beam is a factor of 1.8 and is even greater if the dose-equivalent values are examined. Of course, more cases involving other energies and angles of incidence must be explored before this result can be considered as established. It is curious that the doses due to the photons seem to differ less as depth increases. At present, we have no intuitive explanation for this tendency.

Some data on the corresponding dose curves for volume elements along a midsection of a cylindrical phantom are presented in Figs. 23.15 and 23.16. To some extent the same tendencies discussed above for the slab cases can be seen operating here, but the analogy is not complete. Undoubtedly the curvature of the surface of the phantom, its finite dimensions, and the fact that the beam enters from the top of the cylinder as well as through the lateral surface combine to introduce new complexities. It will be noticed that the dose in the top layer of the phantom is almost constant due to neutrons entering through the top of the cylinder. The higher value of dose where the top meets the irradiated lateral surface is evidently due to the fact that the particular volume element located here is irradiated by neutrons entering through the lateral surface as well as through the top. As expected, the dose from photons is significantly

[29] "Protection Against Neutron Radiation Up to 30 Million Electron Volts," *Natl. Bur. Std. (U.S.), Handbook* **63**, U.S. Govt. Printing Office, Washington, D.C., 1957.

lower in the finite phantom than in the slab, and the difference increases with depth.

What are the implications of these data for personnel dosimetry? The cases presented here are not sufficient to justify any sweeping statements concerning their importance or the measures necessary for taking slant incidence into account in interpreting estimates of dose. Enough evidence is in hand to indicate that, at least for some angles and neutron energies,

1. the surface dose may be significantly higher than for a normal beam;
2. the high-LET component of dose decreases at a faster rate than for the normal beam;

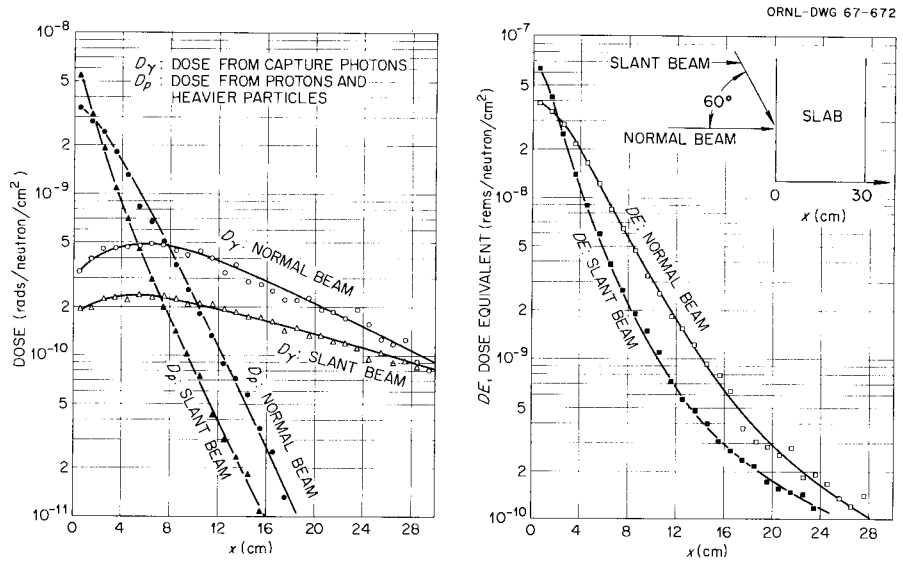

Fig. 23.13. Dose and Dose Equivalent in a Tissue Slab Irradiated by Normal and Slant Beams of Neutrons of Energy 1 Mev.

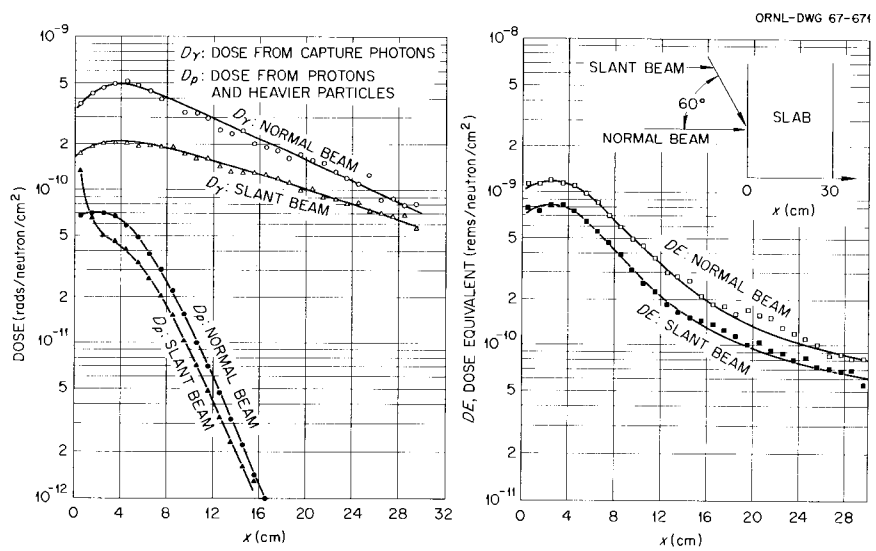

Fig. 23.14. Dose and Dose Equivalent in a Tissue Slab Irradiated by Normal (5 kev) and Slant (10 kev) Beams of Neutrons.

3. the dose from capture photons is substantially less at the surface than for the normal beam, but this difference decreases slowly with depth, and the two are nearly equal at the far side of a thick phantom.

Presumably a good personnel dosimeter would provide an accurate estimate of the increased surface dose, but it would appear that the pattern of depth dose must be inferred from calculated cases just as in the case of a normal beam. Unfortunately, the data now in hand and presented here are not sufficient to provide a basis for such interpretation but do, perhaps, serve to indicate something of the nature of the problem.

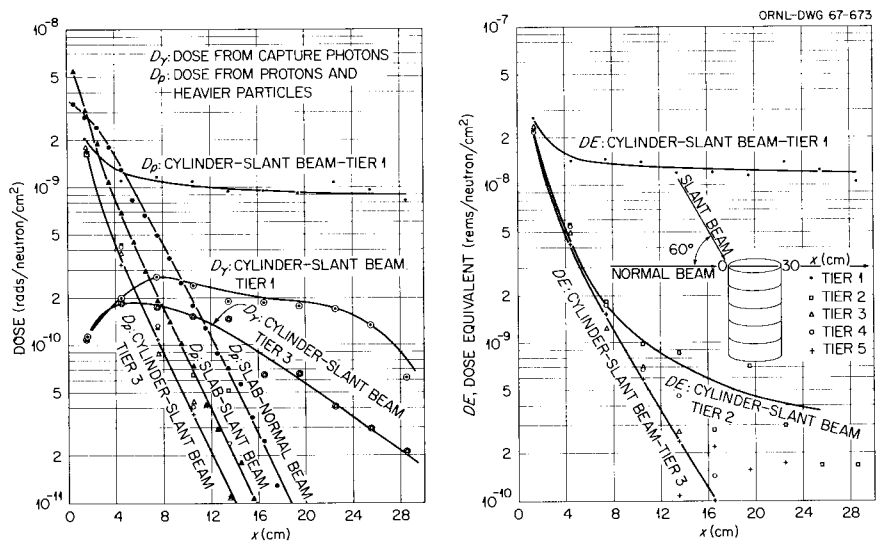

Fig. 23.15. Dose and Dose Equivalent in Tissue Slabs and Cylinders Irradiated by Normal and Slant Beams of Neutrons of Energy 1 Mev.

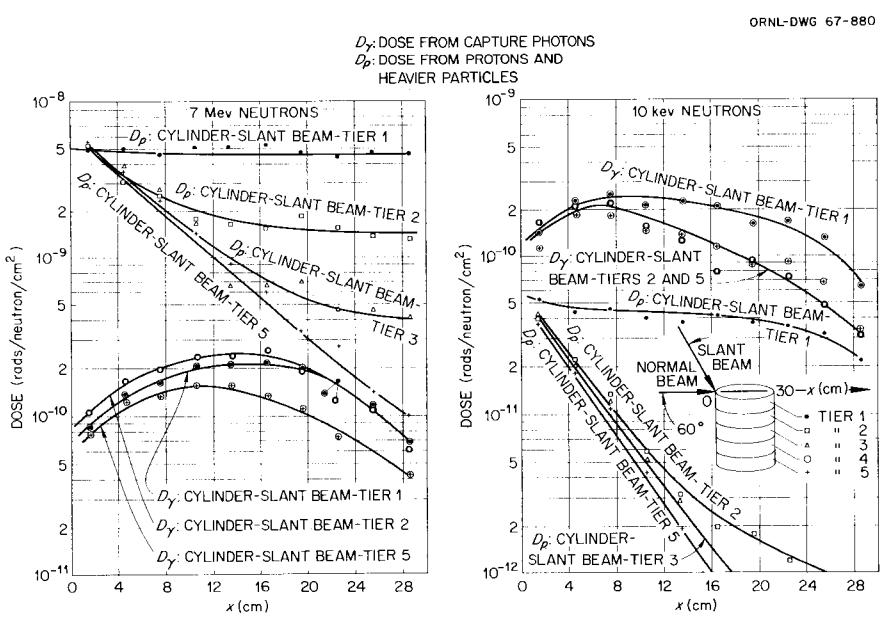

Fig. 23.16. Dose in a Tissue Cylinder Irradiated by Slant Beams of Neutrons of Energy 7 Mev and 10 kev.

THE CALCULATION OF KERMA AS A FUNCTION OF NEUTRON ENERGY

The ICRU[30] has defined kerma as the energy transferred to charged particles per unit mass of the irradiated medium. The units of kerma are ergs per gram, but the concept differs from dose in that the energy in question is not necessarily absorbed in the volume element considered. Thus, if N_p is the number of neutron interactions per gram of material producing charged particles with average energy $\overline{E}_p$, then

$$\text{kerma} = \sum_p N_p \overline{E}_p \,. \tag{1}$$

To compute the average energy deposited locally, $\overline{E}_p$, by a charged particle from an inelastic collision, its cross section, Q value, and the angular distributions of (or partition of energy between) the reaction products must be known. Because the angular distributions are not well known, the assumption is usually made that the charged particle is emitted either (1) with equally probable energies between zero and maximum or (2) isotropically in the center-of-mass system. The equation

$$E_p = E_2 = \frac{2M_1M_2E_1}{(M_2+M_3)^2} + \frac{M_3Q + E_1(M_3 - M_1)}{M_2+M_3}\,, \tag{2}$$

where

M_1 = mass of the incident particle,

M_2 = mass of the reaction product with energy E_2,

M_3 = mass of the reaction product with energy $E_3 = E_1 + Q - E_2$,

Q = Q value for the reaction,

E_1 = energy of the incident particle,

$\overline{E}_2$ = average energy of the reaction product with mass M_2,

is based on assumption 1 and fulfills the basic physical requirements (conservation of energy and momentum) with a minimum of additional assumptions. The average energy $\overline{E}_p$ for elastic collisions was obtained by computing the mean value of

$$\overline{E}_p = E_n \frac{4M_aM_n}{M_a+M_n}\cos^2\theta\,, \tag{3}$$

where θ is the angle of recoil in the laboratory system for a large sample of such collisions, and therefore this value takes account of anisotropic scattering. The summation in Eq. (1) includes all charged particles that may be produced.

If the actual volume element is not infinitesimal, all the complexity of a multicollision calculation of particle histories is involved in estimating kerma. If kerma is considered only conceptually in the limit for infinitesimal volume elements, then one can only calculate a distribution of values of energy transferred per gram or an expected value of the kerma, and these may not be closely related to the physical events occurring in the actual volume element. For example, consider a monoenergetic beam of neutrons of unit fluence incident on a sphere of radius a, where the total interaction cross section is λ. It is easy to show that the number of particles of type p produced by neutrons undergoing their first interaction in this sphere is given by

$$\frac{\pi\lambda_p}{2\lambda^3}\left[(1+2\lambda a)e^{-2\lambda a} - 1 + 2\lambda^2a^2\right]\,, \tag{4}$$

where λ_p is the cross section for the interaction producing charged particles of type p. However, the energy carried by these particles is only a part (albeit major) of the expected average value of kerma for the sphere in that it neglects particles produced by any subsequent interactions (multiple collisions) of the neutrons in the sphere. However, Eq. (4) will be a good approximation to kerma if $\lambda a << 1$. For infinitesimal volume elements dV, N_p equals $\lambda_p\, dV$, and then Eq. (4) becomes equivalent to Eq. (1); but this is only the expected value of kerma for the infinitesimal volume element.

The relationship of kerma and dose is generally not a simple one. If the same amount of energy as that transferred to charged particles produced within the volume element is to be absorbed there, the linear dimensions of the volume must

[30] "Radiation Quantities and Units," International Commission on Radiological Units and Measurements (ICRU) Report 10a, *Natl. Bur. Std. (U.S.), Handbook* **84**, U.S. Govt. Printing Office, Washington, D.C., 1962.

ORNL-DWG. 67-6511

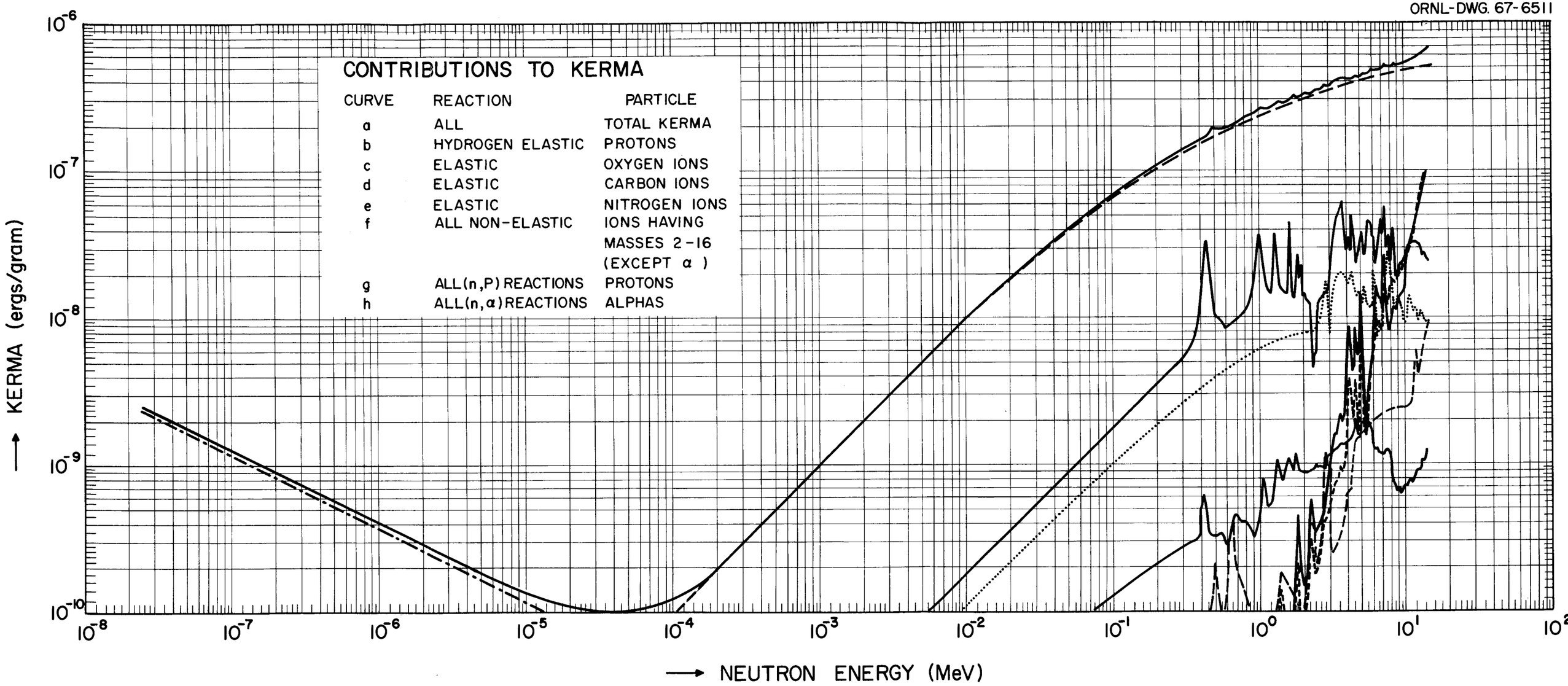

Fig. 23.17. Kerma for Neutrons Incident on Tissue as a Function of Neutron Energy.

be large compared with the range of the charged particles or else there must be a condition of equilibrium so that there is compensation of charged-particle kinetic energy crossing the boundary of the volume element inward and outward. In either case, it is not simple to calculate the energy spectrum of neutrons within the volume element because neutrons which have already made several collisions elsewhere in the phantom will arrive at the point of interest and make a significant contribution to the kerma and dose there. Moreover, the neutron-capture gamma rays from other parts of the phantom will also interact with matter in the volume element, thus adding to both the kerma and the dose. There is, however, a range of neutron energies for which the maximum dose within an anthropomorphic phantom irradiated unilaterally is substantially equal to the neutron kerma at the same point in the phantom. This energy range (0.1 to 14 Mev) is that for which neutron-capture gamma rays contribute little to the maximum kerma or dose and for which the depth-dose curve has a broad peak at the maximum. In Fig. 23.17, kerma in tissue is shown as a function of incident-neutron energy, as obtained from Eq. (1) with $N_p = \lambda_p$, and extending the summation to all reactions which produce charged particles. Figure 23.17 reveals that the total kerma (10^{-2} erg/g) in a small mass is roughly equal to the maximum dose (rads) for the phantom calculations over the range 0.1 Mev $\leqq E \leqq$ 14 Mev, the value of kerma being higher but by less than a factor of 2. This difference is attributed to the averaging of dose over the volume elements of 3 cm thickness used in the phantom calculation.

RESULTS OF THE CALCULATIONS OF THE DOSE IMPARTED TO SMALL SEEDS BY THE HPRR

A seed-irradiation study, in conjunction with the University of Tennessee–AEC Agricultural Research Laboratory, has been carried out at the

Table 23.12. Fast Neutron Dose to Seeds Exposed to Neutrons from the HPRR

Species	Percent of:					Fluence (neutrons/cm^2)	Dose (rads neutrons^{-1} cm^{-2})			D_h/D_T
	Ash	H	O	C	N		Tissue Dose	Total Dose to Seeds = D_T	Dose to H in Seeds = D_h	
Fescue	4.47	6.09	42.10	41.02	2.20	2.4 E12	6000	3616	3038	0.840
Barley	2.38	6.41	43.30	42.80	1.81	3.0 E12	7600	4745	3999	0.843
Clover	4.08	6.79	39.97	43.77	5.65	3.0 E12	7600	4994	4239	0.849
Rice	5.79	6.79	45.23	39.54	1.26	1.3 E12	3100	2150	1836	0.854
Onion	3.99	7.13	26.13	46.95	3.32	2.4 E12	6000	4096	3559	0.869
Cotton	3.65	7.26	36.29	48.07	3.05	9.0 E11	2100	1586	1359	0.857
Alfalfa	3.30	7.53	36.94	47.06	5.80	1.6 E12	3900	2913	2504	0.860
Carrot	6.98	7.63	28.71	51.71	3.89	3.0 E12	7600	5501	4761	0.865
Cucumber	4.24	7.73	27.28	52.49	4.96	2.4 E12	6000	4453	3857	0.866
Tomato	4.23	8.11	30.04	52.42	4.39	3.0 E12	7600	5821	5061	0.869
Flax	3.84	8.29	28.08	55.94	4.07	2.4 E12	6000	4762	4140	0.869
Rape	3.80	9.16	23.60	60.13	2.46	3.0 E12	7600	6490	5715	0.881
Lettuce	4.51	9.68	27.33	54.82	4.42	3.0 E12	7600	6805	6042	0.888

DOSAR facility. The primary objectives were the determination of the energy and spatial distributions of the radiation fields, normalization between irradiations, and the calculation of the absorbed dose delivered to the seeds.

Seeds were exposed to the fast-neutron spectrum of the HPRR during several different irradiations. Care was taken to assure that sample size was small and that the scattering from the floor was minimized. Fourteen species were irradiated during these experiments. Results[31] for each irradiation were reported in units of neutron tissue dose in air.

In addition, a computer calculation of "seed dose" was performed utilizing the measured spectrum, the chemical composition of the seeds as supplied by the University of Tennessee, the integrated fluence incident on each sample, the elastic cross sections for neutrons from BNL-325,[32] and the first-collision dose equation from *NBS Handbook* **75**.[33] Comparison of the calculated first-collision seed dose and the measured dose expressed as "tissue dose in air" indicated agreement within ~10% for the large majority of the species irradiated. These data are shown in Table 23.12.

[31] *Semiannual Progr. Rept. July 1–December 31, 1965*, Agricultural Research Laboratory, AEC, University of Tennessee, Oak Ridge, Tenn., ORO-648.

[32] *Neutron Cross Sections*, BNL-325, 2d ed., 1964.

[33] "Measurement of Absorbed Dose of Neutrons and of Mixtures of Neutrons and Gamma Rays," *Natl. Bur. Std. (U.S.), Handbook* **75**, U.S. Govt. Printing Office, Washington, D.C., 1961.

RESULTS OF THE COMPUTATIONS OF DOSE AS A FUNCTION OF PENETRATION DEPTH IN MOUSE-, RAT-, AND GUINEA-PIG-SIZED CYLINDRICAL TISSUE PHANTOMS

The Monte Carlo code developed primarily for the prediction of dose and dose-equivalent patterns in anthropomorphic phantoms[34] was used to compute dose and dose-equivalent values in mouse-, rat-, and guinea-pig-sized phantoms exposed to the neutron spectrum from the HPRR. The phantoms were assumed to be truncated right circular cylinders[35] with the length and radius adjusted as follows:

	Mouse	Rat	Guinea Pig
Radius, cm	1.25	2.5	3.5
Length, cm	7.5	15	21

Plane, parallel beams of 60,000 neutrons were given the energy distribution shown in ref. 35, and the neutrons were traced (the processes by which neutrons were lost were escape from the phantom and Russian roulette based on the statistical weight of the neutron) in a Monte Carlo fashion[34] until they had produced 1.34, 3.90, and 8.23 collisions/neutron in the mouse, rat, and guinea-pig phantoms respectively. Partial results are shown in Fig. 23.18, with the error limits representing one standard deviation.

[34] J. A. Auxier *et al.*, *Health Phys. Div. Ann. Progr. Rept. July 31, 1966*, ORNL-4007, p. 195.

[35] J. A. Auxier *et al.*, *Health Phys. Div. Ann. Progr. Rept. July 31, 1965*, ORNL-3849, p. 167.

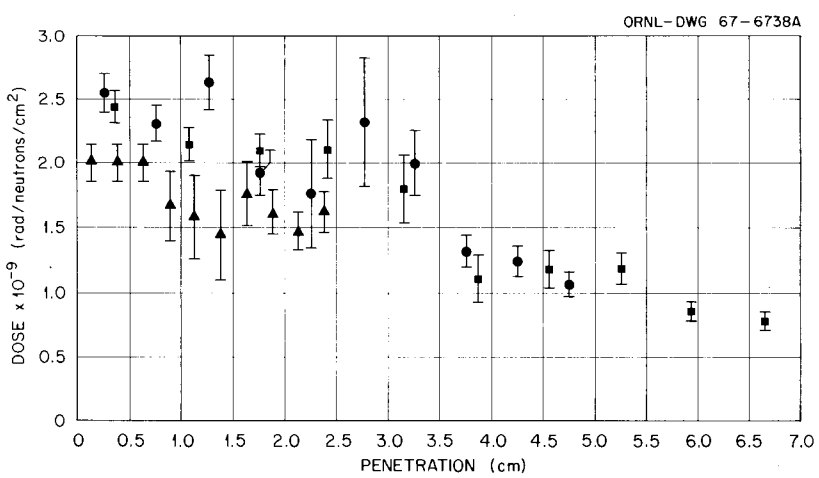

Fig. 23.18. Dose as a Function of Penetration Depth in Mouse-, Rat-, and Guinea-Pig-Sized Cylindrical Tissue Phantoms. △ Mouse, ○ rat, □ guinea pig.

24. HPRR and DLEA Operations

L. W. Gilley[1] F. F. Haywood

J. E. Jackson J. W. Poston W. H. Shinpaugh
D. R. Johnson W. D. Ray[2] D. R. Ward[1]
G. D. Kerr E. M. Robinson

HEALTH PHYSICS RESEARCH REACTOR

The Health Physics Research Reactor (HPRR) continued to operate on a routine basis during the past year. The 120 operating days resulted in a total operation time of 282 hr with an integrated power of 109 kwhr. Since achieving criticality in the fall of 1962, the HPRR has logged a total of 1055 operating hours with an integrated power of 335 kwhr. As in the past years, the reactor has been used primarily by the DOSAR staff. Other users have included ORNL divisions, AEC plants and laboratories, universities, private industry, and foreign guests.

Experiments performed included irradiation of animal and plant systems, instrumentation response and development studies, comparison of nuclear-accident dosimetry systems, and shielding investigations.

The operations staff at the HPRR has been engaged in the training of reactor supervisors and operators for the Army's Aberdeen Pulse Reactor Facility (APRF). Candidates were given instruction in reactor operation, reactor safety, and dosimetry associated with the HPRR. Members of the staff have assisted with many phases of the Aberdeen program and have served on the Initial Operator Qualification Board for the APRF.

During the next reporting period, some effort will be channeled into a further improvement in the burst-rod insertion mechanism. The use of a pulsed neutron source in conjunction with the HPRR, operating in the burst mode, will be investigated.

RADIATION DOSIMETRY STUDIES AT THE HPRR

Dosimetric aspects of the HPRR have been carefully determined and are summarized in a recent document.[3] Studies of parameters such as quantity and symmetry of neutron leakage from the reactor core were included in work that was done primarily to obtain neutron and gamma-ray air-dose curves as a function of distance. These curves are used both for selecting reactor power levels and operating times required to obtain predesignated radiation exposures and, together with a dependable and reproducible normalization channel, for providing quantitative dose information with an estimated accuracy of ±10%.

The fast-neutron leakage from the HPRR is 1.3 neutrons per fission. The "first-collision" absorbed dose rate from neutrons at a distance of 2 m from the reactor is 3.3 ± 0.13 millirads per unit count rate of the normalization sulfur pellet; both source and detector were 2 m above the floor. For this geometry ($H/D = 1$), the scattered-to-total neutron dose ratio is 0.21 and the neutron-to-gamma-ray dose ratio is approximately 7.

RADIATION SURVEY OF THE HPRR

Detectors used in the radiation survey were a Phil miniature G-M counter for gamma-ray dose-rate

[1]On loan from Neutron Physics Division.

[2]On loan from Instrumentation and Controls Division.

[3]D. R. Johnson and J. W. Poston, *Radiation Dosimetry Studies at the Health Physics Research Reactor*, ORNL-4113 (June 1967).

measurements,[4] a Hurst proportional counter and "radsan" dose integrator for fast-neutron dose-rate measurements,[5,6] and a BF_3 proportional counter for thermal-neutron flux measurements. Other detectors used in the study for purposes of intercomparison were a Rossi tissue-equivalent ionization chamber for gamma-ray-plus-neutron dose rates[7] and a Bonner spherical moderating detector for maximum dose-equivalent rates from neutrons.[8]

For purposes of comparison, maximum dose-equivalent rates were obtained from measurements made with the Hurst dosimeter by use of an appropriate quality factor (9.4 for HPRR direct field and 10 for other fields) and of a ratio of maximum to "first-collision" dose equivalent from broad parallel fast-neutron beams (1.3 for HPRR direct field and 1.5 for other fields).[7] Thermal-neutron flux measurements were converted to dose and maximum dose-equivalent rates by use of the conversion factors of 2.5×10^{-11} rad neutron^{-1} cm^{-2} and 1.1×10^{-9} rem neutron^{-1} cm^{-2} respectively.[9]

Data obtained from these comparisons are given in Table 24.1. Results in the direct field of the HPRR gave an added measure of confidence to the calibration of the detectors. Comparisons at the control building of the primary radiation survey instruments with the Rossi dosimeter and Bonner detector, which have a response over the entire neutron energy spectrum, indicated that dose contributions from intermediate-energy neutrons ($0.05 \text{ ev} \leqq E_n \leqq 100 \text{ kev}$) were not significant.

In order to relate "in-air" measurements to the maximum dose equivalent likely to be delivered to a person in the radiation field at the control building, radiation measurements were made about the midsection of a 30-cm-diam by 60-cm water phantom. These data gave a dose-equivalent distribution about the phantom that varied by a factor of 1.5 from lowest to highest. Similar data were obtained using ORNL personnel meters on the phantom during a later series of burst operations. Hence, the scattered radiation field was highly nondirectional and the "first-collision" dose equivalent was selected as the best parameter for relating "in-air" measurements to maximum dose-equivalent rates. Radiation fields inside

Table 24.1. Comparison of Radiation Detectors Used in HPRR Radiation Survey

Radiation Field	Comparison of Measurements	
	$R/(H + P + BF_3)^a$	$B/(H + BF_3)^b$
Direct HPRR field	1.11	1.12
"Skyshine" field outside control building	1.08	0.96
Fields at six locations in heavily shielded areas of control building	1.05 av 1.03–1.10 range	0.85 av 0.66–1.05 range

[a]The R refers to the Rossi tissue-equivalent ionization chamber, the H to the Hurst proportional counter, the P to the Phil miniature G-M counter, and the BF_3 to the BF_3 proportional counter.

[b]The B refers to the Bonner sphere.

Table 24.2. Dose-Equivalent Rates at DOSAR Control Building During HPRR Operations

Survey Location	Dose-Equivalent Rates (millirems/kwhr)			
	Fast Neutron	Gamma Ray	Thermal Neutron	Total
A	48.3	2.76	0.57	51.6
B	11.3	2.67	0.52	14.5
C	0.80	0.99	0.11	1.90
D	4.3	1.13	0.11	5.54
E	1.1	1.07	0.12	2.29
F	0.65	0.71	0.085	1.45
G	0.76	0.66	0.078	1.50
H	0.47	0.53	0.061	1.06
I	0.24	0.26	0.021	0.52
J	0.73	0.71	0.061	1.50
K	<0.10	<0.02	<0.001	<0.12

[4]E. B. Wagner and G. S. Hurst, *Health Phys.* **5**, 20 (1961).

[5]G. S. Hurst, *Brit. J. Radiol.* **27**, 353 (1954).

[6]E. B. Wagner and G. S. Hurst, *Rev. Sci. Instr.* **29**, 153 (1958).

[7]H. H. Rossi and G. Failla, *Nucleonics* **14**(2), 32 (1956).

[8]R. L. Bramblett, R. I. Ewing, and J. W. Bonner, *Nucl. Instr. Methods* **9**, 1 (1960).

[9]"Protection Against Neutron Radiation up to 30 Mev," *Natl. Bur. Std. (U.S.), Handbook* **63**, U.S. Govt. Printing Office, Washington, D.C., 1957.

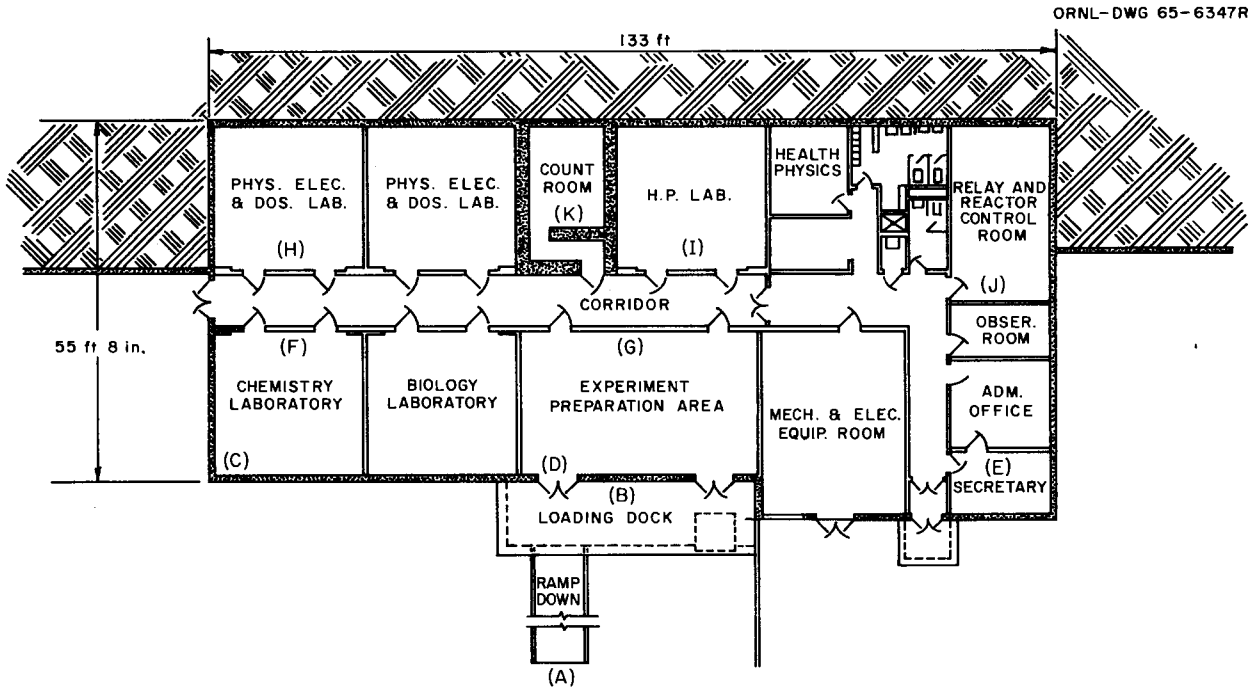

Fig. 24.1. Survey Locations at Control Building of HPRR.

the control building were found to be highly nondirectional also. This method of estimating dose-equivalent rates is in accord with recommendations of the National Committee on Radiation Protection.[10]

Maximum dose-equivalent rates obtained in the above manner are given in Table 24.2 for survey locations shown in Fig. 24.1. Quality factors of 1 and 10 were used to convert dose-rate measurements made with the Phil and Hurst dosimeters, respectively, to dose-equivalent rates. Thermal-neutron flux measurements made with the BF_3 counter were converted to dose-equivalent rates by the conversion factor 2.5×10^{-10} rem neutron^{-1} cm^{-2}.[9]

Results of this survey have provided better data on dose-equivalent rates to personnel in the control building during reactor operations and have been used to modify operational procedures at the facility.

[10] "Permissible Dose from External Sources of Ionizing Radiation," *Natl. Bur. Std. (U.S.), Handbook* **59**, U.S. Govt. Printing Office, Washington, D.C., 1959.

DOSAR LOW-ENERGY ACCELERATOR MODIFICATIONS AND APPLICATIONS

The DOSAR Low-Energy Accelerator (DLEA) was operated 383 times for a total of 115 hr during the past year. The accelerating-voltage levels ranged from 50 to 200 kv, and the beam currents reached 1.85 ma. Protons, deuterons, and helium ions have been accelerated. Experiments performed consisted primarily of instrument calibration with monoenergetic neutrons of 3 and 14 Mev. Although AEC contractors, military and national laboratories, and representatives of two foreign nations have used DLEA, it is primarily used by the DOSAR staff.

Examination of operational data and physical inspection of internal parts indicated that modifications could improve stability and increase beam current. Beam current would gradually diminish during exposures, although it could be readjusted until a maximum was obtained. During such an operation, the beam current fluctuated slightly. Careful inspection of all internal parts revealed electron burns on the ion-source base and gap lens. The ion-source-base exit canal (0.078 in. in diameter) was counter drilled from the back

to 0.115 in. in diameter and to within 0.0625 in. of the face. The gap lens opening was enlarged to an 0.1875-in. diameter, holding the same curvature and finish (Figs. 24.2 and 24.3).

These modifications gave an increase in beam current from 1 to 1.85 ma, and the current remained stable at all beam currents attainable. A single exposure of 4 hr at full power has recently been completed without interruption or fluctuation. Inspection after ~30 hr of operation revealed no electron burns or other operation problems.

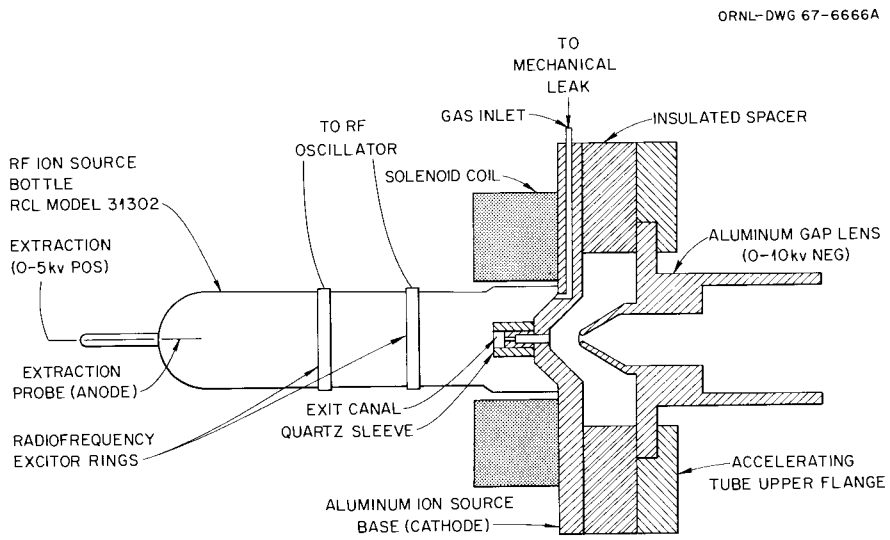

Fig. 24.2. Assembly Drawing for the rf Ion Source for the DLEA.

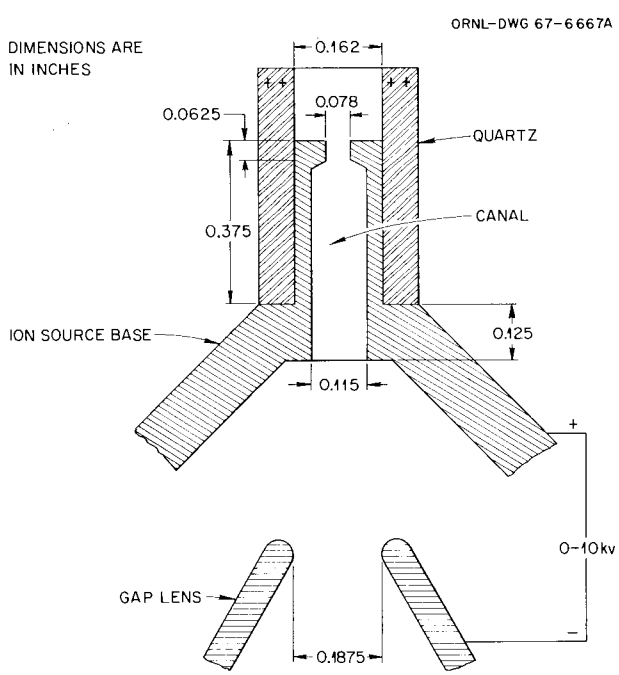

Fig. 24.3. Cutaway Drawing Showing Parts of the rf Ion Source Base and Gap Lens After Modification.

Part V. Internal Dosimetry

W. S. Snyder

25. Internal Dose Estimation

W. S. Snyder
S. R. Bernard
Mary Jane Cook
L. T. Dillman[1]
H. L. Fisher, Jr.[2]
Mary R. Ford
C. F. Holoway
Isabel H. Tipton[3]

CALCULATING THE EFFECTIVE ENERGY PER RADIOACTIVE DECAY FOR USE IN INTERNAL DOSE CALCULATIONS

L. T. Dillman[1]

In making internal dose calculations, it is necessary to determine the effective energy deposited in the organ of reference per radioactive decay. This requires detailed knowledge concerning the decay scheme of the radionuclide involved. Even when decay schemes are well established, considerable tedious work may be involved in computing the effective energy per disintegration. This is particularly true when significant gamma-ray internal conversion or electron-capture processes occur. These processes give rise to x rays and Auger electrons of varying intensities, and the calculation of these intensities is tedious.

This paper describes three computer programs which have been devised as aids to the calculation of the energy of the particles released for each of the following three processes: (1) electron or positron emission, (2) electron capture, and (3) internal conversion of gamma rays. The ultimate goal is a computer code which uses nuclear decay data as input information and calculates the effective energy per decay for the particular organ or organs of interest. The present programs are initial steps toward this goal.

[1]Research participant and consultant to ORNL from Ohio Wesleyan University.

[2]U.S. Public Health Service.

[3]Physics Department, University of Tennessee.

Electron or Positron Emission

For β^+ or β^- decay, one needs the ratio of the average energy of the particle to the end-point energy for each transition under consideration. James *et al.*[4] have computed this ratio for allowed, first-forbidden unique, and second-forbidden unique β^- transitions and have presented their results in graphical form. Their graphs give this ratio as a function of energy for six values of atomic number. Loevinger[5] gives graphs of this ratio as a function of energy for allowed β^+ transitions. A computer code has been written which extends these previous compilations in several ways.

First of all the computer code may be used for any atomic number and for any end-point energy and thus obviates the necessity of graphical interpolation. Second, the code includes first-forbidden unique and second-forbidden unique β^+ transitions. Third, the code calculates the fraction of the emissions in which the initial energy of the β^+ or β^- particle is below a fixed value of energy, for example, 0.03 Mev. This is done because beta radiation of low energy is generally weighted with a quality factor, QF, in estimating dose equivalent; QF is the symbol used for the linear-energy-transfer-dependent factor by which absorbed doses are to be multiplied to obtain, for purposes of radiation protection, a quantity that expresses the dose equivalent delivered to tissue on a common scale for all ionizing radiations. In

[4]M. F. James, B. G. Steel, and J. S. Storey, *Average Electron Energy in Beta Decay*, AERE-M 640 (1960).

[5]R. Loevinger, *Phys. Med. Biol.* 1, 330 (1957).

addition, the absorbed dose may be further multiplied by modifying factors, MF, to take account of other factors that are necessary for calculation of the dose equivalent. For example, ICRP and NCRP assign a QF of 1.7 for beta particles of end-point energy below 0.03 Mev, whereas those above 0.03 Mev are assigned a QF of 1.0. It would seem logical that all electrons or beta-like particles emitted with an initial energy above 0.03 Mev should be assigned a QF of 1.7 for the energy absorbed after they have been degraded to energies below 0.03 Mev; provision is made for evaluating such a part of the energy so this weighting can be used if desired. The discontinuous change in QF at 0.03 Mev is based on quite limited experimental evidence. It may be desirable in the future to use a QF which is a continuous function of energy or which is discontinuous at an energy value different from 0.03 Mev. The code is so written as to make incorporation of either of these a relatively simple matter.

Unlike the work of James *et al.*,[4] the present procedure incorporates a screening correction due to the atomic electrons, and the complicated mathematical functions needed for first- and second-forbidden unique transitions and for the Fermi function are computed from the fundamental equations rather than by using the tables of Rose *et al.*[6] These functions are somewhat dependent on mass number for a given atomic number, and the tables of Rose *et al.*[6] use an average value for the mass number associated with a given atomic number. Use of the fundamental equations leads to greater precision. The ratio of average β^- energy to the end-point energy is quite insensitive to the screening correction, but the ratio of average β^+ energy to the end-point energy is appreciably affected by the screening correction at low values of the end-point energy. Loevinger *et al.*[5] made a screening correction for positrons which was based on the work of Reitz.[7] Reitz's screening correction has been seriously questioned in more recent work by Durand[8] and Brown.[9] A screening correction of the form widely used before the work of Reitz[7] and which is in agreement with the work of Durand[8] has been used in the present work.

Figures 25.1 through 25.6 give the ratios of average β^- energy to end-point energy and of average β^+ energy to end-point energy as determined by this code for allowed, first-forbidden unique, and second-forbidden unique transitions. These ratios are plotted vs energy for ten values of the atomic number of the daughter nuclide. The equations used by the code are given in Appendix A.

Electron Capture

When electron capture occurs, x rays and Auger electrons are generated. Smith *et al.*[10] have developed equations for the calculation of the total "beta-type" energy deposition for cases that are extensions of earlier work by Loevinger *et al.*[11] For electron capture, "beta-type" radiation includes Auger electrons and all x rays of energy less than 0.0113 Mev. This division at 0.0113 Mev is based on the fact that at this energy 95% of the electromagnetic radiation is absorbed in 10 mm of water. This distance is comparable with the ranges of many β^- particles in water. In the general case, "beta-type" radiation also includes internal conversion electrons and gamma rays of energy less than 0.0113 Mev.

We have developed a quite general computer program which analyzes the amounts of radiation of various types that are produced when electron capture occurs. The output of the program lists all x rays of energy sufficiently great that they are not "beta type" and gives the numbers of these x rays per disintegration and their respective energies. The output of the program also lists the number per disintegration and associated average energy of all "beta-type" radiation except Auger electrons of energy less than 0.030 Mev. The number per decay and associated average energy of all Auger electrons with energy less than 0.030 Mev is printed separately since these electrons are assigned a QF of 1.7 rather than 1.0, as for other "beta-type" radiation.

---

[6] M. E. Rose, C. L. Perry, and N. M. Dismuke, *Tables for the Analysis of Allowed and Forbidden Beta Transitions*, ORNL-1459 (1953).

[7] J. R. Reitz, *Phys. Rev.* **77**, 10 (1950).

[8] L. Durand III, *Phys. Rev.* **135B**, 310 (1964).

[9] L. S. Brown, *Phys. Rev.* **135B**, 314 (1964).

[10] E. M. Smith, C. C. Harris, and R. H. Rohrer, *J. Nucl. Med.* **1**, 23–31 (1965).

[11] R. Loevinger, J. G. Holt, and G. J. Hine, "Internally Administered Radioisotopes," p. 801 in *Radiation Dosimetry* (ed. by G. J. Hine and G. L. Brownell), Academic, New York, 1958.

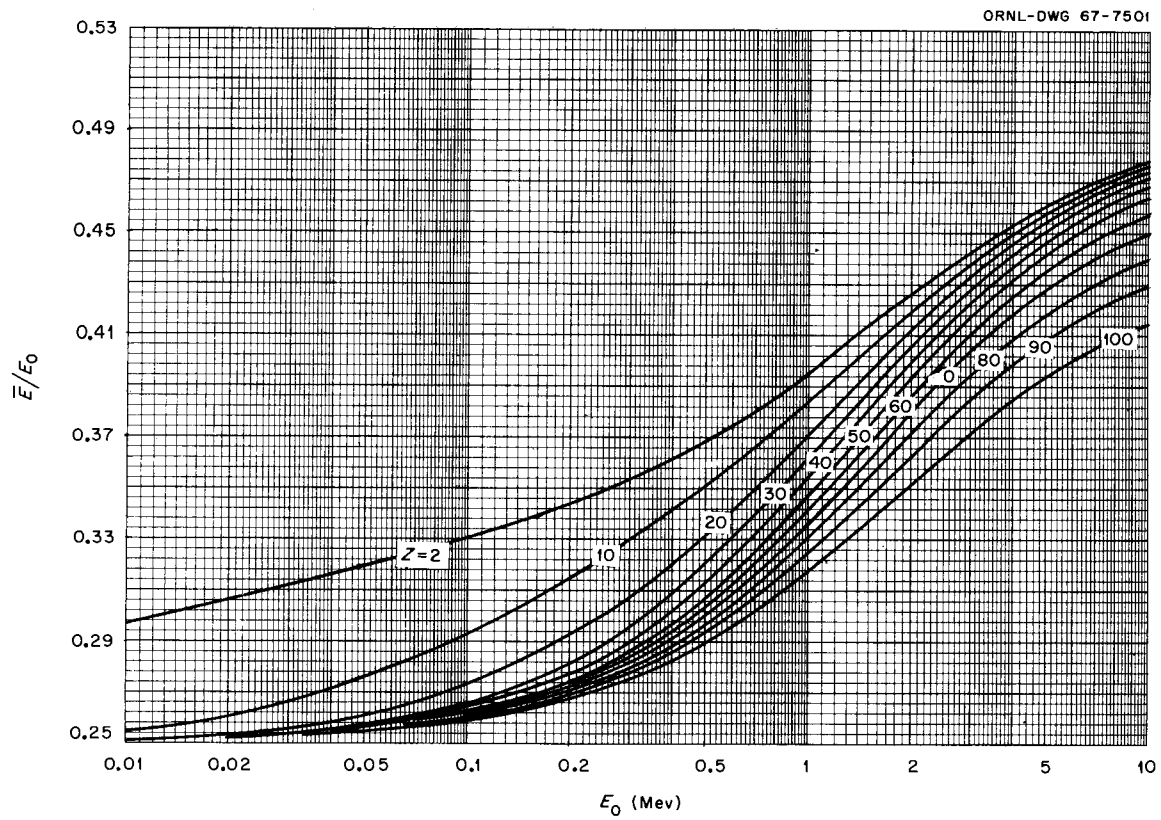

Fig. 25.1. Allowed β^- Transitions.

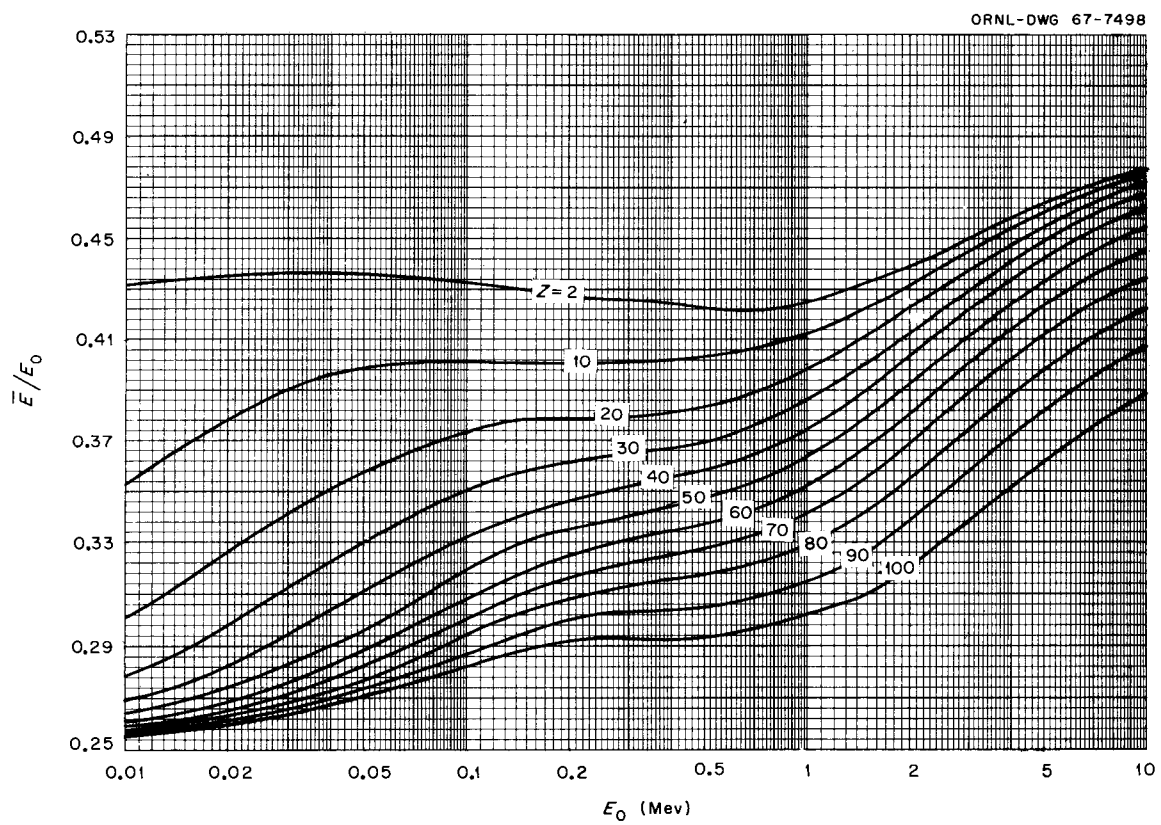

Fig. 25.2. First-Forbidden Unique β^- Transitions.

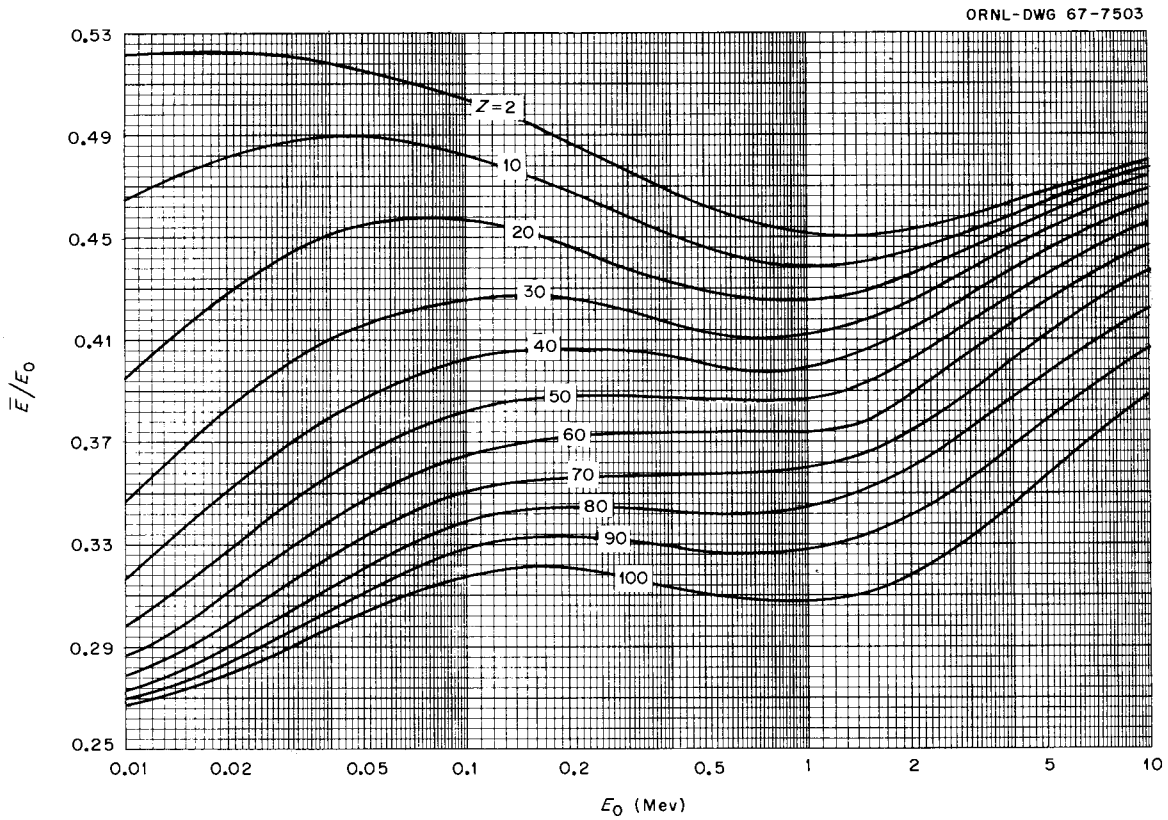

Fig. 25.3. Second-Forbidden Unique β^- Transitions.

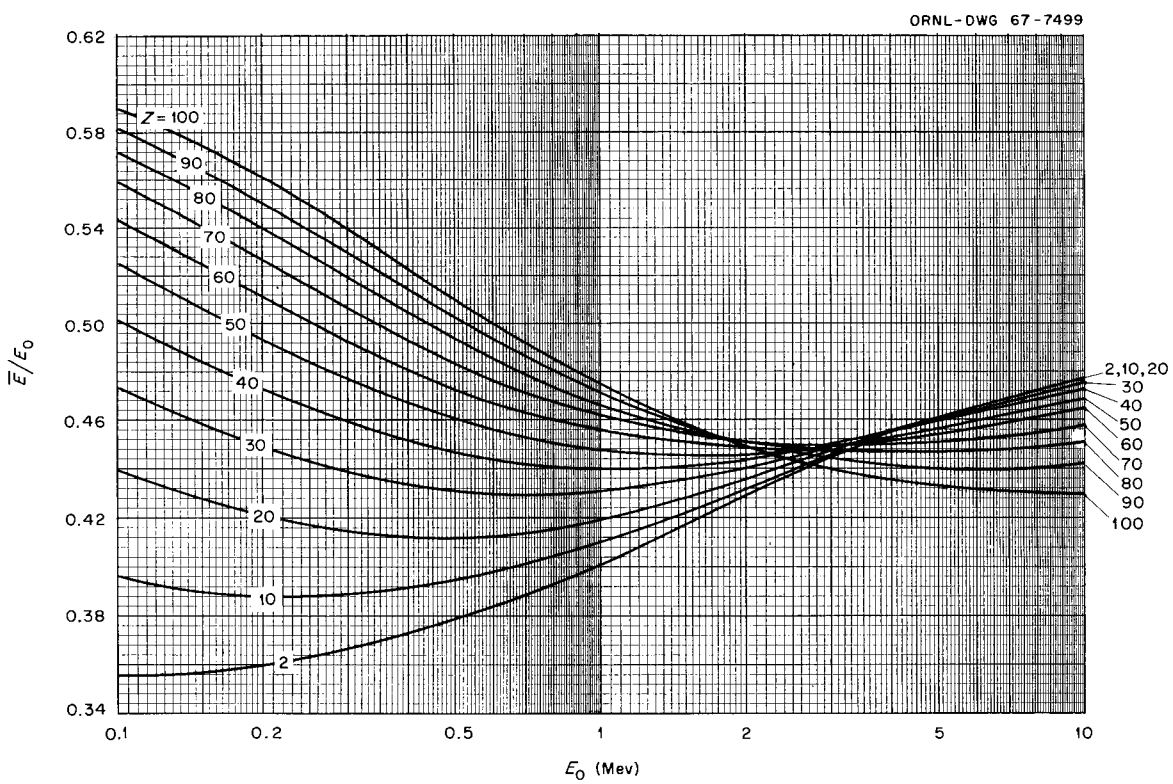

Fig. 25.4. Allowed β^+ Transitions.

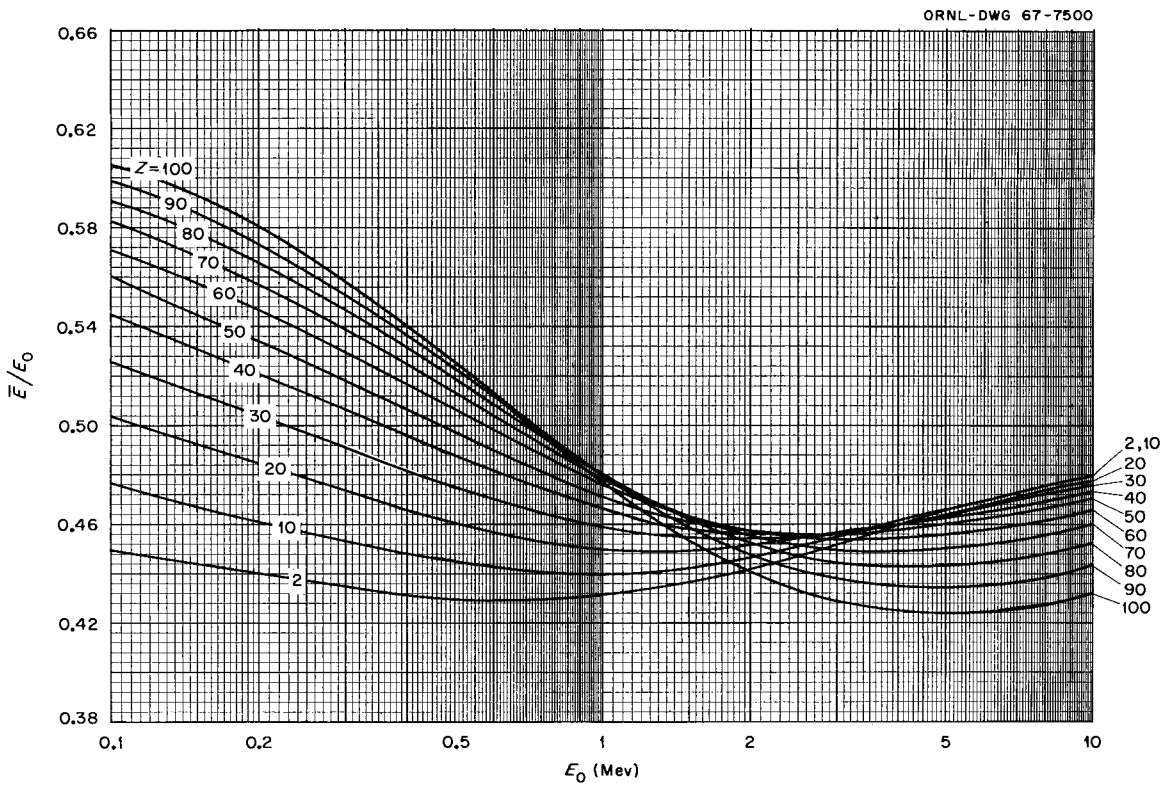

Fig. 25.5. First-Forbidden Unique β^+ Transitions.

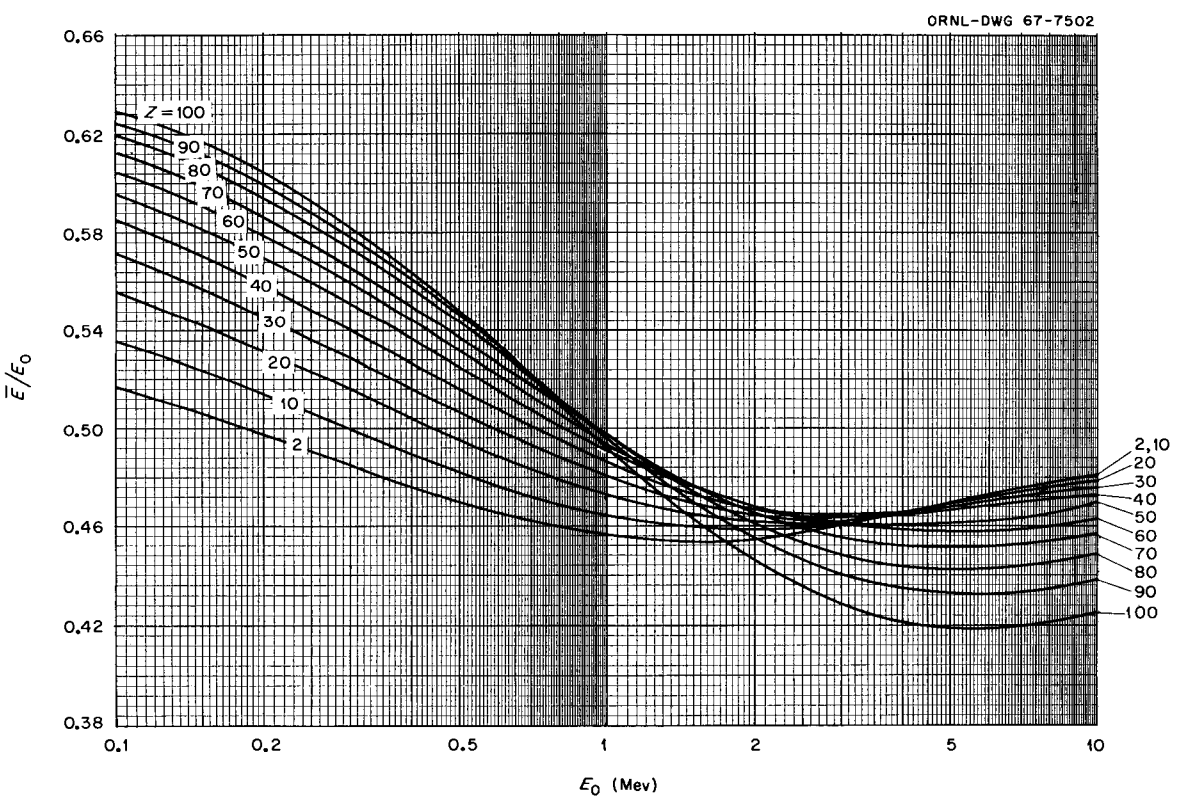

Fig. 25.6. Second-Forbidden Unique β^+ Transitions.

This program extends the work of Smith *et al.*[10] in several ways besides computerization. First of all, their work is limited to atomic numbers less than 82, where the L and M x rays have energies less than 0.0113 Mev, and hence may be considered to be "beta type" and locally absorbed. This limitation is removed in the present work. Second, and most importantly, they state that the fractions f_K, f_L, and f_M, which are the respective fractions of disintegrations that occur by K, L, and M capture, may be determined from $K/L/M$ capture ratios and electron capture branching ratios given in *Nuclear Data Sheets*. However, $K/L/M$ capture ratios are often not given in the *Nuclear Data Sheets*, particularly for the weaker branches. The $K/L/M$ capture ratios as determined from theory are in good agreement with experimental results, but the electron capture branching ratios can be estimated only to orders of magnitude from theory. Hence, the present program uses theoretically computed values of $K/L/M$ capture ratios in conjunction with capture branching ratios given in the *Nuclear Data Sheets*.

The detailed equations involved in the computer program are discussed in Appendix B. The following data for ^{125}I is a typical computer output for electron capture. This example does *not* include the x rays and electrons which are present as a result of the internal conversion of the 0.0353-Mev gamma ray in ^{125}Te which follows the electron-capture process. X rays and electrons arising from internal conversion are included in the example at the end of the following section.

125 I 53 ECA

		FRACTION PER DECAY	ENERGY (MEV)
K-ALPHA1	X-RAYS	.36905	.02747
K-ALPHA2	X-RAYS	.18933	.02720
K-BETA1	X-RAYS	.09964	.03099
K-BETA2	X-RAYS	.02067	.03182
ALL X-RAYS LESS THAN .0113 MEV + ALL AUGER ELECTRONS GREATER THAN .030 MEV		.12913	.00483
ALL AUGER ELECTRONS LESS THAN .030 MEV		2.79170	.00233

The computer output illustrated above is mostly self-explanatory. 125 I 53 means that we are dealing with ^{125}I which has an atomic number of 53; ECA is a mnemonic notation indicating that electron capture is the process under investigation.

Internal Conversion

When internal conversion occurs, one is again faced with the problem of computing the fraction per decay of primary vacancies made in the K, L, and M shells, that is, f_K, f_L, and f_M respectively. Once these fractions are established, the calculations are exactly the same as outlined in the latter part of Appendix B. These fractions may be determined from experimental information concerning the fraction of unconverted gamma transitions per decay, f_r, and experimental information concerning internal conversion coefficients α_K, α_L, α_M, or α_K and $K/L/M$ conversion coefficient ratios. Unfortunately, experimental information concerning internal conversion coefficient parameters is found in many different forms or may be unmeasured. The present computer program does two things in regard to this problem.

First of all, if experimental information is available, the computer will accept a wide variety of forms of the data. The following forms of input data, all of which are sufficient to determine f_K, f_L, and f_M, are accepted by the computer:

1. α_K, α_L ;
2. α_K, K/L ;
3. α_K, K/L, K/M ;
4. α_K, $K/(L+M)$;
5. α_K, K/L, $K/(L+M)$.

For forms 1, 2, and 4, the empirical fact that conversion in the M shell is nearly always about one-third of the conversion in the L shell is used. For example, for form 1 of the input data, we have

$$f_K = f_r \alpha_K ,$$

$$f_L = f_r \alpha_L ,$$

and

$$f_M = \tfrac{1}{3} f_L \ .$$

Forms 3 and 5 of the input data are sufficient to determine f_K, f_L, and f_M uniquely. For example, we have for form 3 of the input data

$$f_K = f_r \alpha_K \ ,$$

$$f_L = f_K/(K/L) \ ,$$

and

$$f_M = f_K/(K/M) \ .$$

Second, the computer program accepts the theoretically computed values of the internal conversion coefficients. We have an entirely separate computer program which computes theoretical internal conversion coefficients by interpolation (cubic equation least-squares fit to the four nearest tabulated values) of the tables compiled by Sliv and Band.[12] This program is a modification of a similar one obtained from the Nuclear Data Group at ORNL. The difficulty with using theoretically computed internal conversion coefficients is that many transitions are admixtures of two different multipolarities, and at the present time it is usually impossible to determine from theory the relative amounts of components of the admixture. A common admixture is magnetic dipole and electric quadrupole radiation. We shall illustrate how the computer program deals with this problem by considering such an admixture.

A quantity called the mixing ratio, δ^2, which is the ratio of intensity of $E2$ (electric quadrupole) radiation to $M1$ (magnetic dipole) radiation, is often experimentally measured and available in the literature. From this the internal conversion coefficients α_K and α_L may be determined by

$$\alpha_K = \frac{\alpha_K(M1) + \delta^2\, \alpha_K(E2)}{1 + \delta^2} \ ,$$

and

$$\alpha_L = \frac{\alpha_L(M1) + \delta^2\, \alpha_L(E2)}{1 + \delta^2} \ .$$

The computer uses the value of δ^2 and theoretically evaluated internal conversion coefficients in the K and L shells to determine α_K, α_L, and α_M. If α_K or K/L or other experimental quantities concerning internal conversion are available in addition to δ^2, the computer uses theoretically evaluated internal conversion coefficients only to supplement the experimental information and make possible a unique determination of α_K, α_L, and α_M.

If no quantities concerning internal conversion parameters have been measured, the computer assumes no mixing of multipolarities (e.g., it would assume 100% $M1$ where $M1$ and $E2$ are a possible mixture) and uses theoretically determined values of α_K, α_L, and α_M. This can, of course, sometimes lead to significant errors, but for most cases it represents the best estimate available in the complete absence of measured data.

The final output of the program is similar to that for electron capture, and since the electron capture decay of ^{125}I, which was illustrated above, results in an internally converted 0.0353-Mev gamma ray, the kind of output obtained is illustrated below:

[12] L. A. Sliv and I. M. Band, issued in U.S.A. as Report 57ICC K1, Physics Department, University of Illinois (K shell). The L shell results appear in Report 58ICC L1.

125 I 53 GEC

		FRACTION PER DECAY	ENERGY (MEV)
GAMMA RAY		.07020	.03530
K-ALPHA1	X-RAY	.37207	.02747
K-ALPHA2	X-RAY	.19087	.02720
K-BETA1	X-RAY	.10045	.03099
K-BETA2	X-RAY	.02083	.03182
ALL X-RAYS AND/OR GAMMA RAYS LESS THAN .0113 MEV + ALL AUGER AND/OR INTERNAL CONVERSION ELECTRONS GREATER THAN .0300 MEV		.26822	.01951
ALL AUGER AND/OR INTERNAL CONVERSION ELECTRONS LESS THAN .030 MEV		3.44394	.00263

The letters GEC are a mnemonic notation to indicate we are dealing with a gamma ray following electron capture. The computer output for the electron capture decay of ^{125}I may be added to this computer output to give the total distribution of radiations emitted in the case of ^{125}I decay. This gives the following results:

Radiations Present in ^{125}I Decay

	FRACTION PER DECAY	ENERGY (MEV)
GAMMA RAY	.07020	.03530
K-ALPHA1 X-RAY	.74112	.02747
K-ALPHA2 X-RAY	.38020	.02720
K-BETA1 X-RAY	.20009	.03099
K-BETA2 X-RAY	.04150	.03182
ALL X-RAYS AND/OR GAMMA RAYS LESS THAN .0113 MEV + ALL AUGER AND/OR INTERNAL CONVERSION ELECTRONS GREATER THAN .0300 MEV	.39735	.01474
ALL AUGER AND/OR INTERNAL CONVERSION ELECTRONS LESS THAN .030 MEV	6.23564	.00250

The last two rows of information are sufficient to determine the total "beta-type" radiation emitted by ^{125}I and give 21.4 kev/disintegration. This compares quite favorably with the value of 20.8 kev/disintegration computed by Smith *et al.*[10]

A number of extensions and improvements in these programs are possible, and further work is in progress. These programs are written in FORTRAN IV and are available from the author.

Appendix A: Beta Decay

The following notations are used:

V_0 = screening potential due to atomic electrons (mc^2 units)

W_0 = end-point total energy (mc^2 units)

W = total energy of negatron or positron (mc^2 units)

ρ = momentum of negatron or positron (mc units)

Z = atomic number of daughter nucleus; Z must be taken positive for negatron emission and negative for positron emission

$F(Z, W)$ = Fermi function

α = fine structure constant = 1/137

R = nuclear radius

A = mass number

$\bar{E}$ = average kinetic energy of the negatron or positron (mc^2 units)

E_0 = end-point kinetic energy (mc^2 units)

The units used throughout the following equations are those in which m (electron mass), c (velocity of light in vacuo), and $\hbar$ (Planck's constant divided by 2π) are assigned values equal to 1. In these units $E = W - 1$ and $\rho^2 = W^2 - 1$.

Neglecting screening corrections, the ratio $\bar{E}/E_0$ in allowed beta decay is given by

$$\frac{\bar{E}}{E_0} = \frac{\bar{W} - 1}{E_0}, \tag{1}$$

where

$$\bar{W} = \frac{\int_1^{W_0} W\, N(W)\, dW}{\int_1^{W_0} N(W)\, dW}, \tag{2}$$

and

$$N(W) = F(Z, W)\, \rho W (W_0 - W)^2, \tag{3}$$

with

$$F(Z, W) = 2(1 + \gamma_0)\, (2\rho R)^{2(\gamma - 1)}\, e^{\pi y} \times \left[\frac{|\Gamma(\gamma_0 + iy)|}{\Gamma(2\gamma_0 + 1)}\right]^2. \tag{4}$$

In this equation for $F(Z, W)$, $\gamma_0 = [1 - (\alpha Z)^2]^{1/2}$, $R = \frac{1}{2}\alpha A^{1/3}$, and $y = \alpha ZW/\rho$.

When screening is taken into account, Eq. (3) becomes

$$N(W) = F(Z, W - V_0)\,[(W - V_0)^2 - 1]^{1/2} \times (W - V_0)\,(W_0 - W)^2, \quad (5)$$

where V_0 is the screening potential in mc^2 units. The screening potential used in the present work is

$$V_0 = \frac{1.13\,|Z|^{4/3}}{\alpha^2}, \quad (6)$$

where V_0 must be taken positive for electrons and negative for positrons. When Eq. (5) is substituted into Eq. (2), it can be shown that the result is equivalent to

$$\overline{W} = \frac{\int_{1-V_0}^{W_0 - V_0} (W + V_0)\,F(Z, W)\,W\rho(W_0 - W - V_0)^2\,dW}{\int_{1-V_0}^{W_0 - V_0} F(Z, W)\,W\rho(W_0 - W - V_0)^2\,dW}. \quad (7)$$

Equation (7) in combination with Eq. (1) was used to determine $\overline{E}/E_0$ for allowed transitions.

For first-forbidden unique transitions, Eq. (3) is modified by a shape function a_1, namely,

$$N(W) = F(Z, W)\;a_1\rho W(W_0 - W)^2, \quad (8)$$

where

$$a_1 = (W_0 - W)^2 L_0 + 9L_1, \quad (9)$$

and for second-forbidden unique transitions, there is a similar modification by a shape function a_2, where

$$a_2 = (W_0 - W)^4 L_0 + 30\,(W_0 - W)^2 L_1 + 225 L_2. \quad (10)$$

The complicated functions L_0, L_1, and L_2 are determined from

$$L_\nu = \frac{1}{2\rho^2 F(Z, W) R^{2\nu}}\,(g^2_{-\nu-1} + f^2_{\nu+1}). \quad (11)$$

The subscript ν may have the value 0, 1, or 2.

Functions f and g are determined from

$$f_n = (W - 1)^{1/2}\,Q_n \times \left\{\text{imaginary part}\,[S_n\;{}_1F_1(a, b; z)]\right\} \quad (12)$$

and

$$g_n = (W + 1)^{1/2}\,Q_n \times \left\{\text{real part}\,[S_n\;{}_1F_1(a, b; z)]\right\}, \quad (13)$$

where

$$Q_n = \frac{(2\rho R)^{\gamma_n}}{W^{1/2}R}\,e^{\pi y/2}\,\frac{|\Gamma(\gamma_n + iy)|}{\Gamma(2\gamma_n + 1)},$$

$$S_n = e^{-i\rho R + in}\,(\gamma_n + iy),$$

$$a = \gamma_n + 1 + iy,$$

$$b = 2\gamma_n + 1,$$

$$z = 2i\rho R,$$

$$\gamma_n = (n^2 - \alpha^2 Z^2)^{1/2},$$

$$e^{2i\eta} = \frac{-n + iy/W}{\gamma_n + iy},$$

and ${}_1F_1\,(a, b; z)$ is the confluent hypergeometric function, which can be represented by

$${}_1F_1\,(a, b; z) = \frac{\Gamma(b)}{\Gamma(a)}\sum_{m=0}^{\infty}\frac{\Gamma(a + m)}{\Gamma(b + m)}\,\frac{z^m}{m!}.$$

The subscript n in the functions f_n and g_n takes on the values -3, -2, -1, $+1$, $+2$, and $+3$ for the various calculations necessary to compute L_0, L_1, and L_2.

When screening is taken into consideration and one integrates from $1 - V_0$ to $W_0 - V_0$, as in Eq. (7), the shape factors represented by Eqs. (9) and (10) become, respectively,

$$a_1 = (W_0 - W - V_0)^2 L_0 + 9L_1 \quad (14)$$

and

$$a_2 = (W_0 - W - V_0)^4 L_0 + 30(W_0 - W - V_0)^2 L_1 + 225 L_2 . \quad (15)$$

Thus, finally, for first-forbidden unique transitions, one has

$$\overline{W} = \frac{\int_{1-V_0}^{W_0 - V_0} (W + V_0)\, F(Z, W)\, W p a_1 (W_0 - W - V_0)^2\, dW}{\int_{1-V_0}^{W_0 - V_0} F(Z, W)\, W p a_1 (W_0 - W_0 - V_0)^2\, dW} , \quad (16)$$

where a_1 is given by Eq. (14). Equation (16), in conjunction with Eq. (2), was used to determine $\overline{E}/E_0$ for first-forbidden unique transitions.

For second-forbidden unique transitions, a_2 as given by Eq. (15) is used in Eq. (16) in place of a_1, and the calculations otherwise proceed in a similar fashion.

Appendix B: Electron Capture

When orbital electron capture occurs, vacancies are created in the various electronic shells. The probability is highest for vacancies to be made in the K shell, if energetically possible. However, a significant number of primary vacancies often are made in the L and M shells. As we shall see, the contributions due to still higher shells are nearly always negligible. For the present work these small contributions may be included with the M-shell contribution.

The $K/L/M$ capture ratios have been studied on the basis of theory by Brysk and Rose[13] and by Bahcall.[14] A number of the results of Brysk and Rose are contained in *Nuclear Spectroscopy Tables*, by Wapstra *et al.*,[15] on pages 59–61. Table 25.1 gives the notations which will be used in the remaining parts of Appendix B.

In Table 25.1, items 4 through 9 are functions of the atomic number and have been tabulated in the literature. Items 4 to 7 may be found in *Nuclear Spectroscopy Tables*,[15] and items 8 and 9 may be extracted from graphs in Chap. XXV, Part A, of *Alpha, Beta and Gamma-Ray Spec-*

[13] H. Brysk and M. E. Rose, *Rev. Mod. Phys.* 30, 1169 (1958).

[14] J. N. Bahcall, *Phys. Rev.* 132, 362 (1963).

[15] A. H. Wapstra, G. J. Nijgh, and R. Van Lieshout, *Nuclear Spectroscopy Tables*, p. 61, Interscience, New York, 1959.

Table 25.1. Notations Used in Appendix B

1. E_n = energy difference of the nuclear levels involved in the nth electron capture branch
2. N_n = the fraction of times the parent nucleus decays via electron capture to the nth branch
3. $\epsilon_{L_I}/\epsilon_K$, $\epsilon_{L_{II}}/\epsilon_{L_I}$, $\epsilon_{L_{III}}/\epsilon_{L_I}$, $\epsilon_{M^+}/\epsilon_L$ = the ratios of electron captures in the various shells or subshells; ϵ_{M^+} means electron capture in the M and all higher shells
4. L_{L_I}/L_K, $L_{L_{II}}/L_{L_I}$, $9L_{III}/L_{L_I}$ = the ratios of certain needed atomic wave function parameters
5. ω_K and ω_L = the K and L shell fluorescent yields respectively
6. E_K, E_{L_I}, $E_{L_{II}}$, $E_{L_{III}}$, E_M = the binding energies in the various shells; E_M is an average over the subshells
7. $K_{\alpha 2}/K_{\alpha 1}$, $K_{\beta 1}/K_{\alpha 1}$, $K_{\beta 2}/K_{\alpha 1}$ = ratios of numbers of $K_{\alpha 1}$, $K_{\beta 1}$, and $K_{\beta 2}$ x rays to $K_{\alpha 1}$ x rays respectively
8. a_{KLX}/a_{KLL} and a_{KXY}/a_{KLL} = ratios of numbers of KLX and KXY Auger electrons to KLL Auger electrons respectively
9. R_{11}, R_{12}, R_{22}, R_{13}, R_{33} = ratios of numbers of KL_1L_1, KL_1L_2, KL_2L_2, DL_1L_3, and KL_3L_3 Auger electrons to KL_2L_3 Auger electrons respectively

trometry, edited by K. Siegbahn. These parameters for each value of Z have been punched onto IBM cards and are used as input data for the computer code.

Electron capture transitions, like other beta transitions, are classed into allowed, first-forbidden, first-forbidden unique, etc., types depending upon spin and parity changes between the nuclear levels involved in the transition. The $K/L/M$ capture ratios are about the same for first-forbidden and allowed transitions; they are also about the same for first-forbidden unique and second-forbidden transitions. Hence we shall consider $K/L/M$ ratios for three cases: allowed, first-forbidden unique, and second-forbidden unique transitions.

Allowed Transitions. – The ratio of capture in the L_{I} shell to that in the K shell is given by

$$\frac{\epsilon_{L_{\mathrm{I}}}}{\epsilon_K} = \frac{L_{L_{\mathrm{I}}}}{L_K}\left(\frac{E_n - E_{L_{\mathrm{I}}}}{E_m - E_K}\right)^2 \times \left(1 + \frac{2.81}{Z} + \frac{13.76}{Z^2} + \frac{75.2}{Z^3}\right) , \quad (1)$$

where the polynomial in inverse powers of Z (atomic number) is a correction to the theory of Brysk and Rose[13] which takes into account the effects of electron exchange and imperfect atomic overlap. This correction was developed by Bahcall,[14] who shows that Eq. (1) agrees with experiment within experimental error.

The ratio of electron capture in the L_{II} subshell to that in the L_{I} subshell is

$$\frac{\epsilon_{L_{\mathrm{II}}}}{\epsilon_{L_{\mathrm{I}}}} = \frac{L_{L_{\mathrm{II}}}}{L_{L_{\mathrm{I}}}} . \quad (2)$$

Electron capture in the L_{III} subshell does not occur in allowed transitions.

We shall designate the ratio of electron capture in M and higher shells to electron capture in the L shell by $\epsilon_{M^+}/\epsilon_L$, and, as indicated above, this has been tabulated as a function of Z.

Designating the total electron capture by ϵ, one may easily show that

$$\frac{\epsilon}{\epsilon_K} = 1 + \frac{\epsilon_{L_{\mathrm{I}}}}{\epsilon_K}\left(1 + \frac{\epsilon_{L_{\mathrm{II}}}}{\epsilon_{L_{\mathrm{I}}}}\right) \times \left(1 + \frac{\epsilon_{M^+}}{\epsilon_L}\right) . \quad (3)$$

Hence the number of vacancies made in the K shell per decay, f_K, is given by

$$f_K = \sum_n N_n \frac{\epsilon_K}{\epsilon} = \sum_n N_n \left[1 + \frac{\epsilon_{L_{\mathrm{I}}}}{\epsilon_K} \times \left(1 + \frac{\epsilon_{L_{\mathrm{II}}}}{\epsilon_{L_{\mathrm{I}}}}\right)\left(1 + \frac{\epsilon_{M^+}}{\epsilon_L}\right)\right]^{-1} . \quad (4)$$

The number of primary vacancies made in the L shell per decay, f_L, is

$$f_L = \sum_n f_{K_n} \frac{\epsilon_{L_{\mathrm{I}}}}{\epsilon_K}\left(1 + \frac{\epsilon_{L_{\mathrm{II}}}}{\epsilon_{L_{\mathrm{I}}}}\right) . \quad (5)$$

The number of primary vacancies made in the M and higher shells per decay, f_{M^+}, is

$$f_{M^+} = \sum_n (N_n - f_{K_n} - f_{L_n}) . \quad (6)$$

In Eqs. (4) to (6) the summation over n is necessary if there is more than one electron capture branch in the decay.

First-Forbidden Unique Transitions. – For first-forbidden unique transitions, the following equations apply:

$$\frac{\epsilon_{L_{\mathrm{I}}}}{\epsilon_K} = \frac{L_{L_{\mathrm{I}}}}{L_K}\left(\frac{E_n - E_{L_{\mathrm{I}}}}{E_n - E_K}\right)^4 \quad (7)$$

and

$$\frac{\epsilon_{L_{III}}}{\epsilon_{L_I}} = 0.511^2 \left(\frac{9L_{L_{III}}}{L_{L_I}}\right) \frac{\left(E_n - E_{L_{III}}\right)^2}{\left(E_n - E_{L_I}\right)^4} ; \quad (8)$$

$\epsilon_{L_{II}}/\epsilon_{L_I}$ and $\epsilon_{M^+}/\epsilon_L$ are the same as for allowed transitions. It follows that the number of vacancies made in the K shell per decay is

$$f_K = \sum_n N_n \left[1 + \frac{\epsilon_{L_I}}{\epsilon_K} \times \left(1 + \frac{\epsilon_{L_{II}}}{\epsilon_{L_I}} + \frac{\epsilon_{L_{III}}}{\epsilon_{L_I}}\right)\left(1 + \frac{\epsilon_{M^+}}{\epsilon_L}\right)\right]^{-1} , \quad (9)$$

$$f_L = \sum_n f_{K_n} \frac{\epsilon_{L_I}}{\epsilon_K}\left(1 + \frac{\epsilon_{L_{II}}}{\epsilon_{L_I}} + \frac{\epsilon_{L_{III}}}{\epsilon_{L_I}}\right) , \quad (10)$$

and f_{M^+} is given by Eq. (6).

Second-Forbidden Unique Transitions. – For second-forbidden unique transitions, the following equations apply:

$$\frac{\epsilon_{L_I}}{\epsilon_K} = \frac{L_{L_I}}{L_K}\left(\frac{E_n - E_{L_I}}{E_n - E_K}\right)^6 \quad (11)$$

and

$$\frac{\epsilon_{L_{III}}}{\epsilon_{L_I}} = \frac{10}{3} \cdot 0.511^2 \frac{\left(E_n - E_{L_{III}}\right)^4}{\left(E_n - E_{L_I}\right)^6} ; \quad (12)$$

$\epsilon_{L_{II}}/\epsilon_{L_I}$ and $\epsilon_{M^+}/\epsilon_L$ are the same as for allowed transitions. Using these results, Eqs. (6), (9), and (10) then apply to give f_K, f_L, and f_{M^+}.

Once f_K, f_L, and f_{M^+} are found by the above equations, we use the results to determine the relative numbers of various x rays and Auger electrons which will be produced. This proceeds as follows:

First of all, it is a simple matter to program the computer, using the information listed in item 7 of Table 25.1 as input, to compute the relative yields of $K_{\alpha 1}$, $K_{\alpha 2}$, $K_{\beta 1}$, and $K_{\beta 2}$ x rays arising from vacancies in the K shell. Let us call these relative yields, normalized to 1, $N_{\alpha 1}$, $N_{\alpha 2}$, $N_{\beta 1}$, $N_{\beta 2}$ respectively. Similarly, one may use the information listed in item 6 of the table to determine the respective energies of these x rays.

Second, the computer uses the information listed in item 8 of Table 25.1 to determine the relative intensities of the KLL, KLX, and KXY Auger electrons. Let us call these relative intensities, normalized to 1, N_{KLL}, N_{KLX}, and N_{KXY} respectively. Similarly one may use the information listed in items 6 and 9 to determine a weighted average energy associated with each of these Auger electron groups.

Then the fractions of $K_{\alpha 1}$, $K_{\alpha 2}$, $K_{\beta 1}$, and $K_{\beta 2}$ x rays per decay and the fractions of KLL, KLX, and KXY Auger electrons per decay, which may be represented by $f_{\alpha 1}$, $f_{\alpha 2}$, $f_{\beta 1}$, $f_{\beta 2}$, f_{KLL}, f_{KLX}, and f_{KXY}, respectively, are

$$f_{\alpha 1} = f_K \omega_K N_{\alpha 1} , \quad (13)$$

$$f_{\alpha 2} = f_K \omega_K N_{\alpha 2} , \quad (14)$$

$$f_{\beta 1} = f_K \omega_K N_{\beta 1} , \quad (15)$$

$$f_{\beta 2} = f_K \omega_K N_{\beta 2} , \quad (16)$$

$$f_{KLL} = f_K (1 - \omega_K) N_{KLL} , \quad (17)$$

$$f_{KLX} = f_K (1 - \omega_K) N_{KLX} , \quad (18)$$

$$f_{KXY} = f_K (1 - \omega_K) N_{KXY} . \quad (19)$$

Then the total vacancies per decay made in the L shell, n_L, are given by

$$n_L = f_L + f_{\alpha 1} + f_{\alpha 2} + 2f_{KLL} + f_{KLX} , \quad (20)$$

and the fraction per decay of L x rays, f_{LX}, is

$$f_{LX} = n_L \omega_L , \quad (21)$$

whereas the fraction per decay of LXY Auger electrons, f_{LXY}, is

$$f_{LXY} = n_L (1 - \omega_L) . \quad (22)$$

We make the approximation in this code that for

both x-ray and Auger processes, only M-shell electrons are involved in the transitions which result from vacancies in the L shell.

The total vacancies per decay made in the M shell, n_M, is

$$n_M = f_M + f_{\beta 1} + f_{KLX} + 2f_{KXY} + f_{LX} + 2f_{LXY} \ . \quad (23)$$

The very low-energy x rays and Auger electrons which result from these vacancies in the M shell will be completely absorbed locally, and we assign an energy equal to the average binding energy in the M shell to these processes.

DISTRIBUTION OF DOSE IN THE BODY FROM A SOURCE OF GAMMA RAYS DISTRIBUTED UNIFORMLY IN AN ORGAN

H. L. Fisher, Jr.[16] W. S. Snyder

When a gamma emitter is present in an organ of the body, only a fraction of the emitted gamma energy is absorbed in that organ. Many evaluations of the absorbed fraction have been published, mostly for highly idealized and perhaps oversimplified cases. The use of an effective radius and a spherical geometry is one instance of such drastic simplification. Although an exact theory of gamma photon interaction with matter is known in detail, application of this theory is usually difficult since an enormous amount of mathematical computation is involved. However, by use of a high-speed digital computer these calculations become feasible. A Monte-Carlo-type calculation has been used to estimate the dose in 22 organs and 100 subregions of an adult human phantom for four initial gamma energies. This report is divided into three parts: a description of the phantom, details of the Monte Carlo method used (described previously[17]), and the dose estimates from a gamma source distributed uniformly in the total body and in the skeleton.

[16]U.S. Public Health Service.

[17]H. L. Fisher, Jr., and W. S. Snyder, *Health Phys. Div. Ann. Progr. Rept. July 31, 1966*, ORNL-4007, p. 221.

The Phantom

Figure 25.7 shows the phantom and the subregions in which dose was determined. The dimensions of the phantom were chosen after consideration of the average size and weight of humans[18–20] and the phantoms designed by Hayes and Brucer.[21] In order to describe the various regions, a coordinate system is needed. As shown in the figure, the origin of the rectangular coordinate system is located at the center of the base of the trunk. The positive z axis extends vertically through the head, the left side of the phantom is taken along the positive x axis, and the rear is taken along the positive y axis. All units of length are in centimeters.

By use of the coordinate system in Fig. 25.7, the body of the phantom may be described as follows. The trunk is an elliptical cylinder given by

$$\left(\frac{x}{20}\right)^2 + \left(\frac{y}{10}\right)^2 \leqq 1 \ ,$$

$$0 \leqq z \leqq 70 \ .$$

The head is also an ellipitical cylinder:

$$\left(\frac{x}{7}\right)^2 + \left(\frac{y}{10}\right)^2 \leqq 1 \ ,$$

$$70 < z \leqq 94 \ .$$

The legs are considered together to be a truncated elliptical cone:

$$\left(\frac{x}{20}\right)^2 + \left(\frac{y}{10}\right)^2 \leqq \left(\frac{100 + z}{100}\right)^2 \ ,$$

$$-80 \leqq z < 0 \ .$$

[18]P. L. Altman and D. S. Dittmer, *Growth Including Reproduction and Morphological Development*, Biological Handbook, Fed. Am. Soc. Exptl. Biol., Washington, 1962.

[19]W. M. Krogman, "Growth of Man," pp. 712–15 in *Tabulae Biologicae*, vol. XX, ed. by H. Denzer *et al.*, Den Haag, 1941.

[20]"Report of ICRP Task Group on the Revision of Standard Man," in preparation.

[21]R. L. Hayes and M. Brucer, *Intern. J. Appl. Radiation Isotopes* 9, 111 (1960).

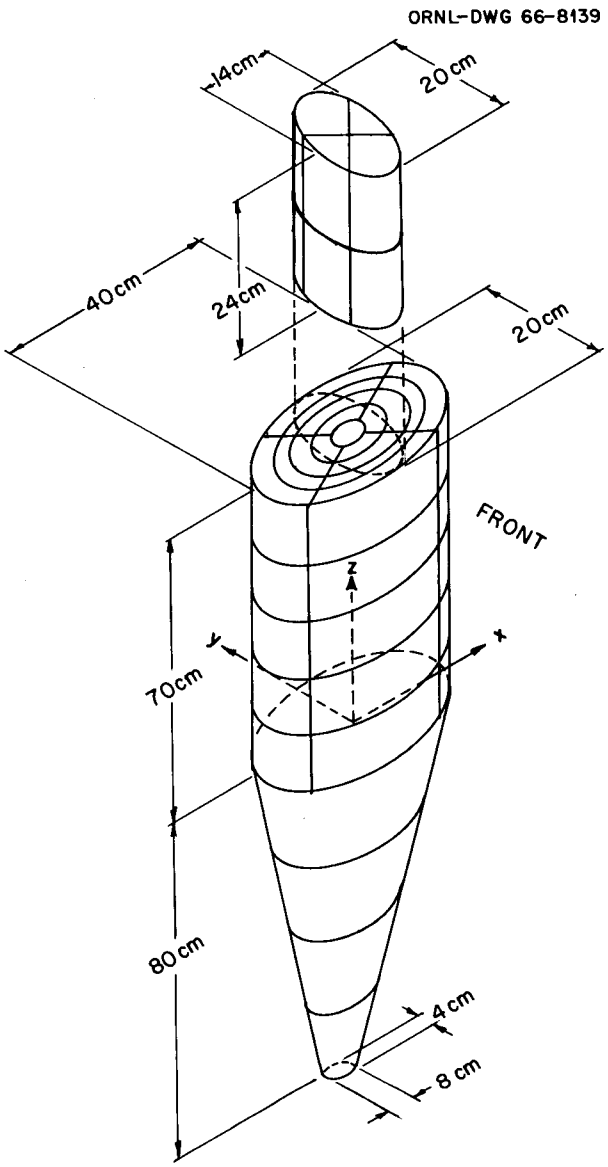

Fig. 25.7. The Adult Human Phantom.

It is now a simple matter for the computer to take any point (x, y, z), substitute it into these inequalities, note whether the inequalities are satisfied, and thereby determine whether this point is inside or outside the phantom and whether it is in the head, trunk, or legs. Except for the head, this phantom is convex. Account has been taken of the photons which transverse the void between the trunk and the head.

The arbitrary subregions into which the phantom was sectioned and in which dose was determined are outlined in Fig. 25.7. The legs were cut into four layers by equidistant horizontal planes; the trunk was divided into five layers by equidistant horizontal planes. Two vertical planes, intersecting at right angles along the central axis of the trunk and having an angle of 45° from either the x or y axis, cut these layers. The final volume element is obtained by four vertical concentric elliptical cutting cylinders. The major axes of these elliptical cylinders are 4, 8, 12, and 16 cm, and the minor axes are 2, 4, 6, and 8 cm. The innermost elliptical cylinder was not cut by the vertical planes. The head was sectioned into two layers equal in thickness and was cut by the same two vertical planes that cut the trunk. Although dose was determined in these arbitrary regions, the results are not presented in this report since the principal purpose is to give organ doses. However, results from the arbitrary regions permit an approximation of the variation of dose throughout the phantom. In particular, if an organ is very small (e.g., ovary, thyroid, pituitary, etc.), the dose estimate may be statistically unreliable on a given calculation, and one may use instead an average dose over one of these layer regions.

Mathematical descriptions of the organs were formulated after consideration of the descriptive and schematic material from several general anatomy references.[22,23] The scaled cross sections of the human body by Eycleshymer and Schoemaker[24] were helpful in locating the positions at which to place the organs as well as an aid in the construction of the organs. The representations of the organs by the mathematical equations given herein are only approximate, and many other geometrically simple approximations might be used. The goal in constructing these mathematical organs was to obtain the approximate size and shape of an average organ through the use of a few simple mathematical equations. If the size and shape approximate those of the real organ, the dose estimate should be correspondingly accurate. To minimize running time and, therefore, cost, the formulas used should be as simple as possible.

The composition of the phantom is tissue[25] of density 1 g/cm^3. There is no low-density area for

[22] H. Gray, *Anatomy of the Human Body*, Lea and Febiger, Philadelphia, 1942.

[23] W. J. Hamilton, *Textbook of Human Anatomy*, Macmillan, London, 1957.

[24] A. C. Eycleshymer and D. M. Schoemaker, *A Cross-Section Anatomy*, D. Appleton-Century, New York, 1911.

[25] "Protection Against Neutron Radiation up to 30 Million Electron Volts," *NBS Handbook* 63, U.S. Dept. of Commerce, 1957.

the lung nor is there a high-density region with modified mass absorption coefficient for bone. However, for gamma energies between 0.2 and 4 Mev, the mass absorption coefficients for bone and soft tissue are essentially the same within several percent. Below 0.2 Mev the photoelectric cross section for bone rises much more rapidly than that for soft tissue. This is one of the major limitations of the present approach. The volume in cubic centimeters of most mathematical organs will be equal to the weight of an average organ in grams. This is not true for the lungs or for regions of bone. The linear dimensions of all organs, including lungs and bones, have been used as the primary basis for developing the mathematical equations.

Figure 25.8 shows an anterior view of some of the larger organs and their positions in the phantom. In the following account, a brief description of each mathematical organ will be given, followed by the mathematical inequalities which must be satisfied for the point (x, y, z) in the coordinate system of Fig. 25.7 to be in the organ. The volumes given were determined by integration.

The volumes of the head, trunk, legs, and total body are 5278, 43,982, 20,776, and 70,036 cm^3 respectively. When there are left and right organs, the equations for only one, the left, will be given. The equations for the other may be obtained by replacing x by $-x$ in the inequalities.

Adrenals. – Each adrenal is half an ellipsoid sitting atop a kidney. The left adrenal is given by

$$\left(\frac{x-4.5}{1.5}\right)^2 + \left(\frac{y-6.5}{0.5}\right)^2 + \left(\frac{z-38}{5}\right)^2 \leqq 1 ,$$

$$z \geqq 38$$

The volume of both adrenals is 15.71 cm^3.

Bladder (Urinary). – The bladder plus contents when moderately full is an ellipsoid given by

$$\left(\frac{x}{6}\right)^2 + \left(\frac{y+4.5}{4.5}\right)^2 + \left(\frac{z-8}{4.5}\right)^2 \leqq 1 ,$$

and the volume is 508.9 cm^3.

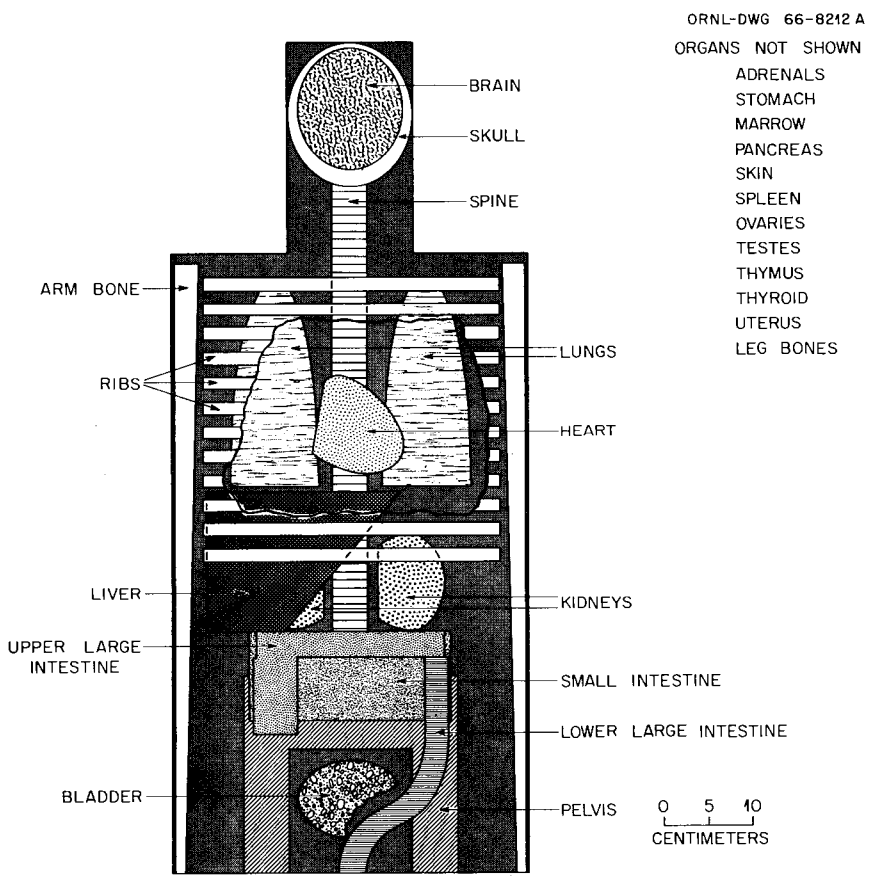

Fig. 25.8. Anterior View of the Principal Organs in the Head and Trunk of the Phantom.

Brain. – The brain is an ellipsoid given by

$$\left(\frac{x}{6}\right)^2 + \left(\frac{y}{9}\right)^2 + \left(\frac{z - 86.5}{6.5}\right)^2 \leqq 1 ,$$

and the volume is 1470 cm^3.

Gastrointestinal Tract. – The form of the gastrointestinal (GI) tract given here represents the mass of the tract itself plus the 24-hr average mass of contents. This is a particularly difficult organ to fix since its volume and location are subject to change between individuals as well as in the same individual. The intestines are taken to be in the somewhat-idealized standard positions. The stomach is the most difficult to represent since its volume will change by nearly an order of magnitude several times in 24 hr. The constant-sized and fixed-position stomach given here is, therefore, not very realistic but should suffice for estimating an approximate dose in that region. The stomach is an ellipsoid,

$$\left(\frac{x - 8}{4}\right)^2 + \left(\frac{y + 4}{3}\right)^2 + \left(\frac{z - 35}{8}\right)^2 \leqq 1 ,$$

and has a volume of 402.1 cm^3.

The small intestine has not been constructed in detail. Instead the volume occupied by the coils of the small intestine is used. This volume, which lies in the pelvic region, is a section of a circular cylinder given by

$$x^2 + (y + 3.8)^2 \leqq (11.3)^2 ,$$

$$-7 \leqq y \leqq 3 ,$$

$$17 \leqq z \leqq 27 .$$

Exclude the portion of the large intestine lying in this volume. The volume is 1696 cm^3.

The upper large intestine is simulated by two cylinders, one with its axis vertical representing the ascending colon and the other an elliptical cylinder with its axis horizontal representing the transverse colon. The upper large intestine is the region satisfying (subregion 1)

$$(x + 8.5)^2 + (y + 4.5)^2 \leqq (2.5)^2 ,$$

$$15.4 \leqq z \leqq 24$$

or (subregion 2)

$$\left(\frac{y + 4.5}{2.5}\right)^2 + \left(\frac{z - 25.5}{1.5}\right)^2 \leqq 1 ,$$

$$-10.5 \leqq x \leqq 10.5 .$$

Its volume is 416.3 cm^3.

The lower large intestine is composed of an elliptical cylinder and an S-shaped figure formed from half of a torus. It is the region satisfying (subregion 1)

$$\left(\frac{x - 9.5}{1.6}\right)^2 + \left(\frac{y + 4.3}{2}\right)^2 \leqq 1 ,$$

$$13.4 \leqq z \leqq 24$$

or (subregion 2)

$$0 \leqq z \leqq 13.4 ,$$

$$\left(\sqrt{E^2 + (z - 6.7 + 6.7m)^2} - 6.7\right)^2 + F^2 \leqq (1.6)^2 ,$$

where

$$E = (x - 4.75)\ 0.7090 - (y - 0.4252)\ 0.7053 ,$$

$$F = (x - 4.75)\ 0.7053 + (y - 0.4252)\ 0.7090 ,$$

$$m = 1 \text{ if } E \geqq 0 ,$$

$$m = -1 \text{ if } E < 0 .$$

It has a volume of 275.8 cm^3.

Heart. – The heart is half an ellipsoid capped by a hemisphere which is cut by a plane. A rotation and translation are then effected. The heart,

$$x_1 = 0.6943\ (x + 1) - 0.3237\ (y + 3) - 0.6428\ (z - 51) ,$$

$$y_1 = 0.4226\ (x + 1) + 0.9063\ (y + 3) ,$$

$$z_1 = 0.5826\ (x + 1) - 0.2717\ (y + 3) + 0.7660\ (z - 51) ,$$

$$\left(\frac{x_1}{8}\right)^2 + \left(\frac{y_1}{5}\right)^2 + \left(\frac{z_1}{5}\right)^2 \leqq 1 ,$$

$$x_1^2 + y_1^2 + z_1^2 \leqq (5)^2 \text{ if } x_1 < 0 ,$$

$$\frac{x_1}{3} + \frac{z_1}{5} \geqq -1 \text{ if } x_1 < 0 ,$$

has a volume of 603.1 cm^3.

Kidneys. – Each kidney is an ellipsoid cut by a plane. The left kidney is given by

$$\left(\frac{x-6}{4.5}\right)^2 + \left(\frac{y-6}{1.5}\right)^2 + \left(\frac{z-32.5}{5.5}\right)^2 \leqq 1 ,$$

$$x \geqq 3 .$$

The volume of both kidneys is 288.0 cm^3.

Liver. – The region of the liver is defined by an elliptical cylinder cut by a plane as follows:

$$\left(\frac{x}{16.5}\right)^2 + \left(\frac{y}{8}\right)^2 \leqq 1 ,$$

$$\frac{x}{35} + \frac{y}{45} - \frac{z}{43} \leqq -1 ,$$

$$27 \leqq z \leqq 43 .$$

Its volume is 1614 cm^3.

Lungs. – Each lung is half an ellipsoid with a section in front removed. The defining inequalities for the left lung are

$$\left(\frac{x-8.5}{5}\right)^2 + \left(\frac{y}{7.5}\right)^2 + \left(\frac{z-43.5}{24}\right)^2 \leqq 1 ,$$

$$z \geqq 43.5 ,$$

$$\left(\frac{x-2.5}{5}\right)^2 + \left(\frac{y}{7.5}\right)^2 + \left(\frac{z-43.5}{24}\right)^2 \geqq 1 \text{ if } y < 0 .$$

The volume of both lungs is 3378 cm^3.

Ovary. – Each ovary is an ellipsoid. The left ovary is given by

$$(x-6)^2 + \left(\frac{y}{0.5}\right)^2 + \left(\frac{z-15}{2}\right)^2 \leqq 1 .$$

The volume of both ovaries is 8.378 cm^3.

Pancreas. – The pancreas is half an ellipsoid with a section removed. It is defined by

$$\left(\frac{y}{15}\right)^2 + y^2 + \left(\frac{z-37}{3}\right)^2 \leqq 1 ,$$

$$x \geqq 0 ,$$

$$z \geqq 37 \text{ if } x > 3 .$$

It has a volume of 61.07 cm^3.

Skeleton. – The skeleton consists of six parts – the leg bones, the arm bones, the pelvis, the spine, the skull, and the ribs. Each piece will be described separately. Each arm bone is the frustum of an elliptical cone. The left one is defined by

$$\left[\frac{(1.4/138)\,(z-69) + (x-18.4)}{1.4}\right]^2 + \left(\frac{y}{2.7}\right)^2 \leqq \left[\frac{138 + (z-69)}{138}\right]^2 ,$$

$$0 \leqq z \leqq 69 .$$

The volume of both arm bones is 956.0 cm^3.

The pelvis is a volume between two nonconcentric circular cylinders described by

$$x^2 + (y+3)^2 \leqq (12)^2 ,$$

$$x^2 + (y+3.8)^2 \geqq (11.3)^2 ,$$

$$y + 3 \geqq 0 ,$$

$$0 \leqq z \leqq 22 ,$$

$$y \leqq 5 \text{ if } z \leqq 14 .$$

Its volume is 606.1 cm^3.

The spine is an elliptical cylinder given by

$$\left(\frac{x}{2}\right)^2 + \left(\frac{y-5.5}{2.5}\right)^2 \leqq 1 ,$$

$$22 \leqq z \leqq 78.5 ,$$

and has a volume of 887.5 cm^3.

The rib volume is that region between two concentric right vertical elliptical cylinders. This

region is sliced by a series of equispaced horizontal planes into slabs, every other slice being a rib. The statements that must be satisfied are

$$\left(\frac{x}{17}\right)^2 + \left(\frac{y}{9.8}\right)^2 \leqq 1 ,$$

$$\left(\frac{x}{16.5}\right)^2 + \left(\frac{y}{9.3}\right)^2 \geqq 1 ,$$

$$35.1 \leqq z \leqq 67.3 .$$

$$\text{Integer}\left(\frac{z - 35.1}{1.4}\right) \text{ is even} .$$

The total rib volume is 694.0 cm^3.

Each leg bone is the frustum of a circular cone. The left one is

$$\left(x - 10 - \frac{8}{79.8} z\right)^2 + y^2 < \left(3.5 + \frac{2.5}{79.8} z\right)^2 ,$$

$$-79.8 \leqq z \leqq 0 .$$

The volume of both is 2799 cm^3.

The skull is the volume between two nonconcentric ellipsoids defined by

$$\left(\frac{x}{6}\right)^2 + \left(\frac{y}{9}\right)^2 + \left(\frac{z - 86.5}{6.5}\right)^2 \geqq 1 ,$$

$$\left(\frac{x}{6.8}\right)^2 + \left(\frac{y}{9.8}\right)^2 + \left(\frac{z - 85.5}{8.3}\right)^2 \leqq 1 ,$$

and has a volume of 846.6 cm^3.

Dose to the entire skeleton is determined by adding together the energies deposited in each part of the skeleton and dividing by the volume of the skeleton, as follows. Let E_i be the energy (in Mev) deposited in region i having a volume V_i. Then the dose in rads to n such regions is

$$D_n = 1.6 \times 10^{-8} \frac{\sum_{i=1}^{n} E_i}{\sum_{i=1}^{n} V_i} .$$

The proportion of marrow in each bone of the skeleton has been given by Mechanik.[26] Using average values for this proportion, f_i, and assuming that the marrow in each region receives the average dose received by that region, the marrow dose is

$$D_n = 1.6 \times 10^{-8} \frac{\sum_{i=1}^{n} f_i E_i}{\sum_{i=1}^{n} f_i V_i} .$$

The proportions, f_i, are skull 0.2, spine 0.5, leg bones 0.4, arm bones 0.3, rib 0.4, and pelvis 0.45.

Skin. – The so-called skin of the phantom was constructed to give the dose at the surface. This region is a layer about 0.2 cm thick just inside the surface of the phantom. For a point to be located in skin, it must be in one of the following six subregions:

1. $z \geqq 93.8$;
2. $70 < z < 93.8$,
$$\left(\frac{x}{6.8}\right)^2 + \left(\frac{y}{9.8}\right)^2 \geqq 1 ;$$
3. $z \geqq 69.8$,
$$\left(\frac{x}{6.8}\right)^2 + \left(\frac{y}{9.8}\right)^2 \geqq 1 ;$$
4. $0 < z < 69.8$,
$$\left(\frac{x}{19.8}\right)^2 + \left(\frac{y}{9.8}\right)^2 \geqq 1 ;$$
5. $z \leqq -79.8$;
6. $-79.8 < z \leqq 0$,
$$\left(\frac{x}{19.796}\right)^2 + \left(\frac{y}{9.799}\right)^2 \geqq \left(\frac{98.485 + z}{98.485}\right)^2 .$$

The total volume of skin is 2677 cm^3.

[26] N. Mechanik, "Untersuchungen über des Gewicht des Knochenmarkes des Menschen," *Z. Anat. Entwicklungsgeschichte* 79(1), 58–99 (1926).

Spleen. – The spleen is defined by the ellipsoid

$$\left(\frac{x-11}{3.5}\right)^2+\left(\frac{y-3}{2}\right)^2+\left(\frac{z-37}{6}\right)^2 \leqq 1$$

and has a volume of 175.9 cm^3.

Testes. – The left testis, an ellipsoid, is given by

$$\left(\frac{x-1.3}{1.3}\right)^2+\left(\frac{y+2.2}{1.5}\right)^2+\left(\frac{z+2.3}{2.3}\right)^2 \leqq 1 .$$

The volume of both testes is 37.57 cm^3.

Thymus. – The thymus is formed by the ellipsoid

$$\left(\frac{x+2}{3}\right)^2+\left(\frac{y+6}{0.5}\right)^2+\left(\frac{z-60.5}{4}\right)^2 \leqq 1$$

and has a volume of 25.13 cm^3.

Thyroid. – The lobes of the thyroid lie between two concentric cylinders and are formed by a cutting surface. The inequalities for this organ are

$$x^2+(y+6)^2 \leqq (2.2)^2 ,$$

$$x^2+(y+6)^2 \geqq (1)^2 ,$$

$$y+6 \leqq 0 ,$$

$$70 \leqq z \leqq 75 ,$$

$$[(y+6)-1\times 1]^2 \geqq 2[x^2+(y+6)^2]T^2 ,$$

where

$$T=\frac{2(\sqrt{2-2})}{5}(z-70)+1 \text{ for } 0 \leqq z-70 \leqq \frac{5}{4},$$

$$=\frac{2(2-\sqrt{2})}{15}(z-70)+\frac{2\sqrt{2-1}}{3} \text{ for } \frac{5}{4}< z-70 \leqq 5 .$$

The volume is 19.89 cm^3.

Uterus. – The uterus is an ellipsoid cut by a plane and is given by

$$\left(\frac{x}{2.5}\right)^2+\left(\frac{y+2}{5}\right)^2+\left(\frac{z-14}{1.5}\right)^2 \leqq 1 ,$$

$$y \geqq -4.5 .$$

It has a volume of 66.27 cm^3.

A computer code has been written which takes a point (x, y, z) and applies the tests for each organ sequentially. For points distributed uniformly in the entire phantom, a CDC 1604 computer using this code can classify the points as to their organ location at an average rate of about 10,000 per minute.

Gamma Dose to Organs

Whole-Body Source. – A source of gamma photons uniformly distributed in the phantom was programmed for the computer. The first objective was to estimate the fraction of the emitted energy that would be absorbed in the phantom. Determination of dose to individual organs will be given later. Photons were given an initial energy E_0, and the energy they imparted in the phantom was recorded. This procedure was followed for seven different initial energies – 0.02, 0.05, 0.2, 0.5, 1.0, 2.0, and 4.0 Mev. There were 1000 photons generated at each energy.

The fractional energy absorption by the total body, which is defined as the ratio of the energy emitted per photon to the average energy absorbed by the total body per photon, was determined from the Monte Carlo data. These results are given in Fig. 25.9. One standard deviation for our data points is less than 1.6% of the mean. An interpolating curve passing through the data points permits the estimation of the fractional energy absorption at other energies. A large number of gamma-emitting radionuclides produce gamma photons with energies in the range 0.1 to 1 Mev, and for such photons the total-body fraction absorption is about 35%. At higher energies the mean free path is larger, permitting a larger percentage of such photons to escape from the phantom and resulting in a lower fractional absorption.

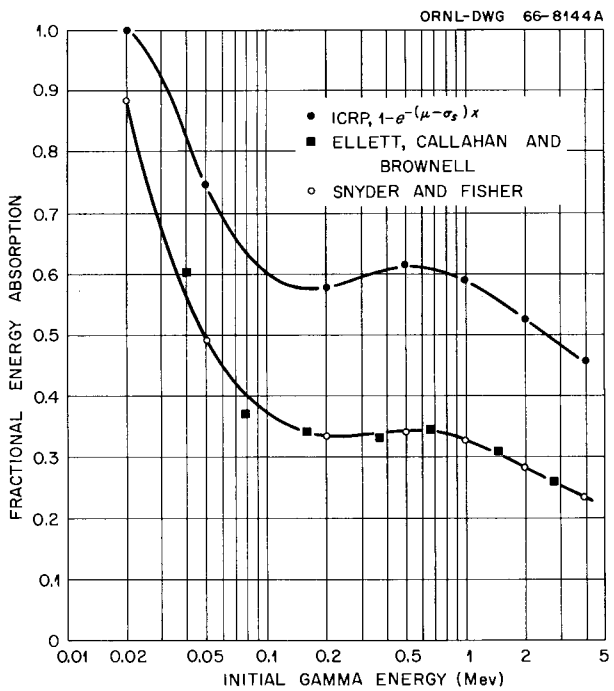

Fig. 25.9. Fractional Gamma Energy Absorption by the Total Body.

Toward lower photon energies, the photoelectric cross section rises steeply, producing an increasing fractional absorption which reaches about 90% at 0.02 Mev.

Also shown in Fig. 25.9 are the Monte Carlo results of Ellett, Callahan, and Brownell[27] for a source uniformly distributed in an ellipsoid. Although their phantom was an ellipsoid, its mass was nearly the same as the mass of the phantom used here, and the fractional absorptions are very similar to those predicted in this paper. The upper curve in Fig. 25.9 gives the fractional energy absorption predicted from the ICRP first-collision formula. In deriving this formula, three major assumptions were made. First, the organ or body is assumed to be spherical. Second, the entire organ or body burden is located at the center of the sphere. Third, a first-collision-dose calculation is then effected to obtain the formula giving the fractional energy absorption:

$$AF = 1 - e^{-(\mu - \sigma_s) r},$$

where r is the radius of the sphere (effective radius), μ is the total gamma cross section at E_0, and σ_s is the Compton scattering cross section at E_0.

It is evident from Fig. 25.9 that the ICRP formula gives a conservative estimate of the fractional absorption, since the Monte Carlo results are seen to be about 55% of those of the ICRP method at intermediate gamma energies.

With the source again uniformly distributed in the phantom, dose to 22 organs was determined. To obtain estimates of dose to individual organs with, at most, 10% statistics required the generation of a larger number of source photons than had been generated in the first case. This was done for initial photon energies of 0.05, 0.2, 0.5, and 1.0 Mev. The number of source photons produced at each energy was 20,000, 30,000, 30,000, and 40,000 respectively.

These results are presented graphically in Figs. 25.10 to 25.13 to permit interpolation. The source is distributed uniformly in the entire phantom, and the dose to various organs in rads per photon emitted by the source is given on the ordinate. The bars on the Monte Carlo data points represent one standard deviation on either side of the mean as estimated from the Monte Carlo calculation. When no bars are given, σ is less than 2%.

Organs located near the center of the phantom, such as the uterus and ovaries, receive a dose of about 1.5 times that of the total body. Most of the organs, however, receive a dose of 1.2 to 1.4 times that of the total body. Of the phantom's organs, the brain receives the lowest dose, 0.45 times that of the total body. This is followed closely by skin, with 0.55 times the body average.

Even with 40,000 initial photons, some organs do not receive a sufficient number of photon collisions to determine the dose received to within 10%. This may be due to the small size of the organ or to its distance from many source photons. An alternative to producing more source photons is to increase the volume in which dose is estimated. This latter procedure was followed. When the standard deviation of dose exceeded 10%, the dose in the arbitrary region(s) (Fig. 25.7) encompassing the organ was taken as the best available estimate of dose received by that organ. When this procedure was necessary, these dose estimates shown in the graphs bear the name of the organ followed by the word "region."

[27] W. H. Ellett, A. B. Callahan, and G. L. Brownell, *Brit. J. Radiol.* 38, 541–44 (1965).

The doses received by the group of organs listed in Fig. 25.13 varied little from each other. Rather than give the doses to each organ individually, the doses received by these organs will lie in the range between the dashed curves in Fig. 25.13.

It is possible to examine the doses received by the organs for very low-energy photons analytically, bypassing the Monte Carlo procedure. At low

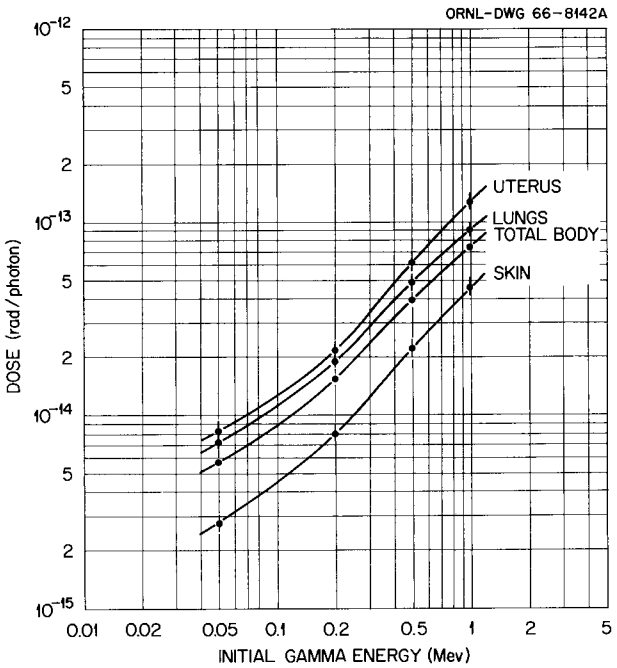

Fig. 25.10. Gamma Dose from a Source Uniformly Distributed in the Body.

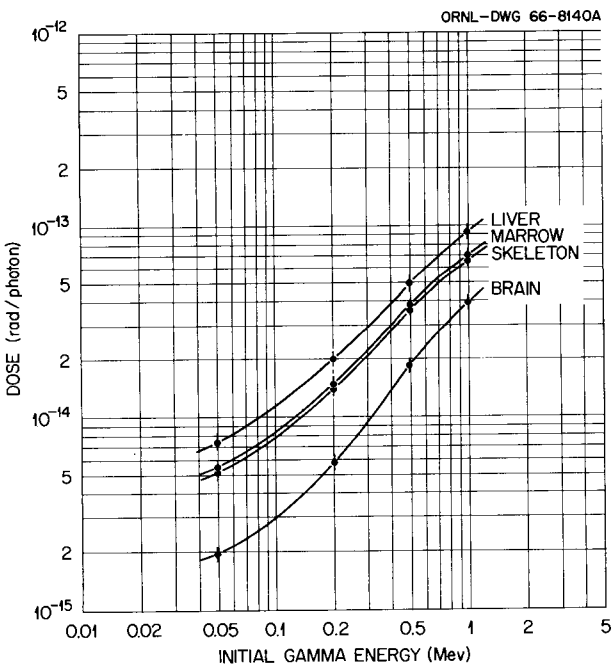

Fig. 25.11. Gamma Dose from a Source Uniformly Distributed in the Body.

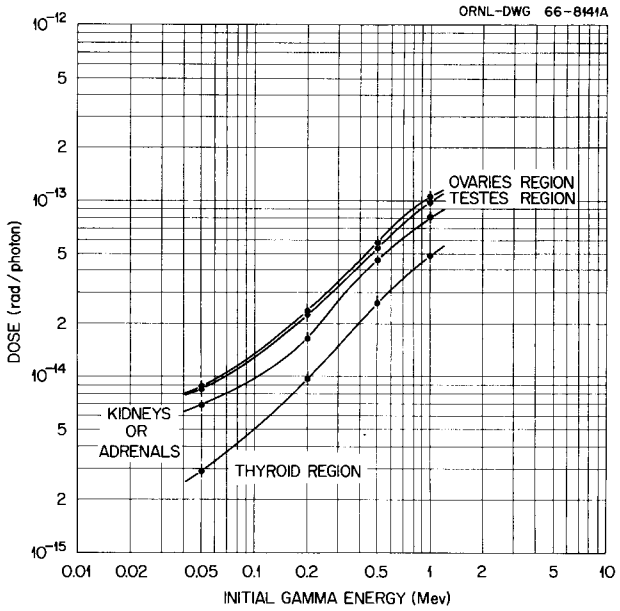

Fig. 25.12. Gamma Dose from a Source Uniformly Distributed in the Body.

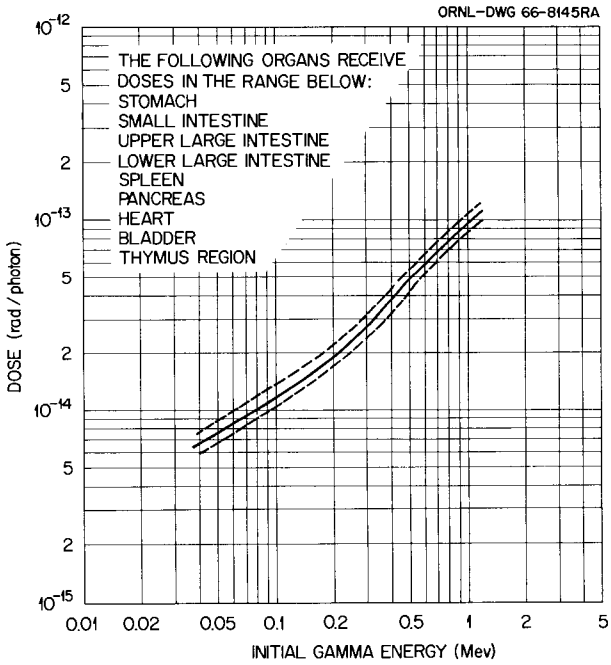

Fig. 25.13. Gamma Dose from a Source Uniformly Distributed in the Body.

photon energies the total cross section is composed almost entirely of that contributed by the photoelectric effect. In addition, the numerical value of this cross section becomes very large, resulting in a small range of the gamma photons before absorption.

If there is a homogeneous medium, infinite in extent, containing a source uniformly distributed throughout which is emitting gamma photons isotropically of energy E_0 Mev at the rate of N_0 per unit time per unit volume, then under steady-state conditions the energy emitted per unit time per unit volume will be equal to the energy absorbed per unit time per unit volume. The dose rate in rads per unit time in any region is then

$$D = \frac{N_0 E_0}{\rho} \, 1.6 \times 10^{-6} \, \frac{\text{erg}}{\text{Mev}} \, \frac{\text{g rad}}{100 \text{ erg}}$$

$$= 1.6 \times 10^{-8} \, \frac{N_0 E_0}{\rho} \, ,$$

where ρ is the density of the medium (g/cm^3). Suppose now that instead of an infinite medium, there is a finite volume of mass W_T grams. Also, suppose that the mean range of the photon is small compared with the dimensions of the volume, so that the result discussed above applies far from the surfaces in the interior with only a small error. If the source produces photons homogeneously distributed in this medium at the rate of n photons per unit time, then the normalized dose in rads per photon for any interior volume which is far from the boundary of the phantom as compared with the mean free path of the photon is

$$D_p = \frac{D}{n} = 1.6 \times 10^{-8} \, \frac{N_0 E_0}{n\rho} = 1.6 \times 10^{-8} \, \frac{E_0}{W_T} \, .$$

In the case of a gamma source in the total body, the dose to interior organs should asymptotically approach

$$D_p \text{ (rads/photon)} = 2.28 \times 10^{-13} \, E_0 \text{ (Mev)}$$

as the mean free path approaches zero. At 0.01 Mev and below, the mean free path of photons in tissue is less than 0.25 cm, and this formula should yield a more reliable result than could be obtained by Monte Carlo even with large photon sample sizes.

The above does not apply to organs located near the surface. Even in this case, however, one may obtain information as to the surface dose by examining a special case. Suppose that a medium, infinite in extent, is cut by a plane and one half of the medium is removed. The dose rate at the newly formed surface will be one-half of the equilibrium dose rate in the infinite medium, by symmetry. The normalized dose at such a surface of a large finite volume is, therefore,

$$D_{ps} = 0.8 \times 10^{-8} \, \frac{E_0}{W_T} \, .$$

Although the phantom has no such plane surface, the radius of curvature of the elliptical cylinder of the trunk is large compared with the mean free path of low-energy gamma photons. An approximate surface dose for a source distributed uniformly in the total body is, therefore,

$$D_{ps} \text{ (rads/photon)} = 1.14 \times 10^{-13} E_0 \text{ (Mev)} \, ,$$

$$E_0 \leqq 0.01 \text{ Mev} \, .$$

These limiting dose rates appear consistent with the Monte Carlo calculations at 0.02 Mev. The organs inside the rib cage of the trunk received doses within 10% of the predicted equilibrium dose, 4.56×10^{-15} rad/photon, while the skin of the trunk received a dose within 10% of the equilibrium surface dose.

Skeletal Source. – A source of gamma photons uniformly distributed in the skeletal region of the phantom was also simulated on the computer. This program was carried out for five gamma energies – 0.2, 0.5, 1.0, 2.0, and 4.0 Mev.

The fractional energy absorption by the skeleton is given in Fig. 25.14. The standard deviation of the data points is less than 2.5% of the mean. Although there is some variation of the absorbed fraction from 0.2 to 1.0 Mev, as shown in Fig. 25.14, an approximate value of 8% could be used over this energy range with little error. The Monte Carlo estimates given here are about a factor of 2 lower than those given by the first-collision, effective-radius method of the ICRP.

In the energy range under consideration, 0.2 to 4.0 Mev, the gamma cross sections for tissue are very similar to those for bone within several percent. Therefore, there should be little error introduced by the use of a tissue phantom, except for the fact that bone is denser than tissue.

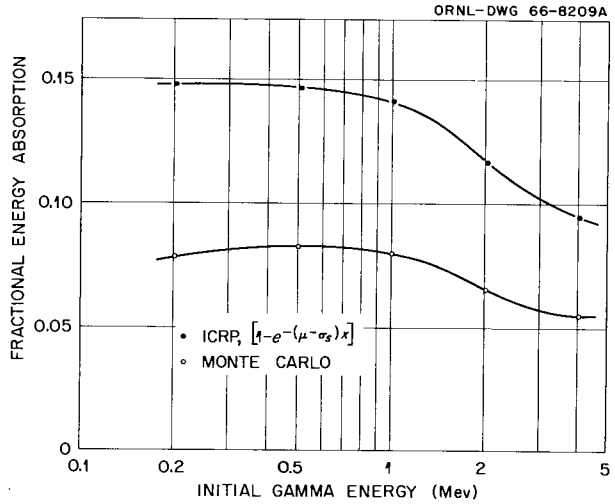

Fig. 25.14. Fractional Gamma Energy Absorption by the Skeleton.

The photoelectric cross section for bone rises steeply with decreasing gamma energy, and although the skeleton is not a compact organ, gamma-ray absorption will be essentially complete at 0.01 Mev and below since the mean free path of these photons will be less than 0.05 cm. In order to obtain a rough estimate for the fractional energy absorption for photons with energies between 0.01 and 0.2 Mev, the entire phantom was considered to be bone. The material in the entire phantom was given the cross section for bone. With the source in bone, the fractional absorption should be more nearly correct for the skeleton than that obtained by using the tissue phantom. However, these results will still be lower than the true values by an undetermined amount for the following reasons. Photons that remain in the skeleton of the phantom will contribute the same amount of energy that a real photon would. However, once a photon escapes from the phantom's skeleton, it will still find itself in a strongly absorbing medium and therefore have a smaller probability of returning to the skeleton than a photon would have if it escaped from skeleton into tissue. A somewhat smaller estimate of the absorbed fraction for the skeleton is obtained, therefore, with the bone phantom at low energies than occurs in the actual situation. With the bone phantom, the fractional energy absorption for the skeleton was 0.81 at 0.02 Mev and 0.41 at 0.05 Mev.

The dose rate to other organs using the skeletal source and the tissue phantom and for energies between 0.2 and 4.0 Mev is given in Figs. 25.15 to 25.18. The notation on these graphs is the same as that described for the total-body source. As expected, the skeleton was the organ with the highest dose. Marrow appears to receive a slightly greater dose than the skeleton but not significantly so. This is because the bones that receive the higher doses happen to contain a greater portion of the marrow. There are compensating factors which would tend to lower the marrow dose, but they are not represented in the model. Marrow is not so uniformly distributed in bone as has been assumed in the model. For a radionuclide that localizes in bone, the marrow should not contain as great a concentration as the bone. This is not the case with the model. Consideration of these factors as well as the Monte Carlo results leads one to believe that the average marrow and average skeletal gamma doses are not very different. The dose estimates to many of the organs or regions were very similar and are not shown separately.

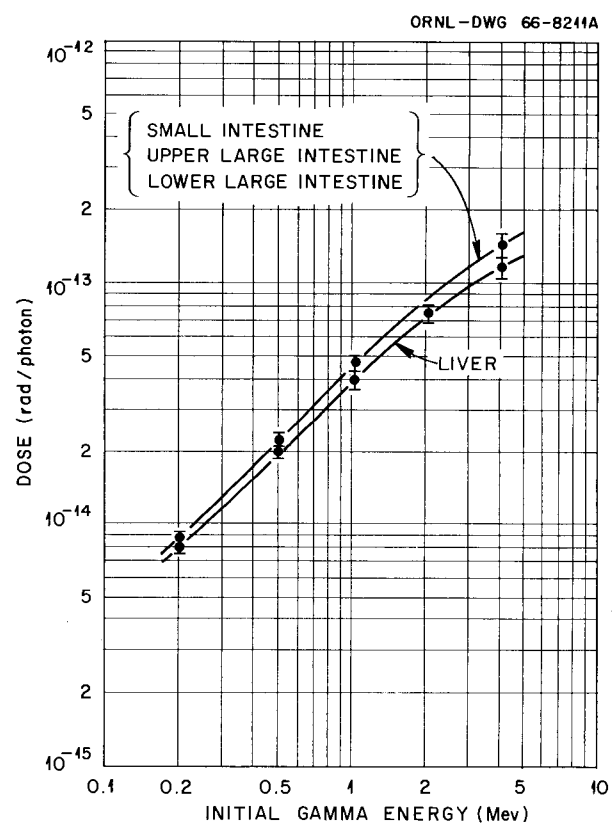

Fig. 25.15. Dose from a Source Uniformly Distributed in the Skeleton.

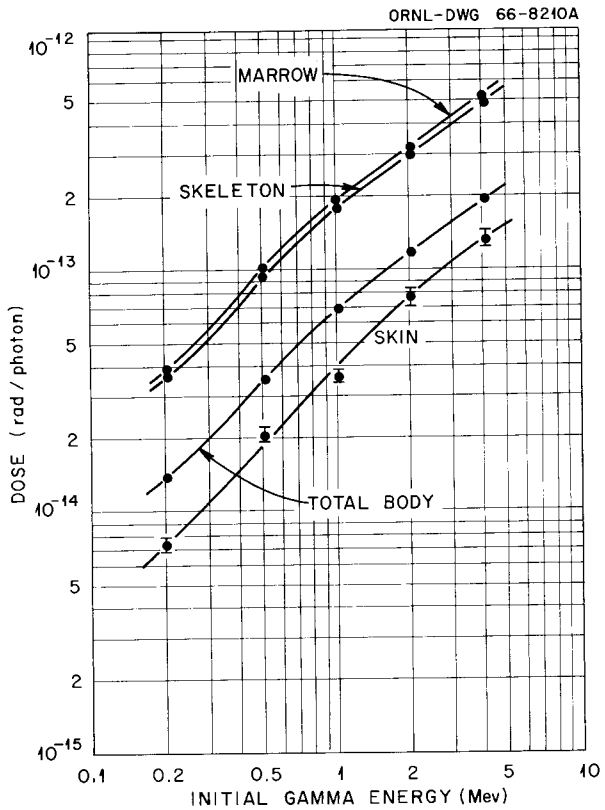

Fig. 25.16. Dose from a Source Uniformly Distributed in the Skeleton.

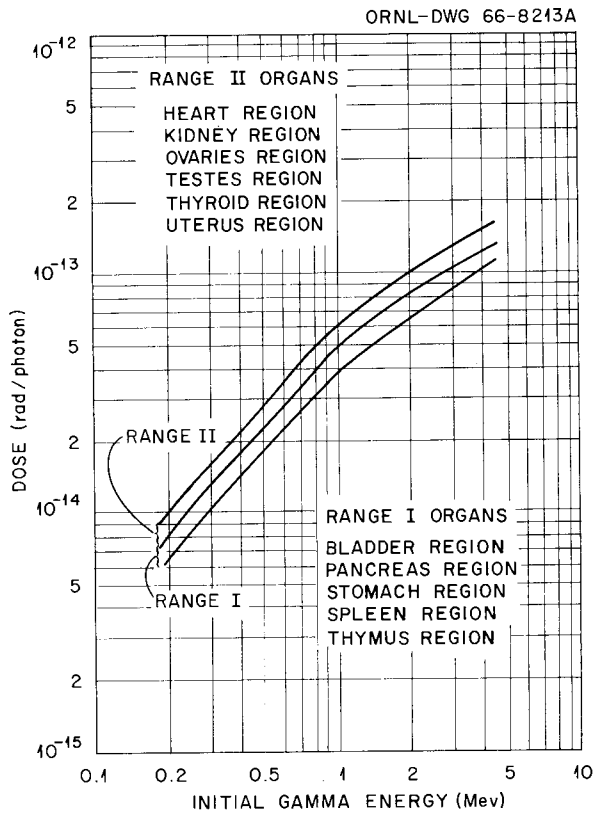

Fig. 25.18. Dose from a Source Uniformly Distributed in the Skeleton.

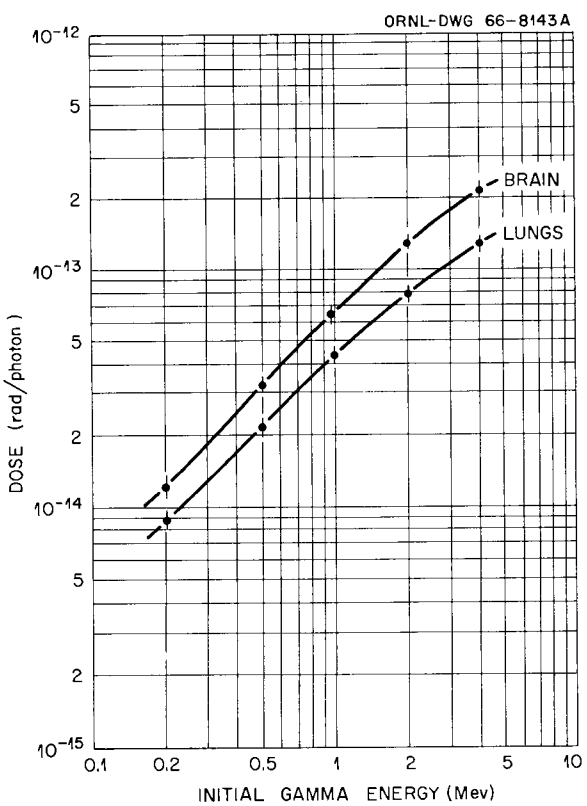

Fig. 25.17. Dose from a Source Uniformly Distributed in the Skeleton.

The doses received by organs listed in the group called range I in Fig. 25.18 received doses between the lower curve and the middle curve in the graph. Similar remarks apply to the organs of range II.

For energies below 0.01 Mev, where absorption is nearly complete, the skeleton would receive a dose in rads per photon of about $1.6 \times 10^{-12} E_0$, where E_0 is the initial gamma energy in Mev. An estimate of dose to the various bones of the skeleton also was obtained from the Monte Carlo code. The part of the skeleton receiving the highest dose was the leg bone, while that receiving the

lowest was rib. For energies between 0.2 and 4.0 Mev, the ratio of the dose in rads per photon of a skeletal part to that of the entire skeleton was formed. These ratios are approximately as follows:

Leg bones/skeleton	$\approx$ 1.4
Spine/skeleton	$\approx$ 1.2
Pelvis/skeleton	$\approx$ 0.8
Arm bones/skeleton	$\approx$ 0.8
Skull/skeleton	$\approx$ 0.6
Ribs/skeleton	$\approx$ 0.5

Conclusion

It appears that a Monte Carlo method of estimating organ doses is feasible under certain conditions. Anatomical differences such as variation of body and organ size have been neglected. Doses have been determined to fixed organ-similar regions of a homogeneous tissue phantom. This gives results that may be extrapolated to many real situations. This paper has examined the dose to organs from gamma sources located in the total body and in the skeleton, although external as well as various other internal sources may be used in conjunction with the Monte Carlo code and phantom.

Acknowledgments

Appreciation is expressed to A. M. Craig, G. G. Warner, and R. T. Boughner of the ORNL Mathematics Division for the programming and computer operations.

THE VARIATION OF DOSE IN MAN FROM EXPOSURE TO A POINT SOURCE OF GAMMA RAYS

W. S. Snyder

A Monte-Carlo-type code has been developed at ORNL which permits one to estimate dose in tissue phantoms for a wide variety of exposure situations. For this paper the code has been used to study the distribution of dose in a homogeneous phantom which has approximately the size and shape of an adult man exposed to a point source of monoenergetic photons.

The trunk of the phantom is taken as a right elliptical cylinder with a height of 70 cm and with semiaxes of the elliptical base as 20 cm and 10 cm (see Fig. 25.19). The arms are considered to be held at the sides and thus are included as part of the above cylinder. The legs are combined to form a truncated elliptical cone, and the head and neck together form a smaller elliptical cylinder. This phantom has about the same masses and dimensions as one designed by Hayes and Brucer[28] and is considered to consist of H, C, N, and O in the proportions given for "Standard Man."[29] Results are presented for the point source positioned directly in front of the phantom at shoulder height or opposite the midpoint of the trunk, and the distance from the midline of the phantom to the source is taken as 1 or 2 m. These four positions, designated *a*, *b*, c, and *d*, are shown in Fig. 25.19. The photon energies used are 1.0, 0.5, 0.15, and 0.07 Mev.

A photon is considered to originate at the source position, the direction being chosen from an isotropic distribution, and the coordinates of the point at which the photon strikes the cylinder are computed. This point marks the beginning of what might be termed the "history" of that photon. Successive collision sites are computed, giving the photon the correct probability for the various alternatives that physical theory predicts as being possible. Thus the distances between successive interaction sites, the interaction type (photoelectric effect, Compton scattering, or pair production), and scattering angle are determined in accordance with the values of the cross sections. Each history, then, constitutes a possible path for a photon, and each history is computed in an unbiased manner according to known physical laws. In a large collection of independently calculated histories, the various interactions and distances between interaction sites should be distributed as theory predicts.

The cross sections are taken from *NBS Circular* **583** and its supplement[30] and are programmed on

[28] R. L. Hayes and M. Brucer, *Intern. J. Appl. Radiation Isotopes* **9**, 113–18 (1960).

[29] *Protection Against Neutron Radiation up to 30 Million Electron Volts, NBS Handbook* **63**, p. 8, U.S. Dept. of Commerce, NBS, Nov. 22, 1957.

[30] G. W. Grodstein, *X-Ray Attenuation Coefficients for 10 keV to 100 MeV, NBS Circular* **583**, 1957; and R. T. McGinnis, *Supplement to NBS Circular 583*, 1959.

ORNL-DWG 66-851

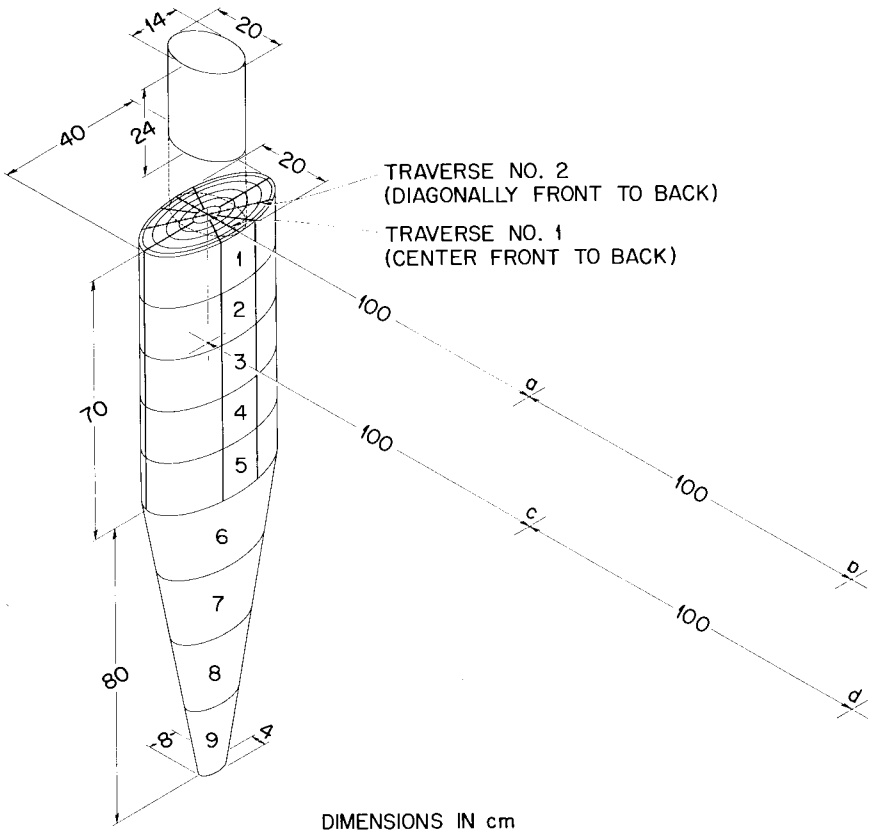

e Regions.

Fig. 25.19. Phantom Dimensions, Source Positions, and Dose Regions.

a separate subroutine. The energy scale is divided into major regions, each corresponding to a decrease of the energy by one-half. Values of the cross sections are listed on magnetic tape at 64 energy values intercalated in each such major region. The machine uses the cross sections corresponding to the nearest listed energy on the magnetic tape. Only the cross sections for the photoelectric effect, pair production, and total cross section are listed, the cross section for Compton scattering being obtained by subtraction.

The trunk region of the phantom is divided into 155 subregions by four equispaced planes perpendicular to the axis of the cylinder, three axial planes making angles of 60° with each other, and five surfaces each of which forms an elliptical cylinder coaxial with the axis of the phantom. The region within the smallest elliptical cylinder was not subdivided by the axial planes in order to improve the statistics on the dose estimates in this region (see Fig. 25.19). The volume elements nearest the surface have a thickness of 1 cm, and the dose in these volume elements may be expected to approximate the reading of a dosimeter exposed on that portion of the surface of the body. These volume elements must be chosen to be large enough so that a significant sample of interactions will occur in the volume to give an acceptably low standard deviation.

The leg region of the phantom is divided into four subregions by three equispaced planes perpendicular to the axis of the cone. The head and neck section, simulated by the smaller elliptical cylinder, is not subdivided.

When an interaction occurs within any one of the volume elements, the energy absorbed in the volume (in Mev) is estimated from the formula

$$E_{\text{absorbed}} = [\sigma_{PE}E_B + \sigma_p(E_B - 1.02) + (\sigma_T - \sigma_{PE} - \sigma_p)E_C]/\sigma_T ,$$

where

σ_T = total cross section,

σ_{PE} = cross section for the photoelectric effect,

σ_p = cross section for pair production,

E_B = energy of the photon before the interaction,

E_C = energy absorbed as a result of a Compton scattering.

The energy absorbed is accumulated for each volume element of the phantom.

When pair production occurs, the positron and an electron are annihilated locally and two photons are released, each having an energy of 0.511 Mev. Photons produced in this way are followed independently, thus producing additional histories. When a photon history has been completed, the total energy contributed to each box by both the parent and the daughter photons, as well as the square of these energies, is accumulated separately. This makes it possible to estimate a variance or standard deviation for the mean energy deposited in each volume element and hence for the average dose in that volume element.

The results obtained are presented in Figs. 25.20 to 25.25. For the trunk section, results are shown graphically for volume elements along two traverses in each layer, one along the minor axis of the elliptical trunk, front to back (traverse 1), and the other running diagonally from front to back (traverse 2) (see Fig. 25.19). Because of the symmetry of the situation, the average dose in any volume element of the trunk can be found from the values given for these traverses. The average dose in the cylinder simulating the head and neck region is shown on the graphs for traverse 1 at the 10-cm position. Results for the leg regions are not presented graphically but are given in a table at the top of the figures. In six cases (E = 0.15

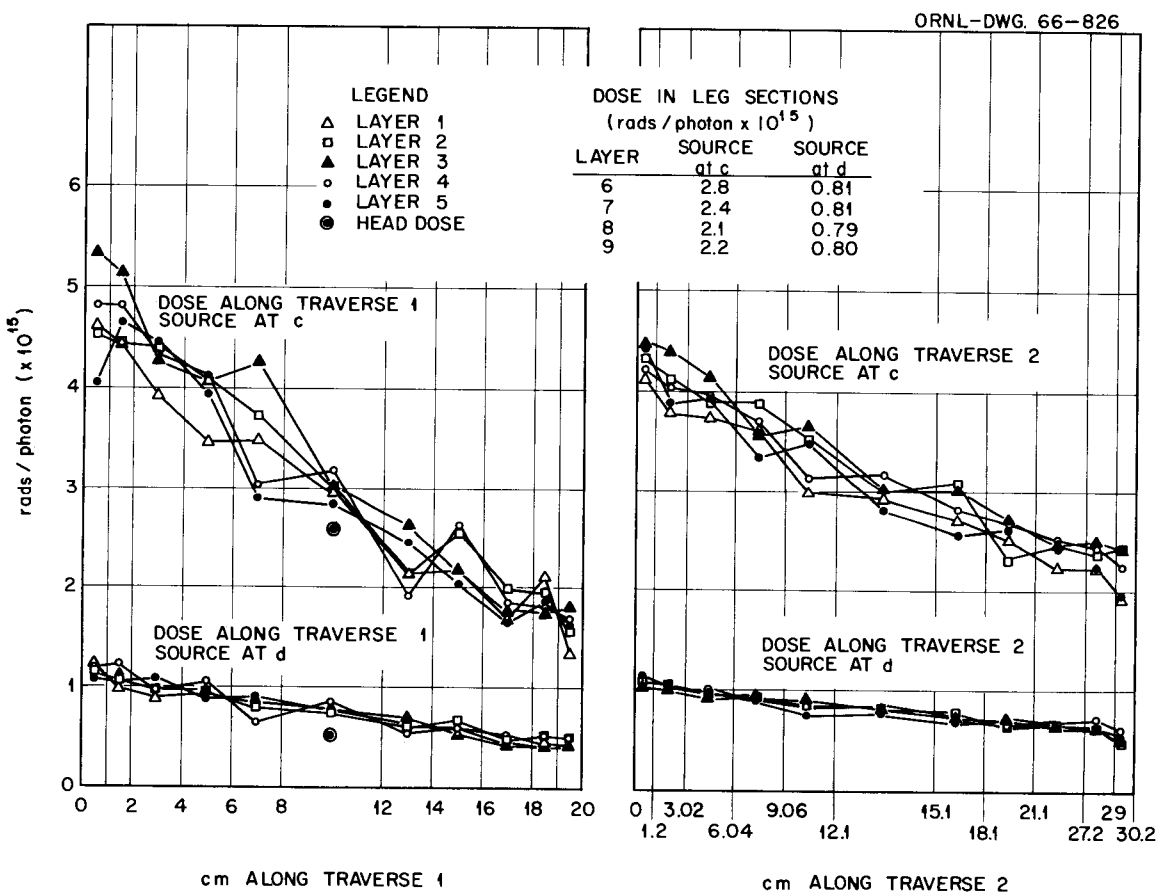

Fig. 25.20. Distribution of Dose in a Tissue Phantom from a Point Source of Photons at Positions *c* and *d*, Energy 1 Mev.

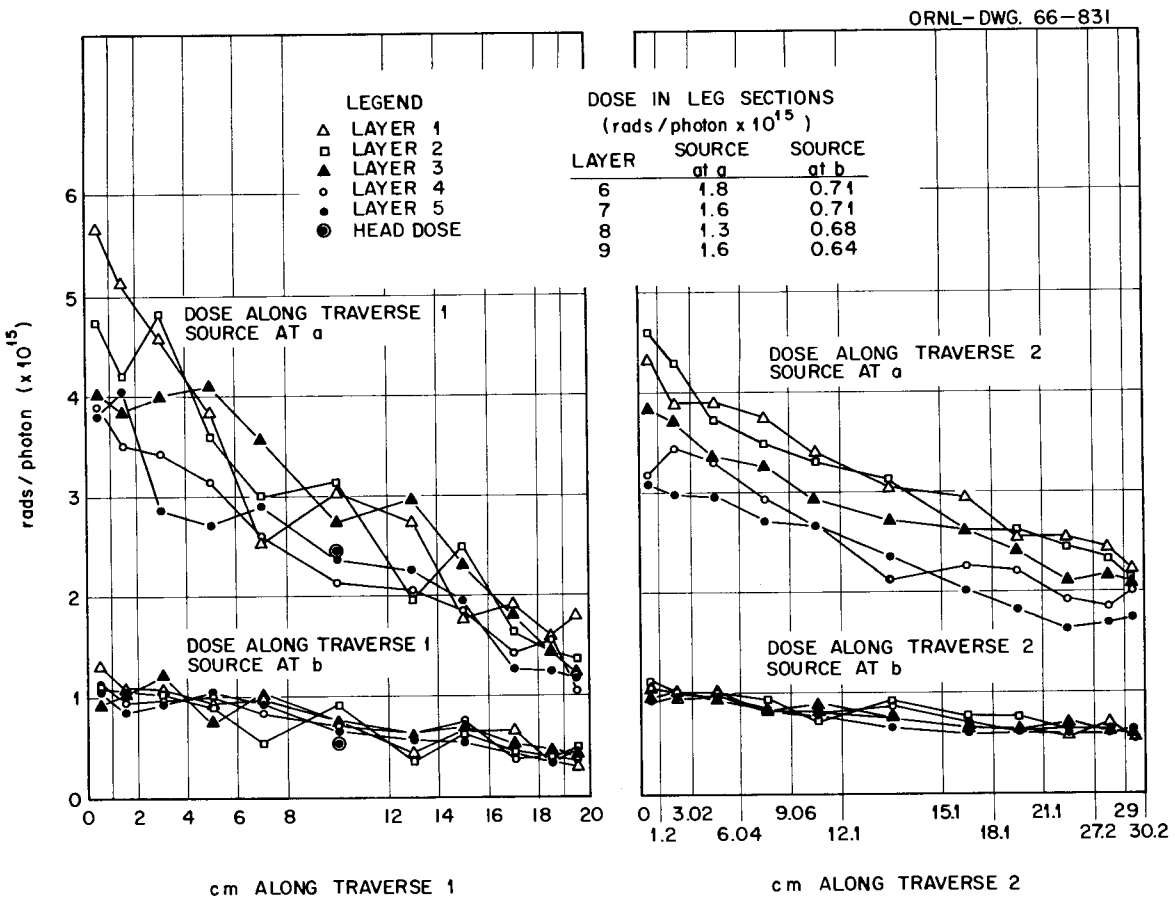

Fig. 25.21. Distribution of Dose in a Tissue Phantom from a Point Source of Photons at Positions *a* and *b*, Energy 1 Mev.

and 1 Mev, source at positions c and *d*; and $E = 0.5$ Mev, source at positions *b* and *d*), 100,000 photons were taken as source; in all other cases 40,000 photons were used. The coefficient of variation (standard deviation expressed as a percentage of the mean) never exceeds 20% for the 40,000 sources nor 11% for the 100,000 sources, and it is much less in the great majority of the volume elements.

The results with the source in positions *b* and *d*, that is, at 2 m from the central axis of the trunk, show less variation from one layer to another than do the results with the source in positions *a* and c. Plausibly, this is due to the fact that the solid angle subtended by similarly placed volume elements in the different layers varies less from one layer to another when the source is 2 m distant than when it is only 1 m distant. Generally, doses to volume elements in the layer at the same height as the source will be higher than at corresponding positions in other layers. However, the statistical fluctuations of the data are so large that one cannot make any very precise interpretation. It is evident that in all cases there is a considerable decrease in dose with distance away from the irradiated surface. In very approximate numbers, the dose to the volume elements near the front exceeds the dose to the volume elements near the back by a factor of about 3 when the source energy is 1 Mev, and the factor increases as the source energy decreases, becoming about a factor of 10 when the source energy is 0.07 Mev. The dose recorded by a film badge might be incorrect by factors of these magnitudes. The dose at corresponding positions varies much less from layer to layer of the trunk section than with depth below the irradiated surface. The variation of dose along traverse 2 is always less than the variation along traverse 1, as would be expected.

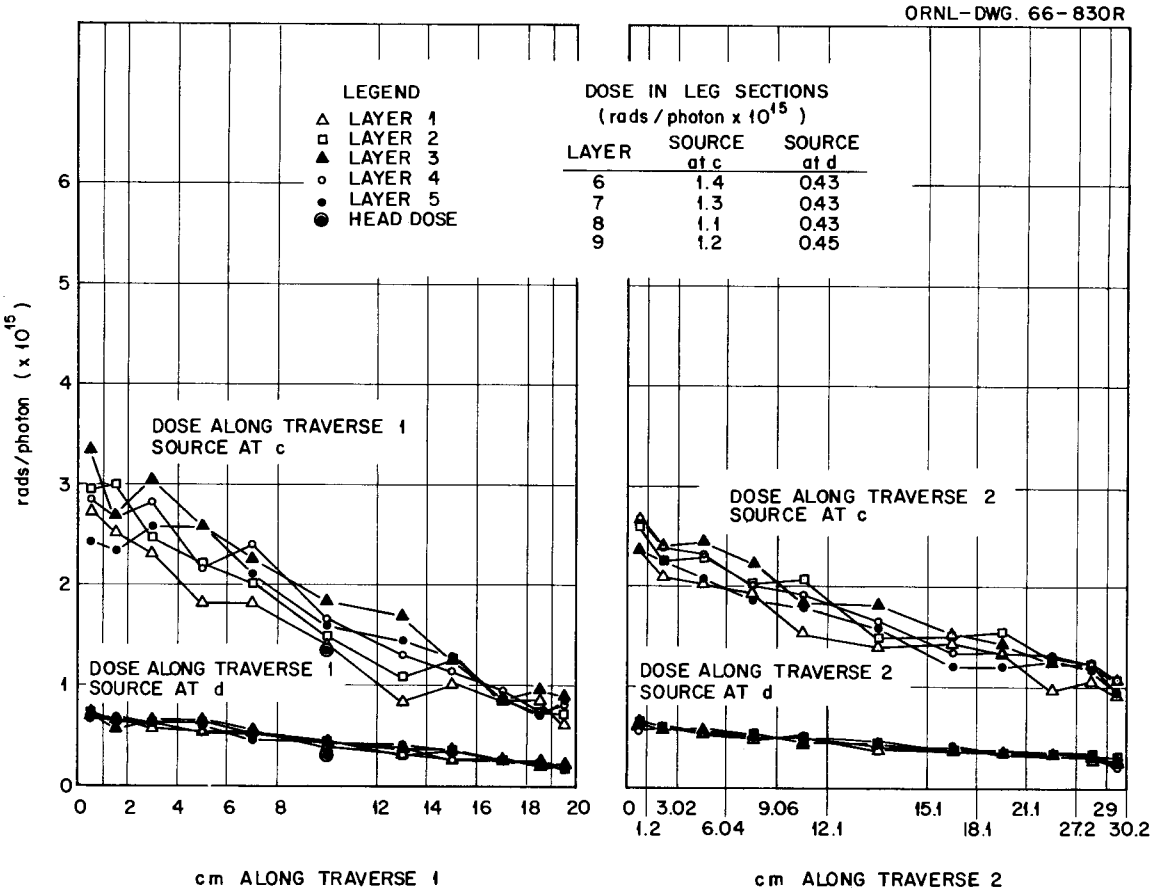

Fig. 25.22. Distribution of Dose in a Tissue Phantom from a Point Source of Photons at Positions c and *d*, Energy 0.5 Mev.

The average dose in the head region, as well as the average dose in the leg regions, is generally slightly lower than the dose to the central region of the trunk. The dose in the leg region tends to decrease, as would be expected, when the layers are farther from the source.

The results obtained in this study have been compared, insofar as possible, with the results of some other studies. Perhaps the closest check is with a study by Jones,[31] who made measurements of dose on and within a phantom of body size from point sources of photons. He reported the dose only as normalized to a "film badge dose" or to an "air dose," and thus only ratios of doses can be compared. As shown in Fig. 25.26, the data obtained in the present study do not agree very closely with those of Jones; however, there is qualitative agreement. The difference may be plausibly accounted for by the experimental and statistical errors and by the fact that his phantom included a complete set of bones. It appears that the presence of the skeleton significantly alters the dose pattern within the body.

It is planned to extend this study to include more energies and other source positions, such as at the side, on the floor, and above the phantom.

AN AGE-DEPENDENT MODEL FOR THE BODILY RETENTION OF CESIUM

H. L. Fisher, Jr. W. S. Snyder

The retention of radioelements by humans was initially determined for the adult since the pro-

[31] A. R. Jones, *Measurement of the Dose Absorbed in Various Organs as a Function of the External Gamma Ray Exposure*, AECL-2240 (October 1964).

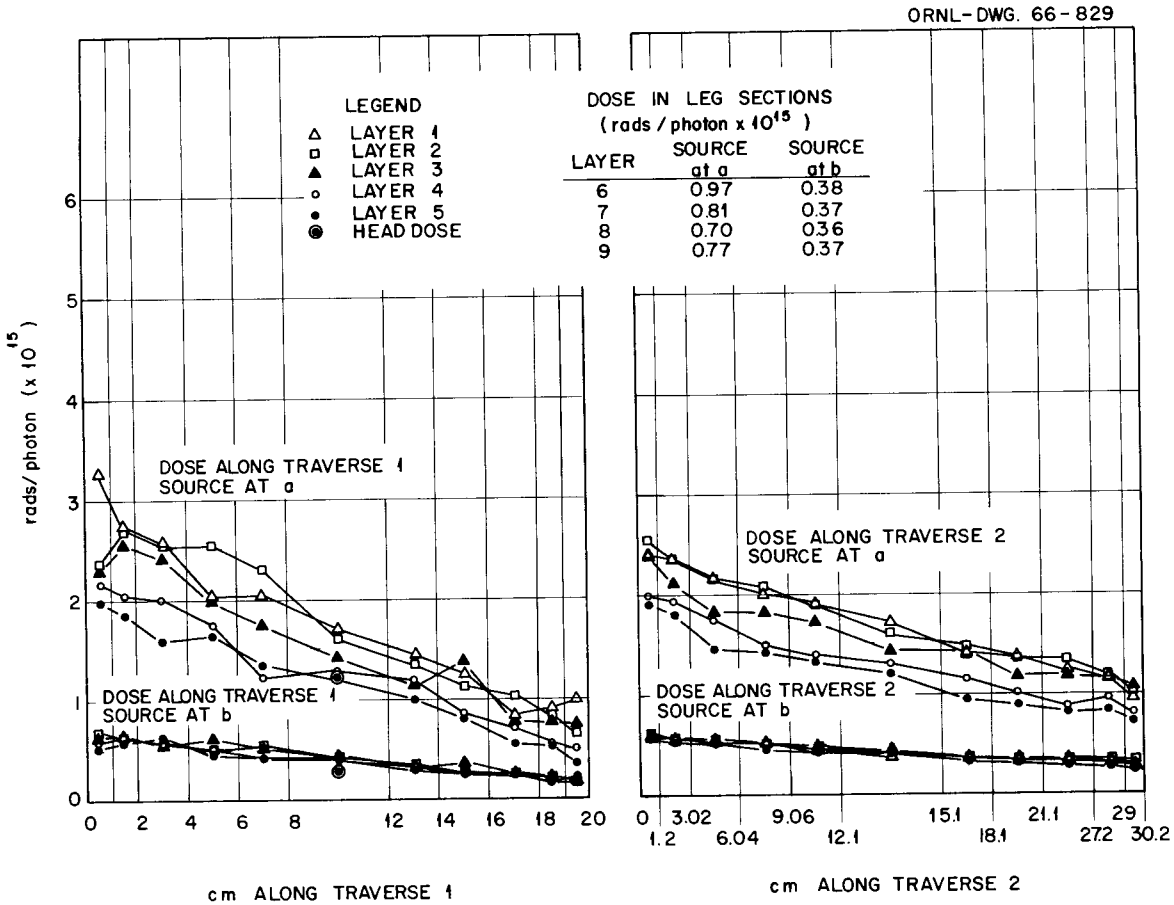

Fig. 25.23. Distribution of Dose in a Tissue Phantom from a Point Source of Photons at Positions *a* and *b*, Energy 0.5 Mev.

tection of radiation workers was a problem of paramount importance and also because more data from accident cases as well as from planned experiments had accumulated for the adult than for individuals of other ages. However, as data accumulated, it was apparent that the retention pattern of a radioelement might vary greatly with age. This appears to be the case for cesium. It is the purpose of this paper to present one theoretical age-dependent compartmental model and apply it to the retention of cesium.

Richmond *et al.*[32] used a two-exponential retention function to fit the observed retention of ^{137}Cs by normal adult males for a period of 550 days after a single oral intake. Except for the first ten days after intake, the second exponential is dominant, contributing more than 99% to the total area under the retention function. Therefore, for purposes of dose estimation or equilibrium level estimation in the adult, the retention of cesium may be considered to be given by a single exponential.

It is well known that a single compartment with an elimination rate proportional to its contents is described by

$$\frac{d}{dt}A(t) = -\lambda\, A(t)\ , \tag{1}$$

where $A(t)$ is the amount of material in the compartment and λ is the decay constant. This equation has a single exponential as its solution. The retention of cesium by the adult apparently may be considered to be retained in a single homogeneous compartment and eliminated in the manner just described.

[32]C. R. Richmond, J. E. Furchner, and W. H. Langham, *Health Phys.* 8(3), 201 (1962).

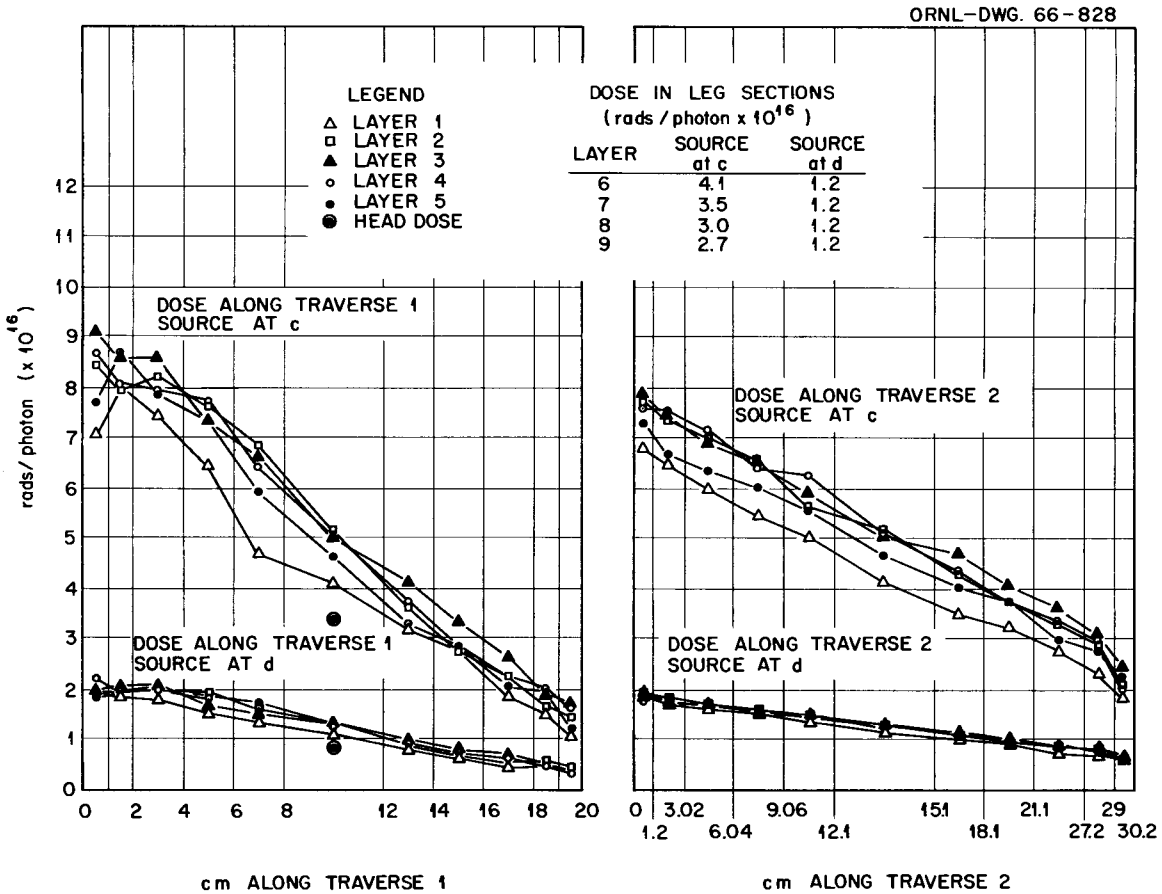

Fig. 25.24. Distribution of Dose in a Tissue Phantom from a Point Source of Photons at Positions *c* and *d*, Energy 0.15 Mev.

To introduce the age dependence into the retention function, consider a single compartment with a definite size or volume, but let the size of this compartment vary with time. In order to write a differential equation governing the kinetics of this compartment, it is necessary to make one assumption. Let us assume that the rate of change of a quantity of material introduced into the compartment is proportional to the concentration of the material in the compartment. The kinetic equation is then

$$\frac{d}{dt}A(t) = -m\frac{A(t)}{W(t)}, \tag{2}$$

where $W(t)$ is the volume of the compartment and m is the constant of proportionality.

There is now the practical problem of determining what should be used as a measure of compartment size. Many different measures might be proposed, for example, weight, muscle mass, body water, or potassium content. Since cesium is rather uniformly distributed throughout the body, let us take body mass to be a measure of compartment size for cesium. This is not to say that mass has physiological significance in cesium retention. What should be inferred is that the true compartmental volume for cesium is assumed to be proportional to body mass.

Although Eq. (2) may be applied directly, there is a simplification that can be made for ^{137}Cs retention. If at time t the change in the compartmental half-life with time is small compared with this half-life, the compartment may be considered to have a constant half-life for material introduced into the compartment at time t. Therefore,

$$T_{1/2} = \frac{W(t)\ \ln 2}{m}. \tag{3}$$

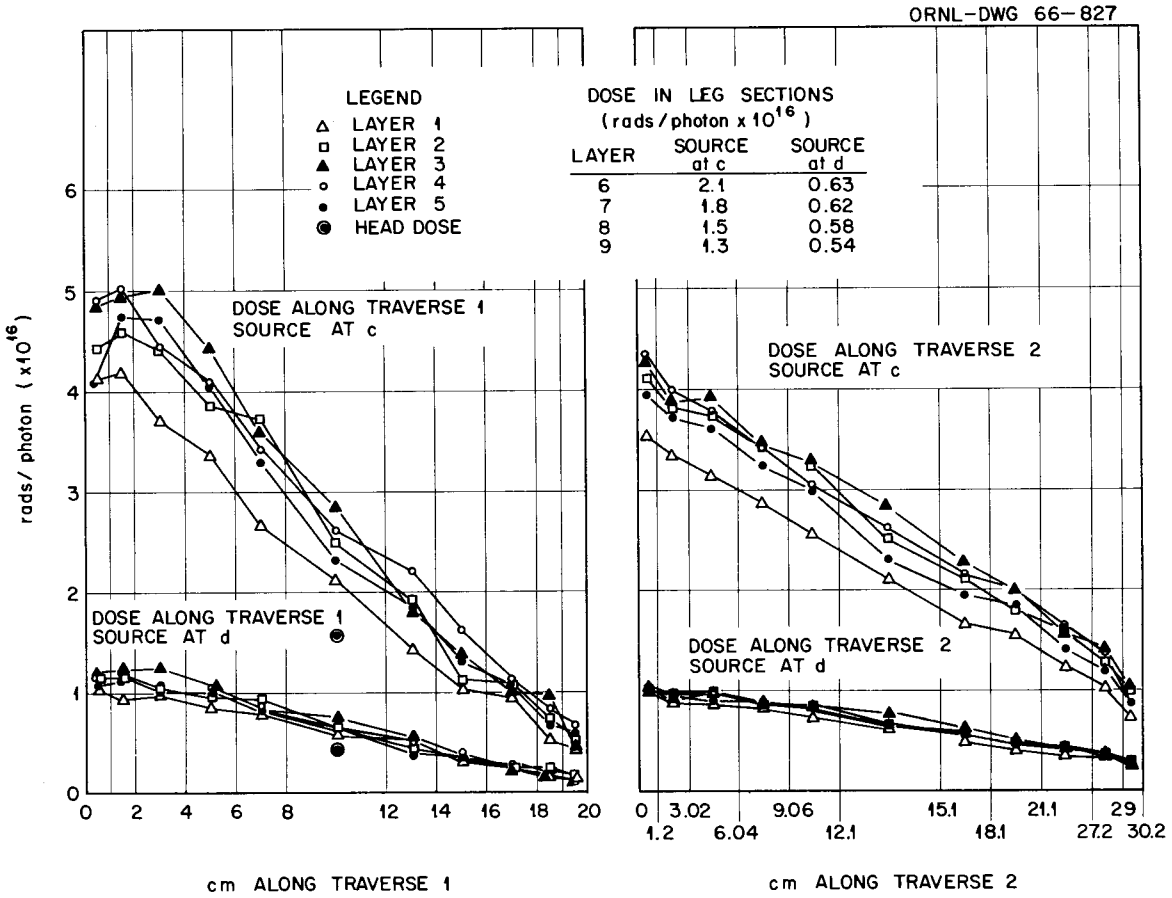

Fig. 25.25. Distribution of Dose in a Tissue Phantom from a Point Source of Photons at Positions c and *d*, Energy 0.07 Mev.

After this simplification, it follows that for a single intake at any time, the elimination is exponential, with a half-life determinable from the volume of the compartment at that time.

If $W(t)$ is a known function, then after determining the proportionality constant m, the time dependence of the compartmental half-life will be determined. The constant m is determined by using the experimentally determined biological half-life for cesium in the adult male and his body mass.

The adult values for body weight and half-life of cesium are used since they have been the topic of many more experiments and are known more precisely. The mass of the adult male is taken to be 70 kg. Although there is a wide range of biological half-times reported in the literature for cesium in adult males, a representative value of 100 days has been chosen. Having determined m from Eq. (2), the relationship between biological half-life for cesium and body mass is given by

$$T_{1/2}(t) = 1.43W(t) . \tag{4}$$

This equation was not derived by considering individuals but was determined for the average of populations of various body masses. The equation should only be used to determine the average biological half-life of a group of grossly normal individuals. Such parameters as percent body fat, environmental temperature, or work activity may greatly influence the biological half-life. However, a group of people of the same age chosen randomly should have an average biological half-life for cesium given by Eq. (4).

The growth curve for body mass from infancy to adulthood is given in Fig. 25.27. The curve for

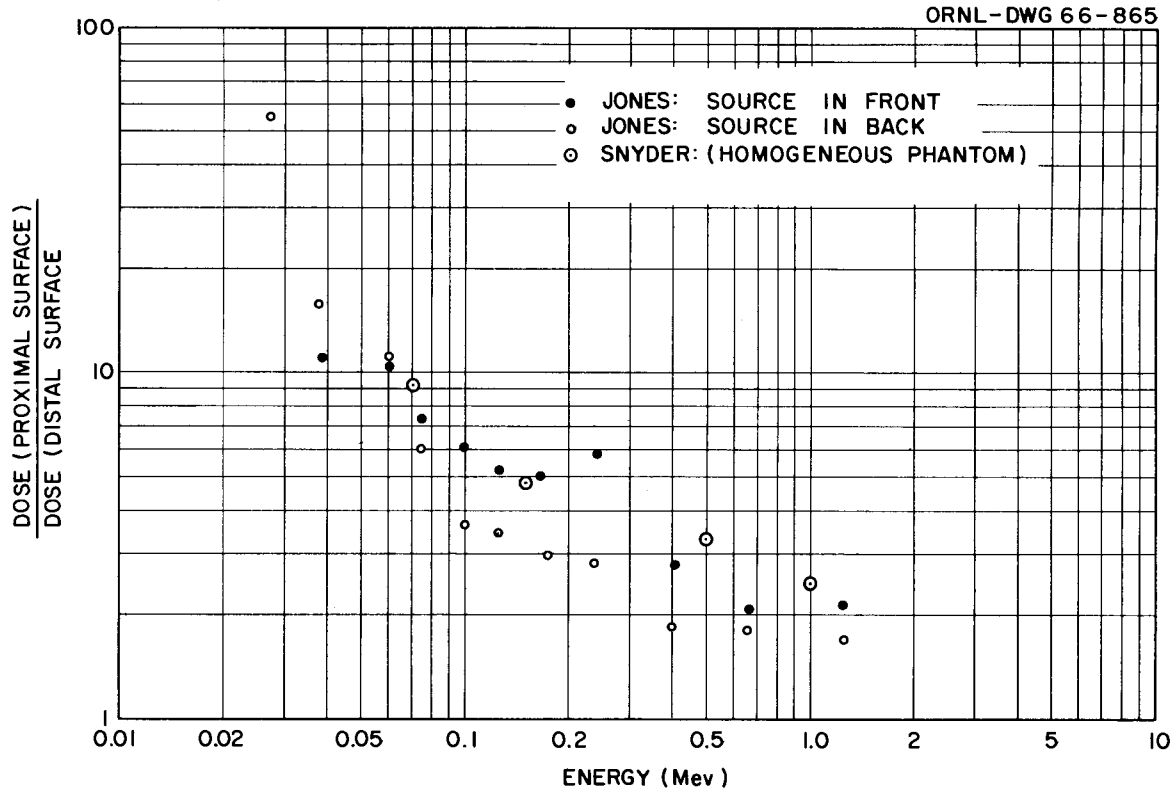

Fig. 25.26. Ratio of Doses on Proximal and Distal Surfaces of a Homogeneous Phantom (Calculated) and of a Phantom with a Skeleton (Experimental).

males is that given by Mitchell;[33] the one for females is taken from ref. 34. Using these curves, the biological half-life for cesium was determined.

In Fig. 25.28 is a comparison of the biological half-life of cesium predicted by the model with some experimental results. The model predicts a cesium biological half-life for the newborn of about 5 days. From this value it increases to the assumed value of 100 days for the adult. Boni[35] has determined the cesium biological half-life of humans from five years of age through adulthood. His method is one in which the body burden of fallout ^{137}Cs, as well as the urinary excretion, is determined. From the single-exponential model and assuming equilibrium conditions, the biological half-life may be determined. For the adult values determined in this way, the range of values about the mean is ±50%. The model given here predicts a half-life about twice as large as Boni's results in the five-to-ten-year age group. However, McGraw[36] has surveyed the literature and given a representative curve for the average half-life. His curve is quite close to the model in the five-to-ten-year age group. It should be pointed out that the variation of the experimental values about McGraw's curve is quite large.

By applying Eq. (4) and using the body weight for females, the half-life of cesium in females was determined and is given in Fig. 25.29. Boni also has measured the biological half-life of cesium in females. As shown, the model predicts a half-life for females of about twice that observed by Boni.

Using measurements of stable cesium in tissue, the daily intake of cesium, and the single-exponential model under equilibrium conditions, Snyder

[33] H. H. Mitchell *et al.*, *J. Biol. Chem.* **158**, 625 (1945).

[34] W. S. Spector, *Handbook of Biological Data*, p. 180, W. B. Saunders, Philadelphia, 1956.

[35] A. L. Boni, "Variations in the Retention and Excretion of ^{137}Cs with Age and Sex," presented at Health Physics Society Meeting, 1966.

[36] T. F. McGraw, *Radiol. Health Data* **6**(12), 711 (December 1965).

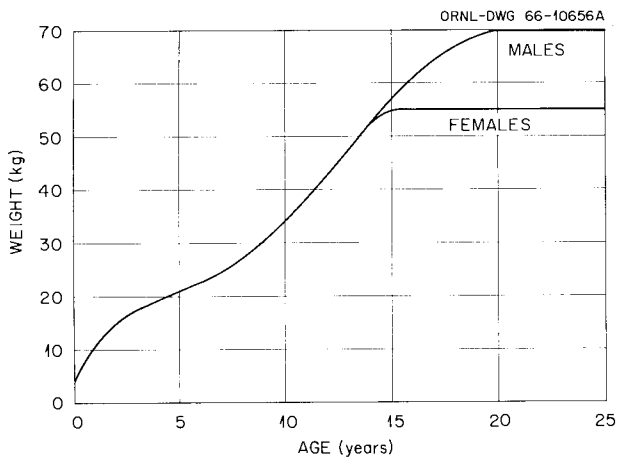

Fig. 25.27. Average Body Weight of Males and Females.

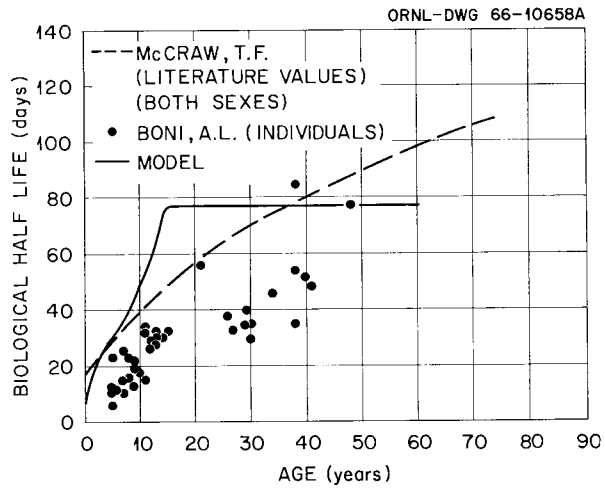

Fig. 25.29. Biological Half-Life of ^{137}Cs in Females.

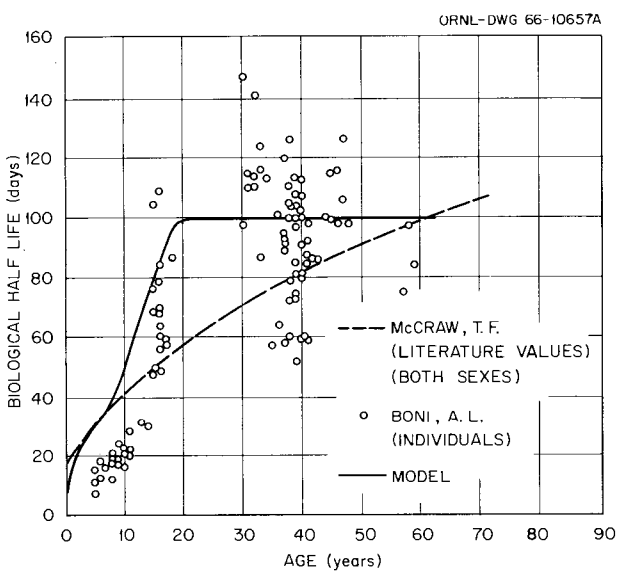

Fig. 25.28. Biological Half-Life of ^{137}Cs in Males.

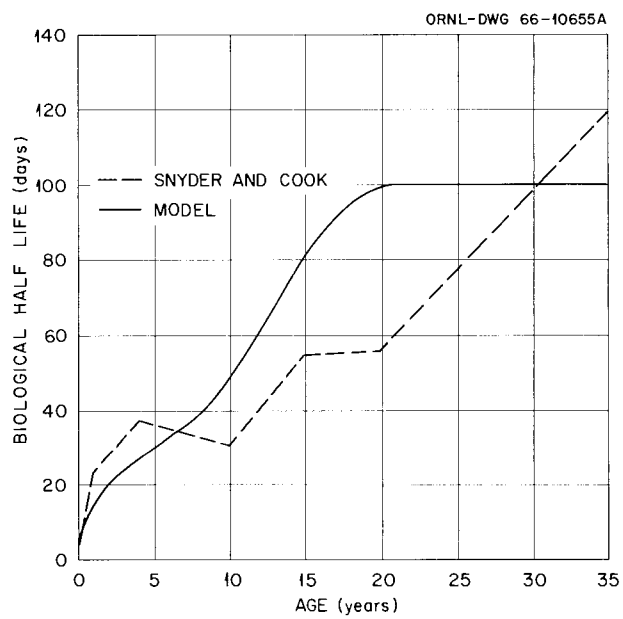

Fig. 25.30. Variation of the Biological Half-Life of Cesium with Age.

and Cook have produced estimates of the biological half-life with age, which are given in Fig. 25.30. During the first five years, the agreement of the model with their values is good. There is agreement for the adult values also; however, the model gives somewhat higher values during the adolescent period.

In this paper we have examined a conceptually very simple age-dependent compartmental model. Application of the model to cesium retention has not been any more successful nor less successful than prior models. It has not explained variation of the biological half-life within an age group. Other parameters besides age are evidently important. However, the model has been derived theoretically with few assumptions, and there is only one arbitrary constant to be determined. The model is capable of accounting for a large part of the variation in half-lives between the various age groups.

Table 25.2. Total Dose Delivered to the Body from a Single Intake of ^{137}Cs

Age (years)	Dose (microrads/μc)		
	Beta	Gamma	Beta Plus Gamma
0	2680	1040	3720
1	2680	1450	4130
5	2680	1650	4330
10	2680	1900	4580
15	2680	2140	4820
20	2680	2390	5070

The total dose delivered to the body of individuals of various ages who have ingested 1 μc of ^{137}Cs has been calculated and is given in Table 25.2. The total dose is directly proportional to half-life and is inversely proportional to body mass. By the model, half-life and mass are proportional. Therefore, total dose is independent of half-life or body mass. This is true when 100% of the emitted energy is absorbed. Beta dose is an example. The fraction of the gamma energy absorbed by the infant is slightly less than half that of the adult, as will be shown later. Therefore, we see the model predicts that for identical single intakes of ^{137}Cs, the infant will receive a beta-plus-gamma total dose of about 75% that of the adult.

Fisher and Snyder[37] have described previously a human phantom and a Monte-Carlo-type calculation which was programmed for a high-speed digital computer. The age-dependent metabolic model described here may be used to estimate the microcurie-days of residence of ^{137}Cs in the body, and the data given in the above report may be used then to obtain an estimate of total dose as well as its distribution in time and in various portions of the body.

Acknowledgment

Appreciation for the coding and computer operations is expressed to Gordon G. Warner of the ORNL Mathematics Division.

[37]H. L. Fisher, Jr., and W. S. Snyder, *Health Phys. Div. Ann. Progr. Rept. July 31, 1966*, ORNL-4007, p. 221.

A DOSIMETRIC STUDY FOR THE ADMINISTRATION OF NEOHYDRIN LABELED WITH ^{203}Hg AND ^{197}Hg

W. S. Snyder Mary R. Ford

Introduction

Brain scanning with the mercurial diuretic chlormerodrin (Neohydrin[38]) labeled with radioactive mercury is now widely used in the localization of intracranial tumors. The isotope of mercury used initially was ^{203}Hg. This isotope was introduced as an agent in brain scanning in 1959 by Blau and Bender,[39] who demonstrated that ^{203}Hg gives a much lower whole-body radiation dose than the conventional agent, ^{131}I-labeled human serum albumin, and it produces scans that compare well with those obtained with ^{131}I. A disadvantage of the mercury, however, is that it accumulates in the kidneys, where it produces a relatively high local dose. More recently, ^{197}Hg has been used. This isotope, because of its shorter half-life and less penetrating radiation, gives a much lower dose to the kidneys than ^{203}Hg. It is considered by some, but not all, clinicians, however, to give less satisfactory scans.[40–42] Because the kidneys lie anatomically not far from the gonads, the magnitude of the genetic dose is a matter of further concern.

Thus an evaluation, with all reasonable precision, of the radiation dose received, especially by the kidneys and gonads, from both ^{197}Hg and ^{203}Hg is needed. We have performed this computation for photons with a Monte-Carlo-type computer code, described previously,[43] which is quite accurate in taking account of the scattering of photons and of the energy deposited in tissue. The dose from beta components is found by conventional techniques, but the estimate is improved

[38]Lakeside Laboratories.

[39]M. Blau and M. A. Bender, *J. Nucl. Med.* **3**, 83 (1962).

[40]D. B. Sodee, *J. Nucl. Med.* **5**, 74 (1964).

[41]M. Blau and M. A. Bender, *J. Nucl. Med.* **5**, 318 (1964).

[42]A. L. Rhoton, Jr., J. Eichling, and M. M. Ter-Pogossian, *J. Nucl. Med.* **7**, 50 (1966).

[43]W. S. Snyder, "The Variation of Dose in Man from Unilateral Exposure to Gamma Rays," presented at Tennessee Valley Industrial Health Conference, Gatlinburg, September 30 and October 1, 1965 (submitted to *Health Physics*).

somewhat by use of computer codes to determine the average beta energy and the number and intensity of beta-like radiations. The metabolic model is derived from data on hospital patients, and the dose estimates based on this model can be adjusted easily to take account of elimination rates appropriate for other patients.

Energy Emitted in the Decay of ^{197}Hg and ^{203}Hg

The decay schemes of ^{197}Hg and ^{203}Hg are given below:

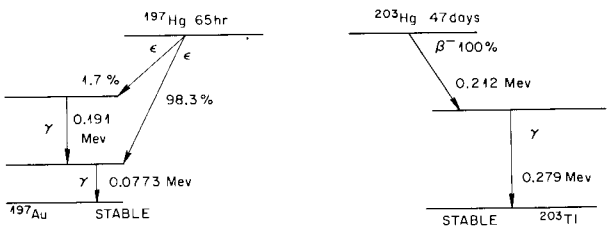

In addition to the energy emitted as shown on the decay schemes, many x rays and Auger electrons of varying energies and intensities arise as a result of gamma-ray internal conversion. This conversion is associated with the gamma decay of both isotopes, and, in the case of ^{197}Hg, the electron capture process accounts for the emission of other x rays and Auger electrons. The calculation of the energy emitted by these processes is tedious and time consuming, and so a computer code developed by Dillman[44] has been used which tabulates the number and energy of these emissions.

The computer output of the gamma and "beta-type" energy emitted per decay of ^{197}Hg and ^{203}Hg is given in Table 25.3. The radiations described as "beta type" include all x rays and/or gamma rays of energy less than 0.0113 Mev, all

[44] L. T. Dillman, "Calculating the Effective Energy per Radioactive Decay for Use in Internal Dose Calculations," this chapter.

Table 25.3. Gammas, X Rays, and "Beta-Type" Energy Emitted by ^{197}Hg and ^{203}Hg

Type of Decay	Radionuclide			
	^{197}Hg		^{203}Hg	
	Energy (Mev)	(%/disintegration)	Energy (Mev)	(%/disintegration)
Gamma	0.191	0.78	0.279	81.6
	0.0773	19.2		
X rays				
$K_{\alpha 1}$	0.0688	37.3	0.0729	6.34
$K_{\alpha 2}$	0.0669	20.5	0.0708	3.50
$K_{\beta 1}$	0.0779	12.9	0.0826	2.23
$K_{\beta 2}$	0.0807	3.47	0.0855	0.63
L			0.01131	5.76
"Beta-type"				
X and/or gamma rays below 0.0113 Mev; Auger and internal conversion electrons above 0.03 Mev	0.0549[a] 0.0158[b]	109[a] 33.5[b]	0.210	19.2
Auger and internal conversion electrons less than 0.03 Mev	0.00398[a] 0.00403[b]	166[a] 203[b]	0.00428	36.6

[a] From gamma decay.
[b] From electron capture.

Table 25.4. Beta Decay of ^{203}Hg

End-Point Energy (Mev)	Fraction per Decay	Betas with Energy Below 0.03 Mev		Betas with Energy Above 0.03 Mev	
		Fraction	Average Energy	Fraction	Average Energy
0.212	1	0.328	0.0249	0.672	0.0490

internal conversion electrons, and all Auger electrons. The output for electrons of energy less than 0.03 Mev is listed separately since these electrons are assigned a quality factor of 1.7 rather than 1 in internal dose calculations.[45] The average energy of the 0.212-Mev beta of ^{203}Hg, also computed by the code of Dillman,[44] is given in Table 25.4. As in the previous case the fraction of the decays in which the initial energy is less than 0.03 is tabulated separately for convenience in applying the quality factor.

Metabolic Characteristics of Neohydrin

The biological data and metabolic characteristics of Neohydrin used in the dose computations are based principally on the clinical experience of Blau and Bender.[39] They found that an injected dose of Neohydrin suitable for scanning purposes (usually 10 μc per kilogram of body weight) is cleared rapidly from the body via the urine and feces. Their data on 20 patients indicate that 50% of the dose is eliminated by the urine during the first 8 hr, and an additional 15% appears in the urine during the next 24 hr. The blood clearance is rapid, with less than 10% remaining after 5 hr. Most of the retained dose accumulates in the kidneys, where about equal amounts are found in the medulla and cortex during the first day. After the first day the concentration in the cortex to that in the medulla is roughly in the ratio of 5/1, and the biological half-life of the long-term component is about 28 days. The remaining few percent of the injected amount is scattered throughout the body, with perhaps some concentrating in the liver.

Based on these data, we have assumed in the computations that 75% of the administered radionuclide is excreted rapidly. Since less than 10% of this 75% is present in blood after 5 hr, according to the curve given in Fig. 2 of Blau and Bender,[39] we have given this deposit an elimination half-time of 1.3 hr. Of the 25% retained, 12% resides in the kidneys with a biological half-life of 28 days – 10% in the cortex and 2% in the medulla. Another 8% is retained in the medulla with a biological half-time of 12 hr. The remaining 5% is assumed to be uniformly distributed in the total body, and this is assigned an elimination half-time of 15 hr, again based on Fig. 2 of Blau and Bender's data.[39]

In addition to these sources of exposure, the urine which flows from the kidneys to the bladder and the amount retained in the bladder will contribute to the dose. This is true especially in the case of the gonads, because they lie in close proximity to the ureter and the bladder. Since the time for urine to pass from the kidneys to the bladder is very short, we have considered the dose from this source to be insignificant, but we have computed the dose from the amount in the bladder. For this computation five voids per day are assumed; that is, 4.8 hr is assumed as a typical period of retention; and because the bladder is near empty during part of each period, 2.4 hr is taken as an average residence time.

Description of the Phantom

The total-body tissue phantom used in the computations is shown in Fig. 25.7. This phantom was designed by the authors for an earlier Monte Carlo computation[46] and is similar to a phantom of Hayes and Brucer.[47] It is considered to consist of H, C, N, and O in the proportions given by standard man and to have a density equal to 1 g/cm^3. The subregions were made originally to show the variation of depth dose from an external source. They are left in these computations to permit the estimation of dose to the ovaries and bladder from the source located in the kidneys.

[45] *Recommendations of the International Commission on Radiological Protection*, ICRP Publication 2, p. 29, Pergamon, London, 1959.

[46] W. S. Snyder, "The Variation of Dose in Man from Exposure to a Point Source of Gamma Rays," presented at Intern. Conf. Radiological Protection in Industrial Uses of Radioisotopes, Dec. 13–15, 1965, Paris (to be published in proceedings).

[47] R. L. Hayes and M. Brucer, *Intern. J. Appl. Radiation Isotopes* **9**, 111 (1960).

When an organ is very small or lies at some distance from the source, the dose estimate averaged over the appropriate subregion is statistically more reliable than the dose estimated in the actual organ.

The internal organs of interest here, the kidneys, ovaries, and bladder, have the same location as corresponding organs described in a paper by Fisher.[48] Also, the size and shape of the ovaries and bladder are identical in the two papers; but the kidneys are described here in somewhat more detail, because Neohydrin concentrates in the kidney cortex, and thus it is necessary to identify the different regions, that is, the cortex, medulla, and papillary region.

The structure of the kidneys was determined from several anatomy references and from consultation with Dr. F. Jones, pathologist, University Hospital, Knoxville, Tennessee. In order to formulate this information as well as possible into a simple mathematical expression usable by the computer, the kidney as a whole is assumed to be an ellipsoid cut by a plane parallel to the major axis. With the rectangular coordinate system located at the center of the base of the trunk in the phantom, as shown in Fig. 25.7, the left kidney can be described by the inequalities

$$\left(\frac{x-6}{4.5}\right)^2 + \left(\frac{y-6}{2}\right)^2 + \left(\frac{z-32.5}{5}\right)^2 \leqq 1 \qquad (1)$$

and

$$x \geqq 4 \ . \qquad (2)$$

The kidneys are assumed to be alike and equal in volume; the combined volume of the two is 305.8 cm^3.

The human kidney is divided internally into three rather well defined regions: (1) the cortex, (2) the medulla, and (3) the papillary region. The cortex caps and surrounds the medulla, which consists of a series of conical masses termed renal pyramids whose apexes project in the form of renal papilla into the cuplike structure known as the papillary region.

[48]H. L. Fisher, Jr., and W. S. Snyder, "Distribution of Dose in the Body from a Source of Gamma Rays Distributed Uniformly in an Organ," presented at First Intern. Congress on Radiation Protection, Sept. 5–10, 1966, Rome (to be published in proceedings).

ORNL-DWG 67-1768R

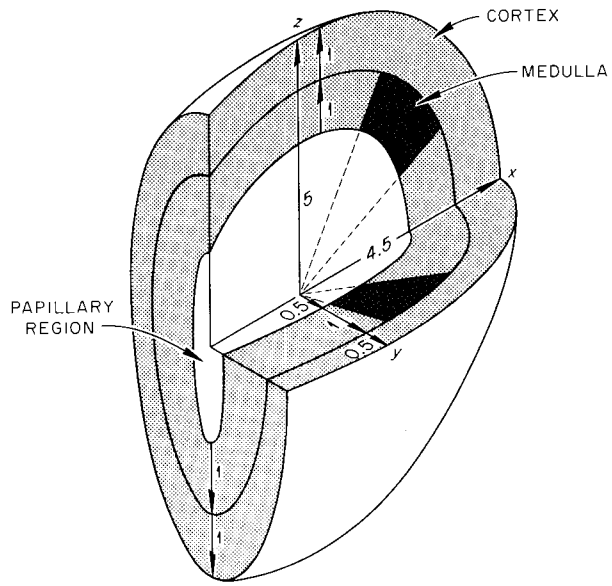

Fig. 25.31. Dosimetric Model of a Human Kidney.

The three sections of the kidney as simulated for computational purposes are shown in Fig. 25.31. The papillary region consists of the points satisfying inequalities (1) and (2) as well as the inequality

$$\left(\frac{x-6}{2.5}\right)^2 + \left(\frac{y-6}{0.5}\right)^2 + \left(\frac{z-32.5}{3}\right)^2 \leqq 1 \ , \qquad (3)$$

and the volume is 15.27 cm^3. Thus the papillary region consists of that portion of the entire kidney defined by (1) and (2) which lies inside a smaller ellipsoid having semiaxes 2.5, 0.5, and 3 cm.

The cortex contains an outer band consisting of the points (x, y, z) satisfying the inequalities (1) and (2) as well as the additional inequality

$$\left(\frac{x-6}{3.5}\right)^2 + \left(\frac{y-6}{1.5}\right)^2 + \left(\frac{z-32.5}{4}\right)^2 \geqq 1 \ . \qquad (4)$$

The volume is 94.17 cm^3. The cortex also contains certain portions of the medullary band to be described later.

The medulla lies in the space between the ellipsoid defining the papillary region and the ellipsoid defining the inner surface of the outer band of cortex. This medullary band consists of points

(x, y, z) satisfying (1) and (2) but not satisfying either (3) or (4), that is, satisfying the opposite inequalities

$$\left(\frac{x-6}{2.5}\right)^2 + \left(\frac{y-6}{0.5}\right)^2 + \left(\frac{z-32.5}{3}\right)^2 > 1 , \quad (3')$$

$$\left(\frac{x-6}{3.5}\right)^2 + \left(\frac{y-6}{1.5}\right)^2 + \left(\frac{z-32.5}{4}\right)^2 < 1 . \quad (4')$$

However, the medulla does not contain all this band. It consists of portions of circular cones having vertexes at the center of the above ellipsoids and half-angles of 17° 42′ which lie in the band defined above, that is, by inequalities (1), (2), (3′), and (4′). There are some 32 such cones distributed so as not to intersect each other. The total volume is 43.5 cm^3.

The portion of the medullary band which is not included in the cones is the additional part of the cortex mentioned above. This consists of points satisfying inequalities (1) and (2), (3′), and (4′) but not inside the cones of the medulla. The volume of the intermedullary portion of the cortex is 18.8 cm^3.

Dosimetry

By use of the physical and biological data and the geometrical configurations described above, the dose to the cortex and medulla of the kidneys and to the bladder and ovaries has been estimated. Estimates are provided per millicurie-hour of residence of ^{197}Hg and ^{203}Hg in the cortex of the kidneys, in the medulla of the kidneys, in the bladder, and in the total body (blood). These estimates are given in Table 25.5 for Neohydrin labeled with ^{197}Hg and in Table 25.6 for the ^{203}Hg label.

The doses were computed for gamma and x rays by use of the Monte Carlo computer code described previously,[45] and the decay data in Table 25.3 were used as input for each source location. In the case of beta and "beta-type" decays, doses were computed only for the organ containing the source, since the range of these emissions is insufficient – about 0.05 cm for the most energetic – to irradiate the other organs of interest. In estimating the dose from "beta-like" radiation, complete absorption of energy in the source region was assumed.

To find the rads per millicurie of intake by use of Tables 25.5 and 25.6, the rads per millicurie-hour for the tissue of interest must be multiplied by the millicurie-hours of residence of the radionuclides in each of the source organs and the results added. The millicurie-hours are given by

$$I \int_0^\infty R(t)\, dt ,$$

where I is the intake (mc) and $R(t)$ is the fraction of the intake present in the tissue of interest t hours after intake.

The activity depositing in the kidney is considered in three parts: (1) a fraction of intake K_1 depositing in the cortex with rather long biological turnover time, T_1 days; (2) a fraction of intake K_2 depositing in medulla with a rather short biological turnover time, T_2 days; and (3) a fraction of intake K_3 depositing in medulla with a rather long biological turnover time, T_3 days. The number of millicurie-hours of residence in kidney for any of the above three fractions is given by

$$I \int_0^\infty R(t)\, dt = \frac{24 I K_i T_r T_i}{0.693(T_r + T_i)} , \quad i = 1, 2, 3 , \tag{5}$$

where T_r is the half-time (days) for radioactive decay and

$$R(t) = K_i \exp\left[-\left(\frac{0.693}{T_r} + \frac{0.693}{T_i}\right)\frac{t}{24}\right]$$

for the respective cases.

The activity (mc) excreted into the bladder from the above deposits is given by

$$I \int_0^\infty R(t) \times \frac{0.693}{24 T_i}\, dt = \frac{I K_i T_r}{T_r + T_i} , \quad i = 1, 2, 3 . \tag{6}$$

This expression must be summed for $i = 1, 2, 3$. If this activity is assumed to reside in the bladder for B hr, the total millicurie-hours of residence in the bladder due to activity eliminated from the kidney deposits may be taken as B multiplied by the sum of the expressions in (6). This estimate neglects radioactive decay, which seems justified. Indeed, if one assumes a uniform intake to the

Table 25.5. Radiation Dose to Various Body Organs from an Injected Dose of 1 mc of ^{197}Hg Neohydrin

Organ	Type of Decay	Location of Source: Cortex		Medulla		Bladder		Whole Body		Total (rads/mc)
		Rads/mc-hr	Rads/mc	Rads/mc-hr	Rads/mc	Rads/mc-hr	Rads/mc	Rads/mc-hr	Rads/mc	
Cortex	Gamma	0.037		0.036		1.3×10^{-4}		7.7×10^{-5}		
	β^-	1.0						2.7×10^{-3}		
	Total	1.0	8.5	0.036	0.10	1.3×10^{-4}	2.7×10^{-4}	2.8×10^{-3}	6.4×10^{-3}	8.6
Medulla	Gamma	0.044		0.062		1.3×10^{-4}		7.7×10^{-5}		
	β^-			2.2				2.7×10^{-3}		
	Total	0.044	0.37	2.3	6.6	1.3×10^{-4}	2.7×10^{-4}	2.8×10^{-3}	6.4×10^{-3}	7.0
Bladder	Gamma	1.5×10^{-4}		1.8×10^{-4}		0.041		8.2×10^{-5}		
	β^-					0.38		2.7×10^{-3}		
	Total	1.5×10^{-4}	1.3×10^{-3}	1.8×10^{-4}	5.2×10^{-4}	0.42	0.85	2.8×10^{-3}	6.4×10^{-3}	0.86
Ovaries	Gamma	2.3×10^{-3}		2.2×10^{-4}		5.1×10^{-3}		1.0×10^{-4}		
	β^-							2.7×10^{-3}		
	Total	2.3×10^{-3}	0.019	2.2×10^{-4}	6.3×10^{-3}	5.1×10^{-3}	0.010	2.8×10^{-3}	6.4×10^{-3}	0.042

Table 25.6. Radiation Dose to Various Body Organs from an Injected Dose of 1 mc of ^{203}Hg Neohydrin

Organ	Type of Decay	Location of Source: Cortex		Medulla		Bladder		Whole Body		Total (rads/mc)
		Rads/mc-hr	Rads/mc	Rads/mc-hr	Rads/mc	Rads/mc-hr	Rads/mc	Rads/mc-hr	Rads/mc	
Cortex	Gamma	0.12		0.11		5.7×10^{-4}		3.1×10^{-3}		
	β^-	1.1						3.1×10^{-3}		
	Total	1.2	73	0.11	1.5	5.7×10^{-4}	1.3×10^{-3}	6.2×10^{-3}	0.015	75
Medulla	Gamma	0.13		0.20		5.7×10^{-4}		3.1×10^{-3}		
	β^-			2.5				3.1×10^{-3}		
	Total	0.13	8.1	2.7	36	5.7×10^{-4}	1.3×10^{-3}	6.2×10^{-3}	0.015	44
Bladder	Gamma	6.7×10^{-4}		6.0×10^{-4}		0.12		3.6×10^{-3}		
	β^-					0.42		3.1×10^{-3}		
	Total	6.7×10^{-4}	0.040	6.0×10^{-4}	8.1×10^{-3}	0.54	1.2	6.7×10^{-3}	0.016	1.3
Ovaries	Gamma	5.9×10^{-3}		5.7×10^{-3}		0.013		4.1×10^{-3}		
	β^-							3.1×10^{-3}		
	Total	5.9×10^{-3}	0.36	5.7×10^{-3}	0.077	0.013	0.029	7.2×10^{-3}	0.018	0.48

bladder for T hr and then a voiding, the correction factor needed to correct for radioactive decay is

$$2\,(T\lambda_r - 1 + e^{-\lambda_r T})/T^2\lambda_r^2\,,$$

and for $T = 4.8$ hr, this is 0.98 and 0.99 for the ^{197}Hg and ^{203}Hg respectively. In addition to activity entering the bladder from the kidney deposits, there is the amount eliminated from the blood, which is assumed to pass through the kidney to the bladder. This is computed by the formula

$$IA \int_0^\infty e^{-(\lambda_r+\lambda_b)t}\lambda_b\, dt = \frac{IA\,\lambda_b}{\lambda_r + \lambda_b}\,, \qquad (7)$$

where $\lambda_r = 0.693/T_r$ is the radioactive decay constant and $\lambda_b = 0.693/T_b$ is the rate of biological elimination. As discussed above, this is used with $A = 0.75$ and $T_b = 1.3$ hr and again with $A = 0.05$ and $T_b = 15$ hr. The sum of the two values obtained from (7) using these data represents the material entering the bladder from blood and must be added to the sum of the three terms obtained from (6). All the activity entering the bladder, that is, the sum of the three terms of (6) and the two terms of (7), is multiplied by B, the residence time in the bladder (i.e., $B = 2.4$ hr), to obtain the total millicurie-hours of residence in the bladder.

In like manner, the millicurie-hours of residence in the whole body (blood) is computed by the formula

$$IA \int_0^\infty e^{-(\lambda_r+\lambda_b)t}\, dt = \frac{IA}{\lambda_r + \lambda_b}\,, \qquad (8)$$

where the terms are defined and used as in (7). In Table 25.7 the numerical values of the constants used in estimating millicurie-hours of residence for the "typical" case described above are given, as well as the corresponding millicurie-hours for each of the reference tissues. These residence times were used to obtain the estimates of dose per millicurie of intake given in Tables 25.5 and 25.6.

If different values of K_i and T_r or of B seem appropriate for a particular patient, formulas (5) and (6) are easily computed to obtain the proper number of millicurie-hours of residence time in the various tissues. Thus the dose estimate is easily adjusted for a particular patient for whom the parameter values given above might not be appropriate. If an entirely different metabolic model is assumed, of whatever kind, and if by its use one can estimate the total millicurie-hours of residence in the various tissues, then, again, one can use the table to obtain the estimate of dose resulting from use of this model. Since individuals may differ rather markedly, there may be cases where this adjustment is of considerable significance.

Table 25.7. Residence Times (mc/hr) of ^{197}Hg and ^{203}Hg in Various Body Organs from an Injected Dose of 1 mc of ^{197}Hg or ^{203}Hg Neohydrin

Organ	Formulas and Constants Used in the Computations	^{197}Hg	^{203}Hg
Total body (blood)	Formula (8)	2.3	2.5
Cortex	Formula (5), $K_1 = 0.10$, $T_1 = 28$ days	8.5	61
Medulla 1	Formula (5), $K_2 = 0.08$, $T_2 = 0.5$ days	1.2	1.4
Medulla 2	Formula (5), $K_3 = 0.02$, $T_3 = 28$ days	1.7	12
Bladder	Formulas (6) and (7), $B = 2.4$ hr	2.1	2.3

USE OF EXCRETION DATA TO PREDICT THE SYSTEMIC BODY BURDEN OF PLUTONIUM

W. S. Snyder Mary R. Ford
G. G. Warner[49]

Health physicists face one of their most difficult problems when they need to estimate the exposure status of an employee who may have been, or is known to have been, exposed to plutonium. In particular, the estimation of the systemic body burden is difficult since the available data suggest that the excretory rate changes, though slowly, with time. Thus, the systemic burden cannot be directly inferred from the excretion rate, but the

[49]Mathematics Division.

time sequence of the exposures is important. In addition, there are wide fluctuations of the amounts excreted per day as have been found in employees[50] as well as in experimental animals.[51] The crowning difficulty is that there are only a few data available which can be used to study the problem and perhaps construct a model.

Langham *et al.*[52] have analyzed the excretion and autopsy data obtained from 15 hospital patients who were given plutonium intravenously. Eleven patients received $^{239}PuNO_3$ complexed with citrate, and four patients received $^{239}PuO_2$. This study provides the best available data on humans concerning retention and excretion as they apply to a systemic burden of plutonium in that the amount entering blood is accurately known, the excretion data are nearly complete, and in six of these cases autopsy data provide evidence on the distribution of the systemic burden as well as a check on the excretion data. These data are limited in three respects: (1) Because the complexing with citrate probably influences the distribution of the systemic burden, emphasizing deposition in bone and deemphasizing deposition in liver, these cases may not be typical of occupational exposure in the majority of cases. (2) The data do not extend very far in time, less than half these patients being available for study up to 40 days postinjection and daily excretion data being available on only two patients for as long as 138 days. (3) These were inactive terminal patients, and this might have some influence on the metabolism and excretion of the plutonium. Langham *et al.*[52] did extend the record by determining the average daily excretion of two of the patients at various times after the close of the experiment and by following the excretion on a few employees who had accumulated measurable amounts of plutonium. He found that by making certain assumptions concerning the employees' exposure, their excretion followed the same trend indicated by the terminal patients. On this basis it is often assumed that the excretion data follow the trend of a power function for times of five years or more, that is, if a unit amount of plutonium enters blood at time $t = 0$, the excretion on day t may be expected to average $at^{-\alpha}$ units, where a and α are constants. As mentioned above, one may expect rather large fluctuations in the day-to-day values.

There is one case of occupational exposure reported in the literature[53] which is not complete enough to be useful for testing or constructing metabolic models but does provide very valuable data. Although neither the exposure nor the amount entering the blood of this employee is known even approximately, the excretion data obtained from scattered samples collected in the course of his employment are available, and the autopsy data are complete and rather detailed. It would be extremely valuable to have more data of this kind, for, although occupational exposures will inevitably lack the precision of the experimental studies, they provide useful data which involve exactly those uncertainties and difficulties the health physicist faces in the practical situation. Hence they are valuable checks on procedures which are proposed for the practical problem of evaluating exposures of plutonium workers. Additionally, one may turn to data on experimental animals to study the problem, but, while valuable, results from animal experiments must be viewed as requiring some confirmation by human data before we can be entirely confident of their applicability to occupational exposure. These remarks are meant to stress the importance of obtaining every bit of human data bearing on the problem whenever possible, as well as to excuse, if excuse be necessary, the analysis which follows and which is open to the charge of overelaboration and refinement of analysis of very few data. However, these are all the relevant data we have found which could be used for this type of analysis.

The first question studied here is that of the extent of individual differences: How different are the 15 patients[52] as far as excretion of plutonium that has entered blood is concerned? The question has been studied previously,[54] and the present studies may be considered as an extension of that study. Langham *et al.*[52] were the first to fit a power function to the excretion data of these patients, that is, to obtain constants a and α so that the function $at^{-\alpha}$ represents approximately

[50] S. A. Beach and G. W. Dolphin, *Assessment of Radioactivity in Man*, vol. II, p. 603, IAEA, Vienna, 1964.

[51] W. J. Bair *et al.*, *Health Phys.* **8**, 639 (1962).

[52] W. H. Langham *et al.*, *Distribution and Excretion of Plutonium Administered Intravenously to Man*, LA-1151 (1950).

[53] H. Foreman, W. Moss, and W. Langham, *Health Phys.* **2**, 326 (1960).

[54] W. S. Snyder, *Health Phys.* **8**, 767 (1962).

the excretion expected on day t. In particular, they gave the three formulas $0.23t^{-0.77}$, $0.63t^{-1.09}$, and $0.79t^{-0.94}$ for urinary, fecal, and total daily excretion respectively. These functions have been extensively used in the interpretation of excretion data to obtain an estimate of body burden. In this study we retain the form of the function, that is, $at^{-\alpha}$, but we analyze the data for each individual to determine what differences exist in the values of a and α that provide the best fit of the function to the data. The values so determined are shown in Table 25.8 together with the values of a and α of best fit when all the data of all the patients are used together.

The values of the parameters a and α given in Table 25.8 are selected in a novel manner. The columns under the subtitle "Point Fit" regard the urinary excretion U_i on day i as a point in a two-dimensional plot, i (days) being the abscissa and U_i (fraction of injected activity excreted on day i) being the ordinate. The values of a and α are chosen to minimize the sum

$$\sum_{i=1}^{n} |U_i - ai^{-\alpha}| = \min , \qquad (1)$$

that is, the sum of the absolute deviations of the data from the formula is minimized. The minimization is accomplished by setting up a mesh, generally on the interval $0 < \alpha < 2$, with a spacing of $\Delta\alpha = 0.01$ for the mesh. A code was designed which selected, in turn, each point of the mesh and, having thus fixed the value of α, used standard techniques to find the minimizing value of the linear parameter a. The value of the sum was computed for each such choice of α and for the minimizing value of a, and the smallest of these values determined the choice of a and α. It is noteworthy that no log transform of the data was used nor was the sum of squares of deviations used. When the formula $at^{-\alpha}$ is used to estimate intake or body burden of an employee, it will be used multiplicatively, and thus any percent deviation by excess or by default of an individual's data from the formula will produce a corresponding percent of error in the estimate. It is for this reason that we chose to minimize the deviations of the data and not the squares of the deviations or the deviations of the logarithms of the data. This procedure produced the values of a and α shown under the subheading "Point Fit."

Table 25.8. Urinary Excretion Formulas, $at^{-\alpha}$, for 15 Individuals Obtained by Minimizing the Sum of the Absolute Deviations

Patient	"Point Fit"		"Area Fit"	
	a	α	a	α
Hp-1	0.24	0.74	0.10	0.42
Hp-2	0.47	1.04	0.17	0.63
Hp-3	0.38	0.99	0.17	0.71
Hp-4	0.44	0.89	0.20	0.54
Hp-5	0.30	1.10	0.11	0.62
Hp-6	0.50	1.21	0.31	0.99
Hp-7	0.24	1.02	0.078	0.64
Hp-8	0.38	0.88	0.16	0.58
Hp-9	0.12	0.48	0.096	0.40
Hp-10	0.41	0.98	0.17	0.60
Hp-12	0.15	0.58	0.087	0.40
Chi-I	0.86	1.85	0.18	0.79
Chi-II	0.25	0.73	0.20	0.66
Chi-III	0.15	0.86	0.071	0.53
Cal-I	0.48	1.19	0.12	0.74
All the patients	0.32	0.93	0.15	0.65

Since the formula $at^{-\alpha}$ is fitted to the 24-hr excretion values, the formula should, strictly, only be used when t is a positive integer, that is, to predict the excretion for a complete day. Thus, it is not a true rate of excretion in the usual sense. When the value of the function does not vary appreciably throughout the day, one may consider it as a rate function and replace the tedious summation of daily values by an integration. Although this procedure is logically based, it points up the basic difficulty of the approach taken here, namely, that excretion is a continuous process and not a discrete one. Even though the individual voids occur at discrete intervals of time, the plutonium is constantly being transferred to the bladder or to the large intestine and is then effectively not a part of the systemic body burden. Thus, it appears more logical on physiological grounds to attempt to determine a true rate of excretion which considers it as a continuous process. Treating the data in this way is in accord with the view

that if a formula is to be used in a certain way, then the procedure used to fit the formula to the data should minimize the deviations from the formula as used; for example, in the present case, if a rate function is wanted so that excretion during a time interval equals $\int f(t)\,dt$ over that time interval, then it is the integral of f that should be used in the minimization process. This is easily done, for if $at^{-\alpha}$ represents the instantaneous rate of excretion, then the excretion over the time interval corresponding to the ith day is given by

$$\int_{i-1}^{i} at^{-\alpha}\,dt = a\left[\frac{i^{1-\alpha}-(i-1)^{1-\alpha}}{1-\alpha}\right]. \qquad (2)$$

The minimizing values of a and α are determined as before, except that the formula

$$\sum_{i=1}^{n}\left|U_i - a\left[\frac{i^{1-\alpha}-(i-1)^{1-\alpha}}{1-\alpha}\right]\right| = \min \qquad (3)$$

is used in place of Eq. (1). The values of a and α so obtained are shown in Table 25.8 under the subheading "Area Fit," for the integral in Eq. (2) represents the area under the curve $at^{-\alpha}$ that corresponds to a daily excretion. It will be noted that there appears to be less spread in the values of a and α for the individual patients when determined in this way than when the "Point Fit" method is used.

As mentioned above, one might prefer to minimize the sum of percent deviations, and the above procedure only minimizes the sum of absolute deviations. It is easy to make the necessary modifications, and thus one obtains

$$\sum_{i=1}^{n}\left|\frac{U_i}{a\,f(i,\alpha)} - 1\right| = \min \qquad (4)$$

with

$$f(i,\alpha) = i^{-\alpha} \text{ or } f(i,\alpha) = \frac{i^{1-\alpha}-(i-1)^{1-\alpha}}{1-\alpha} \qquad (5)$$

and the values of a and α which minimize the sum of the percent deviations. As before, the formula determined by Eq. (4) is to be used essentially by forming sums corresponding to excretion for whole days if $f(i,\alpha) = i^{-\alpha}$ is used, but the second formula given in Eq. (5) is to be used to determine a rate of excretion and the integral used in place of the discrete sum. The values of a and α obtained from Eqs. (4) and (5) for all 15 patients are shown in Table 25.9. This table also contains values of a and α obtained when the data of all patients are used in Eqs. (4) and (5).

Table 25.9. Urinary Excretion Formulas, $at^{-\alpha}$, for 15 Individuals Obtained by Minimizing the Sum of the Percent Deviations

Patient	"Point Fit"		"Area Fit"	
	a	α	a	α
Hp-1	0.28	0.82	0.18	0.65
Hp-2	0.66	1.21	0.17	0.63
Hp-3	0.57	1.20	0.16	0.72
Hp-4	0.44	0.89	0.19	0.56
Hp-5	0.18	0.79	0.11	0.62
Hp-6	0.50	1.21	0.31	0.99
Hp-7	0.48	1.26	0.089	0.75
Hp-8	0.32	0.81	0.23	0.73
Hp-9	0.12	0.47	0.096	0.40
Hp-10	0.73	1.22	0.16	0.72
Hp-12	0.15	0.57	0.12	0.52
Chi-I	0.11	0.61	0.099	0.57
Chi-II	0.17	0.62	0.16	0.60
Chi-III	0.15	0.83	0.083	0.45
Cal-I	0.26	0.88	0.13	0.72
All the patients	0.21	0.73	0.14	0.61

From the data of Tables 25.8 and 25.9, some indication of the extent of individual differences can be observed. Despite the reservations noted concerning the data used here, that is, the sick and immobilized condition of the patients and the limited extent in time of the data, the authors know of no other data available to check on this extent of individual differences. The values of a and α obtained by pooling all the data of all the patients might be considered as "typical" of these parameters so far as our present knowledge permits us to judge. Clearly, the range of the individual values about these "typical" values will produce great differences over long

periods of time, and therefore it is particularly unfortunate that data are not available over a longer period of time. For persons exposed occupationally, the period may extend over many years. For example, in the case reported by Foreman *et al.*[53] the employee worked with plutonium over a period of about 11 years, although not continuously. The data on the isotopic ratio of ^{238}Pu and ^{239}Pu suggest that some of the exposure probably occurred early in this period and that some of it occurred much later. Thus, the formula to be validated should extend over many years – ideally, over a working lifetime.

The previous section was concerned with differences in the broad trends of excretion for different individuals. We turn now to consider the fluctuations of an individual's day-to-day excretion values about his own particular curve. Except for those employees who are subjects of special and intensive study, an individual's excretion curve is unknown, and thus we study also the fluctuation of daily excretion values about the "typical" curve. Some data on this distribution of values appear in Table 25.10, where factors to apply to an individual's curve or to the "typical" curve are given, that is, factors p and P, which correspond to a specified percent of the daily excretion values of the jth individual between $pai^{-\alpha}$ and $Pai^{-\alpha}$, are given. In the case of the "typical" values of a and α, the factors p and P when so applied define a range including a specified percent of all the data of all the patients. The same considerations apply to the formula

$$a\left[\frac{i^{1-\alpha}-(i-1)^{1-\alpha}}{1-\alpha}\right],$$

which is designated in Table 25.11 as the "Area Fit" formula. Values are given only for urinary data, because fecal data are not available in a practical case.

These data are treated more generally by calculating the ratios $R_i = U_i/ai^{-\alpha}$ or $R_i' = (1-\alpha)\,U_i/a\,[i^{1-\alpha}-(i-1)^{1-\alpha}]$ and noting the fluctuations of these ratios. If the ratios R_i, or R_i', are ranked by magnitude, irrespective of the chronological order indicated by i, one has a distribution of values on the real axis. When the ratio R_i equaled 1, the formula predicted the excretion on day i exactly, while values of R_i greater than 1 (less than 1) correspond to cases where the formula predicted too little (too much) excretion. By graphing the cumulative distribution of the R_i or the R_i' for an individual case, one obtains visual presentation of the data. The presentation of these cumulative curves for all the individual cases in one graph produces a complex network of curves, and individual curves are not easily identified. Consequently, only a general region is shown in which all the individual curves lie (see Fig. 25.32 for distribution of values of R_i for the individual cases). Using this region, one can select values of p and P to include any desired percentage of the daily excretion values. Figure 25.33 contains the same presentation for the ratio $R_i' = (1-\alpha)\,U_i/a\,[i^{1-\alpha}-(i-1)^{1-\alpha}]$, and the interpretation is similar. The values of a and α used in Figs. 25.32 and 25.33 are those obtained by minimizing the sum of percentage deviations for the appropriate formula. This would be expected to produce the narrowest region.

The values of a and α may be selected to minimize any one of the four sums defined by Eqs. (1), (3), (4), or (5) when the data of all the patients are used simultaneously. One might expect that the curve so obtained would be more representative of a "typical" or average excretion pattern than any of the individual cases. The values of a and α so obtained are given in Tables 25.8 and 25.9. From these values, the spread of individual fluctuations about the "typical" or group curve is presented in Figs. 25.34 and 25.35. It is evident that the spread of fluctuations is somewhat greater than when the data of each patient are compared with the trend curve obtained by choosing a and α on the basis of his data. The difference in spread of the regions in Figs. 25.34 and 25.35 as compared with the width of the regions in Figs. 25.32 and 25.33 is a measure of the extent of individual differences. In Figs. 25.32 and 25.33, the width is a measure of the extent of daily fluctuations when the curve of best fit for each patient is used for his data. However, in Figs. 25.34 and 25.35, a single formula is used for all the patients, and so the variability due to individual differences is added to the variability due to day-to-day variations.

These data may be used to design a program for a digital computer which uses the entire record of an employee's urinary excretion of plutonium and produces an estimate of his intakes as well as of the plutonium present in bone at any time during exposure or postexposure and which takes into account to some extent the effect of daily fluctuations of data. Other codes of this general type

Table 25.10. Fluctuations of Daily Urinary Excretion Values of Individuals About Their Own Formulas and About the "Typical" Formula of Best Fit—"Point Fit" Formulas Used[a]

Formulas obtained by minimizing the sum of percent deviations

Patient	Percentiles $pf(i)$ and $Pf(i)$ of the Distribution of Excretion Data									
	25%–75%		15%–85%		10%–90%		5%–95%		2.5%–97.5%	
	p	P	p	P	p	P	p	P	p	P
Hp-1	0.93 (1.00)	1.07 (1.15)	0.72 (0.73)	1.10 (1.18)	0.71 (0.71)	1.11 (1.19)	0.65 (0.71)	1.12 (1.20)	0.65 (0.64)	1.17 (1.21)
Hp-2	0.90 (0.66)	1.20 (1.20)	0.77 (0.49)	1.27 (1.37)	0.72 (0.45)	1.33 (1.75)	0.68 (0.41)	1.53 (2.20)	0.66 (0.40)	1.57 (2.27)
Hp-3	0.76 (0.64)	1.08 (1.04)	0.74 (0.61)	1.17 (1.18)	0.65 (0.51)	1.18 (1.37)	0.54 (0.50)	1.27 (2.24)	0.52 (0.43)	1.29 (2.65)
Hp-4	0.82 (1.04)	1.10 (1.72)	0.45 (0.55)	1.25 (1.83)	0.44 (0.54)	1.27 (2.05)	0.34 (0.41)	1.34 (2.30)	0.34 (0.41)	1.34 (2.30)
Hp-5	0.76 (0.56)	1.07 (0.80)	0.73 (0.55)	1.21 (0.86)	0.69 (0.51)	1.22 (0.87)	0.58 (0.45)	1.57 (1.28)	0.45 (0.35)	1.61 (1.38)
Hp-6	0.97 (0.60)	1.03 (0.92)	0.96 (0.54)	1.07 (1.15)	0.93 (0.53)	1.07 (1.32)	0.91 (0.52)	1.17 (1.42)	0.80 (0.48)	1.19 (1.67)
Hp-7	0.86 (0.38)	1.10 (0.58)	0.79 (0.37)	1.14 (1.01)	0.76 (0.35)	1.16 (1.04)	0.72 (0.33)	1.18 (1.43)	0.45 (0.29)	1.33 (1.64)
Hp-8	0.90 (1.03)	1.04 (1.24)	0.85 (0.96)	1.08 (1.30)	0.81 (0.94)	1.17 (1.33)	0.79 (0.86)	1.25 (1.45)	0.63 (0.72)	1.30 (1.80)
Hp-9	0.89 (0.85)	1.12 (1.40)	0.85 (0.74)	1.19 (1.43)	0.77 (0.71)	1.22 (1.47)	0.72 (0.68)	1.28 (1.61)	0.68 (0.66)	1.36 (1.66)
Hp-10	0.96 (0.76)	1.15 (1.18)	0.87 (0.74)	1.17 (1.43)	0.85 (0.72)	1.20 (1.93)	0.74 (0.69)	1.24 (2.27)	0.57 (0.68)	1.27 (2.55)
Hp-12	0.91 (1.00)	1.14 (1.31)	0.82 (0.91)	1.32 (1.61)	0.75 (0.81)	1.56 (1.70)	0.72 (0.76)	2.40 (3.17)	0.68 (0.70)	2.44 (3.25)
Chi-1	0.69 (0.59)	1.31 (1.16)	0.59 (0.48)	1.55 (1.39)	0.52 (0.39)	1.67 (1.46)	0.31 (0.26)	1.96 (1.77)	0.27 (0.22)	2.38 (2.16)
Chi-2	0.63 (0.77)	1.26 (1.53)	0.51 (0.60)	1.46 (1.76)	0.50 (0.55)	1.59 (1.96)	0.47 (0.49)	1.80 (2.12)	0.41 (0.46)	2.08 (2.36)
Chi-3	0.77 (0.44)	1.10 (0.71)	0.69 (0.40)	1.33 (0.75)	0.53 (0.29)	1.88 (1.03)	0.26 (0.14)	1.95 (1.29)	0.26 (0.14)	1.95 (1.29)
Cal-1	0.66 (0.44)	1.20 (0.75)	0.53 (0.38)	1.35 (0.85)	0.41 (0.31)	1.47 (0.93)	0.31 (0.22)	1.61 (1.11)	0.26 (0.20)	1.85 (1.25)

[a]Values in parentheses indicate values of p and P as percentiles of the distribution of values about the "typical" curve, that is, curve of best fit for the data of the group.

Table 25.11. Fluctuations of Daily Urinary Excretion Values of Individuals About Their Own Formulas and About the "Typical" Formula of Best Fit—"Area Fit" Formula Used[a]

Formulas obtained by minimizing the sum of percent deviations

	Percentiles $pf(i)$ and $Pf(i)$ of the Distribution of Excretion Data									
	25%–75%		15%–85%		10%–90%		5%–95%		2.5%–97.5%	
Patient	p	P	p	P	p	P	p	P	p	P
Hp-1	0.89	1.06	0.64	1.12	0.64	1.12	0.57	1.14	0.34	1.16
	(1.01)	(1.28)	(0.73)	(1.31)	(0.73)	(1.36)	(0.64)	(1.38)	(0.49)	(1.41)
Hp-2	0.59	1.06	0.43	1.21	0.39	1.55	0.35	1.76	0.35	2.13
	(0.67)	(1.29)	(0.49)	(1.41)	(0.44)	(1.84)	(0.40)	(2.11)	(0.39)	(2.58)
Hp-3	0.82	1.21	0.77	1.35	0.64	1.44	0.64	1.65	0.55	2.37
	(0.65)	(1.17)	(0.64)	(1.36)	(0.57)	(1.55)	(0.51)	(1.60)	(0.46)	(2.54)
Hp-4	0.68	1.29	0.35	1.39	0.34	1.50	0.26	1.90	0.26	1.90
	(1.07)	(1.93)	(0.55)	(2.03)	(0.54)	(2.07)	(0.41)	(2.68)	(0.41)	(2.68)
Hp-5	0.80	1.05	0.79	1.16	0.70	1.18	0.68	1.20	0.51	1.86
	(0.62)	(0.81)	(0.61)	(0.88)	(0.54)	(0.90)	(0.52)	(0.93)	(0.39)	(1.46)
Hp-6	0.83	1.00	0.81	1.00	0.79	1.02	0.77	1.08	0.67	1.23
	(0.62)	(1.03)	(0.56)	(1.33)	(0.54)	(1.54)	(0.53)	(1.66)	(0.50)	(1.90)
Hp-7	0.96	1.42	0.92	2.05	0.85	2.39	0.73	3.03	0.61	3.14
	(0.38)	(0.62)	(0.36)	(0.98)	(0.35)	(1.20)	(0.33)	(1.66)	(0.28)	(1.86)
Hp-8	0.93	1.07	0.87	1.13	0.83	1.19	0.74	1.30	0.58	1.31
	(0.98)	(1.27)	(0.92)	(1.36)	(0.89)	(1.44)	(0.78)	(1.54)	(0.71)	(2.04)
Hp-9	0.89	1.10	0.85	1.14	0.78	1.18	0.75	1.22	0.69	1.24
	(0.93)	(1.41)	(0.82)	(1.45)	(0.76)	(1.49)	(0.75)	(1.61)	(0.44)	(1.65)
Hp-10	0.94	1.35	0.90	1.68	0.88	1.84	0.84	2.54	0.70	2.62
	(0.77)	(1.21)	(0.76)	(1.55)	(0.73)	(1.73)	(0.70)	(2.65)	(0.69)	(2.90)
Hp-12	0.91	1.18	0.85	1.32	0.77	1.59	0.72	2.34	0.58	2.38
	(1.04)	(1.27)	(0.88)	(1.51)	(0.87)	(1.82)	(0.84)	(2.92)	(0.69)	(2.98)
Chi-1	0.68	1.25	0.56	1.44	0.50	1.58	0.31	1.81	0.27	2.22
	(0.54)	(1.02)	(0.45)	(1.18)	(0.40)	(1.30)	(0.24)	(1.53)	(0.21)	(1.83)
Chi-2	0.63	1.24	0.51	1.44	0.49	1.59	0.47	1.74	0.41	1.97
	(0.74)	(1.45)	(0.59)	(1.69)	(0.57)	(1.84)	(0.55)	(1.99)	(0.48)	(2.23)
Chi-3	0.65	1.01	0.51	1.22	0.35	1.28	0.17	2.40	0.17	2.40
	(0.49)	(0.81)	(0.41)	(0.83)	(0.31)	(1.11)	(0.15)	(1.47)	(0.15)	(1.47)
Cal-1	0.66	1.13	0.58	1.29	0.46	1.42	0.33	1.48	0.30	1.71
	(0.41)	(0.66)	(0.36)	(0.77)	(0.26)	(0.82)	(0.21)	(1.05)	(0.18)	(1.32)

[a]Values in parentheses indicate values of p and P as percentiles of the distribution of values about the typical curve, that is, curve of best fit for the data of the group.

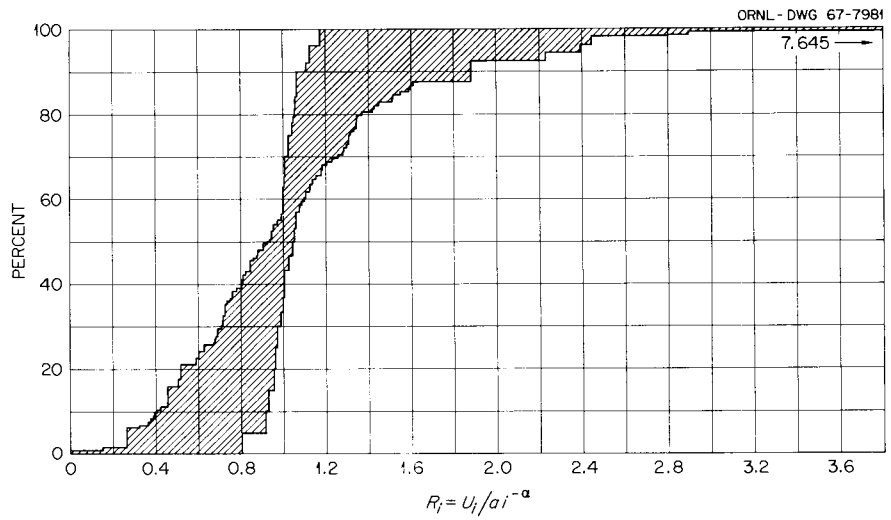

Fig. 25.32. Fluctuations of Daily Urinary Excretion Data of All Patients (Langham, 1950) About Their Own Formula of Best Fit – "Point Fit" Formulas Obtained by Minimizing the Sum of Percent Deviations.

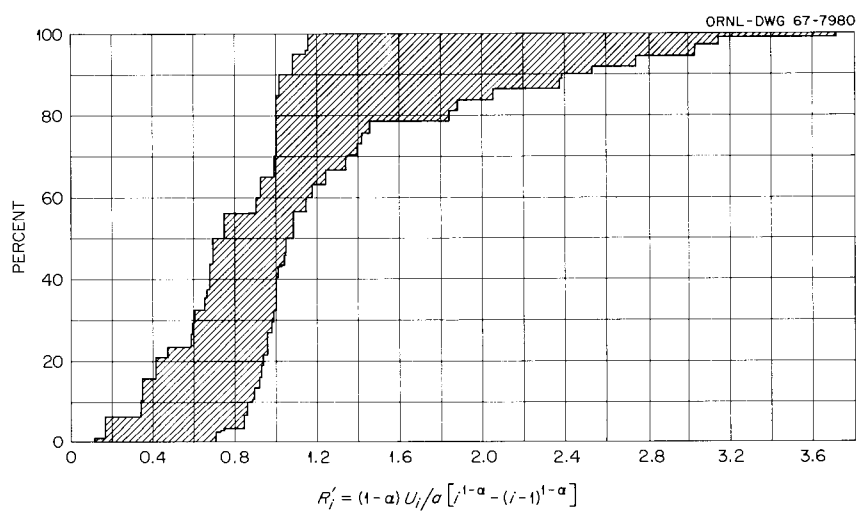

Fig. 25.33. Fluctuations of Daily Urinary Excretion Data of All Patients (Langham, 1950) About Their Own Formula of Best Fit – "Area Fit" Formulas Obtained by Minimizing the Sum of Percent Deviations.

have been described in the literature.[54–56] All these codes are basically of the same general type in that they use the power function $at^{-\alpha}$ describing the trend of urinary excretion following a single intake to blood as a basis for estimating a series of intakes that would be expected to produce the observed excretion pattern as closely as possible. However, these codes have generally used only the trend curve $ai^{-\alpha}$ to estimate the intakes necessary to produce the recorded excretion values and thus took little account of the fact that wide fluctuations of the data are possible and properly should influence the estimates of intake. The present code has been designed to utilize data on the fluctuation of daily excretion levels

[55] J. N. P. Lawrence, *Health Phys.* **8**, 61 (1962).

[56] W. S. Snyder, "The Estimation of a Body Burden of Pu from Urinalysis Data," p. 13 in *Proceedings of the Seventh Annual Meeting on Bio-Assay and Analytical Chemistry*, ANL-6637 (1961).

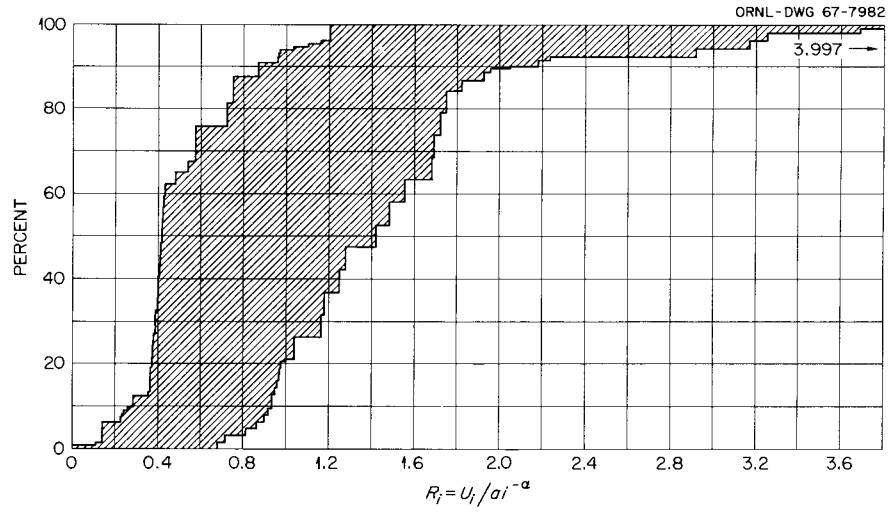

Fig. 25.34. Fluctuations of Daily Urinary Excretion Data of All Patients (Langham, 1950) About the "Typical" Formula of Best Fit – "Point Fit" Formula Obtained by Minimizing the Sum of Percent Deviations.

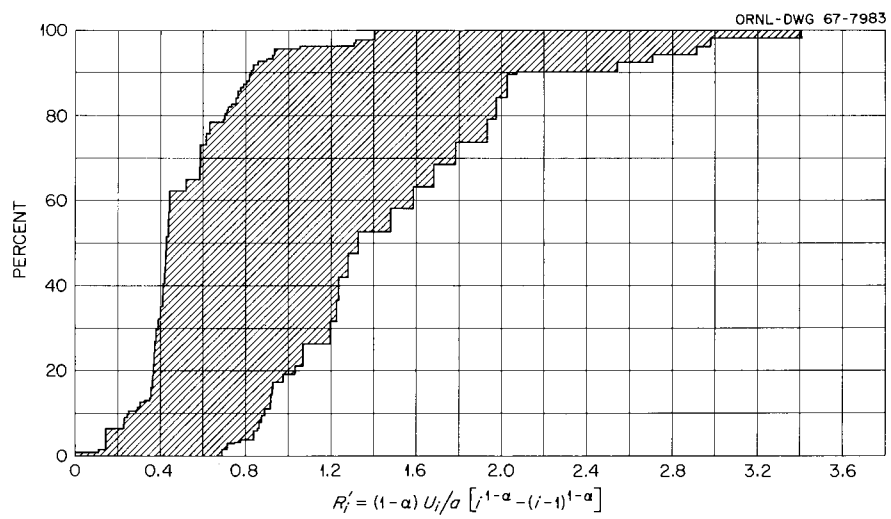

Fig. 25.35. Fluctuations of Daily Urinary Excretion Data of All Patients (Langham, 1950) About the "Typical" Formula of Best Fit – "Area Fit" Formula Obtained by Minimizing the Sum of Percent Deviations.

about the urinary excretion curve $at^{-\alpha}$ and thus reduce somewhat the magnitude and number of intakes that are required.

The code uses as input a value $\Delta \geqq 0$, which represents the supposed level of sensitivity of the analytical methods, that is, the minimum detectable level of activity in a daily urine sample. Any sample value which is less than Δ is regarded as being essentially identical to zero, and no intake is considered necessary to account for the reported activity. If the input specifies zero as the value of Δ, no sample will be rejected by this test. Thus use of this feature of the code is at the discretion of the user.

Two percentage values (p, P) also are included as input for the code. These two values specify a certain range of fluctuation, either high or low, which is considered as acceptable, but excretion values lying beyond the range (whether too high or too low) are considered as not acceptable, that

is, as requiring some modification of the intakes previously estimated. The code is designed to modify the estimates of intake in the latter case so as to produce a pattern of intake which is acceptable if that is possible. For example, if U_i is the first sample value and occurs on day t_1, then the computer will estimate an intake I_1 on a day τ_1 by use of either of the formulas given in Eq. (5). There is some arbitrariness here, both in the choice of the day τ_1 and in the use of the formula which only represents a typical value for the excretion. Actually, the excretion on day t_1 might have been higher or lower than would be predicted by the formula. There is no readily apparent way of deciding whether on any given day excretion was higher or lower than is typically the case, but this should not prevent us from recognizing that this arbitrariness, or uncertainty, is there.

The computer code can be designed to make some allowance for the effect of these fluctuations of the day-to-day data. If the first intake is computed as indicated in the preceding paragraph, that is, on the basis of the formula for the typical or average case, and if the next excretion sample, U_2 on day t_2, shows an activity in excess of what would be expected from the intake I_1, it should be recognized that it is not always necessary to postulate that a new intake occurred on some day between the two sample dates. It may be that the first intake I_1 has been overestimated, and this could occur in several ways, either because the day of intake τ_1 has been wrongly assigned or because excretion happened to be unusually high on the day of the first sample. On the basis of Table 25.10, one can assign a confidence level and use the code so that if U_2 exceeds the excretion predicted on the basis of I_1 but not by more than a factor P, then there is a substantial probability that the excess is due only to a chance fluctuation on the high side. On the other hand, if U_2 exceeds the predicted excretion following an intake I_1 by more than the factor P, there is little likelihood that this is a chance excess, and hence it is likely that some new intake, say I_2, occurred between the sample days t_1 and t_2. However, one postulates such an intake only when the excess above the excretion predicted on the basis of I_1 is so great that it is not likely that a chance fluctuation is responsible for the excess. The numerical value of P can be chosen by the user of the code to correspond to various levels of confidence concerning the extent of daily fluctuations he will allow. In fact, the code can be run for a variety of different levels P and the results compared.

In similar fashion, if the excretion U_2 is less than that predicted on the basis of the first intake, one may decide that I_1 should be reduced. Instead of estimating I_1 solely on the basis of U_1 and the trend curve, say $ai^{-\alpha}$, one may postulate that U_1 is unusually high, say $Pai^{-\alpha}$, and that U_2 occurred on a day when excretion was low, say as given by $pai^{-\alpha}$, or he may use a combination of both assumptions.

The above simple illustration involving only two intakes, I_1 and I_2, and two excretion values, U_1 and U_2, applies in principle to any set of intakes and excretion values. If one has estimated intakes $I_1, I_2, \ldots, I_k$ which correspond to and produce given excretion values $U_1, U_2, \ldots, U_k$, then one may estimate the excretion on a later day from the above intakes. If the actual excretion on this later day does not differ too greatly from that predicted, no new intake need be postulated. If the difference is sufficiently great, one seeks to redefine the intakes $I_1, I_2, \ldots, I_k$ and may, in this way, reduce the difference of the actual and predicted values to lie within the expected limits of variability. Only when this adjustment fails to reduce the difference to within the prescribed factor P does one postulate a new intake I_{k+1} to account for the excess. When many intakes have occurred, the number of possible adjustments is enormous, and the best method of arriving at an acceptable set of intakes is still being explored. However, the principle seems well established, and experience to date with the code indicates it is a definite improvement over methods of estimation which neglect the influence of fluctuations of the excretion data.

26. Stable Element Metabolism

W. S. Snyder
Mary Jane Cook
Cyrus Feldman[1]
F. S. Jones[1]
Peggy L. Stewart[2]
Isabel H. Tipton[2]

In many cases information on the metabolism of stable elements in humans has provided a more reliable basis for calculating maximum permissible concentration (MPC) values than small animal data. Therefore, the study has been extended to include analysis of daily intake and excretion of individuals on *ad libitum* diets. These data are also of interest in interpreting excretion data to estimate dose or body burdens.

A large number of the heavy elements are known to localize in the skeleton. However, owing to the large quantity of $Ca_3(PO_4)_2$ the trace element determinations are more difficult on bone than soft tissues. Since different chemical procedures are needed, much attention has been directed to developing a procedure for the determination of trace elements in bone.

The results of this program are presented in the following sections. The data obtained from these studies will be incorporated with other data for estimating internal exposure to radionuclides.

LONG-TERM STUDY OF INTAKE AND EXCRETION OF STABLE ELEMENTS

Isabel H. Tipton Peggy Lou Stewart

Information on the daily elemental intake and excretion of individuals on their usual diets is difficult to obtain for various reasons. In general the published values for ordinary diets have been obtained from a population different from that for which the values for urine were obtained, which in turn are from a different population from that which provided the values for feces. Almost no information is available for the elemental intake and excretion for a set of the same individuals. Of course individual diets differ greatly even in a fairly homogeneous population, and the difference is even greater among different ethnic groups. In spite of these differences, however, it is reasonable to expect that for normal, adequately nourished human beings, the excretion after intake of an element should follow a general pattern which might be observed by studying the intake and excretion of a few individuals.

At the present time daily diets and excreta of three men are being studied. These men have been, and are, collecting duplicates of their daily diets and saving all excreta for a number of years for Dr. R. A. Kehoe's lead studies at Kettering Laboratory, Cincinnati, Ohio. Since September 1963 this material has been sent to the spectrographic laboratory at the University of Tennessee, where it has been stored frozen until methods for analysis were developed. Only two men participate in the study at one time. One of the men discontinued his part in the program in July 1966, and another man entered the program at that time. Data from a continuous period of such a long duration will allow statistical studies on the influence of time after intake, of intake of other elements, and of other factors on the excretion of an element.

So far analyses for two men for the interval between September 9, 1966, and January 7, 1967, have been completed. The data have been treated by two-month periods. This report includes period

[1]Analytical Chemistry Division.
[2]Physics Department, University of Tennessee.

1, September 9 through November 7, 1966, and period 2, November 8, 1966, through January 7, 1967.

Analytical methods appropriate to the element have been developed. That is, calcium, magnesium, potassium, and sodium have been analyzed by flame photometry; phosphorus by a colorimetric method; and aluminum, barium, beryllium, boron, chromium, cobalt, copper, iron, manganese, molybdenum, nickel, silver, strontium, tin, titanium, vanadium, zinc, and zirconium by emission spectroscopy. (Methods are being developed for analyzing zinc, cadmium, cesium, and rubidium by atomic absorption and lead by emission.) A detailed description of these methods is being prepared for publication. Only a summary indicating the range and precision of the method are included here.

Table 26.1 shows the range of concentrations (in micrograms per gram of dry ashed sample) of which the method is capable. In Table 26.2 an indication is given for the repeatability of the method. Column 1 gives the percent standard deviation for 23 elements resulting from 10 analyses of the same ashed sample of urine (the repeatability for food and feces is comparable). Column 2 shows the percent standard deviations of 7 elements in a sample of food carried 12 times through the entire method of ashing and analysis. For chromium, silver, zinc, and zirconium, the high background in the vicinity of the line contributes to the variability. Vanadium is a varying contaminant of the electrodes for which it is difficult to correct. Since the electrodes in which food samples are burned are different from those in which urine and feces are burned, a differential contamination may be found. Although the precision for beryllium is good in all three types of samples, it appears that this element

Table 26.1. Analytical Methods – Range of Concentration

Micrograms per gram of dry ash

Method	Element	Food		Urine		Feces	
		Low	High	Low	High	Low	High
Flame photometry	Ca	7,000	440,000	260	17,000	5,200	340,000
	Mg	2,100	92,000	260	12,000	5,200	230,000
	K	10,000	460,000	10,000	460,000	5,200	230,000
	Na	10,000	460,000	10,000	460,000	1,000	46,000
Colorimetry	P	10,000	200,000	4,200	84,000	25,000	500,000
Arc emission spectroscopy	Al	40	4,300	4	420	90	14,000
	Ba	1	700	1	200	10	1,400
	Be	0.5	10	0.1	10	0.1	10
	B	2	350	2	300	5	100
	Cr	1	120	2	200	8	300
	Co	0.5	60	1	150	5	125
	Cu	2.5	250	2	100	10	1,300
	Fe	50		5	1,100	100	8,000
	Mn	8	1,200	0.5	150	15	2,300
	Mo	0.2	75	0.5	50	0.5	90
	Ni	1	250	1	85	3	450
	Ag	0.3	100	0.1	20	0.5	125
	Sr	1	450	0.3	15	30	3,000
	Sn	3	1,800	2	85	15	4,000
	Ti	1	350	3	220	15	1,100
	V	1	50	0.5	75	3	120
	Zn	65	3,500	90	2,400	150	16,000
	Zr	1	450	5	800	0.5	525

Table 26.2. Repeatability of Methods

Percent standard deviation

Element	Analytical Method[a]	Total Method (Including Ashing)[b]
Ca	0.93	1.3
Mg	1.4	2.1
K	1.5	
Na	0.66	
P	2.3	
Al	4.3	9.4
Ba	3.1	7.2
Be	1.5	
B	8.4	
Cr	25	
Co	4.2	7.7
Cu	7.6	
Fe	3.3	6.9
Mn	3.1	
Mo	6.0	
Ni	6.0	7.5
Ag	13	
Sr	3.3	
Sn	6.8	
Ti	2.8	
V	6.7	
Zn	12	
Zr	11	

[a]Ten replicates of same sample of ash.

[b]Twelve replicates of same sample of wet material.

is sensitive to the gross composition of the material being analyzed, which is different for food, feces, and urine. These analytical difficulties may be a factor in the apparent imbalance of these elements in the diets and excreta of the two subjects.

With a few exceptions the values for the average daily intake and output over two two-month periods compare very well with the values suggested by the Task Group for Standard Man[3] and with the values for the male and female adult subjects reported by us earlier.[4] In general the disagreement occurs for those elements like vanadium and zirconium for which very little information is available (see Table 26.3).

A preliminary study has been made of the relation of the output of an element in urine to the intake of the same element in food for a period of time previous to the day of output for one individual (subject K-H). Urine values were used because it was assumed that any element appearing in the urine must, of necessity, have crossed the intestinal wall (except what had entered the body through absorption from the lung or through abrasions in the skin).

Multiple regressions have been run of the urinary output of all 23 elements with dietary intake of the element on the same day, the previous day, and two, three, four, five, and six days previous. The equation which predicts the urinary output on any day in terms of the intake of the previous week is

$$y = A + a_1x_1 + a_2x_2 + a_3x_3 + a_4x_4 + a_5x_5 + a_6x_6 + a_7x_7 ,$$

where y is the urinary output (μg), $x_1, x_2, \ldots, x_7$ are the daily intake on the same day (x_1), previous day (x_2), two days previous (x_3), etc. (μg), $a_1, \ldots, a_7$ are the partial regression coefficients, A is an added constant (μg) which indicates the amount of an element which would have been excreted if there had been no intake during the previous week.

Table 26.4 gives the values for the coefficients $a_1, \ldots, a_7$ significantly different from zero at the 99% confidence level, the added constant A, the square of the multiple regression coefficient R, and values for the actual and predicted means for boron and nickel. For both elements it appears that the intake on the day previous may be reflected in the urinary excretion on any day. The values for R^2 indicate that about 20% of the variability in urinary output of these elements can be accounted for by the variability in the intake of the previous week.

For the seven-day lag period, very few elements had coefficients significantly different from zero or R^2 above 0.10. A preliminary study on calcium showed an increase in R^2 from 0.08 to 0.22 by increasing the time of lag from 7 to 14 days. It is obvious that longer periods of dietary intake must be investigated.

With the mass of information about the elemental intake and excretion of the same individual over a long period of time that this study provides, it will be possible to make statistical studies on rhythmic

[3]ICRP Task Group for Revision of Standard Man, report in preparation.

[4]I. H. Tipton *et al.*, *Health Phys.* 12, 1683 (1966).

Table 26.3. Mean Values for Intake and Excretion of Individuals

Micrograms per day

Element	T-P, ♀, 6-12-63 to 7-11-63, 30 Days[a]			T-V, ♂, 6-12-63 to 7-11-63, 30 Days[a]			K-S, ♂						K-H, ♂					
							9-9-66 to 11-7-66, Period 1, 60 Days			11-8-66 to 1-7-67, Period 2, 61 Days			9-9-66 to 11-7-66, Period 1, 60 Days			11-8-66 to 1-7-67, Period 2, 61 Days		
	Food	Urine	Feces	Food	Urine	Feces	Food	Urine	Feces	Food	Urine	Feces	Food	Urine	Feces	Food	Urine	Feces
Al	18,000	1,000	17,000	22,000	1,000	45,000	11,000	880	12,000	13,000	590	14,000	8,700	1,100	8,800	15,000	580	27,000
Ba	1,800	280	600	1,500	560	1,800	570	11	610	520	4.3	590	540	17	590	440	2.8	530
Be							93[b]	1.2	6.8	430[b]	0.24	7.1	110[b]	0.77	10	98[b]	2.8	17
B	420	560	14	350	590	10	1,800	1,100	340	2,000	800	490	1,400	2,300	390	700	990	350
Ca	760,000	140,000	400,000	1,310,000	200,000	920,000	1,600,000	160,000	890,000	1,900,000	130,000	1,100,000	970,000	180,000	790,000	960,000	130,000	880,000
Cr	330	100	10	400	200	160	740[b]	120	110	79	46	82	470[b]	86	87	73	53	67
Co	170	190	40	160	140	60	210	330	57	580	210	23	220	290	32	360	310	23
Cu	1,000	330	710	910	320	1,000	1,500	94	1,600	1,600	20	1,100	1,100	49	1,300	770	19	1,000
Fe				15,000	400	14,000	60,000[c]	1,900	10,000	23,000	540	9,000	16,000	1,700	18,000	14,000	1,100	14,000
	12,000	2,000	9,000															
Mg	280,000	4,000	150,000	320,000	8,000	190,000	260,000	120,000	140,000	370,000	110,000	200,000	160,000	130,000	120,000	170,000	130,000	180,000
Mn	4,400	250	1,200	3,500	320	2,600	3,800	57	2,700	3,300	23	3,900	2,800	63	3,400	2,200	9.4	4,100
Mo	99	150	38	100	71	42	490	140	170	1,400	300	210	170	140	140	520	200	220
Ni	330	170	110	170	92	140	1,100	140	380	720	74	430	450	82	230	380	55	290
P	1,200,000	1,000,000	320,000	1,800,000	1,320,000	470,000	2,900,000	1,400,000	600,000	3,300,000	1,100,000	560,000	1,900,000	1,600,000	560,000	1,700,000	1,200,000	460,000
K							3,100,000	3,000,000	240,000	3,900,000	3,200,000	320,000	1,900,000	2,900,000	290,000	1,600,000	2,700,000	250,000
Ag	44	9	28	35	10	79	340[b]	4.8	120	530[b]	11	180	90[b]	8.0	27	350[b]	8.9	59
Na							4,200,000[d]	5,000,000[d]	28,000	4,300,000[d]	5,000,000[d]	33,000	3,300,000[d]	5,300,000[d]	42,000	3,200,000[d]	4,700,000[d]	31,000
Sr	1,400	240	810	1,200	420	970	1,100	110	890	2,000	58	1,500	1,200	110	1,100	1,500	140	1,200
Sn	1,500	110	2,100	2,500	80	1,600	10,000	100	7,000	7,500	68	2,700	11,000	220	8,200	3,700	86	4,400
Ti	370	300	340	680	310	890	1,000	370	770	1,600	370	310	690	410	400	790	250	430
V							120[b]	40	270	130	34	180	72[b]	32	150	69[b]	26	170
Zn							16,000[b]	2,500	23,000	18,000	1,600	17,000	12,000[b]	2,500	18,000	11,000[b]	1,400	15,000
Zr							1,200[b]	92	180	550	190	320	650[b]	160	170	580[b]	100	180

[a] I. H. Tipton *et al.*, *Health Phys.* 12, 1683 (1966).

[b] The apparent imbalance may be due to analytical problems. See text.

[c] Median value was 18,000.

[d] Both subjects, but especially H, were careless about salting the duplicate meal as well as the one consumed. This gives a spurious negative balance for sodium. Both subjects have corrected this practice and in periods after May 1967 this false negative balance should not occur.

Table 26.4. Regression Equations for Predicting Urinary Output from Dietary Intake: Subject K-H

Coefficients significantly different from zero at $p \leq 0.01$ unless indicated otherwise

		Boron		Nickel	
		Period 1	Period 2	Period 1	Period 2
Days previous	Coefficient				
0	a_1				
1	a_2	0.40[a]	0.32	0.79	0.063
2	a_3				
3	a_4			0.53[b]	
4	a_5				
5	a_6				
6	a_7				
Constant A (μg)		1800	870	28	29
R^2		0.24	0.14	0.27	0.14
Actual mean (μg)		2300	990	83	54
Standard deviation		2100	820	75	71
Predicted mean (μg)		2300	980	83	55
Standard error of estimate		1900	810	68	71

[a] $p < 0.001$.
[b] $p < 0.05$.

variations in excretion patterns of elements and to develop mathematical models relating intake and excretion of a number of elements.

TISSUE ANALYSIS LABORATORY

Cyrus Feldman F. S. Jones

Because bone is one of the most difficult tissues to analyze for trace elements, attention has been directed to improving the overall sensitivity for the detection of trace elements by developing a chemical preconcentration procedure.

The Mitchell-Scott procedure (precipitation of trace elements with a mixture of 8-OH quinoline, tannic acid, and thionalide) was selected for investigation. This procedure proved quite effective for collecting several trace elements, but was ineffective with others (e.g., Mn). It was sometimes difficult to prevent the precipitation of substantial amounts of $Ca_3(PO_4)_2$ along with the trace elements, especially under the conditions necessary to precipitate chromium.

Attempts to circumvent the coprecipitation problem by extracting the trace elements from solutions of bone ash were successful for only a few elements. The presence of phosphate again hampered extractions which would otherwise have been successful. It was therefore decided that the development of a general collection procedure would be greatly facilitated by first eliminating phosphate from the sample.

The most straightforward way to do this in this case would be to adsorb all of the cations on a cation exchange column, allowing the phosphate to pass through the column. However, treating a large sample of bone ash by this method would require a large amount of resin. The resulting reagent blanks would probably defeat the purpose

of the procedure, and a great many studies of trace element recovery would be needed.

It was decided instead to try to remove the phosphate by electrodialysis through anion-permeable resin membranes. This approach would permit the handling of large samples without a commensurate increase in contamination. Although other anions besides phosphate would be removed, few of these are of interest in the present case.

A three-compartment cell was prepared, and the sample (a slightly acid solution of natural or synthetic bone ash) was placed in the center compartment. To avoid problems connected with migration of cations through a cation-permeable membrane and deposition of such ions on the cathode, both walls of the center chamber were made of anion-permeable (i.e., cation-impermeable) resin membrane. The acid used to dissolve the bone ash had to be strong enough to accomplish this dissolution, yet weak enough to leave most of the phosphate in the form of an anion (e.g., $H_2PO_4^-$) rather than the neutral H_3PO_4. The anions of this acid also had to have a relatively low affinity for the anionic resin; the acid itself had to be easily purified and easily eliminated from the solution after processing. Formic acid fulfilled these requirements and was chosen as the solvent. A solution of the formic acid was also placed in the cathode chamber, and a solution of NaOH in the anode chamber. Electrodialysis was carried out at ~20 v, 600 to 700 ma. Migration of phosphate ions toward the anode tended to increase their concentration near the anode compartment wall. Since this favored their migration through the membrane, we refrained from stirring the solution in the center compartment.

Tracer experiments showed that the concentration of phosphorus in the center cell decreased almost exponentially with time. Performance of the cell was therefore measured in terms of the "half-life," that is, the time required to reduce the phosphorus concentration in the center cell to one-half its previous value. Typical results are given in Table 26.5. Unless otherwise noted, the sample consisted of 1 g of $Ca_3(PO_4)_2$ dissolved in 5 ml of HCOOH, pH adjusted to 3, with 10% HCOOH in the anode compartment and 1 *N* NaOH in the cathode compartment. Under the last-named conditions in Table 26.5, less than 4% of the original phosphate remained after 6 hr. This degree of removal proved adequate to permit use of the Mitchell-Scott chemical collection procedure and made it possible to improve the procedure's efficiency for the collection of manganese and chromium. This procedure will now be applied to bone ash and tested for the recovery of trace elements.

Table 26.5. Removal of Phosphate from Calcium Phosphate Solution by Electrodialysis Through Anion Exchange Membrane

Voltage (v)	Current (ma)	Time to Reduce PO_4 by Half (min)	Conditions
10	140–70	820	All compartments stirred
10	135–88	500	Center compartment not stirred
23	365–160	320	
23	410–60	270	20% HCOOH in anode compartment
23	650	80	Same as above; center compartment heated to 65–70°

Part VI. Health Physics Technology

B. R. Fish

27. Aerosol Physics

B. R. Fish

R. H. Boyett
T. G. Clark
G. W. Royster, Jr.
F. G. Karioris[1]
J. L. Thompson
R. L. Walker
W. H. Wilkie, Jr.
B. M. Smith[2]
R. E. Goans[3]

ADHESION OF PARTICLES TO PARTICLES AND TO PLANE SURFACES

B. R. Fish F. G. Karioris
R. L. Walker

Adhesion of particles to surfaces and their adhesion to form agglomerates are of much practical importance in the understanding of air sampling and air cleaning devices. General adhesion phenomena have been treated extensively in the literature during the last 20 years.[4] Although the adhesion of solid particles has been reviewed comprehensively by Corn,[5] most references on adhesion between particles tend to emphasize one or the other phenomenon, implying, and sometimes stating, that others are unimportant. An example of this is in Fuchs'[6] book, where he devotes several paragraphs to the discussion of capillary forces but dismisses electrical charge as having no marked effect.

A more adequate picture of particle adhesion must recognize a variety of physicochemical mechanisms, each becoming important depending upon the properties of the adhering particles and of the ambient environment. Table 27.1 includes a few examples of adhesion forces that may become dominant under some given condition. The table is not exhaustive, ignoring, for example, sintering of particles as well as Stephan's "apparent" adhesion.[7,8]

Preliminary investigations previously reported[8,9] suggest that capillary and electrical forces predominate in many cases; thus we have concentrated our attention on these mechanisms. However, it is clear that under some conditions other adhesion phenomena can become dominant.

Capillary Force Between Two Spheres of Equal Radii

Given two spheres of equal radii R in contact, as in Fig. 27.1, it is seen that the region of contact constitutes a capillary of revolution. Assuming the spheres to be wettable by water, one

[1]Temporary summer employee, Marquette University, Milwaukee, Wis.

[2]On assignment from National Center for Air Pollution, USPHS, Cincinnati, Ohio.

[3]Temporary summer employee, University of Tennessee, Knoxville.

[4]N. A. DeBruyne and R. Houwink (eds.), *Adhesion and Adhesives*, Elsevier, Amsterdam, 1951; and R. Houwink and G. Salomon (eds.), *ibid.*, vol. 2, 1967.

[5]M. Corn, "Adhesion of Particles," chap. XI in *Aerosol Science* (ed. by C. N. Davies), Academic, London, 1966.

[6]N. A. Fuchs, *Mechanics of Aerosols*, Pergamon, Oxford, 1964.

[7]J. J. Bickerman, "Solid-to-Solid Adhesion," p. 166 in *Fundamental Phenomena in the Materials Sciences*, vol. 2 (ed. by L. J. Bonis and H. H. Hausner), Plenum, New York, 1966.

[8]R. L. Walker and B. R. Fish, "Adhesion of Particles to Surfaces in Liquid and Gaseous Media," *Proc. National Tech. Mtg., American Association for Contamination Control, Miami, Fla., May 25–28, 1965.*

[9]B. R. Fish *et al.*, *Health Phys. Div. Ann. Progr. Rept. July 31, 1966*, ORNL-4007, p. 245.

Table 27.1. Summary of Adhesive Forces

Capillary forces	Attractive	Environment controlled
Electrical forces		
Free surface charge	Repulsive	Transient (rapid decay)
Bound volume charge	Attractive or repulsive	Transient (slow decay)
Contact electrification	Attractive	Permanent
Molecular forces	Attractive	Permanent

may expect an equilibrium layer of water to be condensed around the contact point, the size and shape depending on the ambient partial pressure of water.[9]

In Fig. 27.1, ρ is the radius of curvature of the liquid surface at a given point, n is the radius of curvature lying along the normal to the surface, and α is the angle made by the intersection of the tangent to the surface with the line of centers of the spheres. Since the surface is one of revolution about the line of centers, n terminates on this axis. It was shown by Laplace that the surface is one of constant mean curvature and that the normal and the radius of curvature at every point must obey the relation

$$\frac{1}{n} - \frac{1}{\rho} = \frac{\Delta P}{\gamma} ,$$

where γ is the surface free energy (surface tension) of the liquid and ΔP represents a pressure change across the interface from the air into the liquid.

From the geometry and Laplace's relation a differential equation may be derived relating X and α. This may be integrated, using the boundary condition that $\alpha = 0$ and $X = X_0$ at $Y = 0$, to give

$$X \cos \alpha - \frac{\Delta P}{2\gamma} X^2 = X_0 - \frac{\Delta P}{2\gamma} X_0^2 ,$$

which can be referred to contact at the sphere by noting that, at contact, $\cos \alpha = \sin \theta$, where θ is the angle between n at the point of contact and the axis (see Fig. 27.1).

It can be shown that there are an infinite number of such surfaces of revolution having the same mean curvature that can be made to fit geometrically between two spheres. However, the equilibrium surface is the one for which a force balance is possible. In Fig. 27.2, hypothetical cutting planes have been employed to isolate the region of concern, and the unmatched forces acting on the isolated region are shown. At the intersection with the sphere, a force T_s, representing the surface tension of the solid in contact with air (γ_s), acts on the isolated section in a direction tangent to the sphere. The vertical component is

$$F_n = T_s \sin \theta = 2\pi R \gamma_s \sin^2 \theta .$$

This component is the normal force of capillary adhesion between the two spheres and at equilibrium must balance the force due to the liquid surface tension,

$$T_\ell = 2\pi X_0 \gamma ,$$

ORNL-DWG 67-8728

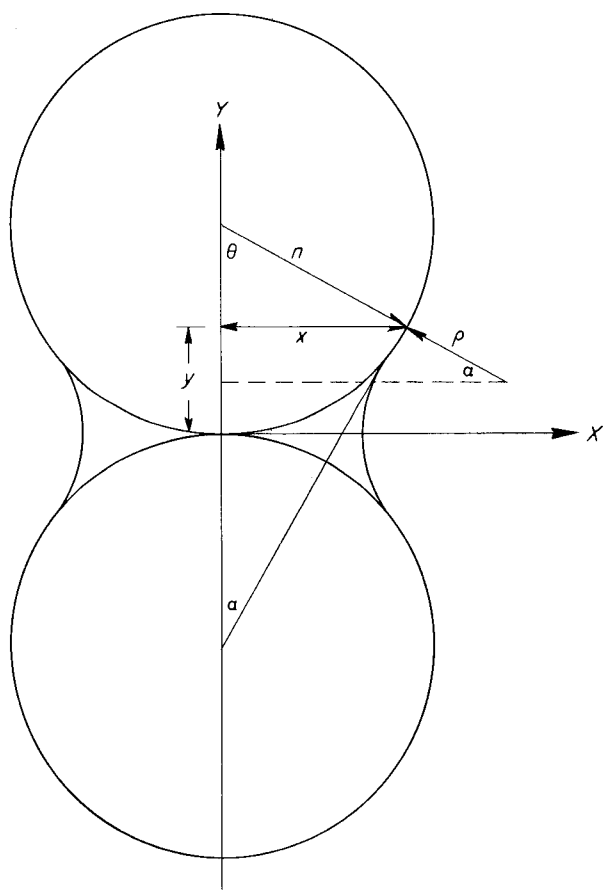

Fig. 27.1. Geometrical Relationships for the Surface of a Liquid Capillary Formed Between Two Spheres of Equal Radii.

ORNL-DWG 67-8729

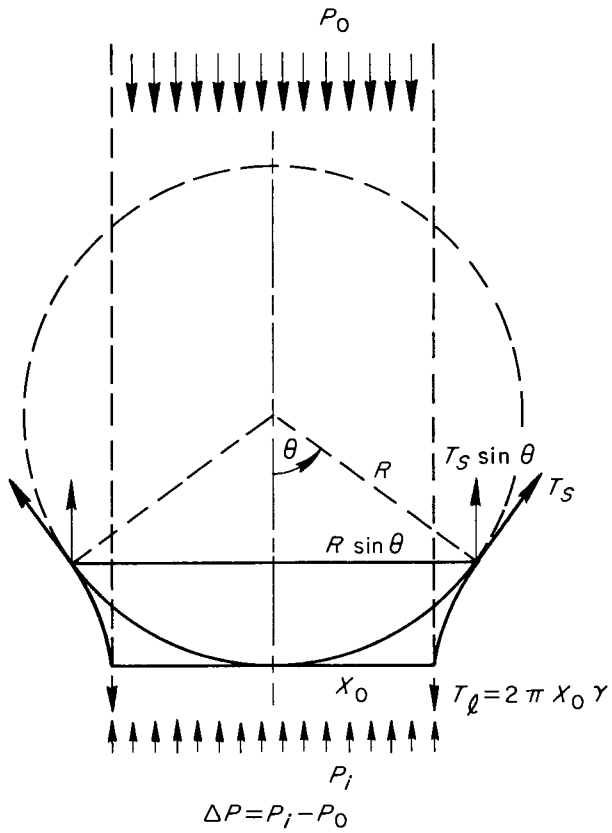

Fig. 27.2. Balance of Forces Acting on a Liquid Capillary Between Two Spheres of Equal Radii.

plus the force due to the differential pressure acting over the minimal cross section,

$$\Delta P \times \text{area} = \pi X_0^2 \, \Delta P \, .$$

Thus, for force balance

$$R\gamma_s \sin^2\theta = \frac{1}{2} \Delta P \, X_0^2 + \gamma X_0 \, .$$

This condition may be combined with that derived above from geometrical considerations to yield an expression for X_0 as a function of known parameters. Two solutions are possible,

$$X_0 = 0$$

and

$$\frac{X_0}{2a} = \frac{(\gamma_s/\gamma) + [(R/2a) - 1]}{(\gamma_s/\gamma) - [(R/2a) - 1]} \, ,$$

where $1/2a$ = constant mean curvature = $\Delta P/2\gamma$ and is a function of relative humidity.

The maximum adhesive force occurs when θ is a maximum, and this requires that the relative humidity be 100%. Under this condition $\Delta P = 0$. The capillary assumes the shape of a catenoid, and $n = \rho$ everywhere on the surface. With this restriction the meridian curve is

$$\frac{Y}{X_0} = \ln\left(\frac{X}{X_0} + \sqrt{\frac{X^2}{X_0^2} - 1}\right) ,$$

a catenary. By imposing known relationships between X, Y, R, and θ at the sphere, an implicit function may be obtained relating R/X_0 and θ; thus

$$\frac{R}{X_0}(1 - \cos\theta) = \ln\left(\frac{R}{X_0}\sin\theta + \sqrt{\frac{R^2}{X^2}\sin^2\theta - 1}\right) ,$$

while $(R/X_0)\sin^2\theta = \gamma/\gamma_s$ remains as a restriction on the possible size of the capillary layer. Numerical solution of these relations shows that there is a limit to the range of θ and R/X_0 that can satisfy all the necessary conditions. The result is that at 100% relative humidity, the equilibrium capillary depends on the ratio γ/γ_s, but in no case can X_0 exceed 0.68 R nor can θ exceed 67°. Finally, it may be seen that the maximum capillary adhesive force between two spheres of equal radii is

$$F_{max} = 2\pi R\gamma_s \sin^2 67° = 5.329 R\gamma_s \, .$$

COULOMETRIC ELECTROLYTIC TANK FOR STUDY OF ELECTRICAL FORCES ON PARTICLES

F. G. Karioris B. R. Fish
J. L. Thompson

The effects of electrical forces on an isolated aerosol particle are reasonably well known.[10] Although the importance of electrical forces in adhesion of particles to surfaces has been recog-

[10] N. A. Fuchs, *The Mechanics of Aerosols*, pp. 107–59, Macmillan, New York, 1964.

nized,[11,12] the physical mechanisms involved are not easy to treat analytically. When a conducting particle contacts a charged capacitor plate in a liquid dielectric medium, the particle acquires a charge and experiences a repulsive force which drives it through the medium until it contacts the opposite plate, where the process is repeated.[13] While in the electric field between the plates, the electrical force on the particle is

$$\mathbf{F} = q\mathbf{E} \tag{1}$$

at distances greater than about 5 sphere radii from either plate. By measuring the speed of the particle and applying Stokes' law, the total charge on the particle can be estimated.

However, the electrical force on a conducting particle in contact with a conducting plane is influenced by mutual interactions, the so-called image charges, with the plane and has not been calculated even when the particle is an idealized sphere. Theoretically, the electrical "lifting" force could be calculated if the charge distribution on the particle were known. Charge area density σ on a conducting surface produces a pressure $\sigma^2/2\epsilon$ and a force normal to the surface given by[14]

$$d\mathbf{F} = \frac{\sigma^2}{2\epsilon} d\mathbf{A} , \tag{2}$$

where ϵ is the permittivity of the medium. The electrical force acting in any direction specified by the unit vector $\mathbf{n}$ can be found by integrating the expression

$$\mathbf{n} \cdot d\mathbf{F} = \frac{\sigma^2}{2} \mathbf{n} \cdot d\mathbf{A} . \tag{3}$$

The variable σ depends on the position of $d\mathbf{A}$ but could be calculated from the electric field E_s at the surface from the well-known expression

$$\sigma = \epsilon E_s . \tag{4}$$

For complicated or mixed boundary conditions, the calculation of E_s is extremely difficult, even when the potentials at the boundaries are known. In such instances, an analog solution such as the electrolytic trough is useful and may be the only means of obtaining quantitative results in certain problems.

The basic theory for the electrolytic trough analog is well known.[15,16] For an isotropic homogeneous conducting medium, Ohm's law may be stated as

$$\mathbf{j} = g\mathbf{E} = -g \nabla V , \tag{5}$$

where $\mathbf{j}$ is the current density (amp/m^2), $\mathbf{E}$ is electric field (v/m), g is conductivity (ohm-meters^{-1}), and V is the potential (v). Since, in a conductive medium,

$$\nabla \cdot \mathbf{j} = -g \nabla \cdot \nabla V = 0 , \tag{6}$$

Eq. (6) reduces to the Laplace equation,

$$\nabla^2 V = 0 . \tag{7}$$

The electrolytic trough analog has been used extensively to simulate the potential distributions for many physical situations which are governed by the Laplace equation.[17,18] This includes electric and magnetic fields, hydrodynamic and aerodynamic fields, temperature fields, elastic stress fields, diffusion, and others. The analog method is used to determine fields which cannot be solved analytically or for which numerical relaxation methods[19] would be extremely tedious. In practice, precision measurements are made of the spatial distribution of potential in the model, and by numerical or graphical analysis of the observed equipotentials, the field is determined in the space between the given electrodes. When the field intensity at a boundary is required (e.g., at the surface of an electrode),[20] the usual pro-

[11] B. V. Deryagin and A. D. Zimon, *Kolloidn. Zh.* **23**, 454 (1961).

[12] M. Corn and F. Stein, *Am. Ind. Hyg. Assoc. J.* **26**, 325 (1965).

[13] B. R. Fish *et al.*, *Health Phys. Div. Ann. Progr. Rept. July 31, 1966*, ORNL-4007, pp. 248–50.

[14] J. Jeans, *The Mathematical Theory of Electricity and Magnetism*, 5th ed., p. 79, Cambridge University Press, New York, 1941.

[15] P. A. Kennedy and G. Kent, *Rev. Sci. Instr.* **27**, 916 (1956).

[16] E. R. Hartill, J. G. McQueen, and P. N. Bobson, *Proc. IEE (London)* **104A**, 401 (1957).

[17] L. Dadda, *L'Energia Elettrica* **1**, 23 (1951).

[18] M. Hackenschmidt, *Technik (Germany)* **18**, 478 (1963).

[19] R. V. Southwell, *Relaxation Methods in Theoretical Physics*, Clarendon, Oxford, 1946.

[20] L. B. Loeb *et al.*, *Rev. Sci. Instr.* **21**, 42 (1950).

cedure is to plot the equipotentials in the intervening space, calculate field intensities by numerical methods, and extrapolate to the boundary.

A more direct measurement of the electric field at a complicated boundary is possible with the electrolytic tank if one carries out the procedure so as to electrodeposit a metal on the surface of interest. When Eq. (5) is multiplied by the electrochemical equivalent z (kg/coulomb) of the metal ion in the electrolyte, the result is

$$z\mathbf{j} = \frac{d}{dt}\frac{dm}{d\mathbf{A}} = \acute{g}z\mathbf{E} \ , \tag{8}$$

and the area density of metal electrodeposited during time t (sec) on a surface at which the field is E_s, ideally, is given by

$$\frac{dm}{dA} = \acute{g}ztE_s = k\sigma_s \ . \tag{9}$$

The area density of metal can be determined by stripping known areas from definite positions and weighing the metal or determining the mass chemically. The constants of proportionality in Eq. (9) can be determined by measuring the conductivity and time or by determining the area density of metal at places on the surface of the model where the field is well known from theoretical considerations.

Despite the appealing simplicity of this approach, there are difficulties with the electrolytic plating method. Equation (8) tells only part of the story, leaving out the important consideration of ionic diffusion effects. A more complete description of the current density field in an electroplating bath is given by

$$z\mathbf{j} = -D \ \mathbf{grad} \ C + \acute{g}z\mathbf{E} \ ,$$

where D is the diffusion constant of the ion and C is its concentration. Although various steps can be taken to minimize the effect of concentration gradient, it cannot be eliminated, and, consequently, analog solutions based on this approach must be considered to be only first-order approximations.

Where applicable, the method is especially suited to problems for which the field at certain boundaries must be determined and for which the field in the space between electrodes is of no interest. Extensive measurements of the three-dimensional potential distribution within the model are not required. Such a coulometric analog tank has been constructed for the determination of surface charge distributions on various shaped conducting particles in contact with a conducting plane. It consists of a 66-cm-high, 45-cm-diam cylindrical polyethylene tank, open at the top and filled to a height of about 60 cm with a copper plating solution. Circular copper electrodes, 0.64 cm thick and closely fitting the inner diameter of the tank, are spaced about 60 cm apart in the solution and with the lower electrode resting on the bottom. The bottom plate is covered with a polyethylene sheet, painted with silver paint, and then very lightly "flashed" with copper in the plating bath to ensure a uniform, low-resistance equipotential surface. Models are made of the particle shapes to be tested, and they are coated with silver paint, "flashed" with copper, and attached to the bottom plate. Tests are made to ensure zero resistance from any part of the particle surface to any point on the plane. The electrode assembly is then placed in the tank, and copper is electrodeposited on the test configuration at room temperature with 1 to 3 v dc, 2 to 4 amp, or about 2 ma/cm^2. The plating liquid is periodically circulated through a charcoal and fiber-glass filter. Copper is plated to sufficient thickness that it may be cut from specific areas and weighed directly on an analytical balance.

To explore the validity of the method, preliminary tests have been made with a hemisphere at the center of the bottom plane. The charge distribution for this configuration is well documented in texts on electrostatics. Using the coordinate system shown in Fig. 27.3, where the radius of the hemisphere is a and σ_0 is the charge density on the plane at a very large distance from the origin, the charge density on the hemisphere as a function of θ is

$$\sigma(\theta) = 3\sigma_0 \cos\theta \ ; \tag{10}$$

while on the plane, at $\theta = 90°$ and a distance $r > a$ from the origin, the charge distribution is

$$\sigma(r) = \sigma_0 \left(1 - \frac{a^3}{r^3}\right) . \tag{11}$$

Equation (10) can be integrated to yield an expression for the cumulative fraction of the charge residing on the sector from 0 to θ, and by applying

the coulometric analog equation, a similar expression can be obtained for the fraction of the total copper mass deposited on the hemisphere which should be found on the sector 0 to θ. Thus,

$$M(\theta) = \frac{\sum_0^\theta \Delta m}{m_{tot}} = \frac{1}{q}\int_0^\theta \sigma(\theta)\, d(\text{area}) = \sin^2\theta \,. \tag{12}$$

By a similar treatment, it can be shown that, on the plane,

$$M(r) = \int_{r_1}^{r_2} dm = k\,\sigma_0 \left\{ \pi \left[r_2^2 - r_1^2 - \frac{2a^3(r_2 - r_1)}{r_1 r_2} \right] \right\} = k\sigma_0\, f(r) \,. \tag{13}$$

The electrodeposited copper is stripped from the hemisphere and the plane in known sectors, and each segment is weighed. The fractional distribution of copper on the hemisphere was calculated and is compared with the theoretical distribution in Fig. 27.4. Similarly, the total quantity deposited on the plane from $r_1 = 4$ cm to r is compared with the theoretical $f(r)$ in Fig. 27.5.

It is obvious from the results of this study of the hemisphere that the electrodeposition analog is far from perfect; nevertheless, it also seems clear that the degree of error resulting from diffusion effects is not so great as to preclude the use of this method for many purposes. Within only a few percent error, the electrical forces on rather complex particle shapes can be determined by this technique.

ORNL-DWG 67-8730

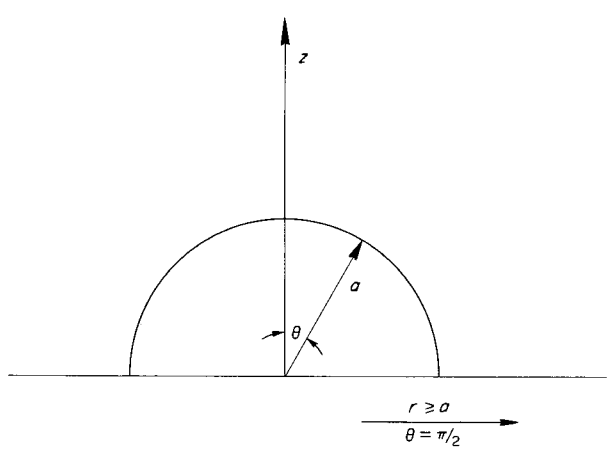

Fig. 27.3. Coordinates for Hemisphere on a Plane.

ORNL-DWG 67-8731

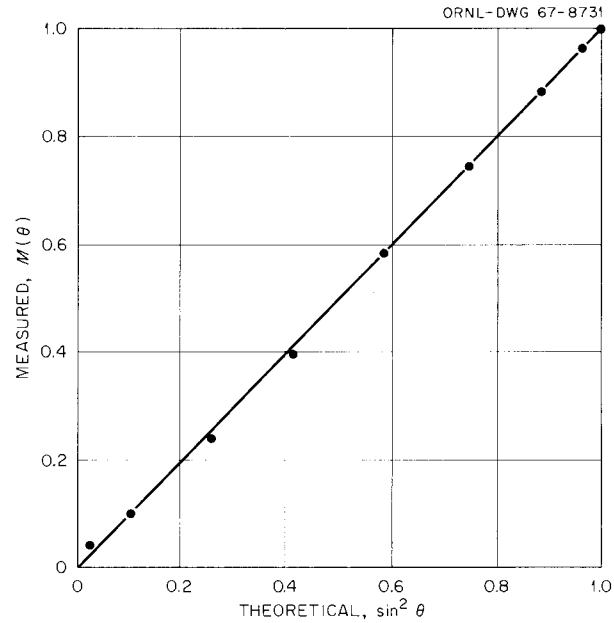

Fig. 27.4. Distribution of Electrodeposited Copper on a Hemisphere in Contact with a Plane Cathode in a Plating Tank. Radius of hemisphere, 3.825 cm.

EXPLODING-WIRE AEROSOL GENERATOR

K. D. Duerksen[21] R. L. Walker
F. G. Karioris[22]

The exploding-wire aerosol generator, described in previous reports,[23] has been replaced by a smaller, more versatile design (Fig. 27.6). The new device is contained in a standard relay rack approximately 1 m high and is mounted on casters. Charge, abort, and fire controls are provided both on the generator itself and on a remote control unit. For open-air shots the remote unit is a safety requirement. However, because of the noise produced by the explosion, most users prefer the remote unit operation even when using an explosion chamber to contain the exploded wire. An

[21] Temporary summer employee, University of Arkansas, Fayetteville.

[22] Temporary summer employee, Marquette University, Milwaukee, Wis.

[23] F. G. Karioris *et al.*, *Health Phys. Div. Ann. Progr. Rept. July 31, 1961*, ORNL-3189, p. 227.

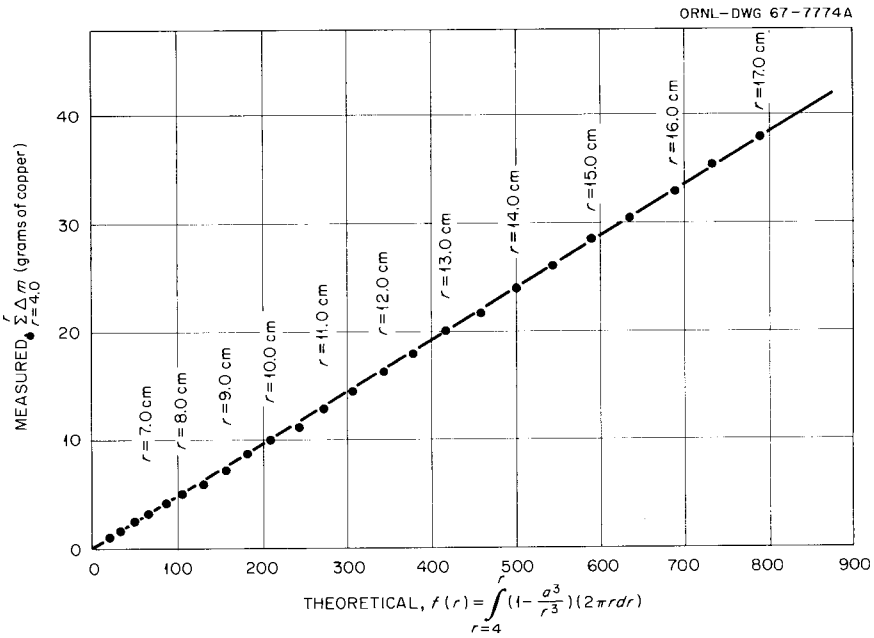

Fig. 27.5. Distribution of Electrodeposited Copper on a Plane in the Vicinity of a Hemispherical Boss. Radius of hemisphere, 3.825 cm.

explosion chamber can range in size and shape from a room to a container that can be fitted over the generator electrodes. For various purposes the size and shape of the electrodes also can be changed.

The system is designed around a commercially available 14-μf, 20-kv capacitor and a companion high-voltage trigger unit.[24] A variable 20-kv power supply is used to charge the capacitor, and a 5-kv and a 300-v supply are used to operate the trigger. Push-button switches are used to activate a series of relays that control the operation of the generator.

In operation the charge switch energizes a vacuum relay, which disconnects one side of the capacitor from ground and turns on the power supplies. When the desired voltage is reached, requiring less than 2 min for full charge, the fire switch may be activated. By means of electromechanical relays, the fire command produces the following sequence of events: (1) all the power supplies are turned off, (2) the capacitor is triggered and discharges the stored energy through a wire placed across its two electrodes, and (3) the vacuum relay (normally closed) is turned off so that both sides of the capacitor are grounded. Another switch can be used to discharge the capacitor without exploding the wire; the same circuit also resets the control sequence back to the beginning if electrical power is lost for any reason. All control functions may be performed from the remote panel except that of turning on the key-locked main power switch.

Aerosols from exploding wires are reproducible spherical particles with diameters in the size range 0.01 to 0.1 μ, which is a most important range in aerosol physics research. Currently, exploding-wire aerosols are being used in studies of the interaction of gases and vapors with dispersed and bulk state particulates (discussed next). In addition, a study of the properties of condensation aerosols generated under various environmental conditions of humidity and radiation field is just beginning.[25]

[24] Tobe Deutschman Laboratories, Canton, Mass.; capacitor ESC 248 A (5 nanohenries inductance); switch SBG 5-TG1 (5 nanohenries inductance).

[25] Supported by Reactor Chemistry Division, Nuclear Safety Program, ORNL.

Fig. 27.6. Aerosol Generator.

INTERACTION OF AIRBORNE VAPORS WITH PARTICULATES

B. M. Smith[26] R. L. Walker
L. E. Stettler[27]

Airborne Particles

Studies are being conducted on the interactions of radioactive iodine vapor (I_2) and sulfur dioxide vapor (SO_2) with airborne particles. Aerosols used in the investigations are generated with an exploding-wire aerosol generator. This aerosol generator is an improved version of the device discussed in previous reports[28,29] and is described in the preceding section of this report. Aerosols generated by this means range from about 0.01 to 0.1 μ in diameter. Silver, platinum, and iron oxide particles are currently being used.

A schematic diagram of the apparatus employed in this work was presented in a previous report.[30] In addition, a gas handling and calibration system was built to allow accurate qualitative and quantitative preparation of various gases, such as SO_2. A schematic diagram of the handling and calibration system is shown in Fig. 27.7.

A wire of the appropriate type is vaporized by means of the exploding-wire device. The resulting

[26]Employee of National Center for Air Pollution Control (NCAPC), USPHS, on assignment to ORNL.

[27]Employee of NCAPC; present address: Aerosol Physics Group, NCAPC, USPHS, Cincinnati, Ohio.

[28]F. G. Karioris *et al.*, *Health Phys. Div. Ann. Progr. Rept. July 31, 1960*, ORNL-2994, pp. 266–69.

[29]F. G. Karioris and B. R. Fish, *J. Colloid Sci.* **17**, 155–61 (1962).

[30]R. L. Walker, *Health Phys. Div. Ann. Progr. Rept. June 30, 1963*, ORNL-3492, pp. 187–89.

ORNL-DWG 67-8732

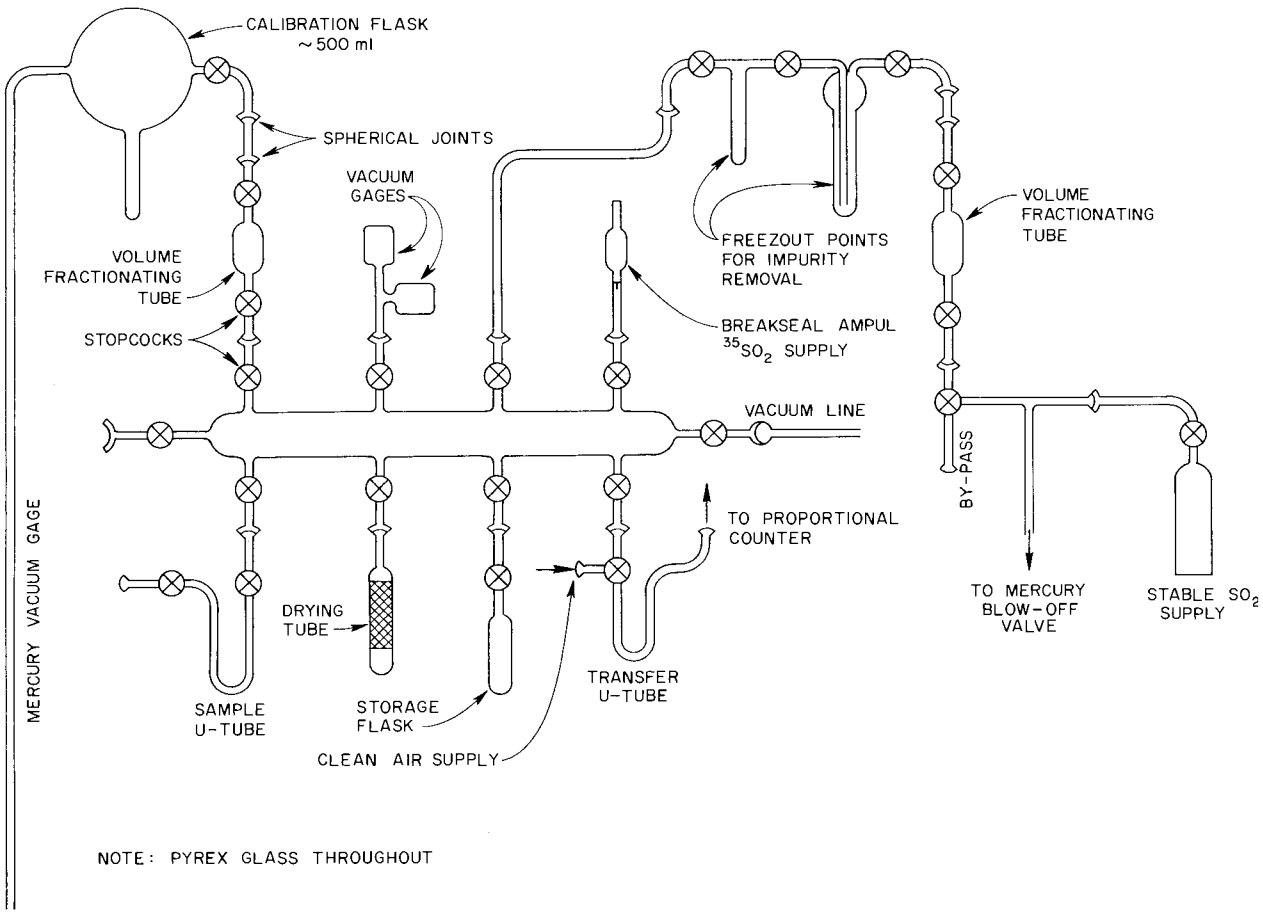

Fig. 27.7. Schematic Diagram of SO_2 Vapor Handling and Calibration System.

aerosol is transferred to a storage tank and diluted with air to produce a concentration of about 10^5 particles/cm^3. From the storage tank the diluted aerosol is transferred to a vapor-aerosol interaction chamber having a volume of 820 liters. Transfer may be made directly, or the aerosol may be conducted through various treatment or sampling devices, such as a Whitby-type ionizer[31] or an aerosol classifier designed by the Aerosol Physics Group and based on data presented by Thomas.[32] The concentration of aerosol in the interaction chamber is usually about 10^4 to 10^5 particles/cm^3 at the beginning of an experiment. The test gas is introduced into the interaction chamber by passing filtered air through a U-tube containing solid iodine or SO_2 while warming the tube with an external heater. Samples for analysis are withdrawn from the interaction tank, first through specially prepared $\frac{3}{8}$-inch copper tubes and then through membrane filters at the ends of the tubes. The sample flow rate is selected so that the vapor of interest will diffuse to the inside wall of the tube while allowing most of the aerosol particles to pass through the tube and be collected on the filter. Tubes for iodine sampling are plated internally with silver for chemisorption of I_2, while those used for SO_2 sampling are coated internally with PbO_2. For analysis, tubes containing chemisorbed $^{127}I_2$ with tracer $^{130}I_2$ or $^{131}I_2$ are cut into segments and counted directly in a scintillation counter. Similarly, tubes containing $^{32}SO_2$ with tracer $^{35}SO_2$ also are cut into segments. The segments are then refluxed in ammonium acetate solution to dissolve the lead sulfate and to produce a specimen suitable for liquid scintillation counting. Filters containing aerosol samples with adsorbed I_2 or SO_2 are counted in the same manner as their respective tube segments. Samples involving stable SO_2 are analyzed by the West and Gaeke wet-chemical method.[33] Samples involving stable I_2 are analyzed by titration of free I_2 in a potassium iodide (KI) solution with sodium thiosulfate.

Typical adsorption curves for SO_2 and I_2 are shown in Fig. 27.8. Airborne SO_2 vapor is observed to be lost to the walls of the interaction chamber with a concentration half-life of 7 hr when no large numbers of condensation nuclei are present. This contrasts with a corresponding half-life for airborne I_2 of only 49 min.

Deposited Particles

A study to screen various aerosols for their ability to sorb I_2, SO_2, and other vapors and gases has been initiated. Aerosols are prepared with the exploding-wire device, and the particles are then collected on membrane filters. To obtain sufficient quantities of the particulates, the aerosols produced by several individual explosions are accumulated on the filter, which is then covered with a clean filter. The two filters are pressure sealed together, and the laminated unit then is exposed to the vapor of interest at a given concentration by passing the vapor-air mixture through the filters.

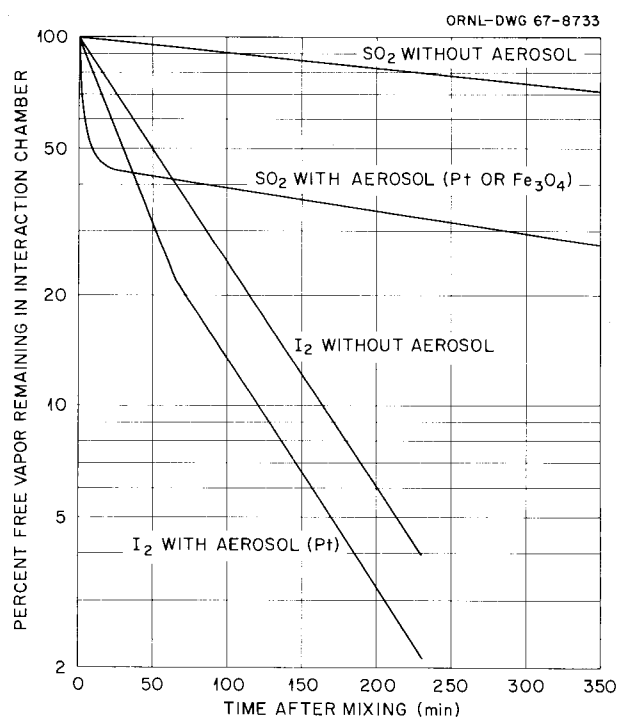

Fig. 27.8. Sorption of SO_2 and I_2 on Aerosols. Initial aerosol concentration, 10^7/liter. Initial SO_2 concentration for Fe_3O_4, 19 ppm; for Pt, 31 ppm. Initial I_2 concentration, 1 ppm.

[31] K. T. Whitby *et al.*, *Generator for Producing High Concentrations of Small Ions*, Tech. Rept. 12, Mechanical Engineering Dept., University of Minnesota, to USPHS, July 1960.

[32] J. W. Thomas and R. H. Knuth, *Intern. J. Air Water Pollution* **10**, 569–72 (1966).

[33] S. Hochheiser, *Methods of Measuring and Monitoring Atmospheric Sulfur Dioxide*, PHS Publication 999-AP-6, U.S. Dept. HEW, PHS, Div. Air Pollution, August 1964.

By screening a large number of different materials, specificities in vapor-particle interactions may be observed that might otherwise remain untested in the more intensive, disperse-state study discussed in the previous section.

Initially, 17 different aerosols were screened with SO_2. Representative results for two different concentrations of SO_2 are presented in Table 27.2. The rate of flow of the vapor-air mixtures through the laminated aerosol filters was in each case 0.4 liter/min. As may readily be observed, SO_2 was not always removed to the same degree at the two different concentrations. This variability in behavior might be expected, considering the several types of surface interactions which are possible. Indicated particle compositions refer to determinations by x-ray diffraction analyses. In many cases, these analyses probably do not accurately represent the composition of the particle surfaces.

Physical adsorption varies directly with vapor concentration. Results show that Mg, Ag, Zr, Cu, Pt, Fe, and Mo particles remove proportionately more SO_2 at the higher concentration. Aluminum aerosol particles (Al_2O_3) differed somewhat in that removal of SO_2 appeared to be proportional to approximately the square of the concentration. Chemisorption, on the other hand, is more time dependent and less concentration dependent. Palladium, nickel, indium, tantalum, tin, and tungsten aerosols removed essentially the same amounts of SO_2 at both vapor concentrations. Lead, cadmium, and gold aerosol particles removed substantially greater amounts of vapor at the lower vapor concentration than at the higher concentration, suggesting a time-dependent reaction. In each case, tungsten particles affected the SO_2 concentration the least.

Similar studies using radioactive iodine are under way.

Table 27.2. Removal of SO_2 from an Air Stream by Deposited Aerosol Particles

Aerosol	Analysis	Amount of SO_2 Removed[a] per Unit Weight of Particulates (μl/g) at an SO_2 concentration of: 21 μl/liter	72 μl/liter
Lead	PbO, $PbCO_3$, $Pb(OH)_3$	16,000	2300
Palladium	Analysis incomplete	1,200	1200
Magnesium	MgO	1,100	3800
Cadmium	CdO	1,100	310
Nickel	Ni, NiO	880	850
Indium	In_2O_3	760	650
Silver	Ag	700	2700
Gold	Au	590	71
Tantalum	Ta, Ta_2O_5	470	260
Aluminum	Al_2O_3	460	5100
Zirconium	Analysis incomplete	440	1800
Copper	Cu_2O, CuO	400	1000
Tin	SnO_2	270	190
Iron	Fe_3O_4	270	660
Molybdenum	MoO_2, MoO_3	160	370
Platinum	Pt	140	710
Tungsten	W, WO_3	39	0

[a]Removal includes retention on particulates as well as possible conversion of SO_2 to other gaseous compounds of sulfur.

INITIAL RETENTION OF PARTICLES ON SKIN

T. G. Clark

Studies have been reported in previous reports on the expected residence time of spherical particles on the arms of human subjects.[34] These data have been reviewed to provide additional information, and further human studies have been undertaken on the degree to which particles impacting on the skin would be retained when subjected to a known removal force. The subjects in these experiments presented their forearms in the path of small spherical wax particles falling vertically at approximately terminal velocities. After initial impaction the arm was inverted slowly, applying a force of 1 *g* to the particles. A count was made of the particles remaining at each step in the procedure. These small spheres were tagged with a zinc sulfide phosphor, and an ultraviolet light was used to visualize their location and number.

The fraction of the particles dropped that were retained after application of a 1 *g* removal force is shown in Fig. 27.9 as a function of particle size. All particles with diameters less than 184 μ

[34]T. G. Clark *et al.*, *Health Phys. Div. Ann. Progr. Rept. July 31, 1966*, ORNL-4007, p. 255.

were retained, while none greater than 714 μ remained on the arm. These sizes are the midpoints of the size ranges shown by the vertical bars. All the data for Fig. 27.9 were taken from one individual, with the exception of one point as noted on the figure. As an indication of the variability between subjects, eight individuals were exposed under similar environmental conditions to falling wax particles ranging from 500 to 595 μ in diameter. As shown in Fig. 27.9, the average fraction retained by the group was 0.18 ($\sigma = \pm 0.21$), with a range from 0 to 0.7.

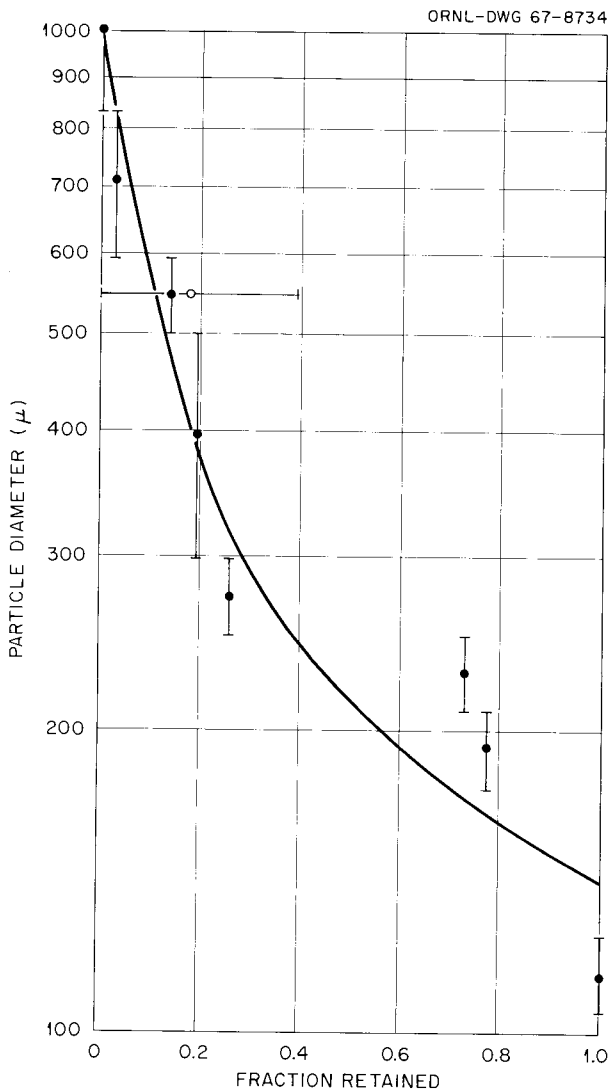

Fig. 27.9. Initial Retention of Falling Particles on Skin as a Function of Particle Size. ⧫, Range and midpoint of diameter; O, mean ± S.D. for eight subjects.

EXPECTED DOSE FROM "HOT" PARTICLES DEPOSITED ON THE SKIN

R. H. Boyett

Analysis of the hazards arising from high-specific-activity particulate sources requires knowledge of the deposition and adhesion of particles to the skin, as discussed in the previous section of this report. In addition to this information on source-skin contact probability, reliable dose measurements also are essential. Data on particle retention, reported previously,[34] provide an estimate of the expected time that particles will adhere to the skin as a function of particle size. In order to derive the expected dose to the skin, dose rate data are integrated over the time that the particle is estimated to remain on the skin.

As an example, the dose measurements from a neutron-irradiated 1-mm-diam uranium dicarbide (UC_2) source[35] (Fig. 27.10) may be corrected

[35] B. R. Fish *et al.*, *Environmental Studies: Radiological Significance of Nuclear Rocket Debris, Progr. Rept. for Period July 1, 1965–June 30, 1966*, ORNL-TM-1686.

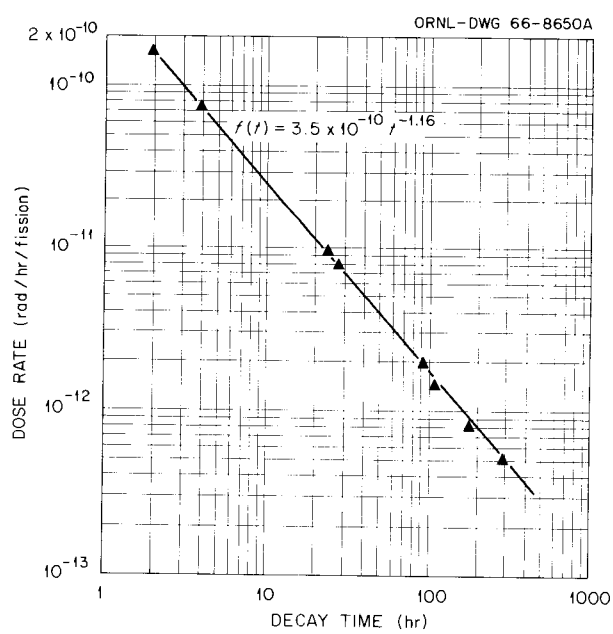

Fig. 27.10. Absorbed Dose Rate Averaged over 1 cm^2 at a Depth of 7.6 mg cm^{-2} in Tissue. Measurements were made with an extrapolation chamber on a 1-mm-diam UC_2 sphere after neutron irradiation (20 min, total 4.46×10^{12} fissions).

for retention time. The straight line in Fig. 27.10 is fitted by $f(t) = 3.5 \times 10^{-10} t^{-1.16}$ rad hr^{-1} fission^{-1}, where t is hours after reactor shutdown. An inspection of retention data[35] shows that a 1-mm-diam UC_2 particle is expected to remain on the skin 2 ($\sigma = \pm 1.4$) hr. Therefore, assuming the particle lands on the skin 2 hr after shutdown, the expected dose (rads/fission) to the skin is given by

$$D_e = \int_{t=2}^{4} f(t)\, dt = 3.5 \times 10^{-10} \int_{t=2}^{4} t^{-1.16}\, dt \,.$$

The upper 1 σ limit of the skin dose (rads/fission) is given by

$$D_u = \int_{t=2}^{5.4} f(t)\, dt \,,$$

and the lower limit is given by

$$D_l = \int_{t=2}^{2.6} f(t)\, dt \,.$$

Based on these calculations, the expected dose to the skin from a 1-mm-diam UC_2 particle which lands on the skin 2 hr after shutdown with upper and lower estimates is: upper 1 σ limit, 2.89×10^{-10} rads/fission; expected, 2.06×10^{-10}; and lower 1 σ limit, 8.09×10^{-11}.

The expected total dose to a 1-cm^2 area calculated as a function of time of first contact with the particle after shutdown is shown in Fig. 27.11. A parallel relationship is seen between the computed curves of the two particle sizes (120 to 145 μ and 1 mm diameter), and for purposes of estimation it may be assumed that intermediate particle sizes would produce approximately parallel curves.

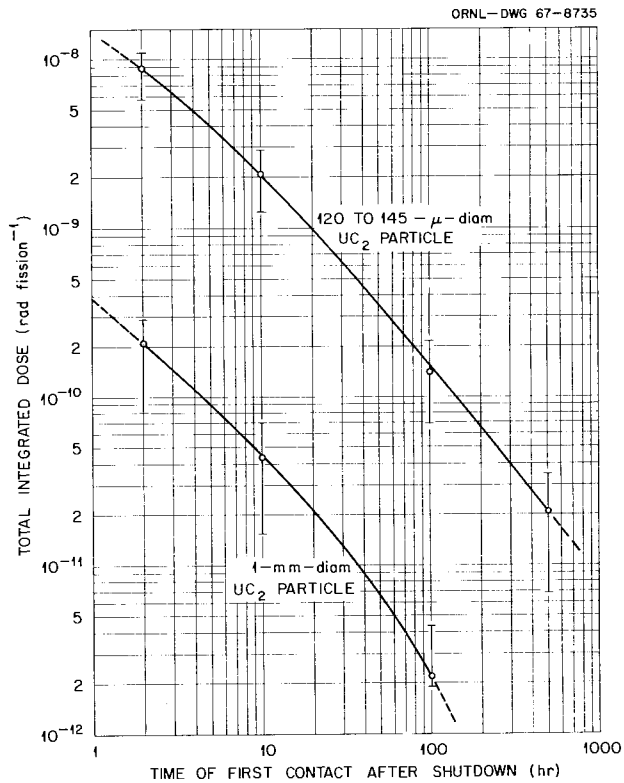

Fig. 27.11. Expected Dose (rads/fission) to Skin Averaged over an Area of 1 cm^2 at a Depth of 7.5 mg/cm^2.

28. Applied Internal Dosimetry

B. R. Fish

P. E. Brown L. B. Farabee
G. R. Patterson, Jr.

ORNL IN VIVO GAMMA-RAY SPECTROMETRY FACILITY

G. R. Patterson, Jr. P. E. Brown

During fiscal year 1967 the ORNL in vivo counting facility continued the program of internal-dose monitoring described in the annual report last year.[1] Basically, the frequency with which employees are scheduled for repeat counts is determined by the potential for exposure in the job or work area.

During the period June 1, 1966, through May 31, 1967, 896 counts were made on 744 persons; approximately 89.8% of the persons counted showed a normal human spectrum on at least one of their counts. A summary is given in Table 28.1 of the data for those counts which indicated measurable amounts of radioactivity other than normal ^{40}K and ^{137}Cs. The amount of ^{137}Cs that is found in nonoccupationally exposed employees due to dietary uptake of weapons fallout has continued to decrease during the period covered by this report. The average ^{137}Cs whole-body burden found in 23 essentially unexposed male employees counted during June 1966 was 0.009 μc, and the average for 64 male employees counted during December of the same year was 0.006 μc. In view of the very low level indicated here [$\sim$0.02% of the maximum permissible body burden (MPBB) for ^{137}Cs] it was decided to discontinue routine computer processing of all counts that by visual inspection of the spectrum appeared to be normal. Since January 1, 1967, only spectra showing indications of something other than normal ^{40}K and ^{137}Cs have been submitted for computer analysis.

The FORTRAN 63 program ALPHA,[2,3] discussed at length in the last report of this series,[1] is still used for analysis of whole-body spectra. A new, improved version, ALPHA M,[4] which is more versatile, supposedly is more accurate, and can be used on the CDC 1604, IBM 7094, or IBM 360, is now available. So far, it has not been demonstrated that ALPHA M has significant advantages over the original version ALPHA for the analysis of whole-body count data. At present, the library of standards available for use with program ALPHA consists of 131 standards on punched cards; this represents multiple counts on 28 different isotopes with differing distributions in the calibration phantom or counted in different count configurations. The library of standards recorded on magnetic tape for repeated use at the computing center is the same as reported last year and includes 36 different standards on 12 isotopes. A new library of 80 different standards on 24 isotopes is being prepared for loading onto magnetic tape and will be used for routine data analysis in the future.

---

[1] B. R. Fish *et al.*, *Health Phys. Div. Ann. Progr. Rept. July 31, 1966*, ORNL-4007, pp. 260–67.

[2] E. Schonfeld, *ALPHA – a Computer Program for the Determination of Radioisotopes by the Least Squares Resolution of the Gamma-Ray Spectra*, ORNL-3810 (July 1965).

[3] E. Schonfeld *et al.*, *Determination of Nuclide Concentrations in Solutions Containing Low Levels of Radioactivity by Least Squares Resolution of the Gamma-Ray Spectra*, ORNL-3744 (January 1965).

[4] E. Schonfeld, *ALPHA M – an Improved Computer Program for Determining Radioisotopes by Least Squares Resolution of the Gamma-Ray Spectra*, ORNL-3975 (September 1966).

Table 28.1. Measurable Radioactivity Found in Routine Whole-Body Monitoring Program June 1, 1966, to May 31, 1967

Isotope	Maximum Amount Detected (μc)	Number of Counts	Number of Persons
^{7}Be	0.31	16	10
^{51}Cr	0.038	2	2
^{58}Co	0.002	5	4
^{60}Co	0.004	16	13
^{65}Zn	0.053	3	3
^{89}Sr	1.450	17	5
^{90}Sr	0.57	61	25
^{95}Zr–^{95}Nb	0.098	18	5
^{103}Ru–^{103}Rh	0.16	22	6
^{106}Ru–^{106}Rh	0.011	5	3
^{131}I	0.58 whole body[a] 0.13 thyroid	7	5
^{137}Cs	0.098	25	14[b]
^{140}Ba–^{140}La	0.004	1	1
^{144}Ce–^{144}Pr	Trace	1	1
^{187}W	0.37	3	1[c]
^{203}Hg	0.48	8	3[d]
Mixed fission products	Trace	6	5

[a]This ^{131}I exposure was detected on a regularly scheduled routine count.

[b]The 14 persons indicated as positive ^{137}Cs deposit cases were found to have significantly more ^{137}Cs than the general Laboratory population. Because of their work areas and assignments, it was felt that their higher burden was due to slight occupational exposure rather than elevated dietary intake. The maximum amount detected still is an insignificant fraction of the MPBB.

[c]This count was made 6 hr after exposure; three days later the indicated body burden was only 0.017 μc.

[d]Two of the indicated three persons received medical tracer injections of ^{197}Hg and ^{203}Hg and, at the time of counting, had relatively small residual burdens of ^{203}Hg. More complete information concerning one of these two cases is presented elsewhere in this report. The employee who showed the somewhat larger body burden listed in this tabulation had been employed only 18 days at the time of his first count; the amount of ^{203}Hg detected at that time resulted from his previous employment.

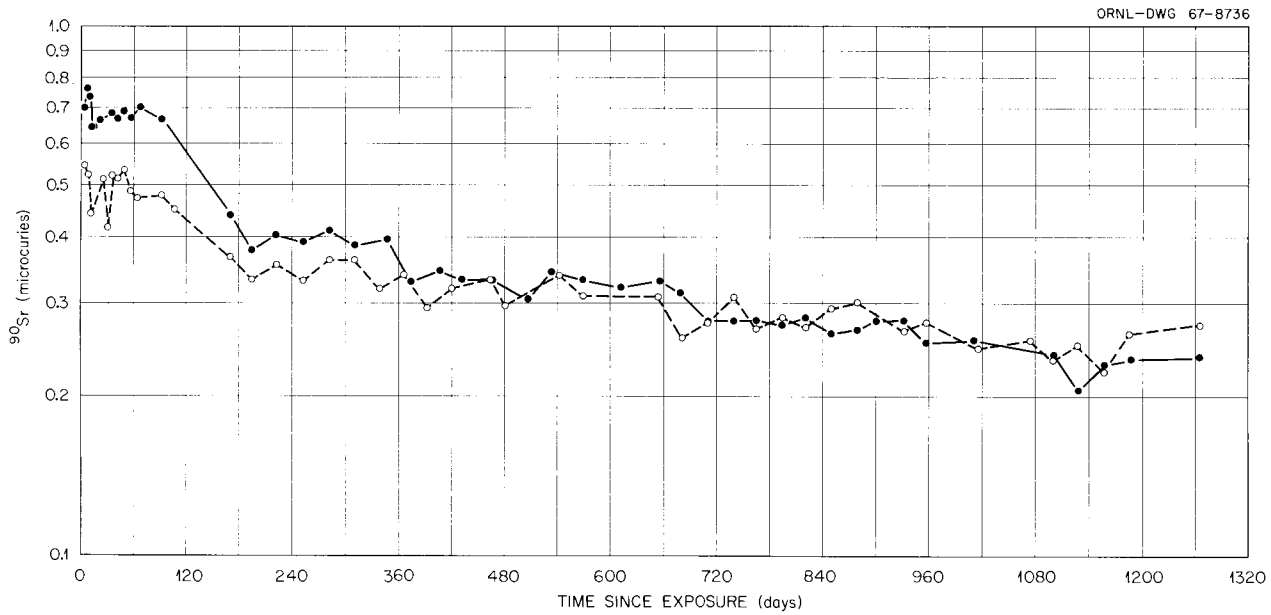

Fig. 28.1. Estimated Lung Burden of Two Subjects Inhaling $^{90}SrTiO_3$.

IN VIVO DETECTION AND MEASUREMENT OF ^{90}Sr-^{90}Y INTERNAL CONTAMINATION

G. R. Patterson, Jr. P. E. Brown

The two employees whose exposure in 1964 to $^{90}SrTiO_3$ by inhalation was reported earlier[5] still are being counted at about one-month intervals using the 8 × 4 in. lead-collimated NaI(Tl) crystal. The estimated chest burdens for these two employees since the time of exposure are shown in Fig. 28.1. During this fiscal year, their estimated chest burdens have averaged approximately 34% of the permissible lung burden for the equilibrium mixture ^{90}Sr + ^{90}Y. Judging from the portion of the curves from 180 days post exposure to 1260 days post exposure, it now appears that the half-time for lung clearance of $^{90}SrTiO_3$ may be in excess of 1800 days. Recent computer analysis of whole-body scan data using a calibration in which 10% of the total body burden is distributed in the skeleton and the other 90% is contained in the lungs suggests that at the end of this fiscal year the whole-body burden for these two employees may be on the order of 0.230 to 0.300 μc. The one who originally had the higher intake still has the higher whole-body burden, although this is not the case for the chest-burden estimates.

On September 2, 1966, despite procedural changes that were intended to prevent recurrence of such exposures, three more persons were exposed to $^{90}SrTiO_3$ contamination during a similar waste-disposal operation. In this case, the person receiving the highest indicated intake was estimated to have approximately 0.57 μc of ^{90}Sr at the time of his first count, only 1½ hr after the incident. On the following day, his chest burden was estimated to be 0.064 μc. On the eighth day following the incident, this employee's whole-body burden was estimated to be 0.093 μc with one-third of this in the chest region. The other two employees involved had somewhat lower initial estimated burdens and showed similar rapid elimination from the body.

ELIMINATION OF INJECTED ^{203}Hg

P. E. Brown

In connection with a medical procedure, unrelated to his work, a male employee received an intravenous injection of 570 μc of ^{197}Hg and about 95 μc of ^{203}Hg on October 28, 1965. When the employee became available for in vivo counting on November 29, a series of measurements was begun.

[5] B. R. Fish *et al.*, *Health Phys. Div. Ann. Progr. Rept. July 31, 1964*, ORNL-3697, pp. 223–25.

At that time, an arc count was made using an 8 × 4 in. NaI(Tl) crystal. The face of the crystal was 6 ft from the subject, which is the maximum distance possible in the existing iron room. A scan was made using a 1 × 1 in. NaI(Tl) crystal, collimated with 2 in. of lead (Fig. 28.2). This showed the activity to be located, principally, in the liver-kidney area.

For the next 140 days counting was done using the 6-ft arc position to determine body burden (Fig. 28.3). After that time both arc and scan counts were made. The effective half-life was observed to be 25 days during this time (day 30 to day 190). Based on this, the estimated biological half-life was 54 days. From day 40, liver and kidney counts were made with the 1 × 1 in. collimated counter. Calibrations and correction factors were determined by placing sources in the liver and kidney sections of a water-filled plastic mannikin. Effective half-lives were found to be about 24 days for activity in the liver and about 53 days in the kidney.

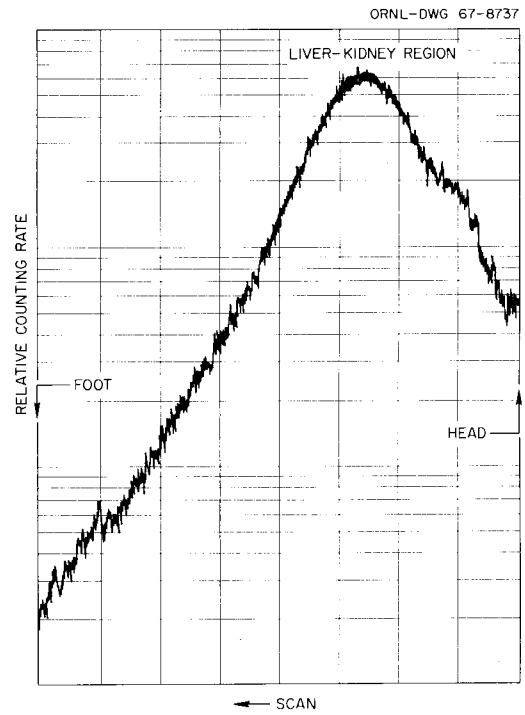

Fig. 28.2. Typical Scan Profile 50 Days After Intravenous Injection of ^{203}Hg.

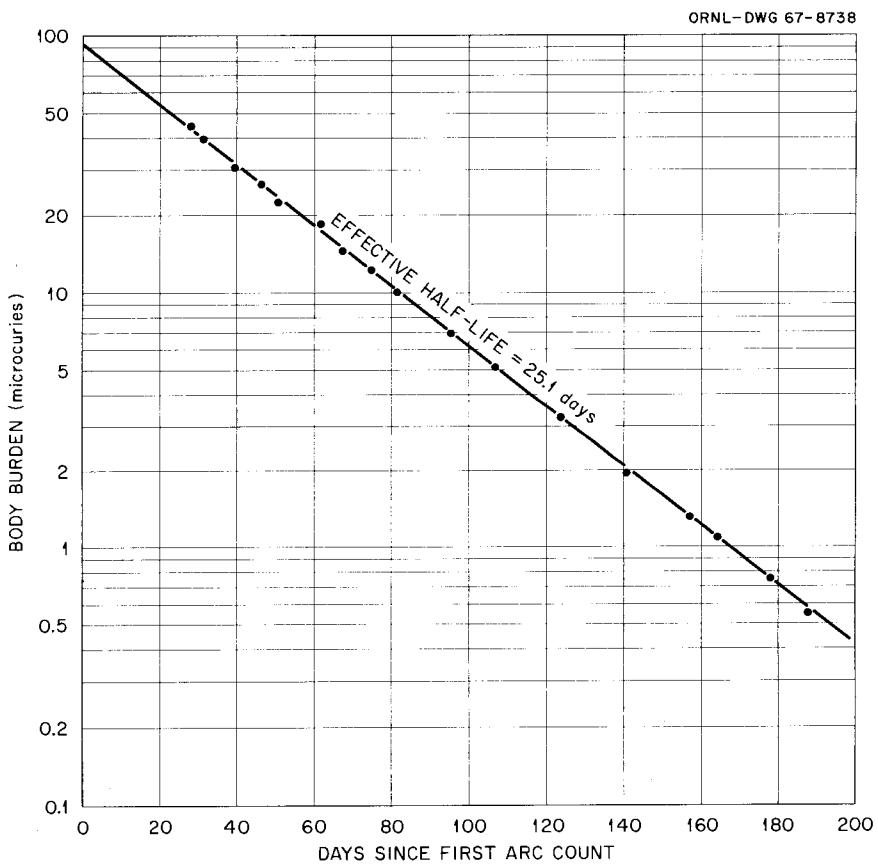

Fig. 28.3. Body Burden of ^{203}Hg Following Intravenous Injection.

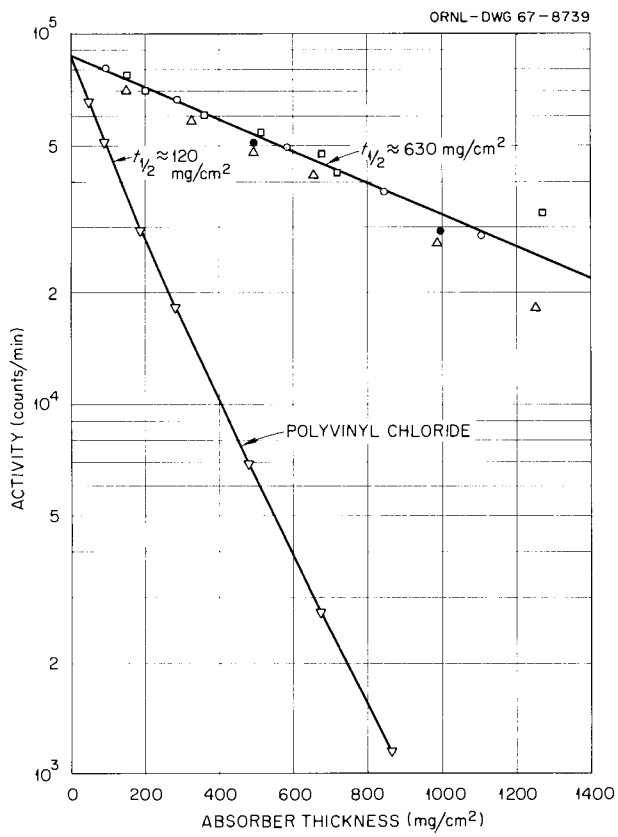

Fig. 28.4. Absorption of 17-kev X Rays from $^{238}PuO_2$. ● Water, ⊙ cellulose acetate, △ pressed ham, ⊡ Lucite.

ABSORPTION OF 17 kev X RAYS FROM TRANSURANIC ELEMENTS

P. E. Brown

A $^{238}PuO_2$ microsphere containing about 82 μc was counted in the iron room of the ORNL In Vivo Gamma Ray Spectrometer Facility using a wound probe described in earlier reports.[1] The energy band 10–20 kev is used to represent the principal x rays of interest, and counts are normalized to the average counting rate observed for zero absorber thickness and are plotted in Fig. 28.4.

A striking difference in the slope of the lines is seen between polyvinyl chloride and other materials tested. This is due primarily to the presence of chlorine atoms in this material.[6] Half-thickness values differed by a factor of about 5.7. For the polyvinyl chloride, $t_{1/2} = 120$ mg/cm², while for the other absorbers $t_{1/2} \approx 680$ mg/cm².

Wound-probe calibrations using Lucite as the absorbing material and calibration techniques reported previously,[1] give detection limits varying from as low as 0.01 nc of ^{239}Pu (containing 2% ^{241}Am) using a 1-mm absorber thickness to 1.39 nc using an absorber 33 mm thick. For pure ^{239}Pu the lower detection limit is 0.01 nc for a 1-mm depth and 2.4 nc for a 33-mm depth in the absorber. Correction for percent of ^{241}Am and depth in tissue is by the same method as outlined in the earlier report.[1] The least-detectable amount of ^{239}Pu based on three standard deviations of the background is shown in Fig. 28.5.

[6] E. Storm *et al.*, *Gamma Ray Absorption Coefficients*, LA-2237 (April 1957).

NEW PROCEDURE FOR RADIOSTRONTIUM ANALYSIS OF ENVIRONMENTAL SAMPLES

L. B. Farabee

The analysis for ^{90}Sr in environmental samples (vegetation, foods, bone, water, etc.) is complicated by the presence of radium in these materials. Provisions for separation from radium are necessary if a direct beta count is to be made for radiostrontium. In most ^{90}Sr procedures, strontium carrier is added to a solution of the ashed sample, and $Sr(NO_3)_2$ is precipitated from 75% HNO_3 solution. Since radium and barium are coprecipitated with Sr(II), a separation from Ra(II) and Ba(II) is necessary before counting the radiostrontium beta.

A new procedure for radiostrontium determination in environmental samples is proposed that would eliminate the $Sr(NO_3)_2$ precipitation as well as the precipitations necessary for Ra(II) separation. In this procedure the radionuclides of Sr(II), Ba(II), and Ra(II) are quantitatively retained on a cation exchange resin while most of the calcium (~1 g) and magnesium (~0.39 g) pass through the resin column as the chelate of tetrasodium ethylenediaminetetraacetate (Na_4EDTA – technical grade). This procedure is similar to the method for radiostrontium analysis of urine.[7] The

[7] L. B. Farabee, "Improved Procedure for Radiostrontium Analysis of Human Urine," presented at 12th Annual Bio-Assay and Analytical Chemistry Meeting, Gatlinburg, Tenn., October 13–14, 1966, CONF-661018.

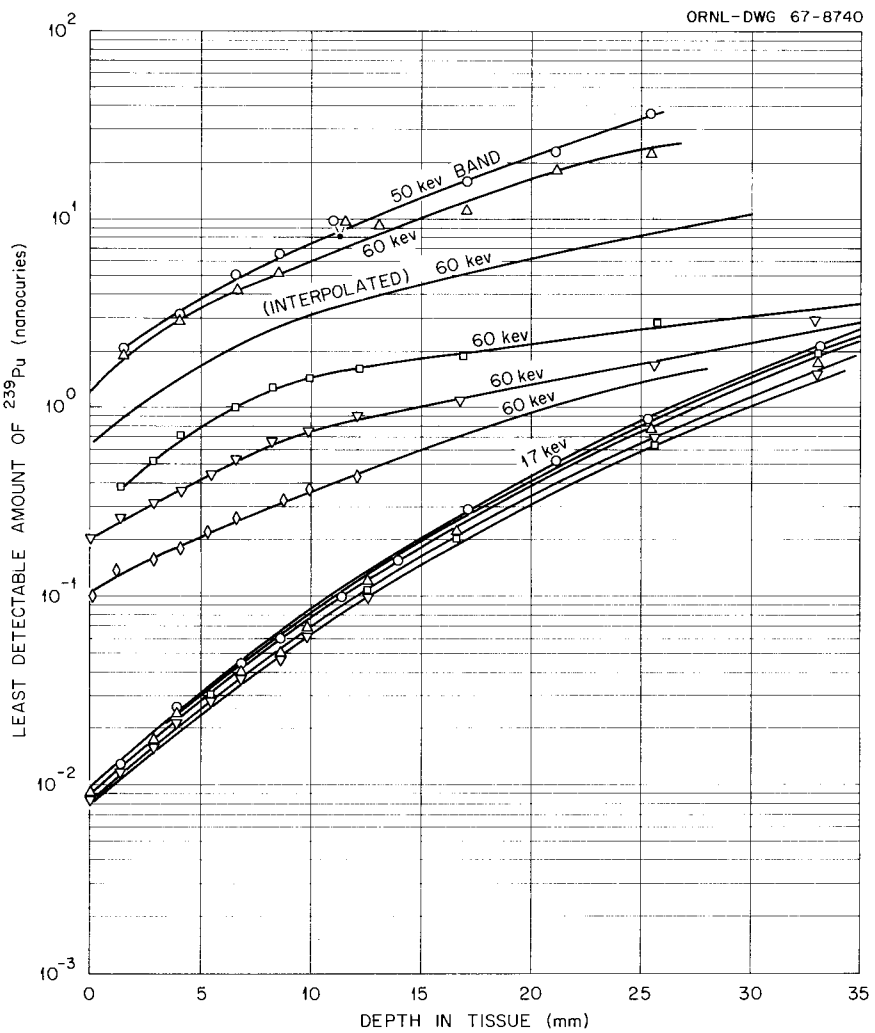

Fig. 28.5. Least Detectable Amount of ^{239}Pu in a Wound. Ratio of ^{241}Am to ^{239}Pu: = 0.000, ⊙; = 0.001, △; = 0.005, ⊡; = 0.010, ▽; and = 0.020, ◇.

Sr(II), Ba(II), and Ra(II) are separated from calcium, magnesium, potassium, ^{137}Cs, etc., in the following way: (1) The ashed environmental sample is solubilized in a minimum of HCl; (2) the volume is built to ~1 liter, and NaOH is added to pH 10; (3) Na_4EDTA is added to chelate all alkaline earths (+10% excess); (4) citric acid is added to give a 0.25% solution; (5) the pH is adjusted to 5.0 with HCl and/or NaOH; (6) this feed solution is passed over a 2.6-cm-ID cation exchange resin column containing 50 ml of Dowex 50-X12 (100–200 mesh) Na^+ at maximum flow rate; and (7) the residual Ca(II) and Mg(II) are washed from the resin with 1250 ml of solution made up of 0.75% Na_4EDTA and 1.00% citric acid at pH 5.0.

The Ra(II), Ba(II), and Sr(II) are retained quantitatively on the resin. The individual radionuclides can be separated sequentially with a solution of 0.04 *M* (1.8%) Na_4EDTA at controlled pH. Duyckaerts and Lejeune[8] demonstrated that separation of individual alkaline earths can be done on a cation exchange resin with EDTA at controlled pH, while Nelson[9] similarly has separated Ra(II) and Ba(II). Optimum conditions for separating Sr(II), Ba(II), and Ra(II) were established by a series of batch-by-batch equilibrium distribution coefficient studies with 1.8% Na_4EDTA,

[8] G. Duyckaerts and R. Lejeune, *J. Chromatog.* **3**, 58 (1960).

[9] F. Nelson, *J. Chromatog.* **16**, 403–6 (1964).

Dowex 50-X12 (100–200 mesh) Na^+, and radioactive tracers ^{85}Sr, ^{133}Ba, and ^{224}Ra. The affinity of each radionuclide to the resin as a function of pH is shown in Fig. 28.6. The separation factor $D_{^{133}Ba}/D_{^{85}Sr} \approx 31$, and $D_{^{224}Ra}/D_{^{85}Sr} \approx 155$ at pH 7.

The radiostrontium can be removed from the resin column by eluting with 1.8% Na_4EDTA at pH 6.8 and a flow rate of 1 to 2 ml/min (Fig. 28.7). No Ba(II) or Ra(II) is eluted in 120 ml of eluate. The radiostrontium fraction can be prepared for counting by recycling the above eluate at pH 5.0 over a 1.0-cm-ID column containing 5 ml of Dowex 50-X12 (100–200 mesh) Na^+ resin. The sodium is removed with 100 ml of 0.5 *N* HCl, and the radiostrontium is recovered with 50 ml of 6 *N* HNO_3. After evaporation of the HNO_3, the radiostrontium is transferred to a stainless steel dish for beta counting. In determining ^{90}Sr at low levels in environmental or bone samples, it is advantageous to allow ^{90}Y to grow to equilibrium and to count both ^{90}Sr and ^{90}Y. This procedure was proven to recover >99% of ^{85}Sr tracer in a variety of samples including grass, milk, leaves, fecal samples, and bone. The radiobarium and radium fractions can be recovered in a manner similar to that for radiostrontium if such an analysis is needed.

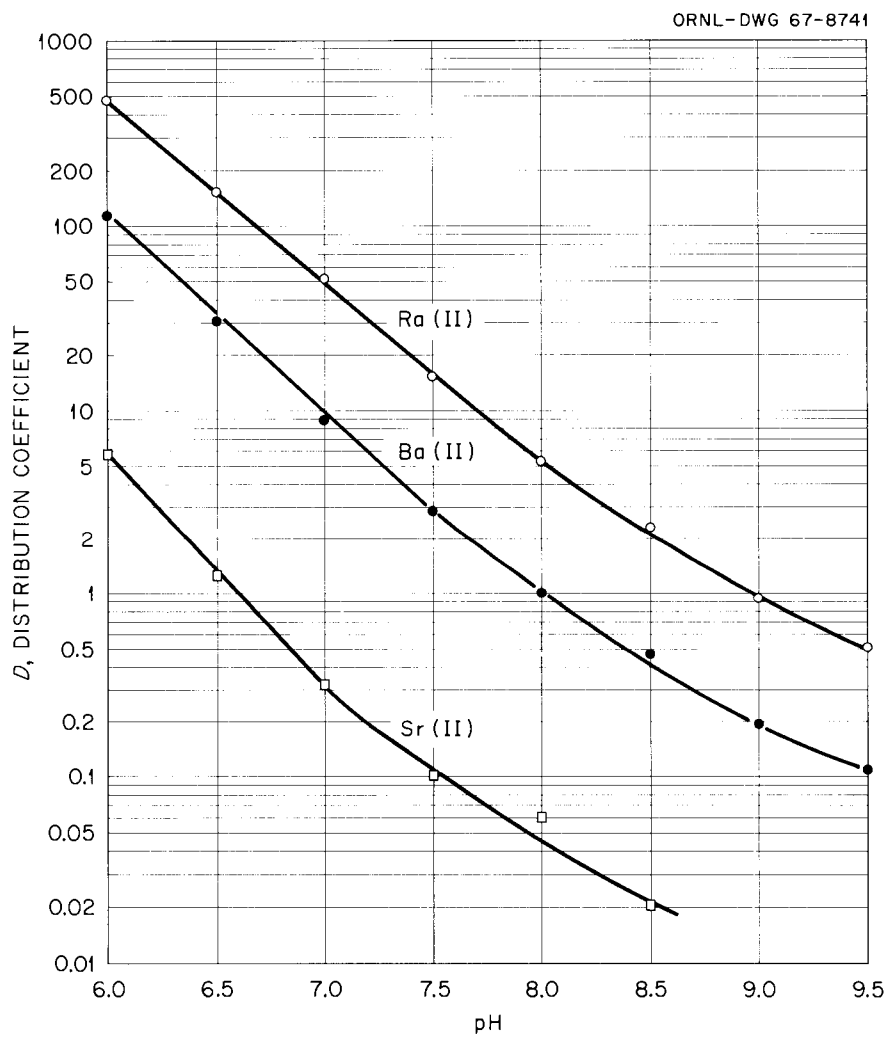

Fig. 28.6. Distribution Coefficients for Radium, Barium, and Strontium with 1.8% Na_4EDTA on Dowex 50-X12 (100–200 Mesh) Na^+ as a Function of pH.

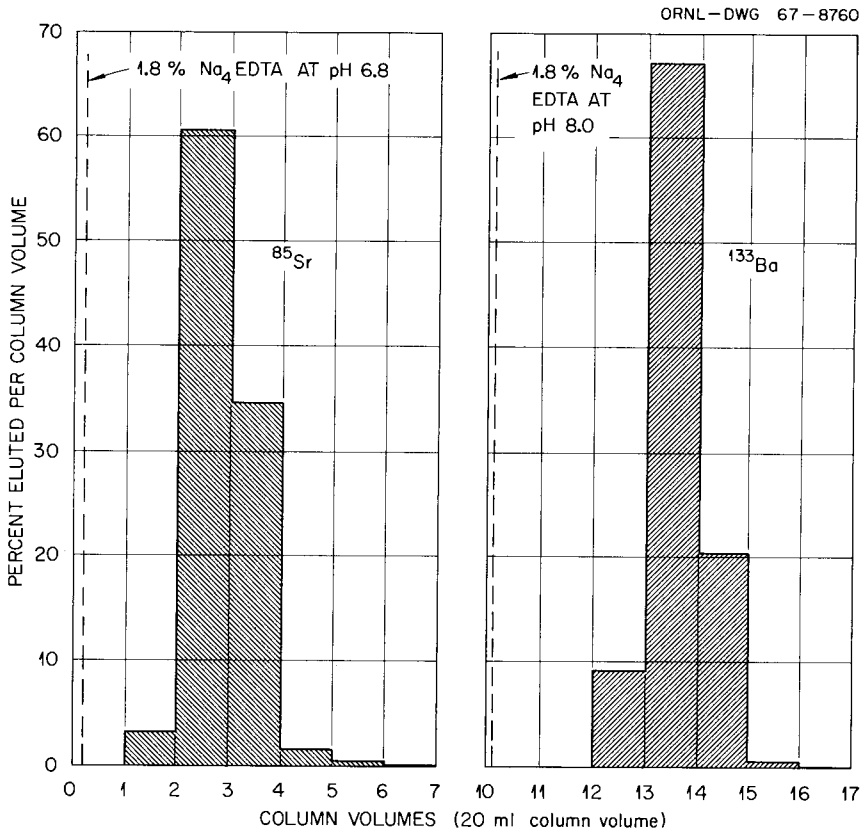

Fig. 28.7. Separation of ^{85}Sr from ^{133}Ba on Resin Column with 1.8% EDTA.

Theses, Papers, Publications, and Lectures

Theses

Scott Cram, E. T. Arakawa, G. E. Jones, and R. D. Birkhoff
Transition Radiation and Low-Energy Bremsstrahlung from Silver and Aluminum Foils Bombarded by Grazing Incidence Electrons, ORNL-TM-1571 (September 1966).

Patricia Dalton and J. E. Turner
Mean Excitation Energies Calculated from Stopping Power and Range Data, ORNL-TM-1777 (June 1967).

H. W. Dickson, L. G. Christophorou, and R. N. Compton
Electron Capture by Hydrogen Halides and Their Deuterated Analogues, ORNL-TM-1724 (June 1967).

J. D. Hayes and E. T. Arakawa
The Optical Properties of Vacuum-Evaporated Films of Tellurium and Amorphous Selenium (in preparation).

W. G. Hendrick, L. G. Christophorou, and G. S. Hurst
An Apparatus for Measurement of Electron Capture at High Temperatures, ORNL-TM-1444 (in preparation).

Larry Johnson and H. C. Schweinler
Oscillator Strength in Magnesium Porphin (in preparation).

S. J. Nalley, M. Y. Nakai, F. W. Garber, R. H. Ritchie, and R. D. Birkhoff
Low-Energy Electron Studies in Aluminum (in preparation).

Margaret S. Riedinger and L. C. Emerson
The Determination of the Optical Properties of Palladium Using Ellipsometry (in preparation).

M. U. Shaikh, D. G. Jacobs, and F. L. Parker
A Study of the Movement of Radionuclides Through Saturated Porous Media, ORNL-TM-1681 (January 1967).

J. L. Stanford, E. T. Arakawa, and R. D. Birkhoff
Photoelectric and Optical Properties of Commercial Platinum, Gold, and Palladium Foils and Evaporated Aluminum and Silver Films in the Extreme Ultraviolet, ORNL-TM-1392 (September 1966).

G. F. Stone and J. H. Thorngate
Experimentally Determined Proton-Recoil Spectra in Tissue-Equivalent Material from 3 and 14 Mev Neutrons, ORNL-TM-1927 (in preparation).

J. C. Sutherland, R. N. Hamm, J. R. Stevenson, and E. T. Arakawa
Optical Properties of Sodium in the Vacuum Ultraviolet, ORNL-TM-1776 (June 1967).

W. A. Thomas, S. I. Auerbach, and J. S. Olson
Accumulation and Cycling of Calcium by Flowering Dogwood Trees, ORNL-TM-1910 (in press).

L. H. Toburen, M. Y. Nakai, R. G. Albridge, R. A. Langley, C. F. Barnett, and R. D. Birkhoff
Part I. The Measurement of High-Energy Charge-Transfer Cross Sections for Incident Hydrogen Atoms and Ions in Various Gases. Part II. The K-, L-, and M-Auger, L-Coster-Kronig and the Conversion-Electron Spectra of Platinum in the Decay of ^{195}Au (in preparation).

H. A. Wright and W. S. Snyder
Differentiability of Set Functions (in preparation).

Papers

E. T. Arakawa, J. L. Stanford, and R. D. Birkhoff
Photoemission Studies in Evaporated Aluminum Films in the Vacuum Ultraviolet, Optical Society of America, October 19–21, 1966, San Francisco, California.

E. T. Arakawa and M. W. Williams
Optical Properties of Sapphire in the Vacuum UV, American Physical Society, April 24–27, 1967, Washington, D.C.

J. C. Ashley
Double-Plasmon Excitation by Charged Particles, American Physical Society, August 29–31, 1966, Mexico City, Mexico.

J. A. Auxier
The Present Status of Neutron Monitoring for Personnel Protection, Symposium on Neutron Monitoring for Radiological Protection, August 29–September 2, 1966, Vienna, Austria.

Multilaboratory Intercomparisons of Neutron Dosimetry Systems, Symposium on Neutron Monitoring for Radiological Protection, August 29–September 2, 1966, Vienna, Austria.

J. A. Auxier and M. D. Brown
Neutron Cross Sections and Reaction Products for H, C, N, and O for the Energy Range from Thermal to 15 Mev, First International Congress of the International Radiation Protection Association, September 5–10, 1966, Rome, Italy.

J. A. Auxier, C. N. Wright, and C. M. Unruh
General Considerations in Nuclear Accident Dosimetry and Standardization, Health Physics Society First Topical Symposium on Personnel Radiation Dosimetry, January 30–February 1, 1967, Chicago, Illinois.

J. Baarli, St. Charalambus, J. Dutrannois, K. Goebel, H. H. Hubbell, T. R. Overton, A. Rindi, and A. H. Sullivan
Hazard from Induced Radioactivity near High Energy Accelerators, Conference on Radiological Protection of the Worker by the Design and Control of His Environment, April 18–22, 1966, Bournemouth, England.

R. D. Birkhoff, W. J. McConnell, R. N. Hamm, and R. H. Ritchie
Electron Flux Spectra in Aluminum – Analysis for Linear Energy Transfer Spectra and Excitation and Ionization Yields, AEC Symposium on Biological Interpretation of Dose from Accelerator-Produced Radiation, March 13–16, 1967, Berkeley, California.

R. P. Blaunstein, L. G. Christophorou, and R. N. Compton
Electron Capture by Organic Molecules, Health Physics Society, June 19–21, 1967, Washington, D.C.

B. G. Blaylock
The Effect of Ionizing Radiation on Competition Between Drosophila melanogaster *and* Drosophila simulans, The Genetics Society of America, September 1–3, 1966, Chicago, Illinois.

The Effect of Ionizing Radiation on Interspecific Competition, The Second National Symposium on Radioecology, May 15–17, 1967, Ann Arbor, Michigan.

R. L. Bradshaw
Rheology of Salt in Mine Workings, Symposium on the Geology and Technology of Gulf Coast Salt, May 1–2, 1967, Louisiana State University, Baton Rouge, Louisiana.

R. L. Bradshaw, T. F. Lomenick, W. C. McClain, and F. M. Empson
Model and Underground Studies of the Influence of Stress, Temperature, and Radiation on Flow and Stability in Salt Mines, International Society of Rock Mechanics, First International Congress, September 25–October 1, 1966, Lisbon, Portugal (presented by T. F. Lomenick).

J. G. Carter, L. G. Christophorou, R. D. Birkhoff, and J. W. Pagel
Organic Scintillators with 2-Ethyl Naphthalene as a Solvent, American Physical Society, December 1–3, 1966, Nashville, Tennessee.

L. G. Christophorou
Interaction of Low-Energy Electrons with Polyatomic Molecules, American Physical Society, December 1–3, 1966, Nashville, Tennessee.

L. G. Christophorou, J. G. Carter, and M-E. M. Abu-Zeid
Optical Emission from Organic Liquids Excited by Electron Impact, Radiation Research Society, May 7–11, 1967, San Juan, Puerto Rico.

L. G. Christophorou, G. S. Hurst, and W. G. Hendrick
Swarm Determination of the Cross Section for Momentum Transfer in Ethylene and in Ethylene Mixtures, 19th Annual Gaseous Electronics Conference, October 12–14, 1966, Atlanta, Georgia.

R. N. Compton and L. G. Christophorou
Negative Ion Formation and Electronic Excitation by Electron Impact in H_2O and D_2O, American Physical Society, December 1–3, 1966, Nashville, Tennessee.

R. N. Compton, L. G. Christophorou, G. S. Hurst, and P. W. Reinhardt
Temporary Negative Ion Formation in Complex Molecules, 19th Annual Gaseous Electronics Conference, October 12–14, 1966, Atlanta, Georgia.

R. N. Compton, R. H. Huebner, L. G. Christophorou, and P. W. Reinhardt
Low-Energy Electron Impact Phenomena in Organic Molecules, Radiation Research Society, May 7–11, 1967, San Juan, Puerto Rico.

K. E. Cowser, Jacob Tadmor, D. G. Jacobs, and W. J. Boegly, Jr.
Evaluation of Environmental Hazards from Release of Krypton-85 and Hydrogen-3 in an Expanding Nuclear Fuel Reprocessing Industry, Health Physics Society Meeting, Washington, D.C., June 18–22, 1967.

D. A. Crossley, Jr.
Tracers in Insect Biology and Ecology, Symposium on Application of Radioisotopes and Ionizing Radiation in Entomology, March 27, 1967, Baton Rouge, Louisiana.

Comparative Movement of ^{106}Ru, ^{60}Co, and ^{137}Cs in Arthropod Food Chains, Second National Symposium on Radioecology, May 15–17, 1967, Ann Arbor, Michigan.

J. W. Curlin
Root Dose from Gamma and Fast Neutron Irradiation of Potted Plants, AIBS Annual Meeting, August 14–19, 1966, College Park, Maryland.

Genetic Differences in Growth Response of Eastern Cottonwood to Nitrogen Fertilization, Soil Science Society of America Annual Meeting, August 21–26, 1966, Stillwater, Oklahoma.

The Use of Radioisotopes in Forest Soils Research, Southern Forest Soils Conference, August 30–31, 1966, Greenville, Mississippi.

Mineral Cycling Research at Oak Ridge National Laboratory, Northwest Forest Soils Workshop, September 16, 1966, Seattle, Washington.

R. C. Dahlman
Carbon-14 Cycling in the Root and Soil Components of a Prairie Ecosystem, Second National Symposium on Radioecology, May 15–17, 1967, Ann Arbor, Michigan.

D. R. Davy
Prediction of Biological Damage from Stopping Power Theory, Sixth Annual Meeting of Physics in Medicine and Biology, August 29–September 2, 1966, Melbourne, Australia.

P. B. Dunaway, L. L. Lewis, J. A. Payne, and J. D. Story
Effects of Acute Ionizing Irradiation in Indigenous Rodents and Shrews, Third International Congress of Radiation Research, June 26–July 2, 1966, Cortina, Italy.

P. B. Dunaway, L. L. Lewis, J. D. Story, J. A. Payne, and J. M. Inglis
Radiation Effects in the Soricidae, Cricetidae, and Muridae, Second National Symposium on Radioecology, May 15–17, 1967, Ann Arbor, Michigan.

L. C. Emerson
Vacuum Ultraviolet Studies of Energy Losses in Solids, American Physical Society, December 1–3, 1966, Nashville, Tennessee.

L. B. Farabee
Improved Procedure for Radiostrontium Analysis of Human Urine, The 12th Annual Bio-Assay and Analytical Chemistry Meeting, October 13–14, 1966, Gatlinburg, Tennessee.

B. R. Fish
Electrostatic Forces of Adhesion Between Particles, Symposium on Electrostatic Effects Associated with Dried Powders, April 25–26, 1967, Fort Detrick, Maryland.

Electrostatic Deposition and Adhesion of Particles on Surfaces, American Association for Contamination Control, Sixth Annual Technical Meeting, May 15–18, 1967, Washington, D.C.

H. L. Fisher, Jr.
Distribution of Dose in the Body from a Source of Gamma Rays Distributed Uniformly in an Organ, First International Congress on Radiation Protection, September 5–10, 1966, Rome, Italy.

An Age-Dependent Model for the Bodily Retention of Cesium, 12th Annual Bioassay and Analytical Chemistry Meeting, October 13–14, 1966, Gatlinburg, Tennessee.

Kenneth Fox, J. E. Turner, and V. E. Anderson
Some Ground-State Energy Eigenfunctions for an Electron-Dipole System, American Physical Society, June 21–23, 1967, Toronto, Ontario.

W. R. Garrett
Elastic Scattering of Electrons by $1s^2 2s^2 2p^q$ *Atoms,* 19th Annual Gaseous Electronics Conference, October 12–14, 1966, Atlanta, Georgia.

L. W. Gilley, L. B. Holland, J. W. Poston, and D. R. Ward
Operation Problems with the Health Physics Research Reactor, American Nuclear Society, June 1966, Denver, Colorado (presented by L. B. Holland).

R. N. Hamm, R. H. Ritchie, and J. C. Ashley
Electron Mean Free Paths in a Free Electron Gas, American Physical Society, August 29–31, 1966, Mexico City, Mexico.

H. Hollister and J. E. Turner
On the Relationship of RBE to LET, Health Physics Society, June 19–21, 1967, Washington, D.C.

R. H. Huebner, R. N. Compton, and L. G. Christophorou
Temporary Negative Ion Resonances in Benzene Derivatives, American Physical Society, December 1–3, 1966, Nashville, Tennessee.

T. D. Jones, J. A. Auxier, J. W. Poston, and D. R. Johnson
Dose Distribution Functions for Neutrons and Gamma Rays in Anthropomorphous and Radiological Phantoms, First International Congress of the International Radiation Protection Association, September 5–10, 1966, Rome, Italy.

S. V. Kaye
The Specific Activity Concept and Internal Dosimetry, Bioenvironmental Subcontractors Meeting for Sea-Level Canal Studies, November 15–17, 1966, Columbus, Ohio.

Environmental Pathways and Internal Dosimetry, Bioenvironmental Subcontractors Meeting for Sea-Level Canal Studies, November 15–17, 1966, Columbus, Ohio.

Distribution and Retention of Orally Administered Radiotungsten in the Rat, Health Physics Society, June 18–22, 1967, Washington, D.C.

S. V. Kaye and S. J. Ball
A Coupled Compartment Model for Radionuclide Transfer in a Tropical Environment, Second National Symposium on Radioecology, May 15–17, 1967, Ann Arbor, Michigan.

G. D. Kerr and J. S. Cheka
Developments in Metaphosphate Glass Dosimetry, Health Physics Society First Topical Symposium on Personnel Radiation Dosimetry, January 30–February 1, 1967, Chicago, Illinois.

G. D. Kerr and D. R. Johnson
Comparison of Radiation Dosimeters at the Health Physics Research Reactor, Health Physics Society, June 18–22, 1967, Washington, D.C.

C. E. Klots
The Optical Approximation in Radiation Chemistry, Chemistry Section, National Bureau of Standards, June 23, 1967, Washington, D.C.

C. E. Klots and J. E. Turner
Factors Involved in the Construction of Useful Degradation Spectra, Radiation Research Society, May 7–11, 1967, San Juan, Puerto Rico.

T. F. Lomenick and O. C. Kopp
Thermal Effects and Stratigraphic Relations on the Deformation of Rock Salt, Annual Meeting of the Geological Society of America, November 14–16, 1966, San Francisco, California.

W. C. McClain
The Effect of Nonelastic Behavior of Rocks, Eighth Symposium on Rock Mechanics, September 14–17, 1966, Minneapolis, Minnesota.

Hydraulic Fracturing as a Waste Disposal Method, IAEA Symposium on Disposal of Radioactive Wastes into the Ground, May 29–June 2, 1967, Vienna, Austria.

W. C. McClain, R. L. Bradshaw, and F. M. Empson
Disposal of High Level Solidified Wastes in Salt Mine, IAEA Symposium on Disposal of Radioactive Wastes into the Ground, May 29–June 2, 1967, Vienna, Austria.

K. Z. Morgan
Development of Health Physics as a Profession, First International Congress on Radiation Protection, September 5–10, 1966, Rome, Italy.

A Comparison and Evaluation of Various Radiation Hazards in Metropolitan Areas, Second Symposium on Health Physics, September 26–30, 1966, Pecs, Hungary.

L. D. Mullins and W. R. Garrett
1-Averaged Exchange Term in the Hartree-Fock Equations, American Physical Society, December 1–3, 1966, Nashville, Tennessee.

D. J. Nelson
Ecological Behavior of Radionuclides in Surface Waters, Reservoir Fishery Resources Symposium, April 5–7, 1967, Athens, Georgia.

Cesium, Cesium-137, and Potassium Concentrations in White Crappie and Other Clinch River Fish, Second National Symposium on Radioecology, May 15–17, 1967, Ann Arbor, Michigan.

J. Neufeld, V. E. Anderson, H. A. Wright, and J. E. Turner
Effects of Phantom Geometry on Dose Distribution, First International Congress of the International Radiation Protection Association, September 5–10, 1966, Rome, Italy.

J. S. Olson
Energy Flow into Deciduous Forests, Second National Symposium on Radioecology, May 15–17, 1967, Ann Arbor, Michigan.

B. C. Patten
Kinetics of ^{134}Cs in Carp, Second National Symposium on Radioecology, May 15–17, 1967, Ann Arbor, Michigan.

H. L. Pray, M. Y. Nakai, and R. D. Birkhoff
Low-Energy Electron Studies in Indium and Magnesium, American Physical Society, December 1–3, 1966, Nashville, Tennessee.

J. R. Reed and D. J. Nelson
Radiostrontium Uptake in Blood and Flesh in Bluegills (Lepomis macrochirus), Second National Symposium on Radioecology, May 15–17, 1967, Ann Arbor, Michigan.

D. E. Reichle and D. A. Crossley, Jr.
Investigations on Heterotrophic Productivity in Forest Insect Communities, Working Meeting on the Principles and Methods of Secondary Productivity in Terrestrial Ecosystems, September 1966, Warsaw, Poland.

Trophic Level Concentrations of Cesium-137, Sodium, and Potassium in Forest Arthropods, Working Meeting on the Principles and Methods of Secondary Productivity in Terrestrial Ecosystems, September 1966, Warsaw, Poland.

S. W. Riggs, J. C. Ashley, L. S. Cram, and E. T. Arakawa
Photon Emission from Al Foils Bombarded by Non-Normally Incident Electrons, American Physical Society, December 1–3, 1966, Nashville, Tennessee.

R. H. Ritchie and W. S. Snyder
Estimation of Dose Distribution Within the Body Resulting from the Y-12 and Vinca Criticality Incidents, IAEA Symposium on Neutron Monitoring for Radiological Protection, August 29–September 2, 1966, Vienna, Austria.

L. L. Robinson, L. C. Emerson, J. G. Carter, and R. D. Birkhoff
Optical Properties of Liquid Water in the Vacuum Ultraviolet, American Physical Society, December 1–3, 1966, Nashville, Tennessee.

A. S. Rogowski and Tsuneo Tamura
Runoff and Erosion Losses of Radiocesium on Captina Silt Loam, Meeting of American Society of Agronomy, August 22–26, 1966, Stillwater, Oklahoma.

W. S. Snyder
Health Physics Aspects of Supersonic Transport, First International Congress on Radiation Protection, September 5–10, 1966, Rome, Italy.

The Use of the Lung Model for Estimation of Dose, 12th Annual Bioassay and Analytical Chemistry Meeting, October 13–14, 1966, Gatlinburg, Tennessee.

Estimation of Internal Dose, AEC Health Protection Meeting, February 14–15, 1967, Albuquerque, New Mexico.

Distribution of Dose in the Body from HTO, Symposium on Instrumentation, Experience, and Problems in Health Physics Tritium Control, February 16–17, 1967, Albuquerque, New Mexico.

Dose Estimation in the Context of Health Physics Regulations and Responsibilities, First International Symposium on the Biological Interpretation of Dose from Accelerator Produced Radiation, March 13–16, 1967, Berkeley, California.

The Use of Excretion Data to Predict the Systemic Body Burden of Plutonium, Symposium on Diagnosis and Treatment of Deposited Radionuclides, May 15–17, 1967, Richland, Washington.

W. S. Snyder, J. A. Auxier, M. D. Brown, T. D. Jones, and R. T. Boughner
Distribution of Dose and Dose Equivalent in an Anthropomorphic Phantom Resulting from Broad-Beam Sources of Monoenergetic Neutrons, American Nuclear Society Winter Meeting, October 30–November 3, 1966, Pittsburgh, Pennsylvania.

J. A. Stockdale and L. G. Christophorou
Molecular Scattering of Thermal Electrons, Radiation Research Society, May 7–11, 1967, San Juan, Puerto Rico.

E. G. Struxness
Ultimate Disposal of Radioactive Wastes, 6th Annual Sanitary and Water Resources Engineering Conference, Vanderbilt University, School of Engineering, June 1, 1967, Nashville, Tennessee.

Permanent Disposal of Radioactive Wastes, 2nd National Symposium on Radioecology, May 15–17, 1967, Ann Arbor, Michigan.

J. C. Sutherland and E. T. Arakawa
Extinction Coefficient, k, *and Imaginary Part of the Dielectric Constant,* ϵ_2, *of Sodium in the Vacuum Ultraviolet,* American Physical Society, April 24–27, 1967, Washington, D.C.

J. C. Sutherland, R. N. Hamm, and E. T. Arakawa
Computer Calculations of Phase Changes upon Reflection from an Absorbing Layer, American Physical Society, December 1–3, 1966, Nashville, Tennessee.

Jacob Tadmor and K. E. Cowser
Underground Disposal of ^{85}*Kr from Nuclear Fuel Reprocessing Plants,* American Nuclear Society Thirteenth Annual Meeting, June 11–15, 1967, San Diego, California.

F. G. Taylor, Jr.
Predicted Seasonal Radiosensitivity of Southeastern Tree Species, American Institute of Biological Sciences, August 14–19, 1966, College Park, Maryland.

Factors Which Affect Prediction and Assessment of Radiosensitivity in Higher Plants, Tennessee Academy of Science, November 25–26, 1966, Johnson City, Tennessee.

Nuclear Characteristics of Populus deltoides *Clones,* Association of Southeastern Biologists, April 20–22, 1967, Columbia, South Carolina.

W. A. Thomas
Cycling of ^{45}*Ca by Dogwood Trees,* Second National Symposium on Radioecology, May 15–17, 1967, Ann Arbor, Michigan.

J. H. Thorngate
Dosimetry, Shielding, and Scattering II, Conference on Principles of Radiation Protection, August 24–26, 1966, Oak Ridge, Tennessee.

Isabel H. Tipton, Judy C. Johns, and Monica Boyd
The Variation with Age of Elemental Concentration in Human Tissue, First International Congress on Radiation Protection, September 5–10, 1966, Rome, Italy.

L. H. Toburen, R. A. Langley, C. F. Barnett, R. D. Birkhoff, and M. Y. Nakai
Charge Exchange Cross Sections for Incident Atomic Hydrogen in Various Gases, American Physical Society, December 1–3, 1966, Nashville, Tennessee.

L. H. Toburen, M. Y. Nakai, and R. A. Langley

Charge Exchange Cross Sections for High Energy Protons and Atomic Hydrogen in Gases, American Physical Society, January 30–February 2, 1967, New York.

J. E. Turner
Penetration of Heavy Charged Particles in Matter, American Physical Society, December 1–3, 1966, Nashville, Tennessee.

J. E. Turner and Kenneth Fox
Minimum Dipole Moment to Bind an Electron to a Finite Dipole, American Physical Society, December 1–3, 1966, Nashville, Tennessee.

Ground-State Energy Eigenvalues and Eigenfunctions for Electron-Dipole System, Radiation Research Society, May 7–11, 1966, San Juan, Puerto Rico.

J. E. Turner, V. E. Anderson, H. A. Wright, W. S. Snyder, and J. Neufeld
Dose from High Energy Radiations in an Interface Between Two Media, AEC Symposium on Biological Interpretation of Dose from Accelerator-Produced Radiation, March 13–16, 1967, Berkeley, California.

R. C. Vehse and E. T. Arakawa
Optical and Photoelectric Properties of Thin Palladium Films in the Far Ultraviolet, American Physical Society, December 1–3, 1966, Nashville, Tennessee.

R. E. Wilems and R. H. Ritchie
Nonlinear Interactions in Bounded Quantum Plasmas, American Physical Society, April 24–27, 1967, Washington, D.C.

The Surface Photoeffect and Surface Secondary Emission from Metal Foils, American Physical Society, December 1–3, 1966, Nashville, Tennessee.

W. H. Wilkie and B. R. Fish
Scintillation Extrapolation Dosimetry of Small Beta-Emitting Sources, Symposium on Solid-State and Chemical Radiation Dosimetry in Medicine and Biology, October 3–7, 1966, Vienna, Austria.

M. W. Williams and E. T. Arakawa
Optical Properties of Single-Crystal MgO, American Physical Society, April 24–27, 1967, Washington, D.C.

M. W. Williams, E. T. Arakawa, and L. C. Emerson
Photon Excitation of Surface Plasmons: Analysis of Data for Al, American Physical Society, December 1–3, 1966, Nashville, Tennessee.

J. P. Witherspoon
Radiosensitivity of Clones of Eastern Cottonwood, American Institute of Biological Sciences, August 14–19, 1966, College Park, Maryland.

Interactions of Fast Neutron Radiation and Growth-Dormancy Cycles in Yellow Poplar Trees, Association of Southeastern Biologists, April 20–22, 1967, Columbia, South Carolina.

Genetic Factors Relating to Radiosensitivity of Populations, Health Physics Society, June 18–22, 1967, Washington, D.C.

Martin Witkamp and M. L. Frank
Cesium-137 Kinetics in Terrestrial Microcosms, Second National Symposium on Radioecology, May 15–17, 1967, Ann Arbor, Michigan.

H. A. Wright, E. E. Branstetter, Jacob Neufeld, J. E. Turner, and W. S. Snyder
Calculation of Radiation Dose Due to High-Energy Protons, First International Congress of the International Radiation Protection Association, September 5–10, 1966, Rome, Italy.

H. A. Wright, J. E. Turner, J. Neufeld, and W. S. Snyder
Calculation of Radiation Dose from High-Energy Nucleons, Health Physics Society, June 19–21, 1967, Washington, D.C.

Edward Yeargers
Ultraviolet Light Effects on Proteins, Symposium on Biologic Effects of Ultraviolet, August 23–26, 1966, Philadelphia, Pennsylvania.

Publications

V. E. Anderson and R. H. Ritchie
Fourier Transform Methods in the Unfolding of Experimental Data, ORNL-TM-1261 (June 1967).

J. C. Ashley
"Transition Radiation from Thin Foils Due to Non-Normally Incident Electrons," *Phys. Rev.* **155**, 208–10 (1967).

J. C. Ashley, L. S. Cram, and E. T. Arakawa
"Photon Emission from Al Foils Bombarded by Non-Normally Incident Electrons," submitted for publication in the *Physical Review.*

Leroy Augenstein, Edward Yeargers, James Carter, and DeVaughn Nelson
"Excitation, Dissipative, and Emissive Mechanisms in Biochemicals," to be published in *Radiation Research.*

J. A. Auxier
"Present Status of Neutron Monitoring for Personnel Protection," pp. 3–14 in *Neutron Monitoring,* IAEA, Vienna, 1967.

"Multilaboratory Intercomparisons of Neutron Dosimetry Systems," pp. 625–29 in *Neutron Monitoring,* IAEA, Vienna, 1967.

"Dosimetry and Exposures in Nuclear Accidents," to be published in *Nuclear Safety.*

"A Discussion of Weapons Effects and Dosimetry," to be published in *Proceedings of First Conference on Long-Range Biomedical and Psychosocial Effects of Nuclear War, Princeton, New Jersey, January 18 Through 21, 1966.*

Report of Trip Abroad by J. A. Auxier During Period August 24, 1966–September 10, 1966, Oct. 12, 1966 (internal memorandum).

"Physical Problems of Dosimetry of Neutrons and Protons," to be published in *Proceedings of Symposium on Accidental Irradiation at Place of Work, Nice, France, April 25 Through 29, 1966.*

J. A. Auxier and M. D. Brown
"Neutron Cross Sections and Reaction Products for H, C, N, and O for the Energy Range from Thermal to 15 Mev," to be published in *Proceedings of First International Congress of the International Radiation Protection Association, Rome, Italy, September 5 Through 10, 1966.*

J. A. Auxier, W. S. Snyder, and T. D. Jones
"Neutron Interactions and Penetration in Tissue," chap. 6 in *Radiation Dosimetry,* vol. 1 (ed. by F. H. Attix and W. C. Roesch), Academic, New York (in press).

J. Baarli, St. Charalambus, J. Dutrannois, K. Goebel, H. H. Hubbell, T. R. Overton, A. Rindi, and A. H. Sullivan
Hazards from Induced Radioactivity near High Energy Accelerators, CERN-DI/HP/84 (April 1966).

R. E. Blanco, J. O. Blomeke, W. J. Boegly, Jr., K. E. Cowser, H. E. Goeller, R. E. Lampton, T. F. Lomenick, and F. L. Parker
Survey of a Site for Nuclear Fuel Processing Plant and Waste Disposal Area at Oak Ridge, ORNL-TM-1748 (Jan. 13, 1967).

B. G. Blaylock
"A Cytogenetic Study of a Natural Population of *Chironomus* Inhabiting an Area Contaminated by Radioactive Waste," pp. 835–46 in *Proceedings of Symposium on Disposal of Radioactive Wastes into Seas, Oceans, and Surface Waters, May 16–20, 1966, Vienna, Austria,* IAEA, Vienna, 1966.

"A Population Cage for Counting Adult *Drosophila* Populations," *Drosophila Inform. Serv.* **42**, 113 (1967).

"Effect of Ionizing Radiation on Interspecific Competition," to be published in *Proceedings of 2nd National Symposium on Radioecology, Ann Arbor, Michigan.*

J. O. Blomeke, R. Salmon, J. T. Roberts, R. L. Bradshaw, and J. J. Perona
"Estimated Costs of High-Level Waste Management," pp. 830–43 in *Proceedings of International Symposium on Solidification and Long-Term Storage of Highly Radioactive Wastes, Richland, Washington, February 15–18, 1966,* CONF-660208 (November 1966).

W. J. Boegly, Jr., R. L. Bradshaw, F. M. Empson, W. C. McClain, F. L. Parker, and W. F. Schaffer, Jr.
"Project Salt Vault: Radioactive Waste Disposal in a Salt Mine," *Proceedings of the 20th Annual Purdue Industrial Waste Conference, Lafayette, Indiana, May 4–6, 1965* (1966).

W. J. Boegly, Jr., and W. L. Griffith
A Survey of Underground Utility Tunnel Practice, ORNL-TM-1714 (February 1967).

R. L. Bradshaw
Current Status, Present Plans, and Future Needs in Project Salt Vault, Jan. 16, 1967 (internal memorandum).

R. L. Bradshaw, T. F. Lomenick, W. C. McClain, W. J. Boegly, Jr., F. M. Empson, and F. L. Parker
"Project Salt Vault: Effects of Temperature and Radiation on Plastic Flow and Mine Stability," pp. 671–84 in *Proceedings of International Symposium on the Solidification and Long-Term Storage of Highly Radioactive Wastes, Richland, Washington, February 15–18, 1966,* CONF-660208 (November 1966).

R. L. Bradshaw, T. F. Lomenick, W. C. McClain, and F. M. Empson
"Model and Underground Studies of the Influence of Stress, Temperature, and Radiation on Flow and Stability in Rock Salt Mines," pp. 429–33 in *Proceedings of the First Congress of the International Society of Rock Mechanics, Lisbon, 25 September to 1 October 1966,* vol. II, 1966.

G. N. Brown and F. G. Taylor, Jr.
"Zinc-65 Distribution and Radiosensitivity of Growth and ^{65}Zn Uptake in Red Oak Seedlings," *Radiation Botany* **6**, 519–24 (1966).

"Interaction of Radiation and Photoperiodism in *Xanthium pensylvanicum:* Effects of Radiation During the Light and Dark Periods of Photoinduction," *Radiation Botany* **7**, 67–72 (1967).

P. H. Carrigan, Jr., and R. J. Pickering
Radioactive Materials in Bottom Sediment of Clinch River: Part B, Inventory and Vertical Distribution of Radionuclides in Undisturbed Cores, suppl. 2B to *Status Report No. 5 on Clinch River Study,* ORNL-3721 (March 1967).

P. H. Carrigan, Jr., R. J. Pickering, T. Tamura, and R. Forbes
Radioactive Materials in Bottom Sediment of Clinch River: Part A, Investigations of Radionuclides in Upper Portion of Sediment, suppl. 2A to *Status Report No. 5 on Clinch River Study,* ORNL-3721 (March 1967).

J. G. Carter and L. G. Christophorou
"Organic Scintillators with 2-Ethyl Naphthalene as a Solvent," *J. Chem. Phys.* **46**, 1883–90 (1967).

J. G. Carter, L. G. Christophorou, and M-E. M. Abu-Zeid
"Emission from Organic Liquids Excited by Electron Impact," submitted for publication in the *Journal of Chemical Physics.*

J. S. Cheka, J. A. Auxier, T. D. Jones, H. H. Hubbell, Jr., and W. S. Snyder
"Estimation of Radiation Dose Received by Survivors of the Hiroshima and Nagasaki Bombings (ORNL-Ichiban)," to be published as *ABCC Research Protocol.*

H. E. Childs, Jr., and G. E. Cosgrove
"A Study of Pathological Conditions in Wild Rodents in Radioactive Areas," *Am. Midland Naturalist* **76**, 309–24 (1966).

L. G. Christophorou and J. G. Carter
"Improved Organic Scintillators in 2-Ethyl Naphthalene: The Role of Excimers," *Nature* **212**, 816–18 (1966).

L. G. Christophorou and R. N. Compton
"Interaction of Low-Energy Electrons with Polyatomic Molecules," to be published in *Health Physics.*

L. G. Christophorou, R. N. Compton, G. S. Hurst, and P. W. Reinhardt
"Dissociative Electron Capture by Benzene Derivatives," *J. Chem. Phys.* **45**, 536–47 (1966).

L. G. Christophorou, G. S. Hurst, and W. G. Hendrick
"Swarm Determination of the Cross Section for Momentum Transfer in Ethylene and in Ethylene Mixtures," *J. Chem. Phys.* **45**, 1081–85 (1966).

R. N. Compton and L. Bouby
"Formation d'ions negatifs dans le glyoxal et le biacetyl," *Comp. Rend.* **264**, 1153–56 (1967).

R. N. Compton and L. G. Christophorou
"Negative Ion Formation in H_2O and D_2O," *Phys. Rev.* **154**, 110–16 (1967).

R. N. Compton, L. G. Christophorou, and R. H. Huebner
"Temporary Negative Ion Resonances in Benzene and Benzene Derivatives," *Phys. Letters* **23**, 656–58 (1966).

K. E. Cowser, L. C. Lasher, L. Gemmell, and S. G. Pearsall
"Operational Experience in the Treatment of Radioactive Waste at the Oak Ridge National Laboratory and Brookhaven National Laboratory," pp. 381–401 in *Proceedings of a Symposium on Practices in the Treatment of Low- and Intermediate-Level Radioactive Wastes, December 6–10, 1965, Vienna, Austria,* IAEA, Vienna, 1966.

K. E. Cowser, W. S. Snyder, C. P. McCammon, C. P. Straub, O. W. Kochtitzky, R. L. Hervin, E. G. Struxness, and R. J. Morton
"Evaluation of Radiation Dose to Man from Radionuclides Released to the Clinch River," pp. 639–71 in *Proceedings of Symposium on Disposal of Radioactive Wastes into Seas, Oceans, and Surface Waters, May 16–20, 1966, Vienna, Austria,* IAEA, Vienna, 1966.

K. E. Cowser, S. V. Kaye, P. S. Rohwer, W. S. Snyder, and E. G. Struxness
Dose-Estimation Studies Related to Proposed Construction of an Atlantic-Pacific Interoceanic Canal with Nuclear Explosives: Phase 1, ORNL-4101 (March 1967).

L. S. Cram and E. T. Arakawa
"Bremsstrahlung and Transition Radiation from Ag Foils Bombarded by Non-Normal Incidence Electrons," *Phys. Rev.* **153**, 455–59 (1967).

D. A. Crossley, Jr.
"Comparative Movement of ^{106}Ru, ^{60}Co, and ^{137}Cs in Arthropod Food Chains," to be published in *Proceedings of 2nd National Symposium on Radioecology, Ann Arbor, Michigan.*

J. Crowell, V. E. Anderson, and R. H. Ritchie
"Ladder Corrections to the Static RPA Dielectric Constant and to Positron Annihilation in Metals," *Phys. Rev.* **150**, 243–48 (1966).

J. W. Curlin
"Clonal Differences in Yield Response of *Populus deltoides* to Nitrogen Fertilization," *Soil Sci. Soc. Am. Proc.* **31**, 276–80 (1967).

J. W. Curlin (with H. C. Jones)
"The Role of Fertilizers in Improving the Hardwoods of the Tennessee Valley," *Proc. TVA Forest Fertilization Symp., Gainesville, Florida* (in press).

J. W. Curlin (with W. M. Ciesla and J. C. Bell, Jr.)
"Color Aerial Photography for Appraisal Surveys of the Southern Pine Beetle," *Photogrammetric Eng.* (in press).

J. W. Curlin and J. P. Witherspoon
"Components and Estimates of Dose to Roots of Potted Plants Exposed to Fast Neutron Radiation," *Health Phys.* (in press).

R. C. Dahlman
"Carbon-14 Cycling in the Root and Soil Components of a Prairie Ecosystem," to be published in the *Proceedings of 2nd National Symposium on Radioecology, Ann Arbor, Mich.*

D. R. Davy
"Personnel Dosimetry for Radiation Accidents" (book review), *Health Phys.* **12**, 1508–10 (1966).

"Prediction of Biological Damage from Stopping-Power Theory," *Health Phys.* (in press).

D. R. Davy and L. H. Peshori
"An Absolute Neutron Dosimeter Based on a Generalized Concept for Radiation Dosimetry," *Health Phys.* **13**, 783–94 (1967).

D. R. Davy, L. H. Peshori, and J. W. Poston
"Sodium-24 Production in Saline-Filled Phantoms Under Neutron Irradiations," *Health Phys.* **12**, 1353–55 (1966).

Wallace de Laguna
Critical Analysis of the Hydrologic Work Carried Out on the Site of the Nuclear Studies Complex at Mol, Report No. 17, C. E. N. Centre d'Etude de l'Energie Nucleaire, Mol, Belgium (1965).

P. B. Dunaway
"Life History and Populational Aspects of the Eastern Harvest Mouse," *Am. Midland Naturalist* (in press).

P. B. Dunaway, J. A. Payne, L. L. Lewis, and J. D. Story
"Incidence and Effects of *Cuterebra* in *Peromyscus*," *J. Mammal.* **48**, 38–51 (1967).

P. B. Dunaway, L. L. Lewis, J. D. Story, J. A. Payne, and J. M. Inglis
"Radiation Effects in the Soricidae, Cricetidae, and Muridae," to be published in the *Proceedings of 2nd National Symposium on Radioecology, Ann Arbor, Michigan.*

P. B. Dunaway (with G. E. Cosgrove and T. P. O'Farrell, J. A. Payne, and H. E. Childs)
"Pathology Survey in Small Mammals," *Bull. Wildlife Disease Assoc.* (in press)

F. M. Empson, W. J. Boegly, Jr., R. L. Bradshaw, W. C. McClain, F. L. Parker, and W. F. Schaffer, Jr.
"Demonstration of Disposal of High-Level Radioactive Solids in Salt," pp. 432–43 in *Proceedings of the Second Symposium on Salt*, vol. 1, The Northern Ohio Geological Society, Inc., Cleveland, Ohio, 1966.

F. M. Empson, R. L. Bradshaw, W. J. Boegly, Jr., W. C. McClain, F. L. Parker, and W. F. Schaffer, Jr.
"Project Salt Vault: Design and Operation," pp. 671–84 in *Proceedings of International Symposium on Solidification and Long-Term Storage of Highly Radioactive Wastes, Richland, Washington, February 15–18, 1966*, CONF-660208 (November 1966).

L. B. Farabee
"Improved Procedure for Radiostrontium Analysis of Human Urine," *Proceedings of 12th Bio-Assay and Analytical Chemistry Meeting, Gatlinburg, Tenn., October 13–14, 1966*, CONF-661018 (June 6, 1967).

B. R. Fish (ed.)
Surface Contamination (Proceedings of a Symposium Held in Gatlinburg, Tennessee, June 8–12, 1964), Pergamon, London (1967).

B. R. Fish, R. L. Walker, G. W. Royster, Jr., and J. L. Thompson
"Redispersion of Settled Particulates," p. 75 in *Surface Contamination* (Proceedings of a Symposium Held in Gatlinburg, Tennessee, June 8–12, 1964). Pergamon, London (1967).

H. L. Fisher, Jr.
"A Computer Code for Estimation of Body Burden of ^{90}Sr Based on O.R. and Bone Remodeling Which Are Age Dependent," p. 147 in *Proceedings of 11th Annual Bioassay and Analytical Chemistry Meeting, October 7–8, 1965, Albuquerque, New Mexico*, CONF-651008 (1966).

H. L. Fisher, Jr., and W. S. Snyder
"An Age-Dependent Model for the Bodily Retention of Cesium," p. 174 in *Proceedings of 12th Annual Bioassay and Analytical Chemistry Meeting, October 13–14, 1966, Gatlinburg, Tennessee,* CONF-661018 (1967).

Kenneth Fox
"Bound States of an Electron in a Point Electric-Dipole Field: Quantization of a Classical Solution," submitted for publication in *Physics Letters.*

Kenneth Fox and J. E. Turner
"WKB Treatment of Bound States in an Electron Dipole Potential," *Am. J. Phys.* **34**, 606–10 (1966).

W. R. Garrett and C. P. Bhalla
"Potential Energy Shift for a Screened Coulomb Potential," *Z. Physik* **198**, 453–60 (1967).

W. R. Garrett and H. T. Jackson
"Electron Photodetachment from O^- and Elastic Scattering from Atomic Oxygen," *Phys. Rev.* **153**, 28–35 (1967).

L. W. Gilley, L. B. Holland, J. W. Poston, and D. R. Ward
"Operation Problems with the Health Physics Research Reactor," *Nucl. Safety* **8**(2), 179–82 (Winter 1966–67).

H. Hollister and J. E. Turner
"The Possible Role of Momentum in Radiation Dosimetry. III. Remarks on the 1962 ICRP/ICRU Report," *Health Phys.* **12**, 949–53 (1966).

H. H. Hubbell
Report of Personnel Exchange Between Oak Ridge National Laboratory and the European Organization for Nuclear Research (CERN), Geneva, Switzerland, During Period September 9, 1965, to August 16, 1966, Oct. 13, 1966 (internal memorandum).

G. S. Hurst and J. E. Parks
"Time-of-Flight Determinations of Electron Diffusion Coefficients and Electron Drift Velocities in Ethylene, Water Vapor, and in Hydrogen," *J. Chem. Phys.* **45**, 282–95 (1966).

D. G. Jacobs
"An Interpretation of Cation Exchange by Alumina," *Health Phys.* **12**, 1565–70 (1966).

"Behavior of Radioactive Gases Discharged into the Ground," *Nucl. Safety* **8**(2), 175–78 (Winter 1966–67).

"Negative Sorption by Alumino-Silicates Having a Limited Degree of Lattice Expansion," pp. 319–29 in *Proceedings of the International Clay Conference, 1966, Jerusalem, Israel,* vol. I.

D. R. Johnson
"*Neutron Detectors,*" book review, *Health Phys.* **13**, 664 (1967).

D. R. Johnson and W. F. Ohnesorge
"Yield, Energy, and Angular Distributions of Neutrons Produced in Graphite, Copper, and Tantalum Targets Irradiated with 63 Mev Protons," to be published in *Atompraxis.*

D. R. Johnson and J. W. Poston
Radiation Dosimetry Studies at the Health Physics Research Reactor, ORNL-4113 (June 1967).

Edith S. Jones
"Microscopic and Autoradiographic Studies of Distribution of Uranium in the Rat Kidney," *Health Phys.* **12**, 1437 (1966).

G. E. Jones, L. S. Cram, and E. T. Arakawa
"Radiation from Thick Silver Foils Bombarded by Grazing-Incidence Electrons," *Phys. Rev.* **147**, 515–17 (1966).

T. D. Jones
Report of Trip Abroad by T. D. Jones During Period September 3 Through 11, 1966, Oct. 13, 1966 (internal memorandum).

Report of Trip Abroad by T. D. Jones During Period February 2–March 6, 1967, Apr. 26, 1967 (internal memorandum).

T. D. Jones, J. A. Auxier, J. W. Poston, and D. R. Johnson
"Dose Distribution Functions for Neutrons and Gamma Rays in Anthropomorphous and Radiological Phantoms," to be published in *Proceedings of First International Congress of the International Radiation Protection Association, Rome, Italy, September 5 Through 10, 1966.*

K. Katoh and J. E. Turner
"A Study of Elementary Particle Interactions for High-Energy Dosimetry," *Health Phys.* (in press).

S. V. Kaye (with J. L. Roti Roti)
Calibration of ^{90}Sr and ^{90}Y Plaques for Irradiating Insects, ORNL-TM-1921 (submitted).

G. D. Kerr and T. D. Strickler
"The Application of Solid-State Nuclear Track Detectors to the Hurst Threshold Detector System," *Health Phys.* **12**, 1141–42 (1966).

N. R. Kevern
"Feeding Rate of Carp Established by a Radioisotopic Method," *Trans. Am. Fisheries Soc.* **94**, 363–71 (1966).

N. R. Kevern, J. L. Wilhm, and G. M. Van Dyne
"Use of Artificial Substrata to Estimate the Productivity of Periphyte," *Limnol. Oceanog.* **11**, 499–502 (1966).

C. E. Klots
"Energy Deposition Mechanisms," to be published as chap. 1 in *Fundamental Processes of Radiation Chemistry* (ed. by Pierre Ausloos).

"Energy Partition Parameters in Radiation Studies Involving Rare Gases," *J. Chem. Phys.* **46**, 3468–74 (1967).

"Statistical Aspects of Autoionization Lifetimes," *J. Chem. Phys.* **46**, 1197–99 (1967).

C. E. Klots and V. E. Anderson
"Ion Loss by Diffusion in the Radiolysis of Gases," *J. Phys. Chem.* **71**, 265–67 (1967).

R. A. MacRae, E. T. Arakawa, and M. W. Williams
"Optical Properties of Vacuum-Evaporated White Tin," submitted for publication in the *Physical Review.*

L. A. Masironi and B. R. Fish
"Direct Observation of Particle Reentrainment from Surfaces," p. 55 in *Surface Contamination* (Proceedings of a Symposium held in Gatlinburg, Tennessee, June 8–12, 1964), Pergamon, London, 1967.

W. C. McClain
"Surface Subsidence Associated with Longwall Mining," *Trans. AIME* **238**, 231–36 (September 1966).

Research Program on Earth Stress Measurement Using Hydraulic Fracturing, January 1967 (internal memorandum).

W. C. McClain and R. L. Bradshaw
"Stress Redistribution in Room and Pillar Salt Mines," *Intern. J. Rock Mech. Min. Sci.* **4**, 245–55 (April 1967).

W. J. McConnell, R. N. Hamm, R. H. Ritchie, and R. D. Birkhoff
"Electron Flux Spectra in Aluminum; Analysis for LET Spectra and Excitation and Ionization Yields," submitted for publication in *Radiation Research.*

E. F. Menhinick
"^{90}Sr Plaques for Beta Radiation Studies," *Health Phys.* **12**, 973–79 (1966).

K. Z. Morgan
"A Comparison and Evaluation of Various Radiation Hazards in Metropolitan Areas," p. 41 in *Proceedings of the II Symposium on Health Physics*, Pecs, Hungary, September 26–30, vol. II, 1966.

M. Y. Nakai, D. A. LaBar, J. A. Harter, and R. D. Birkhoff
"Time-of-Flight Studies of Electrons in the Nanosecond Region," *Rev. Sci. Instr.* **38**, 820–26 (1967).

E. C. Neal, B. C. Patten, and C. E. DePoe
"Periphyton Growth on Artificial Substrates in a Radioactively Contaminated Lake," *Ecology* (submitted).

D. J. Nelson
"Ecology and the Industrial Society" (book review), *Health Phys.* **12**, 1507–8 (1966).

"Microchemical Constituents in Contemporary and Pre-Columbian Clam Shell," *Quaternary Paleoecology*, Yale University Press, New Haven, Conn. (in press).

"The Prediction of ^{90}Sr Uptake in Fish Using Data on Specific Activities and Biological Half-Lives," pp. 843–51 in *Radioecological Concentration Processes* (ed. by B. Åberg and F. P. Hungate), Pergamon, New York.

"Environmental Biology" (book review), *Environ. Sci. Technol.* (May 1967).

"Ecological Behavior of Radionuclides in Surface Waters," *Proceedings of the Reservoir Fishery Resources Symposium* (in press).

"Cesium, Cesium-137, and Potassium Concentrations in White Crappie and Other Clinch River Fish," to be published in the *Proceedings of 2nd National Symposium on Radioecology, Ann Arbor, Michigan.*

D. R. Nelson, J. G. Carter, R. D. Birkhoff, R. N. Hamm, and L. G. Augenstein
"Yield of Luminescence from X-Irradiated Biochemicals," to be published in *Radiation Research.*

Jacob Neufeld
"Reformulation of the Dielectric Constant and of the Conductivity of an Absorbing Medium," *Intern. J. Electron.* **21**, 99–101 (1966).

"Reformulation of the Dielectric Constant and of Ohm's Law in an Absorbing Medium," *Phys. Rev.* **152**, 707–17 (1966).

Jacob Neufeld, V. E. Anderson, Harvel Wright, W. S. Snyder, and J. E. Turner
"Effects of Phantom Geometry on Dose Distribution," to be published in *Proceedings of International Congress of International Radiation Protection Association, Rome, Italy, September 5–10, 1966.*

Jacob Neufeld and C. L. Wiginton
"Cyclotron Excitation of Electromagnetic Waves by a Gyrating Electron Beam," *Phys. Rev.* **148**, 97–103 (1966).

Jacob Neufeld and Harvel Wright
"Discussion of Paper by John M. Cornwall, 'Cyclotron Instabilities and Electromagnetic Emission in the Ultra Low Frequency and Very Low Frequency Ranges,'" *J. Geophys. Res.* **71**, 4200 (1966).

"Excitation of Hydromagnetic Waves by a Helical Proton Stream," *Proceedings of Symposium on Electromagnetic Wave Theory, Delft, September 6–11, 1965* (in press).

T. P. O'Farrell and P. B. Dunaway
"Cell Proliferation as a Function of Metabolism in Three Species of Native Rodents," *Nature* (in press).

"Incorporation and Tissue Distribution of a Thymidine Analog in *Sigmodon hispidus*," *Comp. Biochem. Physiol.* (in press).

J. S. Olson
"Progress in Radiation Ecology: Radionuclide Movement in Major Environments," *Nucl. Safety* **8**, 53–68 (1966).

"Ecology" in *Four Problem Areas in the Recovery from a Large-Scale Nuclear Attack,* National Academy of Sciences, Advisory Committee on Emergency Planning (submitted).

J. S. Olson (ed.)
Systems Ecology and the International Biological Program, National Academy of Sciences, U.S. National Committee for the International Biological Program (submitted).

J. S. Olson (with Victor Obenhaus and Lionel Walford, eds.)
Technology and Man's Relation to His Natural Environment, National Council of the Churches of Christ in the U.S.A. (submitted).

F. L. Parker, M. A. Churchill, R. W. Andrew, B. J. Frederick, P. H. Carrigan, Jr., J. S. Cragwall, Jr., S. L. Jones, E. G. Struxness, and R. J. Morton
"Dilution, Dispersion, and Mass Transport of Radionuclides in the Clinch and Tennessee Rivers," pp. 33–55 in *Proceedings of a Symposium on Disposal of Radioactive Wastes into Seas, Oceans, and Surface Waters, May 16–20, 1966, Vienna, Austria,* IAEA, Vienna, 1966.

B. C. Patten
The Biocoenetic Process in an Estuarine Phytoplankton Community, ORNL-3946 (October 1966).

"Systems Ecology: A Course Sequence in Mathematical Ecology," *BioScience* **16**, 593–98 (1966).

B. C. Patten (with J. S. O'Conner)
"Mathematical Models of Plankton Productivity," *Proceedings of Reservoir Fishery Symposium* (in press).

B. C. Patten and B. F. Chabot
"Factorial Productivity Experiments in a Shallow Estuary: Characteristics of Response Surfaces," *Chesapeake Sci.* **7**, 117–36 (1966).

B. C. Patten and R. L. Iverson
"Photosynthesis and Uptake of Strontium-85 in Freshwater Plankton," *Nature* **211**, 96–97 (1966).

B. C. Patten and G. M. Van Dyne
"Factorial Productivity Experiments in a Shallow Estuary: Energetics of Individual Plankton Species in Mixed Populations," submitted to *Limnology and Oceanography.*

B. C. Patten and M. Witkamp
"Systems Analysis of ^{134}Cs Kinetics in Terrestrial Microcosms," *Ecology* (in press).

J. A. Payne, G. D. Martin, J. D. Story, and G. E. Cosgrove
"Electrophoresis as an Aid in Detecting Pathological Conditions in Wild Mammals," *Bull. Wildlife Disease Assoc.* **3**, 21–22 (1967).

P. T. Perdue
"Inexpensive Liquid Nitrogen Level Control for Cold Traps," *Nucl. Instr. Methods* **44**, 169–70 (1966).

R. J. Pickering, P. H. Carrigan, Jr., T. Tamura, H. H. Abee, J. W. Beverage, and R. W. Andrew, Jr.
"Radioactivity in Bottom Sediment of the Clinch and Tennessee Rivers," pp. 57–88 in *Symposium on Disposal of Radioactive Wastes into Seas, Oceans, and Surface Waters, May 16–20, 1966, Vienna, Austria,* IAEA, Vienna, 1966.

J. W. Poston
Report of Trip Abroad by J. W. Poston During Period July 23, 1966–July 30, 1966, Aug. 18, 1966 (internal memorandum).

J. R. Reed
"Alarm Substances and Fright Reactions in Some Fishes from the Southeastern United States," submitted to *Animal Behavior.*

J. R. Reed and D. J. Nelson
"Radiostrontium Uptake in Blood and Flesh in Bluegills (*Lepomis macrochirus*)," to be published in the *Proceedings of 2nd National Symposium on Radioecology, Ann Arbor, Michigan.*

D. E. Reichle
"Some Pselaphid Beetles with Boreal Affinities and Their Distribution Along the Postglacial Fringe," *Systematic Zool.* **15**, 330–34 (1966).

"Radiocesium Turnover Rates and Energy Flow in Terrestrial Isopod Populations," *Ecology* **48**(3), 351–66 (1967).

"The Temperature and Humidity Relations of Some Bog Pselaphid Beetles," *Ecology* **48**, 208–15 (1967).

"Relation of Body Size to Food Intake, Oxygen Consumption, and Trace Element Metabolism in Forest Floor Arthropods," submitted to *Ecology.*

D. E. Reichle (with E. C. Williams, Jr.)
"Radioactive Tracers in the Study of Energy Turnover by a Grazing Insect (*Chrysochus auratus* Fab.)," submitted to *Oikos.*

D. E. Reichle and D. A. Crossley, Jr.
"Trophic Level Concentrations of Cesium-137, Sodium, and Potassium in Forest Arthropods," to be published in the *Proceedings of 2nd National Symposium on Radioecology, Ann Arbor, Michigan.*

R. H. Ritchie
"On the Possibility of Observing Characteristic Energy Gain by Fast Electrons in Solids," *Phys. Letters* **22A**, 348–49 (1967).

R. H. Ritchie and V. E. Anderson
"The Use of Fourier Transforms in the Unfolding of Experimental Data," *Nucl. Instr. Methods* **45**, 277–81 (1966).

R. H. Ritchie and J. E. Turner
"Electron Capture and Loss in Electron Swarm Experiments," *Z. Physik* **200**, 259–69 (1967).

R. H. Ritchie, M. Y. Nakai, and R. D. Birkhoff
"Low-Energy Electron Mean Free Paths in Solids," in *Advances in Radiobiology,* vol. 3 (in press).

L. L. Robinson, L. C. Emerson, J. G. Carter, and R. D. Birkhoff
"Optical Reflectivities of Liquid Water in the Vacuum UV," submitted for publication in the *Journal of Chemical Physics.*

A. S. Rogowski, W. D. Shrader, H. P. Johnson, and Don Kirkham
"Tile Drainage Experimentation on Webster Soils: Results of Years 1954–1963," *Iowa State J. Sci.* **41**(1), 25–40 (August 1966).

G. W. Royster, Jr., and B. R. Fish
"Techniques for Assessing 'Removable' Surface Contamination," p. 201 in *Surface Contamination* (Proceedings of a Symposium held in Gatlinburg, Tennessee, June 8–12, 1964), Pergamon, London, 1967.

W. F. Schaffer, Jr., W. J. Boegly, Jr., F. L. Parker, R. L. Bradshaw, F. M. Empson, and W. C. McClain
"Project Salt Vault: Design and Demonstration of Equipment," pp. 685–706 in *Proceedings of International Symposium on Solidification and Long-Term Storage of Highly Radioactive Wastes, Richland, Washington, February 15–18, 1966,* CONF-660208 (November 1966).

H. A. Schroeder, J. J. Balassa, and Isabel H. Tipton
"Essential Trace Metals in Man: Manganese. A Study in Homeostasis," *J. Chronic Diseases* **19**, 545 (1966).

H. A. Schroeder, A. P. Nason, Isabel H. Tipton, and J. J. Balassa
"Essential Trace Metals in Man: Copper," *J. Chronic Diseases* **19**, 1007 (1966).

"Essential Trace Metals in Man: Zinc. Relation to Environmental Cadmium," *J. Chronic Diseases* **20**, 179 (1967).

A. F. Shinn
"Kiln-Firing as a Technique for Studying Nest-Building Behavior of Mud-Dauber Wasps," *Nature* **201**, 112 (1966).

W. S. Snyder
"A Dose Estimate Based on Stable-Isotope Data," p. 161 in *Proceedings of 11th Annual Bioassay and Analytical Chemistry Meeting, October 7–8, 1965, Albuquerque, New Mexico,* CONF-651008 (1966).

"The Standard Man in Relation to Internal Radiation Dose," *Am. Ind. Hygiene Assoc. J.* **27**, 539 (November–December 1966).

"The Use of the Lung Model for Estimation of Dose," p. 74 in *Proceedings of 12th Annual Bioassay and Analytical Chemistry Meeting, October 13–14, 1966, Gatlinburg, Tennessee,* CONF-661018 (1967).

"Distribution of Dose in the Body from HTO," p. 22 in *Abridged Proceedings of the Symposium on Instrumentation, Experience, and Problems in Health Physics Tritium Control, February 16–17, 1967, Albuquerque, New Mexico,* SC-M-67-244 (May 1967).

W. S. Snyder, J. A. Auxier, M. D. Brown, T. D. Jones, and R. T. Boughner
"Distribution of Dose and Dose Equivalent in an Anthropomorphic Phantom Resulting from Broad-Beam Sources of Monoenergetic Neutrons," p. 27 in *Proceedings of the Special Sessions on Radiation Transport and Biological Effects, November 1, 1966, Pittsburgh, Pennsylvania,* ANS-SD-4 (1967); *Trans. Am. Nucl. Soc.* **9**(2), 357 (1967) (abstr).

J. A. Stockdale, L. G. Christophorou, and G. S. Hurst
"Capture of Thermal Electrons by Oxygen," submitted for publication in the *Journal of Chemical Physics.*

E. G. Struxness
"Ultimate Disposal of Radioactive Wastes," to be published in *Proceedings of 6th Annual Sanitary and Water Resources Conference, Vanderbilt University, June 1, 1967.*

"Permanent Disposal of Radioactive Wastes," to be published in *Proceedings of 2nd National Symposium on Radioecology.*

E. G. Struxness, P. H. Carrigan, Jr., M. A. Churchill, K. E. Cowser, R. J. Morton, D. J. Nelson, and F. L. Parker
Comprehensive Report of the Clinch River Study, ORNL-4035 (April 1967).

J. C. Sutherland, E. T. Arakawa, and R. N. Hamm
"Optical Properties of Sodium in the Vacuum Ultraviolet," *J. Opt. Soc. Am.* **57**, 645–50 (May 1967).

Jacob Tadmor and K. E. Cowser
"Underground Disposal of ^{85}Kr from Nuclear Fuel Reprocessing Plants," *Trans. Am. Nucl. Soc.* **10**(1), 159 (1967).

Tsuneo Tamura
"Development and Applications of Minerals in Radioactive Waste Disposal," pp. 425–39 in *Proceedings of the International Clay Conference, 1966, Jerusalem, Israel,* vol. I.

"Selective Removal of Cesium-137 and Strontium-90 in Waste Solutions by Minerals," pp. 91–107 in *Proceedings of Conference on Water, Geology, and the Future,* Indiana University, Bloomington, Indiana, 1967.

J. T. Tanner
"Effects of Population Density on Growth Rates of Animal Populations," *Ecology* **47**, 733–46 (1966).

F. G. Taylor, Jr.
"Predicted Seasonal Radiosensitivity of Southeastern Tree Species," *Radiation Botany* **6**, 307–12 (1966).

"*Spiranthes ovalis* Present in Tennessee," *Castanea* **32**, 99–101 (1967).

"Effects of Acute Gamma Radiation on Bud Production and Stem Elongation of Giant Sequoia Seedlings," submitted to *Radiation Botany*.

J. H. Thorngate
"Dosimetry, Shielding, and Scattering. II," to be published in *Proceedings of Conference on Principles of Radiation Protection, Oak Ridge, Tennessee, August 24 Through 26, 1966.*

An Interval Timer Designed for Use During Irradiations at the Health Physics Research Reactor, ORNL-TM-1559 (August 1966).

J. H. Thorngate, J. A. Auxier, F. F. Haywood, and S. Helf
Energy and Angular Distribution of Neutrons and Gamma Rays – Operation BREN, CEX-62.12 (February 1967).

Isabel H. Tipton and Peggy L. Stewart
"Spectrographic Analysis of Biological Materials," *Devel. Appl. Spectry.* **5** (1966).

J. E. Turner
"Calculation of Stopping Power of a Heavy Charged Particle in Matter," to be published in *Health Physics.*

J. E. Turner and Kenneth Fox
"Minimum Dipole Moment Required to Bind an Electron to a Finite Dipole," *Phys. Letters* **23**, 547–49 (1966).

J. E. Turner and Hal Hollister
"On the Relationship of Collision Theory to the Interpretation of Relative Biological Effectiveness," submitted for publication in the *Journal of Physics in Medicine and Biology.*

G. M. Van Dyne
"Application and Integration of Multiple Linear Regression and Linear Programming in Renewable Resource Analyses," *J. Range Management* **19**, 356–62 (1966).

"Use of a Vacuum-Clipper for Harvesting Herbage," *Ecology* **47**, 624–26 (1966).

G. M. Van Dyne and H. G. Fisser
"Influence of Number and Spacing of Points on Accuracy and Precision of Basal Cover Estimates," *J. Range Management* **19**, 205–11 (1966).

G. M. Van Dyne and W. G. Vogel
"Relation of *Selaginella densa* to Site Grazing and Climate," *Ecology* **48**(3), 438–44 (1967).

G. M. Van Dyne and Ingvi Thorsteinsson
"Intraseasonal Changes in the Height Growth of Plants in Response to Nitrogen and Phosphorus," pp. 924–29 in *Proceedings of Tenth International Grassland Conference, July 7–16, 1966, Helsinki, Finland.*

R. C. Vehse, E. T. Arakawa, and J. L. Stanford
"Photoemission Measurements of Silver and Palladium in the Vacuum Ultraviolet," submitted for publication in *Physical Review Letters.*

"Normal Incidence Reflection of Aluminum Films in the Wavelength Region 800 to 2000 Å," *J. Opt. Soc. Am.* **57**, 551–52 (1967).

E. B. Wagner, F. J. Davis, G. S. Hurst, and J. E. Parks
"Time-of-Flight Investigations of Electron Transport in Some Atomic and Molecular Gases," submitted for publication in the *Journal of Chemical Physics.*

R. L. Walker and B. R. Fish
"Adhesion of Radioactive Glass Particles to Solid Surfaces," in *Surface Contamination* (Proceedings of a Symposium held in Gatlinburg, Tennessee, June 8–12, 1964), Pergamon, London, 1967.

H. D. Waller and J. S. Olson
"Prompt Transfers of ^{137}Cs to the Soils of a Tagged *Liriodendron* Forest," *Ecology* **48**, 15–25 (1967).

W. H. Wilkie
Trip Report: Symposium on Solid State and Chemical Radiation Dosimetry in Medicine and Biology, Vienna, Austria, Oct. 3–7, 1966; Discussions at AERE, Harwell, England, and Karlsruhe Nuclear Research Center, Germany, Nov. 11, 1966 (internal memorandum).

W. H. Wilkie and B. R. Fish
"Scintillation Extrapolation Dosimetry of Small Beta-Emitting Sources," in *Solid State and Chemical Radiation Dosimetry in Medicine and Biology* (Proceedings of a Symposium, Vienna, 3–7 October 1966), IAEA, Vienna, 1967.

M. W. Williams, E. T. Arakawa, and L. C. Emerson
"Photon Excitation of Surface Plasmons – Analysis of Data for Aluminum," *Surface Sci.* **6**, 127–31 (1967).

M. W. Williams, R. A. MacRae, and E. T. Arakawa
"Optical Properties of Magnesium Fluoride in the Vacuum Ultraviolet," *J. Appl. Phys.* **38**, 1701–5 (1967).

J. P. Witherspoon
"Effects of Internal ^{137}Cs Radiation on Seeds of *Liriodendron tulipifera,*" *Radiation Botany* (in press).

"Radiosensitivity of Forest Tree Species to Acute Fast Neutron Radiation," to be published in *Proceedings of 2nd National Symposium on Radioecology, Ann Arbor, Michigan.*

Martin Witkamp
"Rates of Carbon Dioxide Evolution from the Forest Floor: Measurement, Environmental Effects, and Relation to CO_2 from Litter," *Ecology* **47**, 492–93 (1966).

"Biological Concentrations of ^{137}Cs and ^{90}Sr in Arctic Food Chains," *Nucl. Safety* **8**, 58–62 (1966).

"Assessment of Microbial Immobilization of Mineral Elements," *Soil Biol.* (in press).

"Aspects of Soil Microflora in Gamma Irradiated Rain Forest," in *The Tropical Rainforest,* ed. by H. T. Odum (submitted).

"Mineral Retention by Epiphyllic Organisms," in *The Tropical Rainforest,* ed. by H. T. Odum (submitted).

"Environmental Influences on Microbial Populations and Activity of the Forest Floor," *Trans. Intern. Congr. Soil Sci., 8th, Bucharest, 1964,* vol. **3**, Soil Biology (in press).

Martin Witkamp, M. L. Frank, and J. L. Shoopman
"Accumulation and Biota in a Pioneer Ecosystem of Kudzu Vine at Copperhill, Tennessee," *J. Appl. Ecol.* **3**, 383–91 (1966).

Martin Witkamp and D. A. Crossley, Jr.
"The Role of Arthropods and Microflora in Breakdown of White Oak Litter," *Pedobiologia* **6**, 293–303 (1966).

Martin Witkamp and M. L. Frank
"Retention of Loss of ^{137}Cs Components of the Groundcover in a Pine (*Pinus virginiana* L.) Stand," *Health Phys.* (in press).

"Cesium-137 Kinetics in Terrestrial Microcosms," to be published in *Proceedings of 2nd National Symposium on Radioecology, Ann Arbor, Michigan.*

Harvel Wright, E. E. Branstetter, Jacob Neufeld, J. E. Turner, and W. S. Snyder
"Calculation of Radiation Dose Due to High-Energy Protons," to be published in *Proceedings of International Congress of International Radiation Protection Association, Rome, Italy, September 5–10, 1966.*

Edward Yeargers
"UV Light Effects on Proteins," to be published in *Proceedings of Symposium on Biological Effects of Ultraviolet, Philadelphia, Pennsylvania, August 23–26, 1966.*

Lectures

S. I. Auerbach

Introduction to Radiation Ecology, Wabash College, July 6, 1966, Crawfordsville, Indiana.

The Importance of Ecology and the Study of Ecosystems, Wabash College, July 6, 1966, Crawfordsville, Indiana.

Current Research in Radioecology, Exhibits Managers' Training Course, Oak Ridge Associated Universities, August 8, 1966, Oak Ridge, Tennessee.

Aspects of Radioecology, Fall Conference of National Association of State Civil Defense Directors, November 15, 1966, Hot Springs, Arkansas.

Ecology and Ecological Research at ORNL, Navy Nuclear Sciences Seminar, Oak Ridge Associated Universities, December 9, 1966, Oak Ridge, Tennessee.

Radiation and Radioisotopes: Their Role in Ecological Research, Department of Ecology and Behavioral Biology, University of Minnesota, May 1, 1967, St. Paul.

J. A. Auxier

The Health Physics Research Reactor and Its Role at the DOSAR Facility, Kernforschungsanlage Julich, August 26, 1966, Julich, Germany.

Selected Aspects of Dosimetry for Human Exposures, Health Physics Society, Lake Mead Chapter, February 14, 1967, Las Vegas, Nevada.

Selected Aspects of Dosimetry for Human Exposures, Health Physics Society, Atlanta Chapter, April 3, 1967, Atlanta, Georgia.

Ichiban: The Dosimetry Program for Nuclear Bomb Survivors of Hiroshima and Nagasaki, Savannah River Laboratory, April 4, 1967, Aiken, South Carolina.

General Problems in Nuclear Accident Dosimetry, Health Physics Society, Savannah River Chapter, April 4, 1967, Augusta, Georgia.

Dosimetry for Human Exposures: Field Experiments and Laboratory Intercomparisons, Health Physics Society, East Tennessee Chapter, July 31, 1967, Oak Ridge, Tennessee.

B. G. Blaylock

Ecological Genetics, Department of Biology, Emory and Henry College, November 14, 1966, Emory, Virginia; Department of Biology, Clinch Valley College, November 15, 1966, Wise, Virginia; Department of Biology, George Peabody College, December 9, 1966, Nashville, Tennessee; Department of Biology, Western Carolina College, December 14, 1966, Cullowhee, North Carolina; Department of Biology, Muskingum College, January 13, 1967, New Concord, Ohio; Seymour Science Club, Catawba College, January 19, 1967, Salisbury, North Carolina; Department of Biology, Virginia Military Institute, February 21, 1967, Lexington, Virginia.

R. L. Bradshaw

Project Salt Vault, Ten-Week Health Physics Course, ORINS Special Training lectures to people responsible for licensing and inspecting of radioisotope users, etc., ORNL, November 7, 1967, Oak Ridge, Tennessee.

L. G. Christophorou

Studies of Electron-Molecule Interactions, Department of Physics, University of Kentucky, April 14, 1967, Lexington.

R. N. Compton

Interactions of Low-Energy Electrons with Complex Molecules, Department of Physics, University of Georgia, October 11, 1966, Athens.

Low-Energy Electron-Molecule Scattering Phenomena, Department of Physics, Tennessee Technological University, February 24, 1967, Cookeville.

Mary Jane Cook

Biological Effects of Radiation, Department of Physics Course on "Special Topics in Health Physics," University of Tennessee, May 4 and 5, 1967, Knoxville.

K. E. Cowser

Movement and Hazards of Radionuclides in Fresh Water, to members of ORINS course in Advanced Isotope Technology, ORNL, August 3, 1966, Oak Ridge, Tennessee.

Clinch River Hazards Analysis, Ten-Week Health Physics Course, ORINS Special Training lectures to people responsible for licensing and inspecting of radioisotope users, etc., ORNL, November 7, 1967, Oak Ridge, Tennessee.

D. A. Crossley, Jr.

Role of Microfauna and Microflora in Breakdown and Transfer of Organic Matter, Seminar on Pesticides, Michigan State University, May 18, 1967, East Lansing.

J. W. Curlin

Soil Activation by Fast Neutrons, Advanced Isotope Technology Course, Oak Ridge Associated Universities, July 13, 1966, Oak Ridge, Tennessee.

Wallace de Laguna

Waste Disposal by Hydrofracturing, Ten-Week Health Physics Course, ORINS Special Training lectures to people responsible for licensing and inspecting of radioisotope users, etc., ORNL, November 7, 1967, Oak Ridge, Tennessee.

B. R. Fish

Radioactivity in Man, ORAU-ORNL Ten-Week Health Physics Course, October 5, 1966, Oak Ridge, Tennessee.

Effects of Air Pollution on the Safety and Well-Being of Society, Reactor Division, ORNL, January 1967, Oak Ridge, Tennessee (2 seminars).

Surface Contamination and Aerosol Physics Research, Atlanta Chapter Health Physics Society, January 9, 1967, Atlanta, Georgia.

In Vivo Detection and Measurement of Transuranic Elements, Transuranium Research Laboratory, ORNL, May 10, 1967, Oak Ridge, Tennessee.

Radiological Health, Radiation Shielding, and Air Pollution, May 5, 1967, University of Texas, Austin (3 seminars).

D. G. Jacobs

Movement of Nuclides Through the Ground, Ten-Week Health Physics Course, ORINS Special Training lectures to people responsible for licensing and inspecting of radioisotope users, etc., ORNL, November 7, 1966, Oak Ridge, Tennessee.

Waste Management, to students at Lenoir Rhyne College, May 12, 1967, Hickory, North Carolina.

Waste Disposal and Environmental Monitoring, Radiation Science Center, March 1, 1967, New Brunswick, New Jersey.

T. F. Lomenick

The Disposal of Radioactive Waste in Terrestrial Environments, Ten-Week Health Physics Course, ORINS Special Training lectures to people responsible for licensing and inspecting of radioisotope users, etc., ORINS, November 8, 1966, Oak Ridge, Tennessee.

K. Z. Morgan

Health Physics Program, U.S. Army Nuclear Science Seminar, Oak Ridge Playhouse, July 19, 1966, Oak Ridge, Tennessee.

Permissible Exposures to Ionizing Radiation, AEC-NSF Basic Institute for Nuclear Science and Engineering, ORNL, August 19, 1966, Oak Ridge, Tennessee.

Establishment of Maximum Permissible Doses and Concentrations, Health Physics Course for PHS Personnel, ORNL, October 6, 1966, Oak Ridge, Tennessee.

Radiation Protection, Past, Present, and Projections, Conference on Principles of Radiation Protection, ORAU, August 24–26, 1966, Oak Ridge, Tennessee.

Health Physics, Sixteenth Naval Nuclear Seminar, ORAU, December 9, 1966, Oak Ridge, Tennessee.

Conflict Between Science and Religion, St. John's Lutheran Church, January 29, 1967, Knoxville, Tennessee.

Health Physics – A New Science and a Challenging Profession, Indiana State University, March 8, 1967, Terre Haute; University of Alabama, June 5, 1967, Birmingham.

D. J. Nelson

Ecological Investigations of Radioactive Waste Releases to the Clinch River, Department of Entomology, Fisheries, and Wildlife, University of Minnesota, January 26, 1967, Minneapolis.

Current Research in Aquatic Ecology, Department of Entomology, Fisheries, and Wildlife, University of Minnesota, January 26, 1967, Minneapolis.

J. S. Olson

Radiocesium Cycling in Deciduous Forests, Advanced Isotope Technology Course, Oak Ridge Associated Universities, July 13, 1966, Oak Ridge, Tennessee.

Tracer Experiments on Forest Ecosystem Relations, Ohio State University Biology Colloquium, November 3, 1966, Columbus.

Systems Ecology, Ohio State University Graduate Ecology Seminar, November 3, 1966, Columbus.

Aims and Methods of Systems Ecology, Notre Dame University, January 9, 1967, Notre Dame, Indiana.

Ecological Models of a Tulip Poplar Forest Tagged with Radiocesium, University of Tennessee Zoology Seminar, February 8, 1967, Knoxville.

Systems Models and Experiments in Forests, Department of Ecology and Behavioral Biology, University of Minnesota, May 1, 1967, St. Paul.

Biological Productivity, Development and Regulation of Ecosystems, University of Minnesota Forest Biology Training Session, June 26, 1967, Minneapolis.

Research Methods and Techniques in Systems Ecology, University of Minnesota Forest Biology Training Session, June 26, 1967, Minneapolis.

F. L. Parker

Radioactive Waste Disposal, ORAU 16th Nuclear Science Seminar (Navy), December 2, 1966, Oak Ridge, Tennessee.

Disposal of Radioactive Wastes, U.S. Army Nuclear Science Seminar, July 20, 1966, Oak Ridge, Tennessee.

Status of Waste Disposal Research, Ten-Week Health Physics Course, ORINS Special Training lectures to people responsible for licensing and inspecting of radioisotope users, etc., ORNL, November 7, 1966, Oak Ridge, Tennessee.

B. C. Patten

Marine Isotopic Studies Off the Coast of Puerto Rico, Advanced Isotope Technology Course, July 13, 1966, Oak Ridge Associated Universities, Oak Ridge, Tennessee.

The Network Variable in Ecology, University of Kentucky, November 2, 1966, Lexington; State University College, February 23–24, 1967, Oneonta, New York; University of Georgia, March 2–3, 1967, Athens; St. Mary's College, March 10–11, 1967, Winona, Minnesota; University of Minnesota, May 12, 1967, Minneapolis; University of Buffalo, June 5, 1967, Buffalo, New York.

D. E. Reichle

Radioactive Tracers in Food Chain Research: Kinetics of Nutrient Cycling and Energy Flow in a Forest Ecosystem, St. Mary's College, Symposium on Ecology, November 1966, Winona, Minnesota.

Food Chain and Energetic Studies in Insects, Advanced Isotope Technology Course, July 13, 1966, Oak Ridge Associated Universities, Oak Ridge, Tennessee.

Bryophyte Succession and the Distribution of Microarthropods in an Illinois Bog, University of Tennessee, Seminar on Bog Ecosystems, April 1967, Knoxville.

Insect Behavior and Its Ecological Significance, University of Tennessee, Graduate Course in Insect Ecology, December 1966, Knoxville.

Pathways of Nutrient Cycling in a Forest Ecosystem, Emory University, March 1967, Atlanta, Georgia.

Radiotracers and the Trophic Dynamics of Forest Arthropods, Northwestern University, March 1967, Evanston, Illinois.

R. H. Ritchie

Radiation Dosimetry, Department of Physics, University of Tennessee, May 25, 1967, Knoxville.

A. S. Rogowski

Inspection of Rainfall Simulator, members of ORINS course in Advanced Isotope Technology, ORNL, August 3, 1966, Oak Ridge, Tennessee.

Soil Plots, Ten-Week Health Physics Course, ORINS Special Training lectures to people responsible for licensing and inspecting of radioisotope users, etc., ORNL, November 7, 1967, Oak Ridge, Tennessee.

Use of Isotopes in Runoff and Erosion Studies, ORINS course in Advanced Isotope Technology, ORNL, August 3, 1966, Oak Ridge, Tennessee.

H. C. Schweinler

The Josephson Effect, Department of Physics, University of Tennessee, April 3, 1967, Knoxville.

W. S. Snyder

Examples of the Variation of Dose Within the Body – Neutrons, Gammas, HTO, Western Pennsylvania Chapter of the Health Physics Society, University of Pittsburgh, November 28, 1966, Pittsburgh.

Monte Carlo Calculations for the Distribution of Dose in the Body from External and Internal Sources of Photons, North Carolina Chapter of the Health Physics Society, Duke University, February 8, 1967, Durham, North Carolina.

Current Activities of the Health Physics Society, Bluegrass Chapter of the Health Physics Society, Holiday Inn, February 11, 1967, Frankfort, Kentucky.

Computer Calculation of Dose, Work Conference on Dosimetry in Total Body Photon Irradiation of Man, ORAU, February 23–24, 1967, Oak Ridge, Tennessee.

Health Physics Society Certification Examination, Baltimore-Washington Chapter of the Health Physics Society, March 21, 1967, Bethesda, Maryland.

The Use of Urinalysis Data to Estimate the Body Burden of Plutonium, Centre d'Etudes Nucléaires, April 20, 1967, Saclay, France; ISPRA, April 24, 1967, Milan, Italy.

Distribution of Dose in an Anthropomorphic Phantom Irradiated by Monoenergetic Neutrons, Centre d'Etudes Nucléaires, April 20, 1967, Saclay, France; Centre de Physique Nucléaire, April 21, 1967, Toulouse, France; ISPRA, April 24, 1967, Milan, Italy.

A Two-Exponential Model for Metabolism of HTO by Man, ISPRA, April 25, 1967, Milan, Italy; Puerto Rico Chapter of the Health Physics Society, May 3, 1967, Mayaguez, Puerto Rico.

Health Physics Aspects of Supersonic Transport, Eastern Idaho Chapter of the Health Physics Society, May 19, 1967, Idaho Falls.

E. G. Struxness

Environmental Monitoring, ORAU, Exhibit Managers, July 29, 1967, Oak Ridge, Tennessee.

Environmental Monitoring, Public Health Agents, State Group, ORNL, October 6, 1966, Oak Ridge, Tennessee; University of Tennessee, March 30–31, 1967, Knoxville; National Science Foundation College Group, Oak Ridge Associated Universities, July 20, 1966, Oak Ridge, Tennessee.

Disposal by Hydraulic Fracturing, Knoxville Science Club, January 20, 1967, Knoxville, Tennessee.

Tsuneo Tamura

Radioactive Waste Disposal, Japan Atomic Forum, October 11, 1966, Tokyo, Japan; Radiation Center of Osaka, October 14, 1966, Kyoto University, Osaka, Japan.

Atomic Wastes: Their Treatment and Disposal, University of Hawaii, October 20, 1966, Honolulu.

Introduction to Waste Disposal Research Program, ORINS course in Advanced Isotope Technology, ORNL, August 3, 1966, Oak Ridge, Tennessee.

Use of Isotopes in Clay Mineralogy Studies, ORINS course in Advanced Isotope Technology, ORNL, August 3, 1966, Oak Ridge, Tennessee.

Clay Mineralogy in Waste Disposal, Ten-Week Health Physics Course, ORINS Special Training lectures to people responsible for licensing and inspecting of radioisotope users, etc., ORNL, November 7, 1967, Oak Ridge, Tennessee.

W. A. Thomas

*Cycling of Calcium in Dogwood (*Cornus florida *L.) Trees,* Department of Ecology and Behavioral Biology, University of Minnesota, May 1, 1967, St. Paul.

J. H. Thorngate

The Research Program at the DOSAR Facility (HPRR), U.S. Army Reserve, 3251st Research and Development Unit, June 6, 1967, Oak Ridge, Tennessee.

Isabel H. Tipton

What Are Little Boys Made of, Kiwanis Club, May 3, 1967, Johnson City, Tennessee.

J. P. Witherspoon

Interactions of Environmental Factors and Ionizing Radiation on Forest Tree Species, Department of Biology, Western Maryland College, October 10, 1966, Westminster; Department of Entomology, Clemson University, November 9, 1966, Clemson, South Carolina; School of Forestry, University of Missouri, December 7, 1966, Columbia; Department of Biology, Woman's College of Georgia, November 2, 1966, Milledgeville; Department of Biology, Winthrop College, January 12, 1967, Rock Hill, South Carolina; Department of Biology, Roanoke College, April 13, 1967, Roanoke, Virginia.

Cycling of Radiocesium in Forest Ecosystems, Department of Entomology, Clemson University, November 9, 1966, Clemson, South Carolina; Department of Biology, Roanoke College, April 13, 1967, Roanoke, Virginia.

Radiation Ecology, AEC Fellows, June 15, 1966, ORNL, Oak Ridge, Tennessee.

HEALTH PHYSICS DIVISION

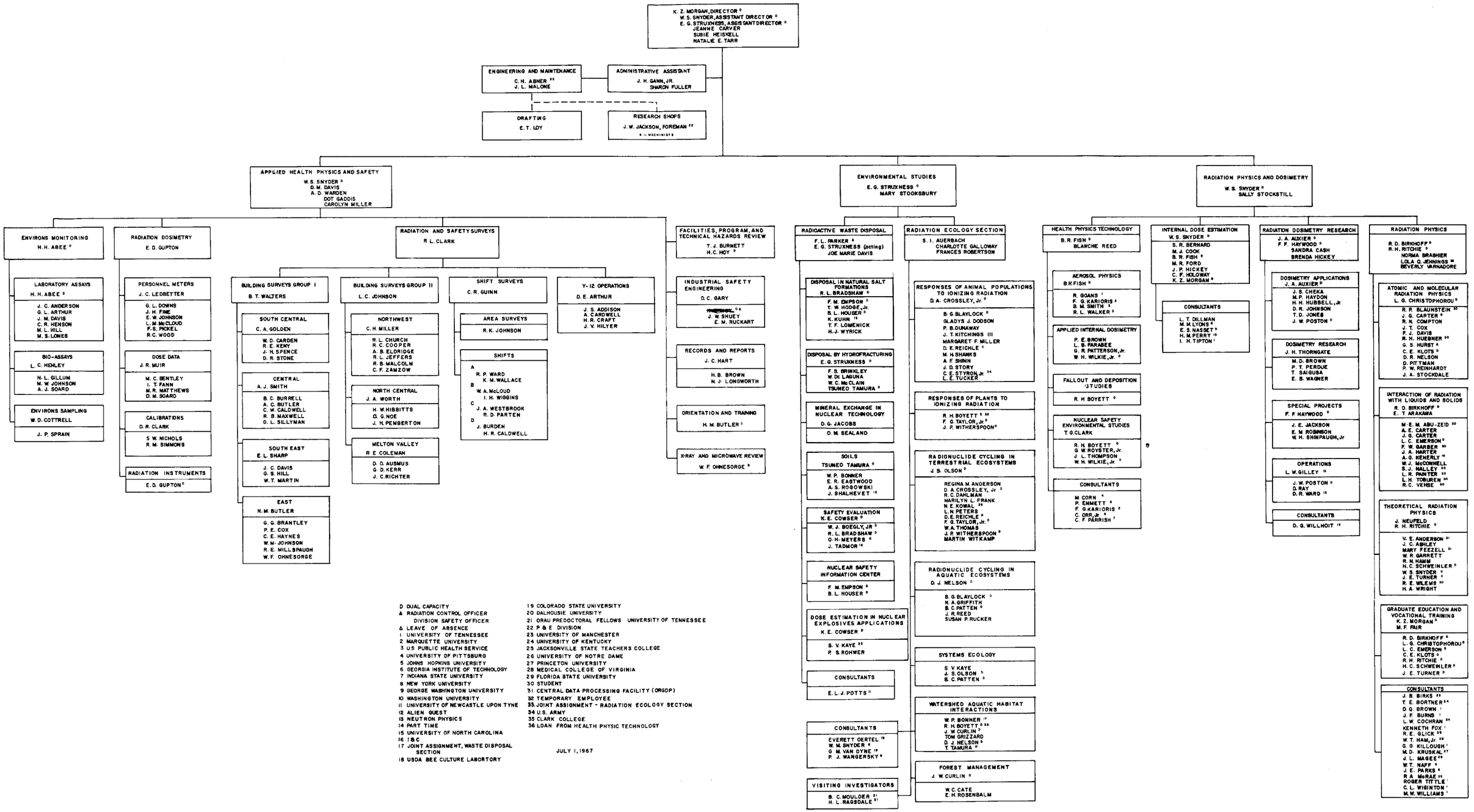

D DUAL CAPACITY
A RADIATION CONTROL OFFICER
DIVISION SAFETY OFFICER
Δ LEAVE OF ABSENCE
1 UNIVERSITY OF TENNESSEE
2 MARQUETTE UNIVERSITY
3 US PUBLIC HEALTH SERVICE
4 UNIVERSITY OF PITTSBURG
5 JOHNS HOPKINS UNIVERSITY
6 GEORGIA INSTITUTE OF TECHNOLOGY
7 INDIANA STATE UNIVERSITY
8 NEW YORK UNIVERSITY
9 GEORGE WASHINGTON UNIVERSITY
10 WASHINGTON UNIVERSITY
11 UNIVERSITY OF NEWCASTLE UPON TYNE
12 ALIEN GUEST
13 NEUTRON PHYSICS
14 PART TIME
15 UNIVERSITY OF NORTH CAROLINA
16 IBC
17 JOINT ASSIGNMENT, WASTE DISPOSAL SECTION
18 USDA BEE CULTURE LABORTORY
19 COLORADO STATE UNIVERSITY
20 DALHOUSIE UNIVERSITY
21 ORAU PREDOCTORAL FELLOWS UNIVERSITY OF TENNESSEE
22 P & E DIVISION
23 UNIVERSITY OF MANCHESTER
24 UNIVERSITY OF KENTUCKY
25 JACKSONVILLE STATE TEACHERS COLLEGE
26 UNIVERSITY OF NOTRE DAME
27 PRINCETON UNIVERSITY
28 MEDICAL COLLEGE OF VIRGINIA
29 FLORIDA STATE UNIVERSITY
30 STUDENT
31 CENTRAL DATA PROCESSING FACILITY (ORGDP)
32 TEMPORARY EMPLOYEE
33 JOINT ASSIGNMENT - RADIATION ECOLOGY SECTION
34 U.S. ARMY
35 CLARK COLLEGE
36 LOAN FROM HEALTH PHYSIC TECHNOLOGY

JULY 1, 1967

ORNL-4168
UC-41 – Health and Safety

INTERNAL DISTRIBUTION

1. Biology Library
2–4. Central Research Library
5. Laboratory Shift Supervisor
6–7. ORNL, Y-12 Technical Library Document Reference Section
8–62. Laboratory Records Department
63. Laboratory Records, ORNL RC
64. H. H. Abee
65. V. E. Anderson
66. E. T. Arakawa
67. J. C. Ashley
68. S. I. Auerbach
69. J. A. Auxier
70. S. E. Beall
71. K. Becker
72. S. R. Bernard
73. R. D. Birkhoff
74. W. J. Boegly
75. P. E. Brown
76. F. R. Bruce
77. T. H. J. Burnett
78. J. G. Carter
79. J. S. Cheka
80. L. G. Christophorou
81. R. L. Clark
82. T. G. Clark
83. W. E. Cohn
84. R. N. Compton
85. M. J. Cook
86. K. E. Cowser
87. D. A. Crossley, Jr.
88. F. L. Culler
89. J. W. Curlin
90. D. M. Davis
91. F. J. Davis
92. P. B. Dunaway
93. L. C. Emerson
94. M. F. Fair
95. L. B. Farabee
96. B. R. Fish
97. M. R. Ford
98. J. A. Gabbard
99. W. R. Garrett
100. J. H. Gillette
101. L. W. Gilley
102. E. D. Gupton
103. R. N. Hamm
104. C. S. Harrill
105. J. A. Harter
106. F. F. Haywood
107. A. Holleander
108. L. B. Holland
109. C. F. Holloway
110. A. S. Householder
111. H. H. Hubbell
112. D. R. Johnson
113. L. C. Johnson
114. T. D. Jones
115. W. H. Jordan
116. M. A. Kastenbaum
117. M. T. Kelley
118. R. F. Kimball
119. C. E. Klots
120. C. E. Larson
121. T. A. Lincoln
122. R. S. Livingston
123. H. G. MacPherson
124. F. C. Maienschein
125. W. J. McConnell
126. A. J. Miller
127. K. Z. Morgan
128. D. J. Nelson
129. D. R. Nelson
130. J. Neufeld
131. J. S. Olson
132. F. L. Parker
133–134. R. B. Parker
135. G. R. Patterson, Jr.
136. R. W. Peelle
137. J. W. Poston
138. H. P. Raaen
139. M. L. Randolph
140. D. E. Reichle
141. P. W. Reinhardt
142. R. M. Richardson
143. R. H. Ritchie
144. E. M. Robinson
145. G. W. Royster, Jr.
146. T. Saigusa
147. H. C. Schweinler
148. H. E. Seagren
149. M. J. Skinner

150. W. S. Snyder
151. J. A. Stockdale
152. E. G. Struxness
153. N. E. Tarr
154. E. H. Taylor
155. J. L. Thompson
156. J. H. Thorngate
157. J. E. Turner
158. A. C. Upton
159. E. B. Wagner
160. A. D. Warden
161. A. M. Weinberg
162. G. C. Williams
163. J. P. Witherspoon
164. Harvel Wright
165. E. K. Yeargers
166. G. Young
167. John E. Cantlon (consultant)
168. John C. Frye (consultant)
169. John B. Hursh (consultant)
170. John L. Magee (consultant)
171. Harold O. Wyckoff (consultant)
172. J. B. Birks (consultant)
173. M. D. Brown (consultant)
174. L. W. Cochran (consultant)
175. Charles Eisenhauer (consultant)
176. Ugo Fano (consultant)
177. Kenneth Fox (consultant)
178. R. E. Glick (consultant)
179. Mary P. Haydon (consultant)
180. W. T. Ham, Jr. (consultant)
181. R. J. Lovell (consultant)
182. R. A. Mac Rae (consultant)
183. R. J. Morton (consultant)
184. J. E. Parks (consultant)
185. T. D. Strickler (consultant)
186. G. E. Thoma (consultant)
187. I. H. Tipton (consultant)
188. G. M. Van Dyne (consultant)
189. Neil Wald (consultant)
190. Donald G. Willhoit (consultant)
191. M. R. Williams (consultant)

EXTERNAL DISTRIBUTION

192–337. Given external distribution
338. Radiation Physics Division, Health and Safety Laboratory, New York Operations, U.S. Atomic Energy Commission
339. Physics Library, Vanderbilt University, Nashville, Tennessee
340. W. W. Grigorieff, Assistant to the Director, Oak Ridge Associated Universities
341. J. A. Swartout, Union Carbide Corporation, New York, N.Y.
342. Laboratory and University Division, AEC, ORO
343–674. Given distribution as shown in TID-4500 under Health and Safety category (25 copies – CFSTI)